NUNC COGNOSCO EX PARTE

TRENT UNIVERSITY
LIBRARY

Digitized by the Internet Archive
in 2019 with funding from
Kahle/Austin Foundation

https://archive.org/details/advancesinchemic0010unse

MOLECULAR BEAMS

ADVANCES IN CHEMICAL PHYSICS

VOLUME X

ADVANCES IN CHEMICAL PHYSICS

EDITOR: I. Prigogine

Faculté des Sciences, Université Libre de Bruxelles, Brussels, Belgium

EDITORIAL BOARD

THOR A. BAK, Universitetets Fysik Kemiske Institut, Copenhagen, Denmark

J. DUCHESNE, University of Liège, Liège, Belgium

H. C. LONGUETT-HIGGINS, The University Chemical Laboratory, Cambridge, England

M. MANDEL, University of Leiden, Leiden, Holland

V. MATHOT, Université Libre de Bruxelles, Brussels, Belgium

P. MAZUR, Institut Lorentz, Leiden, Holland

A. MÜNSTER, Laboratoire de Chimie Physique, Université de Paris, Paris, France

S. ONO, Institute of Physics, College of General Education, Tokyo, Japan

B. PULLMAN, Laboratoire de Chimie Théorique, Université de Paris, Paris, France

S. RICE, Institute for the Study of Metals, University of Chicago, Chicago, Illinois

J. W. STOUT, Institute for the Study of Metals, University of Chicago, Chicago, Illinois

G. SZASZ, General Electric Company, Zürich, Switzerland

M. V. VOLKENSTEIN, Institute of Macromolecular Chemistry, Leningrad, U.S.S.R.

B. H. ZIMM, School of Science and Engineering, University of California at San Diego, La Jolla, California

MOLECULAR BEAMS

Edited by JOHN ROSS

Brown University, Providence, Rhode Island

INTERSCIENCE PUBLISHERS
a division of John Wiley & Sons, New York - London - Sydney

QD453 .A27 v.10 1966

Copyright © 1966 by John Wiley & Sons, Inc.

All Rights Reserved

Library of Congress Catalog Card Number 58-9935

PRINTED IN THE UNITED STATES OF AMERICA

AUTHORS

I. Amdur, Department of Chemistry, Massachusetts Institute of Technology, Cambridge, Massachusetts

James B. Anderson, Mechanical Engineering Department, Princeton University, Princeton, New Jersey

Ronald P. Andres, Mechanical Engineering Department, Princeton University, Princeton, New Jersey

Benjamin Bederson, Physics Department, New York University, New York, New York

Richard B. Bernstein, Theoretical Chemistry Institute and Chemistry Department, University of Wisconsin, Madison, Wisconsin

John B. Fenn, Mechanical Engineering Department, Princeton University, Princeton, New Jersey

Clayton Giese, Department of Physics, The University of Chicago, Chicago, Illinois

E. F. Greene, Metcalf Chemical Laboratories, Brown University, Providence, Rhode Island

Dudley Herschbach, Department of Chemistry, University of California, Berkeley, California

J. E. Jordan, Department of Chemistry, Massachusetts Institute of Technology, Cambridge, Massachusetts

A. L. Moursund, Metcalf Chemical Laboratories, Brown University, Providence, Rhode Island

E. E. Muschlitz, Jr., Department of Chemistry, University of Florida, Gainesville, Florida

Edward J. Robinson, Physics Department, New York University, New York, New York

John Ross, Department of Chemistry, Brown University, Providence, Rhode Island

R. F. Stebbings, General Atomic Division of General Dynamics Corporation, San Diego, California

61264

PREFACE

Studies of molecules in nearly collision-free and unidirectional motion, that is, in molecular beams, have been made for over fifty years. The technique has long been recognized as particularly suitable for the determination of the interaction of a single molecule with another molecule, with a photon, with external fields, or with surfaces. (See the Appendix for some general references.) In principle, at least, molecular beam experiments provide the means for direct measurements of molecular properties. Of course, the properties of macroscopic systems are related to those of their molecular constituents by the theories of statistical mechanics. These relations are always some statistical average of molecular properties, an average which obscures the dependence of the macroscopic measurement on the molecular properties. In practice the removal of all statistical averages even in molecular beam experiments presents extreme problems.

The articles in this volume are reviews of some of the current molecular beam research in the general area of chemical physics. Interest in such experiments has increased sharply in the last ten years, especially among chemical kineticists. The predominant, common theme throughout the volume is molecular interactions.

Elastic scattering is discussed in two articles, one reviewing high-energy scattering and repulsive forces, the other low-energy scattering and a number of quantum-mechanical effects for which both attractive and repulsive forms are of importance. Reactive scattering is the topic of four articles, two on neutral reactions and two on ionic reactions. Information on chemical reactions may be obtained by molecular beam measurements on the scattered chemical product or from the study of elastic scattering in reactive systems. Both methods are reviewed. Ion–molecule and charge-transfer reactions are also discussed in separate articles. The remaining sections of the volume are devoted to inelastic scattering of metastable atoms, the determination of atomic polarizabilities, and the technique of hypersonic beams.

The articles are representative of current molecular beam research in chemical physics, but the selection is by no means complete. For

instance, reviews on nonreactive inelastic scattering, on the use of beams as a technique for molecular resonance spectroscopy, and on the interactions of molecules with surfaces are among the omissions.

I wish to thank my colleague Professor E. F. Greene for much help and advice in editing this volume and Dr. G. P. Flynn for compiling the subject index.

JOHN ROSS

CONTENTS

1. **Beam Measurements of Atomic Polarizabilities**
   By Benjamin Bederson and Edward J. Robinson . . . 1
2. **Elastic Scattering of High-Energy Beams: Repulsive Forces**
   By I. Amdur and J. E. Jordan 29
3. **Quantum Effects in Elastic Molecular Scattering**
   By Richard B. Bernstein 75
4. **Elastic Scattering in Chemically Reactive Systems**
   By E. F. Greene, A. L. Moursund, and J. Ross . . . 135
5. **Collisions of Electronically Excited Atoms and Molecules**
   By E. E. Muschlitz, Jr. 171
6. **Charge Transfer**
   By R. F. Stebbings 195
7. **Ion–Neutral Reactions**
   By C. F. Giese 247
8. **Supersonic Nozzle Beams**
   By J. B. Anderson, R. P. Andres, and J. B. Fenn . . . 275
9. **Reactive Scattering in Molecular Beams**
   By D. R. Herschbach 319

Appendix. Selected References on Molecular Beam Research . . 395

Author Index 397

Subject Index 411

1. BEAM MEASUREMENTS OF ATOMIC POLARIZABILITIES*

BENJAMIN BEDERSON and EDWARD J. ROBINSON

Physics Department, New York University, New York

CONTENTS

I. Introduction 1
II. Theory 2
III. Methods of Calculating Polarizabilities 6
IV. Atomic Beam Experiments 9
A. Alkali Measurements 9
B. Measurements of Metastable $^3P_2$ Argon 20
V. Conclusion 25
References 26

I. INTRODUCTION

Polarizability is a seemingly ubiquitous atomic property which appears as a parameter in the description of many important atomic processes. The calculation of the van der Waals interaction, the description of charge transfer and other ion–atom and electron–atom collision processes, of optical lifetimes, and of optical dispersion all directly involve or are related to the static polarizabilities of ground and excited states of neutral atoms and molecules. In a general sense one can expect that the atomic polarizability will be a useful parameter when dealing with any atomic process in which the outer part of the electronic wave function plays an important role. Direct experimental determinations of atomic polarizabilities provide a very sensitive check on the accuracy of electronic wave functions, where these are

* Some of the work described in this article was supported by the Advanced Research Projects Agency, through the Office of Naval Research, Washington, D.C., under Contract No. NONR-285(60), and by the Defense Atomic Support Agency, through the Army Research Office, Durham, N.C., under Contract No. DA-ARO-D-31-124-G530.

available. In addition, since the approximation methods used in calculating quadrupole shielding factors can also be used to calculate polarizabilities,[1] comparison of such calculations with experiment provides an independent check on these methods, and is therefore helpful in providing more reliable values of nuclear quadrupole moments.

Atomic beam methods would appear to be eminently suited to measuring polarizabilities, because of the absence of particle–particle interactions. Yet, there have been only a few such experiments in recent years, notably the deflection experiments of Chamberlain and Zorn[1] at Yale, and the balance experiments[2-4] by the N.Y.U. group. (The earlier work of Scheffers and Stark[5] is primarily of historic interest.) Our purpose in this article is to discuss these experiments in some detail, and also to briefly describe some of the principal methods by which atomic polarizabilities have been calculated in recent years.

II. THEORY

The energy of an atom in an external field is readily calculable from perturbation theory, provided one has means of estimating the relevant matrix elements. Let an unperturbed atom have a Hamiltonian $\mathscr{H}_0$ with energy $\mathscr{E}_0$. In the presence of an electric field E, the Hamiltonian becomes $\mathscr{H}_0 + \mathscr{H}'$. The perturbation $\mathscr{H}' = -\boldsymbol{\mu}_e \cdot \mathbf{E}$, where the electric dipole operator

$$\boldsymbol{\mu}_e = -\sum_i e\mathbf{r}_i$$

with $\mathbf{r}_i$ the position vector of the ith electron. The first-order perturbation energy is

$$\mathscr{E}_1 = \langle 0|\mathscr{H}'|0\rangle = \langle 0|\boldsymbol{\mu}_e \cdot \mathbf{E}|0\rangle \tag{1}$$

where $|0\rangle$ is the unperturbed state vector. Since $\mathscr{H}'$ is an operator of odd parity, the matrix element in Eq. (1) will vanish if $|0\rangle$ has a definite parity. That is, states of definite parity have zero permanent dipole moments.

The second-order perturbation energy $\mathscr{E}_2$ is given by a summation containing matrix elements of $\boldsymbol{\mu}_e$ between $|0\rangle$ and other states $|k\rangle$ of the form

$$\mathscr{E}_2 = -\sum_{k\neq 0} \frac{\langle 0|\boldsymbol{\mu}_e \cdot \mathbf{E}|k\rangle\langle k|\boldsymbol{\mu}_e \cdot \mathbf{E}|0\rangle}{\mathscr{E}_k - \mathscr{E}_0} \tag{2}$$

The denominator $\mathscr{E}_k - \mathscr{E}_0$ is the energy difference between $|k\rangle$ and $|0\rangle$. Alternatively, if $\hat{n}$ is a unit vector in the direction of $\mathbf{E}$,

$$\mathscr{E}_2 = -E^2 \sum_{k\neq 0} \frac{\langle 0|\boldsymbol{\mu}_e\cdot\hat{n}|k\rangle\langle k|\boldsymbol{\mu}_e\cdot\hat{n}|0\rangle}{\mathscr{E}_k - \mathscr{E}_0} \tag{3}$$

The summation in Eq. (3) may be written explicitly in terms of the rectangular components μ_x, μ_y, μ_z, of $\boldsymbol{\mu}_e$ and a, b, c of $\hat{n}$ as follows,

$$\mathscr{E}_2 = -E^2 \sum_{k\neq 0} \left[\frac{a^2|\langle 0|\boldsymbol{\mu}_x|k\rangle|^2}{\mathscr{E}_k - \mathscr{E}_0} + \frac{b^2|\langle 0|\boldsymbol{\mu}_y|k\rangle|^2}{\mathscr{E}_k - \mathscr{E}_0} + \frac{c^2|\langle 0|\boldsymbol{\mu}_z|k\rangle|^2}{\mathscr{E}_k - \mathscr{E}_0} + \frac{ab\langle 0|\boldsymbol{\mu}_x|k\rangle\langle k|\boldsymbol{\mu}_y|0\rangle}{\mathscr{E}_k - \mathscr{E}_0} + \cdots \right] \tag{4}$$

The polarizability tensor is defined by the relation

$$\mathscr{E}_2 = -\tfrac{1}{2}\mathbf{E}\cdot\alpha\mathbf{E} \tag{5}$$

By comparing Eqs. (4) and (5) it is seen that the (symmetric) tensor components α_{xy}, etc. are given by the relation

$$\alpha_{xy} = 2 \sum_{k\neq 0} \mathscr{R} \frac{\{\langle 0|\boldsymbol{\mu}_x|k\rangle\langle k|\boldsymbol{\mu}_y|0\rangle\}}{\mathscr{E}_k - \mathscr{E}_0} \tag{6}$$

etc., where $\mathscr{R}$ signifies "real part."

If the electric field direction coincides with the axis of symmetry of the atom, then M_J is a good quantum number, the off-diagonal components of α vanish, and the tensor components α_{xx} and α_{yy} (hereafter designated α_x and α_y) are equal. The discussion will be restricted to this case. (It is further assumed that the permanent dipole moment vanishes.) There are then at most two different components of α in each magnetic substate M_J. If use is made of the fact that $\boldsymbol{\mu}_e$ is a so-called $\mathbf{T}$ operator,[6] one whose components satisfy the same commutation rules with the components J_x, J_y, and J_z of the total angular momentum $\mathbf{J}$ as do J_x, J_y, and J_z themselves, the tensor components in the various magnetic substates, $\alpha_x(M_J)$ and $\alpha_z(M_J)$ become

$$\alpha_x(M_J) = A(J^2 + M_J^2 - J) + B(J^2 + J - M_J^2) + C(J^2 + 3J + 2 + M_J^2) \tag{7a}$$

$$\alpha_z(M_J) = 2A(J^2 - M_J^2) + 2BM_J^2 + 2C(J^2 + 2J + 1 - M_J^2) \tag{7b}$$

where

$$A = \left(\sum_{k\neq 0} \frac{|\langle 0|\mu_e|k\rangle|^2}{\mathscr{E}_k - \mathscr{E}_0}\right)\delta_{J-1,J'}, \qquad B = \left(\sum_{k\neq 0} \frac{|\langle 0|\mu_e|k\rangle|^2}{\mathscr{E}_k - \mathscr{E}_0}\right)\delta_{JJ'},$$

$$C = \left(\sum_{k\neq 0} \frac{|\langle 0|\mu_e|k\rangle|^2}{\mathscr{E}_k - \mathscr{E}_0}\right)\delta_{J+1,J'},$$

where μ_e is the absolute value of $\boldsymbol{\mu}_e$, and where J, J' are the total angular momentum quantum numbers of $|0\rangle$ and $|k\rangle$, respectively. The average polarizability, $\bar{\alpha}$, is defined as the average of either α_x or α_z over the magnetic substates. In terms of A, B, and C, $\bar{\alpha}$ is

$$\bar{\alpha} = \tfrac{2}{3}[AJ(2J-1) + BJ(J+1) + C(2J+3)(J+1)] \tag{8}$$

We now show that of the $2(2J+1)$ equations represented by Eq. (7), no more than two are independent. The difference between any two tensor components is a simple multiple of $(A - B + C)$:

$$\begin{aligned}
\alpha_z(M_J) - \alpha_z(M'_J) &= 2(M'^2_J - M^2_J)(A - B + C)\\
\alpha_x(M_J) - \alpha_x(M'_J) &= (M^2_J - M'^2_J)(A - B + C)\\
\alpha_z(M_J) - \alpha_x(M'_J) &= (J^2 + J - 2M^2_J - M'^2_J)(A - B + C)
\end{aligned} \tag{9}$$

It follows from Eqs. (9) that once two independent tensor components are known, all components of all the magnetic substates are determined. It is also easily seen that all the components are equal if $J < 1$, i.e., for atoms with $J \leqslant \frac{1}{2}$ the polarizability is scalar.

The matrix elements of $\boldsymbol{\mu}_e$ are often expressed in terms of the dimensionless oscillator strengths, f_{0k}, which are defined as

$$f_{0k} = \tfrac{2}{3}\,\frac{m(\mathscr{E}_k - \mathscr{E}_0)}{e^2\hbar_2}\,|\langle 0|\mu_e|k\rangle|^2\eta(J, J') \tag{10}$$

where

$$\eta(J, J+1) = (J+1)(2J+3),\ \eta(J, J) = J(J+1),\ \eta(J, J-1) = J(2J-1),$$

and e and m are the electronic charge and mass, respectively. The average polarizability in terms of the oscillator strengths is

$$\bar{\alpha} = \frac{e^2\hbar^2}{m}\sum_{k\neq 0}\frac{f_{0k}}{(\mathscr{E}_k - \mathscr{E}_0)^2} \tag{11}$$

The oscillator strengths satisfy a simple sum rule,

$$\sum f_{0k} = N \tag{12}$$

where N is the total number of electrons in the atom. The summation of Eq. (12) includes oscillator strengths to all possible states of all degrees of ionization and excitation of the atom. A situation that frequently occurs is one in which only oscillator strengths associated with the "first spectrum" of the atom make appreciable contributions to the polarizability. In particular, very often only those transitions which can be represented by the motion of a single electron make appreciable contributions to the polarizability. Under those circumstances there is only one "effective" electron and Eq. (12) becomes, approximately,

$$\sum_k f_{0k} = 1 \tag{13}$$

Eq. (13) is useful in that it sets an approximate upper bound to $\bar{\alpha}$,

$$\bar{\alpha} \leqslant \frac{e^2\hbar^2}{m} \frac{1}{(\mathscr{E}_1 - \mathscr{E}_0)^2} \tag{14}$$

where $\mathscr{E}_1$ is the energy of the state closest in energy to the unperturbed state whose $f_{0k} \neq 0$. If it is known that almost the entire oscillator strength summation arises from a very small number of transitions, and these f_{0k} are known or can be estimated, then the average polarizability can be determined very simply and with some accuracy. (See, for example, Dalgarno and Kingston's calculation of alkali polarizabilities.[7])

The quantity

$$\alpha_z(M_J) - \alpha_x(M_J) = (J^2 + J - 3M_J^2)(A - B + C)$$

is a measure of the polarizability anisotropy, and is zero if $J \leqslant \frac{1}{2}$. It is indirectly related to the atomic quadrupole moment Q defined as

$$Q = e\langle 3z^2 - r^2 \rangle = 2e\langle z^2 - x^2 \rangle \tag{15}$$

with $|M_J| = J$. Eq. (15) can be rewritten as

$$Q = 2e(\langle 0|z^2|0\rangle - \langle 0|x^2|0\rangle),$$

or

$$eQ = 2[\sum_{k\neq 0} |\langle 0|\mu_z|k\rangle|^2 - \sum_{k\neq 0} |\langle 0|\mu_x|k\rangle|^2]$$

Following the procedure leading to Eq. (7), eQ can be expressed in terms of reduced matrix elements as

$$eQ = (-2J^2 + J)(A' - B' + C') \tag{16}$$

where

$$A' = (\sum_{k \neq 0} |\langle 0|\mu_e|k\rangle|^2)\delta_{J-1,\,J'}$$

$$B' = (\sum_{k \neq 0} |\langle 0|\mu_e|k\rangle|^2)\delta_{J,\,J'}$$

$$C' = (\sum_{k \neq 0} |\langle 0|\mu_e|k\rangle|^2)\delta_{J+1,\,J'}.$$

Thus, the polarizability anisotropy and the atomic quadrupole moment differ only in the energy denominators of the sum over dipole matrix elements.

III. METHODS OF CALCULATING POLARIZABILITIES

The polarizability can be calculated, in principle, without evaluating the summation in Eq. (6). Let $|F\rangle$ be the first-order correction to the unperturbed wave function. The wave equation for $|F\rangle$ is then

$$(\mathscr{H}_0 - \mathscr{E}_0)|F\rangle = -\mathscr{H}'|0\rangle \tag{17}$$

If Eq. (17) can be solved for $|F\rangle$, the second-order energy equivalent to Eq. (2) is

$$\mathscr{E}_2 = \langle F|\mathscr{H}'|0\rangle \tag{18}$$

Eqs. (17) and (18) serve as the starting point for all approximate perturbation calculations of the polarizability.

The simplest procedure is to assume that $|0\rangle$ can be represented by a product of one-electron wave functions, (Hartree approximation) and to apply Eq. (17) separately to each orbital. The total polarizability is then the sum of the polarizabilities of the individual one-electron wave functions. This approach neglects exchange and the mutual effect of the induced dipole moments on each other, (i.e., "screening"), but is applicable to systems of any number of electrons. The amount of labor required is simply proportional to the number of orbitals.

The one-electron wave functions are considered to be derivable from a central potential V_{0i}, with eigenvalues $\mathscr{E}_{0i}$, so that they may be written as products of functions of the radial coordinates of the electrons and spherical harmonics. Following Sternheimer, the equation for the radial part of each unperturbed wave function, $P_i(r)$, has the form (in Rydberg units)

$$-\frac{d^2P_i}{dr_i^2} + \frac{\lambda_i(\lambda_i+1)P_i}{r_i^2} + (V_{0i} - \mathscr{E}_{0i})P_i = 0 \tag{19}$$

When the perturbation is turned on, the one-electron form of Eq. (17) separates into two radial parts, P_{i+} and P_{i-} by virtue of the properties of the associated Legendre polynomials. P_{i+} has the angular dependence corresponding to an orbital angular momentum $\lambda_i + 1$ and P_{i-} the angular dependence of orbital angular momentum $\lambda_i - 1$. The equations for $P_{i\pm}$, for unit electric field are

$$-\frac{d^2P_{i\pm}}{dr^2} + \frac{(\lambda_i \pm 1)(\lambda_i + 1 \pm 1)P_{i\pm}}{r_i^2} + (V_{0i} - \mathscr{E}_{0i})P_{i\pm} = rP_i \qquad (20)$$

Eq. (20) is solved numerically for all the orbitals in the configuration, and the polarizability evaluated.

Sternheimer[8] employs the most accurate orbitals available for specific cases, be they Hartree, Hartree-Fock, or whatever. The errors arising from transitions between occupied orbitals tend to cancel out, in the average polarizabilities, and the unperturbed potential is evaluated by using the unperturbed equation, Eq. (19).*

The perturbation method can be extended to a formalism which includes electron exchange (Hartree-Fock approximation) and to one in which the effects of the induced dipoles on one another are also considered (coupled Hartree-Fock approximation). The calculations, however, become exceedingly involved, especially in the coupled approximation, as the number of electrons is increased. The reader is referred to the review article by Dalgarno for a discussion of these methods.[9]

The variational principle can also be used to calculate polarizabilities.[10] The first application of the variational method to this problem was by Kirkwood,[11] whose work was subsequently extended by Buckingham.[12] Let $|0\rangle$ be the exact eigenfunction of the unperturbed problem, and $|v\rangle$ a trial correction to $|0\rangle$. The unperturbed energy is

$$\mathscr{E}_0 = \langle 0|\mathscr{H}_0|0\rangle \qquad (21)$$

* If the central fields for each orbital were exactly the same, the unphysical contributions to the average polarizability due to transitions would exactly cancel. Since the central fields are different for each orbital, this cancellation is only partial. In any event, large errors would be introduced in calculating the anisotropy, since the cancellation will not occur in particular substates, particularly where the anisotropy is due to spurious negative contributions.

If the usual assumptions concerning parity are made, the first-order energy vanishes, and the Rayleigh-Ritz principle gives

$$\mathscr{E}_0 + \mathscr{E}_2 \leqslant \frac{\langle 0'|\mathscr{H}_0 + \mathscr{H}'|0'\rangle}{\langle 0'|0'\rangle} \tag{22}$$

The second-order energy can be expressed by taking the difference between Eqs. (21) and (22),

$$\mathscr{E}_2 \leqslant \frac{\langle 0'|\mathscr{H}_0 + \mathscr{H}'|0'\rangle}{\langle 0'|0'\rangle} - \langle 0|\mathscr{H}_0|0\rangle \tag{23}$$

(Note that if the solution used for the unperturbed problem is not exact, the equal sign in (21) must be replaced by "less than or equal," so that the subtractions used to obtain Eq. (23) can introduce spurious terms.) Small terms in Eq. (23) are neglected, and a trial correction chosen. Buckingham assumes a correction whose orbitals are obtained by multiplying the unperturbed orbitals by $\gamma_i r_i \cos\theta$, where γ_i is an adjustable parameter. (Kirkwood assumed the same adjustable parameter for each orbital.) The γ_i are varied to minimize the energy, and the lower bound for the polarizability (taken to be a scalar) is found to be

$$\alpha \geqslant \tfrac{4}{9} \sum_{l=1}^{n} \{r_l^2 - \sum_{i \neq j} |\mathbf{r}_{ij}|^2\}^2 \tag{24}$$

(The subscripts refer to orbitals, and not electrons.) More involved variational trial functions have been used, and these are discussed by Dalgarno.[9]

All the approximate methods of polarizability calculation are strongly dependent on the form of the approximate unperturbed wave function. In general, these are calculated without including the effects of coulomb correlations on the positions of the electrons, and give wave functions which are too external, resulting in polarizability values which are too large. In fact, it often occurs that the "lower bound," Eq. (24), gives a calculated polarizability greater than the experimental value. The implication is that the more elaborate variational methods, which would raise the lower bound, will be of no great value until more accurate unperturbed wave functions are available.

Sternheimer's[13] treatment of alkali polarizabilities is an interesting case of a calculation (using the perturbation methods described earlier)

which employs unperturbed wave functions for which correlation effects have been taken into account in some approximate manner. The value obtained for sodium with this wave function is 25% lower than that obtained from Hartree-Fock orbitals. Sternheimer has included both the effect of the valence electron and the contribution of the core to the total dipole polarizability. The core contribution involves a calculation of the electric field at the nucleus due to the dipole moment induced in the valence electron charge distribution by the external electric field. Thus, "screening" was approximately taken into account.

IV. ATOMIC BEAM EXPERIMENTS

A. Alkali Measurements

Three related atomic beam methods have been employed in atomic polarizability measurements, namely, "strong field" deflection, "weak field" deflection, and E–H gradient balance. Strong field deflection was first used by Scheffers and Stark[5] in the 1930's to measure the polarizabilities of lithium, potassium, and cesium. An electric field gradient is established transverse to the direction of motion of the atomic beam, and the polarizability is obtained from an analysis of the resulting deflected beam pattern. This deflection pattern is the same as that due to a single magnetic substate in a conventional Stern-Gerlach experiment, except that the transverse magnetic force $\mu_{\text{eff}}(\delta H/\delta z)$ is replaced by the transverse electric force $\alpha E(\delta E/\delta z)$, if the polarizability is scalar. The essential elements of this deflection analysis will be presented here.

A typical deflection experiment geometry is shown in Figure 1. Note that a collimating slit is placed after the field region. If one assumes

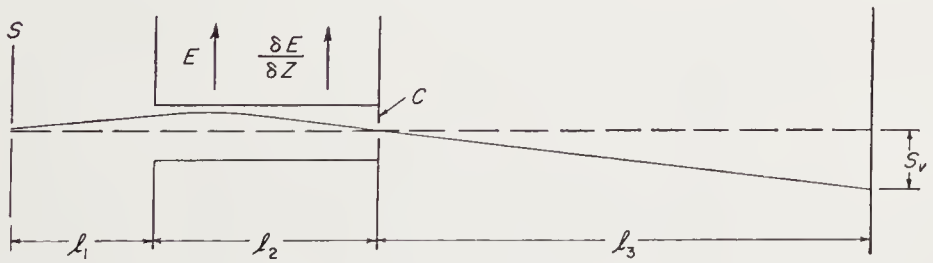

Fig. 1. Electric deflection experimental arrangement. S is atomic beam source, C is collimator placed after deflecting field. S_V is the net atomic deflection in the plane of the detector.

that both the source and collimator widths are negligibly small, then an atom with speed v will be deflected in the plane of the detector by an amount

$$S_v = \frac{F}{2mv^2} l_2(l_2 + 2l_1) \frac{l_3}{l_1 + l_2} \tag{25}$$

where F is the transverse force, and the lengths l_1, l_2, l_3 are defined in Figure 1. The deflection S_B of an atom possessing the most probable oven speed V_B is

$$S_B = \frac{F}{4kT} l_2(l_2 + 2l_1) \frac{l_3}{l_1 + l_2} \tag{26}$$

where $V_B = \sqrt{2kT/M}$ and M is the atomic mass. The beam is assumed to possess the modified Maxwellian distribution

$$I_0(v)dv = \frac{2I_0 v^3 \exp(-v^2/v_B^2)}{v_B^4} \tag{27}$$

Figure 2 shows an undeflected beam intensity pattern $I(s_0)$ in the plane of the detector, as well as a deflected beam intensity pattern $I(s)$. The quantity $I(s)$ can be calculated by integrating the contributions from all elements ds_0 of $I(s_0)$ to the left of s in Figure 2, assuming that

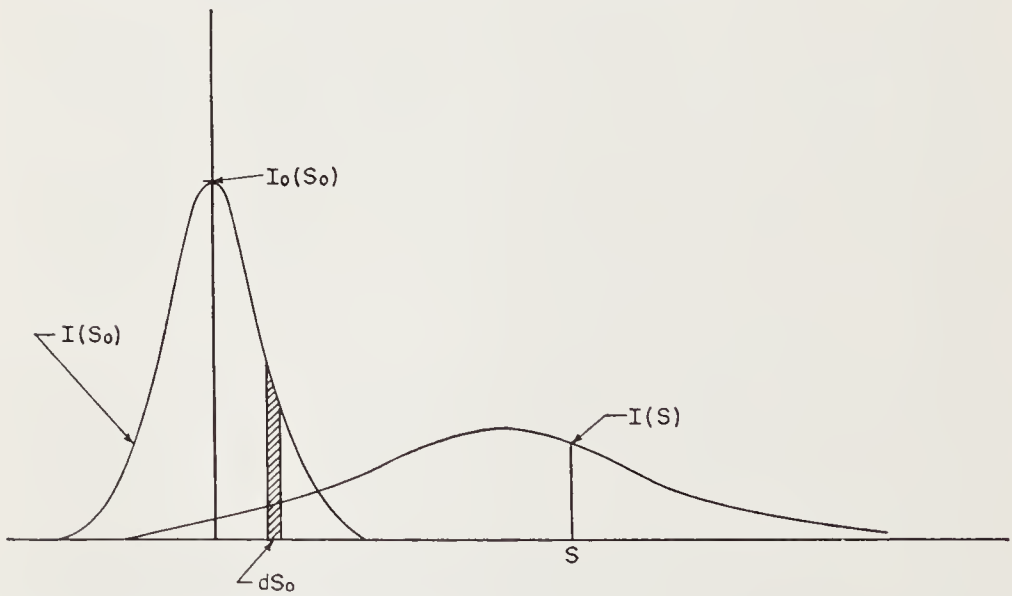

Fig. 2. Idealized undeflected and deflected beam intensity patterns in the plane of the detector, $I(s_0)$ and $I(s)$, respectively.

s_B is positive. Using Eq. (27) to obtain the fractional number of particles in ds_0 which will arrive at s, this integral is

$$I(s) = \int_{-\infty}^{s} \frac{I(s_0)s_B^2}{(s - s_0)^3} \cdot \exp[-s_B/(s - s_0)]ds_0 \tag{28}$$

Kusch and Hughes[14] evaluate Eq. (28) for a rectangular beam shape. If one assumes a trapezoidal beam shape, Eq. (28) yields the rather complicated expression

$$I(s) = \frac{I_0}{d - p}(A) \qquad -d < s < -p \tag{29a}$$

$$I(s) = \frac{I_0}{d - p}(A + B) \qquad -p < s < p \tag{29b}$$

$$I(s) = \frac{I_0}{d - p}(A + B + C) \qquad p < s < d \tag{29c}$$

$$I(s) = \frac{I_0}{d - p}(A + B + C + D) \qquad d < s \tag{29d}$$

where

$$A = (s + d) \exp[-s_B/(s + d)]$$

$$B = -(s + p) \exp[-s_B/(s + p)]$$

$$C = (p - s) \exp[-s_B/(s - p)]$$

$$D = (s - d) \exp[-s_B/(s - d)]$$

and the quantities I_0, d, and p are defined in Figure 3. The designation "strong field" means that s_B is comparable to the beam width, so that no simplification can be made in applying Eqs. (29) when analyzing the deflected beam shape.

An actual experimental beam shape is, of course, a smoothly varying function of position, but it can often be approximated by a best-fitting trapezoid. Trial values of s_B are then inserted into Eqs. (29), to obtain the best fit to the experimentally determined deflected beam shape. The polarizability is then calculated using Eq. (26).

Because of the need for accurate knowledge of various apparatus parameters, including values of both E and the gradient of E at the beam position, and also because of the assumption of a perfect Maxwellian distribution, it is difficult to obtain reliable results by this method.

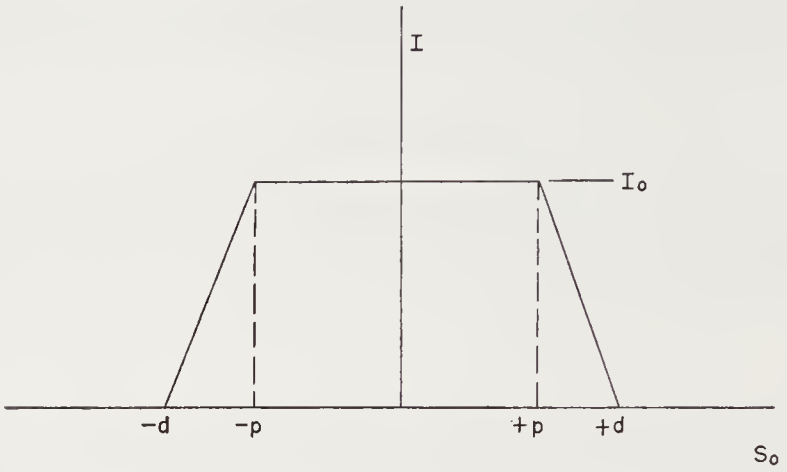

Fig. 3. Geometry parameters for a rectangular beam.

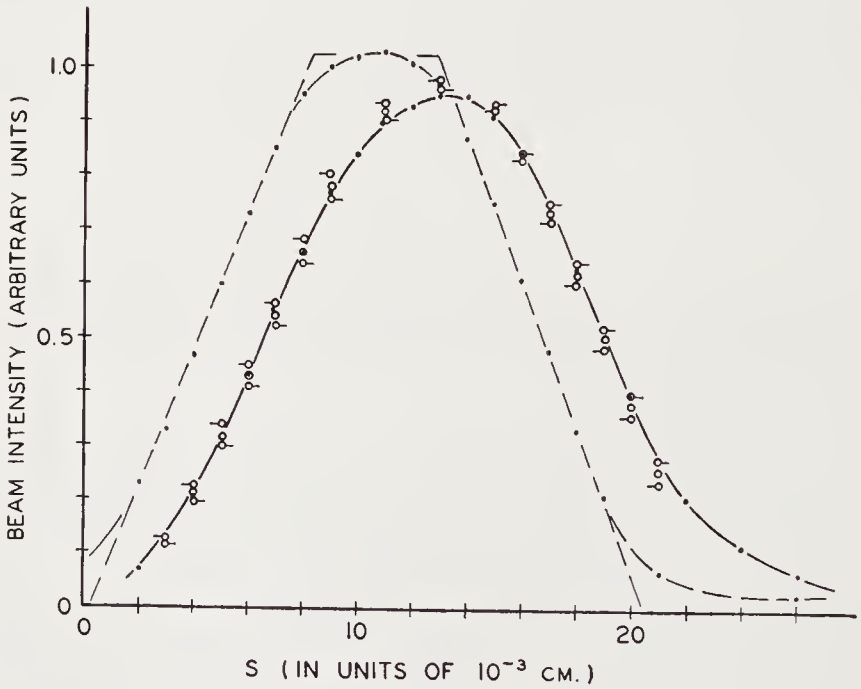

Fig. 4. Undeflected and deflected beam intensity patterns for "strong field" case, for potassium (Chamberlain and Zorn). Calculated points for these values of s_B are represented by o–, o, and –o.

In the Scheffers and Stark experiment, concentric cylinders were used to establish the electric field gradient. Because the beam was rectangular in cross section, the gradient varied significantly over its height, causing additional uncertainty in the measurements. Chamberlain and Zorn[1] used both the strong field and the weak field (described below) deflection methods to measure the polarizabilities of all of the alkalis. They used an equivalent two-wire field geometry of the type which is commonly employed in atomic beam magnetic resonance experiments.[15] This type of field possesses a gradient which is quite uniform along a line perpendicular to the field direction at a distance $1.2a$ from the center of one of the equivalent wires, where $2a$ is the distance between the wire centers. They took considerable care to ensure that the beam possessed an undistorted Maxwellian velocity distribution. Copper ovens were employed to eliminate temperature gradients, and careful shimming of the exit slits probably eliminated effects of local cooling.

Figure 4 shows a typical case of their undeflected and strong-field deflected beam shapes, for potassium. Calculated points for three values of s_B are also plotted, based on the use of Eq. (26). The undeflected beam shape was thus approximated by a trapezoid, while the finite width of the detector was not taken into account. Despite the many experimental uncertainties in this method, the Chamberlain and Zorn large shift determinations of the alkali polarizabilities yielded values in good agreement with other recent experimental and theoretical determinations (see Table I).

In the "weak field" deflection method, s_B is very small compared to the beam width. By expanding $I(s)$ in a Taylor's series about $I(s_0)$, it is easy to show, using Eq. (28), that

$$I(s) = I(s_0) - I'(s_0)s_B + \frac{I'(s_0)s_B w}{2} - \cdots \tag{30}$$

where w is the beam width. If a narrow detector is placed at a linear portion of $I(s_0)$—for example, at the position of half-intensity—the difference in beam intensity with and without an applied electric field is $\Delta I = I'(s_0)s_B$. This method is considerably more straightforward than the strong field method, since s_B is obtained simply from an intensity measurement and knowledge of the slope of the undeflected beam shape at the detector position.* A true Maxwellian distribution and

* This method was also employed[16] to obtain an upper limit on the electron–proton charge difference of five parts in 10^{19}.

TABLE I. Recent Experimental and Theoretical Values of Alkali Polarizabilities (in units of Å^3)

Investigators	Method	Li	Na	K	Rb	Cs
Salop, Pollack, and Bederson, 1961 (4)	*E–H* gradient balance atomic beam method	20 ± 3.0	20 ± 2.5	36.5 ± 4.5	40 ± 5.0	52.5 ± 6.5
Chamberlain and Zorn, 1963 (1)	Weighted average of small-shift and large-shift electrostatic atomic beam deflection method	22 ± 1.5	21.5 ± 1.5	38 ± 3	37.5 ± 3	48 ± 5.5
Bates and Damgaard, 1949 (22)	Calculations based upon f values deduced from calculations of line shapes by the Coulomb approximation	24	23	41	45	56
Dalgarno and Kingston, 1959 (7)	Calculations relying upon experimental and theoretical values of oscillator strengths	24.4 ± 1.2	24.6 ± 1.2	41.6 ± 2.1	43.8 ± 2.2	53.7 ± 5.4
Mizushima, 1958 (23)	Perturbation theory calculation of hfs Stark shift measurement of Haun and Zacharias					51
Sundbom, 1958 (24)	Numerical solution of perturbation equations	20				
Parkinson, 1960 (25)	Numerical solutions of perturbation equations	25				
Sternheimer, 1962 (13)	Sternheimer procedure with semi-empirical core correlation effects	24.9	22.9	44.4	49.1	67.7

accurate knowledge of the beam temperature are, of course, still required. The same geometry factors as in the strong field method must also be known in order to extract the polarizability from s_B. The results obtained by Chamberlain and Zorn by this technique are in good agreement with their large shift values, except for cesium, which is 20% lower. This discrepancy is possibly attributable to self-scattering of the slower beam particles, which would result in a deficiency of slow atoms and a correspondingly smaller value for s_B.

Electric deflection experiments have not as yet been performed using velocity-selected beams, although much of the uncertainty relating to difficulties with the velocity distribution would thereby be eliminated.

In the *E–H* gradient balance method,[2-4] an inhomogeneous magnetic field is established in the same region which contains the inhomogeneous electric field. For atoms possessing a magnetic moment, it is possible to cause the magnetic and electric forces to be equal and opposite for certain magnetic substates. The polarizability determination then reduces to a null experiment, so that geometry factors and the velocity distribution are no longer critical, and the experiment reduces essentially to the measurements of a voltage and a magnetic field. If a normalizing element is used, only the balance voltages need be determined, while the magnetic field is held fixed.

This method was first used by Salop et al.[3] to measure the polarizabilities of the alkalis. The tensor polarizabilities of $^3P_2$ metastable argon have also been measured.[4]* We now briefly review the principle of this method, first as applied to scalar, and, second, to tensor polarizabilities.

Consider an atom traversing a region of space containing both inhomogeneous transverse electric and magnetic fields. We assume that these fields are congruent, that is, the electric and magnetic fields as well as their gradients are proportional, and in the same direction throughout the interaction region. The magnitude of the transverse magnetic force is

$$F_{\text{mag}} = \mu(M_J) \left(\frac{\delta H}{\delta z}\right)$$

* Recently, similar measurements have been performed on $^3P_2$ metastable neon, krypton, and xenon (Robinson, Levine, and Bederson, *Bull. Am. Phys. Soc., Ser. II*, **9**, 90 (1964)).

where $\mu(M_J)$ is the effective magnetic moment of the atom in the magnetic substate M_J, and $\delta H/\delta z$ is the transverse component of the gradient of the magnitude of the magnetic field. The magnitude of the transverse electric force is

$$F_e = \alpha E(\delta E/\delta z)$$

if α is a scalar. Now, the induced electric force, which arises from the dielectric nature of the atomic system, is always directed toward stronger E, while the direction of the magnetic force depends upon the sign of the effective magnetic moment. If the effective magnetic moment is negative,* F_{mag} will be directed toward weaker field. Thus, for such states, it is possible to achieve the balance condition

$$\alpha E \frac{\delta E}{\delta z} = \mu(M_J) \frac{\delta H}{\delta z} \tag{31}$$

In the field region, $\delta E/\delta z = CE$ and $\delta H/\delta z = CH$, where C is a geometry factor which is the same for both fields, because of the assumed E–H congruence. Using these relations in Eq. (31), we obtain

$$\alpha = \mu_{\text{eff}} H/E^2 \tag{32}$$

for a particular magnetic substate, when the E–H gradient balance prevails. Since μ_{eff} is generally an accurately known function of H, the determination of α only requires the measurement of E and H at the balance condition. Thus, the method is independent of the velocity distribution in the beam and the specific values of the field gradients and the apparatus geometry, except where it enters into the calculation of the electric field. Further, it is not necessary to assume the validity of first-order deflection theory (e.g., the use of Eqs. (29)), which introduces a systematic error in the determination of α whose sense and magnitude are very difficult to determine.

* If the energy of the atom in the magnetic field is $\mathscr{E}_{\text{mag}}$, the transverse component of the magnetic force is

$$(F_z)_{\text{mag}} = -\frac{\delta \mathscr{E}_{\text{mag}}}{\delta z} = -\frac{\delta \mathscr{E}_{\text{mag}}}{\delta H}\frac{\delta H}{\delta z}$$

where H is the magnitude of the magnetic field. By definition $-\delta \mathscr{E}_{\text{mag}}/\delta H$ is μ_{eff}, the effective magnetic moment, so that $(F_z)_{\text{mag}} = \mu_{\text{eff}}(\delta H/\delta z)$. Similarly, if the electric energy $\mathscr{E}_{\text{elect}} = -\frac{1}{2}\alpha_z E^2$, the transverse component of the electric force $(F_z)_{\text{elect}} = -\delta \mathscr{E}_{\text{elect}}/\delta z = \alpha_z E\ (\delta E/\delta z)$. Thus the direction of $(F_z)_{\text{elect}}$ and $(F_z)_{\text{mag}}$ can be opposite only when μ_{eff} is negative.

In order to ensure congruency, the electrodes were machined of high permeability soft iron, and also acted as the pole faces of the magnet. If saturation of the iron is avoided, essentially the same boundary conditions are satisfied for both fields, that is, the electrodes are both electrostatic and magnetostatic equipotential surfaces. Therefore these fields should be proportional to each other and in the same direction throughout the region between the electrodes.

The assumption of congruency was tested experimentally by Salop et al. The results of these tests are shown in Figures 5 and 6. Figure 5

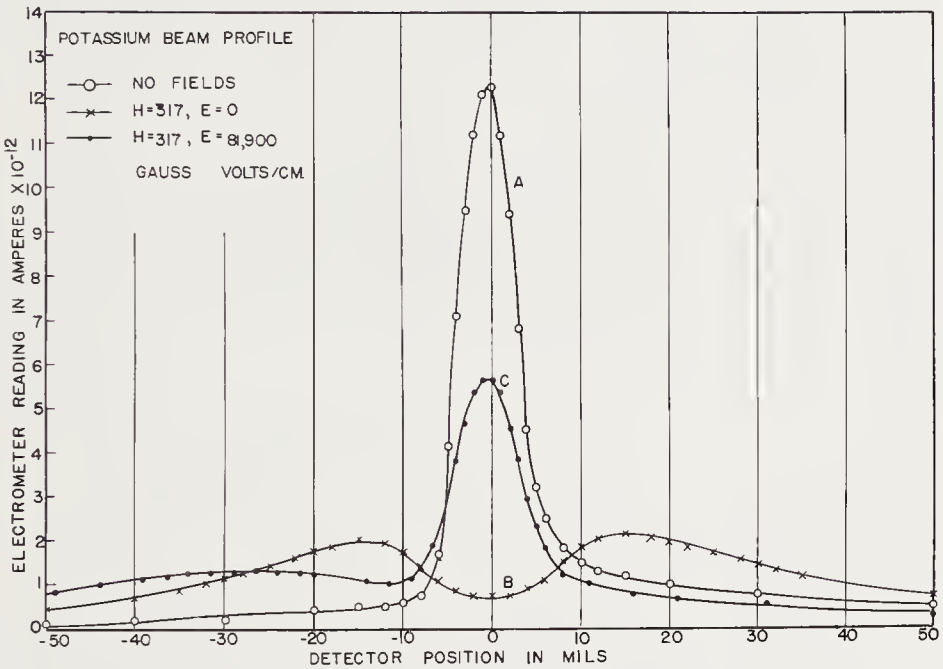

Fig. 5. Qualitative demonstration of E–H gradient balance, using potassium beam (Salop et al.). Curve A represents zero-field beam profile. Curve B represents beam profile with magnetic field, but no electric field. Curve C represents beam profile with magnetic and electric balance fields for one of the two magnetic substates.

represents a qualitative demonstration of E–H field congruency. In this figure, curve A shows a potassium beam profile taken at zero E and H field. Curve B shows a beam profile with $E = 0$, and $H = 317$ gauss. For this field the electronic spin is essentially decoupled from the nuclear spin, for both potassium isotopes (Paschen region), so that $\mu_{\text{eff}} \approx \pm\mu_0$, where μ_0 is the Bohr magneton. The positive (negative) sign refers to negative (positive) substates. The resulting deflection

pattern is thus a conventional Stern-Gerlach pattern, for a spin $\frac{1}{2}$ atom. Curve C shows a profile taken at the same magnetic field, but with an electric field $E = 81{,}900$ V/cm also applied. The left-hand peak ($\mu = +\mu_0$) has shifted further to the left and has been further broadened by the velocity distribution. The right-hand peak ($\mu = -\mu_0$) has shifted to the origin and has sharpened up so as to closely approximate the original beam shape, that is, E–H balance has been attained. It can be seen that the broadening effect of the velocity distribution has been substantially eliminated for the $M_J = +\frac{1}{2}$ substates.

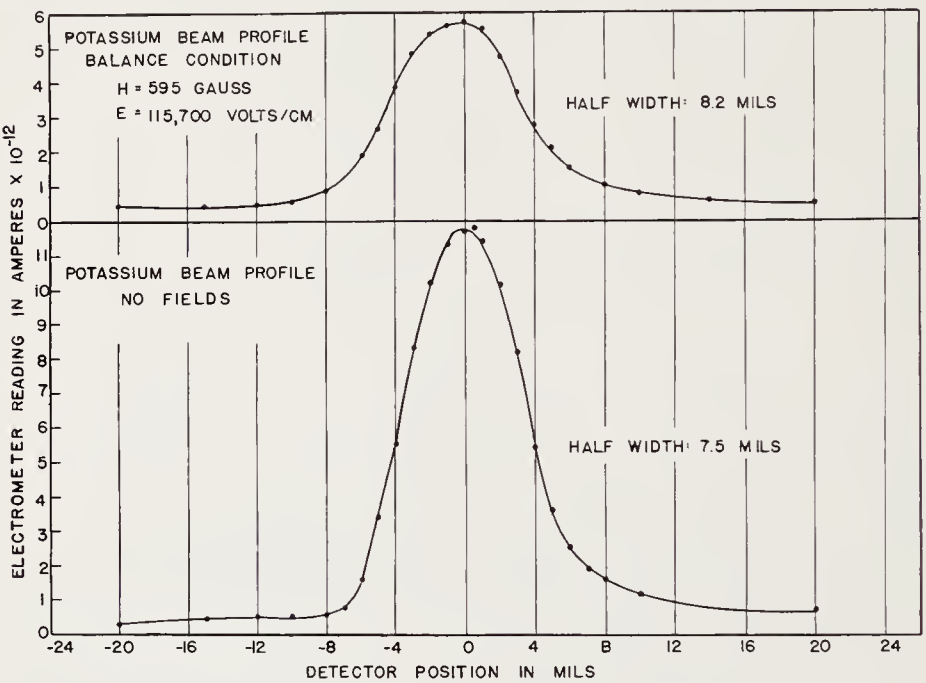
POTASSIUM BEAM PROFILE
BALANCE CONDITION
H = 595 GAUSS
E = 115,700 VOLTS/CM
HALF WIDTH = 8.2 MILS
POTASSIUM BEAM PROFILE
NO FIELDS
HALF WIDTH = 7.5 MILS
ELECTROMETER READING IN AMPERES X 10⁻¹²
DETECTOR POSITION IN MILS
-24 -20 -16 -12 -8 -4 0 4 8 12 16 20 24

Fig. 6. Quantitative demonstration of E–H balance (Salop et al.).

Figure 6 represents a quantitative demonstration of congruency, in which an undeflected profile is compared with a profile taken at the balance fields $H = 595$ gauss and $E = 115{,}700$ V/cm. The half-width of the original beam is 0.0075 in., and the half-width of the balanced peak is 0.0082 in. Thus, the effects due to unbalanced forces, including effects due to imperfect congruency, the finite beam width, fringing fields, etc., altogether produce a 9% broadening of the original beam. It is seen that the fields are congruent to a fairly high degree of approximation.

A cross section of a pair of *E–H* gradient pole faces used is shown in Figure 7, while an overall perspective of the electrode assembly is shown in Figure 8. The magnet yoke assembly lies outside the vacuum envelope,

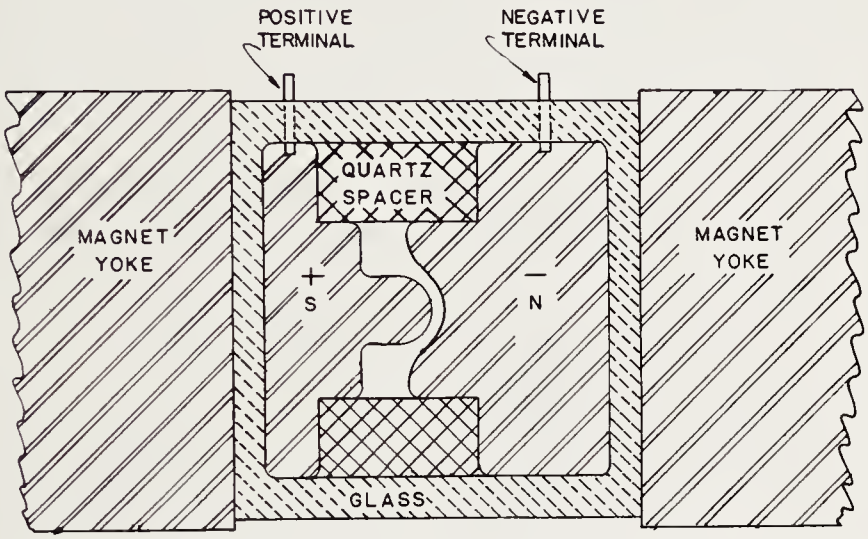

Fig. 7. Cross section of *E–H* gradient pole faces. The glass section serves as vacuum envelope.

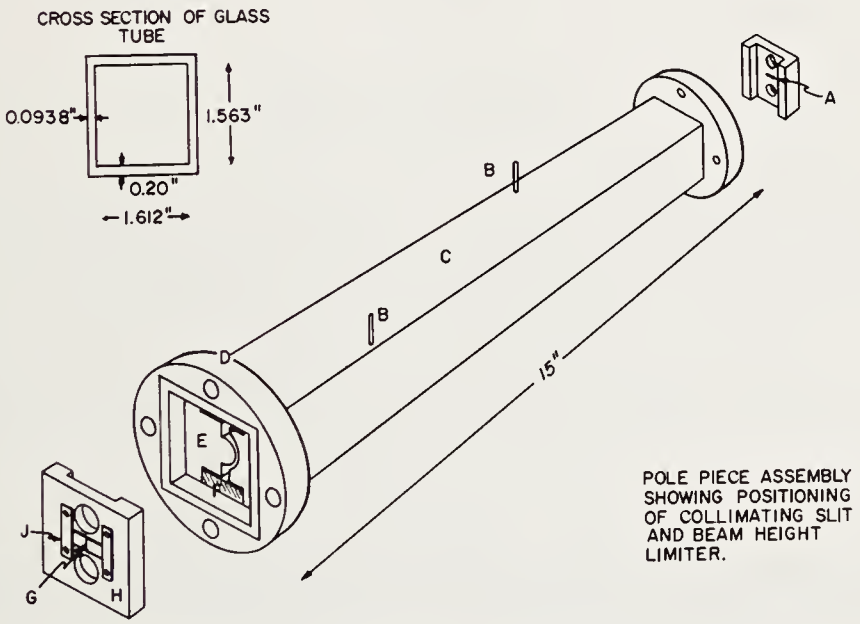

Fig. 8. Overall perspective of pole piece assembly for *E–H* gradient apparatus.

which is defined by the retangular glass tube which surrounds the electrodes. The glass also serves to electrically insulate the electrode-pole faces from the yoke.

In the alkali experiment, measurements were made at magnetic fields at which certain of the substates possess zero moments.* The error in the determination of H thereby contributed only several per cent to the overall experimental error, which was chiefly attributable to uncertainty in locating the precise position of the beam relative to the electrodes.

The results of the alkali polarizability measurements of Salop et al. and Chamberlain and Zorn, as well as a summary of theoretical determinations are presented in Table I.

B. Measurements of Metastable $^3P_2$ Argon

For an atomic system possessing tensor polarizability, $\boldsymbol{\mu}_e$ generally does not lie along the field direction. However, in an E–H balance experiment, the parallel fields establish the z axis as an axis of symmetry in the atom. Thus, $\boldsymbol{\mu}_e$ is in diagonal form with the x and y components of α being equal. The induced dipole moment is

$$\boldsymbol{\mu}_e = \hat{k}\alpha_z E_z$$

The balance relation Eq. (31) becomes

$$\mu_{\text{eff}} \frac{\delta H}{\delta z} = \alpha_z(M_J) E \frac{\delta E}{\delta z} \tag{33}$$

with $\alpha_z(M_J)$ dependent upon M_J through Eq. (7). Should an E–H balance be achieved for more than one substate, then $\alpha_z(M_J)$ for each of these can be separately determined. Eq. (9) can then be used to calculate $\alpha_z(M_J)$ and $\alpha_x(M_J)$ for all M_J. Thus, determinations of $\alpha_z(M_J)$

* μ_{eff} changes sign for certain of the magnetic substates in the intermediate field region. The "zero-moment" field, at which $\mu_{\text{eff}} = 0$, is given by the expression

$$H \approx -\frac{2M_F \Delta W}{(2I+1)g_J \mu_0}$$

for $J = \frac{1}{2}$ atoms, where I is the nuclear spin, g_J is the atomic g factor and ΔW the zero-field hyperfine energy separation. Those employed were $M_F = -2$, $H = 1634$ gauss and $M_F = -3$, $H = 2451$ gauss for ^{133}Cs; $M_F = -2$, $H = 722$ gauss for ^{85}Rb; $M_F = 1$, $H = 1221$ gauss for ^{87}Rb; $M_F = -1$, $H = 316$ gauss for ^{23}Na.

for two values of M_J suffice to yield all the components for α for all M_J.

Pollack et al.[4] have used the E–H balance method to measure $\alpha_z(+1)$ and $\alpha_z(+2)$ of $^3P_2$ metastable argon. The configuration of this state is $1s^2 2s^2 2p^6 3s^2 3p^5 4s$, so that the orbital angular momentum is due to a p hole in the incomplete M shell. The $4s$ electron behaves qualitatively like the valence electron of potassium. In fact, the $4s$ argon wave function calculated by Knox[17] is quite similar to that of the $4s$ electron of potassium[18,19] except for a scaling factor not very different from unity. One expects, therefore, that the average polarizability $\bar{\alpha}$ should be comparable to that of potassium. The anisotropy in α, on the other hand, should not be large, since it arises from the quite small contribution of the p hole to the polarizability. The zeroth-order contribution will actually be negligibly small. However, the anisotropic polarization of the core by the $4s$ orbital will result in an anisotropic core-correlated $4s$ wave function, which could be large enough to observe.

The polarizability of metastable $^3S_1$ helium is quite accurately calculable.[20,21] The argon measurements of Pollack et al. were therefore normalized to the (scalar) $^3S_1$ helium polarizability, thereby eliminating the need to determine H. When using a normalizing element, α is given by

$$\alpha_z(M_J) = \frac{\mu_{\text{eff}}}{\mu_n} \frac{V_n^2}{V^2} \alpha_n \tag{34}$$

where μ_n, V_n, and α_n are the effective magnetic moment, balance voltage, and polarizability of the normalizing element. Since the balance *voltages* appear in Eq. (34), rather than the balance electric fields, no geometry factors need be determined, and the error in α is thereby significantly reduced.

In the experiment of Pollack et al., metastable argon and helium were produced by electron bombardment, and were detected by Auger ejection of electrons from the cathode of an electron multiplier, which activated a scalar counter. Because of the very narrow collimation necessary for good resolution, and the rather long path length through the apparatus, the metastable currents were typically of the order of only several hundred counts per minute.

Because of the normalization to helium, it was only necessary to establish a convenient magnetic field, and to hold it constant throughout the course of a run. The beam intensity was then measured as a

function of electrode potential, for both argon and helium. Two balance peaks should be observed for argon, corresponding to $M_J = +1, +2$, with only one for helium, corresponding to $M_J = +1$. Figure 9 shows an argon run at a magnetic field of approximately

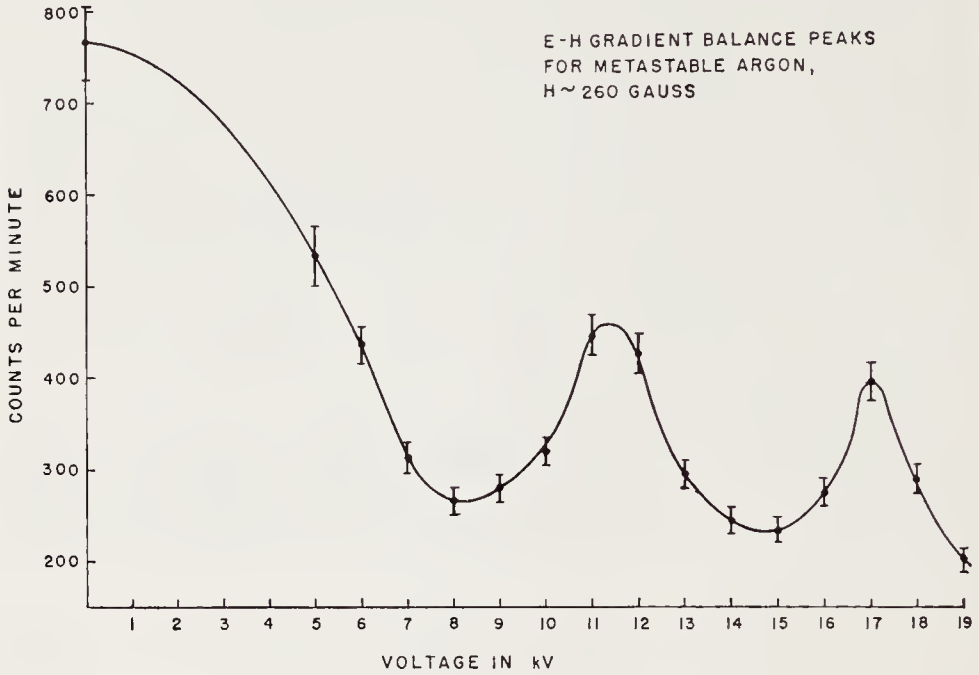

Fig. 9. Beam intensity vs. applied voltage at constant magnetic field of 260 gauss, for beam consisting of $^3P_2$ and $^3P_0$ metastable argon.

260 gauss. It is seen that there are indeed two peaks, balancing at about 11 kV and 17 kV. The corresponding helium peak is at about 13.6 kV. Now, if one assumes that the balance peak at 11 kV is due to the $M_J = +1$ state, the ratio $\alpha_z(+2)/\alpha_z(+1) \approx 1$. However, unless positive identification of the states is achieved, the 11 kV balance peak could instead be attributable to the $M_J = +2$ state, corresponding to a polarizability ratio $\alpha_z(+2)/\alpha_z(+1) \approx 4$. While it is very unlikely that the polarizability ratio should differ greatly from unity, a subsidiary "small shift" experiment was performed in order to definitely identify the substates. In this experiment beam profiles were taken at balance, and also with the applied voltage about 10% below balance, in the vicinity of both peaks. If a triangular beam shape is assumed, and it is

further assumed that $s_B \ll w$, the "weak field" beam shape given by Eq. (30) reduces to

$$I(s) = I(s_0) - I'(s_0)s_B \tag{35}$$

Thus a triangular beam is shifted by a weak field an amount s_B, with negligible velocity broadening. While the small shift deflections were actually comparable to the beam width, still, the beam was only slightly broadened, and the magnitudes of the beam shifts served as rough polarizability determinations.

The net deflection of a beam particle with velocity v_B is given by

$$s_B = \frac{C}{v_B^2}(\mu_{\text{eff}}\delta H/\delta z - \alpha E \delta E/\delta z) = \frac{C'\alpha}{v_B^2}(V_0^2 - (V_0 + \Delta V)^2) \tag{36}$$

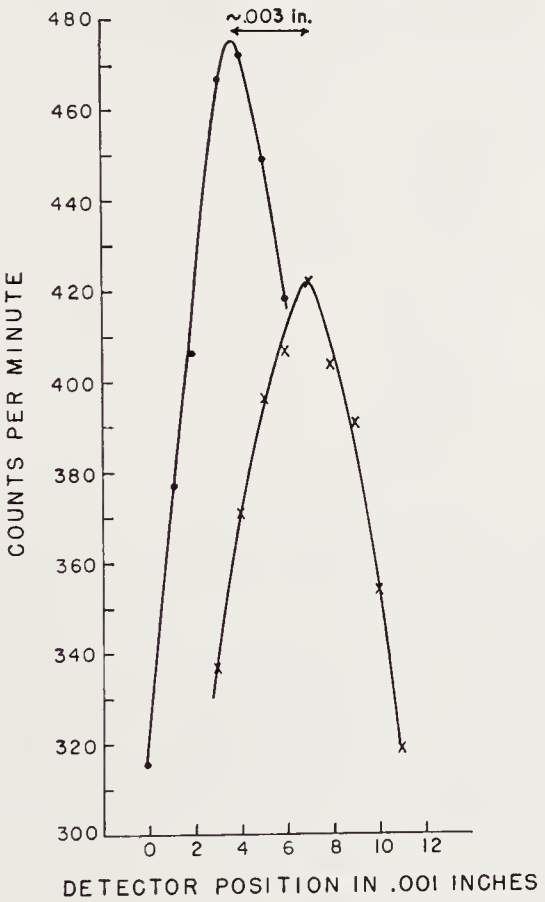

Fig. 10. Balance peak (left) and slightly unbalanced peak (right) for $^3P_2$ metastable argon, $M_J = +1$ substate, at about 11 kV.

where V_0 is the voltage at balance. To first order in ΔV, the ratio $s_B(1)/s_B(2)$ of the two substates is therefore

$$\frac{s_B(1)}{s_B(2)} = \frac{\alpha_1 \Delta V_1 V_{01}}{\alpha_2 \Delta V_2 V_{02}} \tag{37}$$

In this experiment, $\Delta V_1 = \Delta V_2$, and $V_{01}/V_{02} = 11.1/16.9$. The beam profiles are shown in Figures 10 and 11. It is seen that $s_B(1)$ and $s_B(2)$

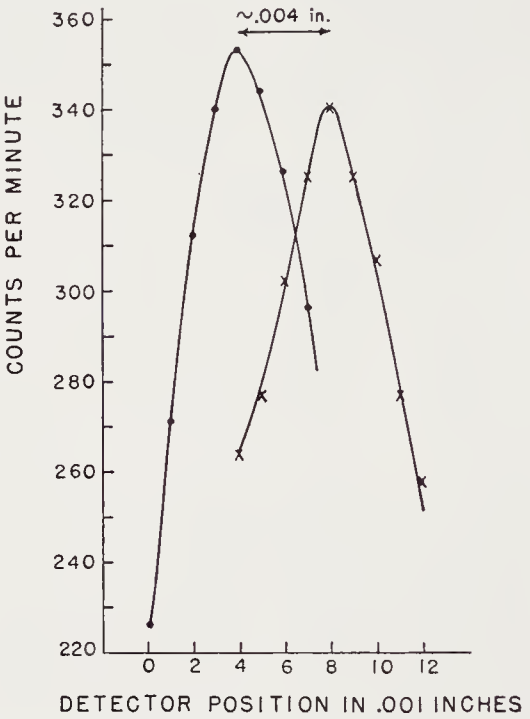

Fig. 11. Balance peak (left) and slightly unbalanced peak (right) for $^3P_2$ metastable argon, $M_J = +2$ substate, at about 17 kV.

are 0.003 and 0.004 in., respectively. Hence, $\alpha_1/\alpha_2 \approx 1$, indicating that the state coming into balance first is indeed $M_J = +1$.

Measurements were then taken in the vicinity of the two argon peaks, and of the helium peak, at several values of the magnetic field. Using the value of 46.6×10^{-24} cm^3 for the polarizability of $^3S_1$ metastable helium,[20,21] the results for $^3P_2$ metastable argon are

$$\alpha_z(+1) = 49.3 \times 10^{-24} \text{ cm}^3$$

$$\alpha_z(+2) = 43.8 \times 10^{-24} \text{ cm}^3$$

The principal sources of error were, first, fluctuations due to the low counting rate, and second, broadening of the peaks due to overlapping by atoms in unbalanced substates, i.e., incomplete resolution. Other error sources included fluctuations in electron gun current, source pressure, and magnetic and electric fields during the course of a run, measurements of the voltage (using an NBS calibrated electrostatic voltmeter), lack of perfect parallelism of the beam with respect to the pole faces, and deviations from the balance condition over the finite beam width. The net assignment of error due to all causes was $\pm 7\%$.

The components of α for all M_J, obtained from Eq. (9), are presented in Table II.

TABLE II

Summary of Measured and Calculated Tensor Polarizability Components for $^3P_2$ Metastable Argon

M_J	Component of α	Polarizability (in units of 10^{-24} cm^2)
0	α_x	46.4
0	α_z	52.4
1	α_x	47.5
1	α_x	50.4
2	α_x	50.4
2	α_x	44.5
	$\bar{\alpha}$	48.4

V. CONCLUSION

Atomic beam methods for measuring polarizabilities have not been heavily exploited thus far. Only the scalar polarizabilities of the ground states of the alkali elements and the tensor polarizabilities of $^3P_2$ metastable argon have been measured, while the tensor polarizabilities of $^3P_2$ metastable neon, krypton, xenon, and mercury are currently being investigated at New York University. In principle, the polarizabilities of the ground states of any element which can be formed in a beam can be measured, using either the small shift, large shift, or E–H gradient balance methods. It is very desirable to employ velocity selection when using the first two methods, although this has not yet

been done. The *E–H* gradient balance method fails, of course, for states which do not possess magnetic moments. It should be noted, however, that for suitably designed *E–H* fields, *nuclear* moments would suffice for an *E–H* gradient balance, rather than the *atomic* moments thus far employed. Therefore, almost all the isotopes of the periodic table can be studied using *E–H* gradient balance.

These remarks can also be applied to molecular systems. Using *E–H* gradient balance, for example, tensor polarizability determinations of specific rotational states can be made. Experimental problems arise because of the generally small molecular polarizabilities and small magnetic moments (of the order of several nuclear magnetons) of diatomic molecules. Thus, long pole faces and very narrow collimation are required. The principal practical limitation on accuracy in such measurements is then voltage breakdown between electrodes at the large electric fields required to obtain observable deflections.

References

1. R. M. Sternheimer, *Phys. Rev.*, **84**, 244 (1951); **95**, 736 (1954); **105**, 158 (1957).
2. G. E. Chamberlain and J. C. Zorn, *Phys. Rev.*, **129**, 677 (1963).
3. B. Bederson, J. Eisinger, K. Rubin, and A. Salop, *Rev. Sci. Instr.*, **31**, 852 (1960).
4. A. Salop, E. Pollack, and B. Bederson, *Phys. Rev.*, **124**, 1431 (1961); also E. Pollack, E. J. Robinson, and B. Bederson, *Phys. Rev.*, **134**, A1210 (1964).
5. H. Scheffers and J. Stark, *Phys. Z.*, **35**, 625 (1934).
6. E. U. Condon and G. H. Shortley, *The Theory of Atomic Spectra*, Cambridge University Press, New York, 1951, p. 60ff.
7. A. Dalgarno and A. E. Kingston, *Proc. Phys. Soc.* (*London*), **A73**, 455 (1959).
8. R. M. Sternheimer, *Phys. Rev.*, **96**, 951 (1954).
9. A. Dalgarno, *Advan. Phys.*, **11**, 281 (1962). Ground-state polarizabilities of the helium isoelectronic sequence have been calculated, using the fully coupled Hartree–Fock approximation, by A. Dalgarno and J. M. McNamee, *Proc. Phys. Soc.*, **77**, 673 (1961). The method has recently been extended to the beryllium sequence by A. Dalgarno and H. A. J. McIntyre, *Proc. Phys. Soc.*, **85**, 47 (1965).
10. J. O. Hirschfelder, C. F. Curtiss, and R. B. Bird, *Molecular Theory of Liquids and Gases*, Wiley, New York, 1954.
11. J. G. Kirkwood, *Phys. Z.*, **33**, 57 (1931).
12. R. A. Buckingham, *Proc. Roy. Soc.* (*London*), **A160**, 94 (1937).
13. R. M. Sternheimer, *Phys. Rev.*, **127**, 1220 (1962).
14. P. Kusch and V. W. Hughes, *Encyclopedia of Physics*, Vol. 37, Part I, Springer Verlag, Berlin, 1959.
15. N. F. Ramsey, *Molecular Beams*, Oxford University Press, London, 1956, p. 397ff.

16. J. C. Zorn, G. E. Chamberlain, and V. W. Hughes, *Phys. Rev.*, **129**, 2566 (1963).
17. R. S. Knox, *Phys. Rev.*, **110**, 375 (1958).
18. D. R. Hartree and W. Hartree, *Proc. Cambridge Phil. Soc.*, **34**, 550 (1938).
19. F. Herman and S. Skillman, *Atomic Structure Calculations*, Prentice-Hall, Englewood Cliffs, N.J., 1963.
20. C. Schwartz, private communication to Pollack et al.
21. A. Dalgarno and A. E. Kingston, *Proc. Phys. Soc.* (*London*), **72**, 1053 (1958).
22. D. R. Bates and A. Damgaard, *Phil. Trans. Roy. Soc.* (*London*), **A242**, 101 (1959).
23. M. Mizushima, *Natl. Bur. Std. Rept.*, **6009**, Boulder, Colorado, 1958.
24. M. Sundbom, *Arkiv Fysik*, **13**, 539 (1958).
25. D. Parkinson, *Proc. Phys. Soc.* (*London*), **A75**, 169 (1960).

2. ELASTIC SCATTERING OF HIGH-ENERGY BEAMS: REPULSIVE FORCES

I. AMDUR and J. E. JORDAN

Department of Chemistry, Massachusetts Institute of Technology, Cambridge, Massachusetts

CONTENTS

I. Introduction 29
II. Fundamental Concepts 31
III. Analysis 33
A. General Features of Elastic Scattering 33
B. Detailed Analysis of Scattering Experiments 35
1. Classical Analysis for Central Forces 35
2. Scattering by a Non-Central Force 47
3. Background Scattering 50
4. Quantum Scattering 53
5. Inelastic Scattering 54
IV. Experimental 57
A. Typical Apparatus 57
B. Modifications 59
V. Results 62
VI. Applications 68
VII. Summary 70
References 71

I. INTRODUCTION

The elastic scattering of high-velocity neutral beams has proven to be a useful method for determining interaction potentials at small internuclear separations. This chapter will critically discuss the experimental and theoretical aspects of such scattering and the reliability of the derived potentials. It will also discuss applications to specific problems where it is necessary to have a quantitative description of the intermolecular potential.

To obtain useful information about the potential at small distances from measured values of macroscopic properties, two general conditions must be simultaneously satisfied. First, there must exist a satisfactory molecular theory, usually statistical mechanical in character, which relates a given macroscopic property to the intermolecular potential. Second, experimental measurements must in most cases be made at extremely high temperatures to insure the presence of a large number of high-energy collisions at the small intermolecular distances at which the potential is effectively determined. Even when it is possible to meet the first condition, as in the case of transport and equilibrium properties of dilute gases of molecules having spherically symmetric force fields and no internal structure, it is usually not possible to meet the second condition. For example, the Ar–Ar potential at 1.7 Å is 10 eV and at 2.25 Å it is 1 eV. To determine the potential in this range from viscosity would require measured values between about 10,000 and 100,000°K.[1] At these temperatures there would be very few uncharged ground-state argon atoms.

The determination of intermolecular potentials from *a priori* calculations based on solutions of the Schrödinger equation, although feasible in principle, is extremely involved in practice, even with assistance from high-speed computers, except for very simple atomic systems.[2–4] Recently, a statistical theory based on the Thomas-Fermi-Dirac method[5] was used to calculate the intermolecular potential for systems of many-electron atoms, but comparison of the theoretical results with experiment shows disparities of about a factor of 2. Spectroscopic data combined with approximate quantum-mechanical calculations have been used to obtain potentials which are internally consistent although it is not always possible to assess their absolute accuracy. The method has thus far been limited to systems such as nitrogen and oxygen interactions where appropriate spectroscopic information is available.[6–9] The elastic scattering of high-velocity neutral beams is thus not only a useful and convenient method for determining repulsive interactions, but in many cases it is the only available reliable method.

In principle, a scattering experiment involves determination of the fraction of the kinetic energy of the center-of-mass system which is converted into potential energy at the distance of closest approach between beam particle and scatterer in a collision producing a known angle of deflection. As the kinetic energy of the system is varied while keeping the angle of deflection fixed, the distance of closest approach

changes and the potential is obtained as a function of separation distance. In practice, a high-velocity neutral beam produced by charge transfer of accelerated positive ions is attenuated in passing through a layer of scattering gas of known length and particle density. Measurement of axial beam intensities by a detector of fixed aperture leads to an apparent total cross section for particles scattered beyond a small, effective angle. Numerical values of the parameters of an assumed potential function are obtained from a comparison of these cross sections, measured over a range of energy, with a theoretical relation which takes account of the geometry of the beam–detector system in analyzing the dynamics of the collision process. Numerous experiments of this sort have been performed. A recent review article by Mason and Vanderslice[10] contains an excellent bibliography and discussion of the experimental approach used by the various investigators.

II. FUNDAMENTAL CONCEPTS

The concept of a two-body intermolecular potential is uniquely defined only if two molecules are fixed in space with a specified distance of separation between their centers of mass. Since this condition cannot be strictly fulfilled in scattering experiments because of the finite velocity of the beam particle relative to the scatterer, an apparent (velocity-dependent) rather than a true (static) potential is operative. If the Born-Oppenheimer approximation is valid—that is, if the nuclear motions of the particles may be regarded as negligibly small in comparison with their electronic motions—the two potentials will be virtually the same. This would be the case for comparatively heavy atoms or molecules with small or moderate relative velocities. It is to be expected, however, that at sufficiently large relative velocities the two potentials might be markedly different.

It is assumed that the force between the beam particle and the scatterer is spherically symmetric. Although the differential equations of motion do not require this assumption, integration of the trajectory equation does require knowledge of the specific form of any angular dependence in the potential function. In experiments involving polyatomic molecules, the measured cross sections are averages over orientations of the scattering systems. Since such experiments are analyzed by assuming the existence of a spherically symmetric potential, it is important to know that this average potential is consistent with the measured cross sections.

It is desirable that the function chosen to represent the potential lead to a tractable solution for the angle of deflection, usually small, as a function of the impact parameter, to facilitate the averaging procedure required for a beam of finite width or diameter. Because of the importance of small internuclear distances in the scattering of high-velocity neutral particles by atoms or molecules, repulsive forces resulting from the overlap of electron clouds strongly dominate the interactions. It is therefore possible to use monotonic potential functions, usually single-term expressions, which represent net repulsion at all distances, since the rapid variation of the total potential with distance makes it unnecessary to include the feeble attraction near the beginning and near the end of the trajectory. A function which has been used very extensively and which has proven quite satisfactory[10] is that for mass points which repel as an inverse power of the distance, namely, $V(r) = K/r^s$, where the parameters K and s are constants. Other potentials which could in principle be used are the various exponential forms, $V(r) = Ae^{-ar^n}$ with arbitrary convenient values of n, and the screened Coulomb potential, $V(r) = Ae^{-ar}/r$. These forms have been used when the beam width or diameter was assumed to be negligibly small,[11-15] but they have not been applied to the case of a beam of finite width or diameter.

Even when it can be shown that deviations from the Born-Oppenheimer approximation are unimportant and that the assumption of a spherically symmetric potential is valid, it is necessary to take account of two additional points before a proper classical analysis can lead to a reliable potential. First, since the analysis assumes that all scattering is elastic, it must be ascertained either that inelastic scattering may be neglected under the conditions of the experiment, or that it is possible to correct the measured cross sections to exclude significant contributions from such scattering. Second, in order to ascribe the derived potential to a specific state of the scattering system, the composition of the beam and of the scattering gas must be known. For example, if it is desired to obtain a potential for the ground state, the concentrations of excited, metastable, or ionized particles in the beam, or in the scattering gas, must be known to be negligibly small; otherwise, suitable corrections must be made. If it is desired to obtain information about the interaction between a metastable beam particle and a normal scattering particle, provision must be made, usually in the detection system, for distinguishing between normal and metastable beam particles.

Finally, having met all conditions necessary for obtaining a meaningful potential from the scattering experiments, the range of interaction distance over which the potential is valid must be determined. The classical dynamical equations which describe the scattering process suggest that all distances, from that of closest approach to infinity, are important when a particle of given energy is deflected through a specified angle. Although this inference is correct from a purely mathematical point of view, it is not physically realistic. Because of the extremely short-range nature of the interaction forces, the potential behaves much like a delta function, and the deflection of the particle is almost completely determined by interactions which occur very near the distance of closest approach, r_0. Stated otherwise, a cross section determined at a single energy essentially leads to a value of the potential at a single distance which may be taken as that of closest approach, and when cross sections are measured over a continuous range of energy, the resultant potential will be valid over a range of distance which lies between the extreme values of the distances of closest approach. It is for this reason that the parameters K and s in $V(r) = K/r^s$ can be considered constants throughout the entire collision trajectory; it is only necessary that they be constant at distances very near r_0. When a single set of parameters cannot represent the potential satisfactorily over the full range of r_0 involved in an experiment, it is possible to use a single function over small successive portions of the range with appropriate different sets of parameters and then to represent the final results by a single smooth curve.[16,17] Since the portions of the range can be chosen as small as desired, the derived numerical values of $V(r)$ will not be influenced significantly by the choice of the convenient inverse power form of potential function.

It is very important that the range be defined conservatively and in a manner consistent with the behavior of the potential to avoid extremely large errors which almost always result from unjustified extrapolation of potentials. In the case of the steeply rising repulsive potentials, such extrapolations are particularly dangerous and can lead to errors of several hundred per cent.[1]

III. ANALYSIS

A. General Features of Elastic Scattering

The general range of the experimental variables in a molecular beam apparatus can be inferred from a simplified treatment of the scattering

process. If the reduced mass of a beam particle and scatterer is μ and if the initial relative velocity of the pair is v_r, the relative scattering angle θ_r is

$$\sin \theta_r = \Delta p_z / \mu v_r \tag{1}$$

where Δp_z is the change in momentum in the direction normal to the incident direction. If the impact parameter b is chosen so that θ_r is small, then

$$\theta_r \cong \frac{\Delta p_z}{\mu v_r} \cong \frac{2b}{\mu v_r^2} \int_{r_0}^{\infty} \frac{F(r)}{\sqrt{r^2 - b^2}}\, dr \tag{2}$$

where r_0, the distance of closest approach in the collision, is approximately equal to b. If $V(r) = K/r^s$, $F(r) = sV(r)/r$ and Eq. (2) becomes

$$\theta_r \cong C \frac{V(r_0)}{E_r} \tag{3}$$

where C, a function only of s, is of order unity and $E_r = \mu v_r^2/2$. A similar result is obtained for $V(r) = Ae^{-ar}$. Equations (2) and (3) show that measurement of θ_r as a function of E_r yields information only about $V(r)$ and not $F(r)$. Since the scattering experiments described in this chapter lead to potential energies of the order of 0.1–10 eV, according to Eq. (3) the product $E_r\theta_r$ must also be of this magnitude.

There are a number of considerations which influence the choice of the individual ranges for θ_r and E_r. The range of energy, E_r, is chosen so that θ_r is small enough to justify the small angle approximation. Generally speaking, this requires that E_r be at least ten times $V(r_0)$. In practice, the energy range is more nearly a thousand times $V(r_0)$ since higher energy beams are more easily formed and detected. It is also important to set an upper limit on the energy. If the beam energy is too high, the effects of inelastic scattering become large and, in addition, the Born-Oppenheimer approximation may no longer be valid. While a precise value cannot be given for the highest desirable energy, later discussion may provide useful guides.

Although $V(r_0)$ and θ_r are not independent, it is desirable that θ_r not be too small. This limitation is not basic to the method, but for computational and analytical ease it is more convenient to use classical, rather than quantum, mechanics to describe the collisions. Quantum considerations, discussed in more detail later, require that θ_r be greater than about 10^{-3} radian.[18]

The discussion so far has been concerned with a single collision, or

the equivalent, the scattering of an infinitesimally narrow beam. In actual experiments the finite dimensions of the beam also affect the experimental results. Such a beam may be treated as a bundle of individual rays, for each of which the scattering cross section is, from Eq. (3), equal to $\pi b^2 = \pi(KC/E_r\theta_r)^{2/s}$. This cross section is different at each point in the path of the beam because it depends on the angle θ_r, which in turn depends on the angle between the axis of the ray and the edge of the detector. The attenuation of an actual beam passing through a target gas involves collisions at all points within the gas. The equation relating the scattered and unscattered beam intensities I and I_0, the scattering gas density n, and the path length Δx, namely,

$$\ln (I_0/I) = nS\Delta x \tag{4}$$

may be applied only if it is recognized that S, the apparent total cross section, represents an average of cross sections for many different rays. The way that this average is obtained will be discussed later, but a few generalizations can be made here.

The apparent cross section will be averaged with respect to scattering angles because the angle is the only variable which is a function of position in the region containing the scattering gas. Thus, an actual experiment involves a range of scattering angles, so that scattering measurements lead to values of $V(r_0)$ which are averages over many values of r_0.

Although it is relatively easy to construct an apparatus whose average scattering angles are large, it is much more difficult to construct one with very small average angles. Enlarging the beam diameter (for a fixed source–detector length) increases the average scattering angle. Decreases in beam size to obtain small average scattering angles, however, are limited by detector sensitivity. Although it is possible to place a detector of very small aperture in the center of a larger beam, this procedure does not result in smaller average scattering angles. Calculations show that the beam size, not the detector size, effectively determines the average scattering angle, since particles may be scattered to the detector as well as from it.[19,20]

B. Detailed Analysis of Scattering Experiments

1. *Classical Analysis for Central Forces*

Details of the analysis will first be presented for a particular configuration of beam, scattering region, and detector. Variations associated

with other configurations will be discussed later. It is assumed that the beam originates far from the scattering region and that the collimation is such that the atoms are all travelling in straight lines parallel to the axis. The beam is assumed to have a circular cross section so that as it traverses the scattering gas it defines a "scattering volume," the right-circular cylinder within which the scattering occurs. Finally, the detector is assumed to be circular, of the same radius as the beam, and coaxial with the beam.

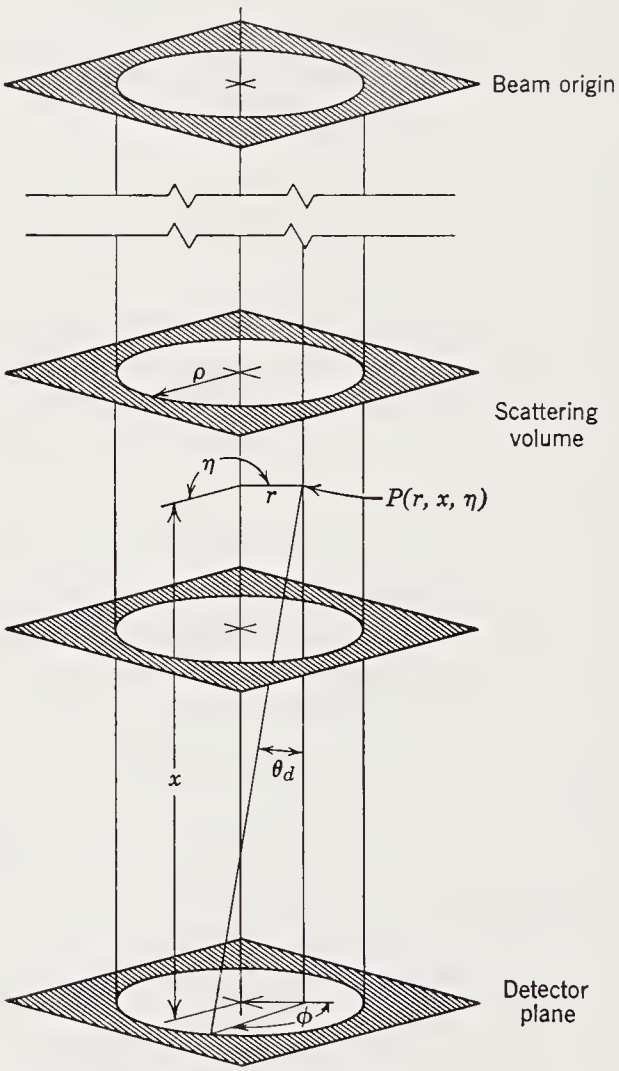

Fig. 1. Scattering volume–detector geometry for a beam of parallel rays. Note that θ_d is the laboratory scattering angle.

Figure 1 shows the arrangement of the beam, scattering volume, and detector. A point $P(r, x, \eta)$ in the scattering volume is defined by the cylindrical coordinates r, x, and η. The radius of the beam is denoted by ρ. The angle θ_d is that angle through which a beam particle must be thrown in order just to miss the detector, and in general will be a function of $P(r, x, \eta)$ and of ϕ, an azimuthal angle about the undeflected trajectory. For the very high beam energies involved here, the thermal energy of the target atoms may be neglected and they may be considered as initially stationary but free to recoil. In such a real system the relative motion of the beam and scattering particles is confined to a plane moving with the constant velocity of the center of mass within it. The most convenient form for the equations of motion and relations derived from them is the same as that for a hypothetical particle of mass m moving with initial velocity v toward a scatterer which is held fixed at all times. Transformation to the center-of-mass coordinate system for a beam particle of mass m_1 scattered by a particle of mass m_2 that is free to move merely involves replacing m by the reduced mass $\mu\,(= m_1 m_2/(m_1 + m_2))$, v by the initial relative velocity v_r, and analogous changes in momenta, accelerations, etc. The angle of deflection is replaced by θ_r, the angle through which the initial relative velocity vector is rotated by the collision.

Let a beam of unit area approach a scatterer initially at P, and consider those particles scattered from the beam which acquire relative velocities whose directions lie in a relative solid angle $d\omega_r$. The function $G(\omega_r)$, the differential scattering cross section, is defined so that $G(\omega_r)d\omega_r$ is the fraction that these particles form of the total scattered particles. The mutual collision cross section, S_p, is the total fraction of the beam scattered by one particle through all space except that subtended by the detector. It is defined by

$$S_p = \int_{\omega_r \neq \omega_{dr}} G(\omega_r)\, d\omega_r \tag{5}$$

where ω_{dr} is the relative solid angle associated with the solid angle subtended by the detector. It will, in general, depend on the nature of the colliding species, their initial relative velocity, and the size and location of the detector. For colliding systems which are not monatomic, it will also depend on the relative orientation of the molecules, but the following derivations will assume that the forces involved are central.

By restricting the problem in this way, the scattering of any beam atom will be symmetrical about its initial direction and S_p can be written

$$S_p = \int_0^{2\pi} \int_{\theta_{dr}}^{\pi} G(\theta_r) \sin \theta_r \, d\theta_r \, d\phi \tag{6}$$

An alternative approach to the problem utilizes an impact parameter b, defined as the perpendicular distance between the undeflected line of flight of the beam particle and a parallel line through the target center. For potential functions which are monotonic, only those beam particles approaching in an area $b \, db \, d\phi$ will be deflected into $d\theta_r$, so that S_p may be written

$$S_p = \int_0^{2\pi} \int_0^{b(\theta_{dr})} b \, db \, d\phi \tag{7}$$

where $b(\theta_{dr})$ is that value of b corresponding to a deflection equal to θ_{dr}.

It should be noted that Eq. (7) is not exactly correct. Setting the lower limit on the integral over b equal to zero represents an oversimplification. Equation (7) states that all particles with impact parameters less than $b(\theta_{dr})$ miss the detector. Actually, some beam atoms whose impact parameters are nearly zero do not miss. For example, if the beam and target atoms are the same mass, the beam atom will be stopped in a head-on collision and the target atom will be accelerated straight along the axis. The detector regards the accelerated particle as unscattered, while Eq. (7) counts it as scattered. In addition, when the beam particle is sufficiently heavier than the scatterer, nearly head-on collisions may cause both particles to be directed toward the detector after the collision. These effects cannot be taken into account in general fashion because the treatment must involve specific features of the detection system; for example, whether it can discriminate between particles which are chemically different and which have different velocities. The total contribution of these effects will be unimportant, however, unless the angle subtended by the detector is quite large, or unless the beam atom is very much heavier than the target atom. Neither case is important here, and Eq. (7) may be integrated to give

$$S_p = \int_0^{2\pi} \frac{[b(\theta_{dr})]^2}{2} \, d\phi \tag{8}$$

where θ_{dr} may be a function of ϕ.

Equation (7) implicitly assumes that the detector is situated in the axis of the beam. If it is placed at some angle to the beam axis, the limits on the integral must be changed accordingly.

For the present type of measurements, it is convenient to locate the detector on the axis, but this restricts the measured cross sections to *total* cross sections. Physically this means that the detector can only measure beam losses. It cannot determine the nature of the event that caused a particle to be removed from the beam, since any interaction that causes a deflection greater than θ_{dr} contributes to the attenuation of the beam and is therefore represented in the quantity S_p. For this reason, it is necessary to consider the extent to which inelastic scattering modifies the total cross section. In addition, it is necessary to assume an analytical form for the potential in order to obtain potential energy information from measured values of the total cross section. Differential cross sections, on the other hand, may be analyzed to give the potential energy directly.[21-23]

The classical analysis of an elastic collision applies the conservation of energy and angular momentum to a system consisting of a beam particle of mass m_1 approaching a target atom of mass m_2 with an initial relative velocity v_r. The relative scattering angle θ_{dr} is given by[24]

$$\theta_{dr} = \pi - 2b \int_{r_0}^{\infty} \frac{dr}{r^2[1 - V(r)/E_r - b^2/r^2]^{1/2}} \tag{9}$$

where E_r is the kinetic energy of relative motion, $\mu v_r^2/2$, and where r_0, the distance of closest approach, is related to b by the equation

$$b^2(\theta_{dr}) = r_0^2[1 - V(r_0)/E_r] \tag{10}$$

The solution of Eq. (9) for small angle deflections (where $\theta_{dr} \sim \sin \theta_{dr}$) and for $V(r) = K/r^s$ is[24,25]

$$\theta_{dr} = KC/E_r r_0^s \tag{11}$$

where C is the ratio of gamma functions

$$C = \sqrt{\pi}\, \frac{\Gamma(s/2 + \frac{1}{2})}{\Gamma(s/2)} \tag{12}$$

It may be noted from Eq. (11) that

$$\frac{V(r_0)}{E_r} = \frac{K}{E_r r_0^s} = \frac{\theta_{dr}}{C} \tag{13}$$

Substitution of Eqs. (10) and (13) into Eq. (8) yields

$$S_p = \frac{1}{2}\int_0^{2\pi}\left[\frac{KC}{E_r\theta_{dr}}\right]^{2/s}\left[1-\frac{\theta_{dr}}{C}\right]d\phi \tag{14}$$

Equation (14) may be expressed in terms of the laboratory coordinate system by making the folllowing substitutions: E_r is expressed in terms of the beam energy E, and the relative angle θ_{dr} is expressed in terms of the laboratory angle θ_d. When θ_{dr} and θ_d are both small,[24]

$$\theta_{dr} = \frac{m_1 + m_2}{m_2}\,\theta_d \tag{15}$$

and when the initial velocity of the target particle v_2 is negligible compared to that of the beam particle v_1, v_r may be replaced by v_1 so that

$$E_r = \mu v_r^2/2 = \frac{m_1 m_2}{2(m_1 + m_2)}\,v_1^2 = \frac{m_2}{m_1 + m_2}\,E \tag{16}$$

Thus $E_r\theta_{dr} = E\theta_d$ and Eq. (14) becomes

$$S_p = \frac{1}{2}\int_0^{2\pi}\left(\frac{KC}{E\theta_d}\right)^{2/s}\left(1-\frac{m_1 + m_2}{m_2 C}\,\theta_d\right)d\phi \tag{17}$$

To relate a theoretical expression to the measured cross section, it is necessary to average S_p over all points P in the scattering volume. Each of these points will, in general, be associated with many values of θ_d and therefore with many values of S_p.

Consider the beam intensity $i(r,x,\eta)$ entering a differential volume $dV = r\,dr\,d\eta\,dx$ at point P along the beam path. (See Fig. 1.) The beam flux at x may be written

$$N(x) = \int_0^{2\pi}\int_0^{\rho} i(r,x,\eta)r\,dr\,d\eta \tag{18}$$

and the loss of flux due to scattering in dV into all space except that subtended by the detector may be written

$$-di(r,x,\eta)r\,dr\,d\eta = i(r,x,\eta)n(x)S_p r\,dr\,d\eta\,dx \tag{19}$$

where S_p is given by Eq. (17). Nonuniformities in the scattering gas density are taken into account by making n a function of x.

Equation (19) must first be integrated over r and η. The result is

$$\begin{aligned} -dN(x) &= n(x) \int_0^{2\pi} \int_0^{\rho} i(r,x,\eta) S_p r \, dr \, dx \, d\eta \\ &= n(x) N(x) \bar{S}_p \, dx \end{aligned} \tag{20}$$

where $\bar{S}_p$ is given by

$$\bar{S}_p = \frac{\displaystyle\int_0^{2\pi} \int_0^{\rho} S_p i(r,x,\eta) r \, dr \, d\eta}{\displaystyle\int_0^{2\pi} \int_0^{\rho} i(r,x,\eta) r \, dr \, d\eta} \tag{21}$$

Integration over x then yields

$$\ln\left(\frac{N_0}{N}\right) = \int_0^D n(x) \bar{S}_p \, dx \tag{22}$$

where D is defined as the total path length of the beam. Equation (22) can be broken up into integrations over two ranges of x; that inside the scattering chamber and that outside. The path length between x_1 and x_2 is inside the scattering chamber and in this region the gas density n_{sc} can be considered to be constant. If $x_2 - x_1 = \Delta x_{sc}$, Eq. (22) becomes

$$\begin{aligned} \ln\left(\frac{N_0}{N}\right) &= n_{sc} \int_{x_1}^{x_2} \bar{S}_p \, dx + \int_0^{x_1} n(x) \bar{S}_p \, dx + \int_{x_2}^{D} n(x) \bar{S}_p \, dx \\ &= n_{sc} \Delta x_{sc} \bar{S}_{sc} (1 + \alpha) \end{aligned} \tag{23}$$

where $\bar{S}_{sc}$ is given by

$$\bar{S}_{sc} = \frac{1}{\Delta x_{sc}} \int_{x_1}^{x_2} \bar{S}_p \, dx = \frac{1}{\Delta x_{sc}} \int_{x_1}^{x_2} \left[\frac{\displaystyle\int_0^{2\pi} \int_0^{\rho} S_p i(r,x,\eta) r \, dr \, d\eta}{\displaystyle\int_0^{2\pi} \int_0^{\rho} i(r,x,\eta) r \, dr \, d\eta} \right] dx \tag{24}$$

and α, the background scattering term, is given by

$$\alpha = \frac{\displaystyle\int_0^{x_1} n(x) \bar{S}_p \, dx + \int_{x_2}^{D} n(x) \bar{S}_p \, dx}{n_{sc} \Delta x_{sc} \bar{S}_{sc}} \tag{25}$$

The background scattering correction α is generally small and may be calculated with sufficient accuracy by using several approximations. The procedures and results of this calculation will be found below.

Equation (24) must be further simplified, since the function $i(r,x,\eta)$ is not known. It is possible to measure the intensity distribution of the beam only at the plane of the detector, and this quantity, $i(r,0,\eta)$, can in general be only indirectly related to $i(r,x,\eta)$. However, Eq. (24) shows that the effect of the distribution will be partially cancelled because $i(r,x,\eta)$ occurs in both numerator and denominator. The equation for $\bar{S}_{sc}$ may therefore be simplified to

$$\bar{S}_{sc} = \frac{1}{\Delta x_{sc}} \int_{x_1}^{x_2} \left[\frac{\int_0^{2\pi} \int_0^{\rho} i(r,0,\eta) S_p r \, dr \, d\eta}{\int_0^{2\pi} \int_0^{\rho} i(r,0,\eta) r \, dr \, d\eta} \right] dx \tag{26}$$

Furthermore, since experimental evidence shows that the intensity is constant across the detector surface in an apparatus where the parallel ray approximation is valid, Eq. (26) further reduces to

$$\bar{S}_{sc} = \frac{1}{\Delta x_{sc} \pi \rho^2} \int_{x_1}^{x_2} \int_0^{2\pi} \int_0^{\rho} S_p r \, dr \, d\eta \, dx = \frac{1}{V} \int_V S_p \, dV \tag{27}$$

Thus $\bar{S}_{sc}$ is simply a volume average of S_p, a not unexpected result Equation (27) may be combined with Eq. (17) and written as

$$\bar{S}_{sc} = \pi \left(\frac{KC}{E} \right)^{2/s} \left\{ \langle \theta_d^{-2/s} \rangle - \frac{m_1 + m_2}{m_2 C} \langle \theta_d^{1-2/s} \rangle \right\} \tag{28}$$

where

$$\langle \theta_d^{-2/s} \rangle = \frac{1}{2\pi V} \int_0^{2\pi} \int_V \theta_d^{-2/s} \, dV \, d\phi \tag{29}$$

and

$$\langle \theta_d^{1-2/s} \rangle = \frac{1}{2\pi V} \int_0^{2\pi} \int_V \theta_d^{1-2/s} \, dV \, d\phi \tag{30}$$

For the geometry in Figure 1

$$\theta_d = \frac{\rho}{x} \left\{ -\frac{r}{\rho} \cos \phi + \left[1 - \left(\frac{r}{\rho} \right)^2 \sin^2 \phi \right]^{1/2} \right\} \tag{31}$$

so that, after substituting $\lambda = r/\rho$, Eq. (29) becomes

$$\langle \theta_d^{-2/s} \rangle = \frac{\rho^{2-2/s}}{V} \int_{x_1}^{x_2} x^{2/s}\, dx \times \int_0^{2\pi} \int_0^1 \{-\lambda \cos\phi + [1 - \lambda^2 \sin^2\phi]^{1/2}\}^{-2/s} \lambda\, d\lambda\, d\phi \quad (32)$$

The integration over x is straightforward and the double integral may be evaluated by substituting $u = \lambda \cos\phi$ and $w = \lambda \sin\phi$. Thus $\langle \theta_d^{-2/s} \rangle$ may be written as XYZ, where

$$X = \frac{x_2^{1+2/s} - x_1^{1+2/s}}{(x_2 - x_1)}$$

$$Y = \sqrt{\pi}\, \frac{\Gamma(\frac{3}{2} - 1/s)}{\Gamma(2 - 1/s)} \quad (33)$$

$$Z = \frac{2(2\rho)^{-2/s}}{\pi(1 - 4/s^2)}$$

An analogous procedure may be followed to calculate $\langle \theta_d^{1-2/s} \rangle$ and this quantity may similarly be expressed as $X'Y'Z'$, where

$$X' = \frac{x_2^{2/s} - x_1^{2/s}}{x_2 - x_1}$$

$$Y' = \sqrt{\pi}\, \frac{\Gamma(2 - 1/s)}{\Gamma(\frac{5}{2} - 1/s)} \quad (34)$$

$$Z' = \frac{2(2\rho)^{1-2/s}}{\pi(2 - 2/s)(2/s)}$$

Equation (28) states that if $\log \bar{S}_{sc}$ is plotted against $\log E$, a straight line with slope $-2/s$ will result. Since the intercept of this curve is a function only of K, s, and apparatus parameters, K may be calculated and the potential function thereby completely specified. The small background correction in Eq. (23), $1 + \alpha$, is actually a function of s so that the determination of K proceeds by successive approximations.

The results obtained thus far have been limited to a beam of parallel

rays striking a detector whose diameter is equal to that of the unscattered beam. Although it is possible to construct an apparatus which essentially satisfies these two conditions, the geometry of some apparatus may not. It is interesting, therefore, to examine different beam-detector geometries.

Since it is extremely difficult to form a beam without some divergence, it is frequently necessary to take this into account. If the rays entering the scattering volume are not parallel, their distribution in initial directions will affect the analysis through the calculation of θ_d. Inclusion of beam divergence in a general analysis is difficult because the extent of the divergence and the degree to which the divergence affects the calculation of $\langle \theta_d^{-2/s} \rangle$ both depend on the specific arrangement of the collimating holes. Unlike the case for parallel rays where the effective radius of the beam is the same as the radius, ρ, of the entrance to the scattering chamber, the effective radius of a diverging beam (in the scattering chamber) is larger than ρ. Depending on the size and location of the detector and the exit hole in the scattering chamber, this effective increase in the size of the beam can result in back-scattering of beam particles which would have missed the detector in the absence of attenuation. Although the calculation of $\langle \theta_d^{-2/s} \rangle$ where back-scattering is important has been carried out for only one geometrical arrangement (to be discussed below), it is possible in several configurations of collimators and detectors to reduce such back-scattering to a negligible quantity even when the divergence of the beam is appreciable. The analysis for such configurations begins with modification of Eq. (19) and proceeds as follows. Let the intensity at point $P(r,x,\eta)$ per unit solid angle with respect to the detector be $i(r,x,\eta)f(\beta)\cos\beta$, where $f(\beta)$ is the distribution of intensity with solid angle and β is the angle between the beam axis and the incoming ray, as shown in Figure 2. Then $2\pi i(r,x,\eta)f(\beta)\cos\beta\sin\beta\,d\beta$ is the intensity at $P(x,r,\eta)$ of beam particles whose initial directions lie in element of solid angle $2\pi\sin\beta\,d\beta$. The loss due to scattering at point P is then written in analogy with Eq. (19).

$$-di(r,x,\eta)f(\beta)2\pi\cos\beta\sin\beta\,d\beta\,r\,dr\,d\eta = i(r,x,\eta)f(\beta)\cos\beta 2\pi\sin\beta\,d\beta n(x)S_p r\,dr\,d\eta\,dx \qquad (35)$$

Integrating this equation over the beam area,* scattering path, and

* Since the effective radius of the beam depends on the amount of divergence, the upper limit on the integral over r will be indicated formally by $\rho(x)$.

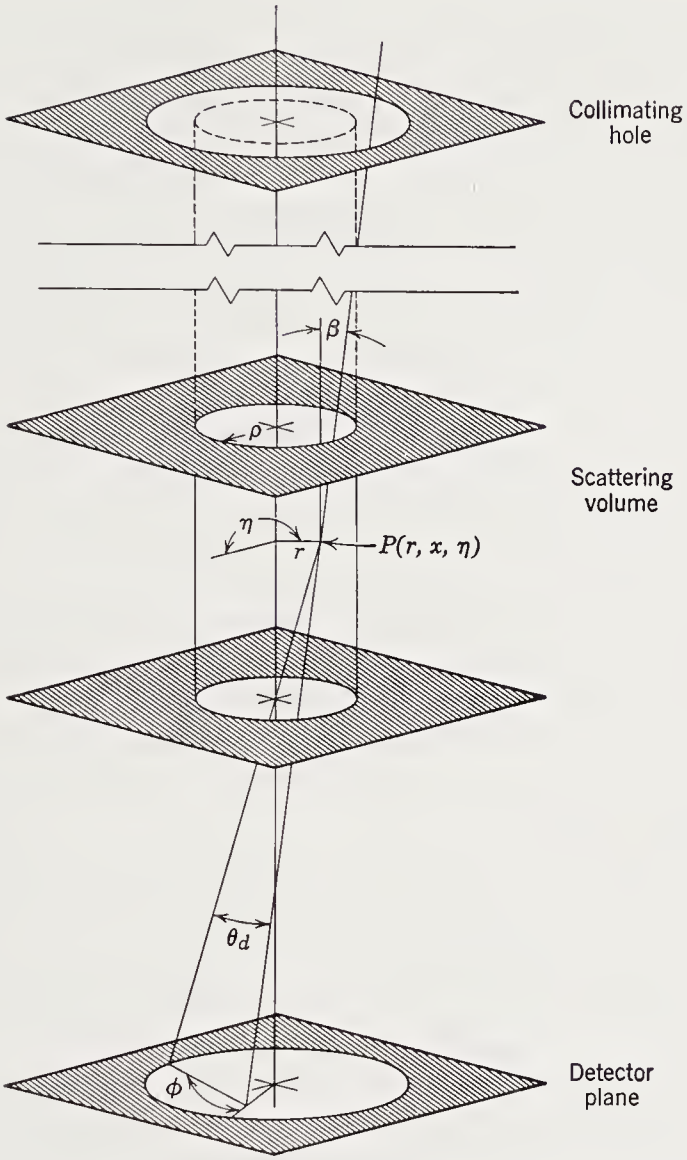

Fig. 2. Scattering volume-detector geometry for a slightly divergent beam.

all incident ray directions gives the expression for the cross section $\bar{S}_{sc}$ analogous to Eq. (24):

$$\bar{S}_{sc} = \frac{1}{\Delta x_{sc}} \int_{x_1}^{x_2} \frac{\int_0^{2\pi}\int_0^{\rho(x)}\int_{\beta_1}^{\beta_2} S_p i(r,x,\eta) f(\beta) \cos\beta \sin\beta \, d\beta \, r \, dr \, d\eta}{\int_0^{2\pi}\int_0^{\rho(x)}\int_{\beta_1}^{\beta_2} i(r,x,\eta) f(\beta) \cos\beta \sin\beta \, d\beta \, r \, dr \, d\eta} dx \quad (36)$$

The limits β_1 and β_2 will depend on the specific geometrical arrangement of the collimating apertures in any given apparatus.

The only cases for which Eq. (36) has been solved are those in which the scattering geometry permits several simplifications. In the first of these[26] it is possible to carry out the analysis by assuming that the source of the beam is a point located at the intersection of lines drawn from the edge of the beam at the detector plane through the edge of the entrance aperture of the scattering chamber. It can be shown that this model can be obtained as a special case of Eq. (36). The actual analysis is similar to that for a parallel beam, and in the limit of very small beam divergence the two treatments become identical. This model is useful for a beam with cylindrical symmetry and with relatively little divergence. Another scattering geometry for which Eq. (36) can be simplified is that where the cross section of the beam is that of a long narrow rectangle taken from the center of a circular beam, an arrangement which reduces the analysis to two dimensions.[19] In addition, several other valid approximations involving the dimensions of the scattering region enables the integration over the scattering volume and over the distribution of initial ray directions to be transferred to an integration along the detector where the intensity distribution $i(r,0,\eta)$ is known. Even with these simplifications, the final integration must be performed numerically.

The case where a narrow detector is placed in the center of a much wider beam is also of interest.[19,20] At first glance, this arrangement appears to offer extremely narrow resolution, but this is actually not the case, because the net decrease in the measured beam flux is sensitive to scattering back to the detector. The net decrease depends primarily on the beam size and only slightly on the detector size so that the value of $\langle \theta_d^{-2/s} \rangle$ for this detector geometry is nearly the same as in the case where the detector is the same size as the beam. It is found by direct scanning that the unscattered beam intensity is reduced by scattering, but that its distribution is only slightly altered. Thus a small detector placed in the center of a large beam will measure nearly the same ratio (N_0/N) as a detector intercepting the entire beam and the two cross sections will be nearly the same. This can be true only if the value of $\langle \theta_d^{-2/s} \rangle$ is approximately the same for both beam-detector arrangements.

The actual calculation of $\langle \theta_d^{-2/s} \rangle$ for a detector smaller than the beam is not as straightforward as the calculation for a beam and detector of equal size. It can be set up in terms of scattered fluxes to and from

the detector, but the exact analysis has not yet been completed for the general case, since scattering from the edges of the beam onto the detector depends critically on the specific intensity distribution. As a result, the calculation of $\langle \theta_d^{-2/s} \rangle$ for this geometry has only been carried out for one special case.[19]

Still another scattering geometry of interest involves a detector which is much larger than the unscattered beam. This arrangement permits large values of θ_d and so may be used to investigate collisions at very small interatomic distances. The calculation of $\langle \theta_d^{-2/s} \rangle$ for this geometry is similar to that for parallel rays.

2. *Scattering by a Non-Central Force*

The foregoing analysis assumes that the colliding particles may be treated as point centers of force. Such spherical symmetry is properly associated with systems of atoms but not with systems involving molecules. In the case of short-range interactions between an atom and a molecule, the important forces probably act between the constituent atoms of the molecule and the free atom; in the case of two molecules, the forces between the constituent atoms are of primary importance. In neither case is it likely that the geometric center of the molecule acts as a point center of force.

In principle, a proper analysis for elastic scattering in which molecules are involved should start with a solution of Eq. (5), using the appropriate angular-dependent potential for a polyatomic system in formulating $G(\omega_r)$. Since it has not yet been possible to solve the equations of motion for this multibody problem, alternative approximate procedures have been developed. One of these procedures, which has been applied to the scattering of He and Ar in N_2 [27] and of He in CH_4 and CF_4,[28] appears to be satisfactory for deducing average molecule–molecule interactions for systems such as N_2–N_2, CH_4–CH_4, and CF_4–CF_4, which in general cannot be measured directly because of the difficulty of forming beams of high-velocity polyatomic molecules. The simplest atom–molecule and molecule–molecule systems, those involving homonuclear diatomic molecules, will be used to illustrate the essential features of the method, since extension to heteronuclear diatomic molecules and to various types of polyatomic molecules involves no new fundamental concepts.

The basic assumption is that the deflection of the beam particle, the atom, is determined by interactions very near r_0. The vibrational

and rotational motion of the scattering molecule is neglected during the very short effective time of its interaction (10^{-15}–10^{-14} sec) with the high-velocity beam atom, so that the potential energy associated with the collisions is assigned to a single atom–molecule orientation. It is further assumed that this potential is the sum of the potentials between the beam atom and each of the constituent atoms in the molecule. Since the molecules in the scattering volume will present all orientations to the beam atoms, the experimental potential is thus an average of the atom–molecule potential for a specified orientation both with respect to beam-detector geometry and the beam atom-scattering molecule geometry.

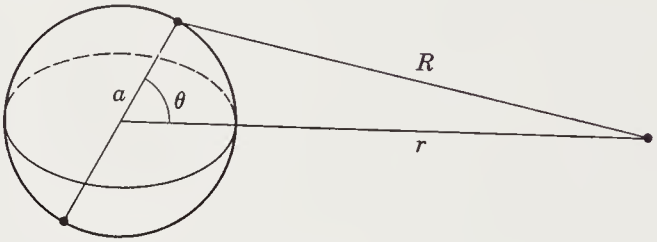

(a)

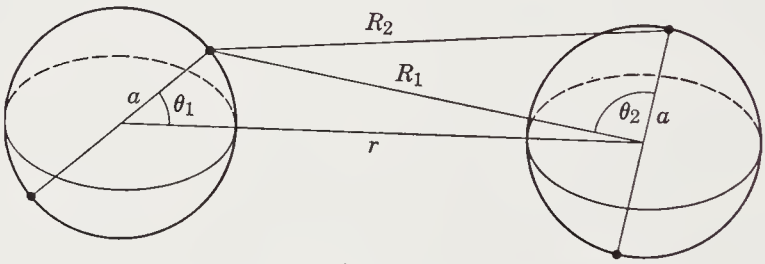

(b)

Fig. 3. (*a*) Atom–molecule coordinate system. (*b*) Molecule–molecule coordinate system.

In terms of the coordinate system in Figure 3*a*, this experimental potential, obtained from appropriate scattering experiments in the same manner as atom–atom potentials, is then assumed to be

$$\langle V(r)\rangle = \frac{K}{r^s} = \frac{1}{4\pi}\int_0^{4\pi} 2V(R)\, d\omega \tag{37}$$

where r is the distance between the center of mass of the molecule and the interacting atom, R is the distance between a constituent atom of the molecule and the interacting atom, and θ is the angle between r and a, the half length of the molecular bond, so that $d\omega = 2\pi \sin\theta \, d\theta$. If $V(R)$ is taken as $K'/R^{s'}$, where $R = r(1 - 2\alpha\cos\theta + \alpha^2)^{1/2}$ with $\alpha = a/r$, Eq. (37) reduces to

$$\langle V(r)\rangle = \frac{K}{r^s} = \frac{2K'}{r^{s'}} \frac{(1+\alpha)^{s'-2} - (1-\alpha)^{s'-2}}{2\alpha(s'-2)(1-\alpha^2)^{s'-2}} \tag{38}$$

A successive approximation procedure may be used to solve for K' and s', the parameters of the interatomic potential, since K, s, and α are known. Because the interatomic potential involves only central force fields, it may be combined with another appropriate interatomic potential to obtain the parameters K'' and s'' of the potential between constituent atoms on the two molecules. The combination rules used for this purpose have been previously tested for rare-gas systems.[29,30] Thus, in analogy with Eq. (37), the average potential between two molecules is

$$\langle V(r)\rangle = \left(\frac{1}{4\pi}\right)^2 \int_0^{4\pi}\int_0^{4\pi} 4V(R_2)\, d\omega_1\, d\omega_2 \tag{39}$$

where R_2, as shown in Figure 3*b* is the distance between constituent atoms on the different molecules, $d\omega_1 = 2\pi \sin\theta_1 \, d\theta_1$ and $d\omega_2 = 2\pi \sin\theta_2 \, d\theta_2$. From the figure, $R_2 = (R_1^2 - 2\alpha R_1 \cos\theta_2 + \alpha^2)^{1/2}$ and $R_1 = r(1 - 2\alpha\cos\theta_1 + \alpha^2)^{1/2}$, so that Eq. (39), with $V(R_2) = K''/R_2^{s''}$, may be integrated to give the following relation for the deduced molecule–molecule potential

$$\langle V(r)\rangle = \frac{4K''}{r^{s''}} \frac{(1+2\alpha)^{s''-3} + (1-2\alpha)^{s''-3} - 2(1-4\alpha^2)^{s''-3}}{4\alpha^2(s''-2)(s''-3)(1-4\alpha^2)^{s''-3}} \tag{40}$$

Sinanôglu has proposed a similar procedure for systems with non-central forces. He regards the atom–molecule experiments as representing averages of cross sections, rather than averages of potentials, over all orientations.[31,32] He has made approximate calculations to compare the two methods and concludes that the averaging of potentials leads to effective interatomic potentials which are somewhat lower than those obtained by averaging cross sections. The difference corresponds to only several per cent in the cross sections and is thus of the same order of magnitude as the experimental uncertainty.

Since it has been shown that the averaging of potentials leads to average molecule–molecule potentials which are consistent with those obtained from high-temperature transport properties,[27,28] it appears that both methods lead to satisfactory results, even though they are substitutes for the correct but intractable procedure of solving the multibody scattering problem for an angular dependent potential. Although the averaging of cross sections is probably a better assumption, the authors are inclined to favor the averaging of potentials simply because it is easier to carry out, particularly for small separation distances where a series expansion in Sinanôglu's treatment encounters convergence difficulties.

3. *Background Scattering*

Background scattering, the beam attenuation due to all gas density except n_{sc}, arises from two sources. The first is the residual pressure in the apparatus because of the limitations of the pumping system. This residual gas density n_0 is the same for both scattered and unscattered beams and can be taken into account by defining n_{sc} as $n_{sc} = n_T - n_0$, where n_T is the total measured scattering gas density. As long as n_0 is constant, it does not influence the measurements. The other source of background scattering is the flow of gas from the entrance and exit of the scattering chamber. Since this incremental background gas density exists only during the measurement of the scattered intensity, its effect cannot be calculated as easily as that of the constant background n_0.

Equation (23) defines the contribution of background scattering as $(1+\alpha)$, where α is given by Eq. (25). This equation cannot be solved as written, but since α is small with respect to unity, simple approximations are permissible. First, the total path length D is broken up into j regions and the average density in each region, $\bar{n}_j$, is taken outside the integral. The quantity α is therefore written as a sum of j terms such that

$$\alpha = \sum_j \frac{\bar{n}_j}{n_{sc}} \frac{\int_{x_j}^{x_{j+1}} \bar{S}_p \, dx}{\Delta x_{sc} \bar{S}_{sc}} \tag{41}$$

where the integration limits imply integration along the length of the jth region. The integrations may be performed as in the evaluation of $\bar{S}_{sc}$, with the result that

$$\alpha = \sum_j \alpha_j = \sum_j \frac{\bar{n}_j}{n_{sc}} \left[\frac{x_{j+1}^{1+2/s} - x_j^{1+2/s}}{x_2^{1+2/s} - x_1^{1+2/s}} \right] \tag{42}$$

The values of $\bar{n}_j$ will depend on the geometric shape of the entrance and exit in the scattering chamber. These are usually tapered holes or slits. Cross sections of typical apertures are shown in Figure 4, together

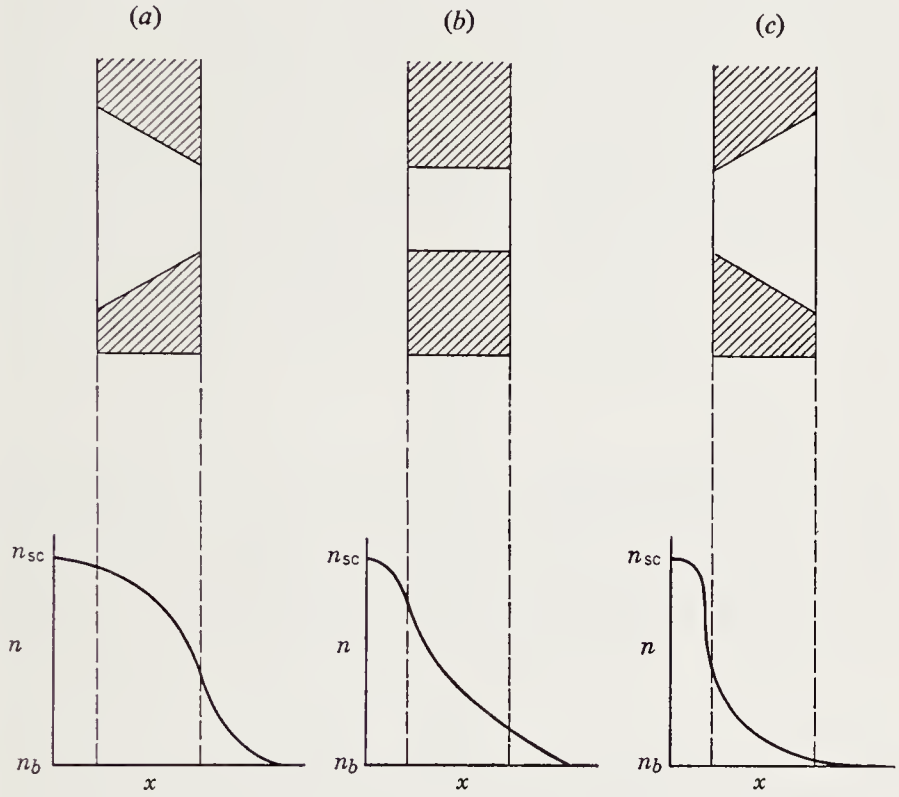

Fig. 4. Cross-section drawings for three typical scattering–chamber apertures. Below each drawing is a plot of the approximate density distribution where it is assumed that the scattering gas is on the left side of the aperture.

with approximate density distributions. Since the smallest value of α will be associated with an aperture in which the density decreases most rapidly, it is clear that an aperture like that in Figure 4*c* is the best one to use.

Three regions are considered for each aperture. The first is that defined by the length of the plate containing the aperture, and the second is that outside the channel where the gas density in the so-called "gas cloud" eventually dies off to n_b. This background density n_b, present when gas is in the scattering chamber, is generally larger than the residual background density n_0, so that the third region

extends from the end of the cloud to the end of the beam path. The value of $\bar{n}_j$ for the last region is n_b, a measured quantity, while the values of $\bar{n}_j$ for the first two regions must be calculated.

Although investigations[33-35] have been reported on the net effusive flow through ducts of diverse geometries, there have been no calculations of the density distribution in flowing gases except for the case of ducts of negligible length.[36] The calculations of $\bar{n}_j$ are therefore approximate and there are no compelling reasons for selecting one approximation over another. All approximations start with the transmission factor of the channel, namely, the ratio of the effusive flow leaving the channel to that entering it. Since this factor only permits the density at the exit of the duct to be established, various arguments[37,38] must be used to deduce the density along the duct. The value obtained for $\bar{n}_j$ in the channel is fairly insensitive to the methods used to estimate the detailed density distribution.

The calculation of $\bar{n}_j$ in the "clouds" is also approximate, but the density there is so low that almost no error in α results. By assuming inverse square falloff at large distance and a simple exponential decrease at the start of the cloud, the density distribution and cloud length may be obtained and $\bar{n}_j$ evaluated for this region. An example of the magnitude of the total background correction is given in Table I. This

TABLE I

Background Scattering Corrections

Region	$\bar{n}_j/n_{sc}$	$\dfrac{x_{j+1}^{1+2/s} - x_j^{1+2/s}}{x_2^{1+2/s} - x_1^{1+2/s}}$	α_j
Upper background	0.0032	8.138	0.026
Upper cloud	0.0742	0.0480	0.004
Upper channel	0.8073	0.0975	0.079
Lower channel	0.2070	0.0813	0.017
Lower cloud	0.0138	0.0719	0.001
Lower background	0.0032	1.248	0.004

Total background correction $= 1 + \sum \alpha_j = 1.131$.

calculation was made for a helium beam scattered by helium gas, for which the potential parameter s was 4.98. The entrance (upper) channel

and exit (lower) channel were circular holes reamed with a 60° taper and oriented as in Figures 4*a* and 4*c*, respectively.

4. *Quantum Scattering*

The criterion[18] for the applicability of classical mechanics to scattering is twofold: (*a*) the uncertainty in the momentum must be small with respect to the total momentum, and (*b*) the uncertainty in the momentum must be small with respect to the change in momentum. Only part (*b*) need be considered here, for part (*a*) is usually quite readily met. The uncertainty in the momentum is given by $\hbar/2r_0$ and in terms of the relative angle θ_{dr}, the criterion for the applicability of classical mechanics becomes

$$\frac{\hbar}{2r_0\mu v_r\theta_{dr}} < 1 \tag{43}$$

If the beam and the detector are the same size, there are some points in the scattering volume where Eq. (43) cannot be satisfied. At the edge of the beam, for example, θ_{dr} is zero. A classical analysis cannot, therefore, be used throughout without introducing some error. This section will briefly investigate the magnitude of this error.

Figure 5 shows the general features of the classical differential cross section $G(\theta_r)$ and the quantum differential cross section $G_q(\theta_r)$. For θ_r greater than a critical angle θ_{cr}, the classical and quantum cross sections are essentially identical, but below $\theta_r = \theta_{cr}$ there are serious discrepancies. To account for these discrepancies, Eq. (6) should be rewritten as

$$\begin{aligned} S_p &= \int_0^{2\pi}\int_{\theta_{dr}}^{\theta_{cr}} G_q(\theta_r)\sin\theta_r\,d\theta_r\,d\phi + \int_0^{2\pi}\int_{\theta_{cr}}^{\pi} G(\theta_r)\sin\theta_r\,d\theta_r\,d\phi \\ &= \int_0^{2\pi}\int_{\theta_{dr}}^{\pi} G(\theta_r)\sin\theta_r\,d\theta_r\,d\phi - \int_0^{2\pi}\int_{\theta_{dr}}^{\theta_{cr}} G(\theta_r)\sin\theta_r\,d\theta_r\,d\phi \\ &\quad + \int_0^{2\pi}\int_{\theta_{dr}}^{\theta_{cr}} G_q(\theta_r)\sin\theta_r\,d\theta_r\,d\phi \end{aligned} \tag{44}$$

When this expression for the cross section is averaged over the scattering volume, the first term gives $\bar{S}_{sc}$. The volume average of the other two terms in Eq. (44) is very involved and tedious because each point in

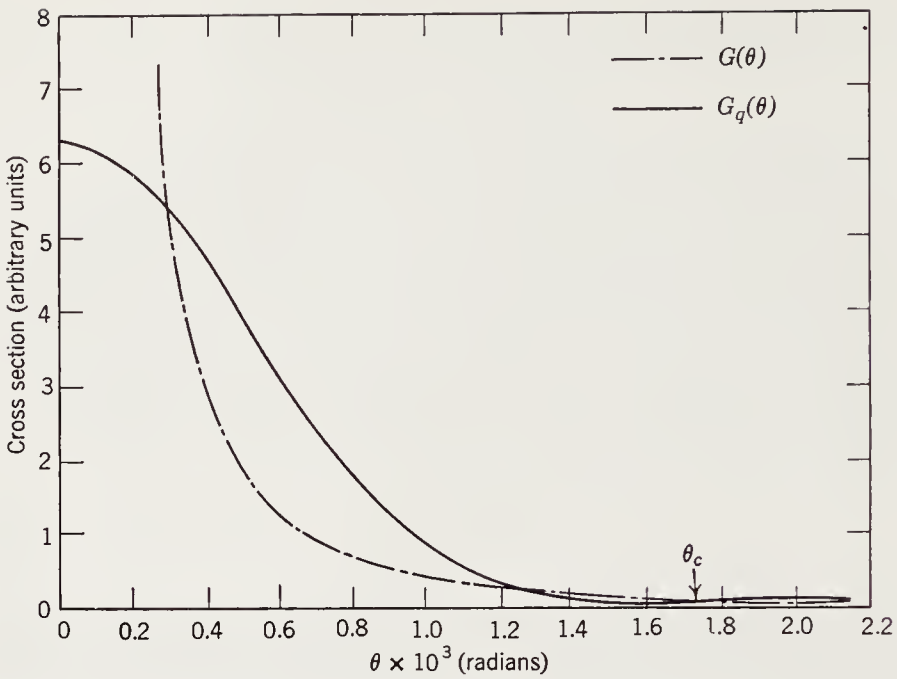

Fig. 5. The differential scattering cross section as a function of scattering angle in the region near $\theta = 0$.

the scattering volume is associated with a range of scattering angles (because the angle between the axis and each point on the detector edge must be considered). Some of these scattering angles may be larger than θ_{cr} and some smaller. The average can be performed, however, if a suitable expression for $G_q(\theta_r)$ is obtained. The calculation has been performed following the "quasiclassical" approach of Landau and Lifshitz.[39] For the cases investigated thus far, the net correction to the measured cross section is only a few per cent and is negative; i.e., applying the correction results in smaller potential energies. This arises from the fact that $G_q(\theta_r)$ is larger than $G(\theta_r)$ in a range of θ_r near θ_{cr}. Because the corrections are small, they are not normally applied to the experimental data.

5. *Inelastic Scattering*

The exact contribution of inelastic scattering to the attenuation of the beam cannot be determined at present. A simple approach will be outlined here, however, which will serve to estimate the error introduced from this source.

The cross section, S_i, for a specific inelastic transition is given by[40]

$$S_i = \int_0^{2\pi} \int_0^{\infty} P_{0i}(E_r,b) b \, db \, d\phi \tag{45}$$

where $P_{0i}(E_r,b)$ is the transition probability between the ground state and state i. Equation (45) is applicable to experiments which measure inelastic cross sections directly, but not to experiments which measure only beam losses. In the latter case, all those rays approaching the scattering center with impact parameters less than $b(\theta_{dr})$ are lost from the beam regardless of whether an inelastic transition occurs; the additional beam loss due to inelastic scattering arises only from those collisions in which the impact parameter is greater than $b(\theta_{dr})$. Thus the cross section for the total scattering beyond the detector becomes

$$S_p = \int_0^{2\pi} \int_0^{b(\theta_{dr})} b \, db \, d\phi + \sum_i \int_0^{2\pi} \int_{b(\theta_{dr})}^{\infty} P_{0i}(E_r,b) b \, db \, d\phi \tag{46}$$

where the sum over i indicates that all inelastic events must be considered in computing the beam losses. It is assumed in Eq. (46) that each inelastic event which occurs results in a deflection large enough for the ray to miss the detector. When this is not the case, the upper limit of infinity must be modified, but this detail will be omitted here.

It is not possible to evaluate Eq. (46) exactly. Although theoretical calculations of $P_{0i}(E_r,b)$ are extremely difficult even for simple cases, and the results in general not reliable enough for the calculation of a correction, they do serve to confirm the expected qualitative behavior of $P_{0i}(E_r,b)$; namely, the transition probability is found to fall off sharply as b increases.[41,42]

The contribution of inelastic scattering to total scattering can be estimated empirically by using experimental values for S_i. Suitable experiments in the energy range of interest are extremely difficult to perform, but measurements of cross sections for ionization (which should be the principal inelastic event in the measurements of present interest) are reported for a few systems. It is found that the ionization cross sections are about 5–20% of the elastic cross sections, and according to Eq. (46) their contribution to the total scattering will be substantially less than that amount. The actual contribution may be estimated as follows.

The ionization probability P_{0i} is represented by the simple function $P_{0i}=e^{-ab}$; all other inelastic processes are omitted. This expression

for P_{0i} is substituted into Eq. (45), the integration is performed, and when the result is set equal to the experimental value of S_i, the parameter a is found to be equal to $\sqrt{2\pi/S_i}$. When the expression for P_{0i}, normalized in this way, is then substituted into Eq. (46), the result is

$$S_p = \frac{1}{2}\int_0^{2\pi} [b(\theta_{dr})]^2 \, d\phi + S_i\{\exp[-b(\theta_{dr})\sqrt{2\pi/S_i}][b(\theta_{dr})\sqrt{2\pi/S_i} + 1]\} \quad (47)$$

The total cross section can be written after volume averaging as

$$\begin{aligned} S_{\text{total}} &= \bar{S}_{\text{sc}}\left\{1 + \frac{S_i}{\bar{S}_{\text{sc}}}\langle\exp[-b(\theta_d)\sqrt{2\pi/S_i}][b(\theta_d)\sqrt{2\pi/S_i} + 1]\rangle_V\right\} \\ &= \bar{S}_{\text{sc}}(1 + \langle f\rangle_V) \end{aligned} \quad (48)$$

Although the value of f calculated from Eq. (48) depends on the function chosen for P_{0i}, it was found that several functions other than the exponential could be used without changing the value of f significantly. It is not expected that $\langle f\rangle_V$ would differ markedly from f and in view of the approximations used, the rather formidable task of volume averaging is not carried out. An estimate of the size of the correction for inelastic scattering can nonetheless be obtained from Table II, where values of f are listed for several actual systems. When ionization cross

TABLE II

Corrections for Inelastic Scattering[a]

System	Energy (V)	$\bar{S}_{\text{sc}}$ (Å^2)	S_i (Å^2)	f	Ref.
He–He	500	4.54	0.04	0.000	26,43
	1500	2.93	0.13	0.000	
He–He	500	2.32	0.04	0.002	17,43
	1500	1.05	0.13	0.012	
He–Ar	500	14.44	0.62*	0.000	29,44
	1500	10.79	0.92*	0.004	
Ar–He	500	12.52	0.00	0.000	29,44
	1500	9.32	0.02*	0.000	
Ar–Ar	500	9.87	1.05*	0.008	17,44
	1500	8.27	2.03*	0.054	

[a] Values of S_i marked with an asterisk are calculated by multiplying the ion–atom ionization cross sections from the reference by 0.7.

sections for neutral particles were unavailable, they were estimated from the corresponding ion–neutral cross sections which are usually found to be about 30% higher than neutral–neutral cross sections.[45] The only appreciable value of f in Table II is that for the argon–argon system, but even here the correction for inelastic scattering is only comparable to the uncertainties from all other sources. Because the correction is so small it is not usually applied.

IV. EXPERIMENTAL

A. Typical Apparatus

The apparatus in which total elastic cross sections are measured can assume a variety of forms depending upon the nature of the ion source, the type of detector, details of the charge transfer, and the structure of the chamber in which scattering occurs. An apparatus[26] whose essential features are shown in block diagram in Figure 6 has been used successfully over a long period. Many of these features are common to all such units, although variations of the fundamental design have been introduced into several other apparatus.

The central part of the apparatus is shown in detail in Figure 7. A low-voltage discharge is maintained at about 0.1 mm pressure between the grounded oxide-coated filament, *1*, and the copper anode, *2*. The copper cathode, *3*, at a negative potential between 0 and 100 V, extracts ions from the discharge and those which drift to the hole in the bottom of the cathode are focused by a hemispherical screen onto the aluminum accelerating electrode, *4*, whose negative potential may be varied between 150 and 2000 V. Some of the positive ions which pass through the 0.5-mm diameter hole in this electrode are converted to high-velocity neutrals by charge transfer and the balance are deflected by a potential difference of about 1000 V across the plates of a condenser *5*. Vycor and Mycalex rings and cylinders are used throughout for insulation and support.

The high-velocity neutral beam enters a narrow scattering chamber, *6*, which localizes the scattering gas. The entrance to the scattering chamber serves as the second beam collimator; this is a 0.5-mm hole in a plate 0.80 mm thick, relieved with a 60° countersink. The bottom plate of the chamber contains the beam exit hole, whose construction is similar to the entrance hole, and a cylindrical nozzle which supports a vane used to intercept the beam.

A $\frac{1}{4}$-in. copper tube, *7*, connects the scattering chamber through a valve to a diffusion pump, or, when a valve is shut, to a McLeod gage.

Gas is introduced into the scattering chamber through a $\frac{1}{16}$-in. tube, *8*, suspended coaxially in the $\frac{1}{4}$-in. tube. The temperature of the scattering gas is measured with a thermocouple attached to the scattering chamber. The scattering pressure is measured with a Pirani gage which is attached to the bottom plate of the chamber and calibrated against a McLeod gage. Thermal detectors of various types are used to measure the beam intensities. Additional details of the Pirani gage and the thermal detectors will be given.

The apparatus, including its 4-in. diffusion pump, is of all-metal construction. Suitably located McLeod gages, ionization gages, and thermocouple gages monitor the pressure in the arc region and the background pressure.

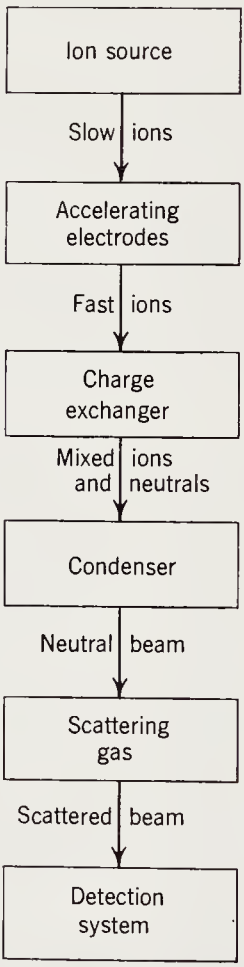

Fig. 6. Block diagram of a scattering apparatus.

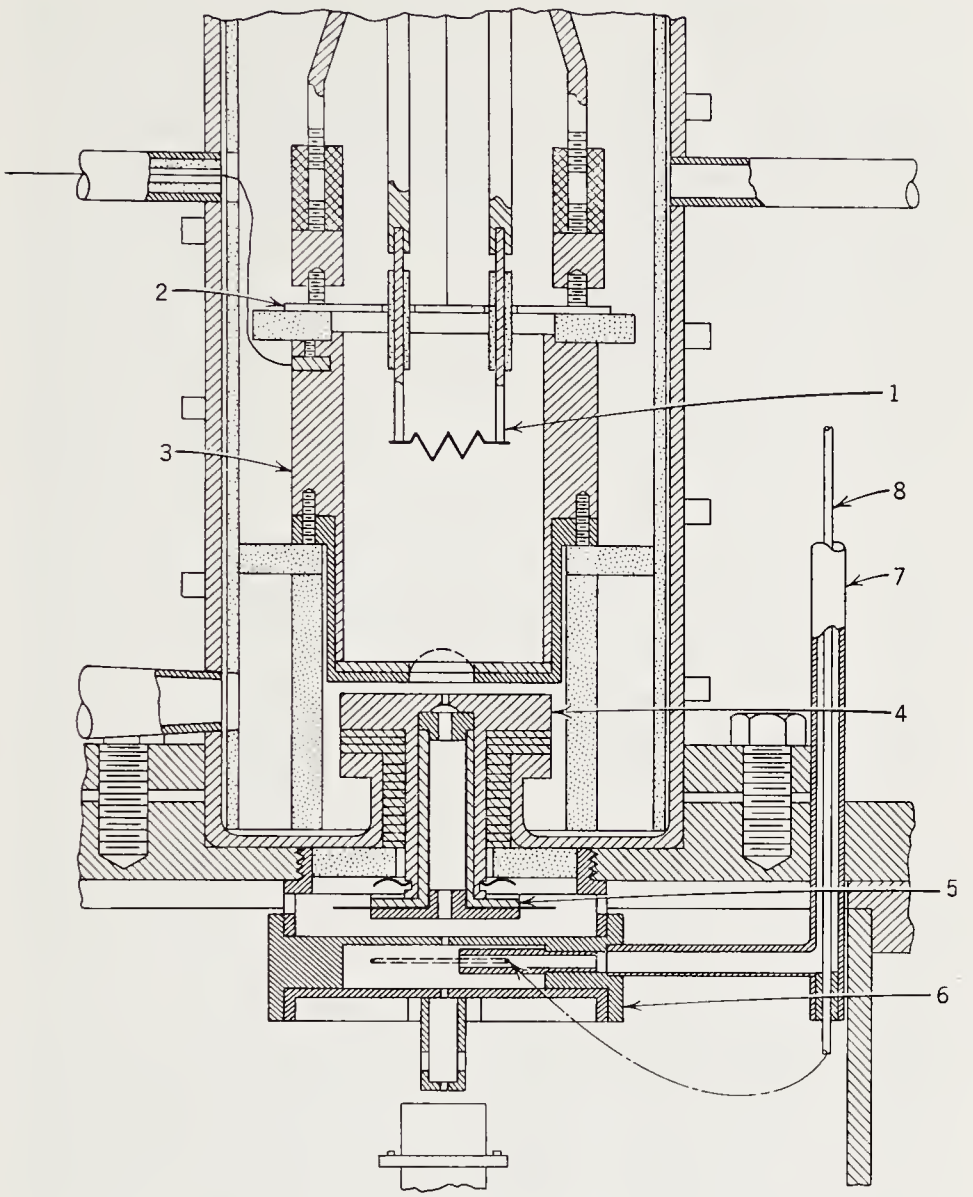

Fig. 7. Details of apparatus.

B. Modifications

A rather different ion source is in operation in another apparatus.[46] In this source, gas at a few microns pressure is admitted into a copper cylinder about 3 in. long and $\frac{1}{2}$ in. in diameter along whose axis there

is a magnetic field of several hundred gauss. Electrons from a tungsten filament are constrained by this field to follow helical paths along the axis, while negative electrodes on each end of the cylinder reflect the electrons back along the axis so that each electron has a long free path and a correspondingly higher ionization probability. In this way the discharge can be maintained at a much lower pressure than is possible without the magnetic field. The ions which are formed are extracted at one end of the cylinder with the same electrode that reflects the electrons and are accelerated to the desired energy in a region of low pressure. This is done to reduce charge transfer during the acceleration, since such premature neutralization would produce a neutral beam with a broad range of energy. The actual energy spread is determined from retarding potential analysis before the ions enter a separate chamber (similar to the scattering chamber) where charge exchange takes place. The spread has been found to be about ± 10 V, and since there is essentially no energy change during the resonant charge transfer, the neutral beam may be assumed to have the same energy distribution. In the apparatus in Figure 7, it is not possible to determine the neutral energy distribution with any accuracy, although it is certain that the average neutral beam energy is somewhat less than that corresponding to the accelerating voltage. It is not expected to be much lower, however, because slow neutrals formed by charge transfer early in the acceleration path have large scattering cross sections and are therefore likely to be scattered before reaching the scattering chamber. A small error in the beam energy produces an error of the same magnitude and direction in the potential parameter K.

It has been indicated that in the cases of interest here, resonant charge transfer is utilized, i.e., the ions are neutralized in a gas with the same ionization potential. Resonant charge transfer cross sections are appreciably higher than nonresonant cross sections, so that impurity ions extracted from the ion source are less likely to be neutralized. Furthermore, the deflection angle, γ, in a charge transfer collision of an ion of mass M and energy E is given approximately by[47]

$$\gamma = \tfrac{1}{2}(\Delta E/E - m/M) \tag{49}$$

where ΔE is the absolute difference in ionization potentials of the two particles and m is the electron mass. Impurity ions or excited metastable ions are therefore deflected more than resonant ions in charge transfer. The geometry of the apparatus assures that neutralized metastables

and impurities will be removed from the beam. (Thermal metastable atoms drifting out of the ion source produce a negligible signal on the detector.)

A variety of gages have been used to measure the scattering gas pressure. These include McLeod gages with specially constructed nozzles extending into the scattering chamber, specially constructed thermocouple gages capable of good accuracy, and Pirani gages. Of these, the Pirani gages have been most satisfactory. They are made of fine platinum wire, mounted inside the scattering chamber and incorporated into a sensitive bridge so that they operate only 2–4° above ambient temperature. The temperature of the scattering gas is therefore not raised appreciably. They are calibrated in place against a McLeod gage under both static and dynamic conditions. (The gas flow out of the chamber is small enough to prevent "anemometer" effects in the gage.) Comparison of the static and dynamic calibrations shows that significant pressure differences can exist between the scattering chamber and an external gage when gas is flowing through the chamber. These differences appear to be extremely sensitive to the dimensions of the nozzle in the chamber which leads to the external gage. An additional advantage of the internal Pirani gage is the rapidity with which it responds to changes in pressure, for example, in the measurement of unscattered and scattered intensities.

Several kinds of thermal detectors have been used to measure beam intensities. These detectors measure the total energy flux in the beam rather than the particle flux itself, but if the beam energy is known, the particle flux may be calculated. In the present case, since only flux ratios are required, the detector design may take a particularly simple form. (For accurate determination of the absolute flux, some sort of reentrant construction would have to be used to assure that the accommodation coefficient on the receiver is unity.) A single junction thermocouple with a flat receiver soldered to the junction,[48] or a multijunction thermopile[49] may be used. These detectors are usually masked with a hole the size of the beam or smaller. In cases where it has been necessary to probe the intensity distribution at the detector plane detector, masks with slits as narrow as 0.001 in. have been used.[46] For even greater resolution, the difficulty of constructing narrow slits has been circumvented by butt-welding a thermocouple from 0.0005-in. wires.[38] Such thermal detectors have sensitivities between 1 and 10 V/W. Their output is fed to a galvanometer whose motion deflects a light beam

and thereby produces an imbalance in the output of two photocells; the resulting differential current is amplified and displayed on a recorder.[50]

Recently, a commercially available thermistor bolometer[51] has been used as a detector. The short time constant of this bolometer allows the beam to be modulated and permits the substitution of a.-c. electronics for the less flexible d.-c. galvanometer arrangement. The mounting of a mechanical chopper, preamplifier, and lamp and photocell (for generating a phasing signal) have created little difficulty.

The use of thermal detectors for high-energy beams has several unique advantages. They are mechanically strong, in most cases not difficult to make, and their outputs are relatively easy to detect. Probably their most important advantage is their insensitivity to background gas. The background gas from the scattering chamber and ion source may be present in quantities far greater than the beam flux, but since this background gas is essentially at thermal energy the detector does not indicate its presence. For example, because fast neutral beams are difficult to ionize efficiently in an ionizing detector, very elaborate beam modulation would be necessary in order to observe the beam signal above the background gas ionization; the special properties of the thermal detector for fast neutral beams avoids these problems.

V. RESULTS

Cross sections obtained in a typical set of measurements[26] are shown in Figure 8 as a function of beam energy. These are total scattering cross sections for a helium beam scattered by helium and were obtained in two separate investigations carried out in essentially the same apparatus. The solid curves were obtained by fitting a straight line to a plot of $\log \bar{S}_{sc}$ vs. $\log E$ by the method of least squares. The average absolute deviation of the points from the curve is 3.1% in Series I and 1.5% in Series II. The value of $1+\alpha$, the correction for background scattering, was 1.197 for Series I and 1.144 for Series II.

The potential functions obtained from the two sets of data differ by only 10% and their average is given by

$$V(r) = 3.47/r^{5.03} \text{ eV} \qquad (0.97 \text{ Å} < r < 1.48 \text{ Å}) \tag{50}$$

The curve calculated from Eq. (49) is shown in Figure 9 (curve *A*) along with some results for other investigations.

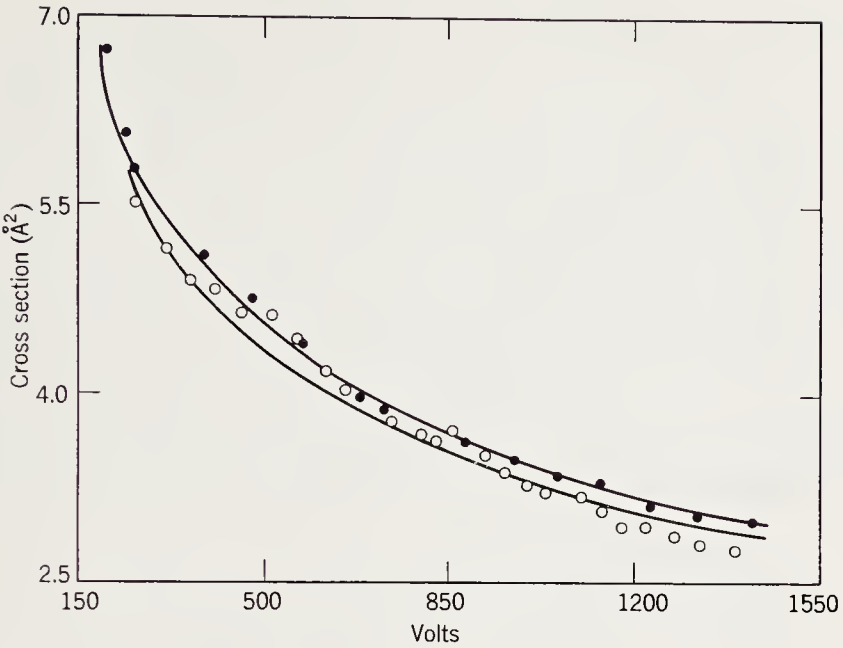

Fig. 8. Total collision cross sections. Open circles, Series I; closed circles, Series II.

An extensive critical compilation of potential functions which have been experimentally determined from scattering has recently been published.[10] Therefore, only those functions which have been reported since that tabulation was published are listed in Table III, which also includes several molecule–molecule potentials which have been derived from the experimental atom–molecule potential functions. The potential function listed for helium–helium was not determined in the usual manner because the system is one for which the potential energy could not be represented over the whole range of r by a single set of parameters, K and s. It was therefore necessary to obtain the potential as a function of distance by using different sets of K and s in successive portions of the range. The function shown in Table III was then used to represent the results with an average deviation of 1.6% and maximum deviation of 4.2%.

Because of the scarcity of independent results with which to compare potentials obtained from the scattering of high-velocity beams, it is difficult to assess directly the reliability of these potentials. As a minimum requirement the potentials must be self-consistent; that is, they must be reproducible. Although, regrettably, virtually all the experimental results have been obtained in a single laboratory, this reproducibility has been repeatedly checked with respect to results in a

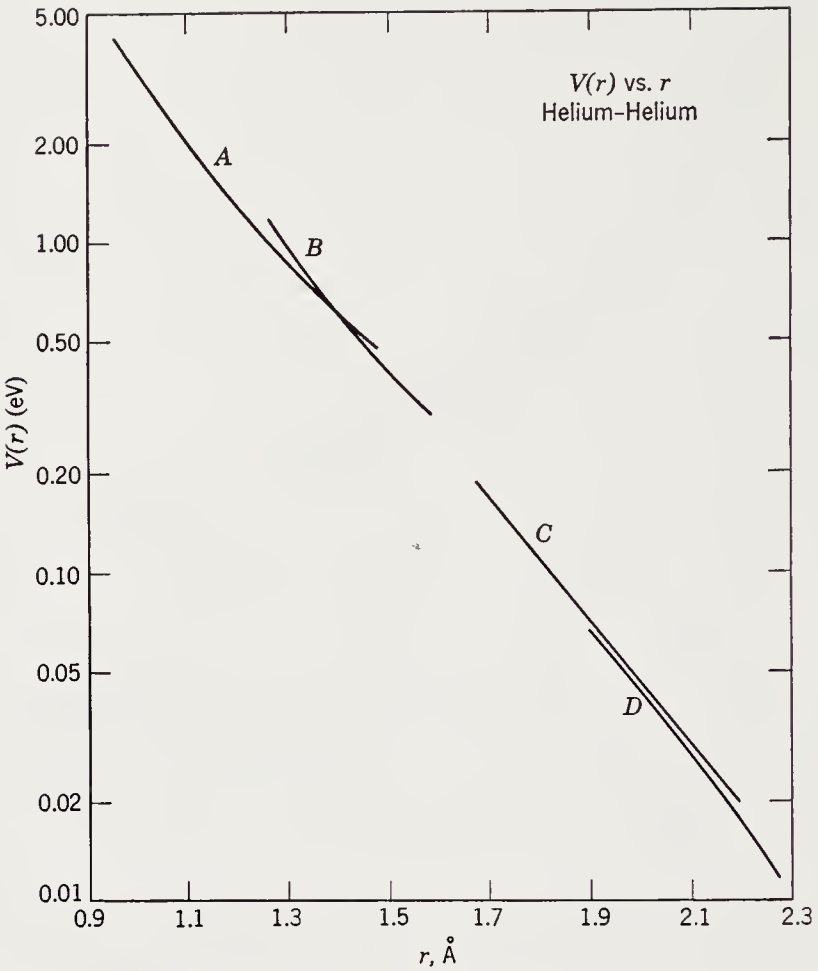

Fig. 9. Helium–helium potential energy vs. distance. Curve *A* (ref. 26) and curve *B* (ref. 19) are obtained from scattering measurements. Curve *C* (ref. 55) is obtained from an analysis of high-temperature thermal conductivity measurements. Curve *D* (ref. 70) is obtained from an analysis of compressibility and viscosity data.

given apparatus. For a specified beam-detector geometry, cross sections measured over wide ranges of conditions in the ion source and over ranges of scattering pressure where only single collisions occur, have an average reproducibility of about 2%. It has also been possible by using apparatus having different types of beam-detector geometry, to obtain potentials for several systems in ranges of separation distance which overlap to some degree. The reproducibility in these cases is comparable to that associated with a single apparatus.

The scattering of helium by helium has been studied more than

that of any other system and has yielded potentials for internuclear separations between 0.52 and 1.59 Å. In addition, there have been many theoretical studies of this potential, so that this system is one which is well suited for critical examination and comparison. At distances greater than about 1 Å there is good agreement between the scattering results and the best quantum-mechanical calculations based on solutions of the Schrödinger equation. Experimental measurements of the thermal conductivity of helium up to 2100°K[55] lead to a potential which almost overlaps the terminal portion of the scattering potential. For r greater than 1 Å the character of the agreement of the potentials obtained from various sources is shown in Figure 9.

Estimates of the errors introduced into the potential from the use of classical mechanics and by the presence of inelastic scattering have been

TABLE III

Summary of Additional Experimental Results

System	Potential function (eV)	Range (Å)	Reference
	A. Atom–Molecule Potentials		
He–He	$\exp(1.07/r)/r$	0.52–0.98	17
Ar–Ar	$386/r^{6.97}$	1.57–2.00	17
Ar–Ar	$3250/r^{9.97}$	1.98–2.41	52,53
Ar–O_2	$1360/r^{8.34}$	2.01–2.50	52,53
Ar–H_2	$159/r^{6.28}$	1.81–2.36	53
Ar–He	$22.2/r^{5.42}$	1.40–1.81	52
Ar–N_2	$567/r^{7.06}$	2.04–2.53	53
Ar–CO	$551/r^{6.99}$	2.09–2.68	53
He–CH_4	$602/r^{9.43}$	1.92–2.37	28
He–CF_4	$6.18 \times 10^6/r^{17.51}$	2.43–2.74	28
He–CH_3F	$386/r^{8.34}$	2.00–2.47	54
He–CH_2F_2	$3.88 \times 10^4/r^{13.33}$	2.22–2.58	54
He–CHF_3	$4.06 \times 10^5/r^{15.43}$	2.33–2.63	54
	B. Molecule–Molecule Potentials		
CH_4–CH_4	$5.64 \times 10^6/r^{15.47}$	2.47–3.06	28
CF_4–CF_4	$1.17 \times 10^{22}/r^{39.27}$	3.43–3.77	28
CH_3F–CH_3F	$1.72 \times 10^{10}/r^{19.61}$	3.41–4.01	54
CH_2F_2–CH_2F_2	$1.14 \times 10^{13}/r^{24.71}$	3.33–3.93	54
CHF_3–CHF_3	$9.11 \times 10^{19}/r^{32.85}$	3.46–3.88	54

discussed in Section II. For the helium system the combined error from both sources might lower the scattering potentials in Figure 9 by 5–10%. The effect of metastable particles in the beam can be shown to have a negligible effect.

As the internuclear separation between two He atoms decreases from 1 to 0.52 Å, there is a marked difference between the potential determined from scattering and that obtained from the best theoretical calculation to date. For example, at 0.52 Å the most recent experimental value is more than 10 eV lower than the theoretical value. There are three possible causes for the discrepancy: (*1*) errors in the experimental measurements or in their analysis; (*2*) increased importance of deviations from the Born-Oppenheimer approximation at higher beam energies and the associated smaller internuclear separations and (*3*) need for still further refinement of the theoretical calculations. It seems unlikely that the first cause is a significant factor in view of the reproducibility and self-consistency of the results above 1 Å and the good agreement of these results with theory and measured transport properties. In addition, as shown earlier, quantum elastic scattering, inelastic scattering, and metastable beam particles cannot alter the reported potentials by more than a relatively few per cent. As the result of an approximate quantum-mechanical calculation, Thorson[56] has suggested that part of the apparent discrepancy at 0.52 Å may be caused by failure of the Born-Oppenheimer approximation and that the nonadiabatic potential obtained from scattering measurements should not be compared with adiabatic potentials calculated from theory except in cases where such nonadiabatic effects can be shown to be small. Thorson's results indicate that no significant discrepancy would be expected for the potentials shown in Figure 9. Finally, it is not yet completely certain that the very careful recent theoretical calculations, such as those of Phillipson,[2] yield potentials at the smaller separation distances which are within an electron volt or less of the true adiabatic value. Although increasing the number of configurations in the original wave function from 13 to 64 decreases the final potential by only 1 eV, it is possible that the convergence is extremely slow and that very many more terms may be required to obtain the correct value. The authors feel that at least a partial answer to the dilemma may be obtained by an experimental approach to the question of the importance of the partial breakdown of the Born-Oppenheimer approximation. Experiments will therefore be made on the elastic scattering of ^{3}He by ^{3}He under

conditions identical to those used for ^{4}He. If the nuclear motion of the system is indeed important at the higher energies and smaller separations, the ^{3}He–^{3}He potential should be lower than that obtained for ^{4}He–^{4}He by a very substantial amount, between 30 and 40%.

Intermolecular potentials for other systems have not been studied as extensively as that for He–He. Theoretical calculations of a statistical nature based on the Thomas-Fermi-Dirac method have been made for the symmetrical rare-gas systems.[5] It is difficult to estimate the accuracy of these calculations except by comparing the results with the quantum-mechanical calculation for He–He and with experimental potentials. For this reason the scattering experiments, which yield potentials which agree within at least a factor of 2 with the corresponding theoretical values, are useful in assessing the reliability of the calculated results, but the inverse comparison throws little light on the reliability of the scattering results. There are, however, several instances where transport properties measured at very high temperatures have yielded potentials whose ranges of validity lie very near or actually overlap those of the scattering potentials. In addition to the measurements of the thermal conductivity of helium previously mentioned,[55] measurements of the mutual diffusion coefficients of He–N_2 up to 1150°K and of He–Ar up to 1100°K have been reported.[57–59] In both cases the potentials derived from the diffusion measurements are in very good agreement with the corresponding results from scattering.[27,29]

Detailed analysis of the various features of the actual scattering experiments, the self-consistency of the derived potentials, and direct comparison of these potentials with those obtained by other means, lead to the definite conclusion that such scattering potentials are, in the vast majority of cases, reliable adiabatic potentials. They are accurate to within 20% in most instances. The exceptions are listed in Tables II and III of reference 10. The potentials reported from the present authors' laboratory prior to 1951 should all be considered unreliable because they were derived from measurements made in an apparatus which, by present standards, must be considered quite primitive. Several systems in this category have been reinvestigated with modified apparatus capable of yielding reliable potentials. However, the He–He potential, recently redetermined, may not be a satisfactory adiabatic potential in the neighborhood of 0.5 Å if future investigation should show that it is seriously velocity dependent in this region.

It is important, in investigating the reliability of potentials obtained from the scattering of high-velocity neutral beams, to avoid extrapolation of theoretical or experimental potentials beyond their known range of validity. Because of the extreme rapidity with which the repulsive potential changes with internuclear separation, such extrapolations are often in serious error.[1] In fact, the absence of such error can only be regarded as an unpredictable, fortuitous coincidence. When, however, there is a small gap between the terminal portion of the potential in one region of interaction distance and the initial portion of the potential in a neighboring region, the unexplored region can be unambiguously determined by interpolation if the two portions of the potential are self-consistent. A situation of this type is well illustrated in Figure 9.

VI. APPLICATIONS

The rapidly increasing interest in the physics and chemistry of the upper atmosphere, combustion, detonation, and high-speed gas dynamics has focused attention on the lack of suitable information concerning equilibrium and gaseous transport properties at high temperatures. Since direct measurements of such properties above about 1000°K are rare, and since extrapolations from low-temperature measurements are almost certain to be in considerable error, accurate calculations of the properties are highly desirable. In general, a satisfactory calculation procedure requires that the actual species present at the densities of interest be known, a suitable formal kinetic theory or statistical mechanical theory exist, and quantitative information be available concerning the potentials of such species in the ranges of internuclear separation of importance at elevated temperatures. Potentials such as those in Table III and in the tabulation of Mason and Vanderslice[10] have been used to calculate virial coefficients of the equation of state and transport properties for the rare gases and molecular nitrogen from 1000 to 15,000°K, and to illustrate the procedure for binary mixtures.[60] Since the potentials were limited to ground-state species, effects of excitation, dissociation, and ionization were not taken into account. Using additional appropriate potential-energy information obtained from sources other than scattering, Vanderslice and co-workers[32] have calculated transport properties of hydrogen and its dissociation products from 1000 to 15,000°K and the

transport properties of air from 1000 to 10,000°K, taking into account atomic species of nitrogen and oxygen.[61,62]

Calculations such as those described above are of sufficient theoretical and practical importance to suggest desirable future extensions of scattering experiments to obtain directly the potential-energy information needed for systems containing excited, dissociated, or ionized species. Potentials for ion–atom or ion–molecule systems are relatively easy to obtain, since ion beams of high intensity in the desired energy range are not difficult to produce, and detection is simpler than for high-energy neutral particles. Additional experiments such as those of Bailey, Muschlitz, Simons, and co-workers,[63] with tractable beam-detector geometry, would be of considerable value. Potentials involving reactive atomic species can be obtained from the scattering of atomic beams of particles such as hydrogen, oxygen, or nitrogen, by similar atomic species or by stable atoms or molecules. For example, beams of high-velocity hydrogen atoms can be produced by selecting the H^+ ions from an accelerated beam containing H^+, H_2^+, and H_3^+, and then neutralizing the pure proton beam. Experiments of this type in which beams of H, N, and O will be produced are in progress in the authors' laboratory. The direct determination of interactions involving excited species poses the most difficult problem. Two approaches seem possible. The first is applicable only to metastable species and involves the scattering of a mixture of ground-state and metastable particles, or if possible, only metastable particles. The method is seriously limited by the difficulty of obtaining sufficiently high intensities of metastable atoms or molecules and by the small number of such species which have sufficiently long lifetimes (greater than about a microsecond) to permit their extraction from the source and their traverse through the scattering chamber before deexcitation occurs. The second approach involves the scattering of stable ground-state particles such as helium or argon, or of ground-state reactive atomic species such as H, through scattering gas which contains known concentrations of excited, dissociated, or ionized species. Scattering gas of this type could be obtained in some cases by suitable temperature control, in others by radiation with light of known intensity and spectral character, and in still others by suitable electric discharge.

In addition to the calculation of high-temperature equilibrium and transport properties of gases, a knowledge of the potential at interaction distances where repulsive forces are dominant is required for the

calculation of vibrational relaxation times of molecules and for properties, such as the dispersion of sound, in which such relaxation phenomena are important.[64,65] Since interactions at close distances are also important in determining molecular structure, Mason and Kreevoy have made use of rare-gas potentials from scattering to estimate magnitudes of energy barriers to intramolecular rotation,[66,67] and Hendrickson has used similar potential-energy information in investigating the stability of conformations in organic systems.[68] A somewhat unusual application to molecular structure has been made in the calculation of the properties of solid and gaseous alkali halides.[69] For example, the Ar–Ar potential has been used as a starting point for obtaining the lattice distance, heat of sublimation, and compressibility of KCl (solid) at 0°K as well as the internuclear separation, heat of dissociation, and vibrational frequency of KCl (gas). Similar calculations have been made for CsI (solid) and CsI (gas) starting with the Xe–Xe potential. For both systems, agreement with experiment is very good. Finally, it would appear that the exchange of kinetic energy or linear momentum between high-velocity gas particles and solid surfaces must depend upon close-distance interactions between the particles of the gas and those of the solid for a gas-free surface, or between the particles of the free gas and those of adsorbed gas if the solid surface is not gas free. Thus, any theoretical calculations of accommodation coefficients for energy or momentum for systems involving high-velocity particles will be concerned with short-range repulsive potentials.

VII. SUMMARY

The elastic scattering of high-velocity neutral beams has been discussed in detail with particular emphasis on the determination of intermolecular potentials at small separation distances. The following points were stressed:

1. Proper interpretation of the results of such scattering experiments must take account of the finite size of the beam, the beam-detector geometry, background scattering, quantum elastic scattering, inelastic scattering, and the possible effect of nuclear motion on the potential.

2. Requirements imposed by the above factors rather sharply determine the nature of the scattering apparatus and the ranges of beam energy, scattering angle, and potential energy.

3. Adiabatic repulsive potentials between neutral particles have

been obtained for a large number of systems from measurements of total cross sections as a function of energy. These potentials are reliable in the majority of cases as judged by their internal consistency and their agreement with results in several instances by independent methods.

4. Information concerning potentials at small separation distances is required for a variety of problems including the calculation of equilibrium and transport properties of gases at elevated temperatures, the determination of the stability of various possible configurations of organic molecules, and the details of the relaxation between translational and vibrational degrees of freedom.

In view of the fundamental importance of a knowledge of the magnitudes of molecular interactions and the wide applicability of the results of the experiments, it is important that the study of the elastic scattering of molecular beams be continued and extended, preferably in a number of independent laboratories.

Acknowledgment

The authors wish to thank the United States Office of Naval Research for support of their work.

References

1. I. Amdur and J. Ross, *Combust. Flame*, **2**, 412 (1958).
2. P. E. Phillipson, *Phys. Rev.*, **125**, 1981 (1962), and references to early work on He–He contained therein.
3. E. A. Mason, J. Ross, and P. N. Schatz, *J. Chem. Phys.*, **25**, 626 (1956).
4. W. Kolos and C. C. J. Roothan, *Rev. Mod. Phys.*, **32**, 219 (1960), and references to early work on H–H contained therein.
5. A. A. Abrahamson, *Phys. Rev.*, **130**, 693 (1963).
6. J. T. Vanderslice, E. A. Mason, and E. R. Lippincott, *J. Chem. Phys.*, **30**, 129 (1959).
7. J. T. Vanderslice, E. A. Mason, and W. G. Maisch, *J. Chem. Phys.*, **31**, 738 (1959).
8. J. T. Vanderslice, E. A. Mason, and W. G. Maisch, *J. Chem. Phys.*, **32**, 515 (1960).
9. J. T. Vanderslice, E. A. Mason, W. G. Maisch, and E. R. Lippincott, *J. Chem. Phys.*, **33**, 614 (1960).
10. E. A. Mason and J. T. Vanderslice, in D. R. Bates, Ed., *Atomic and Molecular Processes*, Academic Press, New York, 1962, Chap. 17.
11. I. Amdur and H. Pearlman, *J. Chem. Phys.*, **9**, 503 (1941).
12. I. Amdur, *J. Chem. Phys.*, **11**, 157 (1943).
13. E. A. Mason and J. T. Vanderslice, *J. Chem. Phys.*, **27**, 917 (1957).
14. R. B. Bernstein, *J. Chem. Phys.*, **38**, 515 (1963).

15. E. Everhart, G. Stone, and R. J. Carbone, *Phys. Rev.*, **99**, 1287 (1955), and subsequent papers by Everhart and co-workers.
16. I. Amdur, *J. Chem. Phys.*, **17**, 844 (1949).
17. I. Amdur, J. E. Jordan, and R. R. Bertrand, in M. R. C. McDowell, ed., *Atomic Collision Processes*, North-Holland Publishing Co., Amsterdam, 1964.
18. D. Bohm, *Quantum Theory*, Prentice-Hall, Englewood Cliffs, N. J., 1951.
19. I. Amdur and A. L. Harkness, *J. Chem. Phys.*, **22**, 664 (1954).
20. P. Kusch, *J. Chem Phys.*, **40**, 1 (1964).
21. F. C. Hoyt, *Phys. Rev.*, **55**, 664 (1939).
22. O. B. Firsov, *J. Exptl. Theoret. Phys.* (*USSR*), **24**, 279 (1953).
23. J. B. Keller, I. Kay, and J. Schmoys, *Phys. Rev.*, **102**, 557 (1956).
24. E. H. Kennard, *Kinetic Theory of Gases*, McGraw-Hill, New York, 1938.
25. M. C. Kells, *J. Chem. Phys.*, **16**, 1174 (1948).
26. I. Amdur, J. E. Jordan, and S. O. Colgate, *J. Chem. Phys.*, **34**, 1525 (1961).
27. I. Amdur, E. A. Mason, and J. E. Jordan, *J. Chem. Phys.*, **27**, 527 (1957).
28. I. Amdur, M. S. Longmire, and E. A. Mason, *J. Chem. Phys.*, **35**, 895 (1961).
29. I. Amdur, E. A. Mason, and A. L. Harkness, *J. Chem. Phys.*, **22**, 1071 (1954).
30. I. Amdur and E. A. Mason, *J. Chem. Phys.*, **25**, 632 (1956).
31. O. Sinanôglu, *J. Chem. Phys.*, **30**, 850 (1959).
32. J. T. Vanderslice, S. Weissman, E. A. Mason, and R. J. Fallon, *Phys. Fluids*, **5**, 155 (1962).
33. P. Clausing, *Ann. Physik*, **12**, 961 (1932).
34. D. H. Davis, L. L. Levenson, and N. Milleron, in L. Talbot, Ed., *Rarefied Gas Dynamics*, Academic Press, New York, 1961.
35. R. P. Iczkowski, J. L. Margrave, and S. M. Robinson, *J. Phys. Chem.*, **67**, 229 (1963).
36. W. M. Howard, *Phys. Fluids*, **4**, 521 (1961).
37. S. Rosin and I. I. Rabi, *Phys. Rev.*, **48**, 373 (1935).
38. I. Amdur, C. F. Glick, and H. Pearlman, *Proc. Am. Acad. Arts Sci.*, **76**, 101 (1948).
39. L. D. Landau and E. M. Lifshitz, *Quantum Mechanics*, Addison-Wesley, Reading, Mass., 1958.
40. H. S. W. Massey and E. H. S. Burhop, *Electronic and Ionic Impact Phenomena*, The Clarendon Press, Oxford, 1952.
41. D. R. Bates, *Proc. Roy. Soc.* (*London*), **A245**, 299 (1958).
42. M. H. Mittleman, *Phys. Rev.*, **122**, 499 (1961).
43. N. G. Utterback, in M. R. C. McDowell, ed., *Atomic Collision Processes*, North-Holland Publishing Co., Amsterdam, 1964.
44. H. B. Gilbody and J. B. Hasted, *Proc. Roy. Soc.* (*London*), **A240**, 382 (1957).
45. T. J. M. Sluyter, J. Kistemaker, and E. deHaas, *Physica*, **25**, 1376 (1959).
46. I. Amdur and J. E. Jordan, to be published.
47. S. K. Allison, J. Cuevas, and M. Garcia-Munoz, *Phys. Rev.*, **120**, 1266 (1960).
48. I. Amdur and H. Pearlman, *Rev. Sci. Instr.*, **10**, 174 (1939).
49. L. Harris, *J. Opt. Soc. Am.*, **36**, 597 (1946).
50. I. Amdur, *Rev. Sci. Instr.*, **9**, 194 (1938).
51. Barnes Engineering Company, Stamford, Connecticut.
52. S. O. Colgate, Ph.D. thesis, Massachusetts Institute of Technology, 1959.

53. J. E. Jordan, Ph.D. thesis, Massachusetts Institute of Technology, 1958.
54. M. S. Longmire, Ph.D. thesis, Massachusetts Institute of Technology, 1961.
55. N. C. Blais and J. B. Mann, *J. Chem. Phys.*, **32**, 1459 (1960).
56. W. R. Thorson, *J. Chem. Phys.*, **39**, 1431 (1963).
57. R. E. Walker and A. A. Westenberg, *J. Chem. Phys.*, **31**, 519 (1959).
58. R. E. Walker and A. A. Westenberg, *J. Chem. Phys.*, **29**, 1139 (1958).
59. R. E. Walker and A. A. Westenberg, *J. Chem. Phys.*, **29**, 1147 (1958).
60. I. Amdur and E. A. Mason, *Phys. Fluids*, **1**, 370 (1958).
61. K. S. Yun and E. A. Mason, *Phys. Fluids*, **5**, 381 (1962).
62. K. S. Yun, S. Weissman, and E. A. Mason, *Phys. Fluids*, **5**, 769 (1962).
63. A series of papers by T. L. Bailey, E. E. Muschlitz, Jr., J. H. Simons, and coworkers appear in *J. Chem. Phys.* (1943–1961).
64. K. F. Herzfeld and T. A. Litovitz, *Absorption and Dispersion of Ultrasonic Waves*, Academic Press, New York, 1959.
65. J. T. Vanderslice and S. Weissman, *J. Chem. Phys.*, **37**, 2247 (1962).
66. E. A. Mason and M. M. Kreevoy, *J. Am. Chem. Soc.*, **77**, 5808 (1955).
67. M. M. Kreevoy and E. A. Mason, *J. Am. Chem. Soc.*, **79**, 4851 (1957).
68. J. B. Hendrickson, *J. Am. Chem. Soc.*, **83**, 4537 (1961).
69. I. Amdur, to be published.
70. E. A. Mason and W. E. Rice, *J. Chem. Phys.*, **22**, 522 (1954).

3. QUANTUM EFFECTS IN ELASTIC MOLECULAR SCATTERING†

RICHARD B. BERNSTEIN

Theoretical Chemistry Institute and Chemistry Department, University of Wisconsin, Madison, Wisconsin

CONTENTS

I. Introduction 75
II. Résumé of Classical Treatment of Potential Scattering 76
III. Résumé of Quantum Scattering Treatment 83
IV. Approximation Methods 88
A. The Radial Wave Function 89
B. The Phase Shifts 91
V. The Scattering Amplitude 94
VI. The Interference Pattern 99
VII. Rainbow Scattering 103
VIII. Low-Angle Scattering 105
IX. Glory Interference Effect at Low Angles 114
X. Total Elastic Cross Section 117
XI. Extrema in Total Cross Sections 120
XII. Maxima in Impact Spectra and the Bound States 124
XIII. Influence of Concurrent Inelastic Processes 126
References 131

I. INTRODUCTION

Observations of elastic scattering of atoms and molecules may be accounted for, to a large extent, by classical mechanics alone. However, a number of important features of the scattering behavior require a quantum-mechanical interpretation; it is these which comprise the subject matter of this chapter.

† This research received financial support from the U.S. Atomic Energy Commission, Division of Research and the National Aeronautics and Space Administration.

Preparatory to a detailed discussion we shall outline the main points of difference between the classical and quantum results. We will compare the classical with the quantum predictions in each case; anticipating somewhat the final conclusions, it is found quite generally that experiment accords with the latter.

First we consider the differential cross sections, designated $I(\theta)$ [or $d\sigma(\theta)/d\Omega$], for elastic scattering by a realistic intermolecular potential. The purely classical description yields a well-known unphysical singularity in the forward scattering, while the quantum treatment predicts a finite $I(\theta)$. The classical inverse-power divergence in the low-angle scattering, $I(\theta) \propto \theta^{-7/3}$, is replaced by a well-behaved small-angle dependence, $I(\theta) \propto e^{-c\theta^2}$, according to the quantum treatment. The classical smooth dependence of differential cross section upon scattering angle is to be contrasted with the strongly oscillatory de Broglie interference pattern in $I(\theta)$ predicted by quantum theory.

With regard to the total elastic cross section, designated $Q(v_r)$ or $\sigma(v_r)$, the classical low angle divergence noted above leads to an infinite value, while the quantum theory correctly yields a finite Q. The simplest quantum-mechanical treatment, considering only the long-range r^{-6} attractive part of the interaction, accounts for the main part of the dependence of the cross section upon relative velocity, $Q \propto v_r^{-2/5}$. A more complete quantum analysis, taking cognizance of the attractive potential well, predicts extrema (resonant behavior) in $Q(v_r)$ and suggests their relation to the bound states of the composite system. None of these features are encompassed within the classical framework.

In the discussion which follows, the emphasis will be upon the deviations from classical behavior predicted by the quantum-mechanical and semiclassical treatments.*

II. RÉSUMÉ OF CLASSICAL TREATMENT[1] OF POTENTIAL SCATTERING

We assume an orientation-averaged, spherically symmetrical potential $V(r)$ with a long-range attraction, an attractive well, and short-range repulsion.†

* Most of the quantum effects with which we shall be concerned may be treated advantageously using the so-called "semiclassical approximation," valid when the de Broglie wavelength of the colliding system is comparable to or less than the "range" of the intermolecular forces. For very low energy collisions where this condition no longer obtains, a full quantum-mechanical treatment is required.

From elementary considerations of energy and momentum conservation one obtains[1] an explicit expression for the classical deflection function, Θ (or χ).

$$\Theta(b,E) = \pi - 2b \int_{r_0}^{\infty} dr/r^2[F_c(r)]^{1/2} \tag{II.1}$$

where

$$F_c(r) = 1 - V(r)/E - b^2/r^2 \tag{II.2}$$

Here b is the impact parameter, E the initial relative kinetic energy or "collision energy" ($E = \frac{1}{2}\mu v_r^2$, where μ is the reduced mass and v_r the magnitude of the relative velocity) and r_0 is the distance of closest approach in the encounter, or the "classical turning point" of the radial motion, the outermost zero of $F_c(r)$. It is recalled that the deflection function[2] Θ is positive for net repulsive and negative for net attractive trajectories; the observable scattering angle is $\theta = |\Theta|$, with $0 \leqslant \theta \leqslant \pi$.

In Figure 1 is shown a typical curve of the dependence of the deflection function upon the reduced impact parameter $\beta \equiv b/\sigma \equiv b^*$ for a definite value of the reduced collision energy $K \equiv E^* \equiv E/\epsilon$. The positive region is associated with domination of repulsion, the negative region with predominance of the attractive forces.

The differential solid-angle scattering cross section is expressible[1-3] directly in terms of the deflection function by the relation

$$\frac{d\sigma(\theta)}{d\Omega} = \sum_{i=1}^{3} b_i \Big/ \sin\theta \cdot \left| \frac{d\Theta}{db_i} \right| \tag{II.3}$$

† It is often convenient to write $V(r)$ in terms of a dimensionless "reduced potential": $V(r) = \epsilon V^*(x)$; ϵ is the depth of the attractive well; $x \equiv r^* \equiv r/\sigma$, where σ is a characteristic length, here the zero of the potential (an alternative choice for a characteristic length is r_m, the position of the minimum in $V(r)$). Any potential with a minimum must contain at least two parameters; thus the function V^* often includes a number of constants governing the shape of the potential. Commonly used forms of the potential describing the interaction of ground-state atoms and molecules include the Lennard-Jones (n,6) the Exp (α,6), the Morse (β), the Kihara (α,12,6) and others, discussed in standard works.[1a] The simplest potential capable of accounting for the gross observed features of molecular scattering is the L.-J. (12,6) function, for which $V^*(x) = 4(x^{-12} - x^{-6})$. For the purpose of numerical or graphical illustration of some of the subsequent relationships between the potential, the angular deflection function, and the scattering cross sections, we shall often employ the L.-J. (12,6) function. Of course, the main body of the formalism itself is quite general and may be applied to any well-behaved, realistic central potential.

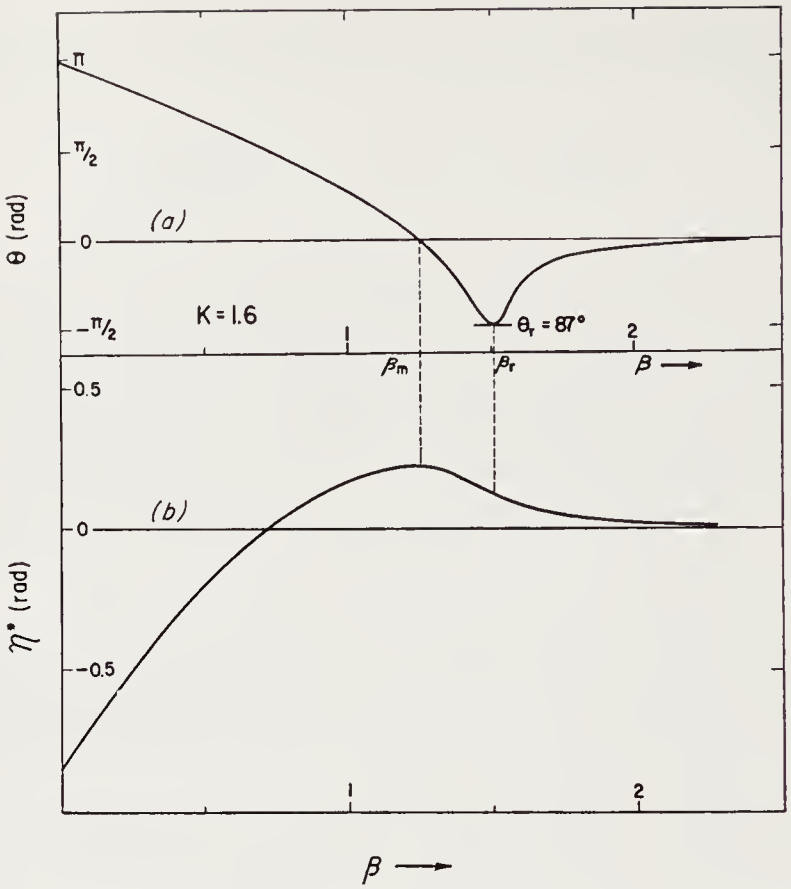

Fig. 1. (*a*) Dependence of the deflection function upon the reduced impact parameter $\beta \equiv b/\sigma$, for an L.-J. (12,6) potential; here the reduced relative kinetic energy $K \equiv E^* \equiv \frac{1}{2}\mu v_r^2/\epsilon = 1.6$; from tabulations in reference 1a. (*b*) The corresponding dependence of the semiclassical reduced phase η^*, defined in Section III, upon the reduced impact parameter β for the same case. Note the minimum in the deflection function at $\beta = \beta_r = 1.52$ rad (corresponding to a "rainbow angle" $\theta_r = 87°$) and the maximum in the reduced phase curve at $\beta = \beta_m = 1.24$, which is also the first zero of the deflection function.

where the summation is over the three† possible branches of the deflection function contributing to the scattering at an angle θ. The forward scattering singularity previously mentioned is immediately evident from Eq. (II.3). A less obvious classical singularity, pointed out by Mason,[3] occurs at $\theta = \theta_r$ (where $d\Theta/db = 0$); it has been termed[2] the "rainbow

† For sufficiently small K, $\Theta(b)$ may pass through $-\pi$, -2π, etc., so that 5, 7, etc. regions contribute to the scattering at a given angle θ. For simplicity hereafter we will assume that there are only three contributing regions.

effect." It is seen that for $\theta > \theta_r$ only one region of the deflection function contributes to the scattering, while three regions do so for $\theta < \theta_r$, i.e., three values of b correspond to a given value of $|\Theta|$. Thus there is a discontinuity as well as a singularity in the classical differential cross section at the rainbow angle (this angle corresponds to the trajectory of maximum attraction between the interacting particles).

In certain applications it is convenient to deal with a "reduced" differential cross section, i.e., $d\sigma(\theta)/d\Omega$ expressed in units of $\pi\sigma^2$, sometimes designated $I^*(\theta)$. Eq. (II.3) may be rewritten, introducing other dimensionless parameters, as follows:

$$I^*(\theta) \equiv \frac{d\sigma(\theta)}{d\Omega} \Big/ \pi\sigma^2 = \sum_{i=1}^{3} \left| \frac{dB_i}{dC} \right| \tag{II.4}$$

where $C \equiv \cos\theta$, $B = \beta^2/2\pi$, and β is the reduced impact parameter.

A suitable graphical presentation of Eq. (II.4) is shown in Figure 2

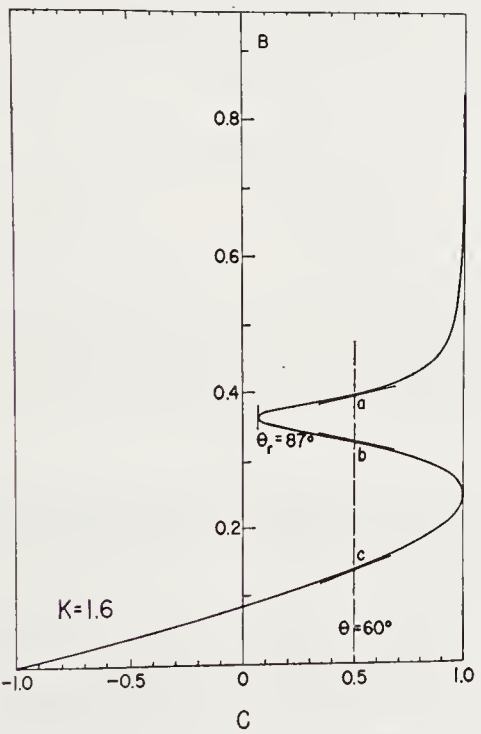

Fig. 2. A BC plot for an L.-J. (12,6) potential with $K = 1.6$. Here $B \equiv \beta^2/2\pi$ and $C \equiv \cos\theta$, so that $I^*(\theta)$ is obtained as the sum of the absolute values of the slopes of the contributing branches. For illustration, at $\theta = 60°$, three branches (a, b, and c) contribute; for $\theta > \theta_r = 87°$ only one branch contributes to $I^*(\theta)$.

(obtained directly from the deflection function of Fig. 1); it may be designated a *BC* plot. At any value of θ (or C), the classical reduced differential cross section $I^*(\theta)$ is given by the sum of the absolute values of the slopes of the contributing branches of the *BC* plot. The forward singularity ($C = 1$) as well as the rainbow singularity and discontinuity are immediately obvious.

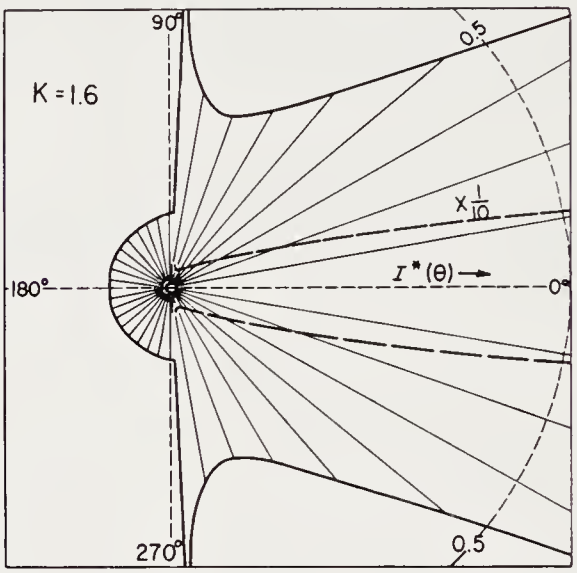

Fig. 3. A polar plot of $I^*(\theta)$ for scattering by an L.-J. (12,6) potential with $K = 1.6$. The outer (solid) curve corresponds to $I^*(\theta)$ directly; the dashed circle corresponds to $I^* = 0.5$; the inner curve (dashed) has been plotted as $\frac{1}{10}I^*(\theta)$. Intensities for $\theta < 11°$ are not shown. The rainbow effect at 87° is evident.

Figure 3 shows a polar plot of $I^*(\theta)$ corresponding to the example of Figure 2. Suggested but not shown is the strong forward divergence; the rainbow effect is clearly seen.

Returning to the deflection function, given by Eq. (II.1), it is well known[1] that except for trivial potential functions, numerical integration is required to evaluate $\Theta(b,E)$ and thus $d\sigma(\theta)/d\Omega$ in the general case. However, for small angles one may employ the Kennard[1b] approximation for the deflection function. For large b (and thus small θ), where $r_0 \cong b$ and $V(r_0)/E \ll 1$, $F_c(r)$ may be suitably expanded and the integration for Θ readily accomplished. For a potential with a long-range

attraction of the form $V = -C^{(s)}r^{-s}$ one obtains†

$$\Theta \cong -(s-1)f(s)C^{(s)}/Eb^s \tag{II.5}$$

and

$$\frac{d\sigma(\theta)}{d\Omega} \cong [(s-1)f(s)]^{2/s}s^{-1}\left[\frac{C^{(s)}}{E}\right]^{2/s}\Big/\theta^{1+2/s}\cdot\sin\theta$$
$$\cong g(s)\left[\frac{C^{(s)}}{E}\right]^{2/s}\cdot\theta^{-2(1+1/s)} \tag{II.6}$$

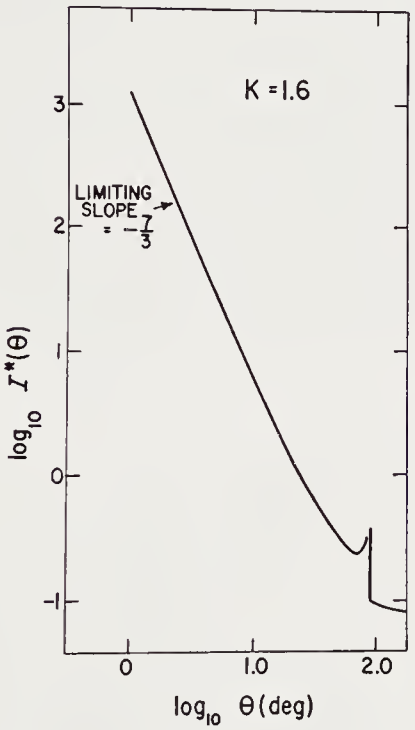

Fig. 4. A log–log plot of $I^*(\theta)$ for scattering by an L.-J. (12,6) potential with $K = 1.6$ (cf. Fig. 3 for the same case). Note the limiting low-angle linearity consistent with a long-range r^{-6} potential.

† For the important practical case of $s = 6$, $f(6) = 3\pi/16$ and

$$\frac{d\sigma(\theta)}{d\Omega} \cong \frac{1}{6}\left(\frac{15\pi}{16}\right)^{1/3}\left[\frac{C^{(6)}}{E}\right]^{1/3}\Big/\theta^{4/3}\sin\theta \tag{II.6′}$$

Specializing for the L.-J. (12,6) potential, for which $C^{(6)} = 4\epsilon\sigma^6$, we obtain the low-angle reduced differential cross section:

$$I^*(\theta)^{(6)} \cong \frac{1}{6\pi}\left[\frac{15\pi}{4K}\right]^{1/3}\Big/\theta^{4/3}\sin\theta \cong \frac{1}{6\pi}\left(\frac{15\pi}{4}\right)^{1/3}K^{-1/3}\theta^{-7/3} \tag{II.6″}$$

where

$$f(s) = \tfrac{1}{2}\pi^{1/2}\Gamma(\tfrac{1}{2}s - \tfrac{1}{2})/\Gamma(\tfrac{1}{2}s) \quad \text{and} \quad g(s) = [(s-1)f(s)]^{2/s}/s$$

Thus a log–log plot of $d\sigma(\theta)/d\Omega$ or $I^*(\theta)$ vs. θ should exhibit linear limiting (low angle) behavior, with a slope of $-2(1 + 1/s)$. Figure 4 shows a log–log $I^*(\theta)$ plot corresponding to the example of Figure 3. The continuously increasing positive deviation of $I^*(\theta)$ from the limiting low-angle behavior, out to the rainbow angle, is quite general for a realistic potential with a well and an inner "core."

Thus the influence of the short-range forces is most easily assessed by examining the angular dependence of the ratio $I^*(\theta)/I^*(\theta)^{(s)} \equiv \rho^*(\theta)$, where the index s refers to the long-range attractive component of the potential, e.g., $s = 6$. Mason[3] has tabulated a function proportional to $\rho^*(\theta)$ for the Exp (α,6) potential over a wide range of reduced collision energies. In Figure 5 we see an example of $\rho^*(\theta)$ for an L.-J. (12,6) potential, corresponding to the case of Figures 1–4.

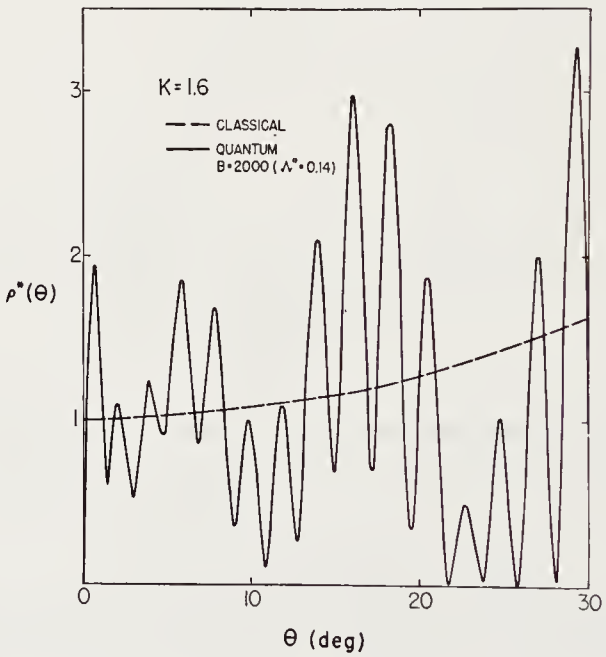

Fig. 5. Plot of $\rho^*(\theta)$, from 0 to 30°, for scattering by an L.-J. (12,6) potential with $K = 1.6$ (cf. Figs. 3 and 4 for same case): The dashed curve is the classical result; the solid curve (see Sec. VI) is a quantum-mechanical calculation for the same K, with $B \equiv 2\mu\epsilon\sigma^2/\hbar^2 = 2000$ (or $\Lambda^* \equiv h/\sigma(2\mu\epsilon)^{1/2} = 0.14$).

Although the true total cross section (for reasons previously mentioned) is not determined within the classical framework, it is of interest to consider the "incomplete" total cross section, namely,

$$\sigma(\theta_0) \equiv 2\pi \int_{\theta_0}^{\pi} \sin\theta \frac{d\sigma(\theta)}{d\Omega} d\theta \tag{a}$$

corresponding to the total cross section for scattering beyond some minimum angle θ_0 (closely related to the angular aperture or "resolving power" of an apparatus). Just as with the differential cross sections, no explicit analytical form can be obtained for $\sigma(\theta_0)$ in terms of the potential constants but, analogous to Eq. (II.6), an approximate form is available for the case of long-range inverse-power potentials. The energy dependence of these cross sections is the same as that of the differential cross sections (cf. Eq. (II.6)). Tabulation of incomplete total cross section functions for the Exp (α, 6) potential are presented in reference 3.

Further information on various classical aspects of elastic molecular scattering theory may be found in references 1–3, as well as in certain articles in a series by Amdur and co-workers[4] and elsewhere.[5]

III. RÉSUMÉ OF QUANTUM SCATTERING TREATMENT[6]

The standard wave-mechanical treatment of scattering by a central potential need not be elaborated here. It will suffice to define terms and outline the procedures required to predict the scattering amplitude and thus differential and total cross sections from an assumed potential.

Following Mott and Massey,[6a] the scattering amplitude $f(\theta)$ is defined by the asymptotic equation for the amplitude function ψ of the colliding system (i.e., by the behavior of the wave function at large interparticle separation r):

$$\psi \sim e^{ikz} + f(\theta)e^{ikr}/r \tag{III.1}$$

where the z axis is the axial direction, θ is the scattering angle and $k = \mu v_r/\hbar = 2\pi/\lambda = [2\mu E/\hbar^2]^{1/2}$ is the incident wave number (λ is the de Broglie wavelength). The differential cross section is given by

$$I(\theta) = |f(\theta)|^2 \tag{III.2}$$

and the total cross section by

$$Q = 2\pi \int_0^{\pi} \sin\theta \cdot |f(\theta)|^2 \, d\theta \tag{III.3}$$

Using the Rayleigh-Faxen-Holtzmark method of partial waves[6a] (expanding $\psi = \sum_l R_l(r)P_l(\cos\theta)$, separating the wave equation, and following standard procedures), one finally obtains the (complex†) scattering amplitude expressed in terms of the phase shifts $\eta_l(k)$:

$$f(\theta) = \frac{1}{2ik}\sum_{l=0}^{\infty}(2l+1)(e^{2i\eta_l}-1)P_l(\cos\theta) \tag{III.4a}$$

where l is the orbital angular momentum quantum number, $P_l(\cos\theta)$ the Legendre function and η_l the lth-order phase shift, defined in terms of the asymptotic behavior of the lth-order radial wave function $G_l(r) \equiv rR_l(r)$:

$$G_l(r) \sim \sin(kr - l\pi/2 + \eta_l) \propto \exp[-i(kr - l\pi/2)] - \exp(2i\eta_l)\cdot\exp[i(kr - l\pi/2)] \tag{III.5}$$

where $G_l(r)$ is the solution of the radial equation

$$[d^2/dr^2 + k^2F(r)]G_l(r) = 0 \tag{III.6}$$

with the inner boundary condition $G_l(0) = 0$. Here

$$F(r) \equiv 1 - U(r)/k^2 - l(l+1)/k^2r^2 \tag{III.7}$$

where $U(r) \equiv (2\mu/\hbar^2)V(r)$. The phase shift η_l thus refers to the displacement of the radial wave function, at large separations, relative to that of the corresponding lth-order spherical Bessel function $j_l(kr)$. We note that $G_l^0(r) \equiv krj_l(kr)$ represents what may be termed a "reference" radial function, i.e., the solution of Eq. (III.6) in the absence of an interaction potential, $V = 0$ (with only the centrifugal potential term remaining). Thus $\eta_l = k \lim_{r\to\infty} \Delta r_z$ where Δr_z is the displacement of (the difference between) corresponding zeros of $G_l^0(r)$ and $G_l(r)$.

† In general, the scattering amplitude may be considered to be the sum of a real and an imaginary part: $f(\theta) = \mathrm{Re}\, f(\theta) + i\ \mathrm{Im}\, f(\theta)$, where

$$\mathrm{Re}\, f(\theta) = \frac{1}{2k}\sum_l (2l+1)\sin 2\eta_l\, P_l(\cos\theta) \tag{III.4b}$$

and

$$\mathrm{Im}\, f(\theta) = \frac{1}{k}\sum_l (2l+1)\sin^2\eta_l\, P_l(\cos\theta) \tag{III.4c}$$

This definition of the phase shift is shown graphically in Figure 6, in which the ordinate (y) is proportional to the radial wave function and the abscissa (x) is the reduced separation $x \equiv r/\sigma$, for an L.-J. potential. The displacement Δx (more properly, evaluated at very large

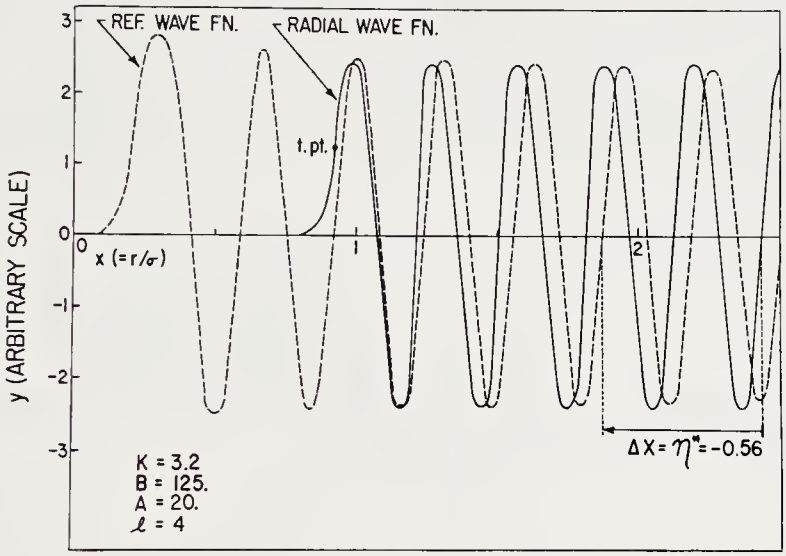

Fig. 6. Typical radial wave function $G_l(r) \propto y(x)$ [solid curve]; for L.-J. (12,6) potential; here $K = 3.2$, $l = 4$, and $A \equiv k\sigma = 20$, $B \equiv 2\mu\epsilon\sigma^2/\hbar^2 = 125$. (See Ref. 6c.) Since $x = r/\sigma$, $\eta^* = \Delta x$ (see text). The classical turning point (inner inflection point in the radial wave function) is designated on the figure. The dashed curve is the "reference" wave function, $y \propto (Ax)j_l(Ax)$.

x where the wave function is sinusoidal) yields directly the so-called "reduced phase"[2,6c] $\eta^* \equiv \eta/k\sigma$ introduced by Ford and Wheeler,[2] which is of considerable importance and will be discussed later.

For the particular case illustrated, the phase shift is seen to be negative, corresponding to the domination of the repulsive branch of the potential. Thus, given any realistic potential function $V(r)$, one solves† (by numerical methods)[6c] the radial equation (Eq. III.6) for successive values of l, evaluating a sufficient number of phase shifts to obtain convergence (to some specified limit of accuracy) in the sum over l in Eq. (III.4). For potentials with a long-range inverse-sixth power radial

† P. O. Löwdin (Quart. Rept. of Molecular Theory Group, M.I.T., Jan. 15, 1962) proposed a general perturbation method for the solution of the one-dimensional wave equation, but this has not yet seen extensive use in the scattering field.

dependence it is found that $\eta_l \sim l^{-5}$, so that convergence presents no practical problem. The behavior of the phases as a function of wave number for various realistic interaction potentials has been investigated in great detail[6c, 7-11] and will not be spelled out here. Figure 1*b* displays a typical "smoothed curve" of η vs. l. Plotted is η^* vs. $\beta \equiv (l + \frac{1}{2})/k\sigma$ for an L.-J. potential at one collision energy; later on, we will identify this β with the reduced impact parameter $b^* \equiv b/\sigma$ in connection with the semiclassical approximation.[2,12]

For practical usage, Eq. (III.2) may be rewritten in terms of real quantities only, as follows:

$$I(\theta) \equiv \frac{d\sigma(\theta)}{d\Omega} = \frac{1}{4k^2}\left\{\left[\sum_l (2l+1) \sin 2\eta_l P_l(\cos\theta)\right]^2 + \left[\sum_l (2l+1)(\cos 2\eta_l - 1)P_l(\cos\theta)\right]^2\right\} \quad \text{(III.8)}$$

and Eq. (III.3) may be reduced using the orthogonality of the Legendre polynomials to yield the simple formula:

$$Q = \frac{4\pi}{k^2}\sum_l (2l+1) \sin^2 \eta_l \quad \text{(III.9)}$$

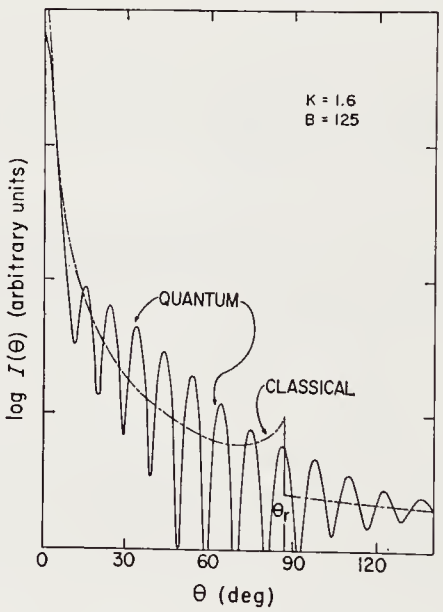

Fig. 7*a*. Semilog plot of $I(\theta)$ for scattering for an L.-J. (12,6) potential; $K = 1.6$, $B = 125$ ($\Lambda^* = 0.56$, $A = 14.1$), comparing quantum with classical calculations. Note region of classical rainbow effect.

Calculated curves of $d\sigma(\theta)/d\Omega$ [and $Q(k)$] for various realistic potentials have appeared often in the literature.[5c, 6c, 9-11] Examples of $d\sigma(\theta)/d\Omega$ plots, for an L.-J. (12,6) potential, are shown in Figures 7 and 8. (An alternative representation of a quantum-calculated angular

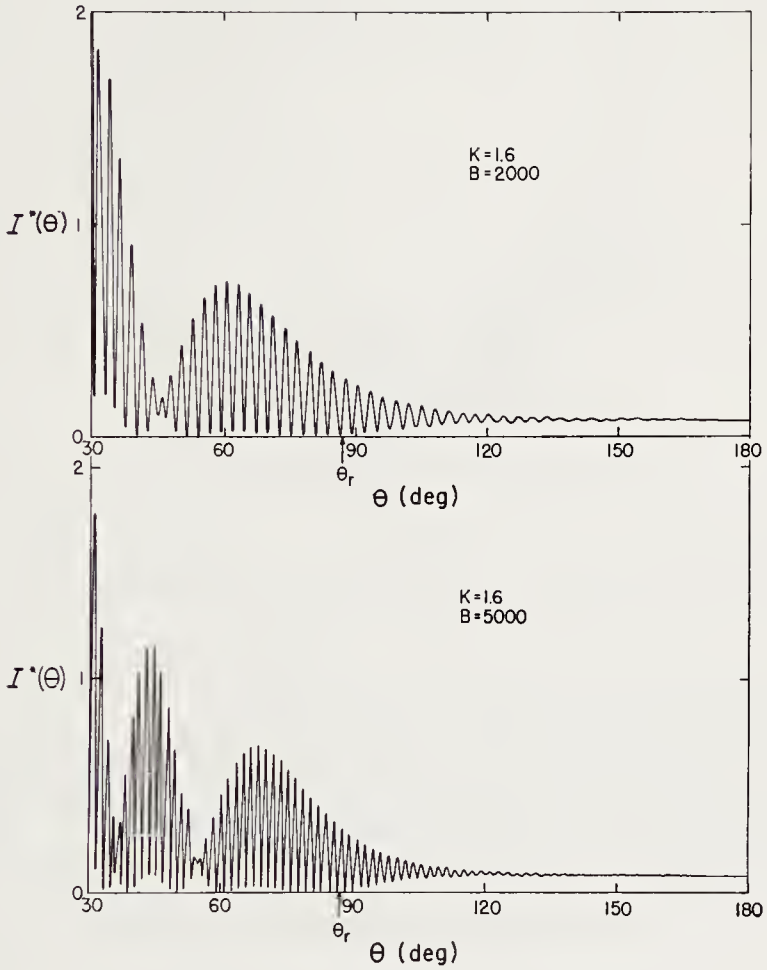

Fig. 7*b*. Plot of $I^*(\theta)$ for an L.-J. (12,6) potential for $K = 1.6$ and $B = 2000$ and 5000, showing development of "semiclassical" effect.

distribution in the form $\rho^*(\theta)$ appears in Figure 5.) Suffice it to say at this point that the differential cross sections show pronounced oscillatory (diffraction-like) behavior, with the periodicity, $\Delta\theta$, decreasing with increasing wave number (Section IX). The total cross sections $Q(k)$ show a general decrease with increasing wave number, but often exhibit broad extrema (and, at very low energies, rather sharp resonances) for reasons

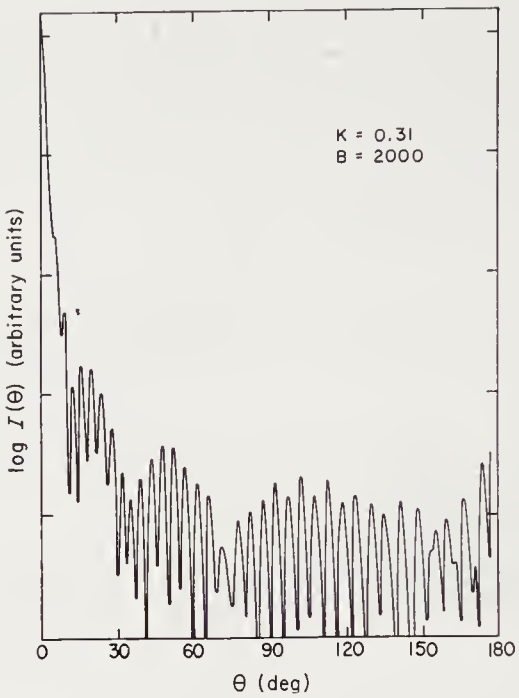

Fig. 8. Semilog plot of $I(\theta)$ as in Figure 7 for $K = 0.31$, $B = 2000$ ($\Lambda^* = 0.14$, $A = 25$). For $K \leqslant 0.8$, no rainbow scattering effect (classical orbiting only).

to be discussed later (Section XI). These nonclassical features will be our main concern in the sections which follow.

The formal inversion problem, i.e., deduction of the potential from the scattering phase shifts, has recently been reexamined by Hylleraas.[12a] Since the formal procedure has not yet been applied to molecular scattering, it will not be elaborated in the present chapter.

IV. APPROXIMATION METHODS

Although the exact quantum treatment of the elastic scattering problem (involving direct numerical integration of the radial wave equation as described in Section III) has been carried out in full on many occasions, suitable approximation methods have always been welcomed by workers in the field. In addition to easing the computational labor of evaluating wave functions, phase shifts, and cross sections, the semiclassical approximation techniques nearly always add insight into the physics, often enabling certain qualitative inferences to be drawn and predictions to be made which would not be possible

otherwise. In certain cases simple approximation formulas may be obtained which describe with good accuracy the main features of a particular quantum effect under consideration.

There are, however, various levels of approximation possible and these may be arranged in some sort of a hierarchy. In this section we shall consider, successively, approximations for

(*A*) the radial wave function, $G_l(r)$

(*B*) the phase shifts, $\eta_l(k)$

(i) phase shifts (no restriction on magnitude)

(ii) "small" phase shifts.

Succeeding sections will be concerned with approximations useful in regard to the scattering amplitude, $f(\theta)$; the interference pattern in $I(\theta)$; rainbow scattering [$I(\theta)$ near θ_r]; low-angle scattering [$I(\theta)$ for small θ]; and the total cross section, $Q(v_r)$.

A. The Radial Wave Function

The Jeffreys-WKBL approximation, recently designated[13] the "asymptotic approximation," AA, for the radial wave function is discussed in many texts; we will base our development here on the presentation of Landau and Lifshitz.[14] As is well known, the approximation is valid only in the limit of a very slowly varying potential ($d \ln V(r)/dr \ll k_r$), i.e., the de Broglie wavelength λ_r small enough that the fractional change in $V(r)$ over a wavelength is negligible. With this assumption the radial differential equation may be simplified and an approximate solution obtained in terms of the Airy function (which is the solution of the radial equation for a potential linear through the turning point). The usual "semiclassical" radial wave functions are written in two forms expressing the asymptotic behavior on the two sides of the classical turning point r_0 (but not *at* the turning point itself, where $\lambda_r = \infty$).

$$G_l(r) \sim \begin{cases} \frac{1}{2}\left[\frac{p_\infty}{|p_r|}\right]^{1/2} \exp\left[-\frac{1}{\hbar}\int_{r_0}^{r} |p_r| dr\right] & (r < r_0) \qquad \text{(IVa.1a)} \\ \left[\frac{p_\infty}{p_r}\right]^{1/2} \sin\left[\frac{1}{\hbar}\int_{r_0}^{r} p_r\, dr + \frac{\pi}{4}\right] & (r > r_0) \qquad \text{(IVa.1b)} \end{cases}$$

Here $G_l(r)$ is the radial wave function normalized to unit asymptotic amplitude, p_r is the "local radial momentum" given by

$$p_r = \hbar k_r \equiv h/\lambda_r = [2\mu(E - V_{\text{eff}}(r))]^{1/2} \qquad \text{(IVa.2)}$$

with the effective potential defined

$$V_{\text{eff}}(r) \equiv V(r) + (l + \tfrac{1}{2})^2\hbar^2/2\mu r^2; \tag{IVa.3}$$

$p_\infty = \hbar k$ is the incident momentum;

$$k_r = k \cdot [F_c(r)]^{1/2} \tag{IVa.4}$$

is the local wave number;

$$F_c(r) = 1 - U(r)/k^2 - (l + \tfrac{1}{2})^2/k^2r^2 = 1 - V(r)/E - b^2/r^2$$
$$= 1 - V_{\text{eff}}(r)/E \tag{IVa.5}$$

$$b = (l + \tfrac{1}{2})/k; \tag{IVa.6}$$

and the turning point is defined by the outermost zero of $F_c(r)$, i.e., $F_c(r_0) = 0$. (Note that the semiclassical $F_c(r)$ differs from the analogous quantum expression (Eq. (III.7)) in the centrifugal term where $(l + \frac{1}{2})^2$ replaces $l(l + 1)$.

Although Eq. (IVa.1b) suffices to evaluate the phase shifts (see below), the apparent singularity at the turning point as $p_r(r_0) = 0$ is a disadvantage for certain applications. Of course, this singularity is only an artifact, due to the use of the asymptotic forms of the Airy integral. It may be removed by an alternative expansion of the Airy function around the turning point,[15] which yields a satisfactory approximation for the wave function (effectively joining Eq. (IVa.1a) with Eq. (IVa.1b) passing smoothly through the turning point.

The solution (valid for $-1 \leqslant z \leqslant 1$) may be represented by[15b]

$$G_l(r) = \left[\frac{k}{F_0'}\right]^{1/6} \cdot \pi^{1/2}[0.35503(1 - z^3/6) + 0.25882z(1 - z^3/12) + \cdots] \tag{IVa.7}$$

where

$$z \equiv [F_0'/k]^{1/3}k(r - r_0) \tag{IVa.8}$$

is the "reduced displacement" from the turning point and

$$F_0' = \left\{\frac{d}{dr}[F_c(r)]\right\}_{r_0} \tag{IVa.9}$$

is proportional to the force at the turning point. The numerical coefficients arise from well-known expansion formulas for the Airy function. It is readily verified that Eq. (IVa.7) satisfies the Airy-like form

of the radial equation near the turning point, and predicts quite accurately the position and amplitude of the first maximum in the wave function (which occurs very near $z = 1$). Beyond the first maximum, i.e., for $z > 1$, one may employ Eq. (IVa.1b) expressed here in a form suitable for numerical computation:

$$G_l(r) = [F_c(r)]^{-1/4} \sin\left[k \int_{r_0}^{r} [F_c(r)]^{1/2}\, dr + \pi/4\right] \qquad \text{(IVa.10)}$$

Thus the radial wave function may be approximated over the entire range $z \geqslant -1$ by the single expression

$$G_l(r) = (1-f)\left[\frac{k}{F_0'}\right]^{1/6} (0.6292 + 0.4588z - 0.1049z^3 - 0.0383z^4 + \cdots)$$
$$+ f[F_c(r)]^{-1/4} \sin[k(r_{\text{eff}} - r_0) + \pi/4] \qquad \text{(IVa.11)}$$

where

$$r_{\text{eff}} \equiv \int_{r_0}^{r} [F_c(r)]^{1/2}\, dr$$

and f is some "joining" function, for example

$$f = [1 + e^{-a(z-1)}]^{-1},$$

with a large a value to effect rapid smoothing.

B. The Phase Shifts

1. *Phase Shifts (No Restriction on Magnitude)*

The JWKB-approximated phase shifts may be obtained directly from the asymptotic form of the AA radial wave function.[6a,6b,14] Comparing the expressions

$$\sin\left[k \int_{r_0}^{R} [F_c(r)]^{1/2}\, dr + \pi/4\right] \qquad \text{(a)}$$

and

$$\sin[kr - l\pi/2 + \eta_l] \qquad \text{(b)}$$

in the limit of large R, we have

$$\eta_l = \lim_{R\to\infty}\left[k \int_{r_0}^{R} [F_c(r)]^{1/2}\, dr - kR\right] + \frac{\pi}{2}(l + \tfrac{1}{2})$$
$$= \frac{\pi}{2}(l + \tfrac{1}{2}) - kr_0 + k \int_{r_0}^{\infty} \{[F_c(r)]^{1/2} - 1\}\, dr \qquad \text{(IVb.1a)}$$

where r_0 is the outermost zero of $F_c(r)$, as usual.† For computational purposes Eq. (IVb.1a) may be transformed to the form

$$\eta_l = \frac{\pi}{2}(l + \tfrac{1}{2}) + kr_0\left\{\int_0^1 \{[F_c(y)]^{1/2} - 1\}y^{-2}\,dy - 1\right\} \quad \text{(IVb.1b)}$$

where $y \equiv r_0/r$. The pole in the integrand is readily dealt with by expanding around the origin, then integrating analytically from $y = 0 \to \varepsilon$ ($\varepsilon \ll 1$) and numerically from ε to 1.

Since Eqs. (IVb.1) involve only a quadrature, whereas the exact solution of the radial equation requires direct numerical integration of the second-order differential equation, the JWKB phase-shift calculation is faster by about two orders of magnitude. For energies high enough (typically $K \equiv E/\epsilon \gtrsim 1$) so that there is no more than a single zero in $F_c(r)$, i.e., above the critical energy for classical orbiting[15d] (or quantum-mechanical tunneling through the centrifugal barrier), the JWKB phases are sufficiently accurate (ca. 0.1%) for all but the most exacting practical applications. Except for the limitation that the absolute uncertainty (in radians) increases with the magnitude of η_l (it is noted that for most purposes one requires η_l modulo π with an accuracy of ca. 0.01 rad), the JWKB approximation procedure imposes no restriction on the size of the phase shifts. In contrast, the Born approximation (mentioned below) is valid only in cases in which the phase shift is small (e.g. $\eta \lesssim \frac{1}{2}$ rad). An alternative form of Eq. (IVb.1b) is[6a,16]

$$\eta_l = k\left[\int_{r_0}^{\infty} [F_c(r)]^{1/2}\,dr - \int_b^{\infty} [F_c^{(0)}(r)]^{1/2}\,dr\right] \quad \text{(IVb.1c)}$$

where $F_c^{(0)}(r) = 1 - (l + \frac{1}{2})^2/k^2r^2$, the expression for $F_c(r)$ in the absence of a potential; b is its zero, i.e., $F_c^{(0)}(b) = 0$ so that

$$b = (l + \tfrac{1}{2})/k.$$

Still another semiclassical route to the phase shifts exists,[17a] but discussion is best postponed (see Sec. V).

† The expression for the phase shift (in this limit) when k and l are such that there are three classical turning points should also contain a contribution from the region between the two inner turning points due to the penetration[6c] of the centrifugal barrier. The implications of this effect have recently been considered.[15c]

2. *"Small" Phase Shift*

When l is sufficiently large (e.g., $l \gg kR$, where R is some "range" parameter of the potential) that the centrifugal term dominates the effective potential (Eq. (IVa.3)), the wave function $G_l(r)$ approaches very closely the Bessel form, $G_l^{(0)}(r)$, and the phase shifts approach zero. Massey and Mohr[16a] showed that Eq. (IVb.1c) could be simplified by suitably expanding $F_c(r)$ to yield the Jeffreys (J)-approximated phase

$$\eta_J \cong \frac{-1}{2k}\int_b^\infty \frac{U(r)\,dr}{[F_c^{(0)}(r)]^{1/2}} = \frac{-\mu}{\hbar^2 k}\int_b^\infty \frac{V(r)\,dr}{[1-(l+\frac{1}{2})^2/k^2r^2]^{1/2}} \qquad \text{(IVb.2a)}$$

so that for $V(r) \sim -C^{(s)}/r^s$

$$\eta_J^{(s)} = \frac{f(s)\mu C^{(s)}}{\hbar^2 k b^{s-1}} = \frac{f(s)C^{(s)}}{\hbar v b^{s-1}} = \frac{f(s)\mu C^{(s)}k^{s-2}}{\hbar^2(l+\frac{1}{2})^{s-1}} = a_s(l+\tfrac{1}{2})^{1-s} \qquad \text{(IVb.3)}$$

where $f(s) = \frac{1}{2}\pi^{1/2}\Gamma(\frac{1}{2}s - \frac{1}{2})/\Gamma(\frac{1}{2}s)$ (see p. 82) and a_s is an obvious abbreviation; of special interest is the coefficient $f(6) = 3\pi/16$. Massey and Smith[18] pointed out an alternative route to the higher order phases (Eqs. (IVb.2a) and (IVb.3)) via the Born (B) approximation:

$$\eta_B \cong -\frac{\pi}{2}\int_0^\infty U(r)[J_{l+\frac{1}{2}}(kr)]^2 r\,dr = -k\int_0^\infty U(r) j_l^2(kr) r^2\,dr \qquad \text{(IVb.4)}$$

Making use of the fact that, for large l, the main contribution to the integral arises from the region outside the first zero of the Bessel function, r_0 (where $r_0 \cong l/k$), and replacing the rapidly oscillatory part of the integrand by its mean value beyond r_0

$$[\text{i.e.,}\quad \langle J_{l+\frac{1}{2}}^2(x)\rangle = (1/\pi x)\cdot(1-l^2/x^2)^{-1/2}],$$

one obtains

$$\eta_B \cong -\frac{1}{2k}\int_b^\infty \frac{U(r)\,dr}{(1-l^2/k^2r^2)^{1/2}} \cong -\frac{1}{2k}\int_b^\infty \frac{U(r)\,dr}{[F_c^{(0)}(r)]^{1/2}} = \eta_J \equiv \eta_{JB} \qquad \text{(IVb.2b)}$$

For an (asymptotic) inverse sixth power potential, the Jeffreys-Born (JB) approximation for the higher-order phases may be written:

$$\eta_{JB}^{(6)} = \frac{3\pi}{16}\frac{\mu C^{(6)}}{\hbar^2}\cdot\frac{k^4}{(l+\frac{1}{2})^5} = \frac{3\pi}{16}\frac{C^{(6)}}{\hbar v b^5} \qquad \text{(IVb.5)}$$

where $l + \frac{1}{2}$ may often be replaced by l. For sufficiently large l (e.g., for $l \gg kR$, or, at least $l > L$ such that $\eta(L) \lesssim \frac{1}{2}$) the accuracy of the JB approximation is adequate (e.g., ± 0.01 rad) for most applications.†

V. THE SCATTERING AMPLITUDE[2,6a,b]

Ford and Wheeler[2] extended the Mott-Massey[6a] semiclassical treatment of the scattering amplitude to yield practical approximation formulas for $f(\theta)$. In the present discussion we shall recapitulate the relevant material and develop certain new relations especially suitable for molecular scattering applications.

Starting with the exact expression, Eq. (III.4), for the scattering amplitude, restricting θ to the region $\varepsilon \leqslant \theta \leqslant \pi - \varepsilon$ (where ε is an infinitesimal angle), making use of the relation

$$\sum_l (2l + 1)P_l(\cos\theta) = 0 \qquad (\theta \neq 0,\pi) \tag{V.1}$$

and the Laplace expansion for the Legendre function for large l, (valid for $\sin\theta \gtrsim 1/l$):

$$P_l(\cos\theta) \sim \left(\frac{2}{\pi l \sin\theta}\right)^{1/2} \sin\left[(l + \tfrac{1}{2})\theta + \frac{\pi}{4}\right]$$
$$= \frac{i}{(2\pi l \sin\theta)^{1/2}} \left\{\exp\left[-i\left(\frac{\pi}{4} + (l + \tfrac{1}{2})\theta\right)\right] - \exp\left[i\left(\frac{\pi}{4} + (l + \tfrac{1}{2})\theta\right)\right]\right\} \tag{V.2}$$

we replace the sum by an integral over l, use l in place of $l + \frac{1}{2}$, and obtain directly the expression:

$$f(\theta) \cong \frac{-1}{k(2\pi \sin\theta)^{1/2}} \int_0^\infty dl \cdot l^{1/2} \cdot [e^{iB_1(l)} - e^{iB_2(l)}] \tag{V.3}$$

where

$$B_1(l) \equiv 2\eta_l + l\theta + \pi/4 \quad \text{and} \quad B_2(l) \equiv 2\eta_l - l\theta - \pi/4. \tag{V.4}$$

Since the terms in the integrand are rapidly oscillating and will, for the most part, destructively interfere, it is appropriate to use the method

† For an L.-J. (12,6) potential, Eq. (IVb.5) may be rewritten[6c]

$$\eta_{JB} = \frac{3\pi}{8} \frac{BA^4}{(l + \frac{1}{2})^5} \quad \text{or} \quad \eta^*_{JB} \equiv \frac{\eta_{JB}}{A} = 3\pi/(8K\beta^5)$$

where $A \equiv k\sigma$, $B \equiv 2\mu\epsilon\sigma^2/\hbar^2$, $K \equiv A^2/B = E/\epsilon$ and $\beta \equiv (l + \frac{1}{2})/A = b/\sigma = b^*$.

of stationary phase.[19] Here we seek values of l, say L, for which one or the other of the B's are stationary, e.g., $(B_1')_L \equiv (dB_1/dl)_L = 0$; the only significant contribution to the integral arises from the regions near the L's. Setting $B_1' = 0$ (Eq. V.4) we have $\eta_L' = -\frac{1}{2}\theta_L$; for the condition $B_2' = 0$, $\eta_L' = \frac{1}{2}\theta_L$ [where $\eta_L' \equiv (d\eta/dl)_L$]. Referring back to Part II on the classical deflection function, we recall that for net repulsive deflections $\theta \equiv \Theta > 0$, while for net attractive trajectories $\theta = -\Theta > 0$ (see also Fig. 1a). Thus for the contributions from the "attractive" branch of the deflection function we have $\eta_L' = \frac{1}{2}\Theta_L$, corresponding to $B_1' = 0$, i.e., domination of the B_1 term in Eq. (V.3). For the contribution from the "repulsive" branch we have, *also*, $\eta_L' = \frac{1}{2}\Theta_L$, corresponding to $B_2' = 0$, and thus domination of the B_2 term. The general relation applicable over the *entire* range of the deflection function is thus:

$$\eta_L' = \tfrac{1}{2}\Theta_L \tag{V.5}$$

It is known as the semiclassical equivalence relationship.†

Returning now to Eq. (V.3), we follow through with the stationary-phase procedure. Anticipating somewhat the final result, we can express $f(\theta)$ as the sum of the three (possible) contributions from the two branches of the deflection function:

$$f(\theta) = f_a(\theta) + f_b(\theta) + f_c(\theta)$$

where a, b, and c refer (see Figs. 1 and 2) to the three regions of l (or impact parameter) corresponding (by the stationary-phase principle) to the specified angle θ. Here a refers to the outermost attractive one, b to the inner attractive one, and c to the inner repulsive one. Of course, if $\theta > \theta_r$ (where θ_r is the rainbow angle), there will be only one region of stationary phase, i.e., near c; however, we will retain the three terms for generality.

† Eq. (V.5) may be utilized[17a] for phase shift evaluation by integration:

$$\eta_L = -\tfrac{1}{2}\int_L^\infty \Theta dl = \frac{-k}{2}\int_b^\infty \Theta db \tag{V.5'}$$

or

$$\eta^* = -\tfrac{1}{2}\int_\beta^\infty \Theta d\beta \tag{V.5''}$$

where the notation is the same as that used previously. Eq. (V.5″) is in a convenient form for the calculation of reduced phases from already available deflection functions. The accuracy attainable is the same as that of Eqs. (IVb.1a) or (IVb.1c). It is noted from Eq. (V.5″) that η attains its maximum value at $\beta = \beta_m = b_0\sigma$ (cf. Fig. 1b).

For each region, we expand $B(l)$ around the stationary values

$$B(l) = B_L + \tfrac{1}{2}B''_L\cdot(l-L)^2 + \tfrac{1}{2}B'''_L\cdot(l-L)^3 + \cdots$$

where $B_L \equiv B(L)$, $B''_L \equiv [d^2B(l)/dl^2]_L = 2\eta''_L$, etc. Thus (for $\theta < \theta_r$) there will be two stationary values, say L_a and L_b, for the B_1 term and one, L_c, for the B_2 term. Considering first the contribution of the outermost term, $f_a(\theta)$, we require evaluation of the integral involving B_1 in Eq. (V.3). Removing the stationary quantities from the integral we obtain

$$f(\theta) \cong \frac{-1}{k(2\pi\sin\theta)^{1/2}}\int_0^\infty dl\cdot l^{1/2}\exp[iB_1(L_a)]\exp\left[\frac{i}{2}B''_L\cdot(l-L_a)^2\right]$$

$$\cong -\frac{1}{k}\left[\frac{L_a}{2\pi\sin\theta}\right]^{1/2}\exp[iB_1(L_a)]\cdot J \qquad \text{(V.6a)}$$

where

$$J \equiv \int_0^\infty dl\cdot\exp[i\eta''_{L_a}\cdot(l-L_a)^2] \cong \int_{-\infty}^\infty dx\cdot\exp[i\eta''_{L_a}\cdot x^2] \qquad \text{(V.6b)}$$

with $x \equiv l - L_a$. For this case, a, $\eta''_{L_a} > 0$ so that[20a]

$$J = \left(\frac{\pi}{\eta''_{L_a}}\right)^{1/2} e^{i\pi/4}. \qquad \text{(V.7)}$$

Making use of Eq. (V.4), we obtain

$$f_a(\theta) = -\frac{1}{k}\left[\frac{L_a}{2\eta''_{L_a}\cdot\sin\theta}\right]^{1/2}\exp[i(2\eta_{L_a} + L_a\theta + \pi/2)$$

$$= \frac{1}{k}\left[\frac{L_a}{2\eta''_{L_a}\cdot\sin\theta}\right]^{1/2}\exp[i(2\eta_{L_a} + L_a\theta - \pi/2)] \equiv Ae^{iB} \qquad \text{(V.8)}$$

Thus $\mathrm{Re}\, f_a(\theta) = A\cos B$ and $\mathrm{Im}\, f_a(\theta) = A\sin B$; the ratio of the real to the imaginary part of the amplitude is then $\mathrm{Re}\, f_a(\theta)/\mathrm{Im}\, f_a(\theta) = \cot B = \cot(2\eta_{L_a} + L_a\theta - \pi/2)$; $\theta \neq 0, \pi$. This ratio approaches zero at low angles; this is of interest in connection with the low angle scattering discussion (Sec. VIII).

For the inner attractive contribution, b, $\eta''_{L_b} < 0$ and thus[20b]

$$J = \left(\frac{\pi}{-\eta''_{L_b}}\right)^{1/2} e^{-i\pi/4} \qquad \text{(V.9)}$$

so that

$$f_b(\theta) = -\frac{1}{k}\left[\frac{L_b}{2(-\eta''_{L_b})\cdot\sin\theta}\right]^{1/2}\exp[i(2\eta_{L_b} + L_b\theta)]$$

$$= \frac{1}{k}\left[\frac{L_b}{2(-\eta''_{L_b})\cdot\sin\theta}\right]^{1/2}\exp[i(2\eta_{L_b} + L_b\theta - \pi)] \qquad \text{(V.10)}$$

For the repulsive contribution, $f_c(\theta)$ is given by the analog of Eq. (V.6) with B_2 in place of B_1. However, $\eta''_{L_c} < 0$, so J is of the form (V.9). Thus we obtain

$$f_c(\theta) = \frac{1}{k}\left[\frac{L_c}{2(-\eta''_{L_c})\cdot\sin\theta}\right]^{1/2}\exp[i(2\eta_{L_c} - L_c\theta - \pi/2)] \qquad \text{(V.11)}$$

Combining Eqs. (V.8), (V.10), and (V.11) we obtain

$$f(\theta) = \frac{1}{k(2\sin\theta)^{1/2}}\left\{\left(\frac{L_a}{\eta''_{L_a}}\right)^{1/2}\exp\left[i\left(2\eta_{L_a} + L_a\theta - \frac{\pi}{2}\right)\right]\right.$$

$$+ \left(\frac{L_b}{-\eta''_{L_b}}\right)^{1/2}\exp[i(2\eta_{L_b} + L_b\theta - \pi)]$$

$$\left. + \left(\frac{L_c}{-\eta''_{L_c}}\right)^{1/2}\exp\left[i\left(2\eta_{L_c} - L_c\theta - \frac{\pi}{2}\right)\right]\right\}; \qquad (\theta \neq 0,\pi) \qquad \text{(V.12)}$$

Utilizing the semiclassical equivalence relationship, with $L_a \cong kb_{L_a}$, we note that the quantity $(L_a/\eta''_{L_a})^{1/2}$ becomes $k[2b/(d\Theta/db)]^{1/2}$, where $d\Theta/db$ is the slope of the deflection function at $b = b_{L_a}$. Similar expressions result at L_b and L_c.

Recalling the classical relation $I_i(\theta) = (b_i/\sin\theta|d\Theta/db_i|)$ (cf. Eq. II.3) it is seen that each of the three terms in Eq. (V.12) is of the proper form:

$$f_i(\theta) = [I_i(\theta)]^{1/2}e^{i\gamma_i} \qquad \text{(V.13)}$$

where γ_i is a phase factor) such that $I_i(\theta) = |f_i(\theta)|^2$. However, there will be interference among the three terms, which will yield a nonclassical angular distribution.

For later applications (Sec. IX) it will be of interest to consider the limiting form of Eq. (V.12) for small angles, $\sin\theta \cong \theta$). Referring to Figures 1*a* and 2, it is seen that for small angles the two inner regions coalesce, i.e.,

$$L_b \cong L_c \equiv L_0, \quad \eta_{L_b} \cong \eta_{L_c} \cong \eta_{\max} \equiv \eta_m,$$

$$\eta'_{L_b} \cong \eta'_{L_c} \cong 0, \quad \text{and} \quad \eta''_{L_b} \cong \eta''_{L_c} \equiv \eta''_0.$$

Thus the contribution of the last two terms of Eq. (V.12) may be approximated by

$$f_{bc}(\theta) \cong \frac{1}{k}\left[\frac{L_0}{2(-\eta_0'')\theta}\right]^{1/2} \exp[i(2\eta_m - 3\pi/4)]$$
$$\cdot\{\exp[i(L_0\theta - \pi/4)] + \exp[-i(L_0\theta - \pi/4)]\}$$
$$= \frac{2}{k}\left[\frac{L_0}{2(-\eta_0'')\theta}\right]^{1/2} \exp[i(2\eta_m - 3\pi/4)]\cdot\cos(L_0\theta - \pi/4)$$
$$\cong 2[I_{b,c}(\theta)]^{1/2} e^{i\gamma_m}\cdot\cos(L_0\theta - \pi/4) \qquad \text{(V.14a)}$$

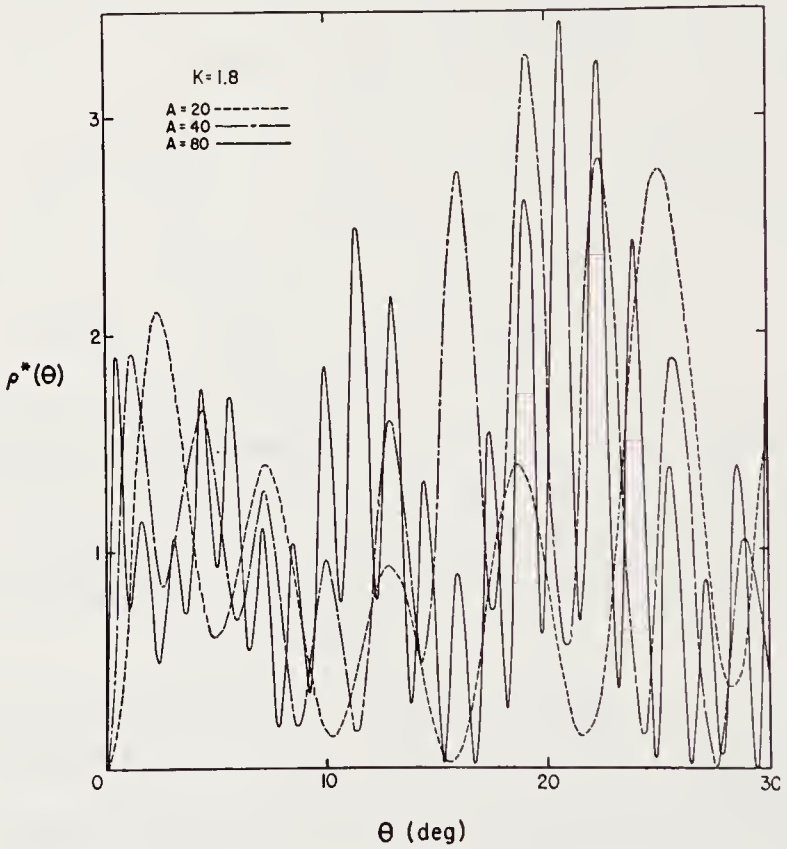

Fig. 9. Interference pattern, $\rho^*(\theta)$, calculated for scattering by an L.-J. (12,6) potential at *constant* $K = 1.8$, with various values of A: 20, 40, and 80, corresponding to values of the quantum parameter $\Lambda^* \equiv 2\pi K^{1/2}/A$ of 0.421, 0.210, and 0.105, respectively. Note the decreasing wavelength of the oscillations (with increase in A) but no significant decrease in the amplitude of the oscillations as the classical limit is approached.

where

$$I_{b,c}(\theta) = b_0/\sin\theta \cdot |d\Theta/db|_{b_0} \tag{V.14b}$$

is the classical contribution from branch b (or c), and $\gamma_m = 2\eta_m - 3\pi/4$ is the phase factor. Recalling the classical result (noting that $|d\Theta/db|_{b_{La}} \ll |d\Theta/db|_{L_0}$, i.e., that $I_a(\theta) \gg I_b(\theta) + I_c(\theta)$ for small angles) we incorporate Eq. (V.14) into Eq. (V.12) and express $f(\theta)$ for small angles in terms of the dominant long-range part:

$$f(\theta) \cong [I_a(\theta)]^{1/2} e^{i\gamma_a} \cdot \left\{1 + 2\left[\frac{I_{b,c}(\theta)}{I_a(\theta)}\right]^{1/2} \cdot e^{i(\gamma_m - \gamma_a)} \cdot \cos(L_0\theta - \pi/4)\right\} \tag{V.15}$$

where

$$\gamma_a \equiv 2\eta_{L_a} + L_a\theta - \pi/2$$

The origin of the interference effects in the angular distribution (e.g., Figs. 5, 7–9) is now apparent.

VI. THE INTERFERENCE PATTERN

For simplicity we restrict the present discussion to angles $\lesssim 30°$ (for which we may replace $\sin\theta$ by θ). From Eq. (V.15) we obtain the following expression for the differential cross section, provided, of course, that $\theta < \theta_r$:

$$I(\theta) = I_a(\theta)\{1 + [Y(\theta)]^2 + 2Y(\theta)\cos\gamma(\theta)\} \tag{VI.1}$$

where

$$Y(\theta) \equiv 2\left[\frac{I_{b,c}(\theta)}{I_a(\theta)}\right]^{1/2} \cos(L_0\theta - \pi/4) \equiv Y_{\max}(\theta)\cos(L_0\theta - \pi/4) \tag{VI.2}$$

and

$$\gamma(\theta) \equiv \gamma_m - \gamma_a = 2(\eta_m - \eta_{L_a}) - L_a\theta - \pi/4. \tag{VI.3}$$

Since $I_a(\theta) = I(\theta)^{(6)}$, Eq. (VI.1) may be rewritten to yield the desired ratio $\rho^*(\theta)$:

$$\rho^*(\theta) = 1 + [Y(\theta)]^2 + 2Y(\theta)\cos\gamma \tag{VI.4}$$

The main factor governing the interference pattern in $\rho^*(\theta)$ or $I(\theta)$ is that involving $Y(\theta)\cos\gamma$; since $2(I_{bc}/I_a) < 1$ for moderately small angles (i.e., θ not too close to θ_r), the Y^2 term is of lesser importance. The oscillatory product may be expressed

$$\cos(L_0\theta - \pi/4)\cdot\cos\gamma(\theta) = \tfrac{1}{2}\{\cos[-\theta(L_a - L_0) + 2(\eta_m - \eta_{L_a}) - \pi/2] + \cos[\theta(L_a + L_0) - 2(\eta_m - \eta_{L_a})]\} \tag{VI.5}$$

From this equation one sees that the "wavelengths" in the pattern of $\rho^*(\theta)$ are $2\pi/|L_a - L_0|$ and $2\pi/(L_a + L_0)$. The shorter of the two wavelengths is designated $\Delta\theta$. Thus

$$\Delta\theta = 2\pi/(L_a + L_0) \tag{VI.6}$$

is the angular spacing between successive minima (or maxima) in the oscillatory function $\rho^*(\theta)$. This is, for practical purposes, the same as the corresponding spacing in $I(\theta)$. It is noted that this spacing is not independent of angle; since L_a decreases with an increase in θ (see Fig. 1), the spacing $\Delta\theta$ increases with θ.

Figure 9 shows an example of a complicated interference pattern in $\rho^*(\theta)$, calculated† for an L.-J. (12,6) potential. The curves refer to one specified reduced collision energy K, with various assumed values of the wave number parameter A; or, alternately stated, for different values of the quantum parameter

$$\Lambda^* \equiv \frac{h}{\sigma(2\mu\epsilon)^{1/2}} = \frac{2\pi}{B^{1/2}} = \frac{2\pi K^{1/2}}{A}$$

For a given K, the deflection function $\Theta(\beta)$ is fully determined (and thus also the classical differential cross section), so differences due purely to quantum effects are clearly displayed. As expected, the periodicity of the oscillations decreases with increasing wave number. Rewriting Eq. (VI.6), we see that

$$A\Delta\theta = 2\pi/(\beta_{\theta a} + \beta_m) \tag{VI.7}$$

for any given K. Figure 10 shows an analysis of the interference pattern of Figure 9 (and of other similar curves at the same K), according to Eq. (VI.7). The agreement between spacings predicted (Eq. (VI.7)) and computed (from $\rho^*(\theta)$ curves) is nearly within the accuracy of the latter determinations, except for a few points at low angles.

Next we consider the amplitude of the oscillations in $\rho^*(\theta)$. Eq. (VI.2) shows that $Y(\theta)$ is governed by the classical intensity ratio $I_{b,c}(\theta)/I_a(\theta)$ or, alternatively expressed, by the classical $\rho^*(\theta)$, which is determined

† The calculations were made via the semiclassical (JWKB) phase shifts (Eq. 1b of Sec. IVb) and the exact summation formula for $I(\theta)$ (Eq. 8 of Sec. III).

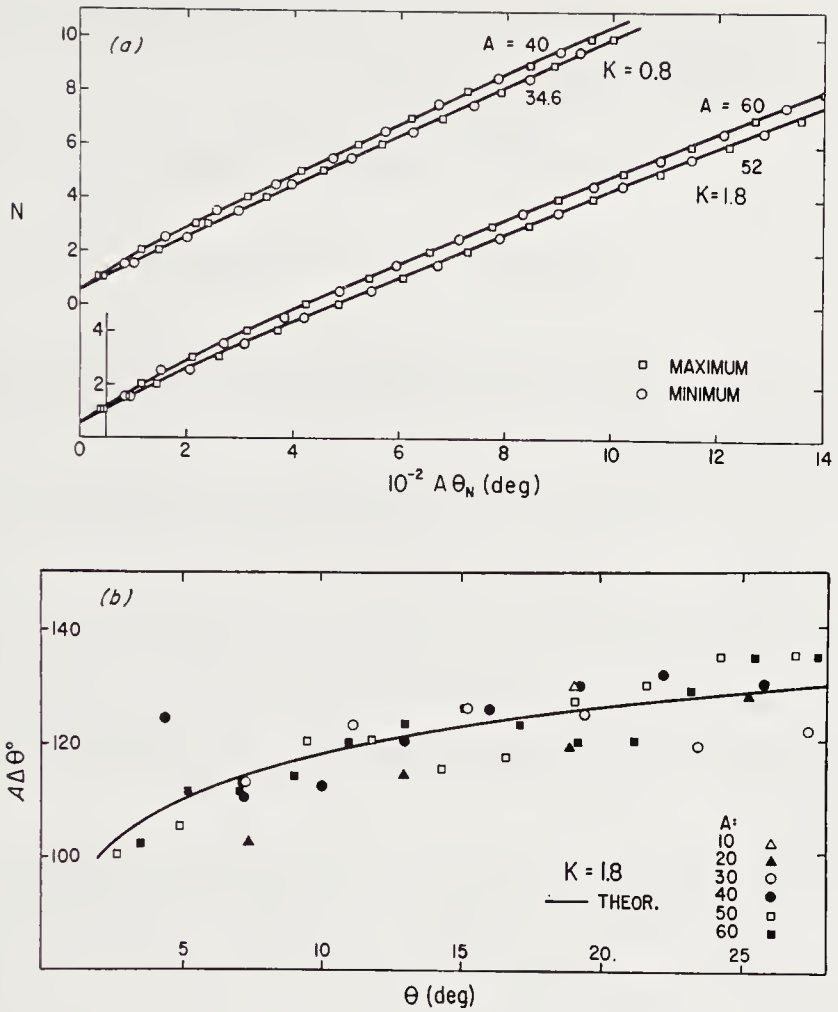

Fig. 10. (*a*) Correlation of interference spacings $\Delta\theta_{\min}$ obtained from calculations of $\rho^*(\theta)$ similar to those of Figure 9; $K = 0.8$ and 1.8. (*b*) Detail for $K = 1.8$ for various values of A: 10, 20, 30, 40, 50, 60, corresponding, respectively to $\Lambda^* = 0.842$, 0.421, 0.281, 0.210, 0.168, 0.140. The product $A\Delta\theta$ is plotted vs. θ, and compared with the theoretical curve: $A\Delta\theta = 2\pi/(\beta_a + \beta_m)$ (Eq. (VI.6)).

solely by K. Thus the amplitude is expected to be independent of the wave number or the quantum parameter. According to Eq. (VI.2) the maximum value allowed for $Y(\theta)$ is

$$Y_{\max}(\theta) = \sqrt{2}\cdot\left[\frac{2I_{b,c}(\theta)}{I_a(\theta)}\right]^{1/2} = \sqrt{2}\cdot[\rho^*_{\mathrm{cl}}(\theta) - 1]^{1/2} \qquad \text{(VI.8)}$$

where $\rho^*_{cl}(\theta)$ is the classical value of $\rho^*(\theta)$. (The minimum value for $Y(\theta)$ is, of course, $-Y_{max}(\theta)$.)

From Eq. (VI.4), $\rho^*(\theta)$ is bounded by

$$[1 + Y_{max}(\theta)]^2 \geqslant \rho^*(\theta) \geqslant [1 - Y_{max}(\theta)]^2 \tag{VI.9}$$

or

$$\{1 + \sqrt{2}\cdot[\rho^*_{cl}(\theta) - 1]^{1/2}\}^2 \geqslant \rho^*(\theta) \geqslant \{1 - \sqrt{2}\cdot[\rho^*_{cl}(\theta) - 1]^{1/2}\}^2. \tag{VI.10}$$

It is found that Eq. (VI.10) predicts quite well the envelope of the oscillations (i.e., the limits on the oscillation amplitude) for the examples of Figures 5 and 9.

Inspection of Figure 9 shows, in addition, a very important implication of Eq. (VI.10) i.e., the overall independence of the amplitude upon wave number (or quantum parameter). Thus, provided $\theta < \theta_r$, i.e., that three terms contribute to the amplitude, we see that while the angular spacing $\Delta\theta$ decreases smoothly to zero with increasing wave number (or decreasing quantum parameter) at constant K, the amplitude of the quantum interferences (oscillations) remains *finite* in the classical limit ($\Lambda^* = 0$). Experimentally, however, small velocity inhomogeneities would tend to mask the oscillations when $\Delta\theta$ becomes too small.

Following upon Eq. (V.15), we have restricted our discussion to small angles ($\theta \lesssim 30°$), but there is no difficulty in generalizing Eq. (V.15) slightly to include the larger angle cases provided, of course, that $\theta < \theta_r$, by keeping the f_b and f_c terms separate. The smallest angular spacing between minima, $\Delta\theta$, then becomes $2\pi/(L_a + L_b)$. Eq. (VI.10) for the amplitude of $\rho^*(\theta)$ should still be approximately correct, with $\rho^*_{cl}(\theta) = 1 + (I_b(\theta) + I_c(\theta))/I_a(\theta)$. The conclusion of the last paragraph about the persistence of the amplitude of the quantum effect is not altered.

However, for angles appreciably beyond the rainbow angle ($\theta > \theta_r$), only one branch of the deflection function contributes to $f(\theta)$; i.e., $f_b(\theta) \cong f_c(\theta) \cong 0$. Thus the quantum oscillations rapidly damp out in the classical limit (cf. Fig. 7*b*). This is the same behavior as that expected for any monotonic potential (for which, of course, the deflection function $\Theta(b)$ is also monotonic) in which case $I(\theta) = |f_a(\theta)|^2 \cong I_{cl}(\theta)$ (cf. Eq. V.13); a familiar example is that of scattering by the rigid-sphere potential.[16b]

The discussion of this section thus confirms the remark by Ford and Wheeler[2] that there exists the possibility of deducing information regarding the phase angles in the scattering amplitude by observing interference of waves scattered out of more than one part of the incident wave front. Experiments showing these interference effects have recently been carried out.[21]

VII. RAINBOW SCATTERING[2]

Ford and Wheeler[2] (FW) applied the semiclassical method to the calculation of the rainbow scattering amplitude for the general case, where Θ_r may be either positive or negative. In the present connection, i.e., for the atomic and molecular scattering problem, Θ_r and thus $(d\eta/dl)_{l_r}$ are invariably negative; $(d^2\eta/dl^2)_{l_r} = \frac{1}{2}(d\Theta/dl)_{l_r} = 0$ by definition of the rainbow condition and

$$(d^3\eta/dl^3)_{l_r} = \tfrac{1}{2}(d^2\Theta/dl^2)_{l_r} \equiv q$$

is always positive. For this special case it seems worthwhile to rederive (and at the same time amend) the FW results, retaining the notation of the previous sections.

The scattering amplitude near the rainbow angle can be expressed

$$f(\theta) = f_a(\theta) + f_b(\theta) + f_c(\theta) = f_r(\theta) + f_c(\theta) \qquad \text{(VII.1)}$$

where f_a and f_b have been combined to give the rainbow contribution to the amplitude, f_r, The repulsive contribution $f_c(\theta)$ is given by

$$f_c(\theta) = [I_c(\theta)]^{1/2} \cdot e^{i\gamma_c} \qquad \text{(VII.2)}$$

where $\gamma_c = 2\eta_{L_c} - L_c\theta - \pi/2$, as in Section V. To evaluate f_r, associated with the attractive branch of the deflection function, we must make use of the function B_1 of Eq. (V.4). Expanding η_l in the neighborhood of the rainbow angle, we find

$$\eta_l = \eta_r - \tfrac{1}{2}\theta_r \cdot (l - l_r) + \tfrac{1}{6}q \cdot (l - l_r)^3 \qquad \text{(VII.3)}$$

This is accomplished by making use of the expansion $\Theta = \Theta_r + q(l - l_r)^2$ and noting that $\theta = -\Theta_r$. The fact that $\eta''_{l_r} = 0$ makes it necessary to extend the stationary phase treatment of Section V to include the cubic terms in Eq. (VII.3). Thus

$$B_1 = 2\eta_r - \theta_r \cdot (l - l_r) + \tfrac{1}{3}q \cdot (l - l_r)^3 + l\theta + \pi/4 \equiv B_1(l_r) + \Delta B_1 \qquad \text{(VII.4)}$$

where

$$B_1(l_r) \equiv 2\eta_r + l_r\theta_r + \pi/4$$

and

$$\Delta B_1 = \tfrac{1}{3}q\cdot(l - l_r)^3 + (\theta - \theta_r)\cdot(l - l_r) + l_r\cdot(\theta - \theta_r)$$

so that

$$\begin{aligned} f_r(\theta) &\cong -\frac{1}{k}\left[\frac{l_r}{2\pi \sin\theta}\right]^{1/2} e^{iB_1(l_r)} \int_{-\infty}^{\infty} e^{i\Delta B_1}\cdot d(l - l_r) \\ &= -\frac{1}{k}\left[\frac{l_r}{2\pi \sin\theta}\right]^{1/2} \exp[i(2\eta_r + l_r\theta + \pi/4)] \\ &\quad \cdot\int_{-\infty}^{\infty} \exp\{i[\tfrac{1}{3}q(l - l_r)^3 + (\theta - \theta_r)(l - l_r)]\}\, d(l - l_r) \\ &= \frac{1}{k}\left[\frac{l_r}{2\pi \sin\theta}\right]^{1/2} e^{i\delta} q^{-1/3}\cdot 2\pi \mathrm{Ai}(x) = [I_r(\theta)]^{1/2}\cdot e^{i\delta} \end{aligned} \tag{VII.5}$$

where

$$\delta \equiv 2\eta_r + l_r\theta - 3\pi/4, \quad x \equiv q^{-1/3}\cdot(\theta - \theta_r),$$

$\mathrm{Ai}(x)$ is the Airy function, and $I_r(\theta) = |f_r(\theta)|^2$. (The above result (correct) for the phase angle δ differs by $-\pi/2$ from that quoted by FW_I.) Thus

$$f(\theta) \cong [I_c(\theta)]^{1/2} e^{i\gamma_c} + [I_r(\theta)]^{1/2} e^{i\delta} \tag{VII.6}$$

and

$$I(\theta) \cong I_c(\theta) + I_r(\theta) + 2(I_c\cdot I_r)^{1/2}\cdot\cos(\delta - \gamma_c) \tag{VII.7}$$

where

$$I_r(\theta) = \frac{1}{k^2}\cdot\frac{2\pi l_r}{\sin\theta}\cdot q^{-2/3}\cdot \mathrm{Ai}^2[q^{-1/3}\cdot(\theta - \theta_r)].$$

Since the principal maximum of $\mathrm{Ai}(x)$ occurs for $x \cong -1$, $I_r(\theta)$ achieves its largest value at an angle significantly smaller than the rainbow angle, namely, where $\theta = \theta_r - q^{1/3}$. As pointed out by FW, the low-resolution rainbow "peak" is spread out over an appreciable angular range and under no conditions (i.e., even at high k) approximates the classical sharp "spike" in the differential cross section at $\theta = \theta_r$.

The interference pattern near the rainbow angle is given by Eq. (VII.7). The differential cross section oscillates between the limits $I_{\max}(\theta)$ and $I_{\min}(\theta)$ where

$$I_{\max}(\theta) = [I_r^{1/2} + I_c^{1/2}]^2 \quad \text{and} \quad I_{\min}(\theta) = [I_r^{1/2} - I_c^{1/2}]^2 \tag{VII.8}$$

with a periodicity governed by $\delta - \gamma_c$. Analogous to the treatment in Section VI (which yielded Eq. (VI.6)) we obtain for the "wavelength" of the oscillations in the neighborhood of the broad rainbow maximum:

$$\Delta\theta = \frac{2\pi}{[d(\delta - \gamma_c)/d\theta]} = \frac{2\pi}{l_r + L_c} . \qquad \text{(VII.9)}$$

As one progresses to angles appreciably larger than the rainbow angle, the amplitude of the oscillations decreases and eventually the nearly monotonic behavior characteristic of single-branch (noninterfering) scattering obtains. On the low-angle side of the rainbow, the three contributions (from the two branches of the deflection function) always produce interference, as discussed in Section V.

Computations[6c,9b,21a] of $I(\theta)$ employing the full phase-shift treatment for monoenergetic scattering by an L.-J. (12,6) potential have not always displayed distinct rainbow maxima which show through the oscillatory pattern (cf. Fig. 7a). However, for values of the quantum parameter Λ^* smaller than about 0.1, the expected effect appears, quite pronounced (cf. Fig. 7b).

There is now ample experimental confirmation of the rainbow scattering phenomenon in atomic and molecular systems via beam-scattering studies in a number of laboratories.[22]† As originally pointed out by Mason,[3] measurements of the energy dependence of θ_r make possible in a rather direct way the evaluation of the potential well depth ϵ for an assumed functional form of the interaction potential. Suitable calculations of rainbow angle vs. K have now been made for the L.-J. (12,6),[1a,22a] Exp(α,6)[3,23], Kihara,[23] and Morse[24,25] potential functions.

The related "tunneling-orbiting" phenomenon has also received a certain amount of attention[1a,2,6c,25a] but the subject has not yet been fully developed and, for reasons of brevity, will not be treated here.

VIII. LOW-ANGLE SCATTERING[26]

Massey and Mohr[16b,27] (MM) first considered the problem of the limiting form of the low-angle behavior of the differential scattering cross section according to quantum mechanics. It was found that for any potential falling off faster than r^{-2}, $I(\theta)$ and thus Q is finite. They also introduced the so-called random-phase (rph) approximation, which

† Recently it has been possible to resolve experimentally[22d] the low-angle satellites of the rainbow maximum (cf. Fig. 7*b*), termed "supernumerary rainbows."[22e]

is especially applicable to the practical heavy-particle case in which a great many phase shifts are required in the sums for the cross sections. Since most of these phases are large (compared to π) and only principal values of the angles are relevant, they (the η_l's) may be considered to be essentially random numbers, for $0 \leqslant l \leqslant L$. The upper limit, L, may be estimated fairly accurately for the rigid-sphere case; here $L \cong kr_0$, where r_0 is the rigid-sphere diameter.

Eq. (III.8) may be expressed as

$$I(\theta) = \frac{1}{4k^2}\left\{\left[\sum_l (2l+1)\sin 2\eta_l \cdot P_l(\cos\theta)\right]^2 + \left[\sum_l (2l+1)\cdot 2\sin^2\eta_l \cdot P_l(\cos\theta)\right]^2\right\} \tag{VIII.1}$$

With the random-phase assumption (strictly valid only in the rigid-sphere case in the limit of very high wavenumber, i.e., $kr_0 \gg 1$) the first term is negligible compared with the second, due to the extensive cancellation in the oscillating $\sin 2\eta_l$ term. In the limit $\theta \cong 0$, upon replacing all terms in $P_l(\cos\theta)$ by 1, we obtain

$$I(0)_{\text{rph}} \cong \frac{1}{k^2}\left[\sum_l (2l+1)\sin^2\eta_l\right]^2 = \left(\frac{kQ}{4\pi}\right)^2 \tag{VIII.2}$$

(making use of the expression for Q which has been given in Eq. (III.9)). The quantity $(kQ/4\pi)^2$ will be designated $I(0)_{\text{rph}}$ hereafter. Removing the average value of $\sin^2\eta_l$ (i.e., $\langle\sin^2\eta_l\rangle_{\text{rph}} = \frac{1}{2}$), we obtain for the rigid-sphere case the well-known result

$$I(0) \cong \frac{1}{k^2}\left[\frac{1}{2}\sum_{l=0}^{L}(2l+1)\right]^2 = \frac{(L+1)^4}{4k^2} \cong \tfrac{1}{4}k^2r_0^4 \tag{VIII.3}$$

and

$$Q \cong 2\pi r_0^2 \tag{VIII.4}$$

For backscattering, i.e., $\theta = \pi$, with $P_l(-1) = (-1)^l$ we find

$$I(\pi) \cong \frac{1}{k^2}\left[\frac{1}{2}\sum_{l=0}^{L}(2l+1)(-1)^l\right]^2 = \frac{(L+1)^2}{4k^2} \cong \tfrac{1}{4}{r_0}^2 \tag{VIII.5}$$

which is the classical result for the differential cross section (classically the scattering would be isotropic with $I(\theta) = \frac{1}{4}r_0^2$ for all θ). The strong nonclassical forward peak (Eq. (VIII.3)), known as the diffraction or shadow scattering contribution, increases in magnitude with increasing

k but is confined to smaller and smaller angles (i.e., $\theta < \theta^*$, where θ^* is the limiting angle) as k is increased[16b]; here $\theta^* \cong \pi/kr_0$. Making use of this, Massey and Mohr[16b] showed that the shadow scattering contributes (approximately) a constant amount, namely πr_0^2, to the total cross section of $2\pi r_0^2$ (Eq. (VIII.4)).

Employing the rph-approximation and taking advantage of the expansion of $P_l(\cos\theta)$ at small angles, they proposed[27] that the low-angle differential scattering cross section was of an exponential form. It will be instructive to derive here the limiting ($\theta \to 0$) functional form of $I(\theta)$ within the framework of the random-phase approximation.

In general, as noted in Section III, the scattering amplitude consists of a real and an imaginary part

$$\mathrm{Re}\, f(\theta) = \frac{1}{2k}\sum_l (2l+1)\sin 2\eta_l P_l(\cos\theta) \tag{VIII.6}$$

$$\mathrm{Im}\, f(\theta) = \frac{1}{k}\sum_l (2l+1)\sin^2 \eta_l P_l(\cos\theta) \tag{VIII.7}$$

[It is noted that for the random-phase case (i.e., $\langle \sin 2\eta_l \rangle_{\mathrm{rph}} = 0$) $\mathrm{Re}\, f(\theta) = 0$; thus the scattering amplitude is pure imaginary and $I(\theta) = [\mathrm{Im}\, f(\theta)]^2$.]

Setting $\theta = 0$ and comparing Eq. (VIII.7) with Eq. (III.9), we obtain the very important general result (known as the optical theorem):

$$Q = \frac{4\pi}{k}\,\mathrm{Im}\, f(0) \tag{VIII.8}$$

from which we derive the useful inequality:

$$[\mathrm{Re}\, f(0)]^2 = I(0) - \left(\frac{kQ}{4\pi}\right)^2 = I(0) - I(0)_{\mathrm{rph}} \geqslant 0 \tag{VIII.9}$$

Thus the (extrapolated) forward differential scattering cross section $I(0)$ may never be *less* than $(kQ/4\pi)^2$. This allows a (partial) consistency check on experimental measurements of low-angle differential cross sections and independently obtained (e.g., via attenuation measurements) total cross sections.

It is convenient to define a dimensionless "forward scattering ratio"

$$j(k) \equiv \frac{I(0)}{I(0)_{\mathrm{rph}}} = 1 + \left[\frac{\mathrm{Re}\, f(0)}{\mathrm{Im}\, f(0)}\right]^2 \geqslant 1 \tag{VIII.10}$$

It is seen that the quantity $(j-1)^{1/2} = \mathrm{Re}f(0)/\mathrm{Im}f(0)$ is a measure of the deviation from the rph-approximation condition. In general, the fractional part of the forward intensity due to the real part of $f(\theta)$ is

$$[\mathrm{Re}f(0)]^2/I(0) = (j-1)/j \qquad \text{(VIII.11)}$$

(with $j = 1$ implying zero for the real part of the forward amplitude).

Figure 11 shows a graph of $j(kr_0)$ for the rigid-sphere potential compared to the L.-J. (12,6) potential (for a specified value of the

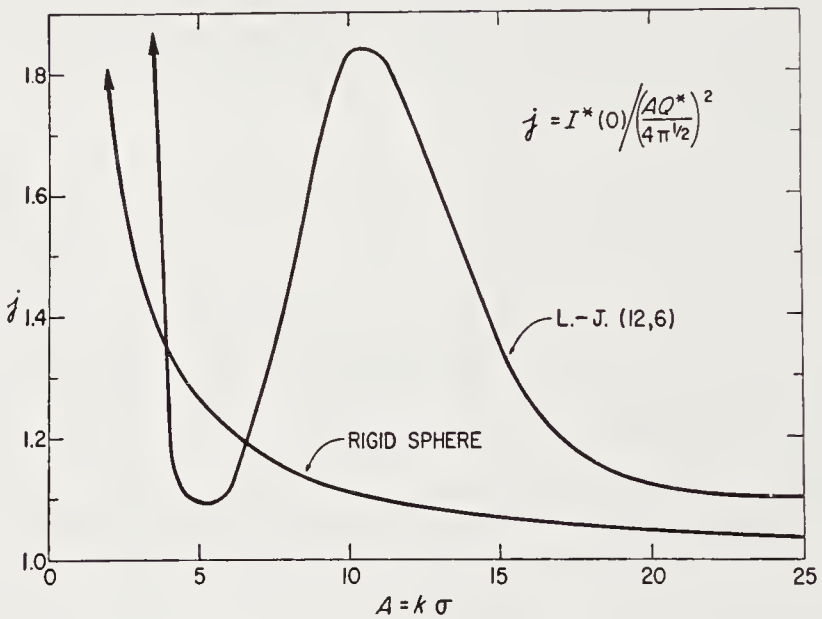

Fig 11. Plot of the "forward scattering ratio" j vs. A ($\equiv k\sigma$) for the rigid sphere potential and for the L.-J. (12,6) potential with $B = 125$.

parameter B). It is seen that *even in the rigid-sphere case* at $A \equiv kr_0 \cong 25$ (i.e., $r_0/\lambda \cong 4$), the ratio $\mathrm{Re}f(0)/\mathrm{Im}f(0)$ is significantly greater than zero (ca. 1/5); for the L.-J. potential it may even exceed unity.

The undulatory behavior in $j(A)$ is characteristic of a realistic interaction potential with a minimum (an attractive well); the origin of the extrema will be discussed in the next section. It will suffice here to call attention to the fact that the velocity dependence of the forward scattering should show such extrema, with the magnitude of the "excess" in j indicating the fractional contribution of the real part of the forward scattering amplitude which originates from the "non-random" phases.

Continuing with the rph-approximation, the low-angle differential cross section is readily evaluated by expanding the Legendre polynomial[28] and replacing the sum over l by an integral as usual. Thus we obtain:

$$I(\theta) = [\mathrm{Im}\, f(\theta)]^2 = \left[\frac{1}{k}\int_0^L 2l\cdot\tfrac{1}{2}\cdot\left(1 - \frac{l^2\theta^2}{4} + \frac{l^4\theta^4}{64} - \cdots\right) dl\right]^2$$

$$\cong \frac{L^4}{4k^2}\cdot\left[1 - \frac{\theta^2 L^2}{8} + \frac{\theta^4 L^4}{192} - \cdots\right]^2$$

$$= I(0)_{\mathrm{rph}}\cdot\left[1 - \left(\frac{k^2 Q\theta^2}{8\pi}\right) + \frac{1}{2}\left(\frac{k^2 Q\theta^2}{8\pi}\right)^2\cdot\frac{5}{6} - \cdots\right]$$

$$\cong I(0)_{\mathrm{rph}}\cdot\exp[-k^2 Q\theta^2/8\pi] \qquad \text{(VIII.12)}$$

where we have made use of Eqs. (VIII.2) and (VIII.3), i.e., $L^2 \cong k^2 Q/2\pi$ and approximated the series $1 - x + \frac{1}{2}x^2\cdot\frac{5}{6} - \cdots$ by e^{-x}, for $x \ll 1$. For low angle scattering by a *rigid sphere* potential, replacing $I(0)_{\mathrm{rph}}$ by $I(0)[=j\cdot I(0)_{\mathrm{rph}}]$, we have

$$I(\theta) = j(kr_0)\cdot\left(\frac{kQ}{4\pi}\right)^2\exp[-k^2 Q\theta^2/8\pi] \qquad \text{(VIII.13)}$$

with $j(kr_0) \to 1$ and $Q \to 2\pi r_0^2$ in the "classical" limit. For this limiting case, as a check, we estimate the contribution ΔQ to the total cross section $Q(=2\pi r_0^2)$ from the strong shadow scattering peak, assuming the exponential approximation for $I(\theta)$ to be valid out to θ^*:

$$\Delta Q = \int_0^{\theta^*} 2\pi I(\theta)\sin\theta\, d\theta \cong 2\pi I(0)_{\mathrm{rph}}\cdot\int_0^{\theta^*}\theta\exp[-k^2 Q\theta^2/8\pi]\, d\theta$$

$$= \frac{8\pi^2}{k^2 Q}\cdot I(0)_{\mathrm{rph}}\left\{1 - \exp\left[-\frac{k^2 Q\theta^{*2}}{8\pi}\right]\right\} \cong \frac{Q}{2}\cdot(0.92) \cong \pi r_0^2 \qquad \text{(VIII.14)}$$

as expected.

Next we reconsider the important problem of low-angle scattering by an inverse-power potential of the form $V(r) = -C^{(s)}/r^s$. In connection with his measurements of small-angle scattering, Pauly[26a] derived an approximate expression (via the Massey-Mohr technique) for the differential cross section at low angles, for an inverse sixth-power potential. He obtained

$$I(\theta) = j(6)I(0)_{\mathrm{rph}}\exp[-c(k^2 Q\theta^2/8\pi)] \qquad \text{(VIII.15)}$$

with $c = 2.08$ and $j = 1.36$. The latter implies, via Eq. (VIII.10), a large and constant ratio of the real to the imaginary part of the forward amplitude, i.e., $\mathrm{Re}f(0)/\mathrm{Im}f(0) = 0.6$; it is large because of the many small and slowly-varying high-order phase shifts associated with this long-range potential. The factor c in the exponent is to be compared to unity for the rph case; it originates from the above source. Helbing and Pauly[26b,c] and Mason et al.[26d] have independently repeated and refined the derivation, extending it to the general case ($s > 5$). Their results are in excellent agreement. For the special case of $s = 6$, they obtained $j = 1.525$ and $c = 2.07$. (This value of j supersedes the less reliable, earlier value quoted above. It yields a still higher real component to the forward amplitude; the ratio $\mathrm{Re}f(0)/\mathrm{Im}f(0) = 0.725$.)

We now outline the derivation of the general case, following along the lines of reference 26d. For the potential above, the higher-order phase shifts are given by

$$\eta_{\mathrm{JB}}^{(s)} \cong a_s l^{1-s} \tag{VIII.16a}$$

where

$$a_s = f(s)\mu C^{(s)} k^{s-2}/\hbar^2 \tag{VIII.16b}$$

according to Eq. (IVb.3).

Expanding the Legendre polynomial (here we carry only first-order terms), and simplifying as usual, Eq. (VIII.1) may be written:

$$I(\theta)^{(s)} \cong \frac{4}{k^2}\left\{\left[J_1 - \frac{\theta^2}{4}J_2\right]^2 + \frac{1}{4}\left[J_3 - \frac{\theta^2}{4}J_4\right]^2\right\} \tag{VIII.17a}$$

where

$$J_1 \equiv \int_0^\infty dl\, l \sin^2\eta \qquad J_2 \equiv \int_0^\infty dl\, l^3 \sin^2\eta_l$$

$$J_3 \equiv \int_0^\infty dl\, l \sin 2\eta_l \qquad J_4 \equiv \int_0^\infty dl\, l^3 \sin 2\eta_l \tag{VIII.17b}$$

Factoring out the most important quantities, we may express $I(\theta)^{(s)}$ in terms of the key integral J_1 and various ratios of integrals:

$$I(\theta)^{(s)} \cong \frac{4}{k^2}J_1^2\left\{\left[1 - \frac{\theta^2}{4}\frac{J_2}{J_1}\right]^2 + \frac{1}{4}\left(\frac{J_3}{J_1}\right)^2 \cdot \left(1 - \frac{\theta^2}{4}\cdot\frac{J_4}{J_3}\right)^2\right\} \tag{VIII.18}$$

Before proceeding, we note that J_1 is closely related to the imaginary part of the forward amplitude and thus to the total cross section. From the definition of J_1 and Eq. (VIII.7) (replacing the sum by an integral over l as usual), we deduce the relations

$$J_1 \cong \frac{k}{2} \operatorname{Im} f(0) = k^2 Q/8\pi. \tag{VIII.19}$$

To evaluate the integrals J_1–J_4 exactly would require an accurate knowledge of η_l for all l. We may circumvent this by following the suggestion of Landau and Lifshitz[29] to replace η_l by η_{JB} throughout, since the principal contribution to the integrals arises from the higher-order phases in any case. All the J integrals may be put into a common standard form; the results may be summarized as follows:

$$J_1 = a^{2/(s-1)}/G(s), \quad \text{where} \quad G(s) \equiv \frac{1}{\pi} \cdot 2^{(3s-5)/(s-1)} \cdot \sin\left(\frac{\pi}{s-1}\right) \cdot \Gamma\left(\frac{2}{s-1}\right) \tag{VIII.20a}$$

$$\frac{J_2}{J_1} = (2a)^{2/(s-1)} \cdot \frac{\frac{1}{2} \sin\left(\frac{\pi}{s-1}\right) \cdot \Gamma\left(\frac{2}{s-1}\right)}{\sin\left(\frac{2\pi}{s-1}\right) \cdot \Gamma\left(\frac{4}{s-1}\right)}$$

$$= J_1 \cdot \frac{2}{\pi} \cdot \tan\left(\frac{\pi}{s-1}\right) \cdot \frac{\left[\Gamma\left(\frac{2}{s-1}\right)\right]^2}{\Gamma\left(\frac{4}{s-1}\right)} \tag{VIII.20b}$$

$$\frac{J_3}{J_1} = \left(\frac{4}{s-1}\right) \frac{\sin\left(\frac{\pi}{s-1}\right) \cdot \Gamma\left(\frac{2}{s-1}\right)}{\sin\left(\frac{\pi}{2} \cdot \frac{s+1}{s-1}\right) \cdot \Gamma\left(\frac{s+1}{s-1}\right)}$$

$$= 2 \tan\left(\frac{\pi}{s-1}\right) \tag{VIII.20c}$$

$$\frac{J_4}{J_3} = (2a)^{2/(s-1)} \cdot \frac{\frac{1}{2}\cos\left(\frac{\pi}{s-1}\right)\cdot\Gamma\left(\frac{2}{s-1}\right)}{\cos\left(\frac{2\pi}{s-1}\right)\cdot\Gamma\left(\frac{4}{s-1}\right)}$$

$$= J_1 \cdot \frac{2}{\pi} \cdot \tan\left(\frac{2\pi}{s-1}\right) \cdot \frac{\left[\Gamma\left(\frac{2}{s-1}\right)\right]^2}{\Gamma\left(\frac{4}{s-1}\right)} \qquad \text{(VIII.20d)}$$

Thus

$$I(\theta)^{(s)} \cong \frac{4}{k^2}\left(\frac{k^2Q}{8\pi}\right)^2 \left\{\left[1 - \frac{k^2Q}{16\pi} f_1(s)\theta^2\right]^2 + \tan^2\left(\frac{\pi}{s-1}\right)\cdot\left[1 - \frac{k^2Q}{16\pi} f_2(s)\theta^2\right]^2\right\} \qquad \text{(VIII.21)}$$

where

$$f_1(s) = \frac{1}{\pi}\tan\left(\frac{\pi}{s-1}\right)\cdot\frac{\left[\Gamma\left(\frac{2}{s-1}\right)\right]^2}{\Gamma\left(\frac{4}{s-1}\right)} \qquad \text{(VIII.22a)}$$

and

$$f_2(s) = \frac{1}{\pi}\tan\left(\frac{2\pi}{s-1}\right)\cdot\frac{\left[\Gamma\left(\frac{2}{s-1}\right)\right]^2}{\Gamma\left(\frac{4}{s-1}\right)} \qquad \text{(VIII.22b)}$$

Squaring terms in Eq. (VIII.21) and dropping only terms involving θ^4, we obtain finally

$$I(\theta)^{(s)} \cong \left(\frac{kQ}{4\pi}\right)^2\left[1 + \tan^2\left(\frac{\pi}{s-1}\right)\right]\cdot\left[1 - \tfrac{1}{2}f_2(s)\frac{k^2Q\theta^2}{8\pi}\right]. \qquad \text{(VIII.23)}$$

Mason et al.[26d] retained the terms in θ^4 and then replaced the quantity in the second bracket by the exponential, yielding a result which may be expressed in our "standard form"

$$\frac{I(\theta)^{(s)}}{I(0)_{\text{rph}}} \cong j(s)\exp\left[-c(s)\frac{k^2Q}{8\pi}\theta^2\right] \qquad \text{(VIII.15′; VIII.24a)}$$

with†

$$j(s) = 1 + \tan^2\left(\frac{\pi}{s-1}\right)$$

and

$$c(s) = \frac{1}{2\pi}\tan\left(\frac{2\pi}{s-1}\right)\cdot\frac{\left[\Gamma\left(\frac{2}{s-1}\right)\right]^2}{\Gamma\left(\frac{4}{s-1}\right)}; \quad [c(6) = 2.07]. \qquad \text{(VIII.24b)}$$

Here we see that for the inverse sth power potential,

$$\mathrm{Re}\, f(0)/\mathrm{Im}\, f(0) = \tan[\pi/(s-1)]$$

Thus the ratio approaches zero as $s \to \infty$ (i.e., the rigid sphere case).

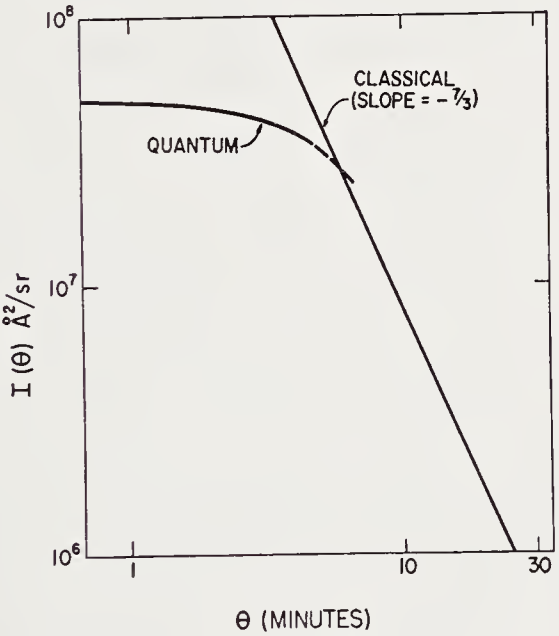

Fig. 12. Log-log plot of $I(\theta)$ at very low angles, calculated[26d] according to Eq. (VIII.24) (quantum), compared with the classical result. The calculations refer to the K–Hg system at a relative velocity of 6.35×10^4 cm sec^{-1}, assuming $C^{(6)} = 8.1 \times 10^{-57}$ erg cm^6.

† It is noted that this result for j is velocity independent, whereas even for the rigid-sphere potential (cf. Fig. 11) j varies with kr_0, only approaching constancy (unity) as $\lambda/r_0 \to 0$. This is due to the significant fractional contribution of the non-random, higher order phases even in this case; however, their relative importance decreases with increasing kr_0.

Helbing and Pauly's[26c] result is identical with Eq. (VIII.24) but expressed slightly differently; they introduce an angle θ_s^* such that the exponential may be expressed as $\exp[-(\theta/\theta_s^*)^2]$; thus for $s = 6$, $\theta^* = 1.965/[k(Q/\pi)^{1/2}]$.

Figure 12 shows a typical plot[26d] of the low-angle differential cross section according to Eq. (VIII.24). The important quantum feature is the leveling off of the differential cross section to a finite value as $\theta \to 0$. This yields, of course, a finite total cross section (in contrast to the classical infinite result) as required; this will be discussed further in the next section.

IX. GLORY INTERFERENCE EFFECT AT LOW ANGLES

For a realistic, nonmonotonic potential, the classical deflection function $\Theta(b)$ will always pass through zero at a finite value of the impact parameter, say b_0; if the collision energy is low enough it may also go through $-\pi$, -2π, etc.[1] Classically (Eq. (II.3)), whenever $\sin\theta = 0$ (provided $d\theta/db$ is finite), a pole (or "glory"[2]) occurs in the scattering at the appropriate angle (zero for a forward glory, 180° for a backward glory).

For simplicity we consider here only the forward glory, which is always found (at all energies) in the scattering by a realistic potential. Figure 1 showed a typical deflection function with the glory impact parameter $b_0 = \beta_m\sigma$ while Figure 2 illustrated the effect on the differential cross section in a graphical way: one notes the vertical tangent (dB/dC) at $C = 1$ (i.e. $\theta = 0$) for $B = (1/2\pi)\beta_m^2$. Thus there are two classical contributions to the divergence in the forward scattering, one from very large impact parameters ($b \to \infty$) and the other from the glory impact parameter. Quantum mechanically these interfere, so we must add amplitudes rather than intensities, as discussed in Section V. In this section we elaborate further on this glory interference, with particular attention to its energy dependence.

Ford and Wheeler[2] first developed an expression for the glory amplitude, making use of the stationary phase approximation. We will rederive their result and combine it with Eq. (V.8) for $f_a(\theta)$, the "outer attractive" contribution to the amplitude. This will yield an equation (essentially, Eq. (VI.1)) for the low-angle scattering which correctly takes into account the important forward glory contribution for a realistic potential. It therefore supersedes Eq. (VIII.24a), intended to

apply only to a *monotonic* (r^{-s}) potential. The oscillatory behavior of the forward scattering ratio $j(k)$ (pointed out in the previous section) is a direct consequence of the glory contribution to the low angle scattering.

The derivation of FW is spelled out for a backward glory, while we choose here to deal specifically with the forward glory effect and its interference with the long-range contribution to the low angle scattering.

Returning to the treatment of Section V, we note that in the present application the Laplace expansion for the Legendre polynomial is not valid, since $\theta \lesssim l^{-1}$. We employ, therefore, one of the expansions in terms of the Bessel function, for example, that of Hilb[28]:

$$P_l(\cos\theta) \sim \left(\frac{\theta}{\sin\theta}\right)^{1/2} J_0[(l+\tfrac{1}{2})\theta] \cong J_0(l\theta) \tag{IX.1}$$

valid for large l and small θ. Here J_0 is the zero-order Bessel function,

$$J_0(l\theta) = \int_0^{2\pi} \exp(il\theta\cos\phi)\, d\phi/2\pi. \tag{IX.2}$$

In the neighborhood of the maximum phase (or the "glory phase"), designated $\eta_m(\beta_m)$ or $\eta_m(L_0)$, we expand η (to the quadratic term only):

$$\eta = \eta_m + \tfrac{1}{2}\eta_m''\cdot(l - L_0)^2 \tag{IX.3a}$$

where

$$\eta_m'' \equiv \left[\frac{d^2\eta}{dl^2}\right]_{L_0} = \frac{1}{2}\left[\frac{d\Theta}{dl}\right]_{L_0} = \frac{1}{2A}\left[\frac{d\Theta}{d\beta}\right]_{\beta_m} < 0. \tag{IX.3b}$$

Then, upon making the usual approximations, and proceeding as before, using Eqs. (V.6b) and (V.9), we obtain the glory amplitude

$$f_g(\theta) \cong \frac{e^{2i\eta_m}}{ik} L_0\, J_0(L_0\theta) \int_{-\infty}^{\infty} \exp[i\eta_m''\cdot(l - L_0)^2]\, d(l - L_0)$$

$$= \frac{1}{k}\left[\frac{\pi}{-\eta_m''}\right]^{1/2} L_0\, J_0(L_0\theta)\exp[i(2\eta_m - 3\pi/4)] = [I_g(\theta)]^{1/2} e^{i\gamma_m} \tag{IX.4a}$$

where

$$\gamma_m \equiv 2\eta_m - 3\pi/4$$

and

$$I_g(\theta) \equiv \frac{\pi L_0^2}{k^2(-\eta_m'')}[J_0(L_0\theta)]^2 = I_g(0)\left[1 - \frac{L_0^2\theta^2}{2} + \cdots\right] \tag{IX.4b}$$

with $I_g(0) \equiv [\pi/(-\eta_m'')](L_0^2/k^2)$. The above expansion of J_0 is useful only for very small angles†: $\theta \lesssim l^{-1}$. Eq. (4a) yields the important results:

$$\operatorname{Im} f_g(0) = [I_g(0)]^{1/2} \sin(2\eta_m - 3\pi/4) \tag{IX.5a}$$

and

$$\operatorname{Re} f_g(0) = [I_g(0)]^{1/2} \cos(2\eta_m - 3\pi/4). \tag{IX.5b}$$

We also recall (from Eq. (VIII.7)) that for the long-range (outer attractive) contribution (cf. Eq. (VIII.17b)),

$$\operatorname{Im} f_a(0) \cong \frac{2}{k}\int_0^\infty dl\, l \sin^2 \eta_{\mathrm{JB}} = \frac{2}{k}\cdot J_1 \tag{IX.5c}$$

In Section VI the interference pattern in the angular distribution arising from the glory effect has been analyzed in detail, but an important feature was intentionally omitted and reserved for the present discussion, namely, the energy dependence (or velocity dependence) of the forward scattering.

We have seen in Section VIII that $j(s)$, the forward scattering ratio for an inverse-s power potential is independent of k (Eq. (VIII.24b)): $j(s) = 1 + \tan^2(\pi/(s-1))$, so that $\operatorname{Im} f(0)/\operatorname{Re} f(0) = \cot(\pi/(s-1)) =$ const.) However, considering the glory contribution (alone), this ratio is seen to be $\tan(2\eta_m - \frac{3}{4}\pi)$, fluctuating from zero (pure positive real) when $\eta_m(k) = \frac{3}{8}\pi$, to ∞ (pure positive imaginary) when $\eta_m(k) = \frac{5}{8}\pi$, to zero again (pure positive real) when $\eta_m(k) = \frac{7}{8}\pi$ and to $-\infty$ (pure negative imaginary) when $\eta_m(k) = \frac{9}{8}\pi$, etc. Thus for a nonmonotonic,

† In Eq. (IX.4b) the Bessel function has been expanded in order to display the angular dependence of the glory scattering at very low angles; however, for $\theta \gtrsim l^{-1}$ this development is no longer valid and the sinusoidal expansion is to be used:

$$J_0(L_0\theta) \sim (2/\pi L_0\theta)^{1/2} \cos(L_0\theta - \pi/4) \tag{IX.6}$$

so that

$$f_g(\theta) = \frac{1}{k}\left[\frac{2L_0}{-\eta_m''}\right]^{1/2} \cos\left(L_0\theta - \frac{\pi}{4}\right) e^{i\gamma_m} \tag{IX.7}$$

identical with Eq. (V.14), obtained in a very slightly different way. Thus

$$I(\theta) = I_a(\theta)\left\{1 + 2\left[\frac{L_0}{L_a}\cdot\frac{\eta L_a''}{(\eta_m'')}\right]^{1/2} \exp[i(\gamma_m - \gamma_a)]\cdot\cos\left(L_0\theta - \frac{\pi}{4}\right)\right\} \tag{IX.8}$$

the same as Eq. (V.15); the discussion of the interference effects in Section VI follows.

realistic potential the forward scattering ratio should show an oscillatory velocity dependence (cf. Fig. 11). The practical implications of this conclusion will be discussed in Section XI.

X. TOTAL ELASTIC CROSS SECTION[10a]

Massey and Mohr[16a] (MM) were the first to develop an approximation formula (in closed form) for the total elastic cross section appropriate for heavy-particle scattering according to an inverse sth power potential. The usual cross section sum (Eq. (III.9)) was broken up into two parts $Q_{\mathrm{MM}} = Q_< + Q_>$, corresponding to two broad regions of angular momentum, the first ($0 \leqslant l \leqslant L$) in which the phase shifts are large and essentially random, where the rph-approximation is applicable, and the second ($l > L$) where they are small (but nonrandom) and for which the JB-approximation is valid. The division was arbitrarily made at $l = L$ such that $|\eta_{\mathrm{JB}}(L)| = \frac{1}{2}$; the result fortunately does not depend very strongly on the choice of the cutoff phase in the neighborhood of, say, $\pi/4$. We shall now briefly outline the MM treatment.

For the rph region, as usual, the sum is found directly:

$$Q_< \cong \frac{8\pi}{k^2} \sum_{l=0}^{L} (l + \tfrac{1}{2}) \cdot \tfrac{1}{2} \cong \frac{2\pi L^2}{k^2} \tag{X.1}$$

while for the JB region we have

$$Q_> \cong \frac{8\pi}{k^2} \int_L^\infty dl\,(l + \tfrac{1}{2}) \sin^2 \eta_{\mathrm{JB}} \cong \frac{8\pi}{k^2} \int_L^\infty dl\, l\, \eta_{\mathrm{JB}}^2 \tag{X.2}$$

(replacing $l + \frac{1}{2}$ by l, the sum by an integral and $\sin \eta_{\mathrm{JB}}$ by η_{JB} for $|\eta_{\mathrm{JB}}| \leqslant \frac{1}{2}$). Substituting for η_{JB} from Eq. (VIII.16a) (or Eq. (IVb.3)) we obtain

$$Q_> \cong \frac{4\pi}{k^2} \frac{a_s^2}{(s-2)} \cdot L^{4-2s} \cong \frac{\pi}{(s-2)} \frac{L^2}{k^2} \tag{X.3a}$$

where we have utilized the cutoff condition to determine L:

$$L = [2 \cdot |a_s|]^{1/(s-1)} = \left[\frac{2\mu C^{(s)}}{\hbar^2} \cdot k^{s-2} \cdot f(s)\right]^{1/(s-1)} \tag{X.3b}$$

As expected, $Q_<$ dominates; the ratio $Q_> : Q_<$ is only $1:(2s-4)$. Thus the MM cross section becomes

$$Q_{\mathrm{MM}} = \frac{\pi}{k^2}\cdot L^2\cdot\left(\frac{2s-3}{s-2}\right) = \pi\cdot\left(\frac{2s-3}{s-2}\right)\cdot\frac{(2a_s)^{2/(s-1)}}{k^2}. \tag{X.4}$$

Substituting for a_s from Eq. (VIII.16b), we obtain directly

$$Q_{\mathrm{MM}} = p_{\mathrm{MM}}{}^{(s)}\cdot[C^{(s)}/\hbar v]^{2/(s-1)} \tag{X.5a}$$

where†

$$p_{\mathrm{MM}}(s) \equiv \pi\cdot\left(\frac{2s-3}{s-2}\right)\cdot[2f(s)]^{2/(s-1)}. \tag{X.5b}$$

A somewhat more accurate[10a] approximation treatment is that of Landau and Lifshitz[29] (LL), in which the entire Q sum is replaced by an integral, and JB phases are used throughout (cf. Section VIII, Eqs. VIII.17). Thus

$$Q_{\mathrm{LL}} = \frac{8\pi}{k^2}\int_0^\infty dl\; l\sin^2\eta_{\mathrm{JB}} = \frac{8\pi}{k^2}\cdot J_1 \tag{X.6}$$

where J_1 is the same as that of Section VIII (evaluated in Eq. (VIII.20a)).

Analogous to Eq. (X.4), we find that

$$Q_{\mathrm{LL}} = \pi^2\cdot(2a_s)^{2/(s-1)}\Big/\sin\left(\frac{\pi}{s-1}\right)\cdot\Gamma\left(\frac{2}{s-1}\right) \tag{X.7}$$

or

$$Q_{\mathrm{LL}} = p_{\mathrm{LL}}(s)\cdot[C^{(s)}/\hbar v]^{2/(s-1)} \tag{X.8a}$$

where‡

$$p_{\mathrm{LL}}(s) \equiv \pi^2\cdot[2f(s)]^{2/(s-1)}\Big/\sin\left(\frac{\pi}{s-1}\right)\cdot\Gamma\left(\frac{2}{s-1}\right). \tag{X.8b}$$

An identical expression for the total cross section results[10a] from the application of still another approximation procedure, namely, that of Schiff.[30] It has been found[10a] that the Schiff-Landau-Lifshitz (SLL) approximation formula for Q yields results in good agreement with calculations involving direct summation based on exact phase shifts.

† Typical values of the dimensionless parameter $p_{\mathrm{MM}}(s)$ are[10a] 10.613, 7.547, 7.062, 6.771, and 6.296 for $s = 4$, 6, 7, 8, and 12, respectively.

‡ Typical values of $p_{\mathrm{LL}}(s)$ are[10a] 11.373, 8.083, 7.529, 7.185, and 6.584 for $s = 4$, 6, 7, 8, and 12, respectively.

The SLL approximation may also be obtained immediately via the optical theorem, making use of Eqs. (VIII.19) and (VIII.20a) for $\mathrm{Im}\, f(0)$ (and, of course, Eq. (VIII.16b) for a_s):

$$Q = \frac{4\pi}{k}\,\mathrm{Im}\, f_a(0) = \frac{8\pi}{k^2}\cdot J_1\,, \tag{X.6'}$$

yielding Q_{SLL} directly.

For the important case of $s = 6$ (London dispersion) we have the result:

$$Q^{(6)}_{\mathrm{SLL}} = 8.083\cdot[C^{(6)}/\hbar v]^{2/5}. \tag{X.9}$$

This implies that a log-log plot of $Q(v)$ should be linear with a slope of $-\frac{2}{5}$. This monotonic velocity dependence would be expected to be applicable to the total cross sections for scattering of neutrals (atoms or molecules) in the thermal energy range, *provided* the influence of the short-range exchange and repulsive forces can be neglected. That this is not the case[6c,31] will shortly become apparent (Section XI).

One possible source of deviation in the behavior of the total cross section for elastic scattering of neutrals at thermal velocities from that predicted by Eq. (X.9) is the neglect of the induced dipole–quadrupole and retardation terms in the long-range potential. By a direct extension of the rph technique, simple approximation formulas have been derived[32] for the (separate) dipole–quadrupole and retardation effects upon Q.

Assuming a potential of the form

$$V(r) \sim -\frac{C^{(6)}}{r^6}\cdot(1 + \beta/r^2) \tag{X.10}$$

the fractional correction on Q_{SLL} (Eq. (X.9) is found to be

$$\frac{\Delta Q}{Q} \cong \frac{2\pi}{3}\frac{\beta}{Q} \tag{X.11}$$

For a retarded potential, given approximately by the expression

$$V(r) \sim -\frac{C^{(6)}}{r^6}\cdot\left(\frac{a}{a + r}\right) \tag{X.12}$$

where a is closely related to the "retardation wavelength," the fractional correction may be shown to be

$$\frac{\Delta Q}{Q} \cong -Q^{1/2}/a\pi^{3/2} \tag{X.13}$$

These deviations are small (for most systems of interest) and opposite in sign. For typical atomic systems in the thermal energy region, the *net* deviation ranges from about -5 to $+10\%$, becoming more positive with increasing relative velocity.

XI. EXTREMA IN TOTAL CROSS SECTIONS[31]

We have already noted (Sections V and IX) that for a realistic potential possessing a minimum, the classical deflection function $\Theta(b)$ passes through zero at the glory impact parameter b_0. Thus the phase shift curve $\eta(l)$ exhibits a broad maximum around $\eta_m(L_0)$, providing a significant fraction of nonrandom phases at intermediate angular momenta. The maximum phase, η_m, increases with a decrease in k, and, if the attractive well is deep enough, $\eta_m(k)$ can pass successively through multiples of $\pi/2$, giving rise alternately to positive and negative incremental contributions, $\Delta Q/\bar{Q}$, to the rph-approximated portion of the MM total cross section. Thus $Q(v)$ should display an undulatory velocity dependence (cf. Fig. 13), with the positions and (magnitudes)

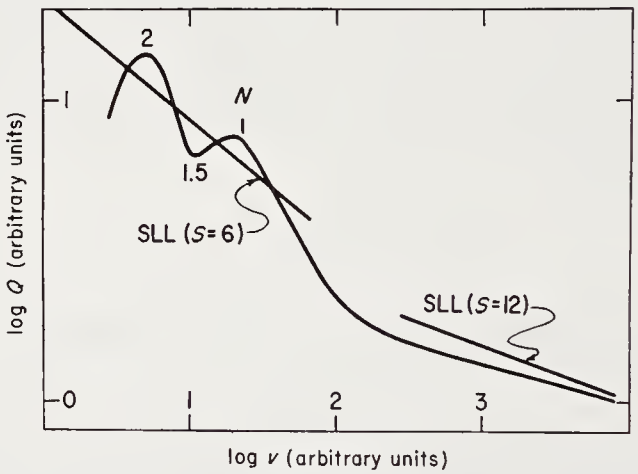

Fig. 13. Log-log plot of $Q(v)$ calculated for an L.-J. (12,6) potential with $B = 125$ The straight lines represent the SLL(6) and SLL(12) approximations. (For additional details see reference 31a.)

of the extrema determined primarily by $\eta_m(k)$ [and $\eta_m''(k)$]. For any given potential one may evaluate the dependence upon wave number of η_m (and η_m''), either by direct or indirect methods, and thus predict the extrema velocities and extrema amplitudes. With an assumed

functional form for the potential, certain of its parameters may thus be deduced from experimental observations of the extrema-effect.

The first quantitative treatment[31] of the extrema effect, following its original prediction,[6c] employed an MM-type semiclassical analysis. This yielded as a condition for an extremum the relation

$$\eta_m(k_N) = (N - \tfrac{3}{8})\pi \qquad \text{(XI.1)}$$

where $N = 1, 2, 3, \ldots$ are indices for maxima (while $N = 1.5, 2.5, 3.5, \ldots$ refer to minima) in the deviation function

$$\Delta Q/\bar{Q} \equiv [Q - Q^{(6)}]/Q^{(6)} \text{ versus } k \text{ or } v.$$

Figure 14 shows an example of such a deviation function for an L.-J. (12,6) potential of specified parameters. A simpler and more exact

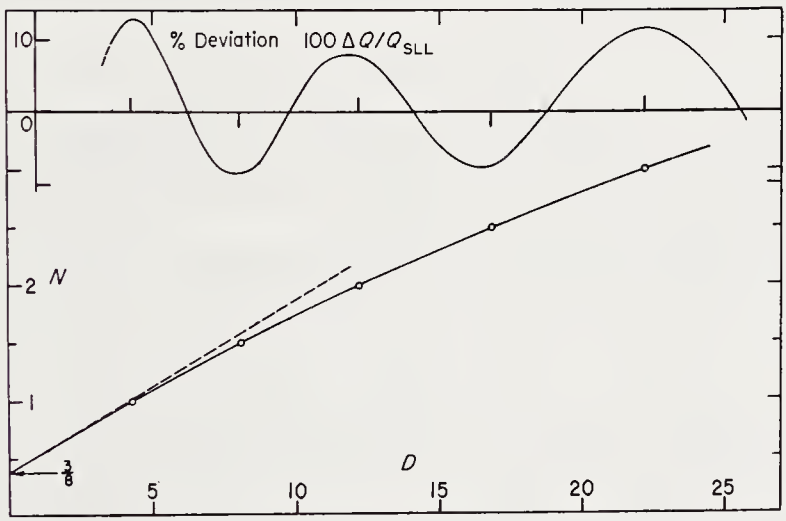

Fig 14. Extrema plot for L.-J. (12,6) potential, with $B = 650$. The upper curve shows the dependence of $\Delta Q/\bar{Q}$ on $D(=B/A)$ while the lower curve shows the indexing of the extrema. (For additional details see references 25, 31, and 34.)

derivation of the deviation function $\Delta Q/\bar{Q}$ was later given by Düren and Pauly,[33] making use of an SLL-type approximation and taking advantage of the optical theorem (Section VIII). We shall briefly outline their procedure and present the results.

Combining Eqs. (VIII.8), (VIII.19), and (IX.5), we obtain the cross

section as the sum of the usual (SLL) long-range outer attractive term and an additional glory term:

$$Q = \frac{4\pi}{k}\cdot[\mathrm{Im}\, f_a(0) + \mathrm{Im} f_g(0)]$$

$$= \frac{4\pi}{k}\cdot\left(\frac{2J_1}{k}\right) + \frac{4\pi}{k}\cdot[I_g(0)]^{1/2}\cdot\sin\left[2\eta_m - \frac{3\pi}{4}\right]$$

$$= Q_{\mathrm{SLL}} + \Delta Q \qquad \text{(XI.2a)}$$

where

$$\Delta Q = \frac{4\pi L_0}{k^2}\cdot\left[\frac{\pi}{-\eta_m''}\right]^{1/2}\cdot\sin(2\eta_m - 3\pi/4) \qquad \text{(XI.2b)}$$

Thus ΔQ is an oscillatory function of $\eta_m(k)$; note that $\langle \Delta Q\rangle = 0$ and $\langle Q\rangle = Q_{\mathrm{SLL}}$. Maxima in the deviation function $\Delta Q/\bar{Q}$ occur when $2\eta_m - \frac{3}{4}\pi = \frac{1}{2}\pi, \frac{5}{2}\pi$, etc. Thus the condition for an extremum may be expressed, as before,

$$\eta_m(k_N) = \pi\cdot(N - \tfrac{3}{8}) \qquad \text{(XI.1)}$$

where indices N define maxima and minima as mentioned earlier.

Eq. (XI.1) is quite general and indicates that it is possible to evaluate the maximum in the phase shift curve, η_m, and its energy dependence directly from observed extrema in $Q(v)$.

The amplitude of the oscillation in $\Delta Q/\bar{Q}$ is (from Eq. (2b))

$$U \equiv \frac{|\Delta Q|_{\max}}{\bar{Q}} = \frac{4\pi L_0}{k^2\bar{Q}}\cdot\left[\frac{\pi}{-\eta_m''}\right]^{1/2} = \frac{4\beta_m}{\bar{Q}}\cdot\left[\frac{2\pi}{-\Theta_0'\cdot A}\right]^{1/2} \qquad \text{(XI.3)}$$

where the usual "reduced" or semiclassical notation (cf. Eq. (IX.3b)) has been introduced. Equations (XI.1)–(XI.3) have been found[33] to reproduce accurately the exact (via summation of phases) calculations of Q for several realistic potential functions. Equation (XI.1) has been employed[31,34] in the analysis of experimental extrema data assuming an L.-J. (12,6) function[34] and Eqs. (XI.1)–(XI.3) in connection with a Kihara potential.[33]

For the L.-J. (12.6) potential it has been found[31] that the maximum reduced phase may be approximated by the expression

$$\eta_m^*(K) \cong \frac{120\pi}{847}\cdot\left(\frac{231}{160}\right)^{1/6}\cdot K^{-1} = \frac{0.4732}{K} \qquad \text{(XI.4)}$$

for $K \gg 1$, so that

$$\eta_m \cong 0.4732D \tag{XI.5}$$

where

$$D \equiv B/A = 2\epsilon\sigma/\hbar v = C^{(6)}/2\hbar v\sigma^5$$

Thus the extremum condition in $\Delta Q/\bar{Q}$ may be expressed (in this case):

$$N - \tfrac{3}{8} \cong 0.3012 \frac{\epsilon\sigma}{\hbar v_N} \tag{XI.6}$$

where v_N is the velocity at which the Nth extremum occurs. A plot of $N - \frac{3}{8}$ vs. v_N^{-1} should pass through the origin (serving to confirm the index assignments) with the initial slope yielding the $\epsilon\sigma$ product (cf. Fig. 14) or, alternatively, the ratio $C^{(6)}/\sigma^5$. For other potentials Eqs. (XI.4) and (XI.5) differ somewhat[34a] (although the limiting inverse energy dependence in Eq. (XI.4) is completely general, following from the v^{-1} functionality of the JB phase shift (Eq. (IVb.3)). Thus a slightly different constant in Eq. (XI.5) results in each case. In reference 33, tabulations of $\eta_m^*(K)$, β_m, and Θ_0' are presented for the Kihara (α,12,6) potential with different values of the parameter α ($-0.3 \leqslant \alpha \leqslant 0.5$), including $\alpha = 0$, the L.-J. (12,6) case; these may be employed in expressions for the deviation function $\Delta Q/\bar{Q}$. In any case, extrema plots of $N - \frac{3}{8}$ vs. v_N^{-1} are all characterized by a limiting linear behavior as $v_N^{-1} \to 0$.

The oscillatory graphs of $\Delta Q/\bar{Q}$ vs. $1/v$ have been termed[31b] elastic atom–atom impact spectra. In such a plot (cf. Fig. 14) the extrema are approximately evenly spaced (at high velocities) so that the indexing of the extrema is readily accomplished. For a (realistic interatomic) potential with an asymptotic r^{-6} form, if one plots, as a function of v^{-1}, the "apparent" value of the potential constant, $C_{\text{app}}^{(6)}$, calculated from Q via Eq. (X.9):

$$C_{\text{app}}^{(6)} = 5.676 \times 10^{-30} v Q^{5/2} \tag{XI.7}$$

(where v, Q, and C are in cgs units), one obtains a similar oscillatory "spectrum." The average value of $C_{\text{app}}^{(6)}$ over the thermal energy range is the "true" value of $C^{(6)}$. Thus, velocity averaging in effect eliminates the influence of the short-range forces upon the total elastic scattering cross section, enabling one to evaluate the long-range attractive constant $C^{(6)}$ directly.[34b]

After assignment of indices it is possible to ascertain *absolute experimental values* of the maximum phase, η_m, as a function of v or k from

Eq. (XI.1). The experimental results may then be concisely expressed in the form of an expansion[34a] of η_m in powers of v^{-1}, say:

$$\eta_m = a_1 v^{-1} - a_2 v^{-2} + \cdots \tag{XI.8}$$

where $a_1 = cC^{(6)} r_m^{-5}$, with c a numerical constant dependent on the assumed functional form of the potential. Thus, since elastic atom–atom impact spectra yield both $C^{(6)}$ and a_1 (and with less accuracy, a_2), for a given functional form of $V(r)$ it is possible to evaluate r_m (and thus ϵ).[34]

XII. MAXIMA IN IMPACT SPECTRA AND THE BOUND STATES[31]

The relationships between differential and total elastic cross sections, extrema velocities (and amplitudes) and the interaction potential have been discussed in previous sections. Given a two-body potential function thus derived from scattering experiments, it is only a matter of straightforward computation[35] to evaluate the energy levels corresponding to all the discrete (vibration-rotation) states of the composite system. There is also a well-known relation[14] between the bound-state energies and the poles in the scattering amplitude as a function of k, the (complex) wave number, occurring in the upper half-plane.

However, only recently has it been pointed out[31] that a rather direct relationship exists between the bound states and the extrema in the total cross sections, i.e., that the maxima in the elastic atom–atom impact spectra serve as "counters" of the vibrational states of the diatom.

A brief outline of this development follows. Assuming the usual semiclassical conditions, it is seen that the maximum phase increases monotonically with decreasing k, while the angular momentum quantum number corresponding to the maximum phase (i.e., L_0, or l_m) decreases smoothly to zero as $k \to 0$. Thus, as the wave number is decreased, η_m approaches progressively closer to the s-wave ($l = 0$) phase shift, $\eta_0(k)$. This, in turn, approaches its zero-velocity limit according to Levinson's theorem[36]:

$$\lim_{k \to 0} \eta_0(k) = n_0 \pi \tag{XII.1}$$

Here n_0 is the number of discrete levels of zero angular momentum, i.e., the number of (rotationless) vibrational states of the diatom. As discussed in the previous section, a maximum in the impact spectrum

occurs once for each time $\eta_m(k)$ passes through integral multiples of π (more accurately, when $\eta_m = \frac{5}{8}\pi, \frac{13}{8}\pi$, etc.); thus the total number of maxima should equal the number of bound states, n_0.

Unfortunately, the semiclassical approximations become less valid as k is decreased. In addition to the onset of the violently nonclassical orbiting-tunneling phenomenon at low energies, another difficulty arises due to the failure of the statistics for the random-phase approximation (we recall that the number of non-negligible phases is roughly $2kr_0$, so that for $kr_0 \lesssim 10$ the rph assumption has no validity). Thus the above bound-state relation is not a rigorous one: indeed, we may anticipate a certain degree of sharp "fine structure" in the impact spectrum at subthermal energies, probably unresolvable experimentally. Nevertheless, there remains a rigorous and direct correlation[31b] between the low-index (high k) extrema and the low-lying vibrational states (quantum number v):

$$N - 1 \leftrightarrow v \qquad \text{(XII.2)}$$

A restatement of the bound-state rule which should be suitable for application in any experimentally feasible situation is as follows:

The observation of m maxima in the elastic atom–atom impact spectrum implies the existence of at least m vibrational states for the di-atom.

The preceding considerations have been applied[34] to experimental extrema observations. In all cases for which the "capacity" of the well for bound states (n_0) was known from the potential parameters it was found that $m \leqslant n_0$ (i.e., neither the number of maxima observed nor the highest index assigned exceeded the theoretical capacity, n_0).

It is clear that the above "level-counting" technique is not dependent on the detailed shape of the potential (so long as the well has a "capacity" for one or more bound states) and should be generally applicable to systems† involving ground-state atoms, metastables, and/or ions.

† Extension to systems involving molecules involves certain obvious complications, including inelastic effects. Cf. Section XIII.

Examples of systems (other than those analysed in reference 34) for which scattering-bound state experiments and/or calculations of this type have been carried out are as follows:

$$\mathrm{K}(^2S_{1/2}) + \mathrm{Kr}(^1S_0) \rightarrow \mathrm{KKr}(^2\Sigma^+) \quad \text{(exp. and calc.)}^{37}$$
$$\mathrm{Li}(^2S_{1/2}) + \mathrm{Hg}(^1S_0) \rightarrow \mathrm{LiHg}(^2\Sigma^+) \quad \text{(exp. and calc.)}^{38}$$
$$\mathrm{He}(^3S_1) + \mathrm{Xe}(^1S_0) \rightarrow \mathrm{HeXe}(^3\Sigma^+) \quad \text{(exp.)}^{39}$$
$$\mathrm{He}(^1S_0) + \mathrm{Li}^+(^1S_0) \rightarrow \mathrm{HeLi}^+(^1\Sigma^+) \quad \text{(calc.)}^{40}$$

A very complete and interesting phase shift computation has recently appeared[40a] dealing with the scattering of atomic hydrogen; the resonances associated with the bound states (for the $^1\Sigma H_2$ molecule) are clearly displayed.

XIII. INFLUENCE OF CONCURRENT INELASTIC PROCESSES

The subject of inelastic collisions of atoms and molecules is not within the scope of the present chapter. Nevertheless it seems worthwhile to consider briefly the question of the influence of concurrent inelastic scattering upon the elastic scattering behavior of molecules.

The simplest situation is the one in which the scattering is inelastic but nonreactive. Here it is known that rotational excitation (and deexcitation) is the most probable path of energy transfer between translation and internal modes. Takayanagi[41] has reviewed in great detail the theory of rotational (and vibrational) transitions in molecular collisions. For the purpose of illustration here, we shall confine our attention to the special case of the atom–diatomic molecule system† following the S-matrix formalism of Arthurs and Dalgarno[42] for scattering by a rigid rotor.

The total cross section for the transition $j \to j'$ may be expressed:

$$Q(j';j) = \frac{\pi}{k^2} \sum_{J=0}^{\infty} (2J+1) \cdot P_{j';j}(J) \tag{XIII.1}$$

where the transition probability is

$$P_{j';j}(J) = \frac{1}{2j+1} \cdot \sum_{l=|J-j|}^{J+j} \sum_{l'=|J-j'|}^{J+j'} |\delta_{\alpha\beta} - S^J_{\beta;\alpha}|^2 \tag{XIII.2}$$

Here J is the total angular momentum quantum number (conserved in the collision) and $S^J_{\beta;\alpha}$ the S-matrix element for the transition from state $\alpha \equiv j, l$ to state $\beta \equiv j', l'$ at given J, defined in terms of a radial wave function with the asymptotic form:

$$G_J^{\beta;\alpha}(r) \sim \delta_{\alpha\beta} \exp[-i(kr - l\pi/2)] - \left(\frac{v}{v'}\right)^{1/2} S^J_{\beta;\alpha} \cdot \exp[i(k'r - l'\pi/2)] \tag{XIII.3}$$

† Detailed calculations for the system He–H_2 have been carried out by Roberts.[43] In addition, the formal procedure[42] has been generalized by Davison[44] to the diatomic–diatomic case; he presented calculations for the H_2–H_2 pair.

(cf. Eq. (III.5)). Here v is the relative velocity associated with the incident channel ($v = k\hbar/\mu = (2E/\mu)^{1/2}$ as usual) and v' the corresponding outgoing relative velocity, given by

$$v' = v[1 - \Delta E/E]^{1/2} = k'\hbar/\mu' \tag{XIII.4}$$

where ΔE is the endothermicity of the transition and k' is the exit channel wave number. The standard expressions for the coupled radial differential equations will not be reproduced here.

Under semiclassical conditions and with the assumption of strong interchannel coupling, a statistical method (analogous to the rph procedure) may be employed[45] to approximate the transition probabilities; one merely calculates the expectation values for the (mod-squared of the) S-matrix elements. Taking advantage of the unitarity of the S-matrix, one finds that for N_J coupled channels

$$\langle |S^J_{\beta;\alpha}|^2 \rangle = 1/N_J \tag{XIII.5}$$

so that for $\beta \neq \alpha$

$$\langle P_{j';j}(J) \rangle = [(2j + 1) \cdot N_J]^{-1} \tag{XIII.6}$$

For $\beta = \alpha$ (elastic scattering) it is found that

$$\langle P_{j;j}(J) \rangle = (2j + 1)^{-1} \cdot \langle |1 - S^J_{\beta;\alpha}|^2 \rangle = (2j + 1)^{-1} \cdot (1 + N_J^{-1}). \tag{XIII.7}$$

From these results it follows that the total (elastic plus inelastic) cross section for scattering to all energetically open channels from state j, i.e., $Q_j^{\text{tot}} \equiv \sum_{j'} Q(j';j)$, is *independent* of the number of coupled channels and is given (approximately) by a formula identical to the Massey-Mohr rph formula (Section X) (which referred, of course, to the total *elastic* cross section in the absence of inelastic scattering). Alternatively expressed, it is found that the elastic cross section is reduced† by an amount just equal to the inelastic cross section, such that

$$Q_j^{\text{tot}} = Q_j^{\text{el}} + Q_j^{\text{inel}} \cong Q_{\text{MM}} \tag{XIII.8}$$

† Since the ratio

$$[\sum_{j'} \langle P_{j';j}(J) \rangle] / \langle P_{j;j}(J) \rangle \leqslant 1 \tag{XIII.9}$$

from Eqs. (XIII.6) and (XIII.7), the total inelastic cross section can never exceed the total elastic cross section, i.e.,

$$\frac{Q_j^{\text{inel}}}{Q_j^{\text{el}}} \leqslant 1 \quad \text{and} \quad \frac{Q_j^{\text{inel}}}{Q_j^{\text{tot}}} \leqslant \tfrac{1}{2} \tag{XIII.10}$$

This result, i.e., "conservation" of total cross section, obtained with a minimum of restrictive assumptions, may well have general validity (e.g., extension to the polyatomic case, as well as inclusion of vibrational excitation) in the field of nonreactive molecular scattering.

For the most general case in which chemically reactive scattering is concurrent, the situation is, of course, much more complicated. Reactive scattering is always accompanied by elastic scattering (as well as inelastic transitions) so a rigorous treatment is expected to be formidable. It is not appropriate here to review the literature in what may be termed the fundamentals of chemical reaction kinetics, but it is relevant to reference the basic collision-theory treatment of Eliason and Hirschfelder[46] (which introduced the concept of the "multichannel" differential chemical reaction cross section) and the important S-matrix formulation of Smith.[47] It appears, however, that the question of the influence of the reactive scattering upon the elastic scattering has not yet been considered in full detail.

In order to obtain a qualitative answer to this question we explore the utility of the optical model for reactive scattering. Here the interaction potential is assumed complex:

$$V(r) = V_0(r) + iW_0(r) \qquad \text{(XIII.11)}$$

with the imaginary part responsible for the absorption (i.e., reaction). Without speculating here on the origin or functional form of Im $V(r)$ we merely recognize[6,14] that the inclusion of this term will yield complex phase shifts and thus reactive scattering.

We make use of the phenomenological "diffraction theory" treatment of Greider and Glassgold.[48] To begin with, we consider as a first approximation the "black-sphere" model (developed long ago for the scattering of neutrons by nucleons).†

Starting with

$$f(\theta) = \frac{1}{2ik}\sum_l (2l+1)(S_l - 1)P_l(\cos\theta) \qquad \text{(XIII.12)}$$

where $S_l \equiv e^{2i\eta_l}$, with η_l complex (say $\eta_l = a_l + ib_l$); we have for the total elastic cross section

$$Q^{\text{el}} = \frac{\pi}{k^2}\sum_l (2l+1)\cdot|1 - S_l|^2 \qquad \text{(XIII.13)}$$

† See, for example, reference 14, Section 117; the small-angle result is the same as that of reference 48, Eqs. V-1,2 for simple diffraction scattering.

for the total reactive (inelastic) cross section

$$Q^r = \frac{\pi}{k^2}\sum_l (2l+1)\cdot[1 - |S_l|^2] = \frac{\pi}{k^2}\sum_l (2l+1)\cdot\beta_l \qquad \text{(XIII.14)}$$

(where $\beta_l \equiv 1 - |S_l|^2$ is the "opacity") and for the total cross section

$$Q^{\text{tot}} = \frac{\pi}{k^2}\sum_l (2l+1)\cdot\{1 - |S_l|^2 + |1 - S_l|^2\}$$

$$= \frac{2\pi}{k^2}\sum_l (2l+1)\cdot[1 - \text{Re}\, S_l] = \frac{4\pi}{k}\cdot \text{Im}\, f(0). \qquad \text{(XIII.15)}$$

Assuming total absorption for all $l < L \cong kR$ (where R is the black-sphere radius) and no interaction† for $l \geqslant L$, we have

$$S_l = 0 \qquad \text{for} \qquad l < L$$

$$S_l = 1 \qquad \text{for} \qquad l \geqslant L \qquad \text{(XIII.16)}$$

so that

$$Q^r = Q^{\text{el}} = \tfrac{1}{2}Q^{\text{tot}} = \pi L^2/k^2 \cong \pi R^2. \qquad \text{(XIII.17)}$$

Thus it is seen that the black-sphere model (Eq. (XIII.17)) gives the same "conservation" result as Eq. (XIII.8), namely,

$$Q^{\text{tot}} = \frac{2\pi L^2}{k^2} = Q_{\text{rph}} = Q^{\text{el}} + Q^{\text{inel}} \qquad \text{(XIII.19)}$$

(recalling Eq. (X.1) for $Q_<$). However, although it is true that the existence of inelastic scattering necessarily implies concurrent elastic (or "shadow") scattering, it will now be shown that the earlier restriction $Q^{\text{inel}}/Q^{\text{el}} \leqslant 1$ *no longer applies* in the case of an absorptive (complex) potential with its associated complex phase shifts.

Rewriting (i.e., redefining)

$$S_l = e^{2a_l}\cdot e^{2ib_l} \equiv (1 - \beta_l)^{1/2}\cdot e^{i\alpha_l} \qquad \text{(XIII.20)}$$

† For small angles this leads to a pure imaginary scattering amplitude (n.b.: contrast with the Born approximation result, namely, pure real forward amplitude),

$$f(\theta \cong \frac{i}{k\theta} L\cdot J_1(L\theta) \cong \frac{iR}{\theta}\cdot J_1(kR\theta). \qquad \text{(XIII.18a)}$$

We note that

$$\text{Im}\, f(0) = L^2/2k \qquad \text{(XIII.18b)}$$

Thus we have the standard formula for "diffraction scattering":

$$I(\theta)_{\text{diff}} \cong R^2\cdot[J_1(kR\theta)]^2/\theta^2. \qquad \text{(XIII.18c)}$$

where α_l and β_l are real (noting that $0 \leqslant \beta_l \leqslant 1$) Eqs. (XIII.13)–(XIII.15) become

$$Q^{\mathrm{el}} = \frac{\pi}{k^2} \sum_{l=0}^{L} (2l+1) \cdot [2 - \beta_l - 2 \cdot (1-\beta_l)^{1/2} \cdot \cos \alpha_l] \quad \text{(XIII.21)}$$

$$Q^{r} = \frac{\pi}{k^2} \sum_{l=0}^{L} (2l+1) \cdot \beta_l \quad \text{(XIII.22)}$$

$$Q^{\mathrm{tot}} = \frac{2\pi}{k^2} \sum_{l=0}^{L} (2l+1) \cdot [1 - (1-\beta_l)^{1/2} \cdot \cos \alpha_l]. \quad \text{(XIII.23)}$$

Assuming maximum opacity ($\beta_l = 1$), Eqs. (XIII.21)–(XIII.23) correctly yield the black sphere results (Eqs. (XIII.17) and (XIII.19). Also, as expected, assuming zero opacity throughout, $Q^r = 0$ and $Q^{\mathrm{el}} = Q^{\mathrm{tot}}$. Moreover, if $\langle \cos \alpha_l \rangle = 0$, then $Q^{\mathrm{tot}} = Q_{\mathrm{rph}}$ as it should.

However, an interesting possibility arises for intermediate opacities: namely, it is readily possible to obtain $Q^r > Q^{\mathrm{el}}$. For example, assuming $\alpha_l = 0$ and β_l constant throughout (independent of l in the range $0 \leqslant l < L$), we have for the ratio of elastic to reactive cross sections:

$$Q^{\mathrm{el}}/Q^{r} = [2 - \beta_l - 2(1-\beta_l)^{1/2}]/\beta_l \quad \text{(XIII.24)}$$

so that the inelastic contribution *exceeds* the elastic for any $\beta_l < 1$. The ratio Q^{el}/Q^r decreases toward zero as the opacity is decreased (with a concomitant reduction of the total cross section toward zero, of course, in the limit of $\beta_l \doteq 0$). Thus we conclude that it is entirely possible for the total reaction cross section to *exceed* one-half of the total scattering cross section.

Returning once again to the question of the influence of the reactive scattering upon the elastic cross section, we may immediately obtain an approximate solution if we assume unit opacity for $l < L$, while all remaining phase shifts η_l ($l \geqslant L$) are unaffected, i.e., pure real, and the same as would obtain in the absence of inelastic scattering.

Employing the generalized optical theorem (Eq. (XIII.15)), we have

$$Q^{\mathrm{tot}} = \frac{4\pi}{k} \cdot \mathrm{Im}\, f(0) = \frac{4\pi}{k} \cdot \{[\mathrm{Im}\, f(0)]_{<} + [\mathrm{Im}\, f(0)]_{>}\} \quad \text{(XIII.25)}$$

where the first term on the right represents the contribution from $l < L$, i.e., the diffraction scattering, and the second one from $l \geqslant L$,

i.e., the residual elastic scattering. Provided L is less than the MM-rph "cutoff" angular momentum, we have

$$[\mathrm{Im}\, f(0)]_{>} = [\mathrm{Im}\, f(0)]_{\mathrm{tot}} - \frac{L^2}{2k} = \frac{k}{4\pi} Q_{\mathrm{SLL}} - \frac{L^2}{2k} \qquad \text{(XIII.26)}$$

while

$$[\mathrm{Im}\, f(0)]_{<} = [\mathrm{Im}\, f(0)]_{\mathrm{black}} = L^2/2k \qquad \text{(XIII.26b)}$$

so that

$$Q^{\mathrm{tot}} = Q_{\mathrm{SLL}} \qquad \text{(XIII.27)}$$

Thus the total cross section is *unaffected* by the reactive scattering, i.e., we see once again the "conservation" of total cross section. However, in view of the result of Eq. (XIII.24) this result cannot be taken as generally applicable. The only conclusion which seems independent of model is expressible by the rather weak inequality

$$Q^{\mathrm{el}} = Q^{\mathrm{tot}} - Q^{r} \leqslant Q_{\mathrm{SLL}} \qquad \text{(XIII.28)}$$

One related point should be noted, i.e., the significant influence of the reactive scattering on the wide-angle differential elastic scattering cross section. This is manifested as a loss in the elastic scattering intensity at large angles[49] (corresponding to small impact parameters), predictable on the basis of simple semiclassical considerations. In terms of the present model, this corresponds to a (rather abrupt) gain in opacity (say, from 0 to nearly unity) for angular momentum (impact parameter) less than some critical value, b_c, say. This leads to a simple estimate of the total reaction cross section: $Q^{r} \cong \pi b_c^2$.

References

1. See, for example, (a) J. O. Hirschfelder, C. F. Curtiss and R. B. Bird, *Molecular Theory of Gases and Liquids*, Wiley, New York, 1964; (b) E. H. Kennard, *Kinetic Theory of Gases*, McGraw-Hill, New York, 1938.
2. K. W. Ford and J. A. Wheeler, *Ann. Phys.* (*N.Y.*), **7**, 259, 287 (1959).
3. E. A. Mason, *J. Chem. Phys.*, **26**, 667 (1957).
4. For references see I. Amdur and J. E. Jordan, this volume, Chap. 2. Also I. Amdur and R. R. Bertrand, *J. Chem. Phys.*, **36**, 1078 (1962); I. Amdur, *Planetary Space Sci.*, **3**, 228 (1961); and other papers in the series which began with I. Amdur and H. Pearlman, *J. Chem. Phys.*, **8**, 7 (1940).
5. (a) E. A. Mason and J. T. Vanderslice, in D. R. Bates, ed., *Atomic and Molecular Processes*, Academic Press, New York, 1962; (b) T. Y. Wu and T. Ohmura, *Quantum Theory of Scattering*, Prentice Hall, Englewood Cliffs, New Jersey, 1962, p. 125; (c) H. Pauly, *Fortschr. Physik*, **9**, 613 (1961).

6. See, for example, (a) N. F. Mott and H. S. W. Massey, *Theory of Atomic Collisions*, Clarendon Press, Oxford, 2nd Ed., 1949; A. Messiah, *Quantum Mechanics*, Wiley, New York, 1962; H. S. W. Massey, *Handbuch der Physik*, **36**, 232 (1956); E. H. S. Burhop in D. R. Bates, ed., *Quantum Theory. I. Elements*, Chap. 9, Academic Press, New York, 1961; (b) T. Y. Wu and T. Ohmura, ref. 5b; (c) R. B. Bernstein, *J. Chem. Phys.*, **33**, 795 (1960); **34**, 361 (1961).
7. See, for example, H. S. W. Massey and R. A. Buckingham, *Proc. Roy. Soc. (London)*, **A168**, 378 (1938); R. A. Buckingham, J. Hamilton, and H. S. W. Massey, *ibid.*, **A179**, 103 (1951); R. A. Buckingham, A. R. Davies, and D. C. Gilles, *Proc. Phys. Soc. (London)*, **71**, 457 (1958); R. A. Buckingham and J. W. Fox, *Proc. Roy. Soc. (London)*, **A267**, 102 (1962).
8. See, for example, J. DeBoer and A. Michels, *Physica*, **6**, 409 (1939); J. DeBoer, *Repts. Progr. Phys.*, **12**, 351 (1949); J. DeBoer and E. G. D. Cohen, *Physica*, **17**, 993 (1951).
9. See, for example, (a) R. P. Marchi and C. R. Mueller, *J. Chem. Phys.*, **38**, 740 (1963); (b) C. R. Mueller and R. P. Marchi, *ibid.*, **38**, 745 (1963); (c) W. A. Sanders and C. R. Mueller, *ibid.*, **39**, 2572 (1963); (d) C. R. Mueller and J. W. Brackett, *ibid.*, **40**, 654 (1964).
10. See, for example, (a) R. B. Bernstein and K. H. Kramer, *J. Chem. Phys.*, **38**, 2507 (1963); (b) R. B. Bernstein, *ibid.*, **38**, 2599 (1963).
11. R. B. Bernstein and F. A. Morse, *J. Chem. Phys.*, **40**, 917 (1964).
12. R. B. Bernstein, *J. Chem. Phys.*, **36**, 1403 (1962).

12a. E. A. Hylleraas, *Physica Mathematica Univ. Oslo*, Rept. 19 (1963). See also L. D. Faddeyev, *J. Math. Phys.*, **4**, 72 (1963).

13. See, for example, B. S. Jeffreys in D. R. Bates, ed., *Quantum Theory I. Elements*, Academic Press, New York, 1961.
14. L. D. Landau and E. M. Lifshitz, *Quantum Mechanics*, Pergamon Press, London, 1959. See also N. and P. Fröman, *JWKB Approximation*, North-Holland Publ. Co., Amsterdam, 1965.
15. (a) D. H. Secrest and J. O. Hirschfelder, *Proc. Natl. Acad. Sci. U.S.*, **47**, 227 (1961); (b) R. B. Bernstein, unpublished notes, Feb. 1961.

15c. C. F. Curtiss and R. S. Powers, *J. Chem Phys.*, **40**, 2145 (1964); S. Choi and J. Ross, *ibid.*, **40**, 2151; C. F. Curtiss, *ibid.*, **42**, 2267 (1965); and others.

15d. J. O. Hirschfelder, R. B. Bird, and E. L. Spotz, *J. Chem. Phys.*, **16**, 968 (1948); also D. A. Stogryn and J. O. Hirschfelder, *ibid.*, **31**, 1545 (1959).

16. (a) H. S. W. Massey and C. B. O. Mohr, *Proc. Roy. Soc. (London)*, **A144**, 188 (1934); (b) *ibid.*, **A141**, 434 (1933).
17. (a) R. B. Bernstein, *J. Chem. Phys.*, **36**, 1403 (1962); (b) *ibid.*, **38**, 515 (1963); (c) F. J. Smith, *Physica*, **30**, 497 (1964).
18. H. S. W. Massey and R. A. Smith, *Proc. Roy. Soc. (London)*, **A142**, 142 (1933).
19. See, for example, (a) H. and B. S. Jeffreys, *Mathematical Physics*, Cambridge Univ. Press, Cambridge, 3rd Ed., 1956; (b) C. Eckart, *Rev. Mod. Phys.*, **20**, 399 (1948); (c) A. Erdelyi, *Asymptotic Expansions*, Dover Publications, New York, 1956.
20. (a) W. Gröbner and N. Hofreiter, *Integraltafeln II*, Springer-Verlag, Vienna, 1961; by transformation of Eq. 313.14a; (b) *ibid.*, Eq. 314.15a.

21. (a) P. J. Groblicki and R. B. Bernstein, *J. Chem. Phys.*, **42**, 2295 (1965); also (b) H. U. Hostettler and R. B. Bernstein, *Phys. Rev. Letters*, **5**, 318 (1960).
22. (a) F. A. Morse, R. B. Bernstein, and H. U. Hostettler, *J. Chem. Phys.*, **36**, 1947 (1962); F. A. Morse and R. B. Bernstein, *ibid.*, 37, 2019 (1962); (b) D. Beck, *J. Chem. Phys.*, **37**, 2884 (1962); D. Beck, E. F. Greene, and J. Ross, *ibid.*, **37**, 2895 (1962); M. Ackerman, E. F. Greene, A. L. Moursund, and J. Ross, *Ninth International Symposium on Combustion*, Academic Press, New York, 1963; (c) E. Gersing, E. Hundhausen, and H. Pauly, *Z. Physik*, **171**, 349 (1963); (d) E. Hundhausen and H. Pauly, *Z. Naturforsch.*, **19a**, 810 (1964); also D. Beck, H. Dummel, and U. Henkel, *Z. Physik*, **185**, 19 (1965); (e) E. A. Mason and L. Monchick, *J. Chem. Phys.*, **41**, 2221 (1964).
23. C. Schlier, *Z. Physik*, **173**, 352 (1963).
24. S. E. Lovell and J. O. Hirschfelder, unpublished calculations.
25. R. B. Bernstein, in M. R. C. McDowell, Ed., *Atomic Collision Processes*, North-Holland Publ. Co., Amsterdam, 1964, p. 895; also *Science*, **144**, 141 (1964).
25a. F. T. Smith, *Phys. Rev.*, **118**, 349 (1960); R. J. Munn, E. A. Mason, and F. J. Smith, *J. Chem. Phys.*, **41**, 3978 (1964); S. Imam-Rahajoe, C. F. Curtiss, and R. B. Bernstein, *ibid.*, **42**, 530 (1965); R. J. Munn, F. J. Smith, E. A. Mason, and L. Monchick, *ibid.*, **42**, 537 (1965).
26. (a) H. Pauly, *Z. Physik*, **157**, 54 (1959); (b) R. Helbing, Diplomarbeit, Bonn Univ. (1961); (c) R. Helbing and H. Pauly, *Z. Physik*, **179**, 16 (1964); also, unpublished report; (d) E. A. Mason, J. T. Vanderslice, and C. J. G. Raw, *J. Chem. Phys.*, **40**, 2153 (1964).
27. R. G. J. Fraser, H. S. W. Massey, and C. B. O. Mohr, *Z. Physik*, **97**, 740 (1935).
28. See, for example, G. Szegö, *Orthogonal Polynomials*, American Mathematical Society, New York, 1959.
29. L. D. Landau and E. M. Lifshitz, *Quantum Mechanics*, Pergamon Press, London, 1959, p. 416.
30. L. I. Schiff, *Phys. Rev.*, **103**, 443 (1956).
31. R. B. Bernstein, (a) *J. Chem. Phys.*, **37**, 1880 (1962); (b) *ibid.*, **38**, 2599 (1963).
32. P. R. Fontana and R. B. Bernstein, *J. Chem. Phys.*, **41**, 1431 (1964).
33. R. Düren and H. Pauly, *Z. Physik*, **175**, 227 (1963); **177**, 146 (1964).
34. E. W. Rothe, P. K. Rol, and R. B. Bernstein, *Phys. Rev.*, **130**, 2333 (1963).
34a. R. B. Bernstein and T. J. P. O'Brien, *Discussions Faraday Soc.*, **40** (to be published).
34b. E. W. Rothe and R. H. Neynaber, *J. Chem. Phys.*, **42**, 3306 (1965).
35. (a) H. Harrison and R. B. Bernstein, *J. Chem. Phys.*, **38**, 2135 (1963); (b) C. L. Beckel and J. Nakhleh, *ibid.*, **39**, 94 (1963).
36. (a) P. Swan, *Proc. Roy. Soc.* (*London*), **A228**, 10 (1955); (b) N. Levinson, *Kgl. Danske Videnskab. Selskab. Mat.-Fys. Medd.*, **25**, No. 9 (1949).
37. E. W. Rothe, R. H. Neynaber, B. W. Scott, S. M. Trujillo, and P. K. Rol, *J. Chem. Phys.*, **39**, 493 (1963).
38. P. J. Groblicki and R. B. Bernstein, see reference 21a.
39. E. W. Rothe, R. H. Neynaber, and S. M. Trujillo, *J. Chem. Phys.*, **42**, 3310 (1965).

40. G. G. Weber and R. B. Bernstein, *J. Chem. Phys.*, **42**, 2166 (1965).
40a. R. A. Buckingham, J. W. Fox, and E. Gal, *Proc. Roy. Soc.* (*London*), **A284**, 237 (1965).
41. K. Takayanagi, *Progr. Theoret. Phys., Suppl.*, **25**, 1 (1963).
42. A. M. Arthurs and A. Dalgarno, *Proc. Roy. Soc.* (*London*), **A256**, 540 (1960).
43. C. S. Roberts, *Phys. Rev.*, **131**, 209 (1963).
44. W. D. Davison, *Discussion Faraday Soc.*, **33**, 71 (1962).
45. R. B. Bernstein, A. Dalgarno, H. S. W. Massey, and I. C. Percival, *Proc. Roy. Soc.* (*London*), **A274**, 427 (1963).
46. M. A. Eliason and J. O. Hirschfelder, *J. Chem. Phys.*, **30**, 1426 (1959).
47. F. T. Smith, *J. Chem. Phys.*, **36**, 248 (1962).
48. K. R. Greider and A. E. Glassgold, *Ann. Phys. N.Y.*, **10**, 100 (1960).
49. D. Beck, E. F. Greene, and J. Ross, *J. Chem. Phys.*, **37**, 2895 (1962); also Chapter 5, this volume. See also D. R. Herschbach, this volume, Chap. 9, and D. R. Herschbach and G. H. Kwei in M. R. C. McDowell, Ed., *Atomic Collision Processes*, North-Holland Publ. Co., Amsterdam, 1964, p. 972.

4. ELASTIC SCATTERING IN CHEMICALLY REACTIVE SYSTEMS*

E. F. GREENE, A. L. MOURSUND,† and J. ROSS

Metcalf Chemical Laboratories, Brown University, Providence, Rhode Island

CONTENTS

I. Introduction 135
II. Experiments 139
III. The Elastic Scattering of K + Kr, K + HCl, K + HBr, and K + HI ... 142
A. Threshold Energies 153
B. Threshold Distances 153
C. Probability of Reaction and Populations of Product States 154
D. Independent Estimates of the Size Parameter r_m 154
E. Total Reaction Cross Section 157
IV. The Elastic Scattering of K + CH_3Br 157
V. The Elastic Scattering of K + $C(CH_3)_4$ and K + CBr_4 160
VI. Conclusion 165
Appendix 166
References 168

I. INTRODUCTION

Molecular beam experiments provide direct information on details of collisions between molecules. A typical experiment involves the scattering of a beam or flux of reactant molecules (A) by an intersecting beam of molecules (B). The initial state for a collision between individual molecules A and B, that is the state prior to any interaction, is specified by the quantum numbers of the internal states of the isolated molecules and by the relative kinetic energy. A number of events may result from a collision. If the internal quantum numbers of the reactants

* This research was assisted by support from the U.S. Atomic Energy Commision and the Advanced Research Projects Agency.

† National Science Foundation Graduate Fellow, 1961–1964.

are unaltered by the interaction, the collision is called elastic. In an inelastic collision the internal quantum numbers of the reactants are changed, while in a reactive collision the chemical identity of the reactants is changed. For given initial conditions, each of these events occurs with a given probability. Studies of each of these types of collisions and the relations between them are useful for an understanding of the details of chemical reactions. In this article we discuss elastic scattering of reactive systems. Reactive scattering is reviewed by D. R. Herschbach in Chapter 9.

The elastic scattering of two-body systems is discussed by R. B. Bernstein in Chapter 3 of this volume. Here we need to refer only to a few characteristic types of scattering. In Figure 1 we show two classical

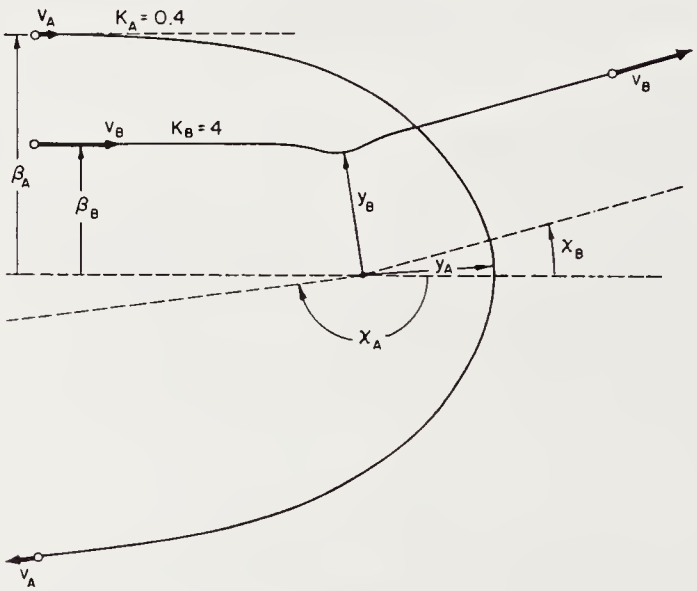

Fig. 1. Two classical trajectories for an elastic collision.

trajectories with their corresponding initial velocities v, reduced impact parameters β, reduced distances of closest approach y, and elastic scattering angles in relative coordinates χ. The variation of χ with β is given in Figure 2 for the corresponding reduced initial relative kinetic energies $K = E/\epsilon$. Such plots are obtained from solutions of the classical equations of motion with the exp-six potential,[1]

$$V\left(\frac{r}{r_m}\right) = \frac{\epsilon}{1-(6/\alpha)}\left\{\frac{6}{\alpha}\exp\left[\alpha\left(1-\frac{r}{r_m}\right)\right] - \left(\frac{r_m}{r}\right)^6\right\} \qquad (1)$$

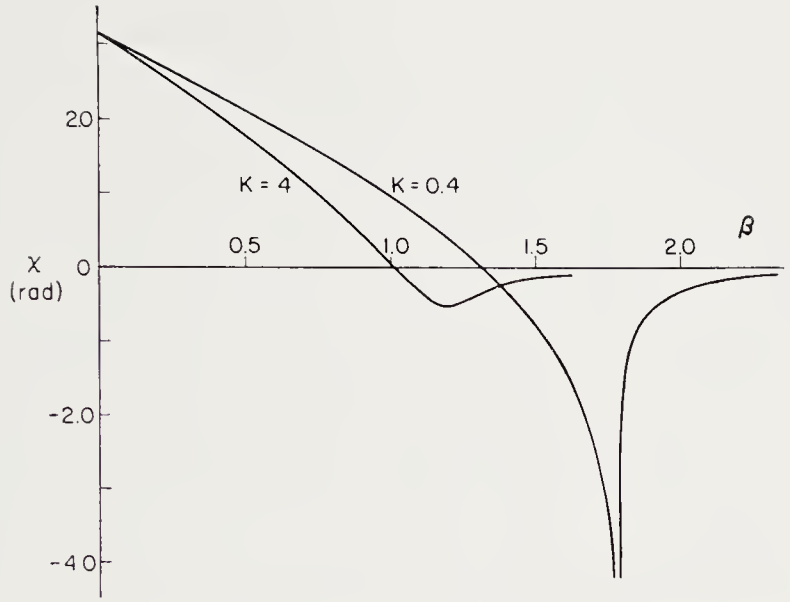

Fig. 2. The classical deflection function (the algebraic value of the scattering angle χ) vs. reduced impact parameter, $\beta = b/r_m$, for the exp-six potential ($\alpha = 12$) at two values of the reduced relative kinetic energy, $K = E/\epsilon$.

where α, r_m, and ϵ are parameters. This potential is plotted for two values of α in Figure 3. The parameters r_m and ϵ are used to form reduced distances and energies, respectively. The relation of the classical differential elastic scattering cross section to the reduced impact parameter is

$$\sigma(\chi) \sin \chi \, d\chi = r_m^2 \beta \, d\beta \tag{2}$$

For some reduced energies, for example at $K = 4$, the deflection function χ has a minimum at an angle called the rainbow angle, χ_r. At this angle the differential scattering cross section becomes infinite, but the infinity is removed by a semiclassical analysis[2] (see Fig. 4). The interference of partial waves of angular momenta related to impact parameters near the reduced impact parameter β_r, which corresponds to χ_r, leads not only to the rainbow scattering patterns but also to oscillations in the differential cross section at angles smaller than χ_r. These are called supernumerary rainbows and have no classical analog.[3]

For the reduced energy $K = 0.4$ the scattering angle χ becomes infinite at some impact parameter β_0. At this singularity, orbiting is said to occur.

The elastic scattering of neutral molecules which may react chemically

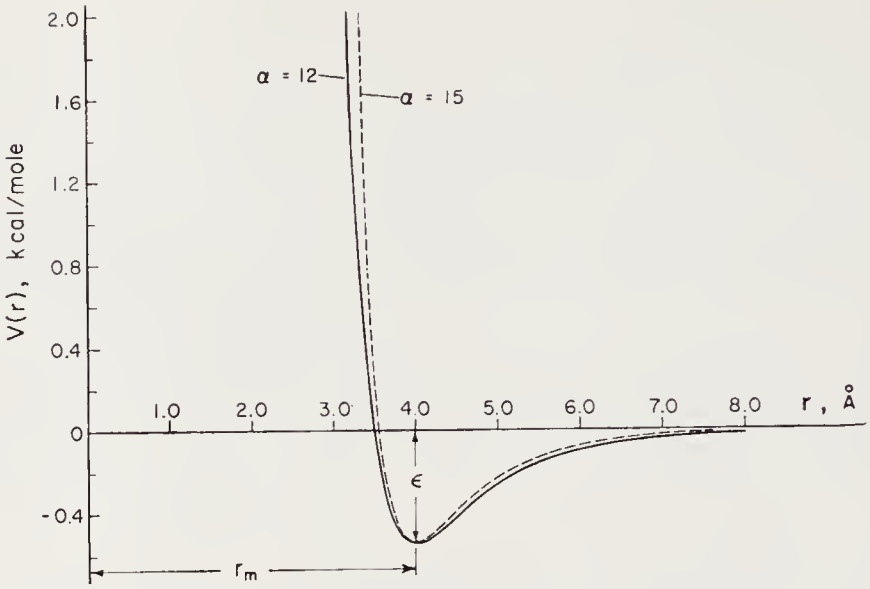

Fig. 3. The exp-six potential, Eq. (1), for two values of the parameter α.

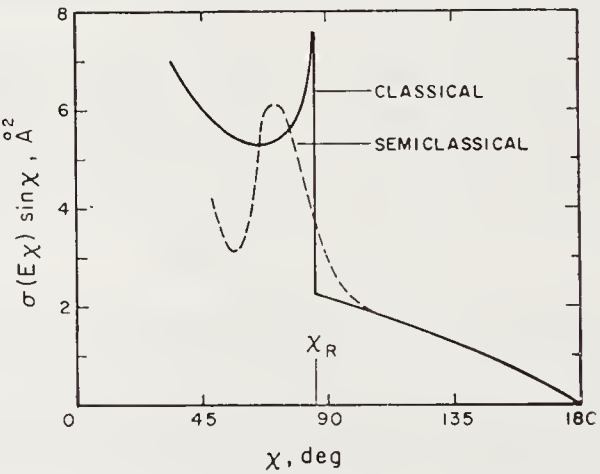

Fig. 4. Calculated differential elastic scattering cross section vs. χ in the rainbow region. The classical rainbow angle is χ_r. [From reference 2.]

has been observed for a number of systems.[4-13] From such measurements it is possible to deduce information about potentials of interaction, threshold (activation) energies, probabilities of reaction as functions of relative energies and impact parameters, typical distances at which reactions occur, distributions of chemical products in final internal quantum states, total reaction cross sections, and the influence

of the conservation requirements of mechanics. In this article we briefly review some experimental results obtained in this laboratory, the interpretation of these results, and the main conclusions which have been drawn for three types of systems. First we discuss the elastic scattering of the reactive systems K + HCl, K + HBr, K + HI, and a nonreactive analog K + Kr. In all four cases the elastic differential scattering cross sections are very similar in that they show rainbow scattering. This is characterized at larger relative kinetic energies by the increase of the polar cross section, $\sigma(\chi) \sin \chi$, to a maximum near the rainbow angle. Such observations indicate that there may be a range of applicability of a model of a spherically symmetric potential for these systems. The rainbow scattering in the three reactive systems is apparently unaffected by the possibility of reaction, and small threshold energies are found. Second, we discuss K + CH_3Br where rainbow scattering is much obscured but present, and again there is a nonzero threshold energy. Third, we discuss the nonreactive system K + $C(CH_3)_4$ which shows rainbow scattering, and compare it with the reactive system K + CBr_4 which does not. The absence of rainbow scattering suggests that even the small angle scattering is affected by reaction. This implies that relatively large distances of closest approach of the reactants suffice for reaction and that no activation energy is required. A model of the reaction based on orbiting collisions is in agreement with the few experimental results.

II. EXPERIMENTS

Experiments on the systems cited above are made with two crossed molecular beams. A schematic diagram of the apparatus is shown in Figure 5. In each case a potassium beam is formed by thermal effusion, collimated and velocity selected by mechanical means, and directed at right angles into a crossed thermal beam of the other reactant. The potassium is detected by surface ionization on a platinum filament.[14]

In an ideal experiment a K beam would be directed into a cross beam of reactant, with each atom and molecule in a given internal quantum state and at a given velocity. In the detection of inelastic collisions the scattered K atom would be velocity selected again, while a simultaneous observation would be made on the internal state of the scattered cross beam molecule. Thus the K scattered due to elastic and inelastic collisions and the scattered chemical product would be detected as a function of the scattering angle, initial relative

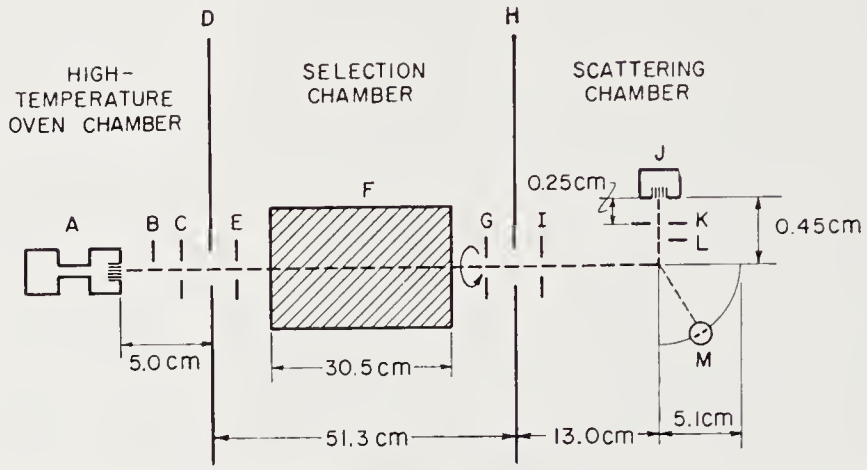

Fig. 5. Schematic diagram of the molecular beam apparatus. *A*, potassium source; *B,L*, beam flags; *C,E,G,I,K*, collimating slits; *F*, mechanical velocity selector; *J*, cross beam source; *M*, detector. The bulkheads *D* and *H* divide separately pumped vacuum chambers.

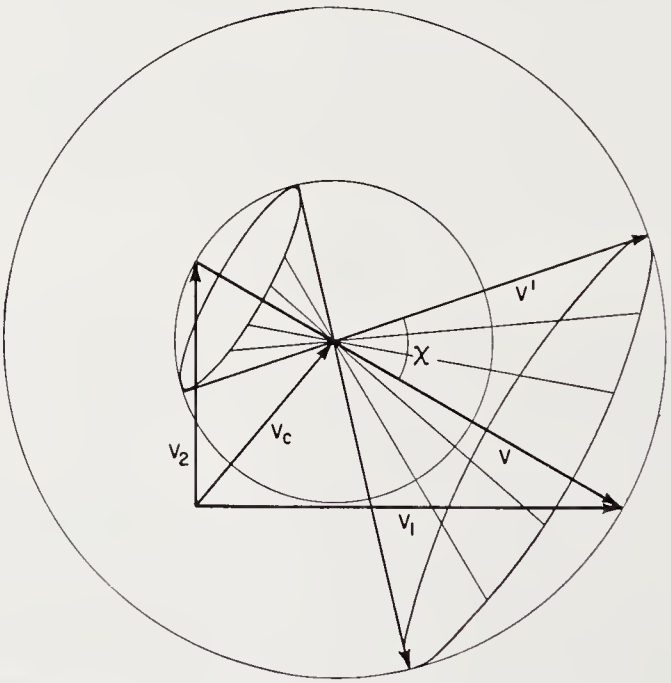

Fig. 6. Vector diagram for elastic scattering. For a collision with initial laboratory velocities V_1 and V_2 and a scattering angle χ in relative coordinates, the scattered particles are observed in laboratory coordinates at the circumferences of the bases of the two cones.

kinetic energy, and the initial and final internal quantum states. The measurements would be made in laboratory coordinates and would have to be transformed to center-of-mass coordinates before comparison with theoretical calculations. Figure 6 is a vector diagram which shows the relations between the coordinate systems for elastic scattering.

The actual experiments we discuss here are far from ideal. They consist of measuring the angular distribution of the flux of scattered potassium in the plane containing the two crossed beams for various values of an average initial relative kinetic energy $\bar{E}$. The detector receives a flux averaged over a small range of laboratory scattering angles determined by the size of the detector and the scattering center. The cross beam molecules are not monitored, nor is the K flux velocity selected again after collision. Hence the experiment records the scattering due to both elastic and inelastic collisions. Vibration–translation energy exchange cannot occur for most of the systems studied because the cross beam molecules are predominantly in their ground vibrational states and the initial relative kinetic energy is too small to produce excitation. Rotation–translation energy exchange may occur, but if it does it apparently leads to only small changes in the differential cross sections; an interpretation of the experiments which neglects the influence of rotation–translation interchange yields consistent results.

The detailed relation of the measured flux of K to the elastic differential scattering cross section is not simple. The mechanical velocity selector transmits K atoms in a range of velocities; the cross beam is not velocity selected and has a thermal distribution of speeds, although its temperature is usually low; in addition, the cross beam has a spatial distribution which gives a substantial range of beam intersection angles. These three factors produce a range of initial relative kinetic energies, and the experimentally measured flux of K is an average over the various distributions. The change from laboratory to relative coordinates also depends on the ratio of molecular velocities and on beam intersection angles and thus needs to be considered in the averaging. An account of the analysis of the experiments has been given elsewhere.[5,6,13] Fortunately, at larger scattering angles the differential cross section is only weakly dependent on energy, so that we may drop the distinction between the effective (average) cross section obtained in the experiments and one determined at a single energy. At smaller scattering angles, in particular in the rainbow scattering region, however, this simplification leads to substantial errors.

III. THE ELASTIC SCATTERING OF K + Kr, K + HCl, K + HBr, AND K + HI

In Figures 7–10 we show effective differential elastic scattering cross sections, multiplied by the sine of the scattering angle, as determined by experiments for one nonreactive system, K + Kr,[5] and three reactive systems, K + HCl,[13] K + HBr,[5,6] and K + HI.[13] In each case measurements were made at a number of average initial relative kinetic energies,

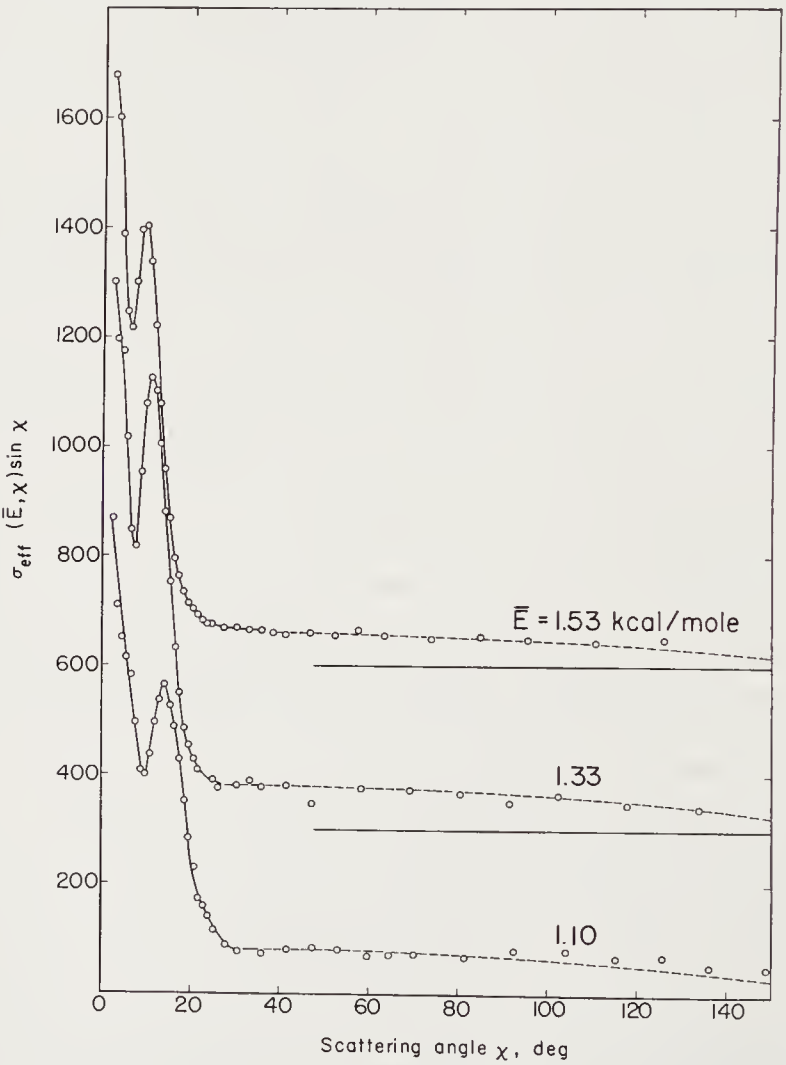

Fig. 7. The differential elastic scattering cross section, in arbitrary units, multiplied by sin χ vs. the relative scattering angle χ for the system K + Kr at three relative energies.

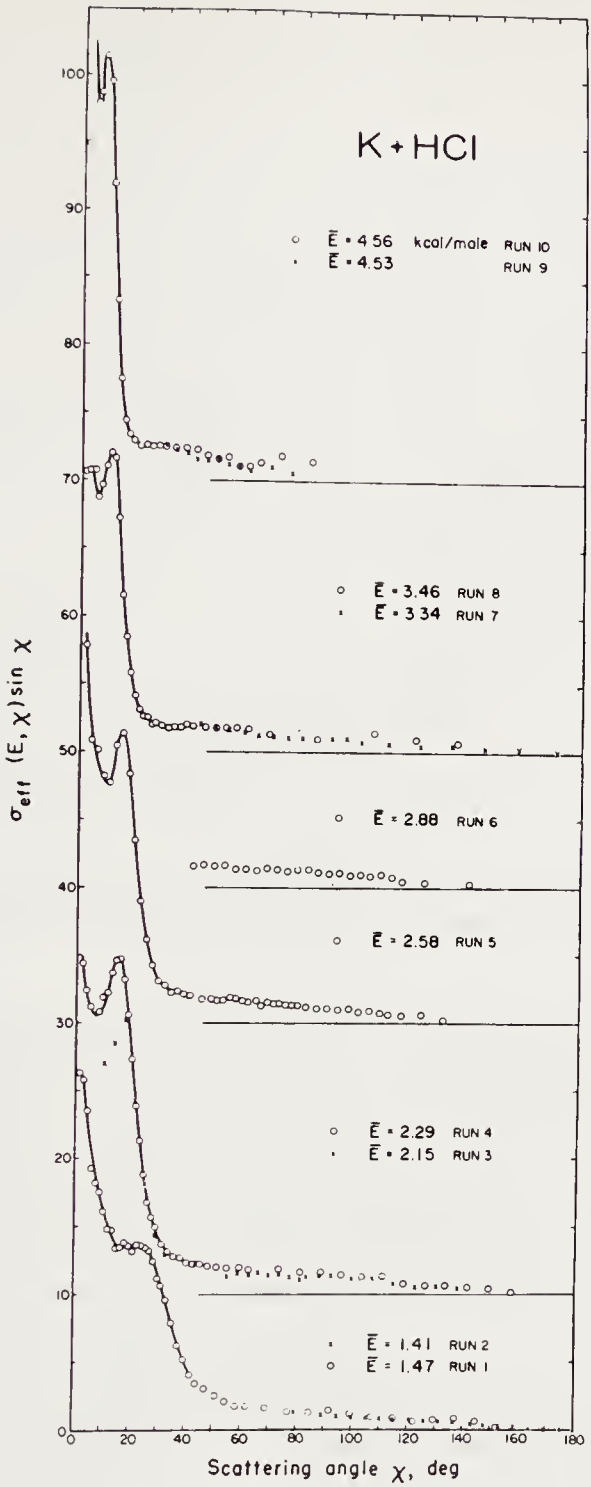

Fig. 8. The differential elastic scattering cross section, in arbitrary units, multiplied by $\sin\chi$ vs. the relative scattering angle χ for the system K + HCl at six relative energies.

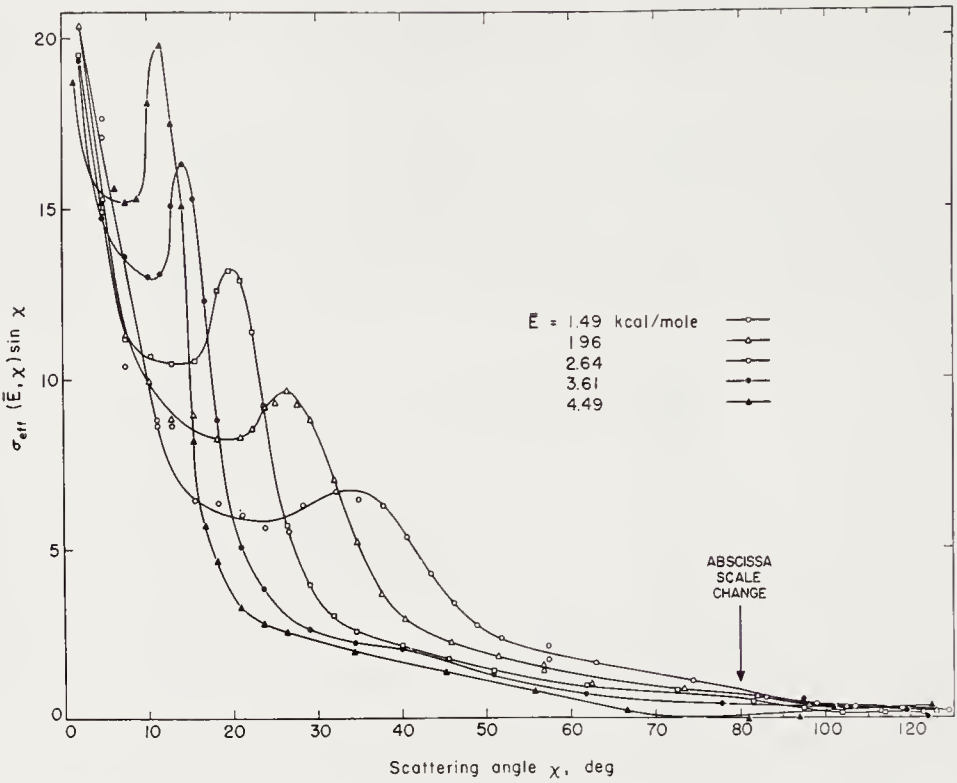

Fig. 9. The differential elastic scattering cross section, in arbitrary units, multiplied by sin χ vs. the relative scattering angle χ for the system K + HBr at five relative energies.

$\bar{E}$. At small angles the cross sections for these four systems have essentially the same form; there is a rapid decrease with increasing χ at very small angles, then for a given $\bar{E}$ there is a maximum in each curve which is displaced to smaller angles with increasing $\bar{E}$, and finally there is a rapid decrease past the maximum. The maxima in the cross sections are evidence of rainbow scattering. By use of the semiclassical theory,[2] the position of the experimentally determined maximum yields the energy parameter ϵ in an assumed analytic form of the potential of interaction, and the rate of decrease of the cross section past the maximum yields the size parameter r_m. Potential parameters for the exp-six potential, Eq. (1), obtained from the scattering experiments on these systems are listed in Table I. For the method of determining the parameters see the Appendix.

The consistency of the potential parameters, first, of all of those for a given system determined at various initial kinetic energies, and,

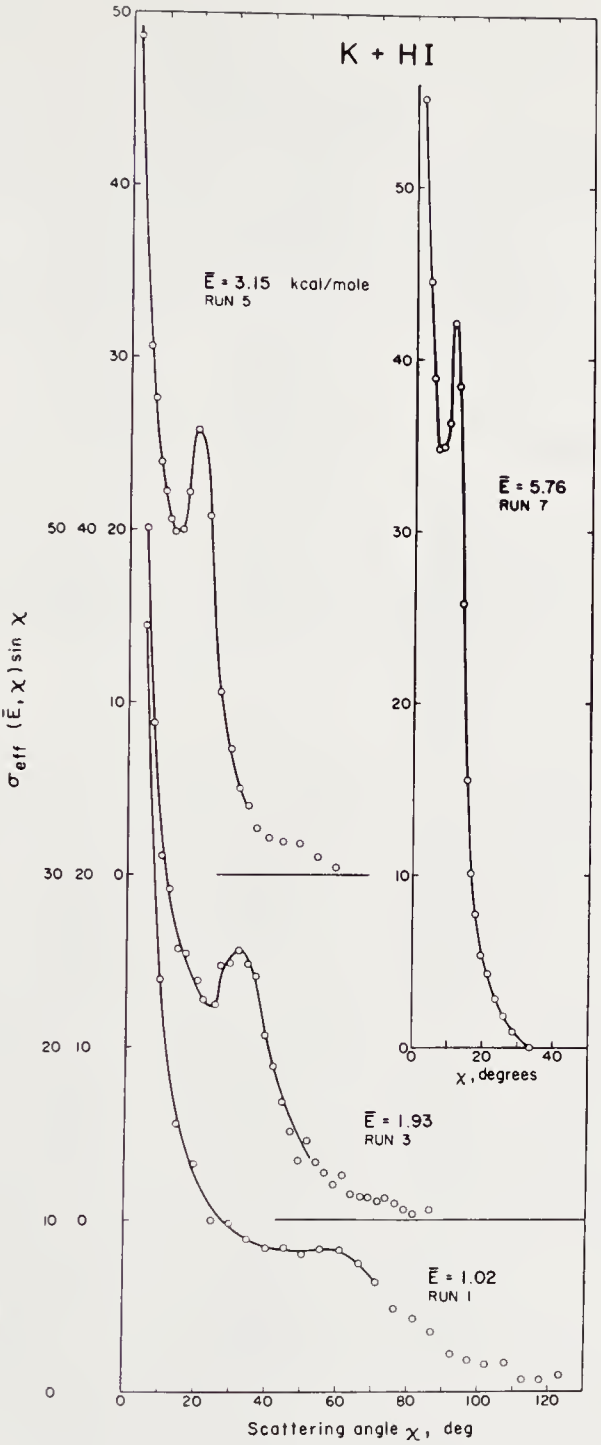

Fig. 10. The differential elastic scattering cross section, in arbitrary units, multiplied by sin χ vs. the relative scattering angle χ for the system K + HI at four relative energies.

TABLE I

Potential Parameters for the Exp-Six Potential, Eq. (1), $\alpha = 12$

System	$\bar{E}$, kcal/mole	ϵ, kcal/mole from rainbow scattering	r_m, Å	r_m, Å, from kinematics
K + Kr[a]	1.10	0.180	5.6	
	1.33	0.176	5.9	
	1.53	0.180	5.4	
Suggested value		0.179 ± 0.005	5.6 ± 0.5	
K + HCl	1.47	0.442	3.3	3.19
	2.15			3.19
	2.29	0.424	4.0	3.20
	2.58	0.471	3.5	3.14
	2.88			3.15
	3.34			3.17
	3.46	0.467	3.8	3.15
	4.53			3.18
	4.56	0.485	4.7	3.18
Suggested value		0.458 ± 0.02	3.3 ± 0.03	
K + HBr	1.49	0.545	5.5	
	1.96	0.566	3.2	
	2.64	0.565	4.4	4.48
	3.61	0.568	4.3	
	4.49	0.592	4.0	
Suggested value		0.567 ± 0.01	4.4 ± 0.4	
K + HI	1.93	0.665	3.8	
	3.15	0.652	4.5	
	5.76	0.697	3.4	<5.4
Suggested value		0.671 ± 0.02	3.9 ± 0.6	
K + CH_3Br	1.12	0.370		
	1.91	0.377		
	2.83	0.376		
	5.01	0.390		
Suggested value		0.378 ± 0.01		
K + $C(CH_3)_4$	1.37	0.417	3.4	
	2.17	0.416	4.3	
	3.69	0.433	5.8	
Suggested value		0.419 ± 0.02		

(*continued*)

TABLE I *(continued)*

System	$\bar{E}$, kcal/mole	ϵ, kcal/mole from rainbow scattering	r_m, Å	r_m, Å, from kinematics
K + CBr_4	1.63	1.0		
	3.18	1.86		
	3.22	1.85		
	4.84	2.66		
	7.14	2.92		
	7.19	2.18		
Suggested value		2.25 ± 0.5		

[a] The potential parameters for this system agree with those determined independently from measurements of the total cross section. E. W. Rothe, R. H. Neynaber, B. W. Scott, S. M. Trujillo, and P. K. Rol, *J. Chem. Phys.*, **39**, 493 (1963).

second, of those of the three hydrogen halide systems, lends support to the assumptions that to a good approximation the potential is spherically symmetric and the rainbow scattering is unaffected by chemical reaction. If the observed rainbow scattering is affected by the exchange of translational and rotational energy, then either this effect is of minor importance or it does not vary appreciably with initial kinetic energy or from one system to another.

For scattering angles larger than the rainbow angle, the elastic differential scattering cross section of the reactive systems is substantially smaller than that of the nonreactive system. This difference may be ascribed to the occurrence of chemical reaction, and a quantitative discussion is possible on the basis of the following simple model. The elastic scattering at large scattering angles is described by classical mechanics, and the potential surface of the system traversed in a collision leading to elastic scattering is adequately represented by the two-body potential of the reactants determined from the rainbow scattering. With this model, for each scattering angle at a given energy there is a corresponding impact parameter b, a distance of closest approach, yr_m, and a potential energy $V(y)$ at the distance of closest approach. As b decreases, χ and $V(y)$ increase. An approximate potential surface for the system K + HBr is shown in Figure 11. It is drawn to be consistent with the present interpretation but must be considered as

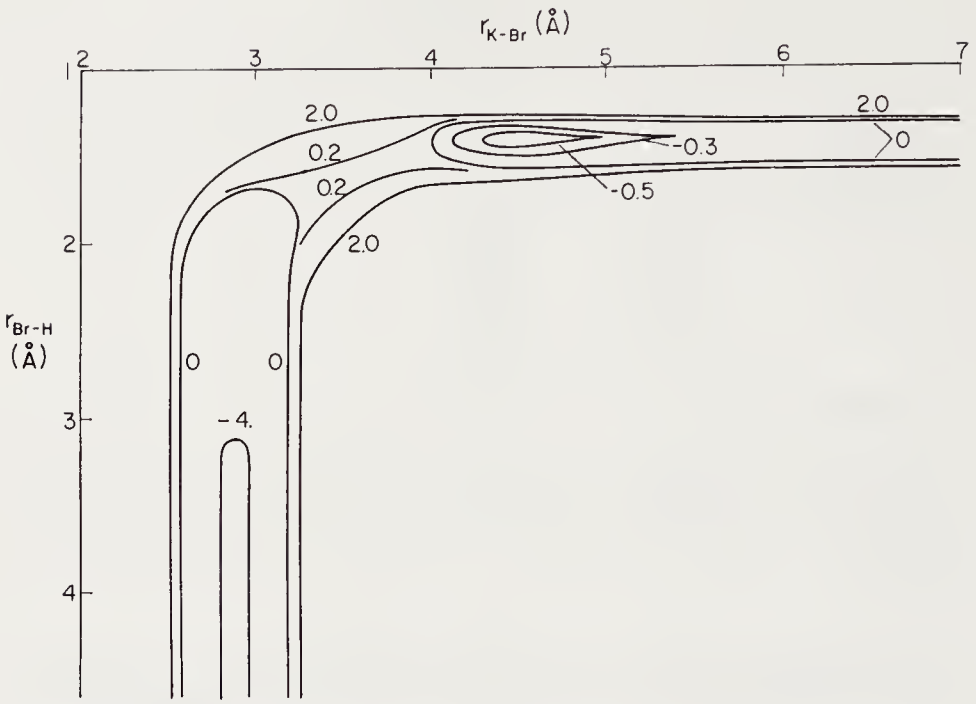

Fig. 11. Postulated potential surface for the reactive system K–Br–H. The interaction of K with HBr is taken to be independent of the orientation of the molecule.

speculative. If the H–Br distance is restricted to be below some upper limit in a collision leading to elastic scattering, or conversely, if reaction occurs when the H–Br distance exceeds a given value in a collision, then the assumption made about the potential surface may have some validity. The utility of the model must be judged by the agreement of its predictions with experiment.

To deduce some consequences of this model, consider a flux of K atoms all with impact parameter b and relative energy E impinging on cross beam molecules. (For convenience we neglect from now on the distinction between E and $\bar{E}$.) A fraction of these K atoms is scattered elastically and the remainder react. The flux of K scattered through an angle χ by the two-body potential is proportional to $\sigma_c(E\chi)$, a calculated classical differential cross section. If $\sigma_c(E\chi)$ is fitted to the experimental scattering cross section at an angle close to the rainbow region, which is assumed to be unaffected by reaction, then for larger scattering angles the experimental scattering cross section is smaller than $\sigma_c(E\chi)$ because some reactant atoms have been lost due to reaction. We can

thus define a probability of reaction,

$$P(E\chi) = \frac{\sigma_c(E\chi) - \sigma(E\chi)}{\sigma_c(E\chi)} \tag{3}$$

but prefer to consider P as a function of E and β or E and $V(y)$. As is mentioned above, this transformation is readily made if the potential parameters α and ϵ are known.

Graphs of the probabilities of reaction for various values of E for the three systems are shown in Figures 12–14. For the endothermic

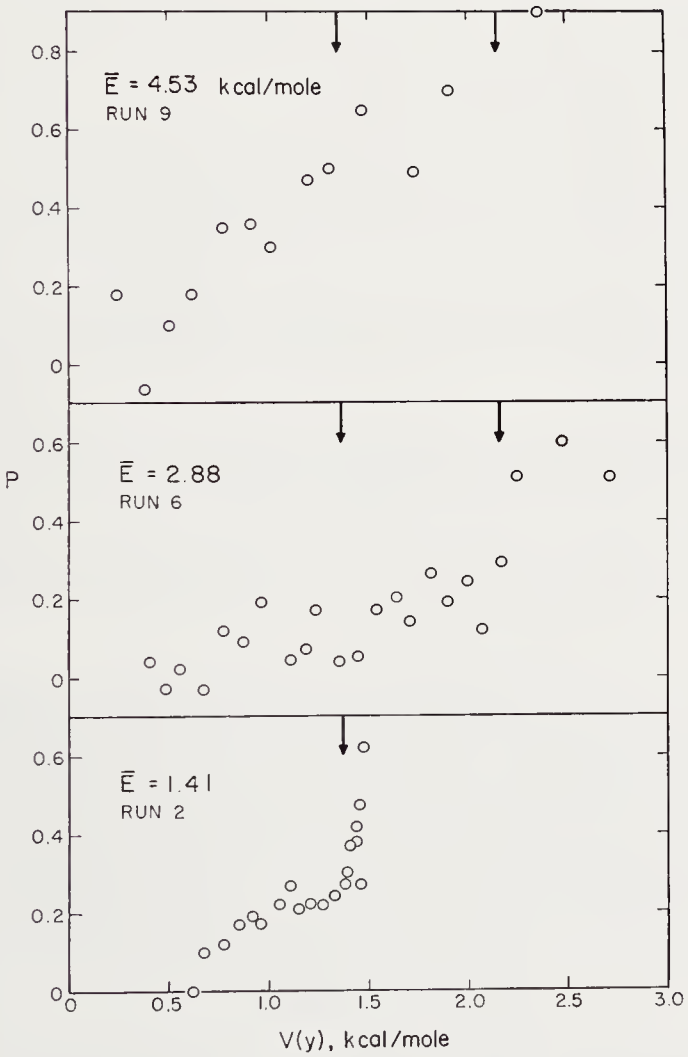

Fig. 12. Probability of reaction vs. potential energy at the distance of closest approach for the reactants K + HCl.

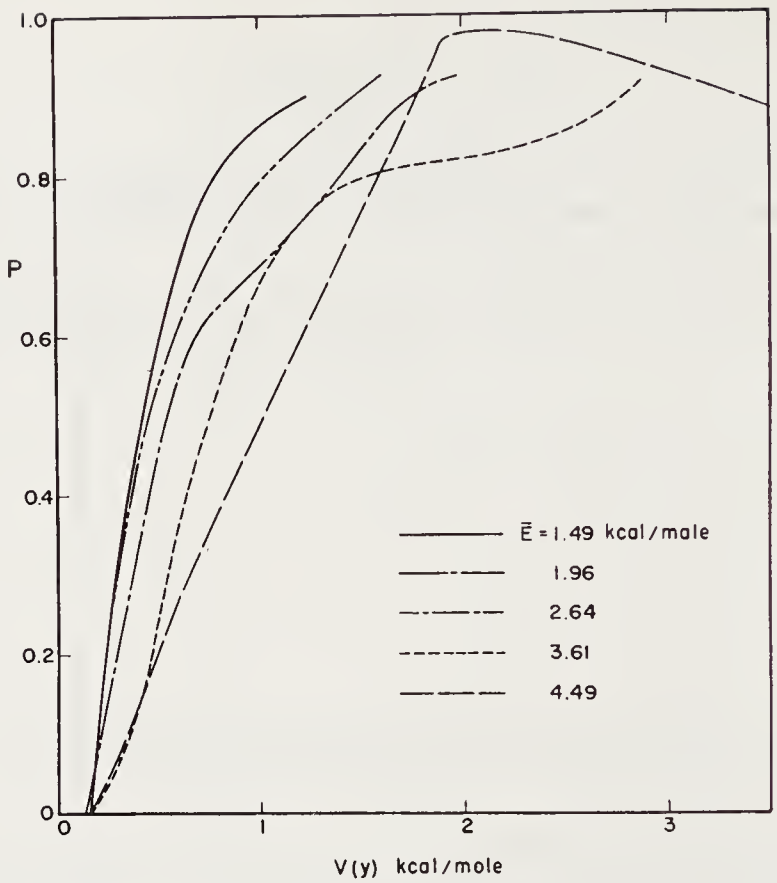

Fig. 13. Probability of reaction vs. potential energy at the distance of closest approach for the reactants K + HBr.

reaction K + HCl, the calculated cross section is fitted without ambiguity to the experiments at scattering angles slightly larger than the rainbow angle, Figure 8. The threshold of the probability of reaction occurs at the threshold angle, that is, the angle at which $\sigma(E\chi)$ begins to differ from $\sigma_c(E\chi)$. The procedure for the two exothermic reactions is less straightforward, since there are no obvious indications here of the onset of chemical reaction. The calculated cross sections are fitted to the experimental curves for K + HI past the rainbow scattering region at values predicted from the height of the rainbow maximum, and for K + HBr at values consistent with the two-body model and a common distance of closest approach of the reactants at threshold. The probabilities of reaction have a distinct and different form for

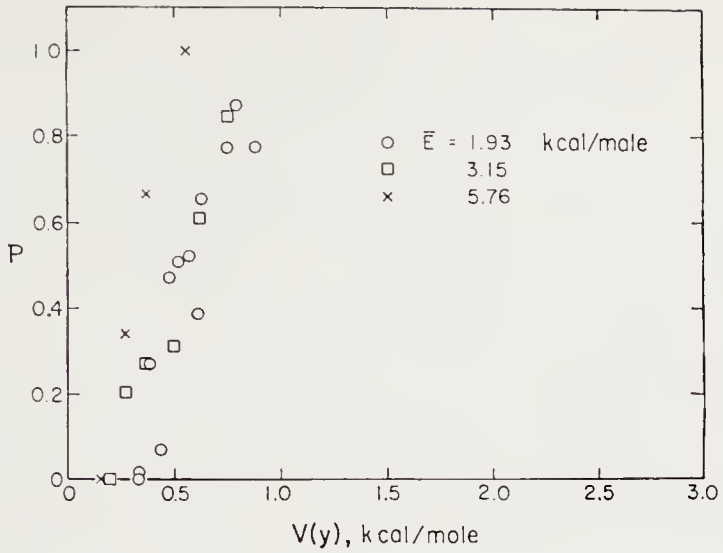

Fig. 14. Probability of reaction vs. potential energy at the distance of closest approach for the reactants K + HI.

each of the three reactions, yet some of their gross features are simply interpreted with the use of the requirement of conservation of angular momentum.

The initial energy of each system K + HX consists of relative kinetic energy E and rotational energy $E_{r,\mathrm{HX}}$. The molecules HX are in the ground vibrational state. The final energy of the products is a sum of their kinetic, E', rotational, $E_{r,\mathrm{KX}}$, and vibrational energy, E_v. Thus we have the equality

$$E + E_{r,\mathrm{HX}} = E' + E_{r,\mathrm{KX}} + E_v + \Delta E_0^\circ \tag{4}$$

where ΔE_0° is the standard energy change of the reaction at 0°K. For the conditions of the experiments, $E_{r,\mathrm{HX}}$ is small compared to E (see Table II), and is neglected. The initial and final angular momenta are each a vector sum of the orbital angular momentum of relative motion, μvb, and the rotational angular momentum, p, of the diatomic molecule. Here μ and μ' are the reduced masses of the reactants and products, respectively. We have the equality

$$\mu vb + p_{\mathrm{HX}} = \mu' v' b' + p_{\mathrm{KX}} \tag{5}$$

and again, as can be seen by reference to Table II, the conditions of the experiments are such that, to a first approximation, p_{HX} may be

TABLE II

Kinematic Data and Distribution of Energy among the Products for K + HX Reactions

System	K + HCl		K + HBr		K + HI	
ΔE_0°, kcal/mole	0.7 ± 1.2		-4.3 ± 1.2		-5.9 ± 1.2	
Threshold energy of reaction, kcal/mole	0.59 ± 0.1		0.15 ± 0.1		0.2 ± 0.1	
Distance of closest approach of reactants at threshold, Å	2.8		3.8		3.4	
Angular momentum of HX, (most probable J), g cm^2/mole sec	1.55×10^{-3} (2)		1.55×10^{-3} (2)		2.19×10^{-3} (3)	
Rotational energy of HX, (most probable J), kcal/mole	0.18 (2)		0.15 (2)		0.22 (3)	
Properties at threshold of reaction						
$\bar{E}$, kcal/mole	1.47	4.56	1.49	4.49	1.02	5.76
Orbital angular momentum, g cm^2/mole sec	0.0312	0.0667	0.068	0.121	0.0528	0.126
Rotational energy of KX, kcal/mole	0.9	4.0	2.52	8.07	1.06	6.18
Rotational quantum number of KX	49	104	104	186	82	200
Sum of final energies of vibration and relative translation, kcal/mole	0	0	3.3	0.7	5.9	5.5
Maximum vibrational quantum state of KX	0	0	5	1	12	11

neglected compared to μvb for the upper range of b, that is, for scattering angles just larger than the threshold angle. Since the reduced mass of the products, μ', is much smaller than that of the reactants, and since the upper limit on the final relative velocity is known, the final orbital angular momentum is small compared to p_{KX} for reasonable estimates of the final impact parameter b'. With these simplifications we have

$$\mu vb \simeq p_{KX} \tag{6}$$

Thus, for the rigid rotor model of KX the equation of conservation of energy, Eq. (4), may be rewritten

$$E = E' + (\mu v b)^2/2I_{KX} + E_v + \Delta E_0^\circ \tag{7}$$

with I_{KX} denoting the moment of inertia of KX. After these preliminaries we may begin a discussion of the probabilities of reaction for the three reactive systems.

A. Threshold Energies

The average thresholds of the probabilities of reaction are listed in Table II. There are no apparent restrictions on these thresholds for the two exothermic reactions, but there is one for the endothermic reaction K + HCl. Here the threshold energy must equal or exceed the change in the energy of reaction at 0°K. The best value available from the literature for this quantity is 0.7 ± 1.2 kcal/mole, which is indistinguishable from the observed threshold 0.59 ± 0.1 kcal/mole.

There are indications in the probability curves for K + HCl (Fig. 12) that for a given initial kinetic energy KCl may be formed in excited vibrational states provided that the impact parameter is such that $V(y)$ exceeds the excitation energy. The vibrational energy spacing of KCl is $\omega = 281$ cm^{-1} or 0.80 kcal/mole. Thus the threshold energy for the reaction leading to formation of KCl in the vth vibrational state is $\Delta E_0^\circ + v\omega$. These values of the threshold energy are shown by arrows in Figure 12 for $v = 1$ and 2. The increase in the probability of reaction is apparent for $\bar{E} = 1.41$ kcal/mole and possibly observable for $\bar{E} = 2.88$ kcal/mole.

B. Threshold Distances

The model we use for the interpretation of the experimental results relates threshold energies directly to threshold distances through the two-body potential $V(y)$. The distances of approach of reactants necessary for reaction are the threshold distances and these are listed in Table II. The threshold distances for the two exothermic reactions are considerably larger than the internuclear distances of the products KBr and KI, even if these are formed in excited vibrational states. The threshold distances for the formation of KCl in the vibrational states $v = 0$ (2.8 Å) and $v = 1$ (2.7 Å), however, nearly equal the equilibrium internuclear distance, 2.67 Å, and the inner classical turning point for $v = 1$, 2.56 Å, respectively.

It is perhaps worth emphasizing at this point that the threshold energies and distances obtained from the interpretation of the experiments depend on the choice of potential but not on any other adjustable parameter.

C. Probability of Reaction and Populations of Product States

The requirement of conservation of angular momentum prescribes the rotational state of the product KX, at least for the larger impact parameters near threshold. (For small impact parameters we cannot neglect either p_{HX} compared to μvb or $\mu' v' b'$ compared to p_{KX}.) Hence we can calculate the sum of translational and vibrational energy of the products KX + H; some typical values are shown in Table II.

We have noted above that the probability of reaction for the system K + HCl increases when an additional vibrational state becomes available. The number of vibrational states available to the product KBr depends very much on the initial kinetic energy for a given value of $V(y)$. We see in Figure 13 that the probability of reaction for this system is qualitatively proportional to the energy available for vibration and translation. This observation is in agreement with the prediction of a statistical theory of chemical reactions in which the reaction probability into given states of products is proportional to the phase space of these states. For the system K + HI we show in Table II that for the conditions of the experiment the energy available for vibration and translation of KI is nearly independent of $\bar{E}$. Thus the same argument predicts reaction probabilities which are almost energy independent. This is just what is observed (see Fig. 14).

D. Independent Estimates of the Size Parameter r_m

Independent estimates of the size parameter r_m may be made from the probabilities of reaction and application of the requirement of conservation of angular momentum.

At threshold the product KCl is formed in the ground vibrational state, so that E_v in Eq. (7) equals zero. If at threshold the products recede from each other with a final translational energy much less than $E_{r,KCl}$, then Eq. (7) reduces to

$$E - \Delta E_0^\circ = (\mu vb)^2 / 2I_{KCl} \tag{8}$$

from which we calculate the threshold impact parameter. We also know the reduced threshold impact parameter $\beta = b/r_m$, because for a

two-body model of interaction of the reactants, β, χ, and $V(y)$ are related by the known solutions of the equations of motion. This independent estimate of the size parameter agrees with the value obtained from the analysis of the rainbow scattering, Table I. If we use the experimental threshold energy taken from the graphs of P vs. $V(y)$ for KCl formed in the first vibrational state, in the cases where such a second threshold is apparent, we can repeat this calculation to obtain another estimate of r_m. This, too, is in good agreement with the other values.

The dependence of the probability of reaction of K + HBr on the initial kinetic energy, E (Fig. 13) may be used for an estimate of the size parameter for this system. We have noticed from the interpretation of the experiments and a simple calculation, that the probability of reaction decreases at fixed $V(y)$ with increasing initial kinetic energy. At some value of E, then, the probability of reaction must become zero because it is impossible to satisfy conservation of energy and angular momentum if reaction occurs. At that threshold E_v and E' in Eq. (7) are zero and, quite similarly to the case of K + HCl discussed above, we obtain the threshold impact parameter b. The value of the initial kinetic energy for which $P = 0$ is obtained at a given $V(y)$ by empirical extrapolation of P vs. E (Fig. 13). For this $E(P = 0)$ and $V(y)$,

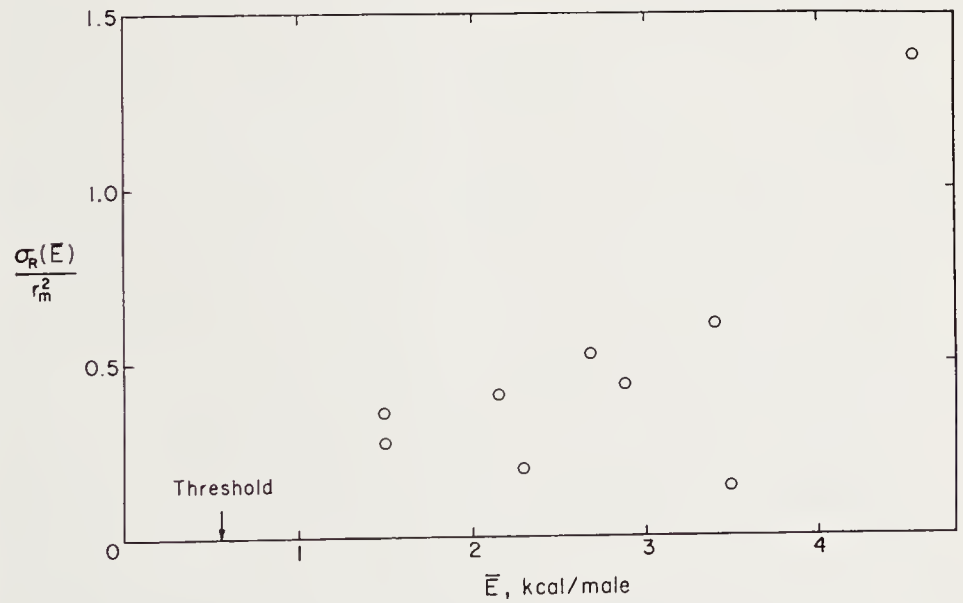

Fig. 15. Energy dependence of the reduced total reaction cross section for K + HCl obtained from elastic scattering measurements.

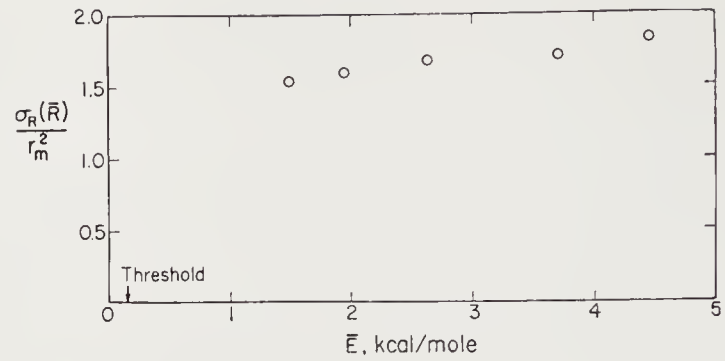

Fig. 16. Energy dependence of the reduced total reaction cross section for K + HBr obtained from elastic scattering measurements.

the two-body model of interaction specifies the reduced impact parameter β and hence r_m is determined. Again this value is in reasonable agreement with those calculated from the rainbow scattering, Table I.

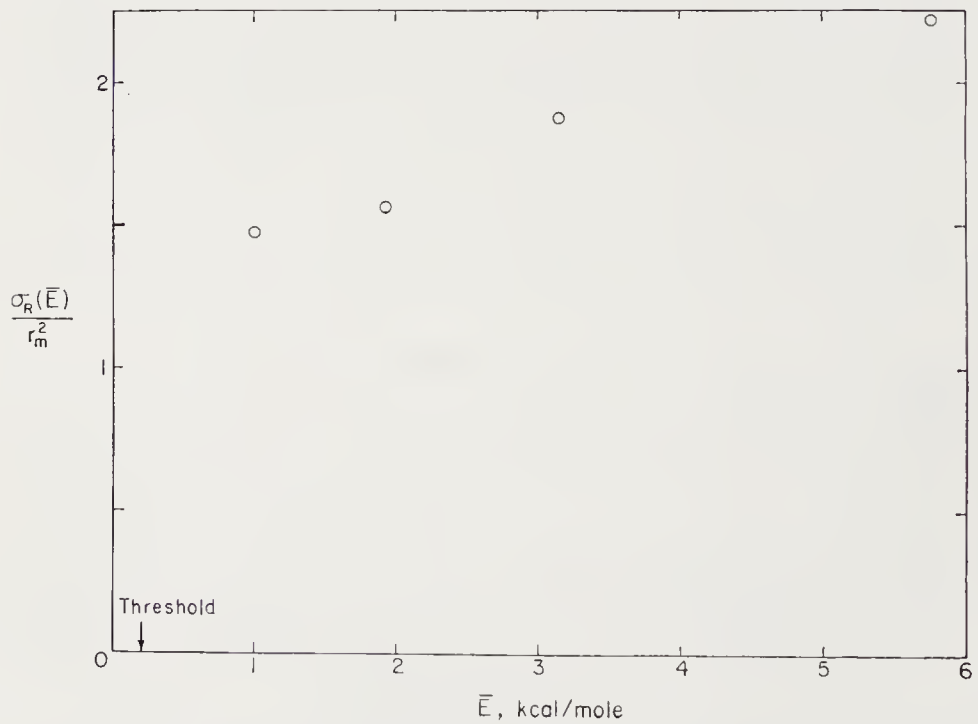

Fig. 17. Energy dependence of the reduced total reaction cross section for K + HI obtained from elastic scattering measurements.

E. Total Reaction Cross Section

The total reaction cross section $\sigma_R(E)$ is obtained from the probability of reaction by integration,

$$\sigma_R(E) = 2\pi r_m^2 \int_0^{\beta_{\text{threshold}}} P(E\beta)\beta \, d\beta \tag{9}$$

Reduced total reaction cross sections so obtained for the three systems are shown in Figures 15–17. Absolute values of the cross sections are obtained by multiplication by r_m^2. Using the recommended values of r_m from Table I, we calculate the following total reaction cross sections at $\bar{E} = 2$ kcal/mole:

$$K + HCl, 4 \text{ Å}^2; \quad K + HBr, 31 \text{ Å}^2; \quad K + HI, 24 \text{ Å}^2$$

IV. THE ELASTIC SCATTERING OF $K + CH_3Br$[10]

Elastic differential scattering cross sections for the system $K + CH_3Br$ are shown in Figure 18. Rainbow scattering is recognizable but clearly very different from the kind observed for the systems discussed above. We do not know the origin of this difference but suspect that it is related to a more significant deviation of the potential of interaction from that of a two-body system. An estimate of the energy parameter ϵ for the exp-six potential is given in Table I.

Abrupt changes in the slopes of the scattering curves are observable for all but the curve at the lowest relative kinetic energy. Again we ascribe this behavior to the occurrence of chemical reaction. For this system, however, the interpretation of the experiments based on a model of two-body interactions is expected to be less valid. Because no better alternative is available, we proceed as above. The probability of reaction is shown in Figure 19. The threshold angles are located at the changes in the slopes of the scattering curves. The size parameter r_m has not been determined because it seems unreasonable to use a two-body theory for this purpose when the rainbow scattering is so distorted. As a first approximation, r_m is taken to be equal to that of $K + HBr$.

The energy dependence of the reduced total reaction cross section is shown in Figure 20. For $r_m = 4.4$ Å, the total reaction cross section is 23 Å^2 at 2 kcal/mole.

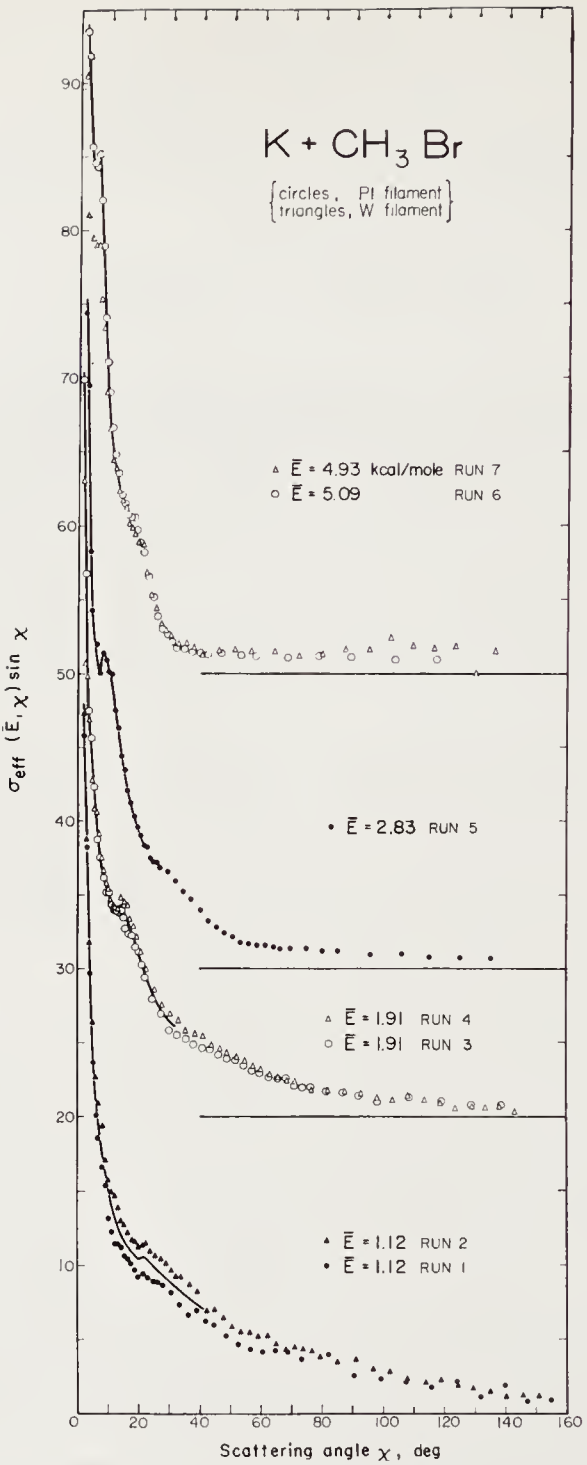

Fig. 18. The differential elastic scattering cross section, in arbitrary units, multiplied by sin χ, vs. the relative scattering angle χ for the system $K + CH_3Br$ at four relative energies.

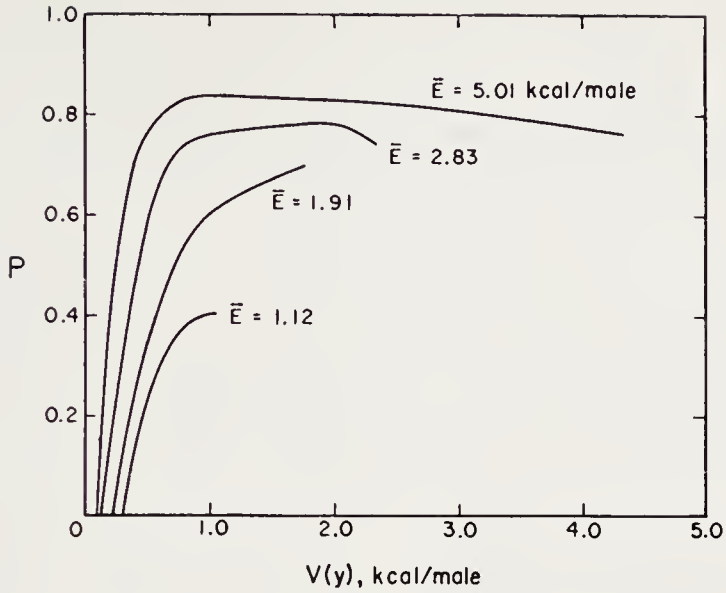

Fig. 19. Probability of reaction vs. potential energy at the distance of closest approach for the reactants $K + CH_3Br$.

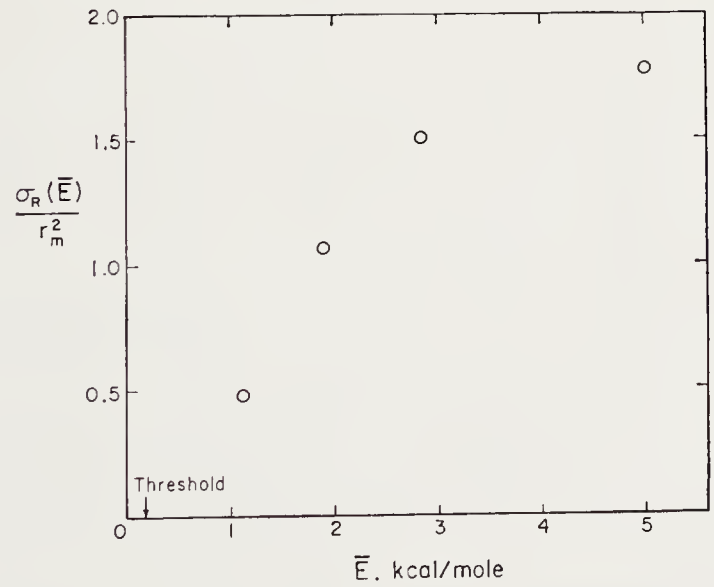

Fig. 20. Energy dependence of the reduced total reaction cross section for $K + CH_3Br$ obtained from elastic scattering measurements.

V. THE ELASTIC SCATTERING OF $K + C(CH_3)_4$ AND $K + CBr_4$*

Elastic differential scattering cross sections of the systems $K + C(CH_3)_4$ and $K + CBr_4$ are shown in Figures 21 and 22. A marked

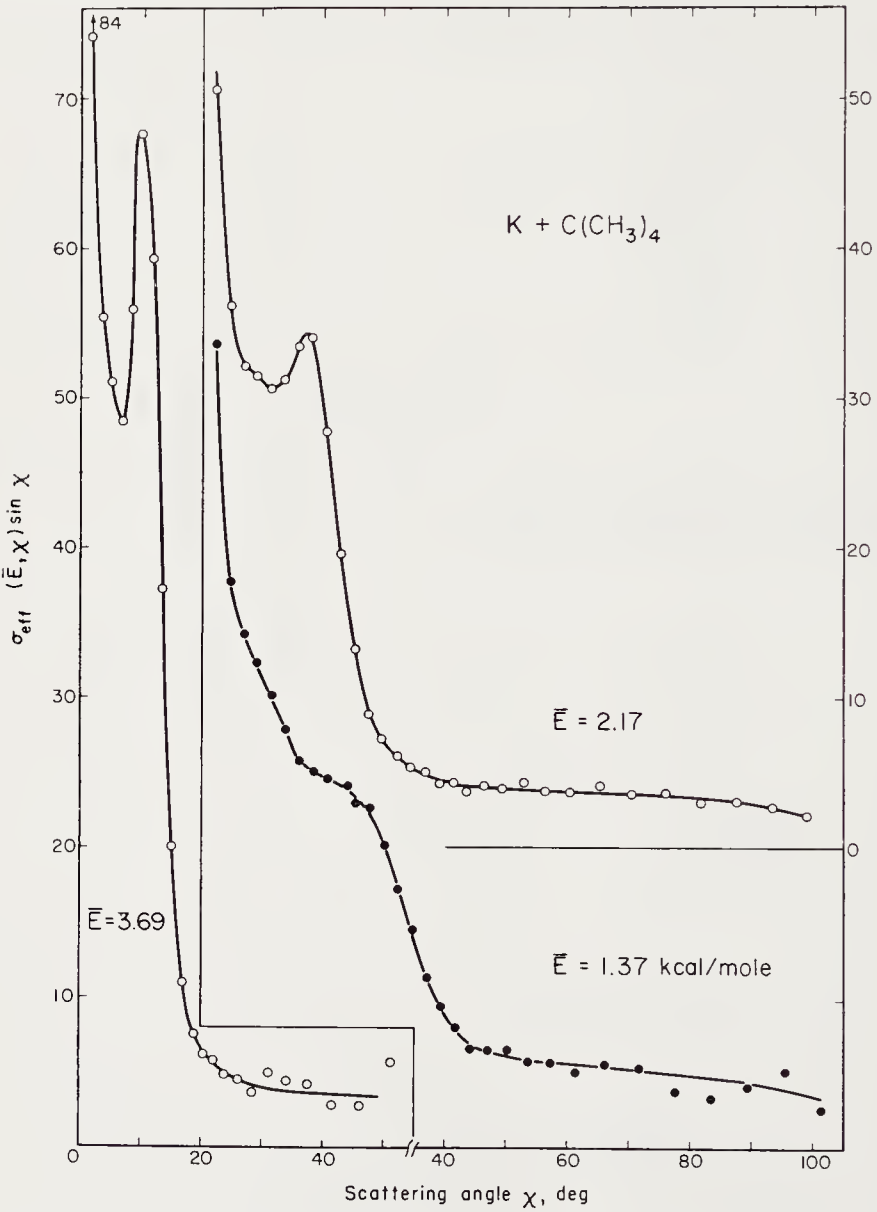

Fig. 21. The differential elastic scattering cross section, in arbitrary units, multiplied by sin χ, vs. the relative scattering angle χ for the system $K + C(CH_3)_4$ at three relative energies.

* Unpublished results.

difference between the two systems is apparent. The nonreactive case shows rainbow scattering similar to that of K + Kr and K + HX. A preliminary estimate of the parameters ϵ and r_m in the potential

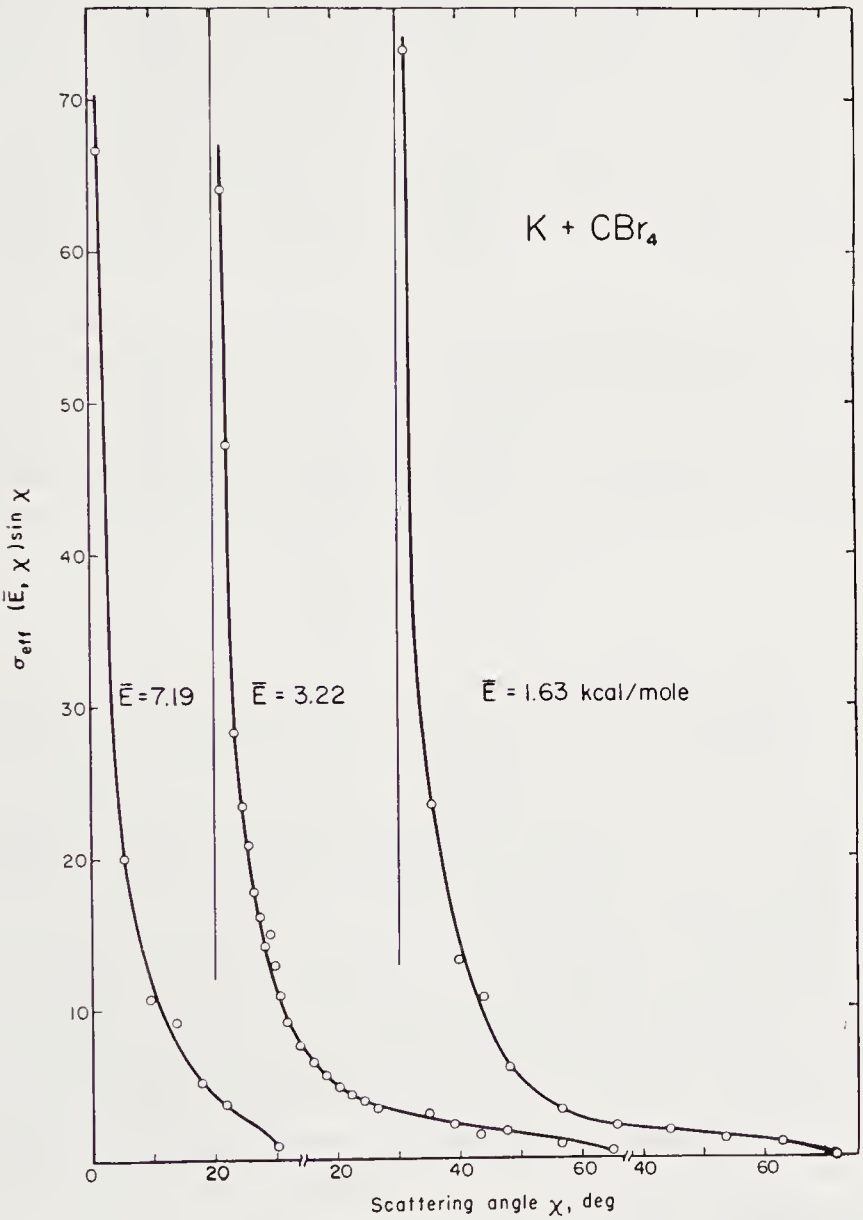

Fig. 22. The differential elastic scattering cross section, in arbitrary units, multiplied by sin χ, vs. the relative scattering angle χ for the system K + CBr_4 at three relative energies.

(Eq. (1)) are listed in Table I. The size parameter varies with energy, which may be due to the inadequacy of the potential function for this system.

The absence of rainbow scattering in the reactive system is evident and provides a clue for a possible model for the reactive collision. Suppose that the reaction cross section has zero threshold energy so that reaction may occur at still larger reduced intermolecular distances than for the systems K + HBr or K + CH_3Br. Now even though the χ vs. β curve (Fig. 2) for a given reduced energy has a minimum (χ_r, β_r), rainbow scattering should not appear if the probability of reaction is nearly unity for impact parameters equal to or smaller than β_r.

The question then remains: What is the threshold distance for reaction? In accordance with previous work on ion–molecule reactions,[15] recombination reactions,[16] and a simple model for triple collisions,[17] we fix the threshold distances for low relative kinetic energies at the point where passage over the rotational barrier is possible. Consider the effective potential energy defined by the equation

$$V(rq) = V(r) + \epsilon q r_m^2/r^2 \tag{10}$$

$$q \equiv \mu v^2 b^2/2\epsilon r_m^2$$

which is shown in Figure 23 for $V(r)$ given by Eq. (1) and for various values of the parameter q. In the range of reduced initial energies $0 \leqslant K \leqslant K_c$, $V(rq)$ has a maximum.* At that point the initial conditions $K = E/\epsilon$ and b are such that the scattering angle is infinite and orbiting occurs. This situation is indicated in Figure 23 by a horizontal line, representing the initial kinetic energy, which is drawn tangent to the effective potential at the maximum. A slight decrease of b at constant K lowers $V(rq)$ slightly so that the particles may approach each other to the inner turning point of $V(rq)$. We therefore choose the threshold distance of reaction at the location of the maximum in $V(rq)$ in the range $0 \leqslant K \leqslant K_c$ and, arbitrarily, at the critical distance r_c/r_m for all K larger than K_c. Furthermore we suppose that the probability of reaction is a step function, zero for distances of closest approach larger than the threshold distance and unity for distances smaller than the threshold distance.

* We do not consider and have not shown in Figure 23 the artificial maximum near the origin which is peculiar to the exp-six potential.

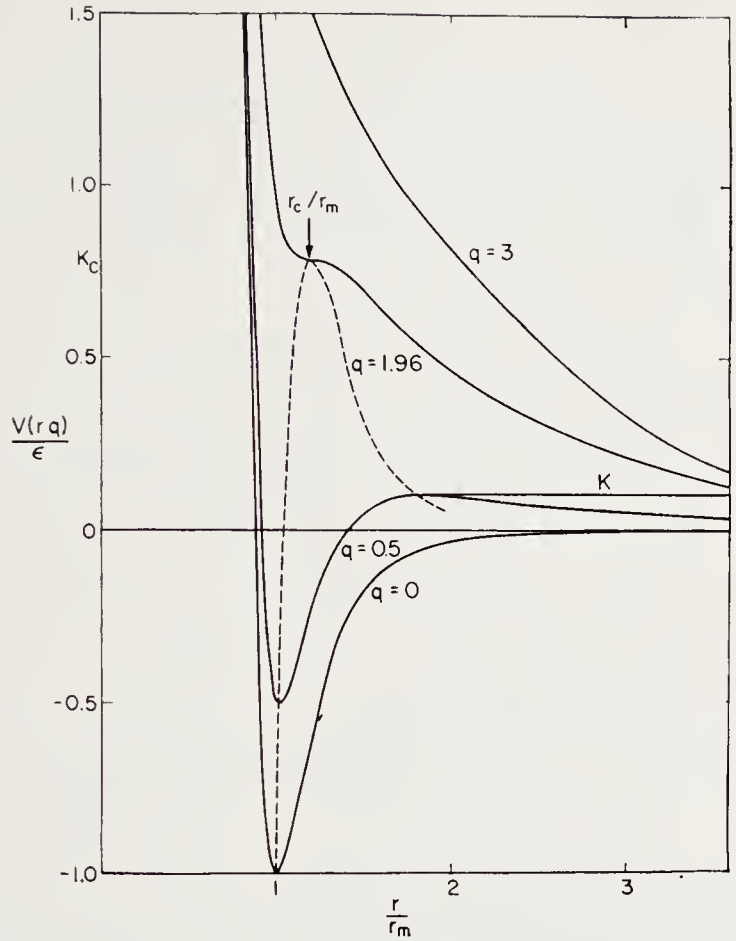

Fig. 23. The effective potential, Eq. (10). The dashed line is the locus of the extrema for different values of $q = \mu v^2 b^2/2\epsilon$.

With this choice we turn again to the curves of χ vs. β and find that now elastic scattering can occur into any given angle only from the outermost branch of the deflection function χ. In Figure 24 we show graphs of the differential scattering cross section for the exp-six potential in the form suggested by Mason[1b]

$$\rho(\chi K) = \left[K\left(1 - \frac{6}{\alpha}\right)\right]^{1/3} \chi^{4/3} \left[\frac{1}{r_m^2}\,\sigma(\chi K) \sin \chi\right] \tag{11}$$

We give the curves of ρ as calculated by Mason corresponding to scattering from all branches of the deflection function (solid lines) and curves of ρ corresponding to scattering only from the outermost

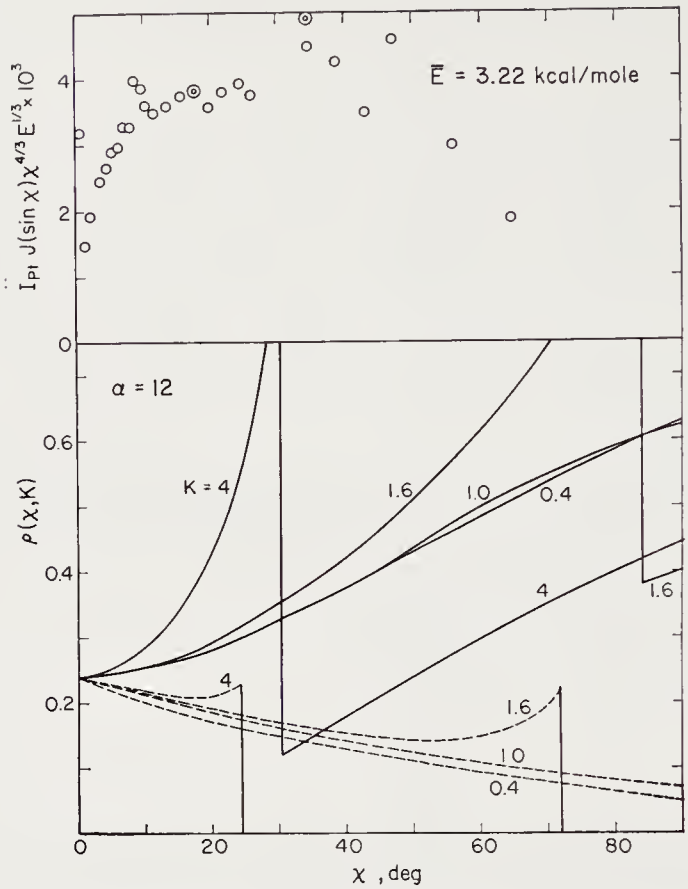

Fig. 24. The elastic scattering cross section plotted in the form of Eq. (11). (*A*) Experiments on K + CBr_4, in arbitrary units. (*B*) Solid lines: Eq. (11) calculated for the exp-six potential, $\alpha = 12$, reference 1b. Dashed lines: The contribution to Eq. (11), calculated for the exp-six potential, $\alpha = 12$, from only the outermost branch of the deflection function $\chi(\beta K)$ (reference 1a).

branch (dashed lines). The latter are terminated at the threshold distances chosen above.

Figure 24 also shows measurements on the elastic scattering of K + CBr_4 reduced to the experimental equivalent of Mason's function $\rho(\chi\bar{E})$. At small angles the measurements do not resemble any calculated curve, a result which is to be expected from the low resolution of the experimental arrangement. The flat portion of the experimental curve and the abrupt decrease show a similarity to the calculated dashed curves. A comparison of the preliminary measurements and the calculated curves at the point of vanishing elastic scattering leads to a

tentative estimate of the energy parameter ϵ for this system (see Table I).

The calculation of the total reaction cross section as a function of energy for this simple model is straightforward. From Eq. (9) we have $\sigma_R(E) = \pi r_m^2 \beta_{threshold}^2$, where $\beta_{threshold}$ is the maximum reduced impact parameter for which the reactants approach within the threshold

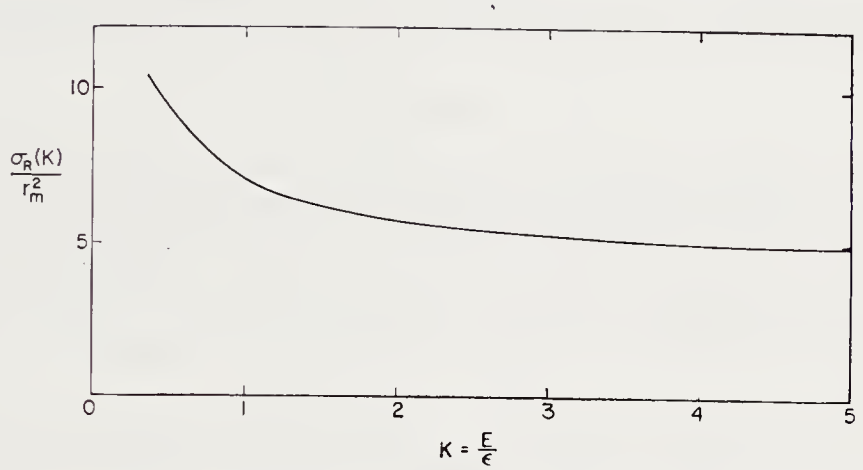

Fig. 25. Calculated energy dependence of the reduced total reaction cross section for K + CBr_4.

distance at the given K. The result is shown in Figure 25. If we guess the size parameter for this system to be about the sum of the C—Br distance in CBr_4 plus r_m for K + HBr (6.4 Å), the total reaction cross section is 236 Å^2 at $E = 2$ kcal/mole. This large value is in qualitative agreement with preliminary results of direct measurements of the product KBr in the reactive scattering for this system.*

VI. CONCLUSION

In this review we have tried to show how measurements of the elastic scattering of chemically reactive species may help to reveal what happens in a reactive collision. An interpretation of the measurements, based on a simple two-body model for the collision, leads to information about the parameters in the interaction potential, the threshold energies and distances, the variation of the probability of reaction with impact parameter (or the potential energy at closest approach), and the energy

* Private communications from D. R. Herschbach and from S. Datz.

dependence of the total reaction cross section. The results obtained so far for a few systems should be supplemented by further studies and should be tested by comparison with theoretical calculations and with measurements of reactive scattering.

Acknowledgments

We are grateful to Mr. K. Westberg and Mr. B. C. Eu for their help with the calculations.

APPENDIX

The potential parameters for the systems K + Kr, K + HCl, K + HBr, and K + HI have been reevaluated from the original data[5,6,13] by essentially the same procedure as given in reference 13. The main difference, and the reason for doing this work, is that the results provide a consistent calculation for all the systems, and these calculations are made with fewer approximations in the extensive numerical computations.

In the text, and in more detail in reference 13, we describe how the flux of K scattered elastically through a relative scattering angle χ is related to an effective differential scattering cross section $\sigma_{\text{eff}}(\chi\bar{E})$. This quantity is an average of the differential cross section $\sigma(\chi E)$ over the remaining distribution of velocities in the two beams and, with some approximations, may be shown to be

$$\sigma_{\text{eff}}(\chi\bar{E}) = 4\pi\left(\frac{m_2}{2\pi kT_2}\right)^{3/2}\frac{v_{10}}{c\bar{v}\mu^2}\int_E dE\sigma(\chi E)\sqrt{E}\,e^{-E/E_{20}} \times \int_{E_1} e^{E_1/E_{20}}\frac{\sqrt{E-E_1}}{E_1}\left[1-\frac{1}{\gamma'}\left|\sqrt{\frac{E_{10}}{E_1}}-1\right|\right]dE_1 \qquad \text{(A1)}$$

The average energy $\bar{E}$ is $\frac{1}{2}\mu[v_{10}^2 + \bar{v}_2^2]$, where μ is the reduced mass of the colliding system, v_{10} is the central K speed transmitted by the velocity selector, and $\bar{v}_2$ is the average speed of the hydrogen halide molecules, $(8kT_2/\pi M_2)^{1/2}$. The constants c and γ' are obtained from the geometry of the velocity selector and determine its transmission and resolution. The relative energy E is written $E_1 + E_2$ with $E_1 = \frac{1}{2}\mu v_1^2$ and $E_2 = \frac{1}{2}\mu v_2^2$, quantities which are proportional to the kinetic energies of the two beams. Similarly we define $E_{20} = \mu kT_2/m_2$ and $E_{10} = \frac{1}{2}\mu v_{10}^2$.

According to the semiclassical analysis of Ford and Wheeler,[2] the elastic scattering cross section in the rainbow region is

$$\sigma(\chi E) \sin \chi = |f_1|^2 \sin \chi + \lambda \beta_r r_m q^{-2/3} \mathrm{Ai}^2(x) \qquad \text{(A2)}$$

In this equation $|f_1|^2$ is the contribution from the positive portion of the deflection function (Fig. 2), λ is the de Broglie wavelength of the translational motion, β_r is the reduced impact parameter at the classical rainbow angle, and Ai is the Airy integral. The symbols q and x are defined by the relations $x = (\chi - \chi_r)q^{-1/3}$ and $q = \xi\lambda^2/4\pi r_m^2$, where χ_r is the rainbow angle and ξ the curvature of the deflection function at χ_r, $\chi - \chi_r = \xi(\beta - \beta_r)^2$.

For an assumed potential, like the exp-six potential Eq. (1) which we choose here, and any specified potential parameters the differential scattering cross section may be calculated from Eq. (A2). The first

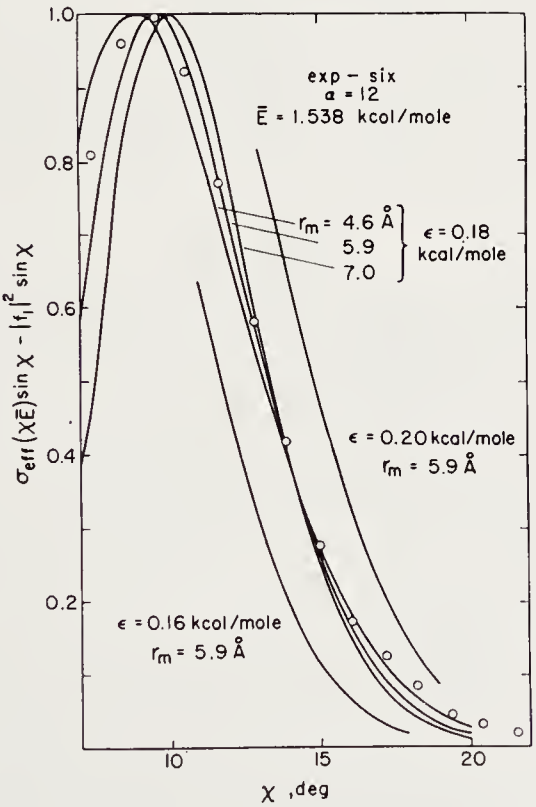

Fig. 26. Effective differential scattering cross section in the rainbow region for the system K + Kr at $\bar{E} = 1.538$ kcal/mole. The experimental points are compared with the solid curves which are calculated with the potential parameters indicated.

term in Eq. (A2) is obtained from the slope of the positive portion of the deflection function $\chi(\beta)$ previously evaluated by Mason[1] for this potential at various reduced energies $K = E/\epsilon$. Then the effective scattering cross section may be calculated from Eq. (A1). The first term $|f_1|^2 \sin \chi$ is a weak function of E and nearly independent of χ in the rainbow region. It is taken as constant in Eq. (A1). This procedure was followed for the systems cited above. A typical plot of $\sigma_{\text{eff}}(\chi\bar{E}) \sin \chi - |f_1|^2 \sin \chi$ is shown in Figure 26 for the system K + Kr for one average relative energy and various sets of potential parameters. Also shown on the graph in Figure 26 are the measurements for this system reduced to the quantity $\sigma_{\text{eff}}(\chi\bar{E}) \sin \chi - |f_1|^2 \sin \chi$. In making this reduction we multiply the experimental points by $[\sigma_{\text{eff}}(\chi\bar{E}) - |f_1|^2]/\sigma_{\text{eff}}(\chi\bar{E})$, which is obtained from Eqs. (A1) and (A2), and then normalize to the calculated curves at the maximum. This procedure is arbitrary, but fortunately $|f_1|^2$ is only about one-fifth of $\sigma(\chi E)$ at its maximum so the results are insensitive to the method used.

From a comparison of the measurements and the calculated curves the potential parameters may be ascertained. See Table I. It is clear that the depth of the potential well, ϵ, may be determined much more precisely than the size parameter, r_m.

References

1. E. A. Mason, (*a*) *J. Chem. Phys.*, **22**, 169 (1954); (*b*) *ibid.*, **26**, 667 (1957).
2. K. W. Ford and J. A. Wheeler, *Ann. Phys., N.Y.*, **7**, 259 (1959).
3. E. A. Mason and L. Monchick, *J. Chem. Phys.*, **41**, 2221 (1964). E. Hundhausen and H. Pauly, *Z. Naturforsch.*, **19a**, 810 (1964).
4. E. H. Taylor and S. Datz, *J. Chem. Phys.*, **23**, 1711 (1955); S. Datz, D. R. Herschbach, and E. H. Taylor, *J. Chem. Phys.*, **35**, 1549 (1961); K + HBr.
5. D. Beck, *J. Chem. Phys.*, **37**, 2884 (1962); K + HBr.
6. D. Beck, E. F. Greene, and J. Ross, *J. Chem. Phys.*, **37**, 2895 (1962); K + HBr.
7. D. R. Herschbach, G. H. Kwei, and J. A. Norris, *J. Chem. Phys.*, **34**, 1842 (1961); K + CH_3I.
8. E. Gersing, E. Hundhausen, and H. Pauly, *Z. Physik*, **171**, 349 (1963); K + $HgCl_2$, K + HgI_2, K + SnI_4.
9. R. Helbing and H. Pauly, *Z. Physik*, **179**, 16 (1964); K + Br_2, K + $HCBr_3$, K + CCl_4, K + HgI_2, K + SnI_4, K + CH_3CH_2I, K + $(CH_2Br)_2$.
10. M. Ackerman, E. F. Greene, A. L. Moursund, and J. Ross, *Ninth Symposium (International) on Combustion*, Academic Press, New York, 1963, p. 669; K + CH_3Br. A recalculation of the data is given in the Ph.D. thesis of A. L. Moursund, Brown University, 1964. There are no important changes in the results.
11. S. Datz and R. E. Minturn, *J. Chem. Phys.*, **41**, 1153 (1964); K + Br_2.

12. K. R. Wilson, G. H. Kwei, J. A. Norris, R. R. Herm, J. H. Birely, and D. R. Herschbach, *J. Chem. Phys.*, **41**, 1154 (1964); K + Br_2.
13. M. Ackerman, E. F. Greene, A. L. Moursund, and J. Ross, *J. Chem. Phys.*, **41**, 1183 (1964); K + HCl, K + HI.
14. S. Datz and E. H. Taylor, *J. Chem. Phys.*, **25**, 389, 395 (1956).
15. G. Gioumousis and D. P. Stevenson, *J. Chem. Phys.*, **29**, 294 (1958).
16. D. L. Bunker and N. Davidson, *J. Am. Chem. Soc.*, **80**, 5090 (1958).
17. S. K. Kim and J. Ross, *J. Chem. Phys.*, **42**, 263 (1965).

5. COLLISIONS OF ELECTRONICALLY EXCITED ATOMS AND MOLECULES

E. E. MUSCHLITZ, Jr.

Department of Chemistry, University of Florida, Gainesville, Florida

CONTENTS

I. Introduction 171
II. Production and Detection of Molecular Beams of Excited Species 172
A. Production 172
B. Detection 174
III. Lifetimes of Excited Species 176
IV. Elastic Collisions 179
A. Total Elastic Cross Sections 179
B. Differential Elastic Cross Sections 184
V. Inelastic Collisions 187
References 191

I. INTRODUCTION

Electronically excited atoms and molecules play an important role in many phenomena. Notable among these are flames, shocks, explosions, electrical discharges, photolysis, and radiolysis. Although the investigation of such phenomena has given some information regarding cross sections for collisions of excited species, the identity of the particles involved must often be inferred and in most cases more than one species is involved. Furthermore, it is virtually impossible to obtain potential functions for interactions between excited and ground-state particles from such experiments. Provided the lifetime of the excited particles is sufficiently long (of the order of a microsecond or greater), molecular beam scattering methods can be used to determine cross sections for both elastic and inelastic scattering of excited particles as well as the interaction potentials. In addition, the individual properties of excited species may be determined, such as polarizabilities, electric

and magnetic moments, and fine and hyperfine structure, by the use of molecular beams of the species concerned. The reader is referred to the general reference by Ramsey[1] and to other chapters of this volume for these applications of molecular beam techniques. Excited atoms or molecules with lifetimes greater than a microsecond are generally described as metastable, the transition to the ground state by the emission of electric dipole radiation being forbidden by one or more selection rules. In this chapter only scattering phenomena involving metastable electronically excited particles and the determination of their lifetimes will be discussed.

II. PRODUCTION AND DETECTION OF MOLECULAR BEAMS OF EXCITED SPECIES

A. Production

Table I lists a number of metastable atoms and molecules that have been produced in molecular beams. The second column of the table

TABLE I

Production of Beams of Excited Atoms and Molecules

Species	State	Method of production[a]	Energy above ground state (eV)
H	$2^2S_{1/2}$	EI,[2,3] CT[4]	10.20
He	2^3S_1	AD,[5] CCD,[6] EI[7,8]	19.82
He	2^1S_0	EI[7,8]	20.61
Li	$(1s2s2p)^4P_{5/2}$	EI[9]	56
N	^2D	RFD[10]	2.38
N	^2P	RFD[10]	3.58
O	^1D	RFD[11]	1.97
Ne	$^3P_{2,0}$	AD,[12] EI,[13] CCD[14]	16.62, 16.71
Ar	$^3P_{2,0}$	CCD,[14] EI[15]	11.55, 11.72
Hg	$^3P_{2,0}$	EI[16]	5.43, 4.64
Hg	$^3D_3$	EI[16,17]	9.05
H_2	$c^3\Pi_u$	EI[18]	11.86
N_2	$A^3\Sigma_u^+$	EI,[15] RFD[10]	6.16
N_2	$a^1\Pi_g$	EI[15]	8.54
O_2	$^1\Delta_g$	CCD,[19] RFD,[11,19]	0.98
CO	$a^3\Pi$	EI[15]	6.01

[a] EI, electron impact; CT, charge transfer; RFD, radio-frequency discharge; AD, low-voltage arc discharge; CCD, cold cathode discharge.

gives the spectroscopic term symbol of the excited state and the third shows the methods of production used. Beams of excited particles have been produced in two major ways: (*1*) by the use of a gaseous discharge and (*2*) by electron impact using a beam of controlled energy electrons.

In the first method, excited particles produced in the discharge are allowed to effuse through a small hole or narrow slit into the vacuum system, and a molecular beam collimated in the usual way by the use of a second hole or slit and differential pumping. A higher intensity of excited particles may be produced by this method; however, it is not very selective and several excited states may result, both molecular and atomic.

In the second method, an electron beam directed at right angles to the molecular beam is used. The electron beam may be located either directly in front or in back of the first collimating hole or slit. If the electron beam were to cross the fully collimated molecular beam, the collimation of the beam would be destroyed to some extent due to recoil of the excited particles. In the case of metastable $2^2S_{1/2}$ hydrogen atoms the angular distribution of the recoiling atoms was measured by Stebbings et al.[20] At electron energies just above threshold, more than two-thirds of the metastable atoms produced recoil at angles between 5 and 15°. Conservation of momentum shows that the recoil angle exhibits a maximum and a minimum value. This may be seen by reference to the Newton diagram in Figure 1. The initial and final

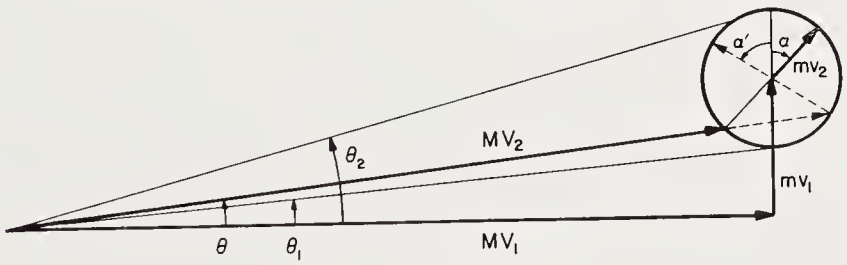

Fig. 1. Newton diagram.

momenta of the molecule are MV_1 and MV_2, respectively, and the vector labeled mv_1 represents the initial momentum of the electron. The inelastically scattered electron has momentum mv_2, a vector with a spherical locus represented by the circle on the diagram. The recoil angle therefore lies between the limits θ_1 and θ_2. Neynaber et al.[21] determined total cross sections for electron scattering from 2^3S helium

atoms by observing the loss in the atomic beam intensity due to recoil of the struck atoms.

An interesting and potentially very useful method was recently demonstrated.[4] A beam of fast positive ions when neutralized by charge-transfer collisions becomes a beam of fast neutral particles. This method was first used by Amdur and co-workers[22] for the production of such beams. Charge-transfer collisions have very large cross sections if the process is a resonant one or nearly so; that is, if very little internal energy must be converted to kinetic energy or vice versa. For the process,

$$H^+ + Cs \rightarrow H(2S) + Cs^+ \tag{1}$$

the energy defect is 0.49 eV in contrast to 9.71 eV for the corresponding process producing hydrogen atoms in the ground state. Therefore most of the charge-transfer collisions will result in the formation of excited hydrogen atoms. Donnally et al.[4] found cross sections of about 40×10^{-16} cm^2 for proton energies in the range of from 0.2 to 3 keV.

For most methods of production that have been used, the resulting beam will contain many particles in their ground states. In general, this is not a disadvantage since methods of detection may readily be employed which are sensitive only to the excited species.

B. Detection

Electronically excited atoms and molecules are capable of ejecting electrons from metal surfaces with fairly high efficiencies and this property has often been used for detection.[23] For the process to take place, the energy carried by the metastable species must exceed the work function of the metal. Surfaces of low work function such as those of the alkali metals have been used successfully for the detection of the $^3P_{2,0}$ states of mercury.[16]

The ejection efficiency for the secondary electrons has been measured in only a few cases. For 2^3S He atoms incident on a gas-covered gold surface, for example, Stebbings[5] found an efficiency of 0.29. Measurements have also been made on platinum,[12,23] molybdenum,[12] and tungsten.[12]

Hagstrum[24] and Varnerin[25] advanced the theory that a metastable atom would be converted to the positive ion at an appreciable distance from the surface. An ion so formed would then undergo an Auger

transition resulting in neutralization and the liberation of a free electron. Thus, the electron ejection efficiency would be the same for the metastable atom as for the ion. Fortunately, for most scattering experiments it is not necessary to know the absolute efficiency of the detector, since ratios of beam intensities are usually determined.

Detection of excited particles in a molecular beam is closely tied to the problem of their identification. In cases where several excited species are present it is often possible to employ a method sensitive to only one of them. A number of specific methods of detection have been used: (*1*) determination of the appearance potential of positive ions formed by electron impact, (*2*) deflection in an inhomogeneous electric or magnetic field, and (*3*) quenching in an electric field.

The first of these methods was used by Foner and Hudson for the identification of excited species formed in gaseous discharges. A molecular beam containing the excited particles is crossed by an electron beam of controlled energy and the positive ions produced are accelerated into a mass spectrometer. Ions produced by electron impact with excited species appear at an electron energy lower than the normal ionization potential by an amount equal to the excitation energy. They identified in this way $^1\Delta_g$ oxygen molecules,[19] $^3\Sigma_u^+$ nitrogen molecules,[10] and ^2D and ^2P metastable nitrogen atoms[10] arising from both radio-frequency and 60-cycle discharges in oxygen and nitrogen.

Deflection in an inhomogeneous magnetic field has been used to determine the relative proportion of 2^1S to 2^3S metastable helium atoms in an atomic beam.[26] McDermott and Lichten[17] employed the atomic beam magnetic resonance method to separate the $^3P_2$ and $^3D_3$ metastable states of mercury and were thereby able to obtain separate electron impact excitation functions for each state.

Lifetimes of metastable species are shortened in the presence of electric fields. Time-dependent perturbation theory shows[27] the lifetime to be inversely proportional to the square of the energy difference between the metastable state and the nearest radiating state. Thus, $2^2S_{1/2}$ hydrogen atoms are easily quenched by small electric fields, the nearest radiating state, $2^2P_{1/2}$, differing in energy by only the Lamb shift. Fite et al.[3] used quenching in an electric field coupled with an ultraviolet photon counter to detect $2^2S_{1/2}$ hydrogen atoms. On the other hand, it is extremely difficult in practice to quench 2^1S helium atoms in this way, the corresponding energy difference being about 0.6 eV in this case.

III. LIFETIMES OF EXCITED SPECIES

Lifetimes of excited species are affected not only by the presence of electric or magnetic fields but also by collisions with other atoms or molecules. The molecular beam method provides an excellent means for the determination of field-free space lifetimes. In fact, such measurements are truly measurements of monomolecular reaction rates in the absence of molecular collisions. It is only necessary to measure the decrease in the intensity of the beam as it passes through a good vacuum. Whether a particle decays by photon emission or dissociation, it and also the products for the most part are lost from the beam. A wide detector must be used which will intercept the penumbra of the beam at all points, and corrections must be made for scattering of the beam from the background gas. With beams from sources at room temperature, the practical limits for the measurement of lifetimes are 10^{-3}–10^{-6} second. These limits could possibly be extended by using low-temperature sources or by utilizing charge transfer as a method of production.

The measurement of lifetimes of excited species using a molecular beam was first attempted by Dunoyer[28] in 1924. It was not until the advent of modern high vacuum and electronics techniques, however, that the method was employed with much success. Muschlitz and Goodman[29] attempted to measure the lifetime of the $A^3\Sigma$ state of molecular nitrogen in this way. The beam used in these experiments contained significant numbers of $a^1\Pi$ molecules so that the measurements were applicable to this state rather than the A state. Lichten[15] repeated these measurements with an improved apparatus obtaining 1.7×10^{-4} sec for the $a^1\Pi$ state. A schematic diagram of his apparatus is shown in Figure 2. A molecular beam is collimated by slits S_1 and S_2. A cylindrical electron beam originating at the indirectly heated cathode, K, crosses the molecular beam in the field-free region in the open-sided box, F. After passage through slit S_3, the beam strikes the magnesium detector, D. Electrons emitted from D are collected on the grid, G. The detector assembly may be moved through a distance of 35 cm. By making measurements both as a function of detector distance and electron energy it was also possible to obtain a lower limit for the lifetime of the A state of 10^{-2} sec. Errors arising from systematic variations in the detector current with distance, such as attenuation of the beam by scattering in the background gas, were allowed for by making comparative measurements with long-lived metastable argon atoms.

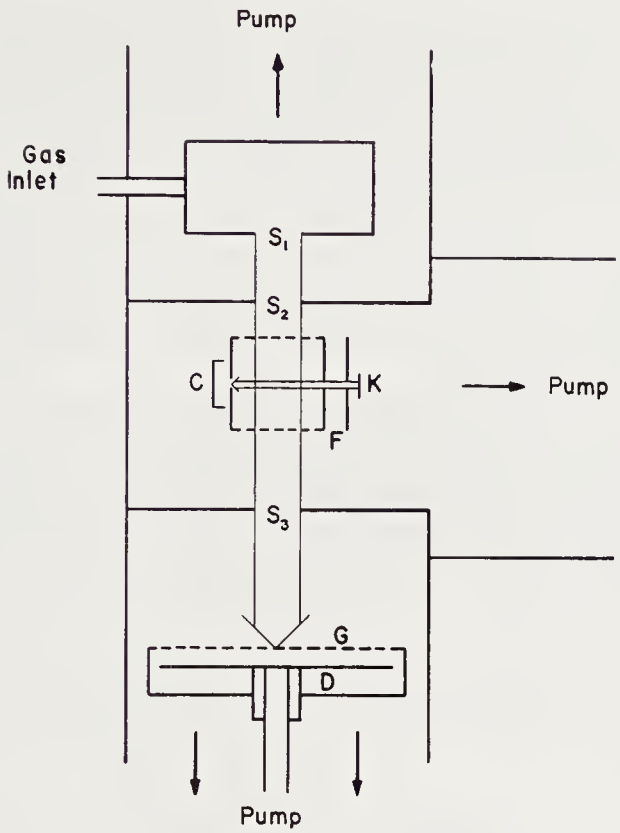

Fig. 2. Apparatus for the measurement of lifetimes.

A small contribution to the detector current arises from photoemission. In these experiments the effect was demonstrated to be less than 5%. It would seem that many of these difficulties might be avoided through the use of a velocity-selected beam in future work.

If a thermal source of molecules is used without velocity selection, the velocity distribution of the molecules in the beam should be taken into account.[15] The intensity of excited molecules of velocity in the range v to $v + dv$ remaining in the beam at a distance x from the point of excitation is

$$I_x(v)dv = I_0(v)dv \exp(-x/\tau v) \tag{2}$$

where τ is the mean lifetime* and $I_0(v)dv$ the corresponding intensity at the point of excitation. The latter quantity is given by the usual Maxwell-Boltzmann distribution:

$$I_0(v)dv = 4\pi I_0(m/2\pi KT)^{3/2}v^2 \exp(-mv^2/2KT)dv \tag{3}$$

* The mean lifetime is related to the half-life by the relation: $\tau_{1/2} = \tau \ln 2$.

The reason for this is that, although the effusion process contributes a factor of v to the normal distribution, the probability that a molecule will be excited by electron impact is proportional to v^{-1}. The beam intensity at x is then obtained by integration of Eq. (2) making use of Eq. (3) for the velocity distribution:

$$I_x = 4\pi I_0 (m/2\pi KT)^{3/2} \int_0^\infty v^2 \exp(-mv^2/2KT - x/\tau v) dv \qquad (4)$$

An analysis of the problem is difficult when a discharge source of excited molecules is used.

Lifetimes of excited species have also been determined by various optical methods,[30-33] but unless such experiments apply or can be extrapolated to sufficiently low pressures, the free-space lifetime is not obtained. Several of these methods are applicable to the determination of much shorter lifetimes than can be measured in beam experiments.

TABLE II

Lifetimes of Excited Atoms and Molecules

Species	Lifetime, seconds		
	Experiment	Calculated	Mechanism
$H(2s)^2S_{1/2}$	$>2.4 \times 10^{-3}$ (3)	0.12 (35)	Double photon emission
$He(1s2s)^3S$	—	$\gg 1$ (27)	Double photon emission
$He(1s2s)^1S$	—	>1 (27)	Double photon emission
$Li(1s2s2p)^4P_{5/2}$	5.1×10^{-6} (9)	1.6×10^{-5} (36)	Autoionization
$N_2\ A^3\Sigma_u^+$	$>10^{-2}$ (15)	—	Electric dipole radiation
$N_2\ a^1\Pi_g$	1.7×10^{-4} (15)	—	Magnetic dipole radiation

Table II gives a summary of recent lifetime measurements as determined by the molecular beam method. The lifetimes of the very long-lived atomic species, for which all types of single photon emission are forbidden, are limited by the probability of the double photon emission process. If magnetic dipole or electric quadrupole radiation is allowed,

the lifetimes are generally shorter. Spin-orbit interaction brings about a violation of the selection rule $\Delta S = 0$ for electric dipole radiation in the case of the $A^3\Sigma_u^+ \rightarrow X^1\Sigma_g^+$ transition in nitrogen.

It should be noted that, in general, the lifetime of an electronically excited molecule depends on the cube of the frequency of the light emitted and hence on the specific vibrational and rotational levels of both the upper and lower states.[30] A discussion of forbidden transitions in both atomic and molecular systems may be found in the review article by Garstang.[34]

IV. ELASTIC COLLISIONS

A. Total Elastic Cross Sections

Collisions between molecules may be classified as elastic or inelastic depending on whether or not the internal energy of one or both of the colliding molecules is altered. If it is not, the collision is elastic; otherwise, it is inelastic. The differential elastic cross section, $I(\varphi)$, is defined as the intensity of particles elastically scattered within the solid angle, $d\omega$, from a beam of unit intensity incident on a single scatterer. The total elastic cross section, Q, is then:

$$Q = \int\int I(\varphi)\, d\omega = 2\pi \int_0^{\pi} I(\varphi) \sin \varphi\, d\varphi \tag{5}$$

Classically, this integral is infinite since $I(\varphi) \rightarrow \infty$ as $\varphi \rightarrow 0$. However, quantum mechanics gives a finite result. For the measurement of total cross sections, the resolution of the apparatus is important, and for thermal energy collisions, it is generally necessary to distinguish scattered molecules at angles as small as a few minutes.[37]

In an experiment the decrease in intensity of a well-collimated beam is determined after passage through a scattering chamber containing gas at a low pressure. At pressures sufficiently low that single collisions predominate,

$$I = I_0 \exp(-NlS) \tag{6}$$

where S is the total absorption cross section; I_0, the initial beam intensity; and I, the beam intensity after passage a distance l through a gas in which the particle density is N. The absorption cross section, S, differs from Q for two reasons. First, there may be inelastic scattering, but in most cases the inelastic scattering cross sections are relatively

small. Second, the collision cross section, Q, refers to target molecules initially at rest. If the average velocity of the scattering gas atoms could be neglected compared to that of the beam atoms, the two cross sections would be the same. The relation between them depends upon the temperatures of the beam source and scattering gas and on the masses of the colliding particles.[38,39]

The first total cross sections for the scattering of excited atoms were reported by Dorrestein and Smit,[40] who used beams of metastable helium atoms. However, the resolution of their apparatus was very poor. Subsequently, Stebbings[5] and Hasted and Mahadevan[12] obtained cross sections at an angular resolution of one degree for the scattering of metastable helium and neon atoms in the rare gases. They used an arc discharge as a source of excited atoms. In a helium discharge, the 2^1S metastable atoms are rapidly destroyed by collisions with slow electrons,[41] so that these experiments pertain to the 2^3S state. Their results are summarized in Table III. Collision cross sections, Q, have

TABLE III

Measurements of Total Cross Sections

System		Stebbings[5]		Hasted and Mahadevan[12]	
Beam	Target	S (Å^2)	Q (Å^2)	S (Å^2)	Q (Å^2)
He*	He	149	111	145	108
He*	Ne	118	107	127	115
He*	Ar	210	197	200	188
He*	Kr	417	406	—	—
Ne*	He	—	—	205	95
Ne*	Ne	—	—	153	115
Ne*	Ar	—	—	277	234

been calculated from their data using the procedure given in reference 38. The collision cross sections increase with increase in the atomic number of the target atom with the possible exception of the symmetrical case He*–He. The cross sections include excitation transfer, which is a resonance process in this case. Still, the total cross section is unusually large, for a recent measurement of the excitation transfer cross section at 300°K gives 4 Å^2.[42] The apparent anomaly for Ne*–He is removed

when the absorption cross sections are converted to collision cross sections.

Recently, Rothe has extended his measurements on the velocity dependence of total cross sections to the scattering of 2^3S_1 helium atoms in the rare gases.[43] The measurements were made at an angular resolution of two minutes with the apparatus shown in Figure 3.

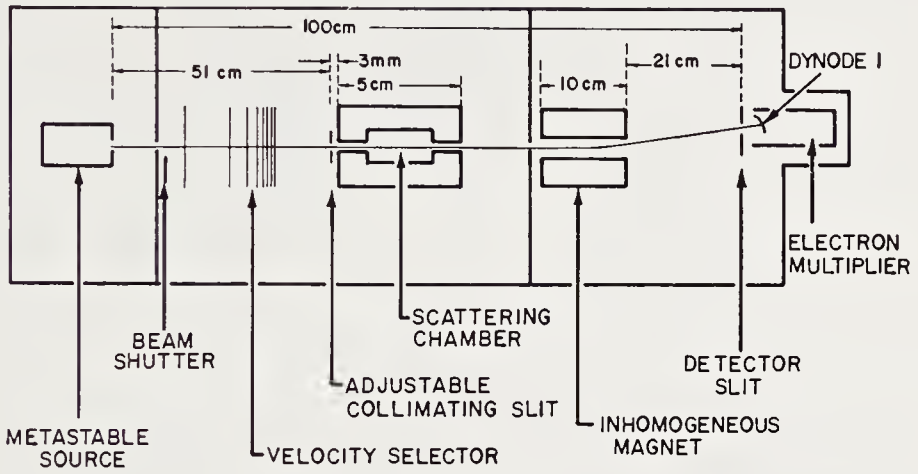

Fig. 3. Apparatus for the measurement of the velocity dependence of the total cross section.

Helium atoms are excited by a DC arc discharge in the source. After collimation, the beam is velocity selected by a slotted disk selector and then passes through the scattering chamber. The unscattered beam is analyzed by an inhomogeneous field magnet and is finally detected on the first dynode of an electron multiplier. Measurements made using the magnet demonstrated that few singlet metastable atoms were present in the beam (the beam intensity was reduced to nearly one-third of its original value when the magnetic field was turned on) and that the cross section for the scattering of 2^3S_1 helium in a given gas is independent of the magnetic sublevel of the triplet state within the experimental error of $\pm 10\%$. The results for the scattering cross sections as a function of relative velocity for the target gases helium and krypton are shown in Figures 4 and 5. Previous results[44] for the scattering of Li in the same gases are shown for comparison. It is seen that the behavior is similar but that the cross sections for the scattering of the metastable atoms are uniformly higher. This is expected because of the

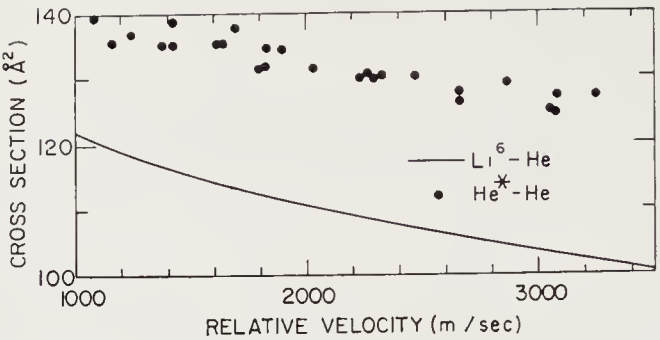

Fig. 4. Scattering of 2^3S, helium in helium, Q vs. relative velocity.

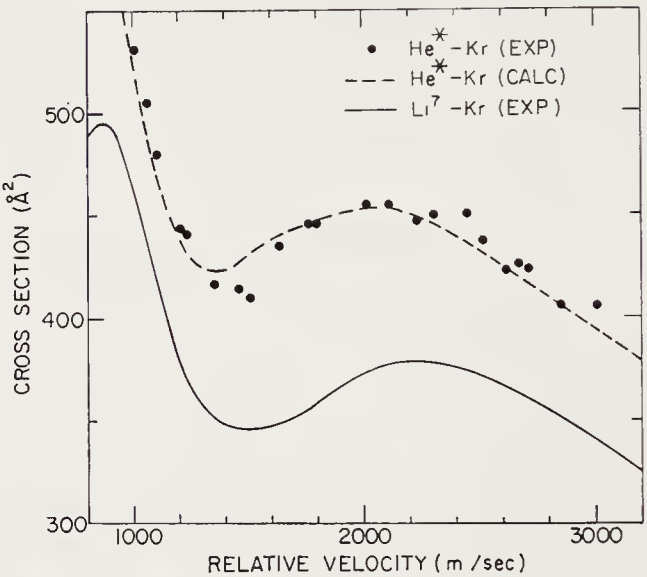

Fig. 5. Scattering of 2^3S, helium in krypton, Q vs. relative velocity.

similarity in structure of the beam particles. Furthermore, the results are consistent with a polarizability of He* [45] higher than Li.[46]

Elastic scattering of thermal energy particles where no chemical interaction exists has generally been interpreted in terms of the Lennard-Jones potential[47]:

$$V(r) = 4\epsilon[(\sigma/r)^{12} - (\sigma/r)^6], \tag{7}$$

in which ϵ is the depth of the potential well and σ, the interatomic separation at $V(r) = 0$. Undulations appear in the cross section vs. velocity curves when both attractive and repulsive branches of the potential influence the scattering angle. When the scattering is determined

primarily by the repulsive branch ("the high velocity region"), the cross section decreases monotonically with increasing velocity, hence the difference in behavior in Figures 4 and 5. The scattering of 2^3S_1 helium in argon also shows undulations. The number of maxima observed in these curves gives a lower limit to the number of diatom bound states (vibrational levels).[47] Table IV summarizes the results.

TABLE IV

Interaction Potential Parameters

System	Minimum number of bound states	ϵ (erg)	σ (Å)
2^3S_1 He–Ar	1	7.7×10^{-15}	4.52
2^3S_1 He–Kr	2[a]	1.2×10^{-14}	4.47

[a] It is very likely that a second maximum exists.

The values of ϵ and σ given are those which give the best fit to the experimental data.[48] The dotted line in Figure 5 is the predicted behavior assuming Eq. (7) for the interaction potential with these values for the potential parameters.

The interaction potential for the system He*–He was first calculated by Buckingham and Dalgarno.[49] Their results are shown in Figure 6 for both singlet and triplet interactions. A deep chemical well exists at about $2a_0$ in both ungerade interactions corresponding to the existence of $^1\Sigma_u$ and $^3\Sigma_u$ excited molecules. The curves are unusual in that a hump exists at larger distances ($\sim 4a_0$). The height of the barrier was calculated by these authors to be 0.29 eV for the triplet interaction and 0.26 eV for the singlet. The magnitude of the van der Waals interaction was underestimated, however, and more recent calculations[50] for the triplet interaction give 0.139 eV at $4.5a_0$ for the height and location of the barrier. Thus, the region within the barrier is classically inaccessible to particles colliding with thermal energies. The long-range repulsion due to the barrier is much softer than the r^{-12} Lennard-Jones repulsion. If a potential well exists due to the van der Waals attraction, it is likely to be quite shallow and occur at an interatomic distance greater than $10a_0$. The experimental results shown in Figure 4 indicate that the scattering is primarily governed by a repulsive interaction. Further work is indicated here over a wider range of relative velocities.

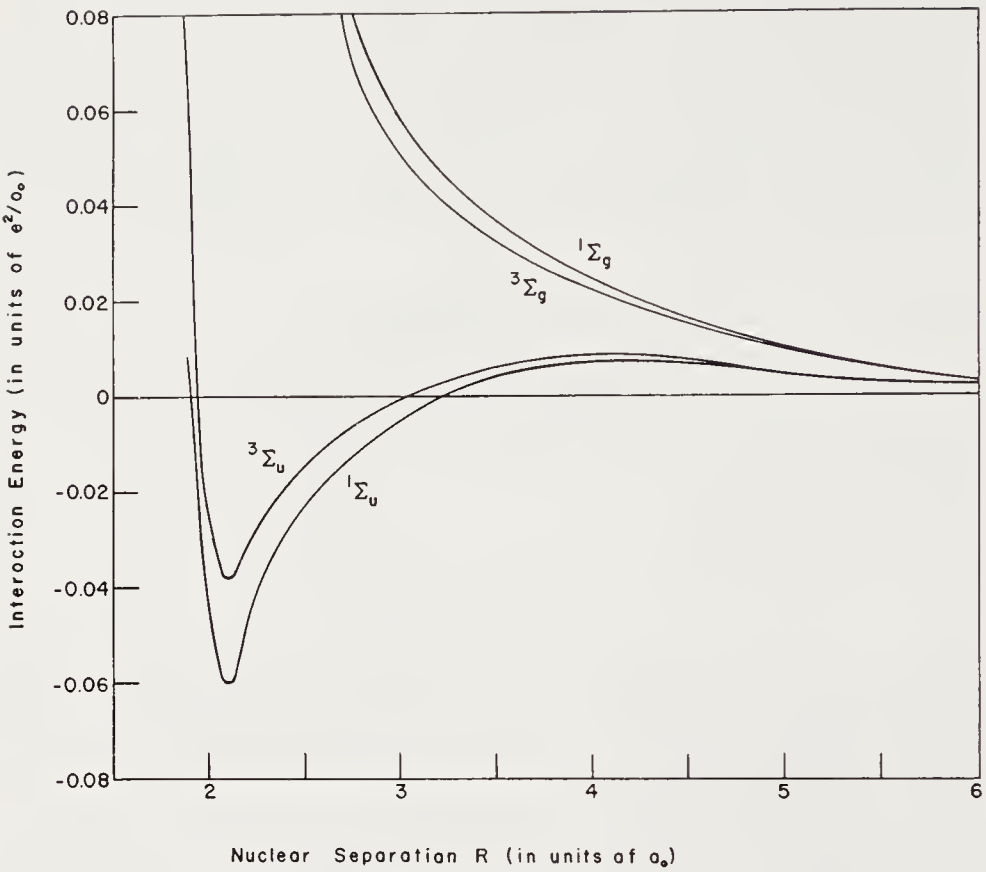

Fig. 6. Calculated interaction potentials for the metastable helium–normal helium interactions.

B. Differential Elastic Cross Sections

Precise measurements of the angular scattering of excited atoms have yet to be made. But, by making measurements of the total cross section as a function of apparatus resolution, approximate values of the angular scattering coefficients have been obtained by Richards.[26] Furthermore, by using electron impact as a means of excitation, beams containing known proportions of the two metastable states of helium were produced. The apparatus used for these measurements is shown in Figure 7. Helium is introduced into the source region at pressures of 20–100 microns. The electron beam is located directly behind the first collimating hole, H_1. Thus, some of the helium atoms effusing through this hole into the forechamber will have been excited by electron impact.

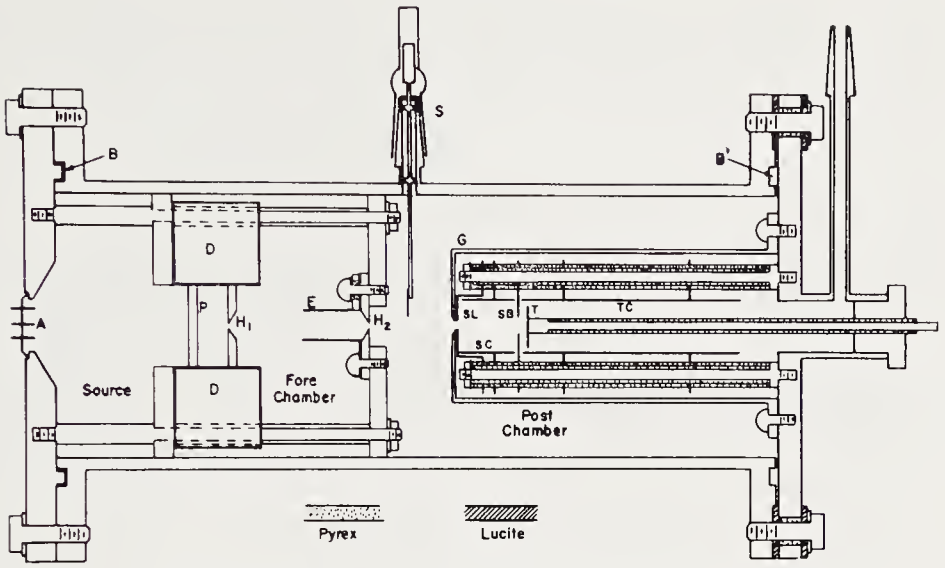

Fig. 7. Apparatus for the determination of elastic and inelastic cross sections.

The collimated beam entering the postchamber through H_2 is 0.5 mm in diameter. It then enters the scattering chamber through a hole in the cylindrical can, G, which separates the scattering region from the postchamber. For the determinations of beam composition as a function of electron energy, the postchamber was lengthened, and an inhomogeneous field magnet inserted between H_2 and G.

With the arrangement of electrodes shown, both the scattered and unscattered portions of the beam may be measured, the latter being the current measured at T. The resolution is altered by changing the diameter of the hole in the plate, SB. Increasing the scattering gas pressure to 150 μ reduces the signal at T to less than 2% of its original value. Photons should still be observed, since their absorption cross section is two orders of magnitude less than that for the excited atoms. Thus, the contribution of photons to the signal may be neglected under the conditions of these experiments.

Measurements of the scattering of He* were made as a function of scattering gas pressure in the range 0–30 μ at three different electron energies. The measurements were then repeated at different angular resolutions. Knowing the beam composition as a function of electron energy, it is possible to calculate from these measurements the cross sections for scattering of both 2^3S_1 and 2^1S_0 helium atoms.[26]

The results for the scattering of metastable helium atoms in helium

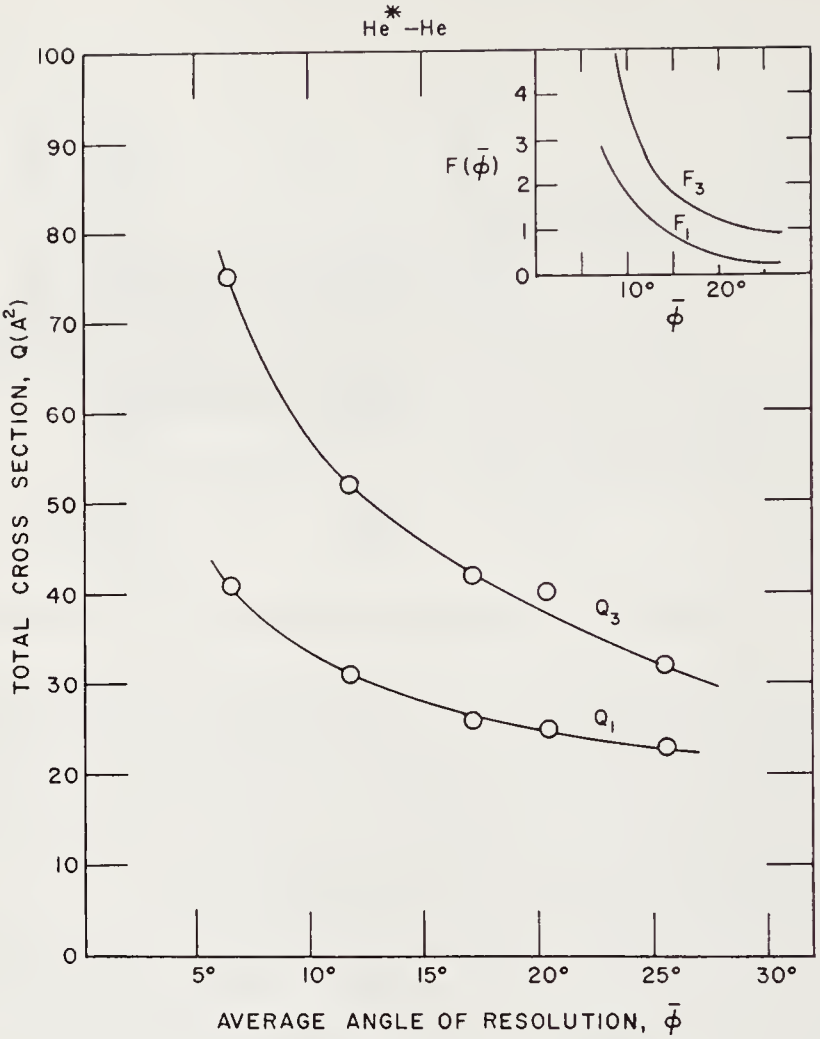

Fig. 8. Scattering of 2^3S_1 and 2^1S_0 helium in helium.

are shown in Figure 8, where Q_3 and Q_1, the total scattering cross sections for triplet and singlet scattering, respectively, have been plotted against the limiting angle of resolution averaged over the scattering path length. The polar angular scattering coefficient,

$$F(\bar{\varphi}) = 2\pi I(\bar{\varphi}) \sin \bar{\varphi} = dQ/d\bar{\varphi} \tag{8}$$

as a function of the average angle of resolution is shown in the upper right-hand corner of the figure.

Larger cross sections are observed for the scattering of the triplet atoms. This is consistent with the calculated interaction potentials

shown in Figure 6. The scattering is influenced equally by the gerade and ungerade interactions, so that the observed cross sections may be considered as a first approximation to be averages of the cross sections for the separate potentials[51]:

$$Q(\text{obs}) = Q(\Sigma_g)/2 + Q(\Sigma_u)/2 \dagger \tag{9}$$

Over the accessible range of the gerade interactions for thermal energy collisions, no appreciable difference exists, while over the range of the ungerade interactions, the triplet interaction is higher, particularly if the maxima were both lower as the more recent calculations indicate.[50] The larger interaction would then give rise to a larger cross section for the scattering of the triplet atoms.

V. INELASTIC COLLISIONS

Several types of inelastic collisions between a metastable excited atom or molecule and another particle may be distinguished:

$$A^* + XY \rightarrow A + XY \tag{10}$$

$$A^* + XY \rightarrow A + XY^* \tag{11}$$

$$A^* + XY \rightarrow AXY^+ + e \tag{12}$$

$$A^* + XY \rightarrow A + XY^+ + e \tag{13}$$

$$A^* + XY \rightarrow A + X^+ + Y + e \tag{14}$$

$$A^* + XY \rightarrow AX^+ + Y + e \tag{15}$$

Eq. (10) represents the conversion of the excitation energy to kinetic energy of separation of the products. Such collisions at thermal energies generally have a low probability, since a crossing point of the potential energy curves must be reached which usually occurs only at close distances of approach corresponding to high intermolecular potential energy. The remaining equations involve a transfer or rearrangement of the internal energy. Eq. (11) is a simple energy transfer, Eqs. (12) and (15) involve the formation of new bonds, and Eqs. (13) and (14) are examples of Penning ionization[52] where the struck molecule is ionized. Reactions producing ions are emphasized here, since ionized

† This equation does not allow for effects arising from interference of particle-waves scattered by the two potentials [F. T. Smith and R. P. Marchi, *Bull. Am. Phys. Soc.*, 9, 709 (1964)].

products are more readily detected and identified. Thus, Eqs. (14) and (15) could be written:

$$A^* + XY \rightarrow A + X + Y \tag{14}$$

$$A^* + XY \rightarrow AX + Y \tag{15}$$

and undoubtedly such reactions also take place. All of these reactions may be considered as proceeding through the formation of a transition species, AXY*.

The process shown in Eq. (12) was first investigated by Hornbeck and Molnar,[53] who showed that the diatomic rare-gas ions are produced in this way. For this process to take place in a thermal energy collision it is necessary that the energy required to ionize A* be less than the dissociation energy of AXY^+ into $A^+ + XY$. Appearance potential measurements demonstrated that the excited atoms were in highly excited states (about 1 eV below the ionization potential) rather than the metastable states. This seems to be true in most cases[54,55]; however, Herman and Čermák have shown the metastable states to be involved in reactions of excited rare-gas atoms with alkali atoms.[56]

Sholette and Muschlitz[57] have measured cross sections for the Penning ionization process, Eqs. (14) and (15), using the apparatus shown in Figure 7. The total beam intensity and the positive ion current drawn to the electrode, *SL*, were separately measured. The cross sections for ionization could then be calculated from the measured scattering pressures, the scattering path length, and the electron ejection efficiency of the metastable atoms. It was assumed that the ions were collected with 100% efficiency. The results of these experiments are summarized in Table V. Metastable helium atoms were used in all cases and separate cross sections determined for both 2^1S_0 and 2^3S_1 states by studying the inelastic scattering as the beam composition was varied in the manner described previously for the elastic cross-section measurements. The measurements of Benton et al.[58] are shown for comparison. They used a time-resolved optical absorption technique to follow the density of helium metastable atoms with time following a pulsed helium discharge. When small amounts of a second gas are introduced, the effective lifetime of the metastable atoms is reduced because of the ionizing collisions.

The beam and optical experiments are in good agreement for the triplet metastable helium collisions, but not for the singlet. Benton et al. remark that their cross sections for the singlet collisions may be

TABLE V

Penning Ionization Cross Sections

Metastable atom	Gas	ΔE (eV)	S (Å^2)	
			SM[57]	BFMR[58]
He(2^3S)	Ar($^1S_0$)	−4.06	8	6.6
He(2^1S)		−4.85	8	55
He(2^3S)	Kr($^1S_0$)	−5.82	9	10.3
He(2^1S)		−6.61	9	64
He(2^3S)	Xe($^1S_0$)	−7.69	12	13.9
He(2^1S)		−8.48	12	103
He(2^3S)	$H_2(^1\Sigma_g^+)$	−4.40	3	6.0
He(2^1S)		−5.19	2	—
He(2^3S)	$O_2(^3\Sigma_g^-)$	−7.6	14	—
He(2^1S)		−8.4	14	—
He(2^3S)	$N_2(^1\Sigma_g^+)$	−4.24	7	6.4
He(2^1S)		−5.03	7	—
He(2^3S)	CO($^1\Sigma^+$)	−5.81	7	—
He(2^1S)		−6.60	7	—

high by a factor of 2 or 3, but their conclusion that a large difference exists between the singlet and triplet cross sections for ionization of a given gas still remains, a conclusion that is hard to understand on theoretical grounds. Ferguson[59] has calculated cross sections for Penning ionization using a simple classical momentum transfer model. The results are in order-of-magnitude agreement with experiment.

In the above experiments, the ions formed were not identified. More recently, Weiss and Muschlitz[60] and Čermák[61] have used a mass spectrometer for this purpose. The rare-gas atoms are excited by electron impact. The excited atoms produced are roughly collimated and enter a collision chamber into which the gas under investigation is introduced. Ions and electrons originating in the excitation region are prevented from entering the collision chamber by appropriate retarding and deflecting fields. Ions produced in the collision chamber are drawn out and accelerated into the analyzing region of the mass spectrometer. Weiss' results for oxygen are shown in the last column of Table VI. In the next to the last column the photoionization cross sections for 20-eV photons[62] are shown for comparison. These cross sections

TABLE VI

Ionization of O_2 on Impact with Metastable He Atoms and with Photons

Products	Energy required, eV	S(20 eV $h\nu$), cm$^2 \times 10^{18}$	S(He*), cm$^2 \times 10^{16}$
$O_2^+(^2\Pi_g) + e$	12.2	25	10.5
$O^+(^4S) + O(^3P) + e$	18.69	1.3	3.5
$O^+(^4S) + O^-(^2P)$	17.25		
$O^+(^2D) + O^-(^2P)$	20.57		

do not vary appreciably near 20 eV. For photoionization, the cross sections are two orders of magnitude smaller and the relative abundance of O^+ much less. The same amount of energy is transferred in the metastable atom collision, since the excited atom must return to the ground state. However, the process is not a simple energy transfer. The probability of reaction depends upon the nature of the $(HeO_2)^*$ complex. The ions HeO^+ and HeO_2^+ are not observed in these experiments. Evidently the complex is not readily stabilized by the loss of an electron. A generalized mechanism for these processes may be written as follows:

$$\begin{array}{c} A^* + XY \rightarrow (AXY)^* \rightarrow AXY^+ + e \\ \qquad\quad \swarrow \quad \searrow \\ (AX)^* + Y \quad A + (XY)^* \rightarrow XY^+ + e \\ \qquad\quad\quad\quad \swarrow \quad \searrow \\ \qquad\quad\quad X + Y \quad X^+ + Y + e \end{array} \tag{16}$$

The excited molecule (AX)* may also decay in the same fashion as shown for (XY)*. The ion products have also been identified in collisions of metastable rare-gas atoms with a number of simple hydrocarbons.[60,61] In general, all fragment ions whose formation is energetically possible are observed.

Beck and Osberghaus[63] have identified the neutral fragments resulting from the monomolecular decay of excited hydrocarbon molecules. The molecules are excited by electron impact and a molecular beam is roughly collimated. The fragment species in the beam are identified by ionization using a second electron beam followed by mass analysis. It is found that radical production occurs very seldom; the excited molecule decays preferentially into two stable molecules.[63,64]

Acknowledgments

The author is indebted to the National Science Foundation and the American Chemical Society Petroleum Research Fund for financial support of his research on metastable atom collisions. This chapter was written while the author held a National Science Foundation Senior Post Doctoral Fellowship.

References

1. N. F. Ramsey, *Molecular Beams*, Oxford Univ. Press, London, 1956.
2. W. E. Lamb, Jr. and R. C. Retherford, *Phys. Rev.*, **79**, 549 (1950).
3. W. L. Fite, R. T. Brackmann, D. G. Hummer, and R. F. Stebbings, *Phys. Rev.*, **116**, 363 (1959).
4. B. L. Donnally, T. Clapp, W. Sawyer, and M. Schultz, *Phys. Rev. Letters*, **12**, 502 (1964).
5. R. F. Stebbings, *Proc. Roy. Soc.* (*London*), **A241**, 270 (1957).
6. V. Hughes, G. Tucker, E. Rhoderick, and G. Weinreich, *Phys. Rev.*, **91**, 828 (1953).
7. G. J. Schulz and R. E. Fox, *Phys. Rev.*, **106**, 1179 (1957).
8. G. M. Smith and E. E. Muschlitz, Jr., *J. Chem. Phys.*, **33**, 1819 (1960).
9. P. Feldman and R. Novick, *Phys. Rev. Letters*, **11**, 278 (1963). Excitation functions and lifetimes of autoionizing states of potassium and rubidium are also given.
10. S. N. Foner and R. L. Hudson, *J. Chem. Phys.*, **37**, 1662 (1962).
11. W. L. Fite and R. T. Brackmann, *Proc. Intern. Conf. Ionization Phenomena Gases, 6th, Paris, 1963*, General Atomic Tech. Report, GA-4313.
12. J. B. Hasted and P. Mahadevan, *Proc. Roy. Soc.* (*London*), **A249**, 42 (1958).
13. G. M. Grosof, P. Buck, W. Lichten, and I. I. Rabi, *Phys. Rev. Letters*, **1**, 214 (1958).
14. A. Lurio, G. Weinreich, C. W. Drake, V. W. Hughes, and J. A. White, *Phys. Rev.*, **120**, 153 (1960).
15. W. Lichten, *J. Chem. Phys.*, **26**, 306 (1957). Appearance potential data are also given for the ^3P states of krypton and xenon.
16. W. Lichten, *Phys. Rev.*, **109**, 1191 (1958).
17. M. N. McDermott and W. L. Lichten, *Phys. Rev.*, **119**, 134 (1960).
18. W. Lichten, *Phys. Rev.*, **120**, 848 (1960).
19. S. N. Foner and R. L. Hudson, *J. Chem. Phys.*, **25**, 601 (1956).
20. R. F. Stebbings, W. L. Fite, D. G. Hummer, and R. T. Brackmann, *Phys. Rev.*, **119**, 1939 (1960).
21. R. H. Neynaber, S. M. Trujillo, L. L. Marino, and E. W. Rothe in *Atomic Collision Processes*, M. R. C. McDowell, ed., North-Holland Publishing Co., Amsterdam, 1964, p. 1089.
22. I. Amdur and A. L. Harkness, *J. Chem. Phys.*, **22**, 664 (1954).
23. R. Dorrestein, *Physica*, **9**, 433, 447 (1942).
24. H. D. Hagstrum, *Phys. Rev.*, **91**, 543 (1953).
25. L. J. Varnerin, Jr., *Phys. Rev.*, **91**, 859 (1953).
26. H. L. Richards and E. E. Muschlitz, Jr., *J. Chem. Phys.*, **41**, 559 (1964).
27. G. Breit and E. Teller, *Astrophys. J.*, **91**, 215 (1940).

28. L. Dunoyer, *Compt. Rend.*, **178**, 1475 (1924).
29. E. E. Muschlitz, Jr. and L. Goodman, *J. Chem. Phys.*, **21**, 2213 (1953).
30. N. P. Carleton and O. Oldenburg, *J. Chem. Phys.*, **36**, 3460 (1962).
31. P. G. Wilkinson and R. S. Mulliken, *J. Chem. Phys.*, **31**, 674 (1959).
32. A. Lurio and R. Novick, *Phys. Rev.*, **134**, A608 (1964).
33. A. V. Phelps and J. P. Molnar, *Phys. Rev.*, **89**, 1202 (1953).
34. R. H. Garstang, in D. R. Bates, ed., *Atomic and Molecular Processes*, Academic Press, New York, 1962, Chap. 1.
35. J. Shapiro and G. Breit, *Phys. Rev.*, **113**, 179 (1959).
36. J. Pietenpol, *Phys. Rev. Letters*, **7**, 64 (1961).
37. P. Kusch, *J. Chem. Phys.*, **40**, 1 (1964).
38. H. S. W. Massey and E. H. S. Burhop, *Electronic and Ionic Impact Phenomena*, Oxford University Press, London, 1952, pp. 390, 391.
39. H. Pauly, *Z. Naturforsch.*, **15a**, 277 (1960).
40. R. Dorrestein and J. H. Smit, *Koninkl. Ned. Akad. Wetenschap. Proc.*, **41**, 725 (1938).
41. A. V. Phelps, *Phys. Rev.*, **93**, 652 (1954).
42. F. D. Colegrove, L. D. Schearer, and G. K. Walters, *Phys. Rev.*, **135**, A353 (1964).
43. E. W. Rothe, R. H. Neynaber, and S. M. Trujillo, *J. Chem. Phys.*, **42**, 3310 (1965).
44. P. K. Rol and E. W. Rothe, *Phys. Rev. Letters*, **9**, 494 (1962). E. W. Rothe, P. K. Rol, R. H. Neynaber, and S. M. Trujillo, in M. R. C. McDowell, Ed., *Atomic Collision Processes*, North-Holland Publishing Co., Amsterdam, 1964, p. 927.
45. A. Dalgarno and A. E. Kingston, *Proc. Phys. Soc.* (*London*), **72**, 1053 (1958).
46. G. E. Chamberlain and J. C. Zorn, *Phys. Rev.*, **129**, 677 (1963).
47. R. B. Bernstein, *J. Chem. Phys.*, **37**, 1880 (1962); E. W. Rothe, P. K. Rol, and R. B. Bernstein, *Phys. Rev.*, **130**, 2333 (1963).
48. R. Düren and H. Pauly, *Z. Physik*, **177**, 146 (1964).
49. R. A. Buckingham and A. Dalgarno, *Proc. Roy. Soc.* (*London*), **A213**, 327 (1952).
50. R. D. Poshusta and F. A. Matsen, *J. Chem. Phys.*, **32**, 307 (1963). The height of the maximum is erroneously given in the text. The authors' Table III yields 0.139 eV.
51. E. A Mason and J. T. Vanderslice, *Phys. Rev.*, **108**, 293 (1957).
52. A. A. Kruithoff and F. M. Penning, *Physica*, **4**, 430 (1937).
53. J. Hornbeck and J. P. Molnar, *Phys. Rev.*, **84**, 621 (1951).
54. M. S. B. Munson, F. H. Field, and J. L. Franklin, *J. Chem. Phys.*, **37**, 1790 (1962).
55. W. Kaul and R. Taubert, *Z. Naturforsch.*, **17a**, 88 (1962).
56. Z. Herman and V. Čermák, *Nature*, **199**, 588 (1963).
57. W. P. Sholette and E. E. Muschlitz, Jr., *J. Chem. Phys.*, **36**, 3368 (1962).
58. E. E. Benton, E. E. Ferguson, F. A. Matsen, and W. W. Robertson, *Phys. Rev.*, **128**, 210 (1962).
59. E. E. Ferguson, *Phys. Rev.*, **128**, 210 (1962).
60. E. E. Muschlitz, Jr. and M. J. Weiss, in M. R. C. McDowell, Ed., *Atomic Collision Processes*, North-Holland Publishing Co., Amsterdam, 1964, p. 1073.

61. V. Čermák and Z. Herman, *Collection Czechoslov. Chem. Commun.*, **29**, 953 (1964); **30**, 169 (1965).
62. N. Wainfan, W. C. Walker, and G. L. Weissler, *Phys. Rev.*, **99**, 542 (1955). G. L. Weissler, J. A. R. Samson, M. Ogawa, and G. R. Cook, *J. Opt. Soc. Am.*, **49**, 338 (1959).
63. D. Beck and O. Osberghaus, *Z. Physik*, **160**, 406 (1960).
64. D. Beck and A. Niehaus, *J. Chem. Phys.*, **37**, 2705 (1962).

6. CHARGE TRANSFER

R. F. STEBBINGS

General Atomic Division of General Dynamics Corporation, San Diego, California

CONTENTS

I. Introduction 195
II. Charge Transfer 197
A. The Near-Adiabatic Hypothesis 197
B. The Collision Cross Section 198
C. Classification of Collisions 199
III. Experimental Methods for Measurement of Charge Transfer Cross Sections 200
A. Slow Particle Detection 200
1. The Condenser Method 200
2. Mass Analysis of the Target Ions 202
B. Fast Particle Detection 206
1. Analysis of Particles After Gas Traversal 207
2. Beam Attenuation in a Transverse Field 209
C. Measurement of Angular and Energy Distribution 212
1. Observations of Incident or Recoil Particles 212
2. Coincidence Detection of Scattered Particles 215
IV. Study of Chemically Unstable Gases 218
A. Crossed Beam Techniques 218
B. Collision Chamber Techniques 222
V. The Influence of Excited Particles upon Charge Transfer 225
A. Metastable Ions in the Primary Beam 225
B. Excited Products of Charge Transfer 228
VI. Theoretical Considerations 234
A. High Velocity Region 234
B. Low Velocity Region 239
C. Energy Resonance 240
References 243

I. INTRODUCTION

Within recent years the experimental and theoretical study of atomic collision processes has been stimulated by the rapid growth of interest

in the physics and chemistry of ionized gases. The ionosphere, aurorae, and the solar corona are but a few of the more familiar, naturally occurring phenomena of interest, while controlled thermonuclear devices, gas discharges, shock waves, and flames provide plasmas which are subject to direct laboratory investigation.

The microscopic understanding of these and related phenomena is frequently hindered through lack of knowledge of the cross sections for the individual atomic processes which together give rise to the observed effects.

One class of reaction which is of particular interest and significance in this context is that involving the transfer of an electron between an ion and a neutral particle; a process variously referred to as charge transfer, charge exchange, electron transfer, or electron capture.

An enormous number of experimental and theoretical investigations of charge transfer processes have been carried out and a number of excellent reviews on the subject are available. Attention is particularly drawn to the work of Massey and Burhop[1] for the development of this field up to the early 1950's; more recent data and techniques are contained in articles by Allison,[2] Allison and Garcia-Munoz,[3] Hasted,[4,5] and McDaniel.[6] The present state of the theory of charge transfer collisions—its achievements and limitations—is summarized in papers by Bates,[7] Bates and McCarroll,[8] and Rapp and Francis.[9]

It is not the intent of this article to provide a balanced review in which areas of greatest experimental or theoretical activity are considered in greatest detail. On the contrary, quite disproportionate emphasis is given to certain areas which, though relatively unexplored, provide data of a new or unusual kind. Within this category fall measurements which shed light upon the state of excitation of the interacting particles. Inasmuch as two ions of the same species, but in different excited states, may, in collision with another particle, show greater dissimilarities than are shown by two ions of quite different species, it is clear that comparison of the results of two experiments is not meaningful unless the reacting particles are identical in all respects. It seems probable that the future course of experiments will in large measure devolve upon the identification and evaluation of the effects of excited particles.

Measurements in which the target particles are chemically unstable are also discussed in some detail. The hydrogen atom measurements are of particular value for the development of the theory of atomic

collisions, for the better understanding of certain phenomena pertaining to the upper atmosphere and interplanetary space, and for the design of thermonuclear devices. The oxygen atom measurements are pertinent to upper air studies.

The study of violent collisions, in which charge transfer is accompanied by appreciable momentum transfer, provides new insight into the understanding of collisions between heavy particles. Rather fragmentary data of this kind are in hand at present and this will doubtless be an active and fruitful area for future research.

In compensation for the special emphasis on these topics, the discussion of the appreciably more numerous measurements derived from more conventional techniques is far from complete and the reader is referred to the review articles mentioned earlier for further details.

II. CHARGE TRANSFER

It is convenient to distinguish between symmetric resonance charge transfer between like atoms

$$X^+ + X \rightarrow X + X^+ \tag{1}$$

and asymmetric charge transfer between unlike systems

$$X^+ + Y \rightarrow X + Y^+ + \Delta E \tag{2}$$

The quantity ΔE is called the energy defect and is the energy change in the electronic transition. When all particles are in their respective ground states, ΔE is simply the difference in the ionization potentials of particles X and Y. The term asymmetric or accidental resonance is given to those reactions between unlike systems in which by chance the energy defect is small or zero.

The energy dependence of the cross section for a particular charge-transfer reaction depends very markedly upon the magnitude of the energy defect and may be discussed in terms of Massey's near-adiabatic hypothesis.[1]

A. The Near-Adiabatic Hypothesis

Under gas kinetic conditions, the cross section for a collision in which an electronic transition occurs will be small unless ΔE is also small. This is because the gradual nature of the collision allows the atomic electrons time to adjust to the slowly changing conditions. The characteristic time of the collision may be written as a/v, where a is the range of interaction of the atoms and v is the relative velocity. The

time involved in the electronic transition is $h/\Delta E$. The condition for a transition to be unlikely may then be written as the inequality

$$\frac{a\Delta E}{hv} \gg 1 \tag{3}$$

which defines the adiabatic region. Within this region the cross section varies as

$$K \exp[-a|\Delta E|/4hv] \tag{4}$$

where K is a constant which depends upon the reaction.

As the velocity rises out of the adiabatic region the cross section reaches a rather flat maximum when $a\Delta E/hv$ is of order unity; the velocity of relative motion is then comparable with the velocity of the atomic electrons concerned in the transition. At higher velocities the cross section falls at a rate determined by the nature of the process, being most rapid for charge-transfer collisions.

It should be recognized that this hypothesis is of use principally for predicting the general behavior of a particular cross section; no indication of the magnitude of the cross section is provided. Exceptions to this qualitative description are not uncommon because ΔE is actually a function of the separation of the colliding particles and should be chosen at the separation at which the transition occurs or is most probable. However, few data are available for interaction energies as a function of the internuclear separation and it has been customary to use ΔE_∞, the value of ΔE at infinite separation. Additional complication in the assignment of the value for ΔE may occur because one or more of the interacting particles may be in an unknown excited state.

When ΔE is small or zero because of accidental resonance, the maximum cross section will occur at very low energy.

In symmetric resonance charge transfer between atomic particles, the cross section increases monotonically as the incident energy decreases, and at thermal energy usually attains a value considerably greater than gas kinetic values, which are of the order of 5×10^{-16} cm^2. The low-energy behavior of resonance charge transfer of molecular ions is less certain, but the cross sections probably do not vanish in the limit of vanishing energy.

B. The Collision Cross Section

Experimental investigation of charge-transfer processes is frequently carried out by passing a beam of energetic ions X^+ through a chamber

containing thermal target gas atoms Y. When simple charge transfer occurs, as in reaction (2), negligible momentum is customarily exchanged and the reaction products are thermal Y^+ ions and energetic neutral particles X, whose trajectories are essentially collinear with those of the primary ions.

The experimental quantity under investigation in such measurements is usually the charge-transfer cross section σ which may be written as ${}_{10}\sigma_{01}$, where the integers denote respectively the charge states of the incident particle, the target, the scattered incident particle, and the recoil. The cross section is defined by

$$dS = I\sigma n dx \tag{5}$$

where dS is a signal characteristic of process (2), I is the primary ion current, n the neutral particle density, and dx the path length over which the signal dS is generated. It is apparent that a collision may be observed in a number of ways as the signals available for observation are (*1*) the attenuation of the primary ion beam, (*2*) the production of slow positive ions, and (*3*) the production of fast neutral atoms, and cross section data have been obtained in each of these ways.

The reduction in the Y atom number density is also a potentially observable quantity, although no measurements of this kind have been recorded.

C. Classification of Collisions

Each of these approaches is subject to certain limitations and ambiguities which stem from the fact that charge transfer, ${}_{10}\sigma_{01}$, is but one of several inelastic collision processes which may occur in energetic ion-atom collisions. The generalized form of equation (2) is

$$X^+ + Y \rightarrow X^{m+} + Y^{n+} + (m + n - 1)e \tag{6}$$

for which the cross section may be written ${}_{10}\sigma_{mn}$ and which includes simple charge transfer ${}_{10}\sigma_{01}$, transfer ionization terms ${}_{10}\sigma_{0n}$ for $n > 1$, ionization terms ${}_{10}\sigma_{1n}$ for $n \geq 1$, and stripping terms ${}_{10}\sigma_{m0} m > 1$. The process whose cross section is given by ${}_{10}\sigma_{mn}$ will be designated as $10/mn$. In the typical case no signal arises uniquely from simple charge transfer and some data analysis is required to derive ${}_{10}\sigma_{01}$. When either of the colliding particles is molecular, the additional possibility of collisional breakup must be considered.

For complete knowledge of an inelastic collision it is necessary to

know the energy, direction of travel, state of excitation, and ionization of all the interacting particles before and after the collision, together with details on the photon emission. Experimental data are available for all these quantities singly and in certain combinations, but in no measurements have all quantities been simultaneously determined.

III. EXPERIMENTAL METHODS FOR MEASUREMENT OF CHARGE TRANSFER CROSS SECTIONS

It is convenient to classify the experimental methods into those in which slow ions are detected and those in which fast ions and neutrals provide the detectable signal.

A. Slow Particle Detection

1. *The Condenser Method*

In this method, as it is customarily applied, a beam of mass-analyzed ions is directed through a collision chamber containing the target gas at sufficiently low pressure that the attenuation of the primary beam is small. The currents of positive and negative charges generated over a well-defined path length are measured.

The method was conceived many years ago by Goldman[10] and has since been used in a large number of investigations. The charge separation is frequently carried out by means of an electric field transverse to the primary beam, and a typical electrode structure is shown in Figure 1. The electric field is maintained between the slow-charge collecting plates S and is made uniform with the aid of guard plates G, which

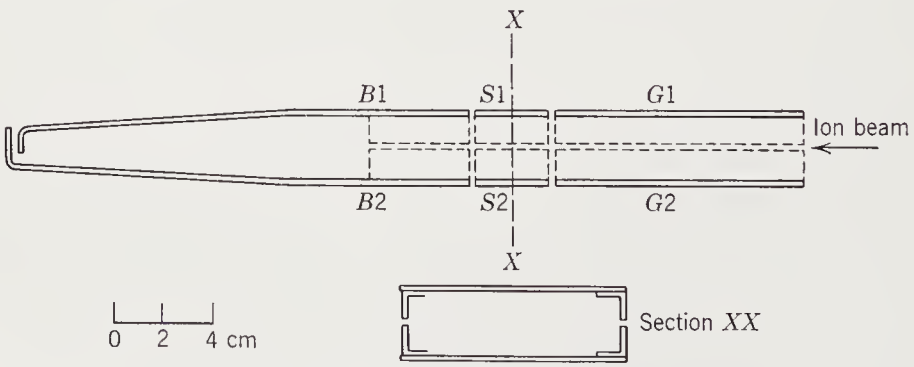

Fig. 1. Electrode structure used by Gilbody et al.[12] for the measurement of total apparent charge transfer cross sections.

are extensions of the main beam-collecting plates *B*. Secondary emission from the negative collecting plate may be suppressed by a negative grid or by a magnetic field parallel to the ion beam axis.

The experimental difficulties of the method arise from effects at the electrode surfaces and from the necessity of ensuring that all the ions and electrons formed over a known path length of gas are collected.

Measurement of the net total charge generated over a definite path length yields the cross section

$$\sigma = -\sum_{mn} (m-1)\,{}_{10}\sigma_{mn} \tag{7}$$

the apparent total charge transfer cross section, which at sufficiently low energies becomes ${}_{10}\sigma_{01}$. Measurement of the total electron current alone provides the cross section

$$\sigma_e = \sum_{mn} (m+n-1)\,{}_{10}\sigma_{mn} \tag{8}$$

which at sufficiently low energies tends to ${}_{10}\sigma_{11}$.

At energies up to a few keV, this procedure has been widely used for the investigation of charge transfer and ionization. At higher energies, where multiply charged ions are formed in appreciable quantity, mass analysis of the slow ions is necessary to provide the fine details of the collision process.

Nonetheless, the condenser method still finds application at higher energies as a check on the calibration of the mass spectrometer and as a means of measuring the apparent total charge transfer cross section. Particular care must be exercised in the design and operation of the charge collection system because the ions and electrons may be formed with appreciable kinetic energy. The normal procedure is to increase the collection field until further increase produces no change in the collected current (saturation conditions). Fields as large as 100 V/cm are not uncommon, since at ion energies of tens of keV, electrons may be produced with energies up to several hundred electron volts.

Extensive use of this experimental technique has been made by Hasted, Gilbody, and collaborators,[11,12] who have correlated the experimental data for a large number of collision processes with the aid of Massey's adiabatic hypothesis. Some typical data are shown in Figure 2.

Variations of the condenser method have been used in a number of experiments. Low-energy scattering of D^+ and rare-gas ions has been

studied by Cramer and co-workers,[13,14] while Utterback and Miller[15] examined N_2^+–N_2 collisions. Donahue and Hushfar,[16] Bailey,[17] and Moe[18] have also made use of this technique.

2. *Mass Analysis of the Target Ions*

When the mass spectrum of the slow ions is required, they are customarily extracted from the collision region by a weak electric field and accelerated prior to mass analysis. From measurements of the currents of the various secondary ion species as a function of the collision chamber pressure it is possible to determine the cross sections for production of ions with different charge/mass ratios. In general, the measured cross sections are not unique to a particular process but are the aggregates of those for several processes. Thus the cross section for production of n times ionized target particles includes $10/1n$ (positive ion ionization), $10/0n$ (transfer ionization), which for $n = 1$ is simple charge transfer, and $10/mn$ (combinations of stripping and ionization).

Measurements of this kind have been made by Fedorenko, Afrosimov, and Kaminker,[19] who determined not only the charge/mass ratios of the secondary ions but also their angular distribution.

When the target particle is molecular, charge transfer may lead to the appearance of both molecular and atomic ions. The identification

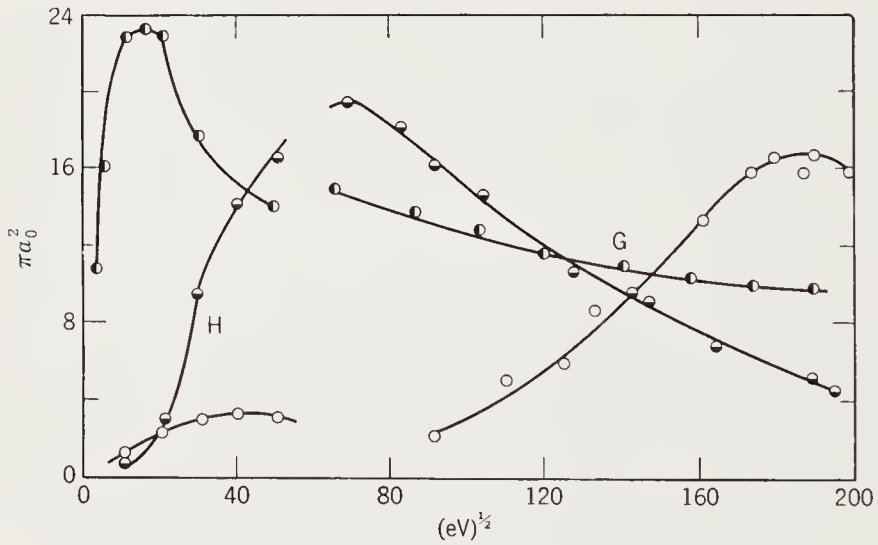

Fig. 2. Charge transfer cross sections, Hasted (H), Gilbody (G); ○ C^+ in Ar, ◒ H^+ in N_2, ◐ Ar^+ in H_2. The cross sections in units of πa_0^2 are plotted against the square roots of the ion energies.

of these ions requires mass analysis, and the most extensive measurements of this nature have been carried out by Lindholm and his associates,[20] who used the apparatus shown in Figure 3. The primary ions

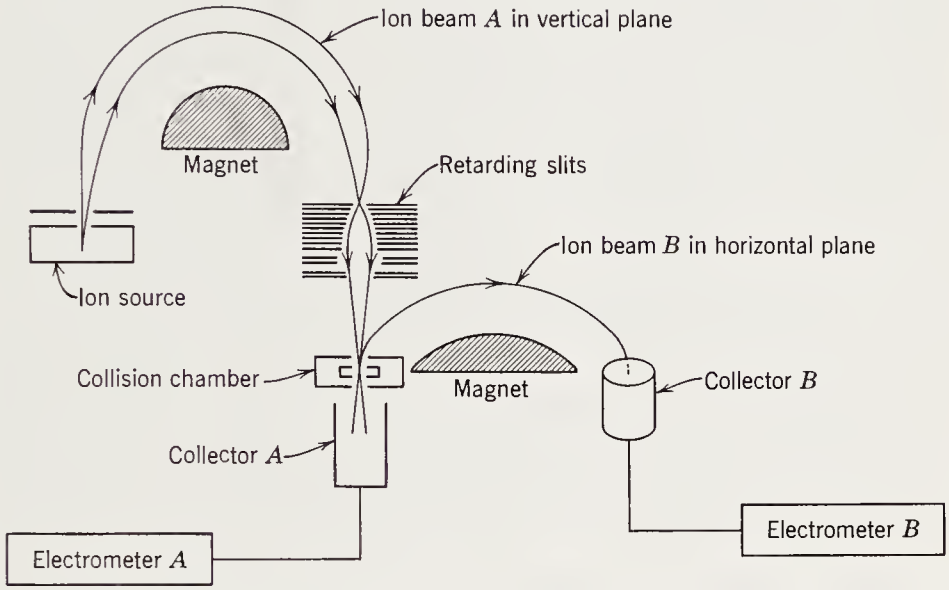

Fig. 3. Experimental arrangement of Lindholm et al.[20] for mass analysis of slow ions resulting from charge transfer.

were produced in an ion source of the Heil type and accelerated to 2000 eV for analysis in a 180° permanent magnet A. They were then retarded in a 12-element electrostatic lens system to the desired collision energy. After passing through the collision chamber, the primary ions (A) were collected in a Faraday cup and measured with a vibrating reed electrometer. The ionized fragments (B), obtained from the gas molecules, were extracted from the collision chamber by means of a weak electrostatic field, accelerated, and then analyzed in a second mass spectrometer. The cross section for charge transfer may then be expressed as

$$\sigma = K(B/A) \tag{9}$$

where A and B are the intensities of the primary and secondary currents, respectively, and K is a constant.

In order to check and calibrate the apparatus, the collisions of He^+, Ne^+, Ar^+, and Kr^+ ions in their parent gases were investigated, and using absolute measurements of other workers, the constant K was

determined. It was observed that the value of K was invariant for these processes, and the cross sections for a large number of charge-transfer reactions involving dissociation were subsequently determined on the (incorrect) assumption that all measurements with different fragments were characterized by the same K value.

Measurements of dissociative charge transfer have also been reported by Stebbings, Smith, and Ehrhardt,[21] who used the apparatus shown in Figure 14. A detailed description of this apparatus is given in Section IV-A, and it is sufficient, for the present, to say that the atomic and molecular ions resulting from charge transfer in He^+–N_2 and He^+–O_2 collisions were analyzed in a 180° magnetic mass spectrometer. The molecular ions which were formed with little kinetic energy were collected with high efficiency; the atomic ions, on the other hand, resulted from the dissociation of excited molecular ions and could, in consequence, possess several electron volts of kinetic energy. The central problem in these measurements was, therefore, the determination of the collection efficiency for the energetic atomic ions relative to that for the molecular ions. Once this ratio was determined, the mass-

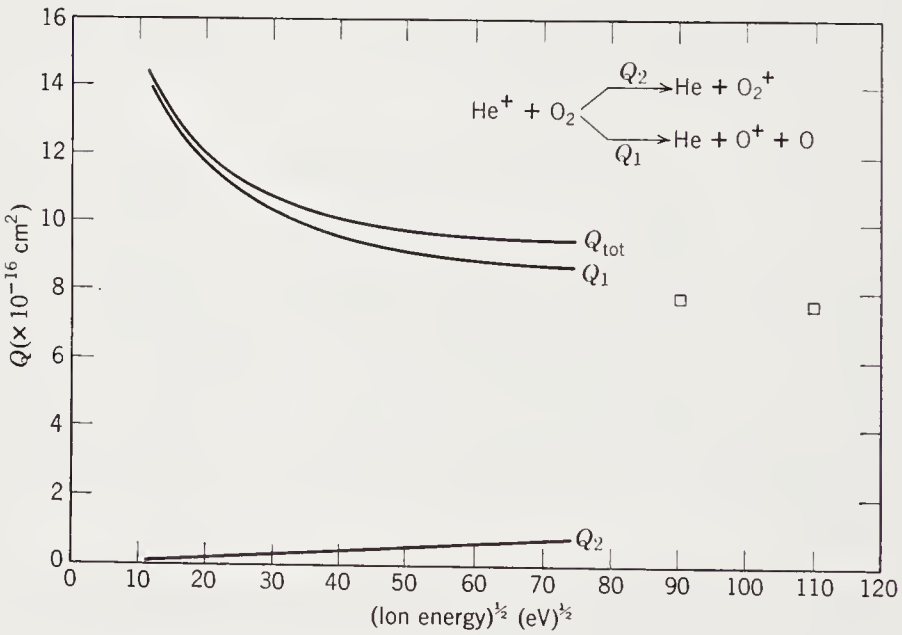

Fig. 4. Measurements by Stebbings, Smith, and Ehrhardt[21] for charge transfer between He^+ and O_2. Q_{tot} is the cross section for total slow ion production; Q_1 and Q_2 are the cross sections for production of O^+ and O_2^+ ions. Also shown (□) are values obtained by Stier and Barnett[28] for total charge transfer.

analyzed ion signals were appropriately weighted and the total charge transfer cross section, which was determined in a second measurement, correctly apportioned between the two competing processes.

The results are shown in Figure 4 and it is seen that by far the greatest contribution to the total He^+–O_2 cross section comes from collisions involving dissociation. The energy dependence of this process indicates that it is one of accidental resonance. It would appear that the $c^4\Sigma_u^-$ state of O_2^+ recently identified by LeBlanc,[23] which lies at 24.56 eV above the ground state of O_2, is the immediate product of the reaction, with dissociation then occurring to produce the observed O^+ ions.

$$He^+(^2S) + O_2(X^3\Sigma) \rightarrow He(^1S) + O_2^+(c^4\Sigma_u^-) + 0.02eV \qquad (10)$$

The experimental data for He^+–N_2 collisions are shown in Figure 5 and are seen to be rather similar to the oxygen data except that the resonance would now seem to be less exact. It seems likely that the N_2^+ ion is formed in the $(c^2\Sigma_u^+)$ state, followed by predissociation giving

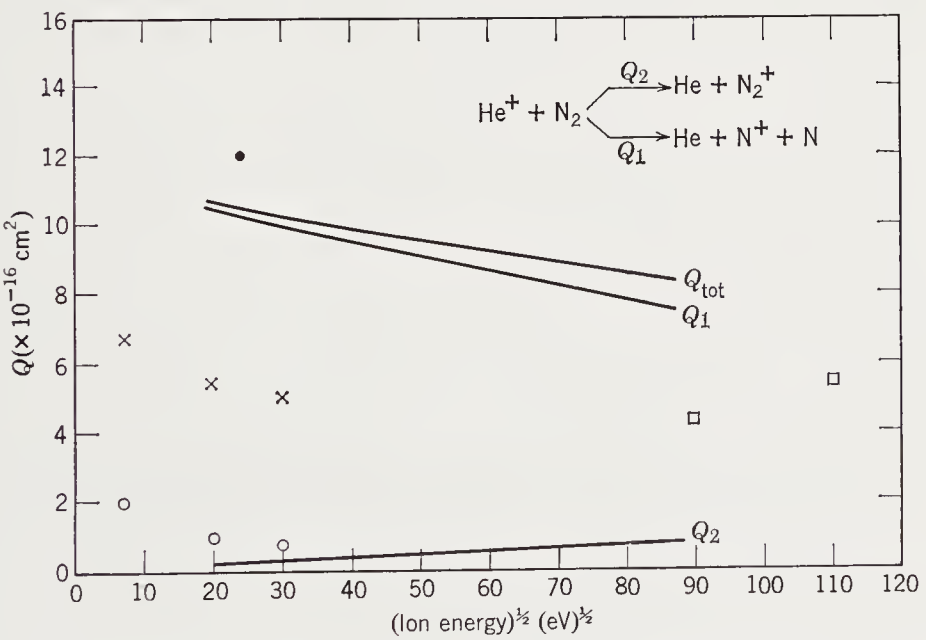

Fig. 5. Measurements by Stebbings, Smith, and Ehrhardt[21] for charge transfer between He^+ and N_2. Q_{tot} is the cross section for total slow ion production; Q_1 and Q_2 are the cross sections for production of N^+ and N_2^+ ions. Also shown are values for N^+ ion production by Lindholm[20] (●), Wolf[22] (×), and Gustafsson and Lindholm[20] (○). Total charge transfer values obtained by Stier and Barnett[28] (□) are also shown.

$N(^4S)$ and $N^+(^3P)$. The rather large discrepancies between the various values reported for this process illustrate the difficulties in obtaining absolute cross sections in ion–neutral collisions using mass spectrometric detection of the slow products. It is of interest to note that the efficiency of detection of the slow molecular ions was about 20 times greater than that for the more energetic atomic ions.

Giese and Maier[24] have studied dissociation of CO by impact of He^+, Ne^+, and Ar^+ ions at low energy. Hasted, Lee, and Hussain[25] have reported measurements of electron capture by doubly charged rare-gas ions (excluding helium) in their own gas, in which the singly charged target ions were mass analyzed.

There is a clear requirement for more measurements of this kind. The experimental difficulties are less at high primary ion energies when strong fields may be applied at the interaction region without perturbing the motion of the primary ions. Under the influence of sufficiently strong fields, all secondary ions, regardless of their initial kinetic energy, may be collected with uniform efficiency. At low ion energy the techniques of Giese and Maier may find general application.

B. Fast Particle Detection

The experimental studies of charge transfer employing fast particle detection have employed a variety of techniques which provide different types of data. An excellent review of this work is given by Allison and Garcia-Munoz.[3] The experimental methods may be conveniently grouped into three general categories.

In the first of these a monoenergetic beam of ions X^+ is passed through a chamber containing the target gas Y, and charge-changing collisions occur, resulting in a fast particle beam containing all the possible charge states which X can assume together with neutral X atoms. This beam enters a region of high vacuum where transverse fields are used to separate the beam into its various charged components. From measurements of the currents of ions in various charge states, relationships between the cross sections for the electron capture and loss processes are determined.

In the second method a transverse magnetic or electric field is applied throughout the chamber in which the charge-changing collisions occur, so that spatial separation of the various charged components of the beam occurs immediately upon their production. The detector is positioned to collect those particles which suffer no charge-changing

collisions and the measurement is one of attenuation of the primary beam.

In a small fraction of collisions, charge transfer is accompanied by appreciable momentum transfer. Experimental investigation of these so-called "violent" collisions proceeds through measurement of the angular distribution of the scattered products.

1. *Analysis of Particles after Gas Traversal*

a. Equilibrium Beam Method. Many of the experiments in which the fast particle beam is analyzed after collision have been modeled on the equilibrium beam method. In the simple case when only two charge states of the incident particle are possible, the ratio of the charged to neutral components in a beam passing through a gas is determined by the relative magnitudes of the cross sections for electron capture σ_{10} and electron loss σ_{01}. A shortened notation is used here where only the initial and final charge states of the projectile are indicated. The final charge states of the target particle are neither known nor susceptible to measurement in this arrangement. If the fractions of fast particles in the singly charged and neutral states are designated as F_1 and F_0, respectively, then the change of the fast-particle fraction with distance through the gas of number density, n, is given by

$$dF_1/dx = n(\sigma_{01}F_0 - \sigma_{10}F_1) \qquad \text{where } F_0 + F_1 = 1. \tag{11}$$

If the target is sufficiently thick, $dF_1/dx \to 0$ and the beam achieves equilibrium fractions given by

$$F_{1\infty} = \frac{\sigma_{01}}{\sigma_{01} + \sigma_{10}} \qquad F_{0\infty} = \frac{\sigma_{10}}{\sigma_{10} + \sigma_{01}} \tag{12}$$

The cross sections themselves are evaluated from measurements of F_1 and F_0 as a function of gas thickness using the equations

$$\sigma_{01} = \frac{F_{1\infty}}{nx} \ln\left[\frac{1 - F_{1\infty}}{F_{1(nx)} - F_{1\infty}}\right] \tag{13}$$

$$\sigma_{10} = \frac{F_{0\infty}}{nx} \ln\left[\frac{1 - F_{1\infty}}{F_{1(nx)} - F_{1\infty}}\right] \tag{14}$$

where $F_{1(nx)}$ is the fraction of singly charged ions resulting from traversal of gas thickness nx (number density $\times$ path length).

The spatial separation of the charged from the neutral beam components is achieved through the use of magnetic fields[26,27] or by electrostatic deflection.[28,29] Faraday cups are frequently used to collect the charged particle beams, while the neutral beams are commonly measured using secondary emission detectors or calorimetry. Electron multipliers, scintillators, proportional counters, and solid-state junction devices may also be employed for the detection of both charged and natural particles.

The use of the above equations to derive collision cross sections requires a system in which only two charged states and two cross sections are involved. Even in the simplest realizable system, in which a primary proton beam is employed, three possible charge states exist, namely, H^-, H, and H^+, and as a consequence the number of processes competing to provide the equilibrated beam is too large to permit the evaluation of all the pertinent cross sections. The method is in fact limited to the evaluation of σ_{01}, σ_{10}, $\sigma_{\bar{1}0}$, and $\sigma_{0\bar{1}}$ in systems where multiple ionization is impossible.

b. Method of Single Collisions. Of more widespread application is the technique of fast beam analysis after traversal of a thin gas target. Measurement of the capture cross sections of singly and doubly charged ions in their own gases has been performed by Flaks and Solov'ev.[30] The cross sections were determined from measurements of the fast ions and atoms produced in the capture process. Measurements of σ_{01} for Ne^+, Ar^+, Kr^+, and Xe^+ in the energy range 3–30 keV are in agreement with the theory of Firsov.[31] The σ_{21} cross sections for Ne^{2+}, Ar^{2+}, Kr^{2+}, and Xe^{2+} increase continuously with ion energy in the range 6–60 keV. Results for σ_{20} for these ions suggest that the capture of two electrons is a resonant process.

Flaks and Solov'ev[32] also reported values for σ_{21} and σ_{20} for Ne^{2+}, Ar^{2+}, Kr^{2+}, and Xe^{2+} in collision with foreign inert gas atoms.

The apparatus used by McGowan and Kerwin[33] is shown in Figure 6, and is basically a high-intensity inflection mass spectrometer. Ions formed in the field-free source were accelerated by a Nier-type gun into the magnetic analyzer, where the pressure was maintained at about 10^{-4} torr. The regions before and after the magnetic analyzer were shielded against its fringe magnetic field and constituted two collision region of known dimensions. The collector was suitable for the detections and measurement of both charged and neutral particles. A double grid high-pass ion filter enabled the energy distribution of the

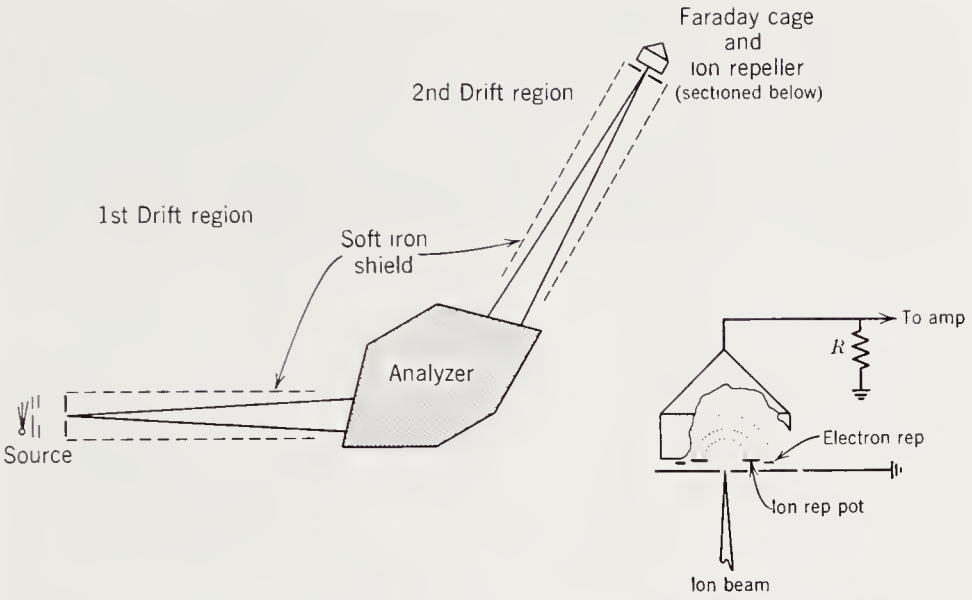

Fig. 6. Schematic diagram of apparatus used by McGowan and Kerwin.[33]

ions to be determined. Because of collisions within the drift regions, the mass spectrum contained a number of broad bands in addition to the primary ion peaks. These so-called Aston bands resulted from collisions in which ions suffered a change in their m/q ratio. In general, these ions occupy mass positions and possess energies different from those of the parent ions, and it may be shown that the products of reactions which occur within the first drift region will focus at a charge/mass position $(m/q)_b$ given by

$$(m/q)_b = (m_f/q_f)^2(q_i/m_i) \tag{15}$$

where the subscripts i and f refer to the initial and final ions. Collisions which occur after mass analysis in the second field-free region give products which occur at the parent mass position. Separation of the parent and product ions may be obtained in these circumstances using the high-pass energy filter, which allows the study of fast neutral products or of products which have charge exchanged and have more energy per charge than the parent. In this way a number of 10/01 collisions have been studied in the second drift region. A discussion of these results is included in Section V-A.

2. *Beam Attenuation in a Transverse Field*

In this method a mass-analyzed beam of the particles under study enters the collision region across which is maintained a transverse

field, and a collector is placed to collect those particles which emerge unscattered from the collision chamber. Particles which suffer a charge-changing collision follow a different trajectory in the transverse field and are not collected, even if the original charge state is restored in a subsequent collision. The apparatus used by Stier and Barnett[28] in this manner for the determination of the charge-transfer cross sections for protons in a number of gases is shown in Figure 7. A beam of protons

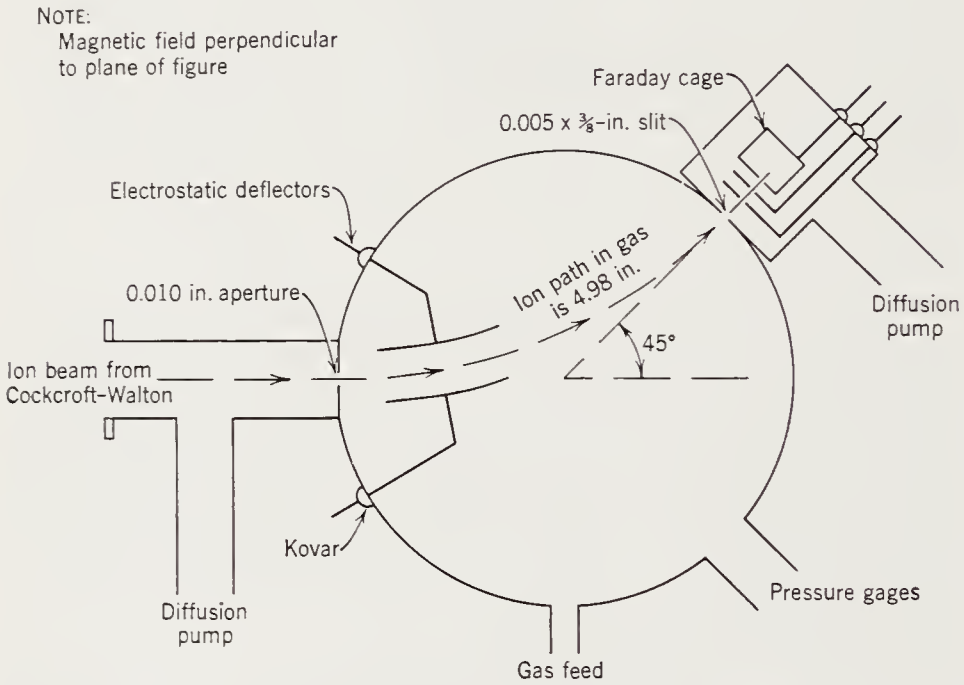

Fig. 7. Experimental arrangement of Stier and Barnett[28] for measuring electron capture cross sections of protons.

from a Cockroft-Walton machine entered a differentially pumped gas cell where it was deflected through an angle of 45° by a transverse magnetic field. The emergent beam was collected in a Faraday cage located behind guard electrodes which were biased to prevent secondary emission. To eliminate the effects of small-angle elastic scattering, the ion beam was moved across the exit slit by a linear electrostatic sweep voltage and the emergent beam was integrated. From measurements of the integrated beam intensity as a function of the cell gas pressure, the adsorption cross section was determined. In the proton measurements the cross section for transfer of two electrons is considerably smaller

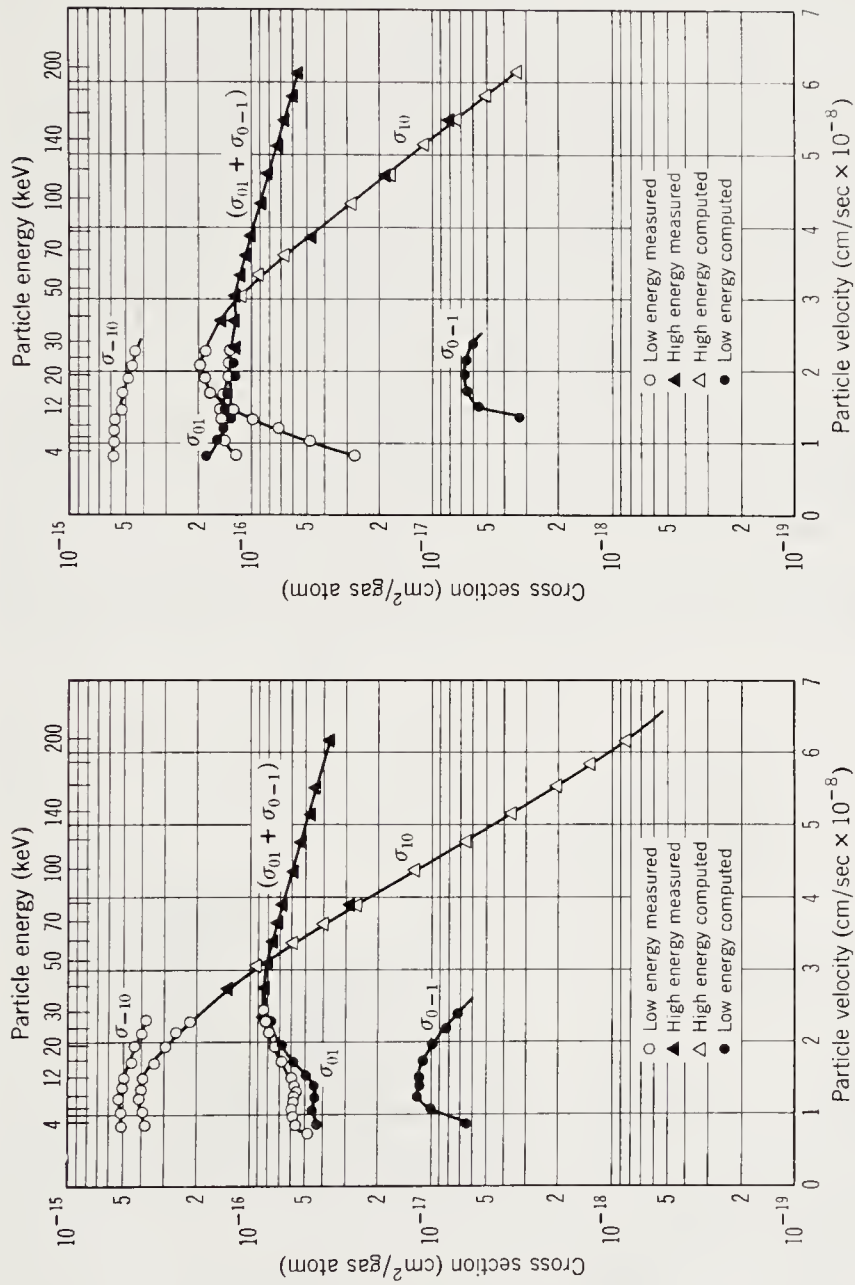

Fig. 8. Results of Stier and Barnett[28] for electron capture and loss for hydrogen ions and atoms (left) in H_2 and (right) in He.

than that for one-electron transfer and the σ_{10} cross section was, therefore, alone under study.

Figure 8 shows some results of Stier and Barnett for charge-transfer and electron-loss cross sections, the first being the results for H^+ and H in H_2, and the second being for the same fast particles in He. In addition to showing the general magnitude and energy dependence of the various cross sections, comparison of the maxima in the charge-transfer cross sections illustrates the shifting of the maxima toward higher energies, as the energy defects in the collision processes increase, in accordance with the adiabatic considerations.

C. Measurement of Angular and Energy Distribution

1. *Observations of Incident or Recoil Particles*

As stated in Section II-B, charge transfer is customarily accompanied by negligible momentum transfer. However, in a small fraction of collisions, large angle scattering of projectile and recoil particle may occur. These deflections result from violent encounters in which the fast projectile passes very close to the target particle. In general, the scattering angle in such collisions increases with the number of electrons transferred. Investigations of the angular and charge distribution

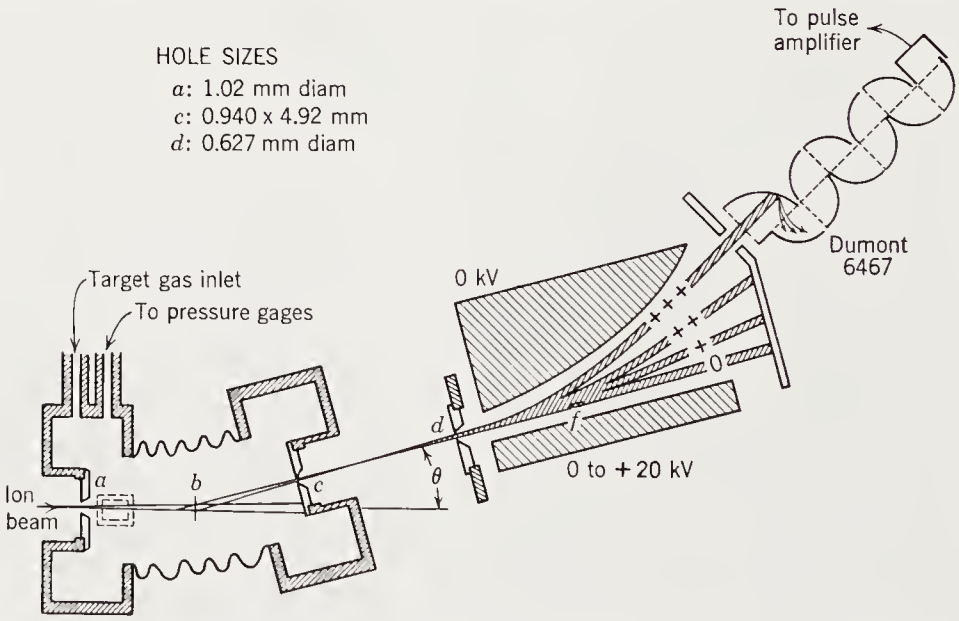

Fig. 9. Apparatus used by Ziemba et al.[37] for the investigation of resonant charge transfer in violent collisions.

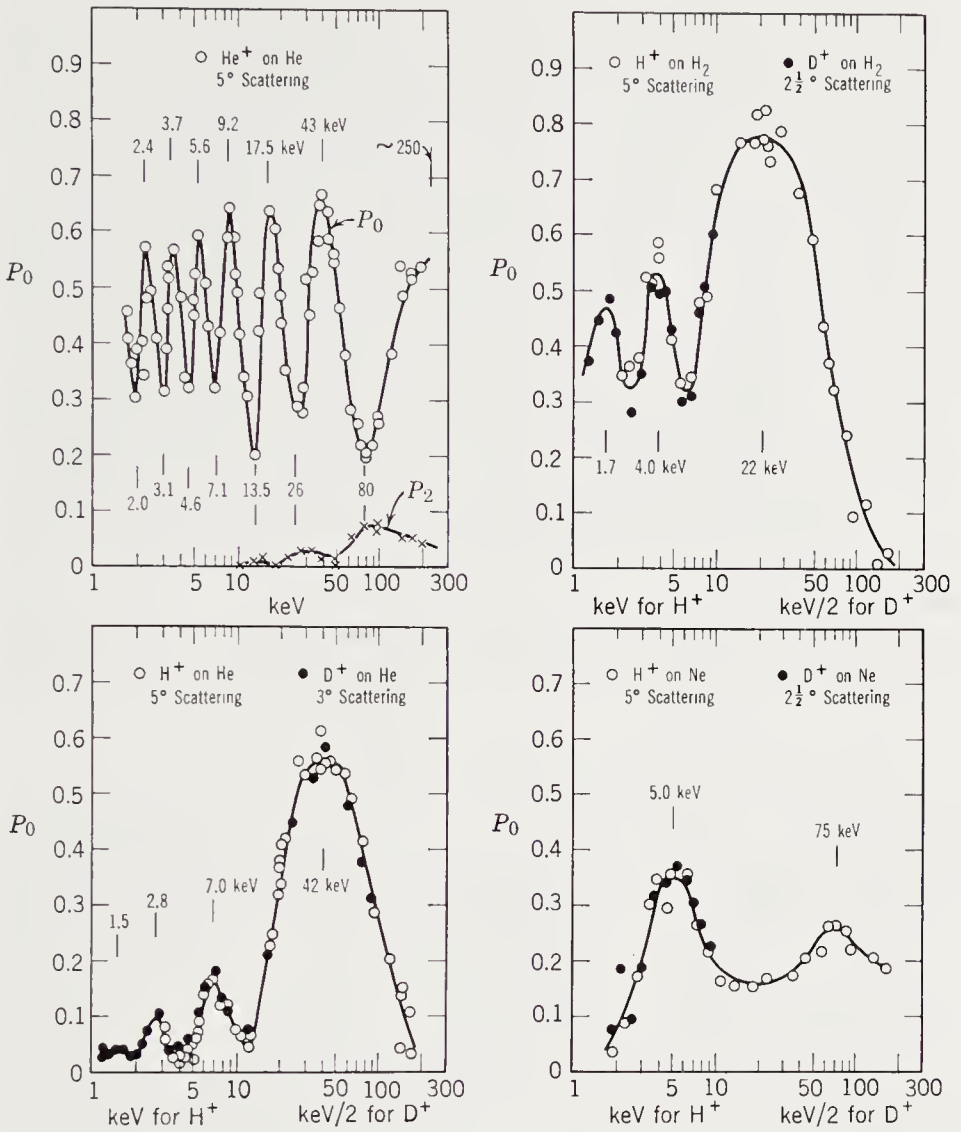

Fig. 10. Results of Ziemba et al.[37]

of the scattered particles have been conducted by Everhart and his colleagues.[34] Resonant charge transfer in violent collisions was first observed by Ziemba and Everhart,[35] who determined the differential scattering of He^+ by He, in the energy range 1–200 keV. The incident ion after a single collision, which was hard enough to result in a 5° deflection, was analyzed to determine whether it had gained or lost electrons. The capture probability plotted against incident ion energy showed seven pronounced peaks. This effect was attributed by Ziemba

and Russek[36] to the resonant process 10/01. The angle 5° was chosen as representative of large-angle scattering and is large enough to ensure deep interpenetration of the colliding particles during the collision. The apparatus used by Ziemba et al.[37] is shown in Figure 9. A mass-analyzed beam from a Cockroft-Walton accelerator was passed into a collision chamber containing the target gas at a pressure of about 1 μ. Collisions which occurred near b and which resulted in scattering in the proper direction allowed particles to pass through the resolution holes c and d. The electrostatic analyzer following hole d separated the scattered particles according to their charge state before they entered the multiplier detector. The several charged states were successively deflected into the detector by applying different voltages to the analyzer. Although a knowledge of the absolute counting efficiency was not necessary for a determination of the fractions P_n in a given charge n, it was assumed that the relative counting efficiency was independent of the charge.

Some data obtained by Ziemba et al.[37] are shown in Figure 10. The results for scattering at 5° in He^+–He collisions show maxima for P_0

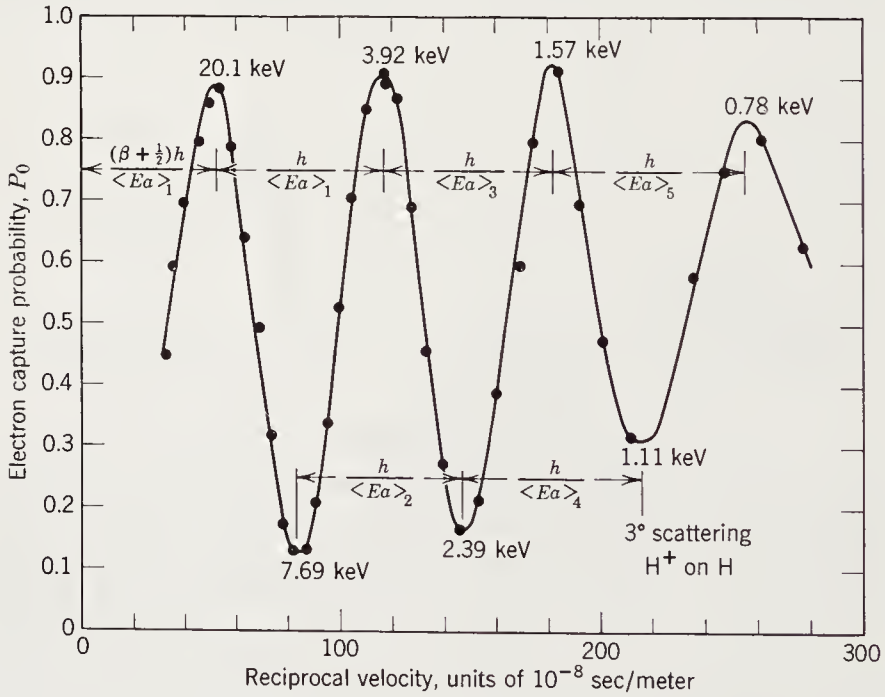

Fig. 11. Results of Lockwood and Everhart[34] for resonant electron capture in violent proton–hydrogen atom collisions.

at 2.4, 3.7, 5.6, 9.2, 17.5, and 43 keV. Peaks for P_2 (He^{2+} production) occur where P_0 is a minimum. A theoretical treatment of these results, based upon the impact parameter method, is given by Ziemba and Russek.[36] Also shown in Figure 10 are data for collisions between H^+ and D^+ with H_2, He, and Ne. More recently, Morgan and Everhart[38] have measured the energy and charge states of recoil particles in Ar^+–Ar collisions. From these data the inelastic energy-loss cross section is determined as a function of incident energy and scattering angle. Lockwood and Everhart[34] have studied resonant electron capture in violent proton–H atom collisions. These latter measurements are of particular significance for the development of the theory of such collisions. In Figure 11 is plotted the electron capture probability versus reciprocal velocity for the H^+–H collisions. The even spacings of the maxima and minima are characteristic of resonant electron capture.

Fedorenko, Filippenko, and Flaks[39] have investigated Kr^+, Kr^{2+}, Kr^{3+}, and Ne^{2+} in total or partial neutralization in neon and krypton. Ogurtsov and Flaks[40] have measured charge transfer of Xe^{3+} and Xe^{4+} in neon.

2. *Coincidence Detection of Scattered Particles*

In the foregoing measurements attention has been focused upon the scattering and charge state of either the fast or the slow particles resulting from the collision. The derived cross sections are, therefore, the summation of those for all the possible charge states of the unobserved particles. In a recent investigation, Afrosimov et al.[41] investigated individual events in atomic collisions through analysis of the scattering and charge states of both interacting particles, using coincidence techniques. This method allows the determination of the impact parameter, the distance of closest approach between the nuclei, and the inelastic energy loss for a known elementary collision event. Results are reported for the 10/*mn* and 00/*mn* collisions of atoms and ions of argon with argon atoms at 50 keV. Coincidences were recorded between incident and recoil particles in collisions with impact parameters smaller than atomic dimensions, when an appreciable scattering and kinetic energy transfer takes place. Under these conditions the kinematics of the collisions and the energy loss may be determined with adequate accuracy. Inasmuch as each of the colliding particles may lose one or more electrons, a large number of fundamental processes are observable. All measurements were made under single-collision con-

ditions, and the experimental arrangement is shown in Figure 12. A monoenergetic beam of ions separated by a monochromator M was collimated by slits S_1–S_5 and entered a collision chamber C_3 filled with gas. After collision the particles were investigated with two analyzers A_2 and A_3 which could be rotated in the horizontal plane about the center of the collision chamber C_3. After passing through the collimators K_1 and K_2, which determined the scattering angles of the particles under observation, they were mass analyzed in a magnetic field. Following this analysis, individual charged particles were recorded by detectors D_1 and D_3, while neutral particles were detected at D_2 and D_4. The efficiency of ion detection was of the order of 90% and was the same for neutrals with energy greater than 10 keV. Afrosimov et al. have examined a large number of fundamental processes involving the formation of recoil ions from Ar^+ to Ar^{5+} and the scattering of incident particles in the charge states Ar^0 to Ar^{6+}. From measurements of the scattering angles of the incident particles and of the recoil particles, the magnitude of the inelastic energy loss may be unambiguously determined. In addition, these measurements allow evaluation of the scattering angle in the center-of-mass system from which one may

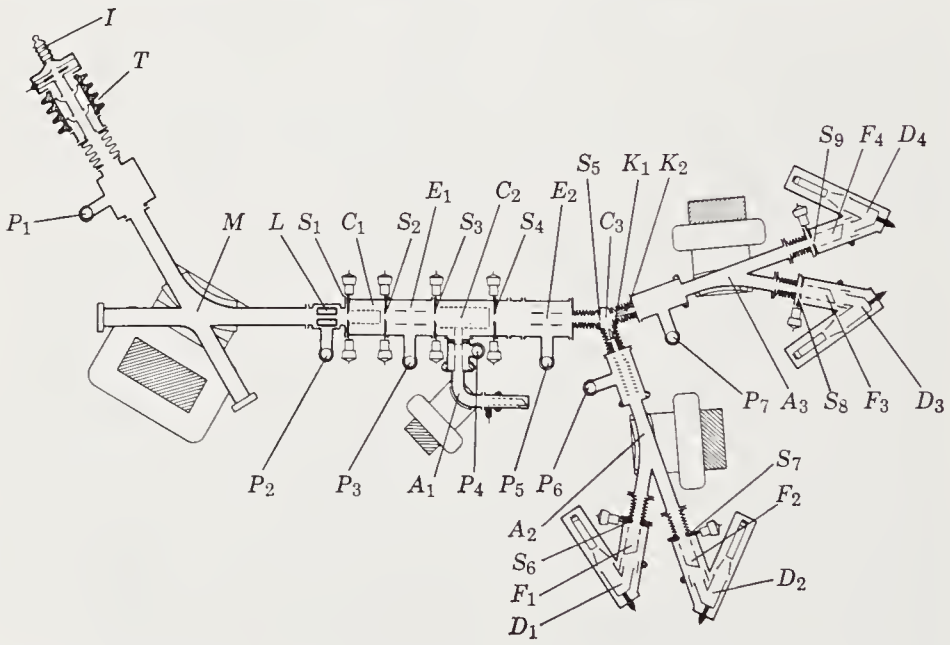

Fig. 12. Apparatus used by Afrosimov et al.[41] for coincident observation of the incident and recoil particles.

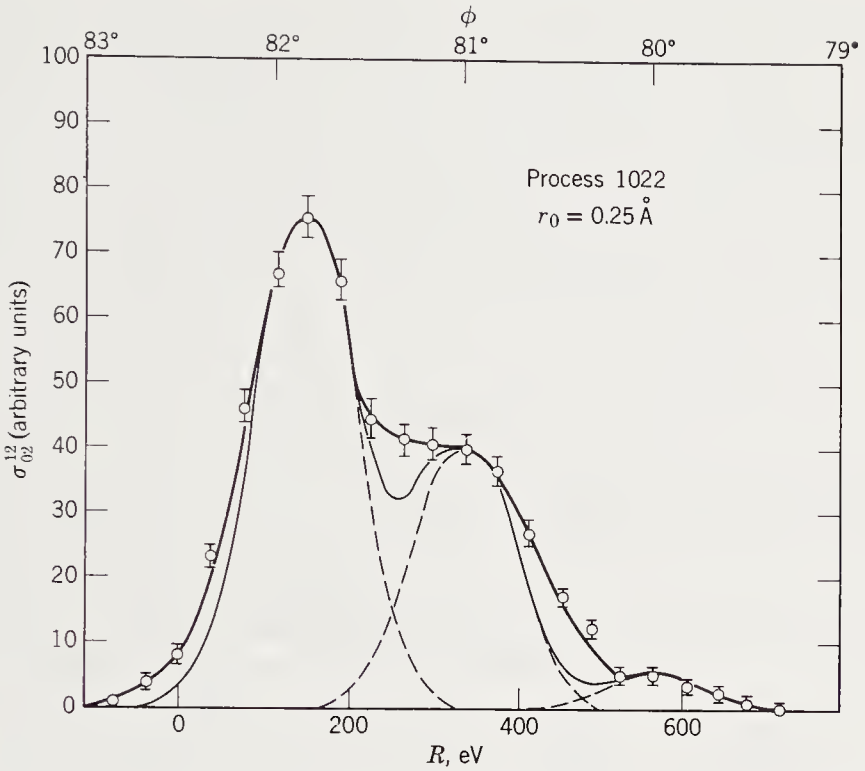

Fig. 13. Variation of the 10/22 cross section (Eq. (16)) with inelastic energy loss R. Solid line: experimental. Dashed line: instrument function contours. Thin line: theoretical value of $_{10}\sigma_{22}$ for infinitely narrow energy loss lines. The distance of closest approach between the nuclei is 0.25Å.

calculate the impact parameter and the distance of closest approach of the nuclei using the relationships obtained by Kaminker and Fedorenko.[42] They investigated the dependence of the probabilities of a number of these processes upon the inelastic energy loss at different impact parameters and distance of closest approach of the nuclei. In Figure 13 is shown the dependence of the cross section for the process 10/22

$$Ar^+ + Ar \rightarrow Ar^{2+} + Ar^{2+} + 3e \qquad (16)$$

in relative units on inelastic energy loss R at an impact parameter of 0.235 Å and the distance of closest approach between the nuclei of 0.25 Å. It is seen that at a fixed impact parameter the cross section exhibits three maxima. Such structure has been observed in all the processes studied; moreover, if losses for ionization are subtracted from the inelastic energy loss, the characteristic energy losses are 37 ± 9, 268 ± 11,

and 471 ± 15 eV. At the present time, theory is unable to account for these observations. Quantum-mechanical treatments are inadequate, but simplified statistical treatments are being attempted by Russek and Thomas[43] and by Firsov.[31] It is noted by Afrosimov et al. that the characteristic energy losses do not correspond to the energies necessary to remove electrons from the M, L, and K shells of an argon atom. They surmise that these energy losses may result from excitation of collective oscillations in the electron shells of the colliding particles.

IV. STUDY OF CHEMICALLY UNSTABLE GASES

A. Crossed Beam Techniques

With the single exception of the proton–hydrogen atom measurements of Lockwood and Everhart,[34] all techniques of measurement so

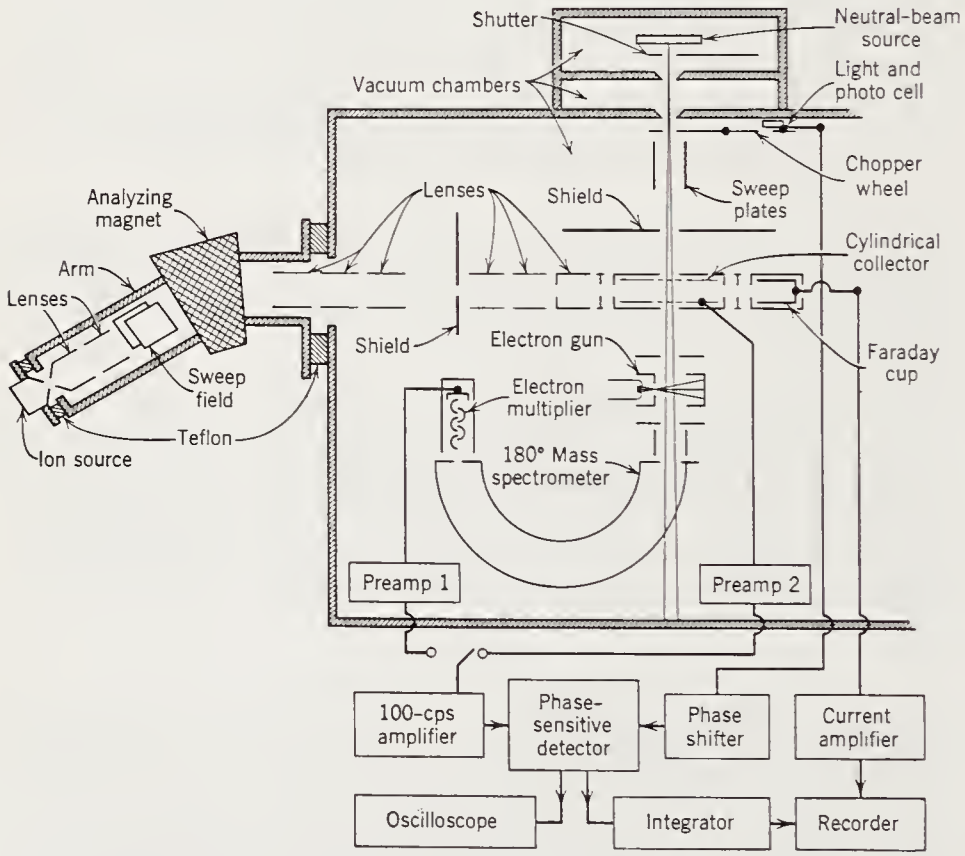

Fig. 14. Crossed beam apparatus for the measurement of collision cross sections of chemically unstable target gases.

far described were developed for the study of chemically stable gases. When the target particles are chemically unstable, techniques which utilize collision chambers are in general unsuitable because of the rapid recombination of condensation of these particles at the chamber walls. This limitation is avoided by the use of beam techniques which were first applied successfully by Fite, Brackmann, and Snow[44] to the study of H^+–H collisions. Their original measurements have subsequently been improved and extended and a recent version of the equipment used by Fite, Smith, and Stebbings[45] for the study of collisions between H^+, O^+, and He^{2+} ions and H atoms is shown in Figure 14.

Atomic hydrogen was produced through thermal dissociation of hydrogen molecules in an electrically heated tungsten furnace. The H atoms which issued from a small orifice in the wall of the furnace were collimated into a fine beam as they passed through a vacuum buffer chamber into the experimental chamber. The neutral beam was then interrupted, at a frequency of 100 cps, by a rotating toothed wheel before entering an electric field, which removed any charged particles. A final collimating aperture limited the neutral beam before it entered the interaction region.

The ions were extracted from an electron bombardment source of the Heil type, analyzed in a 30° magnetic mass spectrometer, focused and collimated into a fine beam which intersected the H-atom beam inside a cylindrical electrode whose axis coincided with that of the ion beam. The potential of this cylinder was maintained negative to that of the surrounding electrode so that slow ions resulting from charge transfer were unable to escape from the potential well in which they were formed and were collected on this cylinder. Two apertures through which the neutral beam passed were positioned diametrically in the cylinder. On leaving the interaction region, the primary ions passed through a final defining slit before collection in a positively biased Faraday cup. The dimensions of the orifices in the interaction region were such that all ions that passed through this final slit necessarily passed through the neutral beam. A 180° magnetic mass spectrometer was provided to sample the charge transfer ions and also, when used with an electron gun, to determine the composition of the neutral particle beam. In the hydrogen atom measurements this mass spectrometer was used only to determine the degree of dissociation of the neutral beam; all charge-transfer measurements were made with the non-discriminating cylindrical collector.

The charge-transfer signal which arose from the interaction of the two beams was distinguishable from the much larger signal arising from collisions between the ions and the residual gas because the former occurred at the modulation frequency and in a specific phase, while the latter signal was DC plus some noise at the modulation frequency. The use of narrow-band amplifiers and phase-sensitive detectors provided high discrimination against unwanted background signals.

The experimentally observed quantities were the signal current (S) of slow charge-transfer ions and the primary ion current (I). The ratio (S/I) of these two quantities is related to the required cross section by a proportionality constant which is determined by the neutral beam parameters. With the conditions affecting the neutral beam kept constant, measurements of this ratio, determined as a function of the primary ion energy, gave relative cross sections. Absolute values for the H^+–H cross section were then obtained by measuring the ratio of the cross sections of the hydrogen atom and the hydrogen molecule at a given ion energy and then multiplying this ratio by the previously determined absolute molecular cross section. In measuring the ratio of cross sections, advantage was taken of the fact that the amount of gas flow per unit time in the beam was constant and independent of both the furnace temperature and degree of dissociation in the furnace. Once the H^+–H cross section was absolutely determined, relative cross section data for another primary ion, e.g., O^+, were normalized by measuring the signal per unit current (S/I) for O^+ and H^+ ions incident on the same neutral H beam. These values of S/I were proportional to the corresponding charge-transfer cross sections, and the O^+–H cross section could thus be determined directly. An essentially similar procedure was used for the normalization of the cross sections for collisions of other ions with H atoms. In Figure 15 are shown some experimental data. In this work, particular emphasis was placed upon results at low ion energies, and for this reason the cylindrical slow-ion detector was substituted for the more conventional condenser plates which had been used in earlier studies. The deflection of the low-energy primary ions which would have resulted from the transverse condenser field was thus avoided. Inasmuch as the cylindrical collector does not allow unequivocal elimination of the effects of ionization, the condenser method was used at higher collision energies when positive-ion ionization becomes important. Charge transfer in H^-–H collisions[46] and N^+–H collisions[47] has also been investigated in this way.

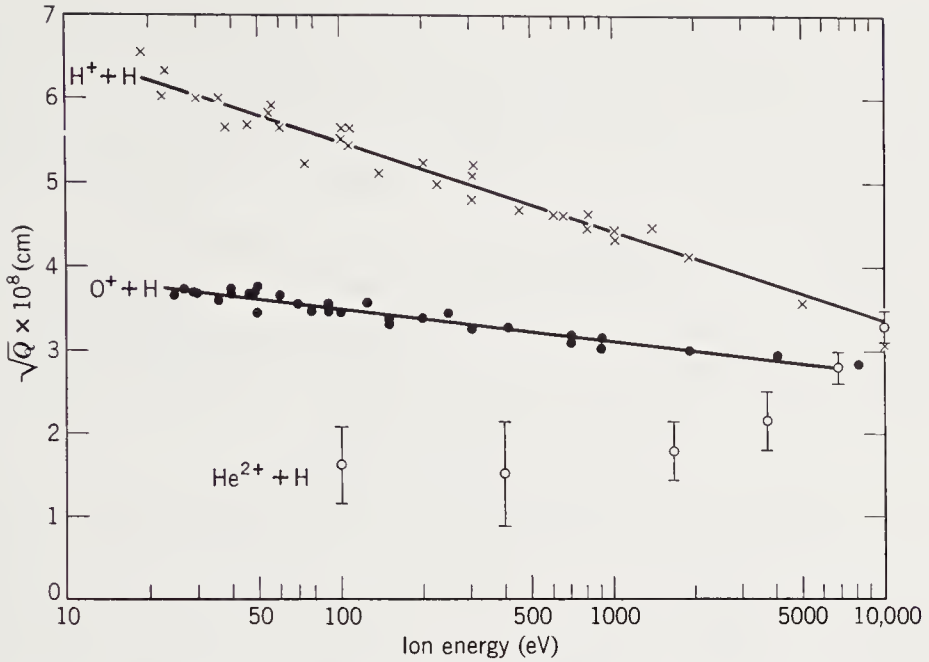

Fig. 15. Results of Fite, Smith, and Stebbings[45] for charge transfer between H atoms and H^+, O^+, and He^{2+} ions.

The apparatus illustrated in Figure 14 has also been used for the investigation of charge transfer between O atoms and H^+, O^+, O_2^+, N^+, N_2^+, and NO^+ ions.[48,49] The experimental method was similar to that used for the H-atom work except that the oxygen atom source was a radio-frequency discharge. Whereas in the hydrogen measurements the neutral beam was normally more than 95% dissociated, the dissociation in the oxygen beams never exceeded 40%. In order to determine the atomic cross section at a particular ion energy, the signal current at the cylindrical detector was measured for the molecular beam and for the partially dissociated beam. Then for constant mass flow in the neutral beam

$$S_f = kQ_2$$

$$S_n = k[Q_2(1 - D) + \sqrt{2}Q_1 D] \tag{17}$$

where S_f and S_n are the signals per unit primary ion current with the radio frequency off and on, respectively; k is a constant determined by the neutral beam parameters and the signal current detection sensitivity; and Q_1 and Q_2 are the respective cross sections for charge transfer between the ions under investigation and atoms and molecules of

oxygen. Measurements of S_f, S_n, and D, the dissociation fraction, permit Q_1 to be evaluated if Q_2 is known. D was determined with the mass spectrometer as the fractional drop in the molecular content of the neutral beam as the radio-frequency excitation was applied. Some results for charge transfer in O-atom collisions are shown in Figures 16 and 17.

Crossed beam techniques have also been applied by Chkuaseli, Nikoleishvili, and Guldamashvili[50] to the study of resonance charge transfer in potassium and cesium within the energy range 5–30 keV. The absolute magnitudes of the measured cross sections are about 50% higher than those calculated by Firsov[51] and by Demkov.[52]

B. Collision Chamber Techniques

More conventional techniques have also been applied to the study of resonance charge transfer in the alkali metals. The apparatus used by Marino, Smith, and Caplinger[53] for the study of cesium is shown in Figure 18. Cesium ions, produced by surface ionization of atoms diffusing through a heated porous tungsten plug, were accelerated, mass analyzed, and focused into the charge-transfer chamber. This

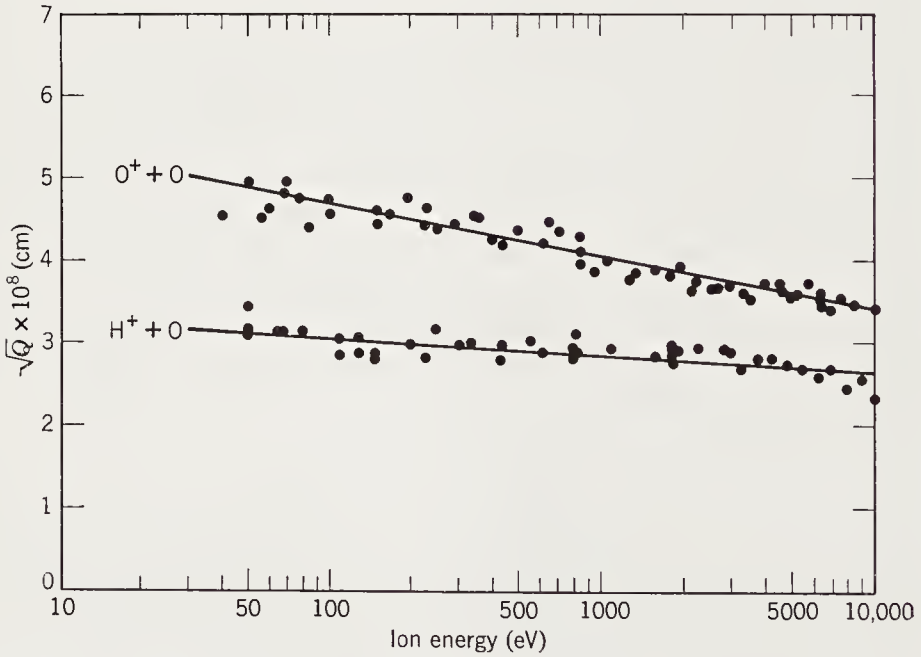

Fig. 16. Results of Stebbings, Smith, and Ehrhardt[49] for charge transfer between O atoms and O^+ and H^+ ions.

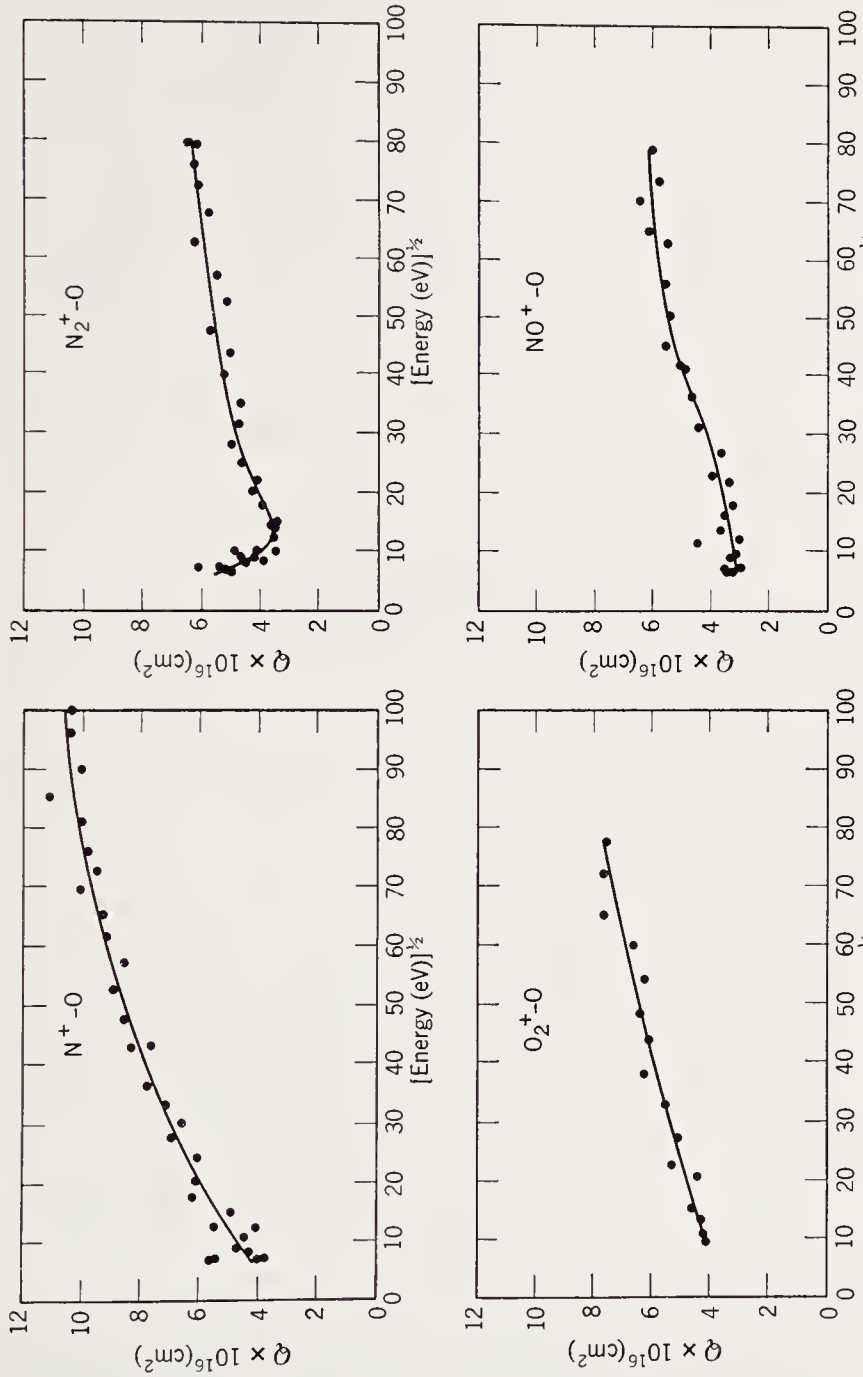

Fig. 17. Results of Stebbings, Smith, and Gilbody[48] for charge transfer between O atoms and N^+, N_2^+, O_2^+, and NO^+ ions.

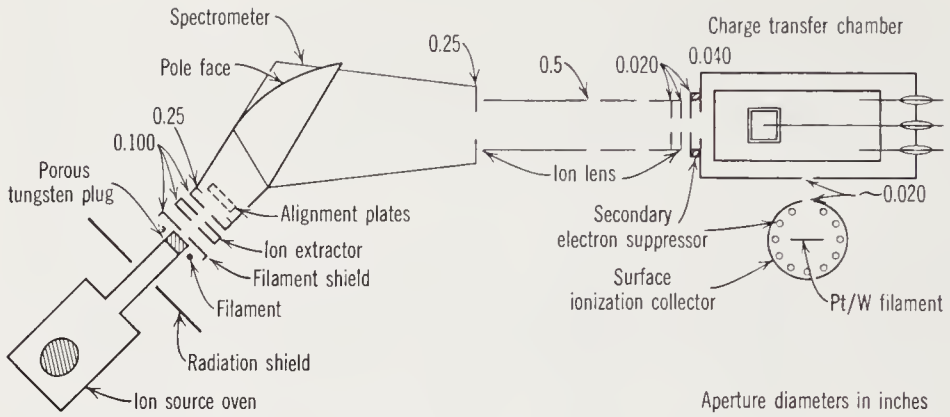

Fig. 18. Apparatus used by Marino, Smith, and Caplinger[53] for the study of resonance charge transfer in cesium.

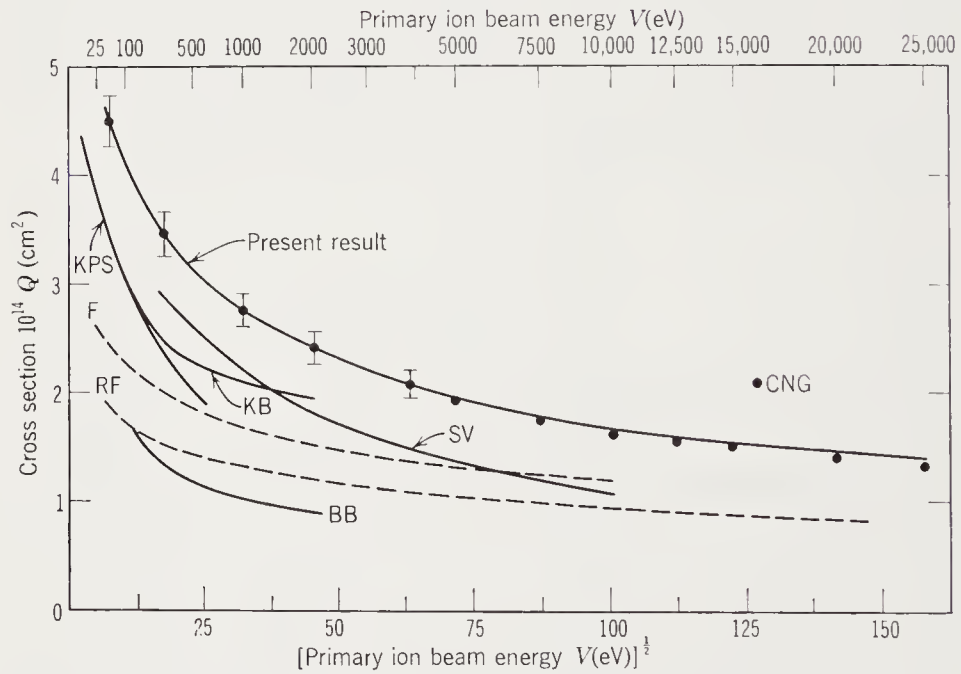

Fig. 19. Resonance charge transfer in cesium. The measurements of Marino, Smith, and Caplinger[53] are indicated as "Present result." Also shown are measurements by Chkuaseli, Nikoleishvili, and Guldamashvili[50] (CNG); Speiser and Vernon[54] (SV); Kushnir and Buchma[55] (KB); Kushnir, Palyukh, and Sena[56] (KPS); Bukhteev and Bydin[57] (BB); Firsov[51] (F); and Rapp and Francis[9] (RF).

chamber contained neutral cesium atoms at a pressure which was controlled by the temperature of a reservoir containing cesium metal. The atom density in the chamber was determined with a surface ionization detector. Slow ions which resulted from charge transfer were collected on the parallel plates P while the primary beam was collected on Q. Measurement of the above quantities together with knowledge of the electrode dimensions allowed evaluation of the cross sections. The results are shown in Figure 19, together with those of other investigations. It is seen that good agreement is obtained between the crossed beam measurements of Chkuaseli et al. and those of Marino et al., who point out that the remaining measurements may well be in error due to incorrect measurement of the vapor pressure of cesium in the collision chamber.

V. THE INFLUENCE OF EXCITED PARTICLES UPON CHARGE TRANSFER

A. Metastable Ions in the Primary Beam

The existence of excited species in ion beams and their influence on the measurement of collision cross sections has long been recognized, and several attempts have been made to assess the contributions to measured cross sections arising from such excited ions. Hasted and collaborators[11] have interpreted structure observed in their total cross-section curves as arising from the presence, in their primary ion beam, of long-lived excited ions. Lindholm and co-workers,[58] in their investigation of the mass spectra of complex molecules, have been able to determine the recombination energies which are appropriate to their ion beams and thus are able in favorable circumstances to identify the presence of excited ions. Neither technique allows evaluation of the individual cross sections appropriate to each metastable ion because the composition of the primary ion beam in terms of these excited states is unknown. Only the total cross section associated with all states of the parent ion beam is determinable and may be written as

$$Q = \sum_n Q_n F_n \tag{18}$$

where F_n is the fraction of the ion beam in a state n and Q_n is the cross section for ions in that state. Lindholm and co-workers[20] demonstrated very clearly the influence on the composition of an O^+ ion

beam of its mode of production. Thus they obtained beams of O^+ ions from the dissociative ionization of CO, N_2O, and CO_2 and took them into collision with various gases. In collision with N_2, the charge-transfer cross sections were observed to differ by a factor greater than 4, clearly demonstrating the varying compositions of the ion beams in terms of their excited states.

When an electron-impact ion source is used, the resulting ion-beam composition is sensitive to the energy of the bombarding electrons. At sufficiently low electron energy, ions may be formed only in their ground

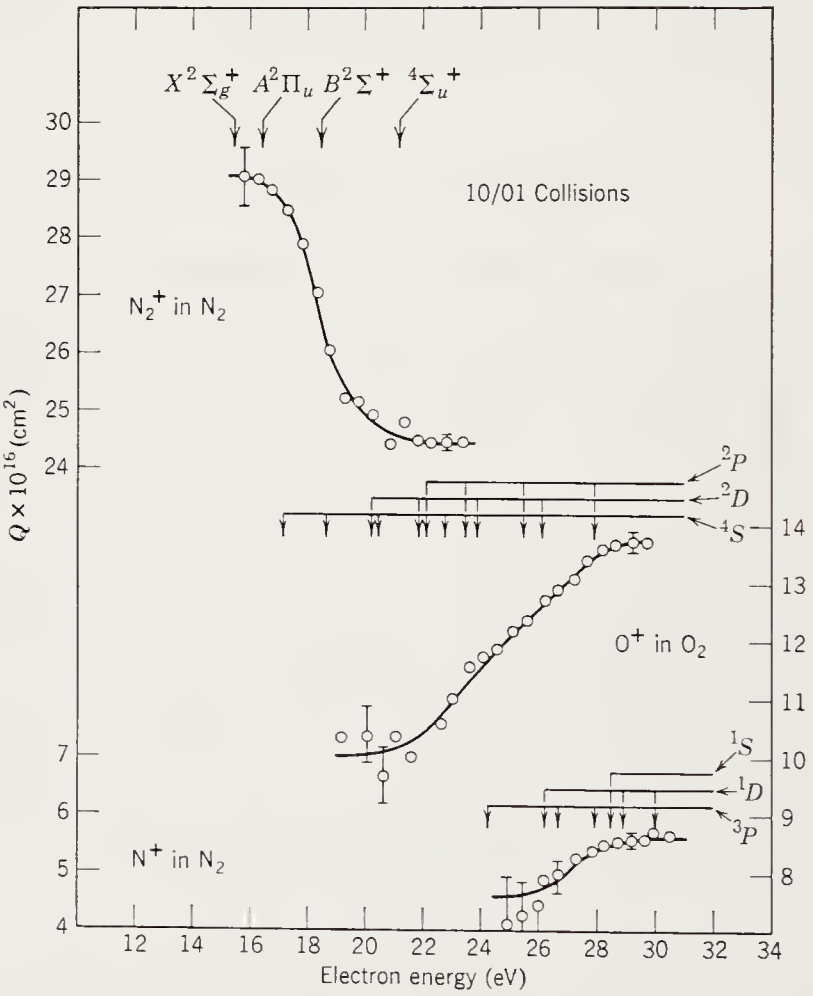

Fig. 20. Cross sections obtained by McGowan and Kerwin[60] for the 10/01 reactions of O^+ in O_2, N^+ in N_2, and N_2^+ in N_2 as a function of the beam composition (i.e., ionizing electron energy). The arrows indicate thresholds of various states.

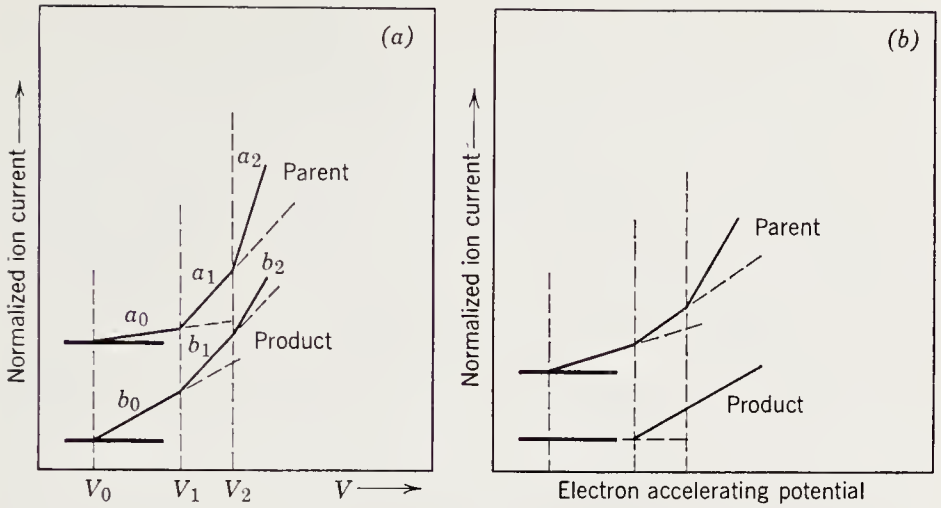

Fig. 21. Comparison of appearance potential curves of parent with product ion at fixed ion kinetic energy.

state. As the energy is increased, the production of excited ions becomes energetically possible and measurement of a charge-transfer cross section, at a fixed ion energy, as a function of the electron energy in the ion source, provides information upon the cross sections for the excited ions. This technique has been exploited by Amme and Utterback[59] and by McGowan and Kerwin.[60] The former authors used the technique of slow-ion detection and operated at ion energies within the range 40–1000 eV. The energy of the electrons in the ion source was carefully controlled and it was determined that for N_2^+–N_2 charge transfer, at fixed ion energy, the 10/01 cross section decreased by about 15% when the electron energy was raised from 17 to 23 eV. These results are in accord with those of McGowan and Kerwin, which are shown in Figure 20, together with other data. In the case of O_2^+–N_2 charge transfer, for electron energies below 18 eV the cross section obtained by Amme and Utterback was strongly nonresonant, approaching zero below 100 eV. For electron energies above 22 eV the cross section appeared to have resonance form.

With reference to Figure 20, it is seen that for the 10/01 reaction for O^+ in O_2, the ground state ion has a cross section nearly 50% lower than that obtained when the beam is saturated with ground state and long-lived excited ions. Information regarding the cross sections for metastable ions may, in principle, be obtained through comparison of the appearance potential curve of the product ion with that of the

parent. These curves are obtained by plotting the ion currents as a function of the bombarding electron energy, and a simple case is shown in Figure 21*a*, where the appearance potential curve for the product is seen to have the same structure as the parent. This is to be expected, since the various increases in product current simply reflect the increased parent ion current as the ionizing energy of the source electron beam causes various states of the parent ion to be excited. However, as different metastable or long-lived excited states are formed in the beam, the collision cross section changes and, therefore, the slope of the product curve may change relative to that for the parent. Figure 21*b* illustrates the case where the product is not produced until the parent has reached a certain state of excitation. Even from this point on, the two curves do not necessarily contain all the same breaks. As a consequence of the differences observed in some parent and product curves, it is often simple to identify known states and, in many instances, to identify the onsets of previously unobserved metastable or long-lived ions. From the appearance potential curve of the parent ion one may extract the relative concentrations of the different ions from the relative slopes and the energy intervals above onsets in a manner similar to that described by Marmet.[61] From the ratio of the differences of parent to product slopes it is possible to determine the relative cross sections for these states. McGowan and Kerwin have applied these techniques also to the study of collision-induced dissociation.

B. Excited Products of Charge Transfer

Information on the state of excitation of the collision products may occasionally be inferred from the measured ion spectrum, but more detailed information of this nature is provided by experiments which utilize a light-sensitive detector to observe the photon decay of excited collision products. The detector is typically a photomultiplier or a photon counter which is used in conjunction with a suitable means of wavelength identification.

In a number of investigations, the region of interaction between a mass-selected ion beam and a target gas has been viewed and information obtained on the states of both the projectile and target particles. When both the incident and target particles are of the same chemical species, the origin of the observed radiation may be traced because of the Doppler shift in the fast-particle spectrum.

Collisions between protons and N_2 have been studied in the energy

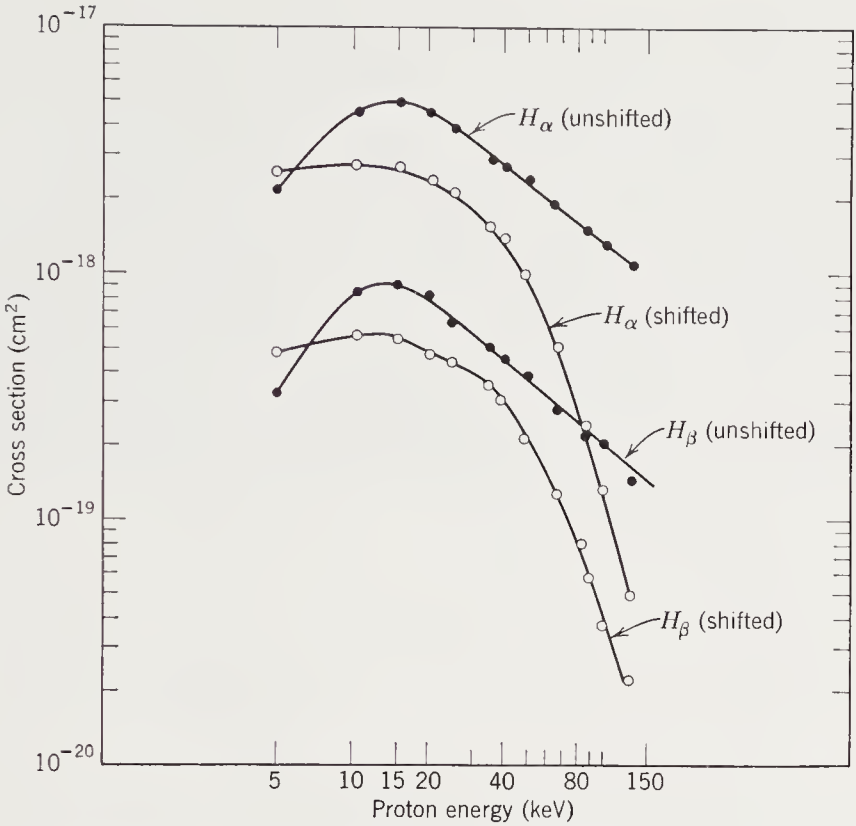

Fig. 22. Measurements by Hughes, Lin, and Hatfield[63] of the H_α and H_β emission produced by proton impact on H_2.

range 1.5–4 keV by Carleton and Lawrence,[62] who used a spectrometer–photomultiplier detector. In addition to the study of N_2 excitation they observed the Balmer β line resulting from electron capture and concluded from measurements at different target pressures that their signal included contributions from direct capture into excited states plus capture into the ground state followed by excitation in a subsequent collision. Proton collisions with H_2 have been examined by Hughes, Lin, and Hatfield[63] within the range 5–140 keV. The Balmer emission resulting from dissociative excitation of the target molecules was distinguished from that arising from electron capture into excited states of the fast particles because of the Doppler shift of the latter radiation. Absolute cross sections for the production of the H_β and H_α by proton impact on H_2 were measured up to 140 keV and are shown in Figure 22.

In the work of Dunn, Geballe, and Pretzer,[64] the absolute cross section for Lyman-α production was determined as a function of the ion energy for a number of ion–neutral pairs. A beam of mass-analyzed ions was focused into a collision region which was viewed by an iodine-filled oxygen-filtered photon counter.[65] The counter is sensitive within the wavelength interval 1080–1317 Å, but between these limits the molecular oxygen is strongly absorbing except at seven transmission windows. The overall system is sensitive, therefore, only to wavelengths lying within these windows, one of which lies precisely at the wavelength of Lyman α. Dunn et al. compared Lyman-α production from H_2 by proton and electron impact and used the previously determined absolute cross section for the latter process to normalize the proton data. The H^+–H_2 cross section was then used as a standard against

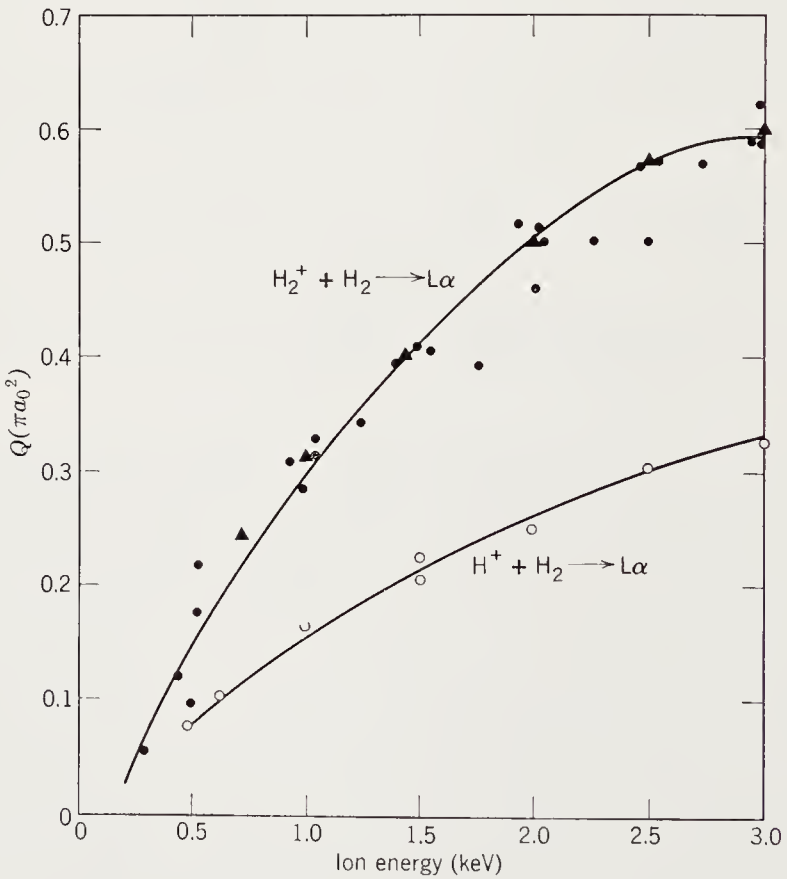

Fig. 23. Lyman-α production resulting from impact of H^+ and H_2^+ ions with H_2. The radiation was observed normally to the ion beam axis (from ref. 64).

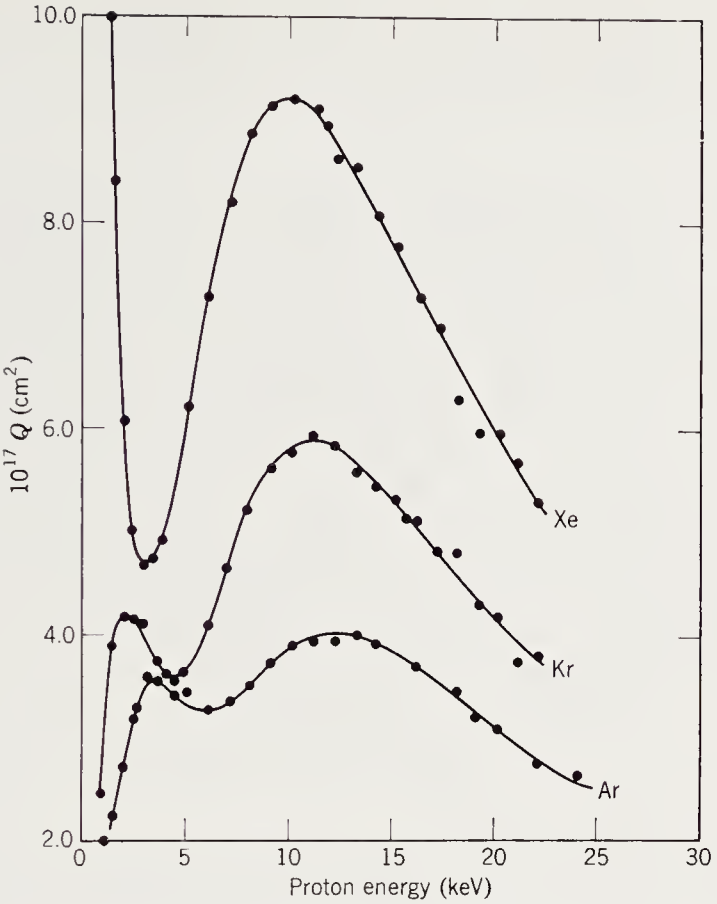

Fig. 24. Measurements by Pretzer, van Zyl, and Geballe[66] of Lyman-α production in proton–rare-gas atom collisions.

which to compare Lyman-α production cross sections in other target gases. Results are shown in Figure 23 for hydrogen ion impact on H_2. Interpretation of these data is complicated because in each case a number of processes may be operative. For example, in H^+–H_2 the following processes lead to Lyman-α production:

$$H^+ + H_2 \rightarrow H^{*L\alpha} + H_2^+ \qquad \Delta E = 11.9 \text{ eV}$$
$$H^+ + H_2 \rightarrow H^{*L\alpha} + H^+ + H \qquad \Delta E = 14.6 \text{ eV}$$
$$H^+ + H_2 \rightarrow H^+ + H + H^{*L\alpha} \qquad \Delta E = 14.6 \text{ eV}$$
$$H^+ + H_2 \rightarrow H + H^+ + H^{*L\alpha} \qquad \Delta E = 14.6 \text{ eV}$$

Discrimination between the radiation coming from fast and slow particles by virtue of the Doppler shift could not be made by Dunn et al. because their counter was fixed normal to the ion beam. Measure-

ments by Pretzer, van Zyl, and Geballe[66] for proton–rare-gas collisions have been made using the same techniques. The well-defined structure which they observe in the data shown in Figure 24 is as yet not understood.

Electron capture into excited states of H^+ and He^+ incident upon H_2, He, Ne, and Kr has been studied by de Heer, van Eck, and Kistemaker.[67] The spectral lines originating from these encounters were observed within the region 200–1250 Å using a calibrated vacuum spectrograph so that absolute cross sections could be obtained. Within the energy range of their measurements, 5–35 keV, they found that the probability of capture into an excited state decreased with increasing principal quantum number. In general, the capture cross sections for the $2P$ and $3P$ states of H and He show, as a function energy, a behavior similar to the total capture cross section. At 30 keV, about 5% of the captured electrons were found in the $2P$ state and 0.5% in the $3P$ state. The measurements of Dunn et al. and Philpot and Hughes[68] show a similar dependency upon the principal quantum number. Some measurements of Lyman-α production are common to the work of de Heer et al. and of Geballe and his associates. It is found that although the relative curve shapes are quite similar, the absolute values obtained by de Heer et al. are higher by a factor of 2 or 3 than those taken using the photon counter.

Charge transfer into the metastable $2S$ state of atomic hydrogen was observed by Cristofori et al.[69] for protons with energies in the range 7–40 keV incident on hydrogen and helium gas. The metastable atoms were quenched in an electric field and the resulting Lyman-α photons were detected with a calibrated oxygen-filtered Bendix multiplier. The absolute cross sections so obtained were lower than those obtained theoretically using the Born approximation.

Observations on the Doppler shift of the radiation emitted by excited recoil particles have been used by Mandelberg[70] to determine the energy transfer in fast molecular ion collisions. In this work a beam of H_2^+ and H_3^+ ions in the energy range 25–75 keV was incident upon a target of H_2, and the collision products were spectroscopically examined. From the Doppler shift of the Balmer H_α line at 6565 Å Mandelberg determined that the energy of the emitting atoms was about 1 keV less than that of the incident molecular ions. It was observed that this energy difference was greater for H_3^+ ions than for H_2^+ ions.

An entirely different detection scheme was used by Riviere and

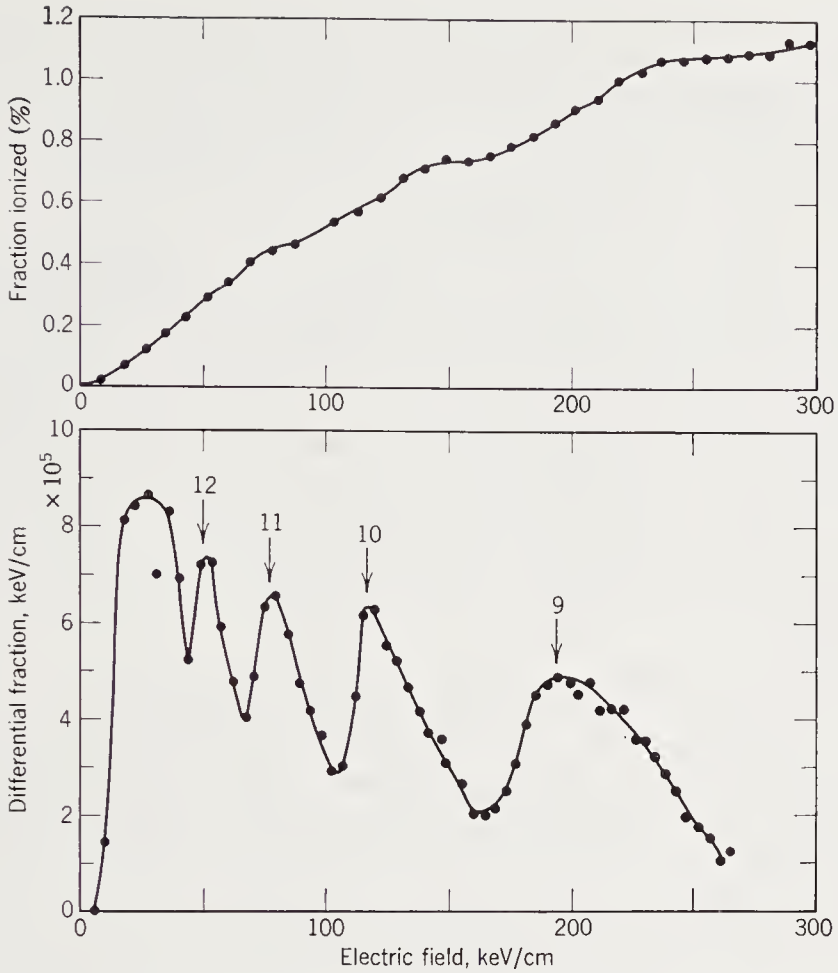

Fig. 25. Upper part: Ionization of 200 keV hydrogen atoms as a function of the applied electric field. Lower part: Rate of increase of the fraction of neutral atoms which were ionized as a function of the applied field.

Sweetman[71] for the investigation of electron capture into excited states by fast protons. They took advantage of the fact that in an electric field a potential barrier separates the excited atomic electron from a point at lower potential outside the atom. At sufficiently high electric fields the barrier disappears and the electron can move freely away from the proton. In their experiments, highly excited hydrogen atoms were ionized by passing them into an intense electric field that was maintained between two highly polished stainless steel electrodes placed 1 mm apart. After passing through the high-field region the beam was magnetically analyzed and the components were detected by CsI

scintillation counters. The results of measurements of the ionization of 200-keV H atoms, resulting from H^+–H_2 charge transfer, are shown in Figure 25. The ionized fraction of the beam is shown as a function of the applied electric field, together with the rate of change of the ionized fraction. The structure is interpreted as showing the successive ionization of the excited states of the hydrogen atom.

Using electric field ionization, Riviere and Sweetman have measured the cross section for H-atom formation in the $n = 14$ excited state through H^+–H_2 collisions within the energy range 25–100 keV. The equilibrium value for the excited atom population was also measured for a thick hydrogen target over the same energy range. Equilibrium populations of the sum of $n = 8$, 9, 10, and 11 states for thick targets of He, Ne, Ar, Kr, and Xe have been obtained at an energy of 50 keV.

This ingenious technique is limited to the study of highly excited neutral particles because of the large field strengths involved. For ionization of a ground-state H atom, a field of order 10^8 volt/cm is required.

VI. THEORETICAL CONSIDERATIONS

In theoretical studies of charge transfer there are two main approximations: a high-velocity approximation in which the perturbation causing transitions is taken to be the interaction potential, and a low velocity approximation in which the perturbation is taken to be the relative motion.

A. High-Velocity Region

When the velocity of relative motion of the colliding systems is high, the cross section for a given process may be obtained by use of a first-order approximation in which it is assumed that the incident and scattered waves associated with the relative motion are plane (wave treatment), or, alternatively, that the nuclei are classical particles of infinite mass (impact parameter treatment).

The wave treatment gives the cross section for a collision in which there is a transition from an initial state p to a final state q to be

$$Q(p \cdot q) = \frac{M^2 v_q}{2\pi^4 v_p} \int_{-1}^{+1} |N|^2 d(\cos\theta) \tag{19}$$

where

$$N = \int \psi_p^* V \psi_q d\tau \qquad \text{and} \qquad \cos\theta = \bar{v}_p \cdot \bar{v}_q \tag{20}$$

M is the reduced mass of the system, v_p and v_q are the initial and final velocities of relative motion, ψ_p and ψ_q are the corresponding wave functions suitably normalized, and V is an interaction potential.

The simplest charge transfer process and the one which has received most theoretical attention is

$$H_A(1s) + H_B^+ \rightarrow H_A^+ + H_B(1s) \tag{21}$$

where A and B identify the nuclei.

The instantaneous interaction for the systems on the right of reaction (21) includes a nuclear–nuclear (*nn*) term and a nuclear–electron (*ne*) term and may be written as

$$e^2\left\{\frac{1}{|r_a - r_b|} - \frac{1}{r_a}\right\} \quad \text{(post)} \tag{22}$$

and for the systems on the left it is

$$e^2\left\{\frac{1}{|r_a - r_b|} - \frac{1}{r_b}\right\} \quad \text{(prior)} \tag{23}$$

Use of either the post or prior expression leads to the same result, provided exact atomic eigenfunctions are used.

In the original work of Brinkman and Kramers,[72] and Oppenheimer,[73] the nuclear–nuclear term was neglected and the cross section $Q^{(ne)}$ was evaluated, using only the *ne* term of the interaction potential. Subsequently, Bates and Dalgarno,[74] and Jackson and Schiff[75] included an empirical *nn* term to allow for defects in the elementary treatment which originate from the nonorthogonality of the initial and final atomic eigenfunctions. Use of the (*ne* + *nn*) interaction leads to serious mathematical complexity in even the simplest case. However, with the aid of a high-speed computer, Mapleton[76] calculated $Q^{(ne+nn)}$ for the 1*s*–1*s*, 1*s*–2*s*, 1*s*–2*p*, 1*s*–3*s*, 1*s*–4*s*, 1*s*–5*s*, and 1*s*–3*p* transitions. It is observed that $Q^{(ne+nn)}$ is smaller than the corresponding $Q^{(ne)}$ by a factor which varies only slowly with the impact energy and which is almost independent of the transition.

Similar calculations on

$$H(1s) + He^{2+} \rightarrow H^+ + He^+(1s, 2s, \text{or } 2p) \tag{24}$$

were carried out by Schiff,[77] but distortion effects arising from the Coulomb repulsion between the products were not properly taken into account.

It is now known that direct use of neither the (ne) or $(ne + nn)$ interaction is correct, although the use of these simple interactions yields results which possess the correct general characteristics and which may be quite accurate.

The defects in this elementary treatment of the problem originate from the nonorthogonality of the initial and final atomic eigenfunctions. Explicit account of the nonorthogonality has been taken by Bates[78] and by Bassel and Gerjuoy[79] in deriving a more complex interaction potential. An improved version was used by McCarroll[80] to evaluate the charge-transfer cross section $Q^{(\text{ortho})}$ for H^+–H collisions.

None of the processes involving only one electron has been studied experimentally in the high-energy region. Measurements on processes involving several electrons are available, but the significance of any comparison which may be made with theory is obscured by the uncertainty due to the approximate eigenfunctions used in the calculations.

A number of detailed calculations on processes involving several electrons have been carried out. The earliest were those of Bransden, Dalgarno, and King,[81] who evaluated

$$Q^{ne}(1s^2/1s, 1s) \quad \text{for} \quad \text{He}(1s)^2 + \text{H}^+ \rightarrow \text{He}^+(1s) + \text{H}(1s) \tag{25}$$

representing the normal helium atom by a rather crude variational eigenfunction.

Subsequently, Mapleton[82] calculated $Q^{(ne+nn)}(1s^2/n'l', n''l'')$ for the additional $/n'l', n''l'')$ combinations: $/1s, 2s)$, $/1s, 2p)$, $/1s, 3s)$, $/1s, 3p)$, $/1s, 3d)$, $/2s, 1s)$, $/2p, 1s)$, $/2s, 2s)$, $/2s, 2p)$ and $/2p, 2s)$. From the results he was able to calculate the cross section

$$Q^{(ne+nn)}(1s^2/\Sigma\Sigma) = \sum_{n'l', n''l''} Q^{(ne+nn)}(1s^2/n'l', n''l'') \tag{26}$$

for $\text{He}(1s^2) + \text{H}^+ \rightarrow \text{He}^+ + \text{H}$. All the calculations were done with the post and prior forms of the $(ne + nn)$ interaction, which lead to different cross sections because of the approximate nature of the helium eigenfunction. The post and prior values of the total cross section $Q^{(ne+nn)}(1s^2/\Sigma\Sigma)$ do not differ by more than 20%, and in Figure 26 a comparison is made between the mean of these values and the measured cross sections of Stier and Barnett,[28] Barnett and Reynolds,[83] and Allison.[2]

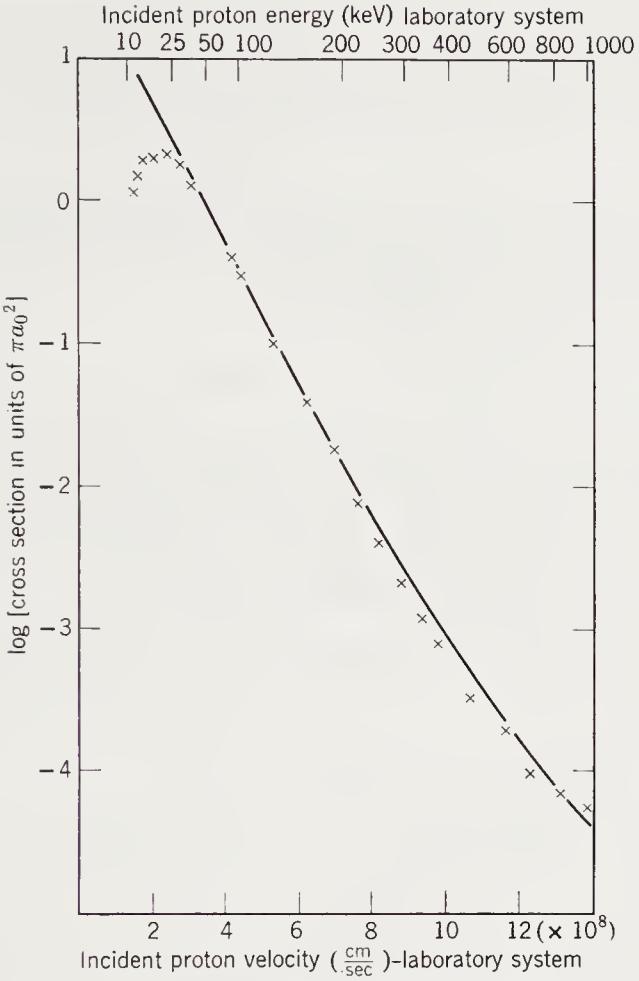

Fig. 26. Electron capture from helium atoms by protons. The full line is the arithmetic average of the total capture cross sections calculated by Mapleton[82] using the prior and post interactions. The crosses represent measurements by Stier and Barnett,[28] Barnett and Reynolds,[83] and Allison.[2]

Tuan and Gerjuoy[84] have studied

$$H_2(X'\Sigma_g^+) + H^+ \rightarrow H_2^+(1s\sigma^2\Sigma_g^+ \quad \text{or} \quad 2p\sigma^2\Sigma_u^+) + H(1s)$$

and showed that, in contradiction to earlier belief, a hydrogen molecule may not be regarded as approximately equivalent to two hydrogen atoms as far as charge transfer at high energies is concerned.

Effects arising from the difference between the interaction on the colliding systems when the initial state and in the final state may be

quite important for charge transfer. In symmetric resonance, there are no such distortion effects because the initial and final states are identical. However, McCarroll and McElroy[85] found that for the process

$$H(1s) + He^{2+} \rightarrow H^{+} + He^{+}(1s) \tag{27}$$

distortion raises the cross section considerably at moderate energies because the Coulomb repulsion reduces the separation between the initial and final potential energy surfaces.

McElroy[86] has also considered

$$H(1s) + He^{2+} \rightarrow H^{+} + He^{+}(2s, 2p) \tag{28}$$

which is of special interest because it is an example of accidental energy resonance. If no allowance is made for distortion, the cross sections tend to infinity with decreasing energy. When allowance is made for distortion, however, the cross section tends to zero in the manner determined experimentally by Fite, Smith, and Stebbings.[45]

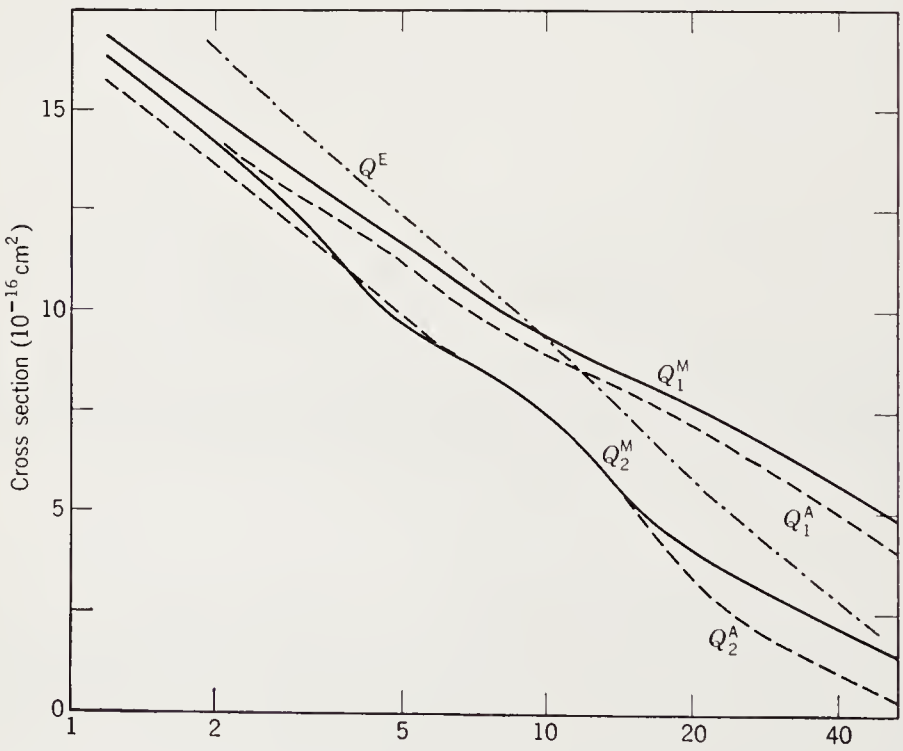

Fig. 27. Comparison of theory and experiment for proton–hydrogen atom charge transfer. The energy of the incident protons is given in units of keV.

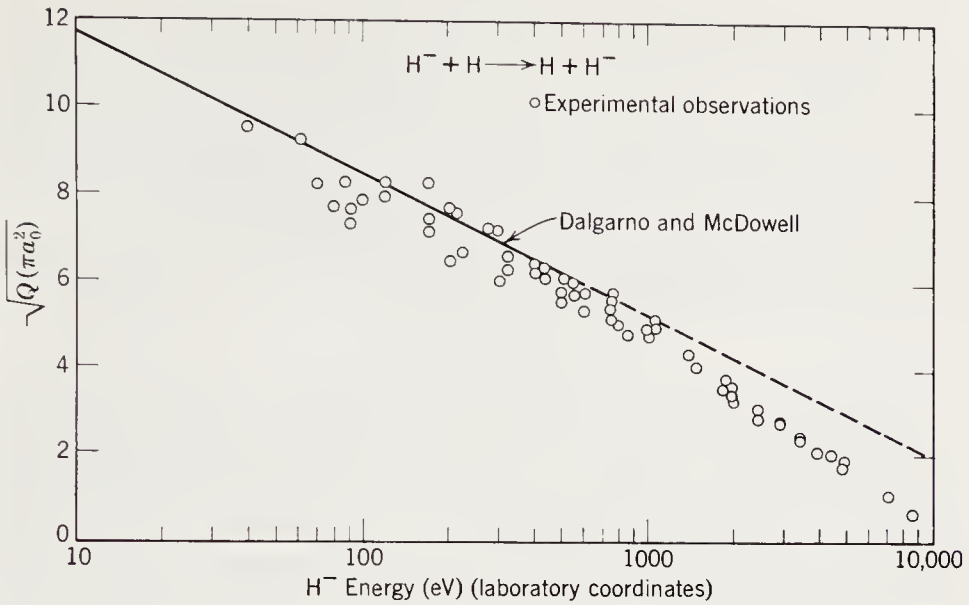

Fig. 28. Cross section for charge transfer between H^- ions and hydrogen atoms. The experimental observations of Hummer et al.[46] are compared with the *pss* calculation of Dalgarno and McDowell.[92]

B. Low-Velocity Region

When the velocity of relative motion of the two atomic systems becomes much smaller than the orbital velocity of the bound electron, the process may be treated as semiadiabatic, and the method of perturbed stationary states[87] may be employed. In this approximation the wave function describing the colliding systems is expanded, using the set of eigenfunctions of the quasi-molecule formed in the collision. Ferguson[88] has obtained the cross section for symmetric resonance charge transfer in H^+–H collisions in this way and his results are shown in Figure 27. In deriving Q_2^M, account was taken of the change in the translational motion of the active electron, while allowance for this was excluded in evaluating Q_1^M. Q_1^A and Q_2^A are the corresponding cross sections obtained by McCarroll[80] based on an expansion in atomic eigenfunctions using the high-velocity approximation. At low energies, Q_2^M should be most accurate and at high energies Q_2^A should be most accurate. In agreement with the early experimental data of Fite et al.,[89] Q^E for total charge transfer is quite satisfactory in the low-energy region and it is possible that the discrepancy at high energies is due to the contribution from nonresonant processes.

Cross sections have been obtained for the following simple resonance charge-transfer processes using the *pss* approximation without allowance for the effect of the change in the translational motion of the active electron: $H(1s)$–H^+ (Dalgarno and Yadav[90]); $H(2s, 2p)$–H^+ (Boyd and Dalgarno[91]); $H(1s)$–$H^-(1s)^2$ (Dalgarno and McDowell[92]); $He(1s)^2$–$He^+(1s)$, $He(1s^2)$–He^{2+} (Ferguson and Moiseiwitsch[93]).

Comparison of the H^-–H computations with the experimental data of Hummer et al.[46] is given in Figure 28.

C. Energy Resonance

A number of more complicated symmetrical resonance charge-transfer processes have been treated, using very approximate spherically symmetrical atomic wave functions (Firsov,[51] Demkov,[52] Gurnee and Magee,[94] Karmohapatro and Das,[95] Karmohapatro,[96] Rapp and Francis[9]). It has been shown in a number of treatments (Demkov,[52] Dalgarno and McDowell,[92] Iovitsu and Ionescu-Pallas[97]) that in the case of symmetrical resonance charge transfer, the cross section σ varies with velocity v as

$$\sigma = a - b \ln v \tag{29}$$

when a and b are constants for a given process. The treatments do not allow for the effect of the force between the systems upon their relative motion and therefore fail at sufficiently low velocities.

The cross sections for a number of resonant processes computed by Rapp and Francis[9] using the impact parameter method are shown in Figure 29.

It is seen that the magnitudes of the cross sections at a particular velocity are strongly dependent on the magnitude of the ionization potential, and for atoms other than those listed the cross sections may be determined by interpolation in terms of their ionization potentials. Agreement with the experimental values is in many cases quite satisfactory, particularly when cognizance is taken of the possibility that many experiments were complicated by nonresonant processes, arising from excited primary ions and capture into excited states.

In addition, Rapp and Francis have obtained approximate cross sections for a number of asymmetric nonresonant reactions, using a two-state approximation (cf. Bates and McCarroll[8]). These calculations were made in terms of the ΔE of the reaction and the "average" ionization potential of the two atoms. Comparison with experimental

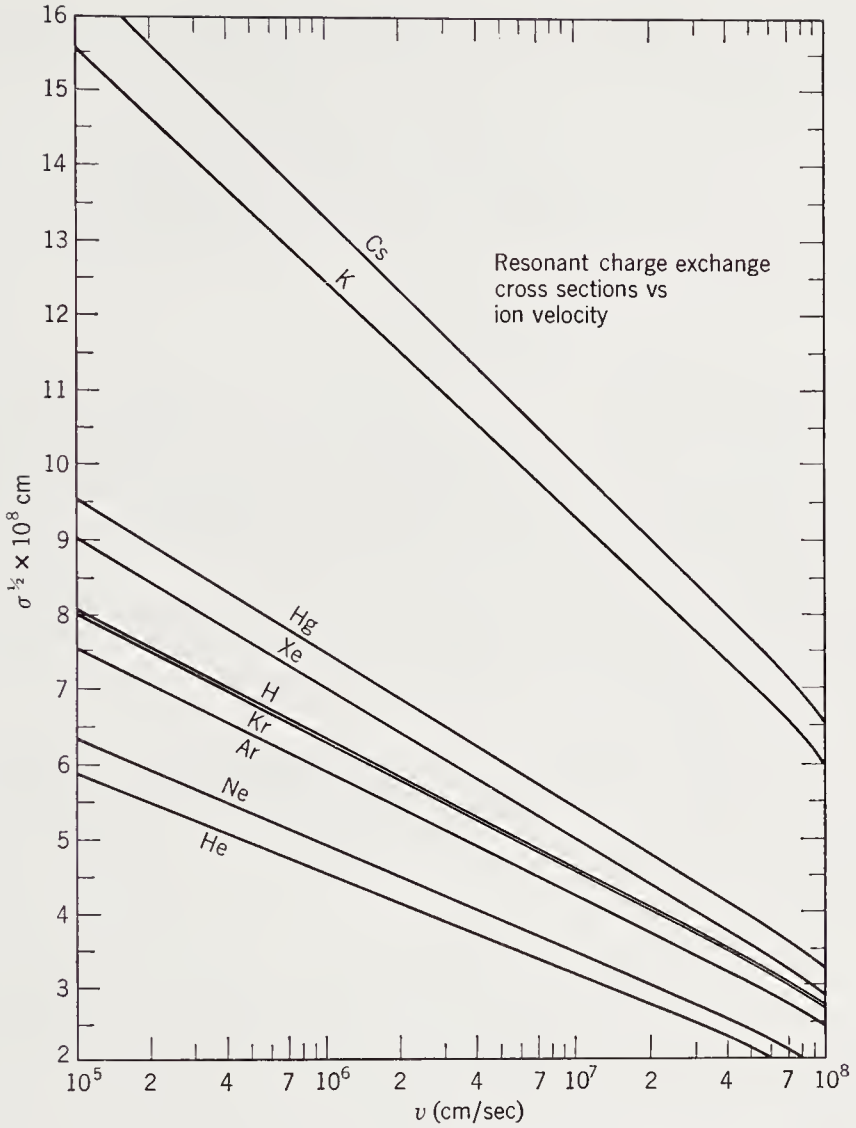

Fig. 29. Cross sections for resonant charge transfer between monatomic ions and their parent gases calculated by Rapp and Francis.[9]

data, which again probably include processes involving excited states, is not a reliable test of the theory, although qualitatively such a comparison suggests that the calculations give the correct energy variation of the cross section, but with some error in absolute magnitude. Rapp and Francis also indicate the approaches which may be used for extrapolating experimental data to lower velocities, where the impact parameter method is not applicable.

Accidental resonance charge transfer has been discussed in a number of theoretical[94,98] papers. Two processes of more than casual interest in this context are

$$O^+(^4S) + H(1s) \rightarrow 0(^3P_J) + H^+ \begin{Bmatrix} -0.01 \text{ eV } (J=0) \\ +0.00 \text{ eV } (J=1) \\ +0.02 \text{ eV } (J=2) \end{Bmatrix} \tag{30}$$

which is influential in determining the composition of the earth's high atmosphere[99] and

$$He^{2+} + H \rightarrow He^+(2p) + H^+ \tag{31}$$

which is a one-electron problem and may be treated theoretically with high precision.

Process (30) and the inverse reaction have been studied experimentally[45,49] (Figs. 15 and 16) and it is observed that within the measured energy range the energy variation of the cross sections is of the form characteristic of symmetric resonance charge transfer. Within the experimental uncertainty it is observed that at the same collision velocity the cross section for reaction (30) exceeds that for the inverse process by a factor of 9/8, a result in accord with simple statistical weight considerations.

Because O and H have the same ionization potentials, the cross sections for charge transfer in O^+–H collisions and H^+–H collisions

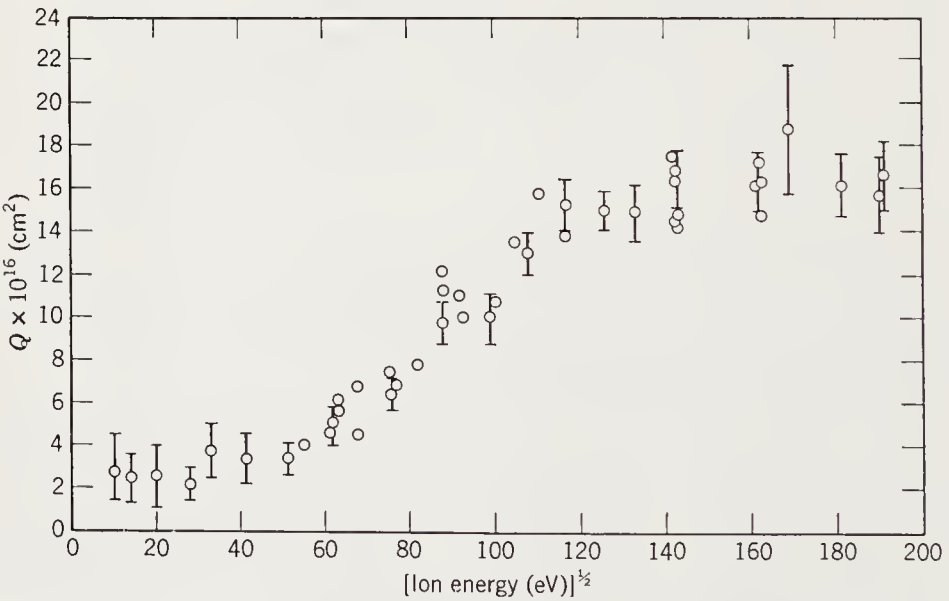

Fig. 30. Cross section for charge transfer between He^{2+} ions and atomic hydrogen measured by Fite, Smith, and Stebbings.[45]

should be approximately in the ratio 3/8, at velocities above that for the maximum cross section in the asymmetric process (Rapp and Francis). The experimental data indicate the ratio to be 0.35; in view of the very approximate nature of the theory, this agreement is good.

Process (31) has already been discussed; the nonresonance behavior observed experimentally (Fig. 30) is in keeping with theoretical predictions and arises from the Coulomb repulsion between the product ions.

References

1. H. S. W. Massey and E. H. S. Burhop, *Electronic and Ionic Impact Phenomena*, Oxford University Press, Oxford, 1952.
2. S. K. Allison, *Rev. Mod. Phys.*, **30**, 1137 (1958).
3. S. K. Allison and M. Garcia-Munoz, in D. R. Bates, Ed., *Atomic and Molecular Processes*, Academic Press, New York, 1962.
4. J. B. Hasted, *Advances in Electronics*, Vol. XIII, Academic Press, New York, 1960, p. 1.
5. J. B. Hasted, in D. R. Bates, Ed., *Atomic and Molecular Processes*, Academic Press, New York, 1962.
6. E. W. McDaniel, *Collision Phenomena in Ionized Gases*, Wiley, New York, 1964.
7. D. R. Bates, in D. R. Bates, Ed., *Atomic and Molecular Processes*, Academic Press, New York, 1962.
8. D. R. Bates and R. McCarroll, *Phil. Mag. Suppl.*, **11**, 39 (1962).
9. D. Rapp and W. E. Francis, *J. Chem. Phys.*, **37**, 2631 (1962).
10. F. Goldman, *Ann. Physik*, **10**, 460 (1931).
11. H. B. Gilbody and J. B. Hasted, *Proc. Roy. Soc.* (*London*), **A238**, 334 (1956); **A240**, 382 (1957).
12. H. B. Gilbody, J. B. Hasted, J. V. Ireland, A. R. Lee, E. W. Thomas, and A. S. Whiteman, *Proc. Roy. Soc.* (*London*), **A274**, 40 (1963).
13. W. H. Cramer and J. H. Simons, *J. Chem. Phys.*, **26**, 1272 (1957).
14. W. H. Cramer and A. B. Marcus, *J. Chem. Phys.*, **32**, 186 (1960).
15. N. G. Utterback and G. H. Miller, *Rev. Sci. Instr.*, **32**, 1101 (1961).
16. T. M. Donahue and F. Hushfar, *Phys. Rev. Letters*, **3**, 470 (1959).
17. T. L. Bailey, *Proceedings of the Thirteenth Gaseous Electronics Conference*, 1960.
18. D. E. Moe, *Phys. Rev.*, **104**, 694 (1956).
19. N. V. Fedorenko, V. V. Afrosimov, and D. M. Kaminker, *Soviet Phys. Tech. Phys.*, **1**, 1851 (1957).
20. E. Gustafsson and E. Lindholm, *Ark. Fys.*, **18**, 219 (1960); E. Pettersson and E. Lindholm, *ibid.*, **24**, 49 (1963); E. Lindholm, *ibid.*, **8**, 433(1954).
21. R. F Stebbings, A. C. H. Smith, and H. Ehrhardt, *J. Chem. Phys.*, **39**, 968 (1963).
22. F. Wolf, *Ann. Phys.*, **30**, 313 (1937).
23. F. J. LeBlanc, *J. Chem. Phys.*, **38**, 487 (1963).
24. C. F. Giese and W. B. Maier II, *J. Chem. Phys.*, **39**, 197 (1963).

25. J. B. Hasted, A. R. Lee, and M. Hussain, *Proceedings of the Third International Conference on the Physics of Electronic and Atomic Collisions*, North-Holland Publ. Co., Amsterdam, 1964.
26. F. Ribe, *Phys. Rev.*, **83**, 217 (1951).
27. J. H. Montague, *Phys. Rev.*, **81**, 1026 (1951).
28. P. M. Stier and C. F. Barnett, *Phys. Rev.*, **109**, 385 (1958); **103**, 896 (1956).
29. Yu. F. Bydin and A. M. Bukhteev, *Dokl. Akad. Nauk SSSR*, **119**, 1131 (1958).
30. I. P. Flaks and E. S. Solov'ev, *Soviet Phys. Tech. Phys.*, **3**, 564 (1958).
31. O. B. Firsov, *Soviet Phys. JETP* (*English Transl.*), **9**, 1076 (1959).
32. I. P. Flaks and E. S. Solov'ev, *Soviet Phys. Tech. Phys.*, **3**, 577 (1958).
33. J. W. McGowan and L. Kerwin, *Can. J. Phys.*, **41**, 316 (1963).
34. E. Everhart, R. J. Carbone, and G. Stone, *Phys. Rev.*, **98**, 1045 (1955); E. N. Fuls, P. R. Jones, F. P. Ziemba, and E. Everhart, *ibid.*, **107**, 704 (1957); P. R. Jones, F. P. Ziemba, H. A. Moses, and E. Everhart, *ibid.*, **113**, 182 (1957); G. J. Lockwood and E. Everhart, *ibid.*, **125**, 567 (1962).
35. F. P. Ziemba and E. Everhart, *Phys. Rev. Letters*, **2**, 299 (1959).
36. F. P. Ziemba and A. Russek, *Phys. Rev.*, **115**, 922 (1959).
37. F. P. Ziemba, G. J. Lockwood, G. H. Morgan, and E. Everhart, *Phys. Rev.*, **118**, 1552 (1960).
38. G. H. Morgan and E. Everhart, *Phys. Rev.*, **128**, 667 (1962).
39. N. V. Fedorenko, L. G. Filippenko, and I. P. Flaks, *Soviet Phys. Tech. Phys.*, **5**, 45 (1960).
40. G. N. Ogurtsov and I. P. Flaks, *Soviet Phys. JETP* (*English Transl.*), **15**, 502 (1963).
41. V. V. Afrosimov, Yu. S. Gordeev, M. N. Padov, and N. V. Fedorenko, *Ionization Phenomena in Gases*, SERMA, Paris, 1964.
42. D. M. Kaminker and N. V. Fedorenko, *Zh. Tekhn. Fiz.*, **25**, 2239 (1955).
43. A. Russek and M. T. Thomas, *Phys. Rev.*, **109**, 2015 (1958).
44. W. L. Fite, R. T. Brackmann, and W. R. Snow, *Phys. Rev.*, **112**, 1161 (1958).
45. W. L. Fite, A. C. H. Smith, and R. F. Stebbings, *Proc. Roy. Soc.* (*London*), **A268**, 527 (1962).
46. D. G. Hummer, R. F. Stebbings, W. L. Fite, and L. M. Branscomb, *Phys. Rev.*, **119**, 668 (1960).
47. R. F. Stebbings, W. L. Fite, and D. G. Hummer, *J. Chem. Phys.*, **33**, 1226 (1960).
48. R. F. Stebbings, A. C. H. Smith, and H. B. Gilbody, *J. Chem. Phys.*, **38**, 2280 (1963).
49. R. F. Stebbings, A. C. H. Smith, and H. Ehrhardt, *Proceedings of the Third International Conference on the Physics of Electronic and Atomic Collisions*, North-Holland Publ. Co., Amsterdam, 1964.
50. D. V. Chkuaseli, U. Nikoleishvili, and A. Guldamashvili, *Soviet Phys. Tech. Phys.*, **5**, 770 (1961).
51. O. Firsov, *Soviet Phys. JETP* (*English Transl.*), **21**, 1001 (1951).
52. Yu. N. Demkov, *Leningrad State University, Scientific Notes*, **No. 146**, 74 (1952).
53. L. L. Marino, A. C. H. Smith, and E. Caplinger, *Phys. Rev.*, **128**, 2243 (1962).
54. R. Speiser and R. Vernon, A. R. S. Rept. 2068-61, October, 1961.
55. R. Kushnir and I. Buchma, *Bull. Acad. Sci. USSR*, **24**, 989 (1960).

56. R. Kushnir, B. Palyukh, and L. Sena, *Bull. Acad. Sci. USSR Phys. Ser.* (*English Transl.*), **23**, 995 (1959).
57. A. Bukhteev and Yu. F. Bydin, *Bull. Acad. Sci. USSR Phys. Ser.* (*English Transl.*), **24**, 966 (1960).
58. H. von Kock and E. Lindholm, *Ark. Fys.*, **19**, 123 (1961); P. Wilmenius and E. Lindholm, *ibid.*, **21**, 97 (1962).
59. R. C. Amme and N. G. Utterback, *Proceedings of the Third International Conference on the Physics of Electronic and Atomic Collisions*, North-Holland Publ. Co., Amsterdam, 1964.
60. J. W. McGowan and L. Kerwin, *Can. J. Phys.*, **41**, 316 (1963); **41**, 1535 (1963); **42**, 2086 (1964).
61. P. Marmet, D.Sc. thesis, Laval University, Quebec, 1960.
62. N. P. Carleton and T. R. Lawrence, *Phys. Rev.*, **109**, 1159 (1958).
63. R. H. Hughes, S. Lin, and L. L. Hatfield, *Phys. Rev.*, **130**, 2318 (1963).
64. G. H. Dunn, R. Geballe, and D. Pretzer, *Phys. Rev.*, **128**, 2200 (1962).
65. R. T. Brackmann, W. L. Fite, and K. E. Hagen, *Rev. Sci. Instr.*, **29**, 125 (1958).
66. D. Pretzer, B. van Zyl, and R. Geballe, *Phys. Rev. Letters*, **10**, 340 (1963).
67. F. J. de Heer, J. van Eck, and J. Kistemaker, *Ionization Phenomena in Gases*, SERMA, Paris, 1964.
68. J. L. Philpot and R. H. Hughes, *Phys. Rev.*, to be published.
69. F. Cristofori, G. E. Frigerio, N. Molho, and P. G. Sona, *Ionization Phenomena in Gases*, SERMA, Paris, 1964.
70. H. I. Mandelberg, *Ionization Phenomena in Gases*, SERMA, Paris, 1964.
71. A. C. Riviere and D. R. Sweetman, *Proceedings of the Fifth International Conference on Ionization Phenomena in Gases*, Vol. II, North-Holland Publ. Co., Amsterdam, 1962, p. 1236.
72. H. C. Brinkman and H. A. Kramers, *Koninkl. Ned. Akad. Wetenschap. Proc.*, **33**, 973 (1930).
73. J. R. Oppenheimer, *Phys. Rev.*, **51**, 349 (1928).
74. D. R. Bates and A. Dalgarno, *Proc. Phys. Soc.*, **A65**, 919 (1952).
75. J. D. Jackson and H. Schiff, *Phys. Rev.*, **89**, 359 (1953).
76. R. A. Mapleton, *Phys. Rev.*, **126**, 1477 (1962).
77. H. Schiff, *Can. J. Phys.*, **32**, 393 (1954).
78. D. R. Bates, *Proc. Roy. Soc.* (*London*), **A247**, 294 (1958).
79. R. H. Bassel and E. Gerjuoy, *Phys. Rev.*, **109**, 335 (1958).
80. R. McCarroll, *Proc. Roy. Soc.* (*London*), **A264**, 547 (1961).
81. B. H. Bransden, A. Dalgarno, and N. M. King, *Proc. Phys. Soc.*, **A67**, 1075 (1954).
82. R. A. Mapleton, *Phys. Rev.*, **122**, 528 (1961).
83. C. F. Barnett and H. K. Reynolds, *Phys. Rev.*, **109**, 355 (1958).
84. T. F. Tuan and E. Gerjuoy, *Phys. Rev.*, **117**, 756 (1960).
85. R. McCarroll and M. B. McElroy, *Proc. Roy. Soc.* (*London*), **A226**, 422 (1962).
86. M. B. McElroy, *Proc. Roy. Soc.* (*London*), **A272**, 542 (1963).
87. N. F. Mott and H. S. W. Massey, *Theory of Atomic Collisions*, 2nd ed., Oxford Clarendon Press, 1933.
88. A. F. Ferguson, *Proc. Roy. Soc.* (*London*), **A264**, 540 (1961).

89. W. L. Fite, R. F. Stebbings, D. G. Hummer, and R. T. Brackmann, *Phys. Rev.*, **119**, 663 (1960).
90. A. Dalgarno and H. N. Yadav, *Proc. Phys. Soc.*, **A66**, 173 (1953).
91. T. J. M. Boyd and A. Dalgarno, *Proc. Phys. Soc.*, **72**, 694 (1958).
92. A. Dalgarno and M. R. C. McDowell, *Proc. Phys. Soc.*, **A69**, 615 (1956).
93. A. F. Ferguson and B. L. Moiseiwitsch, *Proc. Phys. Soc.*, **A74**, 457 (1959).
94. E. F. Gurnee and J. L. Magee, *J. Chem. Phys.*, **26**, 1237 (1957).
95. S. B. Karmohapatro and T. P. Das, *J. Chem. Phys.*, **29**, 240 (1958).
96. S. B. Karmohapatro, *J. Chem. Phys.*, **30**, 538 (1959).
97. I. P. Iovitsu and N. Ionescu-Pallas, *Soviet Phys. Tech. Phys.*, **4**, 791 (1960).
98. D. R. Bates and N. Lynn, *Proc. Roy. Soc.* (*London*), **A253**, 141 (1959).
99. A. Dalgarno, *Ann. Geophys.*, **17**, 16 (1961).

7. ION–NEUTRAL REACTIONS

C. F. GIESE

Department of Physics, University of Chicago, Chicago, Illinois

CONTENTS

I. Introduction 247
II. General Comments 248
III. Recent Refinements in Technique 250
IV. Low-Energy Charge Transfer 252
A. Energetics of Reactions 252
B. Low-Energy Asymmetric Near-Resonance Charge Transfer 254
C. Threshold Behavior of Endothermic Charge Transfer 256
V. Ion–Molecule Reactions 258
A. Information Obtained from Variation of Electron Energy 258
B. Temperature Effects 259
C. Repeller Effects 260
D. Isotopic Effects 262
E. Persistent Complexes 264
F. Theory of Ion–Neutral Reactions 265
VI. Miscellaneous Aspects of Ion–Neutral Reactions 268
VII. Future Prospects 269
References 271

I. INTRODUCTION

The subject of low-energy ion–neutral reactions has enjoyed very intensive coverage by reviewers.[1,2] Rather than add an additional and unnecessary compendium of apparatus descriptions and tables of data on the huge number of reactions which are now known, the present reviewer chooses to stress the high points of the subject, the problems which need more work, and suggestions for future progress. References directly relevant have been cited, but no particular attempt has been made to mention every recent paper. Mass spectrometric measurements predominate, because the author is a mass spectroscopist. Ion mobility and gas discharge measurements are neglected almost entirely.

During the last few years there have been many improvements in technique. The results from these more powerful methods show the need for refinements in theory, and these refinements are beginning to appear. A heightened interest in the interplay between theory and experiment, as well as the great practical interest in ion-neutral interactions in astrophysics, plasma physics, and radiation chemistry, should make this an exciting corner of chemical physics for some time to come.

II. GENERAL COMMENTS

The general low-energy ion–neutral reaction is

$$A^+ + B \rightarrow C^+ + D \quad \text{or} \quad A^- + B \rightarrow C^- + D \tag{1}$$

A, B, C, and D can be quite general. The subject thus includes elastic or inelastic scattering in which only energy is transferred, charge transfer, and interactions in which at least one heavy particle is transferred, i.e., chemical-type reactions. Elastic scattering dominates in mobility experiments, in which the effects observed are the result of many collisions. The complex task of interpreting these experiments in terms of single scattering encounters is a subject unto itself, and is not covered in this review. Low-energy charge transfer has aspects in common with the chemical-type ion–neutral reactions, and so both of these subjects are treated in this review.

The subject of single-encounter elastic and inelastic but nonreactive scattering of ions is relatively untouched. There has been a great increase in measurements recently on the comparable processes for electrons, and the next few years may bring about the same development for ions.

The experimental problem in studying reactions is one of specifying as many parameters of the reaction as possible. Ideally one would want to specify the precise states of A^+, B, C^+, and D, including rotational angular momentum, and the angle of emergence of, say, C^+, relative to the direction of travel of A^+. All present experiments fall far short of this ideal.

Let us consider first the primary ion A^+. Except for glow discharge experiments, and one or two cases in which photoionization was used,[3] and possibly field ionization,[4] the ions are currently all obtained by electron impact ionization. The limitations upon the selection of A^+ are thus precisely the limitations of electron impact spectroscopy. Obviously, one can use a low electron energy and discriminate against

excited states, but one cannot obtain a pure beam of excited states. State selection on the basis of magnetic or electric moments by deflection in inhomogeneous fields is not possible because of the charge on the ions. Limitation to low-energy states by using low-energy electrons can be done only when sufficient sensitivity is available to accommodate the low primary ion intensity thus obtained. Rotational energies are essentially the thermal distribution appropriate to the ion source temperature, and no attempt has yet been made to control this parameter alone, independent of all others. The control over ion kinetic energy depends on the technique used. In the classic mass spectrometric studies, the ion source chamber is also the reaction chamber, and ion kinetic energies vary between thermal energy and some maximum determined by the ion extraction voltage applied across the reaction chamber. In these experiments, the primary ion identity itself must be determined from the variation of secondary ion intensity with electron energy, along with corroborative information of various sorts. A variation due to Čermák permits use of a conventional ion source in a way which provides better control over primary ion energy. To obtain better control over the primary ion identity and kinetic energy, one may use a separate ionization chamber with differential pumping and/or a mass analyzer between it and the reaction chamber. In these experiments, the premium is upon low-energy ions, particularly when mass analysis is used, because it is very difficult to operate a mass spectrometer at low voltage and still transmit a useful current of ions.

The identity of the reactant B is usually unambiguous, particularly if A^+ and C^+ are identified. Separate differential pumping of the reaction chamber is the surest technique. Up to the present, atoms or molecules which have appreciable vapor pressure at room temperature or slightly elevated temperatures have been used primarily for the target particles B, except for the case of hydrogen atoms[41] or oxygen atoms.[104] The states of B are governed in general by the appropriate thermal energy distribution. Specific state selection by inhomogeneous fields seems some way off at present, because of the low neutral beam densities which can be obtained this way, even using focusing devices.

The identification of C^+ is trivial if a mass spectrometer is used, but the states of C^+ and D are obtainable only indirectly. In principle one could detect C^+ and D in coincidence, passing D through some state-selecting device, but this is very difficult at present, again because of intensity problems. Determination of the angle of emission of C^+ is now

possible, giving differential cross sections, but it is a difficult experiment and can be done only at moderately high ion kinetic energies and with fairly large cross sections.

III. RECENT REFINEMENTS IN TECHNIQUE

Refinements in technique in this area are occurring rapidly. A number of workers are now attempting to study ion–neutral reactions with a mass-analyzed or otherwise selected ion beam which interacts with the neutrals in a reaction chamber, the products from which are then analyzed with a mass spectrometer. Lindholm's pioneering work using two mass spectrometers has resulted in a whole series of reports[5–13] primarily on charge-transfer and charge-transfer induced dissociations. Lehrle, Robb, and Thomas[14] describe a time-of-flight mass spectrometer which has a separate ion source for production of primary ions. No mass selection is used here, but with differential pumping and control of electron energy, considerable discrimination can be achieved in selection of primary ions. Ions are retarded from 1 or 2 kV down to final energies as low as about 30 eV. Tal'roze and co-workers[15] have described an apparatus with one sector-field mass spectrometer which transmits a primary ion beam at right angles to the ion chamber of a second sector-field instrument. A review by Tal'roze[1] describes some results obtained with this apparatus, notably the reaction $Xe^+ + C_2H_4 \rightarrow CH_2^+ + Xe + CH_2$, which has an abrupt onset at approximately the expected energetic threshold. In all of these, the primary ion beam passes at right angles to the direction of extraction of secondaries. In Lindholm's case this is done specifically to discriminate as much as possible against reactions in which appreciable momentum transfer occurs between projectile ion and target molecule. If one wishes to study cases in which momentum transfer occurs, it is more convenient to pass the primary ion beam longitudinally through the reaction chamber. The second, or analysis, mass spectrometer can then be used to measure either the primary or secondary ion currents. Giese and Maier[16,17] have described such an arrangement using a 1-inch radius, 90°, round pole primary spectrometer combined with a 12-inch, 60°, sector-field instrument. It has proved possible to obtain usable ion currents at kinetic energies down to less than 1 eV, often without retardation or with relatively little retardation. The use of the apparatus for endothermic reaction studies[16] clearly shows that the energies of the ions are well defined even at these

low energies. The equipment has been used successfully without any differential pumping of the primary ion source and the reaction chamber; however, this lack has handicapped the measurements, and now the ion source and reaction chamber are both differentially pumped,[18] with the result that background problems and problems of specification of the reactants are very much reduced.

Čermák and Herman[19] have developed a very clever technique for achieving a degree of selection of the primary ion energy, using just a conventional mass spectrometer ion source with electron collector, or trap, beyond the ionization chamber. The electrons pass through the ionization chamber at an energy e_0 below the ionization potential in question, and then are accelerated to above the threshold e_T as they approach the positive (e_p relative to ionization chamber) trap electrode. Primary ions are thus produced which are accelerated backwards and enter the ionization chamber with an energy distribution which starts at $e_T - e_0$, builds up to a peak at e_p, and cuts off beyond. These primary ions proceed across the ionization chamber, producing secondary ions by reactions. By careful choice of the voltages, a fairly narrow band of primary ion energies can be selected. This particular mechanism for production of secondary ions was also observed by Crable and Kearns.[20]

A variation is to use a trap electrode which has a deep cavity in it and which thus serves as an equipotential ionization chamber.[21,22] This produces a more nearly monoenergetic primary ion beam. The Čermák technique is now in use in a number of laboratories.[21–24] It is possible to achieve very strong discrimination against detection of primary ions, so that secondary ions are much easier to distinguish.

Tal'roze[1] has described a pulsing technique for varying the residence time of primary ions within the ion source, using a pulsed electron burst followed by pulse ion drawout. Recently, a number of workers[25–31] have improved differential pumping to the extent that very high pressures in the range up to 1.0 torr can be used in the ionization reaction chamber, enabling them to detect relatively improbable reactions, to use as the ionizing agency α or β rays, and to detect consecutive reactions or higher order reactions.

Fite and co-workers[32] have succeeded in performing crossed-beams experiments on a few reactions and getting the angular distribution of the products.

By monitoring with a mass spectrometer the ions emerging from afterglows as functions of time after pulsing the discharge, Fite and co-

workers[33] are able to study reactions of ions with neutrals in the afterglows. Knewstubb and Tickner[34–36] have described an apparatus for the mass spectroscopy of steady-state glow discharges, and have discussed the information on reactions of ions which can be obtained with the apparatus, with the notable inclusion of termolecular, i.e., three-body, reactions.

IV. LOW-ENERGY CHARGE TRANSFER

In low-energy charge transfer there are three interesting matters: the energetics of charge transfer-induced dissociations of molecules, the behavior of the cross section for exothermic near-resonance charge transfer at very low energies, and the problem of threshold behavior for endothermic charge transfer.

A. Energetics of Reactions

Lindholm, with co-workers, in a long series of papers,[5–13] has investigated charge transfer-induced dissociation processes in molecules. In these studies he makes the attractive assumption that the ion kinetic energy does not enter into the picture at all, and the ion upon neutralization delivers to the target molecule an amount of energy equal to the difference in total energy of the initial ion, often excited, and the neutralized ion, again often excited. This difference, called the recombination energy, or RE, by Lindholm, can assume a rather large number of values in many cases. Nevertheless, Lindholm is able to extract from the cross-section measurements rather detailed fragmentation patterns for methanol, ethanol, propane, and butane, as well as information on the dissociation of H_2, N_2, and CO. The technique is therefore competitive with, and is to be compared with, electron and photon impact studies of ionization and fragmentation. These comparisons are made in the relatively few cases where they are possible.[9,10,12,13]

In general, one may say that qualitatively and, within limits, quantitatively, the comparison is satisfactory. This shows that the ion impact technique certainly can give information on dissociation processes. Close comparison with other measurements, however, reveals some pronounced differences. An example is the mass 43 fragment from propane,[12] for which Lindholm gets an appearance potential of over 12 eV, while photoionization[37] gives 11.5 eV *or less*. The behavior near the threshold in Lindholm's experiment seems to be based primarily on

COS^+ and CH_3OH^+ as projectile ions. The recombination energies for both of these are very uncertain. That selected for COS^+, for example, is but one of a number of spectroscopically acceptable values. Thus the difference in this specific case may be explained, but it appears that at present, the method is not in general reliable for energy resolution of better than perhaps 0.5 eV.

The role of ion kinetic energy in the reactions is not fully clear. Its influence is probably reduced when the ion kinetic energy is very low, but then the probability for forming stable neutral products is increased. This possibility, ignored in the analysis, would complicate the energetics. Further, the analysis of the cross sections to give fragmentation curves is so complicated and involves so many judgments that one wonders whether the curves are unique.

Tal'roze[38] has obtained some information on the importance of ion kinetic energy. Cases in which ion kinetic energy clearly is important are the dissociative ionization of N_2 and CO. These involve rare-gas ions whose recombination energies are well defined. The dissociative ionization of CO by He, Ne, and Ar ion impact has been studied by Giese and Maier[16] using longitudinal geometry[17] rather than transverse geometry as in Lindholm's apparatus.[9] The endothermic processes involving Ne^+ and Ar^+ show sudden onsets with ion kinetic energy. The thresholds in ion kinetic energy lead, using known ionization potentials and assuming that ground-state products are formed, to $D(CO) = 11.1 \pm 0.2$ eV, in good agreement with the accepted bond energy. Since at threshold all product particles must be brought to the same velocity (or have zero velocity in the barycentric system), a rather intimate collision must be involved. Thus these are perhaps not charge-transfer processes in the usual sense, and are not to be interpreted in terms of the Massey criterion,[39] which would predict a very small cross section, with the energy defects involved, at these low ion energies. The cross sections for these processes are quite large, in the range of geometrical cross sections, showing that in an intimate collision the interconversion of translational and electronic energy proceeds rather efficiently. Recent measurements[18] show that ion impact-induced dissociations of N_2 and N_2O also give cross sections with sharp onsets. The thresholds for N_2 agree with the presently accepted (9.76 eV) N_2 bond energy. Tal'roze[1] has measured the cross section for the reaction $Xe^+ + C_2H_4 \rightarrow Xe + CH_2^+ + CH_2$ in the vicinity of the threshold, obtaining evidence for a rather abrupt onset at threshold.

B. Low-Energy Asymmetric Near-Resonance Charge Transfer

An interesting problem attracting much attention in recent years is the behavior, as ion kinetic energy approaches zero, of the cross section for charge transfer in the case of near-resonant exothermic processes. The most discussed[40] case is the reaction

$$O^+(^4S) + H(1s) \rightarrow O(^3P_J) + H^+ \quad \begin{cases} -0.01 \text{ eV}, J = 0 \\ +0.00 \text{ eV}, J = 1 \\ +0.02 \text{ eV}, J = 2 \end{cases} \tag{2}$$

which is of great importance to ionic equilibrium in the ionosphere. The topic is discussed here, even though the lowest energy at which experimental results[41] are available up to now is about 25 eV. (A further discussion will be found in the article by Stebbings in this volume.)

In symmetric resonance, owing to the symmetry of the potential, one does not describe the state of the system as a single electron eigenfunction, but rather as a linear combination of the gerade and ungerade electron eigenfunctions. For example, the simple sum of gerade and ungerade functions represents the electron situated entirely on one atom. This is the initial state. As the encounter proceeds, the *phases* of the coefficients change because at finite distances the gerade and ungerade combinations have different energy. The change in phase means that when the particles separate, there is some probability that the electron has transferred from one charge center to the other.

The case of asymmetric resonance is quite different. Here the two atoms are distinguishable, and even though the states of the separate systems which correspond to the electron being on one atom or the other are degenerate or nearly so, they correspond to different electronic states. Charge transfer now means a transition between these states.[42] Perfectly adiabatic behavior would then result in no charge transfer at all, since as the internuclear distance decreases to a minimum and then increases, the system would simply avoid all crossings and reemerge in the same state it started out in.[43] The theoretical problem is then to treat, at low velocities of encounter, the delicate interplay of the off-diagonal elements of the interaction Hamiltonian, which tend to produce a transition between the two states, and the diagonal elements. If these diagonal elements are very different, it means that the energies of the two states are different, and this difference inhibits transitions at low velocities. Recent theoretical treatments have differed primarily in their treatment of these diagonal elements.

Bates and Lynn[42] regarded the difference in diagonal matrix elements

as decisive and concluded that reactions such as (2) would have small cross sections at low energy. They also pointed out, however, that the attractive potential between ion and neutral increases their relative velocity and that proper account must finally be taken of this effect.

Rapp and Francis,[44] in their calculations of cross sections, use spherical hydrogen-like orbitals to represent the electron on either charge center. With these, for exact resonance, the diagonal matrix elements are equal and the separation of states does not occur. They treat no other assumption. The authors also consider the effect of the polarization force and conclude that for resonant asymmetric charge transfer, the cross section will probably be determined by the critical impact parameter at which classical orbits lead into direct collisions. The cross section would then go as $1/v$ as predicted for ion–molecule reactions.[45]

In a later paper, Bates[46] performs calculations in which he at first neglects the differences in diagonal matrix elements, later estimating their importance only for the case of fairly large energy deficit.

The authors above have used the "impact parameter method" in which the influence of any forces in the encounter upon the trajectory of the particles is ignored. Takayanagi[47] treats the relative motion quantum-mechanically. It is then apparently sufficient to assume a finite exothermicity for the reaction to show that the outgoing wave representing charge-transfer products remains finite as ion kinetic energy goes to zero.

The most direct experimental evidence on this matter is contained in a paper by Fite et al.,[41] who give the cross section for the reaction (2) down to a laboratory energy of 25 eV, or 1.47 eV in the barycentric system. Down to this energy, the cross section is like that of a resonance process. The authors point out, however, that the dropoff suggested by Bates and Lynn may still occur at lower energies, it being difficult or impossible at present to state exactly at what energy the dropoff will occur, if at all. They also have measured the cross section for $He^{2+} + H \rightarrow He^{+} + H^{+}$, which for He^{+} in the $2s$ or $2p$ state is in near energy resonance. Two problems exist here. The experimental cross section includes all possible states of He^{+}. Further, this case is different because the coulomb repulsion between He^{+} and H^{+}, which is not present between He^{2+} and H, spreads the two states, between which there must be a transition for charge transfer to take place, so far apart in energy as to inhibit transition and prevent resonance-like behavior. The experimental cross section does show rather a nonresonant form.

Rapp[40] summarizes the experimental and theoretical situation and concludes that the cross section for reaction (2) for ionosphere velocities (4.5×10^5 cm/sec) is very likely greater than 2×10^{-16} cm^2 and is probably more like 20×10^{-16} cm^2. This is done by comparing the results of Fite et al.[41] with the theoretical curves of Rapp and Francis,[44] for various energy defects ΔE. This very probably settles the issue as far as the role of reaction (2) in the ionosphere is concerned.

It appears very likely now that processes of the type $A^+ + B \rightarrow A + B^+$, for which accidental resonance or near-resonance obtains, do have very large cross sections at low energies and one has a choice of theoretical explanation for this behavior. The case of $A^{2+} + B \rightarrow A^+ + B^+$ is quite different, and this is easily understood. For further understanding of the behavior of the former type of reaction, a number of experiments should be of great value. Further refinement of techniques will permit reaction (2) to be studied at still lower ion kinetic energy. A study of $O^+(^2D) + N_2(X^1\Sigma_g^+, v = 0) \rightarrow O(^3P) + N_2^+(A\ ^2\Pi_u, v = 1)$ would be highly interesting since it is a case of near-resonance like reaction (2) but of less symmetrical character.[42] Further, it is worthwhile to study molecular cases such as $AA^+ + AA \rightarrow AA + AA^+$ as well as $AB^+ + AB \rightarrow AB + AB^+$ down to very low energies to test the proposition of Bates and Lynn[42] that these are not really to be regarded as cases of symmetric resonance. Stebbings, Turner, and Smith[48] have measured charge-transfer coefficients for O_2, N_2, NO, O, N, and NO ions in the molecular gases down to 30 eV, using a crossed-beams method. The cross sections remain quite large for all processes down to low ion kinetic energy and for molecular ions in their parent gases, the cross sections increase rapidly at low energies. Henglein and Muccini[24,49] have obtained some results on molecular resonance charge transfer which seem to indicate that the cross sections are quite large for primary ion energies from 5 to 40 eV. Curran[50] has evidence for large cross sections at very low ion kinetic energies for the charge-transfer process $X^- + NO_2 \rightarrow NO_2^- + X$, with X = O, SF_6, SF_5, and Cl. Similar results[51] for X = CS and NH_2 have also appeared.

C. Threshold Behavior of Endothermic Charge Transfer

If a charge-transfer process is endothermic, then there will be some ion kinetic energy below which charge transfer is not possible. This ion kinetic energy is that energy which, converted to energy in the barycentric system, equals the energy defect. The Massey criterion,[39] however,

predicts that the cross section near threshold will be very small since in the adiabatic region it varies as

$$K \exp[-a|\Delta E|/4hv] \tag{3}$$

(see Section II-A in the chapter on "Charge Transfer"). This equation, and indeed the present state of theory in the near-adiabatic region, gives no information on absolute cross sections, i.e., on the constant K, and experimental results at low energy are scanty as well. Some charge-transfer cross sections at fairly low energies are anomalously large,[52] however, giving some hope that near threshold the cross section may still be large enough to measure.

Very recently at this laboratory[53] the cross section for the reaction

$$Kr^+ + D_2 \rightarrow D_2^+ + Kr \tag{4}$$

has been measured just above threshold. At the expected threshold energy for this endothermic, pure charge transfer reaction, which is 17 eV in the laboratory system for the $^2P_{1/2}$ state of Kr^+, the cross section rises sharply. Above 40 eV and up to 100 eV. the cross section is almost flat and has a value of roughly 10^{-17} cm^2. This case is only one step removed from the simplest system, namely, atomic ion + atom. This one step may be decisive, however, because a triatomic composite system may have a lifetime against breakup which is long compared with the lifetime of the diatomic system. During this lifetime, enough mixing of states may occur so that the particular channel involved in reaction (4) becomes accessible. The question as to whether abrupt onsets occur for atomic charge transfer at threshold remains, and should be given some attention.

Another possibility is that of determining the ionization potentials of large molecules. There is good evidence[37] that for many molecules the vertical ionization potential measured in photoionization or electron impact ionization is far above the energy for an adiabatic transition giving the true ionization potential. The reason is apparently that the shapes of ground-state molecule and ion are different and the Franck-Condon principle, well obeyed in a fast transition, makes a transition to the ground-state ion very unlikely. In a slow process such as an ionic charge-transfer collision, however, there may be enough time for readjustment so that the adiabatic transition becomes possible.

V. ION–MOLECULE REACTIONS

Reactions involve the transfer of a heavy particle or a more complicated rearrangement, rather than simply the transfer of an electron. The number of known reactions is very large.[1,2] No attempt is made here to consider all types of reactions. Rather, the following sections discuss a variety of the more important aspects of the subject.

A. Information Obtained from Variation of Electron Energy

Perhaps the most informative technique for study of reactions, particularly when primary ions are formed by electron impact and react in the same chamber, is the variation of electron energy. In these cases it is the standard method for identification of the primary ion. When a product can be formed by either of two primary ions, one can hope to separate the contributions of the two primary ions by studying the variation of product ion and primary ions with electron energy, provided the appearance potentials of the primary are sufficiently different.[54,55] This type of experiment pushes the method to the extreme, however, and in general the manipulation of electron energy to study reactions is prey to all of the familiar difficulties of electron appearance potential measurements. Electrons from a filament have a rather large energy spread, and any energy analysis is accomplished only with a considerable loss in intensity. Contact potentials and stray fields are a problem and so is space charge unless electron currents are rather low. However, with proper calibration of the energy scale, much can be done in the identification of the primary ion, even to showing that excited ions are involved. A number of recent papers are good examples of the use of the technique. Henglein[56] reports on reactions of a variety of ground-state and excited ions, including a case involving acrylonitrile in which the reaction occurs *only* from the ground-state ion and not from the excited ion. Excited ions appear to live 10^{-6} sec or more. Čermák and Herman[57] demonstrate the apparent existence of the $^4\Sigma$ excited state of N_2^+ by observing the formation reaction of N_3^+ in N_2, varying the electron energy.

A refinement on the control of electron energy is the technique originated by Čermák and discussed in Section III. Henglein and Muccini[24,49] use the technique in studying many electron and proton transfer reactions. Their results are covered in other sections of this review.

If an ion–molecule reaction is endothermic for primary ions in their ground state, the difference in appearance potentials for primary and secondary ions gives the endothermicity of the reaction, provided ion kinetic energies are small or unimportant. One clear case in which the energetics are known is $H_2^+ + He \rightarrow HeH^+ + H$, for which the appearance potential difference is nicely consistent with the known endothermicity.[58–60]

B. Temperature Effects

One technique for investigating ion–molecule cross sections at low energies which at first glance has great appeal is to study the effect of temperature. Gioumousis and Stevenson[61] have treated the problem of formation of secondary ions in the ion source of a mass spectrometer in a thorough way, starting from a Boltzmann equation for the ion flux. The integration to obtain a total production rate becomes elementary because if the microscopic cross section σ varies as $1/v$, v being the relative velocity of ion and neutral (see Section V-F), then the product $v\sigma(v)$ appearing in the integral becomes simply a constant. The prediction is then that the phenomenological cross section Q will be independent of temperature. The experiments of Stevenson and Schissler[62] on ArH^+ and ArD^+ formation show no temperature dependence. Tal'roze,[1] however, has found some decrease with temperature, perhaps as $1/T$. For more complex systems, the temperature effect appears to be stronger. However, no experiments appear to show strong temperature effects.

Unfortunately it is difficult to vary the temperature of an ion source by more than say 300°C, equivalent to 0.03 eV in kinetic energy. Thus the variation in energy is relatively small compared with the energy an ion obtains after acceleration over a very short distance, even when a typical minimum repeller voltage of 0.5 V is used. Thus, when measurements show no temperature effect, one may say that this is consistent with an $E^{-\frac{1}{2}}$ or $1/v$ dependent cross section, but it is difficult to state how sensitive this measurement is, i.e., to what extent it rules out other forms of $\sigma(E)$. As an example, Boelrijk and Babeliowsky[63] have calculated some predicted phenomenological cross sections for the case in which $\sigma(E) = \sigma_1 E^{-\frac{1}{2}} - \sigma_H$ for $E \leqslant E_c$ and $\sigma = 0$ for $E > E_c$. For a case in which $E_c = 1.5$ eV and repeller voltage is 2 eV, the phenomenological cross section is predicted to drop only 5% from 400 to 600°K, showing

that even for a case which is quite different from a simple $E^{-\frac{1}{2}}$ dependence, the temperature effect is small.

It remains true, however, that varying the temperature is the best way to make small changes in the energy of the reactions. For good sensitivity to any temperature effect, one must have a weak ion drawout field. This could be done by making the primary ions by photoionization, passing the photon beam through a carefully designed reaction chamber in which the fields would be well known. No source magnet or electron space charge effects would interfere, and the absence of a hot filament would mean that the gas temperature could be precisely determined. This reaction chamber could be cooled or heated, thereby extending the possible temperature range. This experiment is now feasible, and is perhaps the best possibility for studying the very low energy behavior of cross sections. The precise selection possible with photoionization also means that the state of the primary ion could be better determined.

C. Repeller Effects

In experiments on ion–molecule reactions occurring in the ionization chamber of a mass spectrometer, the measured quantity is an effective cross section averaged over ion kinetic energies from thermal to a maximum determined by the voltage applied to a repeller electrode. This repeller electrode is typically just a plane element located behind the ionization volume, producing an approximately uniform field accelerating ions out of the chamber.

If the microscopic cross section for an ion–molecule reaction has the form $\sigma(E) = \sigma_0 E^{-\frac{1}{2}}$, then the average or phenomenological cross section should have the form $Q = Q_0 Er^{-\frac{1}{2}}$, where Er is the repeller voltage.[61] Many ion–molecule reactions exhibit this kind of repeller voltage variation, particularly those[2] involving H_2 or H_2^+. In general, one may not study the behavior at very low repeller voltages with much confidence, because the effects of space charge, contact potentials, and accelerating voltage penetration become too important. Thus, the repeller voltage effect is not as sensitive a test of the form of $\sigma(E)$ as one would wish. A further problem is that as the repeller voltage is varied, there may well be differential variation in the extraction efficiency or transmission for secondary ions as compared with primary ions; this problem has concerned a number of workers. Reuben and Friedman[64] consider the discrimination at the first slit in the ion source and conclude that any discrimination present would be that associated with differences in

velocity distributions of the ions. They conclude from measurements of peak width that D_2^+ and D_3^+ ions have only thermal energy distributions while the greater energy spread of H^+ and D^+ ions from H_2, HD, and D_2 can easily be detected. The sensitivity of the technique is about 0.25 eV. A remaining problem in this kind of experiment is that one cannot be sure that a small energy spread, undetectable by peak width measurement, might not cause some changes in relative extraction efficiency. Note also that the peak width measurements unfortunately are made not on total ion currents, but on selected fractions of ion currents, i.e., the transmitted ions.

Many reactions show repeller voltage effects differing from an $Er^{-\frac{1}{2}}$ dependence.[2,65–67] Boelrijk and Hamill[68] have considered this effect and suggest that collisions which are nearly head-on require a different treatment than the glancing collisions which dominate the conventional low-energy ($E^{-\frac{1}{2}}$) cross section. Collisions with impact parameter less than the impact parameters corresponding to the ordinary gas–kinetic cross section σ_K are treated separately. The reaction cross section is written as $\sigma(E) = (\sigma_1 E^{-\frac{1}{2}} - \sigma_0) + \sigma_K$ in which $\sigma_1 = P_L\sigma_L$, or a reaction probability P_L times the cross section for surmounting the centrifugal barrier, σ_L. A portion of the cross section $\sigma_0 = P_L\sigma_K$ is removed and reintroduced as $\sigma_K = P_K\sigma_K$, where P_K, the reaction probability for head-on collisions, need not equal P_L. For energies greater than E_t, at which the term in parentheses is zero, $\sigma(E) = \sigma_K$. For direct comparison with the curves of average cross section versus repeller voltage, the appropriate integral of $\sigma(E)$ is used. For instance, the result fits ArH^+ formation well down to $E^{-\frac{1}{2}} = 0.3$, but curves for D_3^+ and DO_2^+ formation depart markedly at $E^{-\frac{1}{2}} < 0.8$.[68] The difference is perhaps related to the fact that ArH^+ formation is dominated by $Ar^+ + H_2 \rightarrow ArH^+ + H$, for which the barycentric energy is only $\frac{1}{21}$ times the laboratory energy, while for $D_2^+ + D_2 \rightarrow D_3^+ + D$ and $D_2^+ + O_2 \rightarrow DO_2^+ + D$ the fractions are $\frac{1}{2}$ and $\frac{4}{5}$, so that in the latter two reactions one is dealing with much higher barycentric energies.

For many systems, at higher energies, $\sigma(E)$ drops off below its value expected from the $E^{-\frac{1}{2}}$ dependence. It is not clear whether this is because any complex formed dissociates too quickly for reaction, if the energy is high, or products are formed with energies above their dissociation limits, i.e., they dissociate immediately. Recent direct measurements[17] of $\sigma(E)$ have been made using two mass spectrometers in tandem. These show, in cases in which the barycentric energy reaches

several electron volts, that $\sigma(E)$ drops off much more sharply with E than an $E^{-\frac{1}{2}}$ dependence. Clearly, it will be necessary to take nonreactive or dissociative collisions into account in the theory of ion–neutral reactions.

Moran and Hamill describe further changes in the repeller effect to be expected when the neutral molecule has a permanent dipole moment, and the formula obtained is compared with their experimental results.[69]

A notable exception to the typical monatomic decrease of integrated cross section with repeller voltage occurs for $H_2^+ + He \rightarrow HeH^+ + H$,[59] for which a definite dropoff occurs at low repeller voltage. A similar effect occurs with $H_2^+ + Ne \rightarrow NeH^+ + H$.[70] The repeller curves can be fitted by assuming an effective threshold in ion kinetic energy. However, it has not been possible so far to find a threshold in ion kinetic energy for this reaction using a separated primary ion beam.[60] Further, the variation of secondary ion intensity with electron energy[59,70] reveals no evidence for conversion of translational energy into internal energy. That is, if one found low-energy tails on the curves of secondary ion intensity versus electron energy, with elevated repeller voltage, it would show that H_2^+ ions in low vibrational states, but with increased kinetic energy, were capable of reaction. This effect is not seen. The present suggested interpretation is that there is a competition, at low ion kinetic energies, between reaction and ion deexcitation,[70] with the latter dominating at very low ion kinetic energies. These experiments are very interesting and bear on an important aspect of our understanding of reactions. The issues are not settled, and more work seems to be needed.

Just as for studying temperature effects, the use of photoionization would be attractive for work on repeller effects. Very simple geometry could be used, and in the absence of magnetic fields or space charge, the results would be usable down to very weak extraction fields, or very low average ion energies.

D. Isotopic Effects

The study of isotopic effects is a standard technique in chemical kinetics used to gain information on details of the reaction mechanism. The technique has not been exploited very much in ion–neutral reactions as yet. The results up to now appear to be consistent with the idea that when the ion and neutral combine to form a composite ion for which no stable counterpart is known, and when the reaction is

simple, as in $CH_4^+ + CD_4$,[71] no thorough mixing occurs, and the model of a loosely coupled complex held together by polarization forces applies. On the other hand, when the composite ion has a stable counterpart and when reactions are more complex, as in the system $CD_4^+ + C_2H_4$,[72] much more complete mixing occurs and one thinks of a strongly coupled composite ion. Certainly the data are still scanty, and more experiments will be needed to determine the parameters which determine the properties of the intermediary, and the form of competition between different labeled reaction channels.

Reuben and Friedman[64] have studied the isotopic effects in reactions in various mixtures of H_2, D_2, and HD. In reactions of, say, H_2 and D_2 mixtures there are trivial isotopic effects produced simply by differences in reduced mass. The case of $HD^+ + HD$ is more interesting. Here it is seen that at low repeller voltage HD_2^+ is favored over H_2D^+ by 7%. Reuben and Friedman consider the centrifugal barrier for formation of linear complexes HDDH, DHHD, and HDHD and conclude that on H_2D^+ should be favored by 20%, since the second form would be favored over the other two. They note that the lower zero-point energy of HD_2^+ will favor its formation. However, the zero-point energy difference is small compared with the exothermicity of the reaction, and it is improbable that this mechanism could produce so large an isotopic effect. The barrier presented to outgoing particles was not considered by Reuben and Friedman, but it would favor the most symmetric division of mass between product ion and neutral,[73] i.e., it would favor H_2D^+ formation.

Henglein and Muccini,[49] using the Čermák technique (see Sec. III), have studied isotopic effects in methane and water and found proton transfer strongly favored over deuteron transfer, with the ratio increasing as ion kinetic energy increases.

Using the technique of separate mass selection of primary ions, Giese[74] has studied the reaction of HD^+ ions with HD, and of HD^+ ions with all rare-gas atoms. In the former case the formation of H_2D^+ ions is favored, with the ratio H_2D^+/HD_2^+ increasing with energy to over 3 at 3.5 eV. The ratio can be determined only down to 1.3 eV by this technique, because of the difficulty of separating the true H_2D^+ secondary ions from D_2^+ ions which leak through the primary mass spectrometer even when it is set to mass 3. When very low-energy primary ions are obtained by passing ionizing electrons directly through the reaction chamber and using only a small drawout voltage, the ratio

found by Reuben and Friedman[64] is reproduced. With He, Ne, Ar, and Kr, the results are very striking. If we let $R = \sigma(XH^+)/\sigma(XD^+)$, for He, R drops as ion energy increases; with Ne it drops less rapidly, and levels off. With Ar, R rises slightly and with Kr, considerably more so. With Xe, the reaction cross section is very small, surprisingly, and it is not possible to measure R.

The calculations of Light[75] (see Section V-F) offer the most promising approach to these isotopic effects, which are assumed to represent the competition of two outgoing channels presumably fed by the same ingoing channel. Agreement of theoretical prediction and experiment is not very good now, and it is clear that more work is needed. The isotopic experiments are capable of providing much information on the details of these reactions, and much more work should be done on isotopic effects by the classic single mass spectrometer technique and with mass analysis of the primary ions as well.

E. Persistent Complexes

A particularly interesting kind of reaction which falls into a separate category from all others is the formation of "persistent complexes."

$$A^+ + B \rightarrow AB^+ \tag{5}$$

The interest here lies in the question of stability of the complex. If the complex does not radiate (the cross section for radiative capture is very small), the long life must occur simply because the energy of excitation which obviously is above the dissociation limit for at least one channel (the entrance channel) is shared among many oscillators, and for small excitations an appreciable time can elapse before all oscillators reach again the proper configuration to permit dissociation. Pottie and Hamill[76] reported the first evidence for these complexes. Henglein[77] and Field[78] have found some other cases. Ionic complexes of Xe and C_2H_2 are apparently formed following radiolysis of the gas mixture.[31] Another example is the formation of N_4^+.[79] In order to be sure that some kind of neutral reaction, for example on the filament, was not actually involved, Giese[60] has verified the reactions cited by Pottie and Hamill, using separately mass-analyzed primary ions. The cross section drops off very fast with increasing ion kinetic energy, and secondary ions could be seen only when the primary ions were retarded to perhaps 0.1 to 0.2 eV or less. This is consistent with the fast decrease with increasing repeller voltage seen by the other workers. It is hoped that

much more can be done with these reactions in the future because the predictions of the lifetime of such a complex is a problem very similar, if not identical, to that of the dissociation of an excited molecular ion produced by other means, as by photoionization.[37] These experiments may prove to be a powerful complementary means for studying these unimolecular processes, because the energy of excitation can be varied directly by precise increments by varying the ion energy.

F. Theory of Ion–Neutral Reactions

The familiar formulation of the theory of ion–neutral reactions, and the one most used at present to compare with experiment, is that of Gioumousis and Stevenson.[61] This theory depends on the assumption that reaction occurs if and only if the ion gets very close to the neutral at some stage of the trajectory. The sole attractive potential is taken to be the classical ion-induced dipole moment potential, which varies as r^{-4}. This is a central potential, and one may treat the motion in one dimension by introducing a repulsive centrifugal potential. The attractive r^{-4} potential and the centrifugal potential combine to give a total potential which has a maximum, or barrier. The necessary condition for a close encounter becomes simply that the particles have enough energy to surmount the barrier. This condition gives a critical impact parameter b_{max} for a given laboratory energy E, in electron volts. The cross section is then[61]

$$\sigma = \pi b_{max}^2 = 5.33 \times 10^{-16}(\alpha m/\mu)^{\frac{1}{2}} E^{-\frac{1}{2}} \text{ cm}^2 \tag{6}$$

with m the primary ion mass, μ the reduced mass, and α the polarizability in units of 10^{-25} cm^2.

This treatment has ignored the barrier which outgoing particles must surmount, analogous to the barrier for incoming particles. Rosenstock[73] has considered the effect of this barrier. The barrier will be lower, the larger the reduced mass, for a given outgoing channel. Reuben and Friedman,[64] in attempting to understand some isotopic effects in hydrogen, consider the same effect and find that it predicts an isotopic shift opposite to that observed. Hamill and co-workers[68] have attempted to take account, in a semiempirical way, of head-on collisions which are effectively nonreactive at higher energies. This modification has been introduced to attempt to explain repeller curves and is discussed in the section on repeller effects. Eyring and co-workers[80] have given a treatment of some ion–molecule reaction rates using the absolute

reaction rate theory. As has been the case before, the agreement between experiment and theory for $H_2^+ + H_2 \rightarrow H_3^+ + H$ is spectacularly good. In other cases the agreement is much poorer, and the disagreement is attributed to errors in the calculation of the entropy change for transitions to and from the the activated complex.

Apart from some isolated attempts by authors to explain specific effects seen in their experiments, there has been no real change in the theoretical treatment of very low-energy reactions since the work of Gioumousis and Stevenson,[61] and no change in basic approach since the early work of Eyring and co-workers.[81] It is true that in many cases the theory appears to err only by factors of 2 or 3 or less, and for the prediction of reaction rates, this is really rather good performance. However, in other cases, such as the important reaction $O^+ + N_2 \rightarrow NO^+ + N$, there is evidence[82] that the effective rate constant is smaller than about 0.1 times the theoretical value. In addition, experimental results on isotopic effects in ion–molecule reactions are now available,[64,74] and these effects are not treated at all by the theory as it stands.

Very recently, Weingartshofer and Clarke[83] have measured the cross section for $H_2^+* + H_2 \rightarrow H_3^+ + H$, as a function of the vibrational excitation of H_2^+*, obtained by using ionizing electron beams with carefully controlled energy. The results show that reaction does not occur for H_2^+* in states above the third excited state. This result is strikingly at variance with the theory based on the ion–dipole potential.[61]

Suppose we make the assumption that reactions occur only for intimate collisions, ignoring for the present questions as to the lifetime of the composite system, and whether it may be treated as a "complex molecule" or an "activated complex." Then the problem of calculating a reaction cross section may be divided into two parts; first, the cross section for an intimate collision and second, the probability that when the collision takes place the system will follow a particular outgoing channel. The latter problem is now being attacked intensively by John Light[75] at the University of Chicago, who assumes that all available outgoing channels compete, the probability that a particular channel will be followed being determined by the fraction of total phase space available in that channel. The channels included are nonreactive scattering, charge transfer, and reaction. The phase space must be computed with proper constraints to insure conservation of angular momentum and total energy and that the product formed is not in so high a rotational state

that it will dissociate and not be seen as a product. The effect of the centrifugal barrier presented to outgoing particles[73] is built into these calculations. A calculation by Firsov[84] treats the phase space for the reaction $H_2^+ + H_2 \rightarrow H_3^+ + H$, but errs in that angular momentum is not conserved in the calculation.[75]

A second area in which much theoretical work may be forthcoming is that of calculation of the cross sections for intimate collisions. These cross sections are governed by the force between ion and neutral. Many workers have expressed doubts as to the accuracy of the ion–dipole representation of the potential. Certainly at *very* large distances the ion–dipole potential is accurate, and the pivotal impact parameters for ion–neutral reactions are large. The question as to whether the ion–dipole approximation is good enough is thus not easy to answer.

Arthurs and Dalgarno[85] have considered the effect of a permanent quadrupole moment possessed by the neutral. The leading term in the potential in such a case varies as r^{-3}, and will predominate over the r^{-4} term at very low energies. The predicted effect becomes important only in cases such as ion mobility at reduced temperatures.

One ion–neutral system for which the accurate potential is available is the $H^+ + H$ system (energy of H_2^+).[86] Obviously, no chemical reactions can take place in this system, but it serves as a test case for which the cross section for intimate collisions may be computed,[87] using the usual centrifugal potential added to the quantum-mechanical potential, and assuming that the collision is adiabatic, i.e., the system remains at minimum electronic energy throughout. The cross section thus obtained behaves qualitatively like the cross sections for $H_2^+ + H_2 \rightarrow H_3^+ + H$ obtained with mass analysis of the primary ion beam.[17] Clearly, all systems in which reactions occur are much more complicated than $H^+ + H$ and the question as to whether the $1/r^4$ potential is accurate enough for them, as well as what to do if it is not, will require much more work. However, qualitative predictions[87] based on the presence of a quantum-mechanical resonance potential similar to that in the $H^+ + H$ system are consistent with the results of Weingartshofer and Clarke[83] and also with the observation that reaction of HD^+ with Ar and Kr is efficient, but that with Xe is inefficient.[74]

Another case which needs further consideration is that of neutral reactants which have permanent electric dipole moments, as H_2O. The problem is the difficult one of a rotating molecule with permanent dipole moment interacting in a collision with an ion. Moran and

Hamill[69] have analyzed some measurements on reactions involving neutrals with permanent dipole moments in terms of smooth transition between limiting cases in which the dipole either orients in the position of minimum energy or else rotates freely so that the permanent dipole effect averages out.

A totally different treatment of reactions, suitable for high ion energies (hundreds of electron volts) has been given by Bates, Cook, and Smith.[88] At such high energies, polarization forces and binding energies can be ignored, and calculation of a reaction cross section corresponds to calculation of the probability, following an impulsive collision, that a particular group of atoms emerge with small enough relative velocity so that they stick together.

VI. MISCELLANEOUS ASPECTS OF ION–NEUTRAL REACTIONS

Dehmelt and Major[89] have done a most ingenious experiment on spin orientation of He^+ ions which succeeds because of their very subtle use of ion–neutral reactions. Orientation takes place because of the exchange

$$Cs(\uparrow) + He^+(\downarrow) \rightarrow Cs(\downarrow) + He^+(\uparrow)$$

which takes place between a beam of optically polarized Cs atoms and He^+ ions trapped in an electrostatic quadrupole trap. Ions are removed from the trap by the charge transfer $Cs + He^+ \rightarrow Cs^+ + He^*$ which has an energy defect of 0.1 eV for He* in the singlet state, or 0.9 eV for the triplet state. Thus, by the Massey criterion, for low-energy ions, one expects the singlet cross section to be much larger than the triplet (and both of these to be much smaller than the spin exchange cross section). Accordingly, the rate of loss of ions changes when the polarization of Cs atoms is switched on and off.

Dawson and Tickner[90] have evidence for formation of H_5^+ in a hydrogen glow discharge.

The formation of H_3^+ has been detected in a field ionization experiment[4] but the formation occurs under conditions when H^+ formation drops off and, further, it does not occur, although H_2^+ is formed, above certain surfaces of the field-ion tip. Thus it is doubtful that the familiar reaction $H_2^+ + H_2 \rightarrow H_3^+ + H$ is involved here.

The evidence for secondary reactions occurring on surfaces in the mass spectrometer ion source[91,92] suggests that one must be careful to

insure that secondary ions produced with the aid of such a surface reaction are not attributed to gas-phase reactions.

Calculations of the properties of ions resulting from reactions remain rather few in number, with HeH^+ the ion whose binding energy is best determined.[93] A lower limit of 2.14 eV for the binding energy of He_2^+ has been calculated.[94] Comes[95] has restudied the formation mechanism for He_2^+ and from the experimental results along with several theoretical considerations, concludes that the process is $He(3^3P) + He(1^1S) \rightarrow He_2^+ + e^-$. Hoyland and Lampe[96] have made a single-center single determinant calculation on CH_3^+, CH_3, CH_4, and CH_5^+ to obtain their relative energies, giving a value for the proton affinity of CH_4 of 7.26 eV.

Elastic scattering measurements furnish perhaps the best information on the interaction potential between ion and neutral, and therefore, on reaction cross sections. An experiment which measures just the total elastic scattering cross sections for deflections greater than some minimum angle is capable only of measuring two parameters in a potential function,[97] for example, k and n in the expression $V = -kr^{-n}$. Since the true potential contains a repulsive term which is probably important even at low energies,[98,99] it would be more informative to measure differential elastic scattering cross sections at low energies. Experiments of this sort are now beginning to appear.[100]

The relationship between scattering cross sections of H^+ in CH_4, CF_4, C_2H_6, and C_2F_6 and the interaction energies between the ion and neutral are treated by Cloney and Vanderslice.[101] A striking result is that there is apparently no minimum in the interaction energy in H^+ of CH_4, even though the proton affinity of CH_4 is known to be large. The suggestion is made that the scattering is far from adiabatic, and the normal CH_5^+ curve is not traced by the proton–CH_4 system. An analysis[102] of Ar^+ scattering and charge transfer in Ar gives a determination of the Ar_2^+ binding energy. The result is an apparent upper limit of 0.056 eV, which is surprisingly low.

Shock tube research is developing rapidly, and the time-dependent spectroscopy of ions in the shock tube is providing another means for investigating the reactions of the ions with ambient neutrals.[103]

VII. FUTURE PROSPECTS

The most exciting prospects for the future are experiments which will fix, or measure, more of the collision parameters. Results from these

experiments will provide more stringent tests for theory and will spur its refinement.

Refinements are being added in gradual stages. For example, primary ions H_2^+ have now been prepared by electron impact with energy-selected electrons.[83] These ions react in the chamber in which they are formed. In the future, one may hope to combine the electron energy selection with mass and energy selection of the primary ions, using a separate reaction chamber. An even more powerful experiment would be to obtain the primary ions by photoionization. This experiment is possible with the photon fluxes available now. Presenting the neutral reactants to the ion beam in the form of a crossed beam[32] permits use of chemically active neutrals such as hydrogen atoms[41] or oxygen atoms.[104] It is possible that selection of particular states of the neutrals will be done using familiar molecular beam techniques. The angular distribution of the products of interaction should be much more informative than the total cross sections. Kinetic energy analysis of the product ions either alone or combined with the angular distribution would also be highly revealing. Angular distributions are just beginning to be determined.[32,100] It should be most attractive in the future to combine more and more of these refinements into one experiment. The major detriment is intensity. All of these refinements are achieved at the expense of intensity.

Very low intensities can be tolerated, if the background is also very low, when using ion counting. In nuclear physics the background is reduced by using coincidence techniques. In chemical physics these techniques have not been used nearly to the extent that they might be. A wide variety of detectors, such as scintillators, geiger tubes, solid-state detectors, etc., is available for particles, neutral or charged, with kinetic energies in the range of millions of electron volts. While low-energy ions may be accelerated into electron multipliers to produce countable pulses, low-energy neutrals in general are not easily detected with good efficiency; typically, they must be ionized and then detected. This detection difficulty has probably been the greatest problem in experimental work in chemical physics. An additional difficulty is that thin windows, so useful in confining target gases in nuclear physics, are not usable in chemical physics. In spite of these problems, there appears to be no fundamental difficulty to prevent carrying much of the impressive technology of nuclear physics over into chemical physics, and this will permit some very powerful experiments.

References

1. V. L. Tal'roze, *Pure Appl. Chem.*, **5**, 455 (1962).
2. F. W. Lampe, J. L. Franklin, and F. H. Field, *Progress in Reaction Kinetics*, Pergamon Press, New York, 1961, Vol. I, Chap. 3, p. 67.
3. F. J. Comes and W. Lessmann, *Z. Naturforsch*, **17a**, 704 (1962).
4. T. C. Clements and E. W. Müller, *J. Chem. Phys.*, **37**, 2684 (1962).
5. E. Lindholm, *Z. Naturforsch.*, **9a**, 535 (1954).
6. E. Lindholm, *Arkiv Fysik*, **8**, 257 (1954).
7. E. Lindholm, *Arkiv Fysik*, **8**, 433 (1954).
8. E. Gustafsson and E. Lindholm, *Arkiv Fysik*, **18**, 219 (1960).
9. H. von Koch and E. Lindholm, *Arkiv Fysik*, **19**, 123 (1961).
10. P. Wilmenius and E. Lindholm, *Arkiv Fysik*, **21**, 97 (1962).
11. E. Lindholm and P. Wilmenius, *Arkiv Kemi*, **20**, 255 (1963).
12. E. Pettersson and E. Lindholm, *Arkiv Fysik*, **24**, 49 (1963).
13. W. A. Chupka and E. Lindholm, *Arkiv Fysik*, **25**, 349 (1963).
14. R. S. Lehrle, J. C. Robb, and D. W. Thomas, *J. Sci. Instr.*, **39**, 458 (1962).
15. V. L. Tal'roze, L. L. Dekabrun, G. D. Tantsyrev, E. L. Frankevich, O. D. Vetrov, A. K. Lyubimova, G. K. Lauroskaya, V. I. Epofeev, V. D. Grishin, V. E. Skurat, and A. Ya. Yukhvidin, *Instr. Exptl. Technol.*, **1**, 936 (1960).
16. C. F. Giese and W. B. Maier II, *J. Chem. Phys.*, **39**, 197 (1963).
17. C. F. Giese and W. B. Maier II, *J. Chem. Phys.*, **39**, 739 (1963).
18. W. B. Maier II, *J. Chem. Phys.*, **42**, 1790 (1965). See also W. B. Maier II, *J. Chem. Phys.*, **41**, 2174 (1964).
19. V. Čermák and Z. Herman, *Nucleonics*, **19**, No. 9, 106 (1961).
20. G. F. Crable and G. L. Kearns, *J. Chem. Phys.*, **36**, 558 (1962).
21. A. Galli, A. Giardini-Guidoni, and G. G. Volpi, *Nuovo Cimento*, **26**, 845 (1962).
22. A. Galli, A. Giardini-Guidoni, and G. G. Volpi, *J. Chem. Phys.*, **39**, 518 (1963).
23. J. H. Futrell and T. O. Tiernan, *J. Chem. Phys.*, **39**, 2539 (1963).
24. A. Henglein and G. A. Muccini, *Z. Naturforsch.*, **17a**, 452 (1962).
25. F. H. Field, H. N. Head, and J. L. Franklin, *J. Am. Chem. Soc.*, **84**, 1118 (1962).
26. C. E. Melton, *J. Chem. Phys.*, **33**, 647 (1960).
27. S. Wexler and N. Jesse, *J. Am. Chem. Soc.*, **84**, 3425 (1962).
28. J. S. Dahler, J. L. Franklin, M. S. B. Munson, and F. H. Field, *J. Chem. Phys.*, **36**, 3332 (1962).
29. M. S. B. Munson, F. H. Field, and J. L. Franklin, *J. Chem. Phys.*, **37**, 1790 (1962).
30. C. E. Melton, *J. Chem. Phys.*, **37**, 562 (1962).
31. P. S. Rudolph, S. C. Lind, and C. E. Melton, *J. Chem. Phys.*, **36**, 1031 (1962).
32. B. R. Turner, R. F. Stebbings, M. A. Fineman, and W. L. Fite, *Bull. Am. Phys. Soc.*, **7**, 488 (1962).
33. W. L. Fite, J. A. Rutherford, W. R. Snow, and V. A. J. van Lint, *Discussions Faraday Soc.*, **33**, 264 (1962).
34. P. F. Knewstubb and A. W. Tickner, *J. Chem. Phys.*, **36**, 674 (1962).
35. P. F. Knewstubb and A. W. Tickner, *J. Chem. Phys.*, **36**, 684 (1962).
36. P. F. Knewstubb and A. W. Tickner, *J. Chem. Phys.*, **37**, 2941 (1962).
37. B. Steiner, C. F. Giese, and M. G. Inghram, *J. Chem. Phys.*, **34**, 189 (1961).

38. V. L. Tal'roze, *Bull. Acad. Sci. USSR* (*English Trans.*), **24**, 1006 (1960).
39. H. S. W. Massey and E. H. S. Burhop, *Electronic and Ionic Impact Phenomena* Oxford University Press, New York, 1952.
40. D. Rapp, *J. Geophys. Res.*, **68**, 1773 (1963).
41. W. L. Fite, A. C. H. Smith, and R. F. Stebbings. *Proc. Roy. Soc.* (*London*), **A268**, 527 (1962).
42. D. R. Bates and N. Lynn, *Proc. Roy. Soc.* (*London*), **A253**, 141 (1959).
43. D. R. Bates, *Quantum Theory I. Elements*, Academic Press, New York, 1961, Chap. 8, p. 293ff.
44. D. Rapp and W. E. Francis, *J. Chem. Phys.*, **37**, 2631 (1962).
45. D. P. Stevenson and G. Gioumousis, *J. Chem. Phys.*, **29**, 294 (1958).
46. D. R. Bates, *Discussions Faraday Soc.*, **33**, 7 (1962).
47. K. Takayanagi, *Sci. Rep. Saitama Univ., Ser. A.* **4**, No. 2 (1962).
48. R. F. Stebbings, B. R. Turner, and A. C. H. Smith, *J. Chem. Phys.*, **38**, 2277 (1963).
49. A. Henglein and G. A. Muccini, *Z. Naturforsch.*, **18a**, 753 (1963).
50. R. K. Curran, *Phys. Rev.*, **125**, 910 (1962).
51. K. Kraus, W. Müller-Duysing, and H. Neuert, *Z. Naturforsch*, **16a**, 1385 (1961).
52. H. B. Gilbody and J. B. Hasted, *Proc. Roy. Soc.* (*London*), **A238**, 334 (1956).
53. W. B. Maier II, *J. Chem. Phys.*, **42**, 1790 (1965).
54. D. Hutchison and L. Pobo, paper presented at ASTM, E-14 meeting, Chicago, June, 1961.
55. A. G. Harrison and J. M. S. Tait, *Can. J. Chem.*, **40**, 1986 (1962).
56. A. Henglein, *Z. Naturforsch.*, **17a**, 37 (1962).
57. V. Čermák and Z. Herman, *Collection Czech. Chem. Commun.*, **27**, 1493 (1962).
58. W. Kaul, U. Lauterbach, and R. Taubert, *Z. Naturforsch.*, **16a**, 624 (1961).
59. H. von Koch and L. Friedman, *J. Chem. Phys.*, **38**, 1115 (1963).
60. C. F. Giese, unpublished results.
61. G. Gioumousis and D. P. Stevenson, *J. Chem. Phys.*, **29**, 294 (1958).
62. D. P. Stevenson and D. O. Schissler, *J. Chem. Phys.*, **29**, 282 (1958).
63. N. A. I. M. Boelrijk and T. P. J. H. Babeliowsky, *J. Am. Chem. Soc.*, **84**, 3592 (1962).
64. B. G. Reuben and L. Friedman, *J. Chem. Phys.*, **37**, 1636 (1962).
65. F. H. Field, J. L. Franklin, and F. W. Lampe, *J. Am. Chem. Soc.*, **79**, 2419 (1957).
66. R. F. Pottie, A. J. Lorquet, and W. H. Hamill, *J. Am. Chem. Soc.*, **84**, 529 (1962).
67. L. P. Theard and W. H. Hamill, *J. Am. Chem. Soc.*, **84**, 1134 (1962).
68. N. Boelrijk and W. H. Hamill, *J. Am. Chem. Soc.*, **84**, 730 (1962).
69. T. F. Moran and W. H. Hamill, *J. Chem. Phys.*, **39**, 1413 (1963).
70. T. F. Moran and L. Friedman, *J. Chem. Phys.*, **39**, 2491 (1963).
71. C. D. Wagner, P. A. Wadsworth, and D. P. Stevenson, *J. Chem. Phys.*, **28**, 517 (1958).
72. F. W. Lampe and F. H. Field, *Tetrahedron*, **7**, 189 (1959).
73. H. Rosenstock, *U. S. At. Energy Comm. Rep.*, JL1-650-3-7, TID-4500 (1959).

74. C. F. Giese, *Bull. Am. Phys. Soc.*, **9**, 189 (1964).
75. J. C. Light, *J. Chem. Phys.*, **40**, 3221 (1964).
76. R. F. Pottie and W. H. Hamill, *J. Phys. Chem.*, **63**, 877 (1959).
77. A. Henglein, *Z. Naturforsch.*, **17a**, 44 (1962).
78. F. H. Field, *J. Am. Chem. Soc.*, **83**, 1523 (1961).
79. M. Saporoschenko, *Phys. Rev.*, **111**, 1550 (1958).
80. T. S. Ree, T. Ree, H. Eyring, and T. Fueno, *J. Chem. Phys.*, **36**, 281 (1962).
81. H. Eyring, J. O. Hirschfelder, and H. S. Taylor, *J. Chem. Phys.*, **4**, 479 (1936).
82. V. L. Tal'roze, M. I. Markin, and I. K. Larin, *Discussions Faraday Soc.*, **33**, 257 (1962). However, see also Ref. 22, in which Professor Tal'roze is quoted as stating that the upper limit to the reaction is 10 times larger than in the original article.
83. A. Weingartschofer and E. M. Clarke, *Phys. Rev. Letters*, **12**, 591 (1964).
84. O. B. Firsov, *Soviet Phys., JETP*, **15**, 906 (1962).
85. A. M. Arthurs and A. Dalgarno, *Proc. Roy. Soc.* (*London*), **256A**, 540, 552 (1960).
86. D. R. Bates, K. Ledsham, and A. L. Stewart, *Phil. Trans. Roy. Soc.* (*London*), **246**, 215 (1953).
87. C. F. Giese, paper presented at the ASTM E-14—GAMS Mass Spectrometry Conference, Sept. 14–18, 1964, Paris, France. Forthcoming in conference Proceedings.
88. D. R. Bates, C. J. Cook, and F. J. Smith, *Proc. Phys. Soc.* (*London*), **83**, 49 (1964).
89. H. G. Dehmelt and F. G. Major, *Phys. Rev. Letters*, **8**, 213 (1962).
90. P. H. Dawson and A. W. Tickner, *J. Chem. Phys.*, **37**, 672 (1962).
91. P. Marmet and J. D. Morrison, *J. Chem. Phys.*, **36**, 1238 (1962).
92. G. E. Moore, *J. Appl. Phys.*, **32**, 1241 (1961).
93. A. A. Evett, *J. Chem. Phys.*, **24**, 150 (1956).
94. P. N. Reagan, J. C. Browne, and F. A. Matsen, *J. Am. Chem. Soc.*, **84**, 2650 (1962).
95. F. J. Comes, *Z. Naturforsch.*, **17a**, 1031 (1962).
96. J. R. Hoyland and F. W. Lampe, *J. Chem. Phys.*, **37**, 1066 (1962).
97. C. E. Baker, J. M. McGuire, and E. E. Muschlitz, Jr., *J. Chem. Phys.*, **37**, 2571 (1962).
98. E. A. Mason and J. T. Vanderslice, *J. Chem. Phys.*, **27**, 917 (1957).
99. E. A. Mason and J. T. Vanderslice, *J. Chem. Phys.*, **28**, 253 (1958).
100. W. Aberth and D. C. Lorents, *Bull. Am. Phys. Soc.*, **9**, 411 (1964).
101. R. D. Cloney and J. T. Vanderslice, *J. Chem. Phys.*, **36**, 1866 (1962).
102. R. D. Cloney, E. A. Mason, and J. T. Vanderslice, *J. Chem. Phys.*, **36**, 1103 (1962).
103. W. Roth, *J. Chem. Phys.*, **37**, 925 (1962).
104. R. F. Stebbings, A. C. H. Smith, and H. B. Gilbody, *J. Chem. Phys.*, **38**, 2280 (1963).

8. SUPERSONIC NOZZLE BEAMS*

J. B. ANDERSON, R. P. ANDRES, and J. B. FENN

Beam Kinetics Laboratory, School of Engineering and Applied Sciences, Princeton University, Princeton, New Jersey

CONTENTS

I. Introduction 275
II. Basic Principles of Nozzle Beam Operation 277
A. General Considerations 277
B. Theoretical Nozzle Beam Performance 279
C. Comparison of Nozzle and Oven Beams 282
III. Some Design Considerations and Experimental Results 282
A. Pumping Speed Requirements 283
B. The Nozzle–Jet System 284
C. The Skimmer 292
IV. Applications of Nozzle Beams 304
A. Sampling Experiments and Their Interpretation 304
B. Direct Studies with Beam Molecules 306
V. Energy Limitations and the Use of Mixed Gases 308
A. The General Problem of Energy 308
B. Nozzle Beams and Mixed Gases 311
C. Related Experiments with Gas Mixtures 313
References 315

I. INTRODUCTION

Those who have read the other articles in this volume may have become aware that molecular beam research is constantly plagued with difficulties in detecting the bits of information being sought. In all too many situations the investigator seems to be peering through a glass darkly just on the ragged edge of total blindness. Consequently, there has been a lot of attention paid to the problem of increasing the critical

* Preparation of this article was made possible by Grant NSF G 19087 from the National Science Foundation. Partial support was also provided by the Office of Naval Research through Project SQUID Contract Nonr 1858(25), NR-098-038.

ratio of signal to noise in molecular beam experiments. In this endeavor the developments in modulation techniques and detector specificity have contributed a greal deal. Another and obvious approach is to try to increase beam intensity. For this purpose, multiparallel effusive sources have been developed in the form of clusters of small tubes, crinkled foil assemblies, and the like. All of these variations on the theme of increasing usable signal have been helpful but still have left much to be desired.

A little more than a decade ago Kantrowitz and Grey made a most powerful suggestion which seemed to promise beam intensities orders of magnitude greater than could be achieved by any effusion technique. They suggested that the effusive flow field of the conventional oven beam be replaced by a supersonic jet.[1] This idea was tried almost immediately by Kistiakowsky and Slichter, who soon discovered that the critical problem in implementing the Kantrowitz-Grey suggestion was the provision of enough pumping capacity to handle all the gas which even a small supersonic jet admitted into the system.[2] It was not until the pioneering work of Becker and Bier in 1954 that the effectiveness of supersonic jets as beam sources was adequately demonstrated.[3] The success obtained by Becker and his associates together with the increasing availability of large vacuum pumps at moderate cost has resulted in a gradually growing activity in the development of what we shall call "nozzle beams." This activity has accelerated in the past two years so that now there are more than a dozen groups who have built or are building apparatus based on the Kantrowitz-Grey idea.

In spite of all the work that has been done, it must be recognized that nozzle beams are still in a relatively early stage of development. They have yet to become the prolific sources of scientific information that their oven cousins have been for many years. Although there is no present reason to doubt that they will ultimately fulfill their promise, there is still much to be done before they can be regarded as perfected. In this article we will attempt to review what has been accomplished in designing, building, operating, and understanding nozzle beam systems. We will try to define what we regard as important problems to be solved and to indicate some possible future uses for nozzle beams in the study of problems of interest to chemical physicists.

It is inevitable that this communication will be more of a progress report on the state of an art than a critical review of scientific data. What is really involved at this point is the engineering development of a

principle into a useful tool. The tangible results obtained by the use of nozzle beams are thus far few. Consequently, we hope we will be forgiven if much of what we say smacks of qualitative opinion and speculation rather than quantitative fact and certain knowledge. We also hope we will be able to persuade the reader that there are exciting rewards well worth the hard work which they will require to be realized. We would be remiss if we did not also emphasize that the interest and activity in nozzle beam development is growing so rapidly that any summary of its status is almost bound to be obsolete by the time it appears in print. We therefore urge the reader not to construe what appears here as the latest word. In fact we earnestly hope that the reach of progress will have well exceeded our present grasp of its prospects.

II. BASIC PRINCIPLES OF NOZZLE BEAM OPERATION

A. General Considerations

In Figure 1 are shown representations of a nozzle beam apparatus and its classical oven beam counterpart. It is convenient to consider that the first defining element in a nozzle beam system is the skimmer and that it plays a role analogous to the effusive slit in the oven of a conventional beam apparatus. The figure shows schematically the flow field downstream of the slit and the skimmer, respectively. In the oven beam the source gas is at rest relative to the slit. In the nozzle beam the source gas is traveling with a mean velocity relative to the skimmer. Physically there are three consequences of this mean motion:

1. For a given upstream density the mass flow per unit area into the first defining element of the beam apparatus is increased.

2. The fraction of the total mass flow in the first defining element which persists on the axis or center line is higher than in the case of an effusion source. This focusing is due simply to the fact that at high Mach numbers there is imposed on the beam molecules a mean velocity in the axial direction which is large with respect to the radial velocities due to their random thermal motion. The spatial distribution has an ellipsoidal rather than a spherical shape.

3. The fraction of total flux within a given energy interval is higher in a nozzle beam. This is due to the decrease in temperature during the adiabatic expansion to supersonic velocity. For example, in an effusion beam only about 11% of the total flux is within 5% of the mean molecular velocity. In a supersonic beam at a Mach number of 10, about

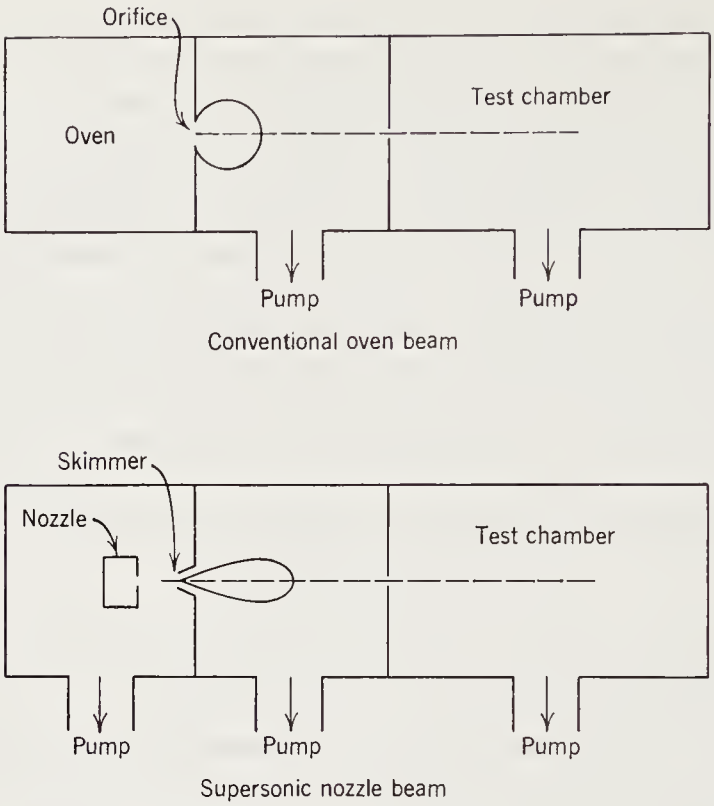

Fig. 1. Schematic representation of oven beam and nozzle beam systems. The closed curves downstream of the slit and skimmer represent the relative intensity distributions.

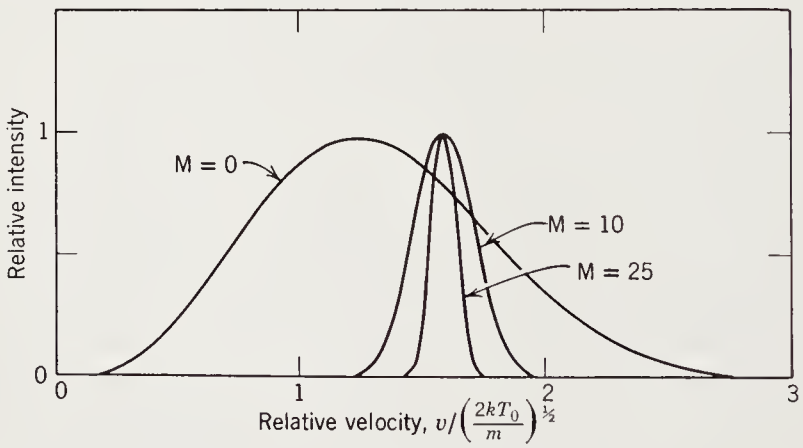

Fig. 2. Theoretical axial velocity distributions for nozzle source beams of monatomic gases with Mach number at the skimmer entrance as indicated. The distribution for an oven beam is also shown ($M = 0$).

47% of the molecules have velocities within 5% of the mean. At a Mach number of 20 this fraction becomes about 80%. The variation of the velocity distribution with Mach number is shown in Figure 2. Moreover, in cases where internal degrees of freedom are excited at the source temperature, relaxation of these during expansion will compress the range of internal energy states of molecules in the beam.

These factors are cumulative in their contribution to useful beam intensity. In principle they permit overall gains of several orders of magnitude, substantial fractions of which have been achieved by various investigators.

B. Theoretical Nozzle Beam Performance

In order to provide a frame of reference for the understanding of beam performance it is in order to derive what we shall call the "theoretical intensity" of a nozzle beam. This development is a natural extension of the original analysis of Kantrowitz and Grey[1] which has been refined by Parker et al.[4]

Provided that molecular collisions downstream of the skimmer may be neglected to a good approximation, the various properties of the beam are determined simply by the density and velocity distribution of the gas at the skimmer entrance. This distribution was assumed by Kantrowitz and Grey to be of the form

$$dn = n\left(\frac{m}{2\pi kT}\right)^{\frac{3}{2}} \exp\left[-\frac{\mathrm{m}}{2kT}(c-u)^2\right] d^3c \qquad (1)$$

where n, T, and u are the density, translational temperature, and mean velocity of the gas, m is the mass of a molecule, k is the Boltzmann constant, and c is the molecular velocity. Such an equilibrium distribution includes classical oven beams as a special case when u is zero. In this case the density and temperature are determined simply by the pressure and temperature in the oven. In a nozzle beam, however, n, T, and u all depend on the extent of expansion before the skimmer. They are usually found by assuming that the flow in the nozzle–jet system is isentropic and may be treated by the techniques of continuum gas dynamics up to the skimmer entrance. But, if the density in the jet becomes low enough, it is impossible for the gas to maintain these isentropic gradients and a transition to free molecular flow may be observed ahead of the skimmer. In order to account for such cases when the distance to the skimmer l_s is larger than the distance at which

such a transition occurs, l_1, we shall extend the treatment of Kantrowitz and Grey by assuming a model in which the flow is isentropic up to a spherical surface of transition and free molecular downstream from this surface. The results of Kantrowitz and Grey are then included as the case when $l_s \lessapprox l_1$. That this too is an oversimplification is obvious. However, the performance predicted by this model serves as a convenient standard by which to judge the actual behavior of real beams. In passing it should be noted that we have neglected the effect of collisions of jet molecules with background molecules in the nozzle chamber or with molecules reflected from the skimmer surfaces. We shall have more to say about the importance of these effects later.

In general, then, the theoretical flux of beam molecules through an orifice coaxial with the jet is given by the expression

$$I(r,x) = n_1 \pi r_s^2 \left(\frac{m}{2\pi k T_1}\right)^{\frac{3}{2}} \times \int_0^\infty \exp\left[-\frac{m}{2kT_1}\left\{(c - u_1 \cos\theta_2)^2 + u_1^2 \sin^2\theta_2\right\}\right] \times c^3\, dc \cos^4\theta_1 \frac{1}{x^2} \tag{2}$$

where $\sin\theta_2 = (l_s/l_1)\sin\theta_1$. The various lengths and angles in this expression are defined in Figure 3. We have assumed here that r_s, the

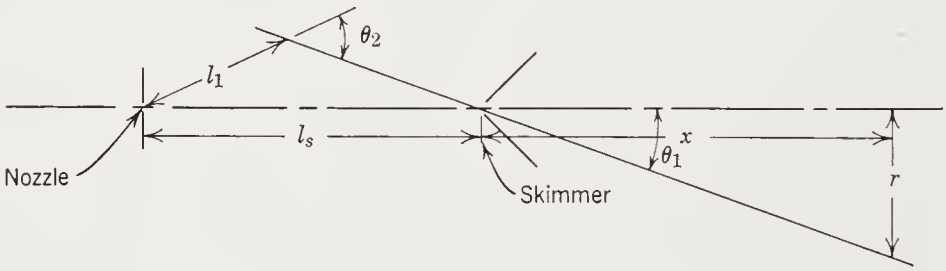

Fig. 3. Schematic diagram indicating the geometry and dimensions used in the development of expression for theoretical intensity.

radius of the skimmer entrance, is small with respect to l_1, l_s, and x and have subscripted the density, temperature, and mean velocity to indicate that they refer to the gas at l_1. With the speed ratio defined as

$$w_1 = \left(\frac{mu_1^2}{2kT_1}\right)^{\frac{1}{2}} \tag{3}$$

this expression may be integrated to yield

$$I(r,x) = n_1 \pi r_s^2 \left(\frac{2kT_1}{m}\right)^{\frac{1}{2}} \frac{1}{\pi x^2} \cos^4\theta_1 f(w_1) \tag{4}$$

where

$$f(w_1) = (\tfrac{3}{4}w_1 \cos\theta_2 + \tfrac{1}{2}w_1^3 \cos^3\theta_2) \times (\operatorname{erfc}[-w_1 \cos\theta_2]) \times (\exp[-w_1^2 \sin^2\theta_2]) \times \frac{1}{2\pi^{\frac{1}{2}}}(1 + w_1^2 \cos^2\theta_2)(\exp[-w_1^2])$$

In most situations the second collimating orifice will, of course, be on the beam axis. Making this simplification and taking the case of a conventional oven beam, we obtain

$$I_{\text{oven beam}} = n_s \pi r_s^2 \tfrac{1}{4} \left(\frac{8kT_s}{\pi m}\right)^{\frac{1}{2}} \frac{1}{\pi x^2} \tag{5}$$

For supersonic flow at the skimmer entrance our general expression may also be simplified when the speed ratio is greater than about 4. In this case, as we will discuss later, the density resulting from the sonic nozzles generally used is inversely proportional to the square of the distance from the nozzle and the error integrals and exponential terms may be replaced by their limiting values, therefore

$$I_{\text{nozzle beam}} \cong n_s (l_s/l_1)^2 \pi r_s^2 u_1 \frac{1}{\pi x^2} (w_1^2 + \tfrac{3}{2}) \tag{6}$$

or, in terms of Mach number M_1 and the specific heat ratio γ,

$$I_{\text{nozzle beam}} \cong n_s \pi r_s^2 u_1 (1/\pi x^2)(l_s/l_1)^2 (\tfrac{1}{2}\gamma M_1^2 + \tfrac{3}{2}) \tag{7}$$

for $M_1 > 4$. If $l_s < l_1$ then u_1, l_1, and M_1 simply become u_s, l_s, and M_s. We have written this expression in terms of the density at the skimmer entrance to make a comparison with oven beams more meaningful. It should be noticed that as long as the point skimmer approximation is valid and $n_s \sim l_s^{-2}$, beam intensity becomes independent of nozzle–skimmer distance when $l_s > l_1$ if no collisional losses occur. It is perhaps worth elaborating a bit on why Mach number is used in connection with beams. The reason is purely one of convenience. Because the local

speed of sound is a measure of temperature, Mach number becomes equivalent to a measure of ordered motion (mean gas velocity) relative to random thermal motion. Most tabulations of gas properties in flow situations are in terms of Mach number rather than the more meaningful speed ratio. Consequently, it is useful to cast the pertinent equations in terms of this variable.

C. Comparison of Nozzle and Oven Beams

In order to compare performance of an oven beam and a nozzle beam, we consider the density at the first defining orifice to be the same for both. We assume the temperature of the oven to be equal to the temperature of the gas before expansion in the nozzle. It is then easy to show from Eqs. (5) and (7) that the ratio of total intensities is, at any axial distance

$$\frac{I_{\text{nozzle beam}}}{I_{\text{oven beam}}} \cong \left(\pi \frac{C_p}{k}\right)^{\frac{1}{2}} \gamma \mathrm{M}_{\text{eff}}^2, \tag{8}$$

where C_p is the heat capacity of the gas at constant pressure and $\mathrm{M}_{\text{eff}} = (l_s/l_1)\ \mathrm{M}_1$ is the effective Mach number. Thus at an effective Mach number of 10 with a diatomic gas like nitrogen, for example, an ideal nozzle beam can in principle provide 470 times the total beam intensity of an oven beam operating under comparable conditions. An effective Mach number of 20 would provide 1860 times as much intensity. It should be noted that this effective Mach number corresponds to the jet static temperature or the beam velocity distribution only when $l_s \leqq l_1$. When l_s is greater than l_1 the beam velocity distribution or temperature is dependent upon M_1.

III. SOME DESIGN CONSIDERATIONS AND EXPERIMENTAL RESULTS

There are three characteristic features of a nozzle beam system which differ markedly in degree or kind from their counterparts in an effusive beam apparatus. These are the pumping speed requirements, the nozzle–jet complex, and the skimmer. It seems appropriate to discuss the function of these components in the light of both theory and experience to date. Although we will not endeavor to specify optimum design details, we will try to point out the important factors which must be taken into account.

A. Pumping Speed Requirements

The total gas flow in a nozzle beam system is orders of magnitude greater than that in typical effusive beam apparatus. Fortunately, most of this gas which is introduced initially through the nozzle is removed upstream of the skimmer and does not contribute to the load aft of the skimmer. In fact, it is clear from comparison of Eqs. (5) and (7) that the ratio of axial beam intensity to skimmer mass flow in a nozzle beam is higher by a factor of about $\frac{1}{2}\gamma\ M_{\text{eff}}^2$ than the ratio of beam intensity to effusive mass flow in an oven beam. Consequently, for a given total intensity, the pumping speed required in the high-vacuum region is substantially lower for a nozzle beam than for an oven beam. Even the large improvements in the ratio of total intensity to total flow which can be obtained with multiparallel channel sources cannot overcome this advantage of the nozzle beam if reasonably high Mach numbers are achieved. Moreover, this advantage is still further enhanced by the narrow velocity distribution which accompanies high Mach number. Thus, for usable intensity in a particular velocity interval, the nozzle beam can be much less demanding of high-vacuum pumping speed than any effusive beam. All the usual economies obtained by differential or staged pumping are equally realizable in both kinds of systems and have been used.

Upstream of the first defining element, skimmer or effusive aperture, the situation is, of course, entirely different. The oven in an effusive system requires no auxiliary pumping at all. The nozzle exhaust chamber in a nozzle system must be provided with enough pumping capacity to remove all of the total nozzle flow except the minute fraction which passes through the skimmer. In terms of size and cost this requirement depends largely on the pressure which can be tolerated in the nozzle exhaust chamber and at which the bulk of the nozzle mass flow must be removed. In early nozzle beam work the nature of this requirement had not been documented and its importance not completely realized. Nozzle beam systems were built with as little as 25 liters sec^{-1} capacity at 0.10 torr by Campargue[5] and as much as 5000 liters sec^{-1} at 0.001 torr by Deckers and Fenn.[6] The importance of this first-stage pumping has been recently brought into focus by Bier and Hagena,[7] Fenn and Anderson,[8] and Anderson et al.[9] We will enlarge upon its nature in our subsequent discussion of the nozzle–jet system and show that in general the higher the pumping speed in the nozzle exhaust chamber the

more effectively can beams be produced. Apropos of our present discussion of pumping requirements, we call attention to some relatively recent and pertinent developments. Knuth investigated sorption pumping and found that high speeds could be realized at the price of some inconvenience in regeneration.[10] Knuth and Iacobellis have designed, built, and operated a radial-flow turbomolecular pump for use in a nozzle beam system and obtained speeds of the order of 10,000 liters sec^{-1}.[11] Cryopumping with liquid nitrogen has been used with success by Hagena and Henkes for producing beams of readily condensable substances such as carbon dioxide.[12] McGinn takes advantage of a liquid helium supply to provide extremely large pumping speeds even for "permanent" gases.[13] Fristrom is investigating the use of porous-wall nozzles which in principle permit the withdrawal of a substantial fraction of the total nozzle flow at relatively high pressures.[14] He is also experimenting with pulsing the nozzle flow, a technique which has been successfully exploited by Hagena[15] and Bier and Hagena.[16] It is clear that using an intermittent duty cycle will effectively enhance the available pumping capacity not only in the nozzle exhaust chamber but in the rest of the system as well. This approach reaches its ultimate in the shock-tube driven systems about which we will have more to say.

B. The Nozzle–Jet System

As originally conceived by Kantrowitz and Grey, the nozzle was of the conventional converging–diverging type designed in accordance with well-known principles to give a particular Mach number at the exit. There are a number of special considerations that clearly apply to such nozzles for beam systems. The Mach number should be as high as possible; thus, the ratio of the exit area to throat area must be large, e.g., 536 for a Mach number of 10, 15,400 for a Mach number of 20. The advantages of high intensity and narrow velocity distribution promised by the theory are consequent to the absence of collisions between molecules after they have passed the skimmer. This implies a low density in the jet at the skimmer entrance and in the nozzle exhaust chamber. At the same time, the nozzle mass flow must be relatively low so that the pumping system required to maintain these low densities will not be exorbitantly large. Therefore, the nozzle throat area or diameter must be small. The combination of small dimensions and low densities means low Reynolds numbers which are characteristic of flow regimes in which viscous effects such as boundary layers become

important. It is an all too familiar problem in the field of low-density gas dynamics that nozzles designed to give streams or jets at high Mach number and low density inevitably give rise to very thick boundary layers in the diverging section. The result is that the "isentropic core" of the nozzle exit flow becomes very small and often disappears altogether. Each of the early nozzle-beam systems nevertheless used converging–diverging nozzles generally designed to give an exit Mach number of about 4. Because of the viscous effects there were great uncertainties as to the true state of the gas at the skimmer inlet. For this reason it was not possible to make meaningful comparison of actual and theoretical performance. Some persuasive empirical evidence that nozzles were not performing as "designed" was obtained by Becker and Bier.[3] They found essentially the same beam intensities when they cut off the diverging section of their nozzle altogether so that they had a simple converging nozzle with sonic velocity at the throat.

It is possible to describe the flow field from a sonic nozzle expanding into a zero pressure region by a method-of-characteristics solution of the equations relating to inviscid compressible flow. Numerical computations for this problem were first reported by Owen and Thornhill, who also suggested that the centerline gas in a free jet expanding into a region of finite pressure was unaware of the ambient pressure until it reached the so-called jet Mach disk.[17] A schematic representation of the structure of such a jet is shown in the upper part of Figure 4. Thus, in the region between the nozzle exit and the Mach disk, the Mach number along the centerline should be uniquely determined by the distance from the nozzle exit. This property of free jets from sonic nozzles offers the possibility of avoiding many of the boundary-layer problems in ordinary nozzles and has been seized upon by workers in the field of low-density gas dynamics. Sherman, in particular, has exploited this approach.[18] He has extended the Owen-Thornhill type of computation to specific heat ratios other than 1.4 and to a larger range of axial distances.[19] Ashkenas and Sherman developed a number of analytical expressions which are capable of accurately describing a number of the properties of the flow field including the axial and radial Mach number distributions and the relation between the distance from the nozzle exit at which the Mach disk occurs and the pressure ratio across the nozzle.[20] These relations were confirmed with experimental data for flow situations in which the Reynolds numbers are high enough for viscous effects to be negligible.

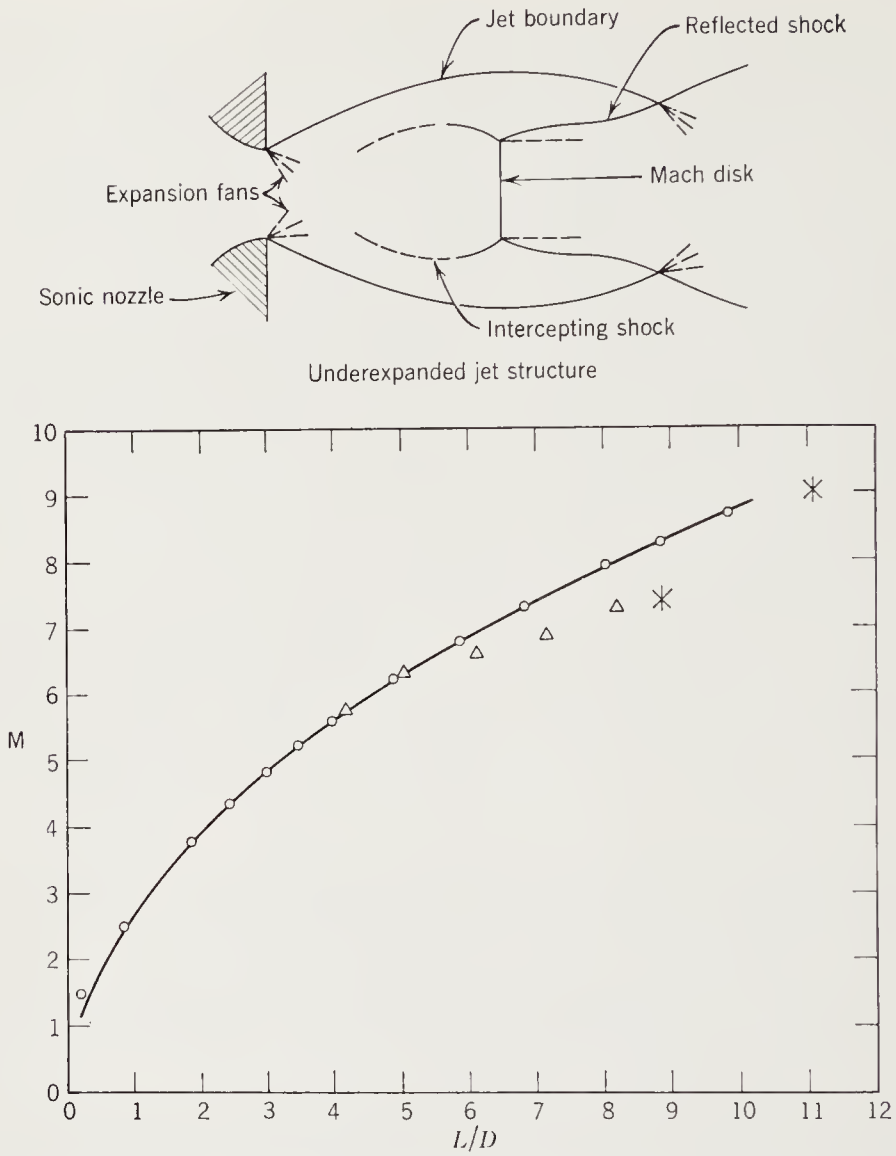

Fig. 4. Schematic structure of underexpanded jet. The solid curve below shows axial distribution of Mach number according to the calculation of Owen and Thornhill. Circles are experimental points by Reis for 200-torr nozzle pressure. Triangles are for 50-torr nozzle pressure. Asterisks indicate Mach disk location.

More specific to our present discussion is the work of Reis and Fenn, which showed that even for the small nozzles used in generating beams, a simple measurement of nozzle discharge coefficient could result in a suitable correction for viscous effects by leading to an effective throat

diameter in terms of which the theoretical inviscid solutions accurately described the real situation.[21] In the bottom part of Figure 4 are shown the experimental Mach numbers as determined by Pitot measurements in nitrogen jets from a 1.6-mm diameter nozzle. The solid curve represents the Owen-Thornhill computation. It is clear that for substantial axial distances the computation seems to be a reliable representation of Mach number under at least some experimental conditions.

As indicated by the triangles in Figure 4, Reis and Fenn observed that there was a definite departure from the Owen-Thornhill curve at large axial distance, indicating a Mach number deficiency. This departure occurred closer to the nozzle as the upstream nozzle pressure was decreased. It was speculated that this Mach number lag might be due to the decrease in collision frequency as the gas density decreased. Further work in our laboratory as reported by Anderson et al. has now pretty well shown that the apparent excess pressure corresponding to low Mach numbers was due to viscous effects at the probe.[9] As it turns out, there is indeed a Mach number lag corresponding to a "freezing" of translational static temperature in the jet, but a Pitot tube measurement alone, even appropriately corrected, is incapable of reflecting it. This incapability is due simply to the fact that the "freezing" of translational temperature corresponds to the transition from continuum (isentropic) expansion to free molecule (nonisentropic) expansion. Only if the constancy of entropy during expansion can be assumed is it possible to convert a Pitot impact pressure to a Mach number. Otherwise, it is necessary to know an additional jet gas property. An obvious candidate is the free-stream static temperature, which is particularly important because it determines the velocity distribution in the beam. Conversely, a measurement of velocity distribution in the beam, which must be known in any event, can lead in principle to a specification of the static temperature in the jet at the skimmer entrance. Accordingly, the direct measurement of velocity distributions has been recognized as a critical experimental objective.

The first measurements of velocity distribution in nozzle beams extracted from jets were made by Becker and Henkes.[22] They used a time-of-flight method in which they chopped the beam by a rotating shutter and observed the time–density pattern of the beam segments downstream from the chopper by means of an ionization detector. Hagena and Henkes introduced some improvements.[12] Phipps, Griffith, and Scott used a multidisk rotating velocity selector.[23] In all of these investigations

there were uncertainties stemming from the possibility of skimmer interaction with the jet gas (about which we will have more to say) and the lack of pumping speed in the nozzle exhaust chamber, which severely limited the range of conditions which could be achieved in the jet. The apparent Mach numbers (on the order of 5 or less) corresponding to the measured velocity distributions were much lower than had been hoped for or might have been expected. More recently, Bier and Hagena, by exploiting the pulsed nozzle technique to overcome the nozzle chamber pumping speed limitation, were able to achieve apparent

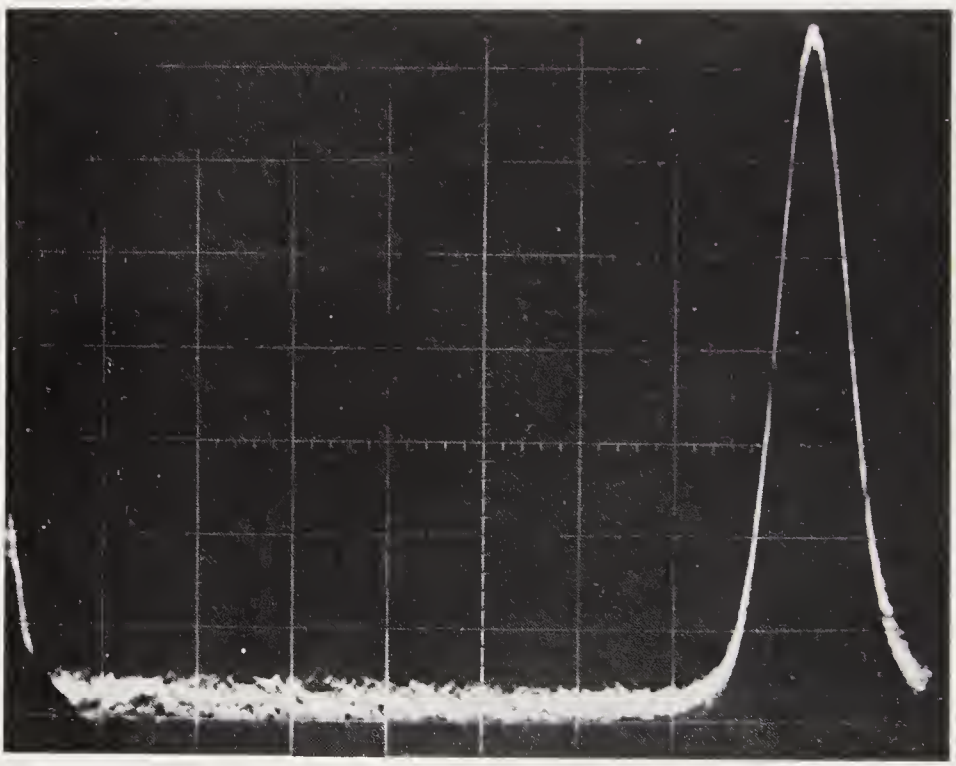

Fig. 5. Typical oscillograph trace obtained in measurement of beam velocities by the time-of-flight technique. The distribution of velocities corresponds to a Mach number of 18 at the skimmer entrance.

Mach numbers as high as 25 with helium.[16] Anderson and Fenn[24] used a time-of-flight technique similar to that of Becker and Henkes. A typical oscillogram trace is shown in Figure 5. Over a wide range of experimental conditions they were able to show that there was indeed a Mach number limitation corresponding to a "freezing" of the

translational jet temperature when the density in the jet reached a critical value which could be characterized by the stagnation density of the gas and the diameter of the nozzle. Their results for argon can be summarized by the equation:

$$M_T = 1.17\ Kn_0^{-0.4} \tag{9}$$

where M_T is the terminal or maximum Mach number achieved in the jet and Kn_0 is the ratio of viscosity-based mean free path in the nozzle stagnation chamber to the nozzle diameter. This correlation has been found to hold for nozzles as small as 0.02 mm in diameter and as large as 4.85 mm in diameter. It is to be expected but it has not yet been shown that gases other than argon will obey a relationship similar to Eq. (9) in which the Knudsen number exponent is $(1 - \gamma)/\gamma$.

If the density in a free jet can get so low that continuum expansion stops, it is very natural to ask whether the background molecules in the nozzle exhaust chamber might not permeate the jet and perhaps scatter molecules from the axis which might otherwise appear in the beam. Fenn and Anderson addressed themselves to this question and found that such scattering effects indeed occurred and were responsible for many cases of low beam intensities which had been observed.[8] They were able to show that the axial distance at which appreciable penetration of background molecules to the axis occurred could be represented by a nozzle Knudsen number dependence similar to the one for terminal Mach number in Eq. (9). The axial distance along the jet at which background gas began to attenuate the beam significantly was always slightly downstream of the point at which Mach number freezing occurred. The amount of attenuation was describable by a simple classical exponential scattering relation in terms of the scattering distance and the density of the background gas.

The observation that translational energy can be "frozen" during the expansion from small nozzles invites the question as to whether other kinetic processes may not show substantial lags. Internal degrees of freedom such as rotation and vibration generally have much longer relaxation times than translation. When such internal degrees are excited ahead of the nozzle, it is clear that the extent of their relaxation during the expansion process must be documented if the energy states of the molecules in the final beam are to be known. We will discuss later what little work has been done on this problem. More pertinent to our present discussion is the possibility of condensation in the jet. This can

occur even with the rare gases which have no internal degrees of freedom. Condensation in supersonic flows is a well-known phenomenon in high Mach number wind tunnels and steam turbines. In these systems the onset of nucleation and subsequent condensation generally manifests itself in observable effects only when the particles of condensed phase have grown to macroscopic size. In experiments with nozzle source beams the problem is much more critical because of the prospective sensitivity of results to very small aggregates of molecules, even dimers and trimers, which might pass unnoticed in other situations.

Becker and his co-workers[25,26] appear to have made the first observations of nucleation and condensation in nozzle beam systems. When they refrigerated their nozzle they found for a given source pressure a critical source temperature at which there was an abrupt increase in apparent beam intensity that they identified with the appearance of a condensed phase. Bentley[27] and Henkes,[28] working independently, reported direct evidence of the existence of microscopic clusters in a carbon dioxide jet from a small nozzle. They were able to obtain a measure of the actual concentrations of these various cluster species by crossing an electron beam with the molecular beam extracted from the jet and obtaining a mass analysis of the ions formed. More recently, Henkes[29] used mass spectrometry to investigate highly condensed hydrogen beams obtained by cooling the nozzle with liquid hydrogen. Greene and Milne[30] and Milne[31] have observed cluster populations in beams of several gases from nozzle sources at room temperature.

While it is clear that mass spectrometry of clusters in nozzle source beams may be a very powerful technique for the study of homogeneous nucleation, it is also apparent that nucleation and condensation must be avoided completely if nozzle beams are to realize their full investigative potential. In their examination of this problem in terms of what is now known, Anderson et al.[9] tentatively conclude that condensation effects should be negligible with many gases even at room temperature if source pressures are below 1 atm. Moreover, the onset of condensation is such a sensitive function of temperature that modest increases in source temperature should provide a substantial safety factor. Bier and Hagena,[16] on the other hand, suggest that condensation occurs more easily. There is some possibility that the relatively abrupt increases in beam intensity which they observed with increasing source pressure and which they identify as the onset of condensation may in fact be due to other causes related to skimmer behavior.

It seems in order at this point in our discussion to summarize the consequences of the various points we have mentioned and to set forth an overall picture of the jet–nozzle complex and its implications with respect to system design as they seem to be emerging. Simple sonic converging nozzles or orifices appear to be most useful because they avoid the boundary layer problems of nozzles with diverging sections and because they are easier to fabricate. The general flow characteristics of the jets from such nozzles are reasonably predictable, if not completely understood. Upstream of the Mach disk the axial distribution of density can be accurately approximated except within a few nozzle diameters of the nozzle exit by assuming that the flow field corresponds to that from a point source located near the nozzle exit plane. That is, the density decreases inversely with the square of axial distance. When the density decreases to a certain critical value, which can be characterized in terms of a nozzle Knudsen number, a transition from isentropic continuum to nonisentropic free molecule flow occurs over a relatively short axial distance, resulting in what might be loosely termed a "surface of transition." Upstream of this surface, the temperature or Mach number on the jet axis is accurately calculable as a function of distance by well-known methods of continuum fluid mechanics. Downstream of this surface the density continues its inverse square with distance decrease but the temperature remains constant and the Mach number becomes "frozen."

Slightly downstream of the transition surface, at a point which can also be characterized by a nozzle Knudsen number, the density of the jet becomes so low that background gas in the nozzle exhaust chamber begins to scatter jet molecules which otherwise would contribute to beam intensity aft of the skimmer. This attenuation is describable in terms of a simple classical exponential scattering law.

With respect to equipment design and operation this overall picture invites the following general conclusions. Pressure ratios across the nozzle should be as high as possible in order to permit the highest possible Mach numbers before the Mach disk is reached. It is advantageous to realize high pressure ratios by low background pressures in the nozzle exhaust chamber in order to obtain low jet densities at high Mach number and to minimize the effect of background scattering. These factors suggest that to make maximum use of available pumping speed, small-diameter nozzles and high source pressures are desirable. On the other hand, high source pressures may introduce condensation

problems. Moreover, small nozzles mean small values of the ratio of mean free path to Mach number in the jet. We will find in the next section that large values of this ratio at the skimmer entrance are desirable. The optimum design compromise will depend somewhat on the experiment to be performed but in general will be dictated by available pumping speed.

C. The Skimmer

The shape and dimensions of a typical skimmer and a nozzle configuration are shown in Figure 6. In the case of the skimmer these are

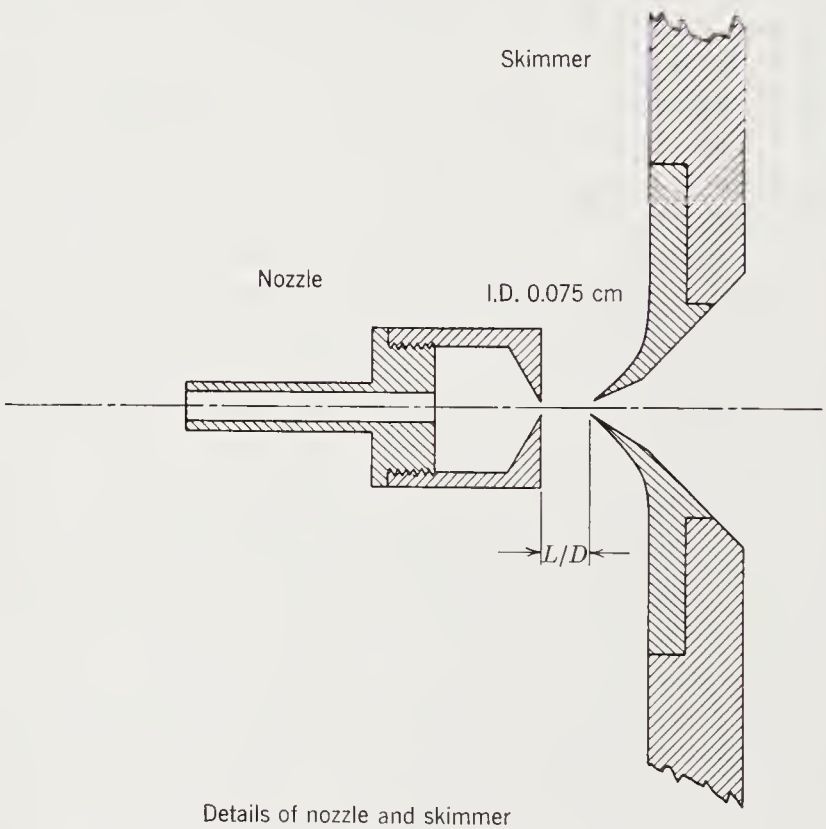

Fig. 6. Construction details for typical nozzle and skimmer.

not arbitrary but stem from careful consideration of somewhat conflicting requirements. Because it is immersed in a supersonic stream, the skimmer must give rise to a so-called bow shock wave like any other object whose maximum dimensions perpendicular to the flow direction

are large with respect to the mean free path in the stream gas. We consider the case of a body which is a sharp pointed cone. For a number of reasons this turns out to be a practical skimmer shape. From theory and experiment in continuum gas dynamics there is a well-established relationship between the Mach number of the free stream and the maximum included angle of a sharp pointed cone which can result in so-called "attachment" of the bow shock wave to the cone apex or tip. If the cone angle is greater than a critical value for a particular Mach number the shock wave will be detached. That is to say, there will be a finite distance between the shock wave and the cone tip. In this region the gas will be in the thermodynamic post-shock state of subsonic Mach number and high temperature. Clearly, if the gas passing through the skimmer is in this post-shock state, all the prospective advantages of the supersonic beam theory will be lost. Therefore, the cone angle must be such that the shock wave will be attached, i.e., as close as possible to the cone apex. It turns out that if the included cone angle is 60° or less, all bow shock waves at Mach numbers above about 1.5 will be attached. At higher Mach numbers, slightly greater angles could be tolerated but about 60° is a convenient design criterion and has been widely used.

Even if the shock wave is attached, there is no implicit assurance that the skimmer flow will indeed be supersonic. To examine the situation at the cone tip we must take a more microscopic view. A shock wave is usually between two and ten free-stream mean free paths thick. This means that the average molecule of gas passing through a shock wave must undergo at least a few collisions in passing from the free stream to the post-shock state. If the lateral dimension of the conical tip of the skimmer, i.e., the diameter of the inlet, is of the order of a free-stream mean free path, it is intuitively reasonable to expect that when the bow shock is attached in macroscopic terms the gas reaching the inlet will not have undergone all the collisions necessary to achieve the post-shock condition. If the mean free path in the free stream is substantially larger than the critical skimmer dimension, the inlet diameter, it seems possible that the gas flowing through the skimmer into the very low-pressure region aft may approach the free-stream condition. The minimum ratio of free-stream mean free path to skimmer inlet diameter, i.e., the skimmer Knudsen number, necessary to avoid collisional perturbation of the free-stream state is not obvious. We will explore this problem further, content now with the observation that the skimmer inlet diameter must be of the order of the free-stream mean free path.

There also exists the possibility of collisional perturbation of the skimmer flow by molecules reflected from the skimmer surfaces aft of the inlet. In order to minimize this effect, the edge of the skimmer opening must be as sharp as possible and the included internal angle of the skimmer cone must be as large as possible. How close it can come to the external angle and how sharp the edge of the skimmer opening can be depend directly on how adept we are in fabrication.

These *a priori* considerations lead to a skimmer design typified by the example in Figure 6. There have been some variations. Bier and Hagena reported results with conical skimmers of several angles.[16] They found, as we have in our own laboratory, that with smaller internal included angles there is somewhat more apparent scattering loss at high jet densities. At low jet densities the effect of internal angle is less pronounced, but increasing external angle seems to result in larger losses. It will be recognized that the situation in the vicinity of the skimmer inlet is analogous to the case of the effusion aperture in a classical oven beam. There it has long been recognized that the critical dimension (width if a slit, diameter if an orifice) must be less than the mean free path of the gas in the oven if the effusion flow field from which the beam is drawn is to be unperturbed by collision effects. It might be expected that collision effects would be much more serious in supersonic beams because of possible loss of the narrow velocity distribution which is so desirable. In effusion beams the velocity distribution is inherently completely random and cannot very well be further spread. The question becomes whether the collisionless skimmer flow assumed in the Kantrowitz-Grey analysis can be actually realized in practice even if we take all the *a priori* precautions we have cited. We note already the seeds of contradiction in the fact that jet densities must be high if Mach numbers are to be high, and low if collisionless flow through the skimmer is to be achieved with skimmer inlet diameters of any reasonable size.

The earliest data reported by Becker and Bier and by Parker, Kuhlthau, Zapata, and Scott indicated that observed intensities were somewhat below those which might have been expected from theory.[3,4] The situation was not clear at that time because there were substantial uncertainties as to Mach number and density at the skimmer entrance. Consequently, meaningful comparisons with theory could not be made. The already mentioned work of Reis and Fenn indicated that the Mach number in the jet at the skimmer entrance could be fairly well approxi-

mated by the Owen-Thornhill calculation in terms of the distance between the nozzle and the skimmer. On this basis, Deckers and Fenn found that observed intensities were substantially below theory. This observation was confirmed subsequently by Scott and Drewry[32] and by Bier and Hagena,[7,15] who also found that velocity distributions were broader than the theory predicted. Before we undertake an explanation of these departures from ideality it is in order to present some typical experimental results in detail.

In Figure 7 are shown some measured intensities with nitrogen at a source temperature of 300°K at various source pressures as a function of distance between the nozzle exit and the skimmer. Also indicated on the abscissa are the Mach numbers in the free stream, based on the assumption that the state of the gas on the jet axis is correctly described by the previously mentioned Owen-Thornhill calculation. These results, reported by Deckers and Fenn,[6] were obtained with a nozzle diameter of 0.8 mm and a skimmer diameter of 1.6 mm. The intensities relate to a position 10 cm downstream from the skimmer inlet. We note in passing that Deckers and Fenn observed that the inverse square relationship of intensity to distance from the skimmer was accurately followed out to a distance of at least 60 cm as predicted by the theory. This indicates no appreciable scattering due to background gas aft of the skimmer.

There are a number of features of the curves in Figure 7 which deserve attention. In the first place, the observed intensities are attractively high. We estimate that with an oven beam at 300°K having a circular effusive orifice of the same size that maximum intensities at 10 cm would be approximately 7×10^{14} molecules/cm^2-sec, only about 10% of the highest values shown in the figure. More interesting, for our present purpose of comparing theory with experiment, is the shape of the curves and the relative effect of pressure. The theoretical expression for ideal performance in no way explains the sudden decrease in intensity with increasing distance which the curves for 50- and 100-torr nozzle pressure show. The theory also does not explain the rise in intensity with further increases in distance to a maximum value. There is nothing in the theory to account for the fact that between 10 and 20 nozzle diameters a higher intensity is obtained with 50-torr nozzle pressure than with 100-torr nozzle pressure. We hasten to emphasize that these curves are not unique to our apparatus, but are entirely typical of those obtained by all other groups who have reported such data.

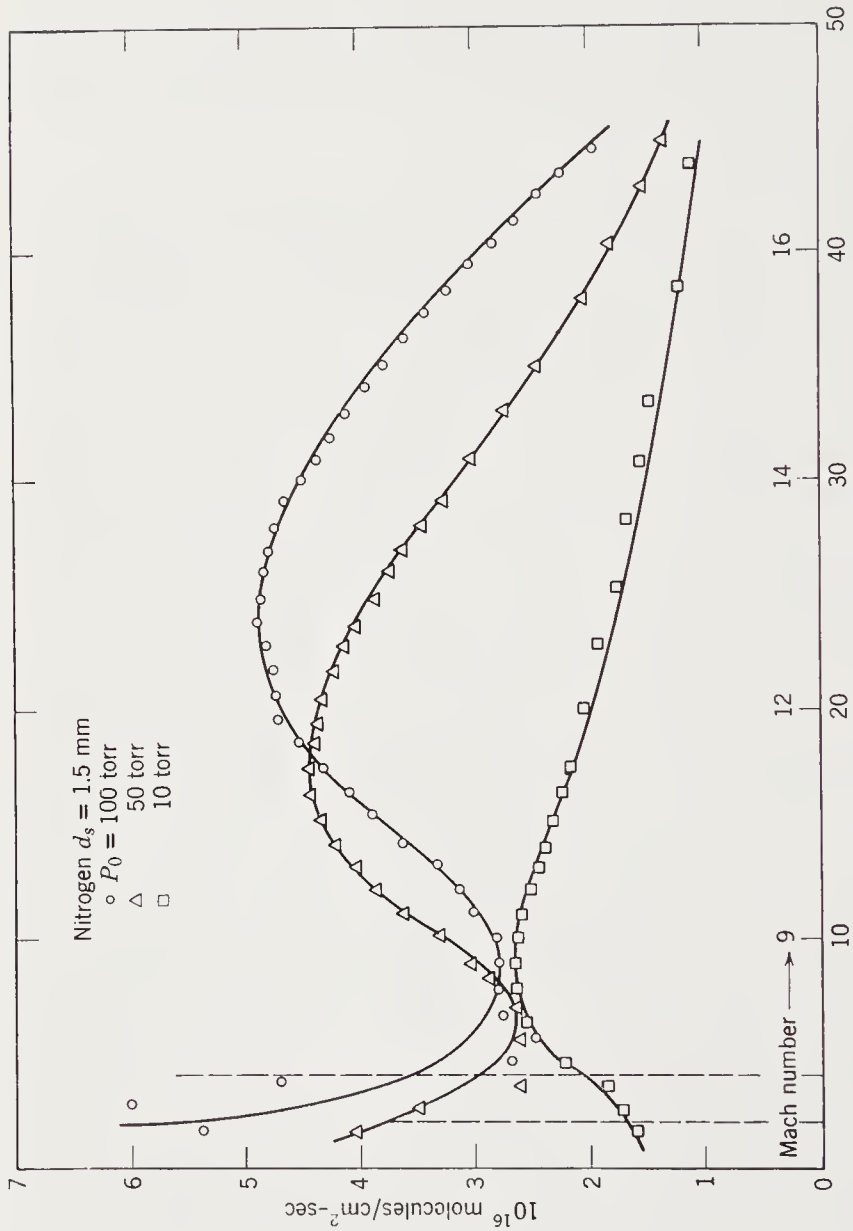

Fig. 7. Measured beam intensities at various nozzle pressures as a function of nozzle–skimmer distance (Mach number). Data are from Deckers and Fenn for nitrogen at room temperature. Dotted lines represent distances for 50- and 100-torr nozzle pressures beyond which Reis could not swallow shock using a pumped probe.

In an attempt to explain the behavior indicated in Figure 7, Fenn and Deckers[33] proposed that under many experimental conditions there was a normal shock wave at the skimmer inlet. This shock was "swallowed" in the higher pressure cases when the skimmer was close to the nozzle. In such a "swallowed shock" condition there is in fact no shock wave in the stream tube entering the skimmer and the skimmer in effect becomes a nozzle and free expansion to high Mach number occurs downstream of the skimmer with no shock losses. As the distance between the skimmer and the nozzle increases at a particular nozzle pressure, the gas density at the skimmer inlet decreases and viscosity effects cause the shock wave to "pop out" or form in front of the skimmer inlet, resulting in an abrupt decrease in beam intensity over a very short increase in nozzle skimmer distance, due perhaps in part to a slight decrease in skimmer flow but mostly to thermalization accompanying the post-shock state. At the relatively low density represented by the 10-torr case in Figure 7, the relative flow resistance in the skimmer due to viscosity is never low enough to permit the shock wave to be swallowed. This concept of a normal shock, sometimes detached and sometimes swallowed, is consistent with observations made by Reis and Fenn in their study of mass flow through a probe similar in shape and dimension to the skimmer. We have used the continuum concept of viscosity to explain this shock behavior. It is just as effectively interpreted in terms of the increase in penetration distance of molecules reflected from the skimmer inlet surfaces as the stream density is decreased.

This model which accounts for the abrupt decrease in intensity with distance close to the nozzle by postulating the formation or appearance of a shock in front of the skimmer inlet was further pursued by Fenn and Deckers as follows. As the nozzle–skimmer separation is increased beyond the point at which the minimum in intensity appears, the stream density becomes lower, the shock wave becomes thicker, and the skimmer inlet penetrates the shock zone further and further. Thus the gas actually entering the skimmer becomes less and less completely "shocked" until finally at low enough densities the gas entering the skimmer is in the free-stream condition. By such a phenomenological argument, Fenn and Deckers arrived at the idea that the ratio of observed intensity to theoretical intensity should correlate in terms of the dimensionless group, Knudsen number divided by Mach number, computed in terms of free-stream properties at the skimmer entrance, the skimmer entrance diameter being the characteristic dimension by

which the Knudsen number is defined. The success of this proposed correlation is shown in Figure 8, where data are plotted for nitrogen over a wide range of experimental conditions. All the data of Figure 7 are included together with other data from our laboratory using a smaller skimmer. Whether the normal shock picture is correct or not, it is clear that the plot of beam "efficiency" against Kn/M is a very compact way of presenting and comparing intensity data. The "universality" of this relation is indicated by the inclusion of intensity data for nitrogen presented by Scott and Drewry which are represented by the solid circles.[32] In a private communication Professor Scott has told us that all of his data for nitrogen and argon fall in this same pattern. Our own results with argon show a similar behavior. The apparent differences between our results and those from the University of Virginia, i.e., the fact that the latter tend to show a higher efficiency, are probably due to differences in detector calibration. On this score we suspect that their data are probably more accurate than ours. Also included in Figure 8 is one point for hydrogen from the original paper of Becker and Bier (indicated by the arrow). Only for this one point was there sufficient supporting information for us to estimate the theoretical intensity and the value of Kn/M.

The apparent success of Kn/M as a correlating parameter does not, of course, necessarily confirm the validity of the model which Fenn and Deckers proposed to account for skimmer interference. It is possible to "explain" the qualitative features of the correlation in Figure 8 by any of a number of models which have been suggested and which will be mentioned below. Moereover, there are difficulties in justifying any particular definition of Knudsen number because of conceptual uncertainty in the meaning of "mean free path." It is not at all clear, for example, whether the appropriate distance between collisions should be based on a coordinate system moving with the molecules as used in Figure 8 or one at rest relative to the laboratory, i.e., the skimmer, as discussed by Muckenfuss.[34] Even the definition of a collision is arbitrary and it is quite clear that a viscosity-based hard-sphere diameter for the jet molecules is very crude approximation at the extremely low temperatures in a high Mach number jet from a room-temperature source. It seems more likely that the disturbing collisions are between free stream molecules and those reflected from the skimmer surfaces. Such collisions occur at an energy roughly equivalent to the thermal collisions in the source. This equivalence

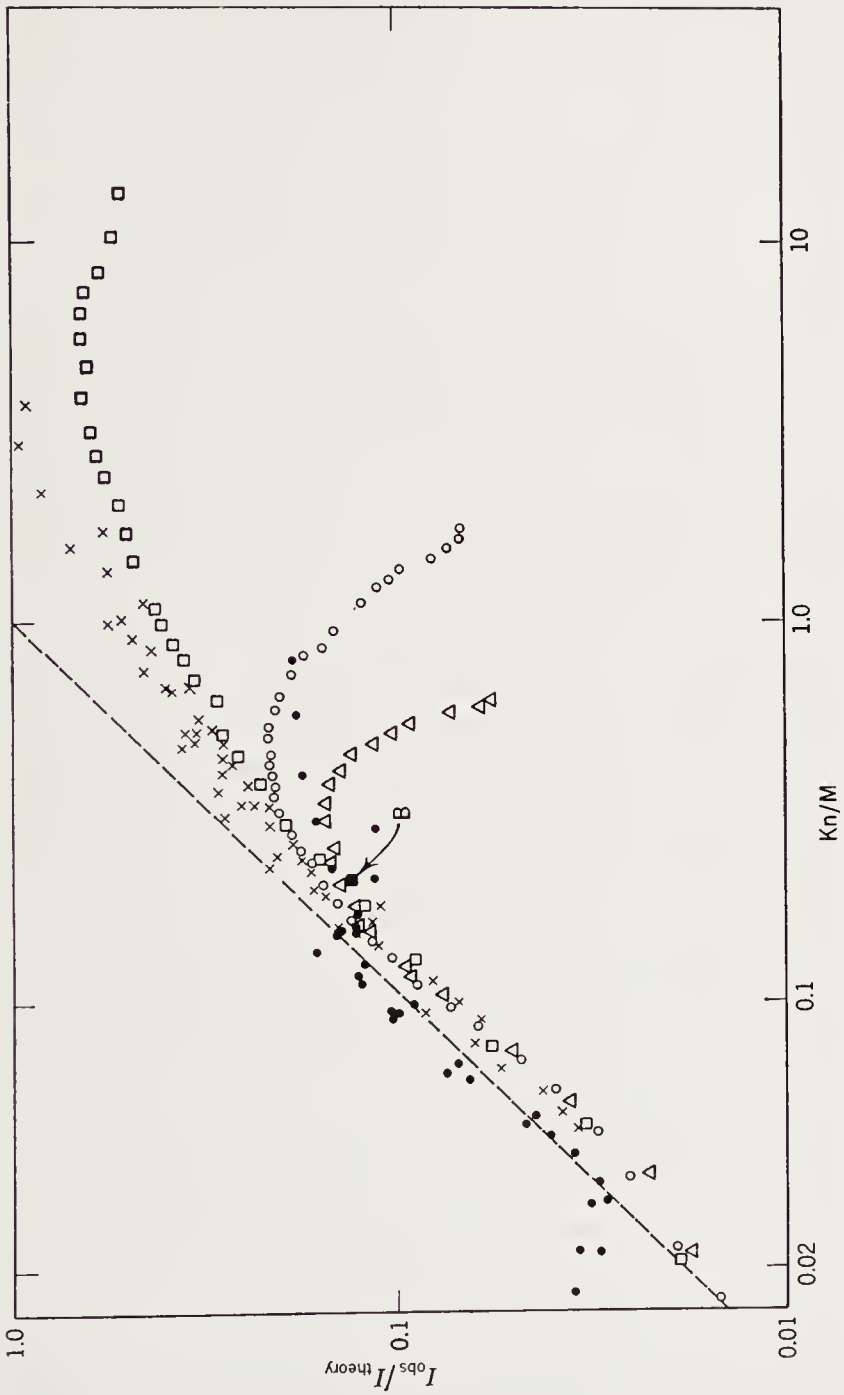

Fig. 8. Ratio of observed to theoretical intensity as a function of Knudsen number/Mach number based on free-stream conditions. Open points are from Fenn and Deckers for nitrogen at nozzle pressures of 100 torr (triangles), 50 torr (circles), and 10 torr (squares) with a 1.6-mm skimmer. Crossed points are for various pressures with 0.4 mm skimmer. Solid points are for nitrogen from Scott and Drewry. Arrow indicates single point for hydrogen from Becker and Bier.

may account for the apparent effectiveness of the use by Fenn and Deckers of a collision diameter based on a source temperature–viscosity cross section. No matter what model is chosen it seems intuitively reasonable that a Knudsen number, however defined, is an inverse measure of the number of collisions which occur. Therefore, the approach to theoretical intensity should be proportional to such a Knudsen number. The Mach number in the denominator of Kn/M would seem to be a measure of the sensitivity of the system to disturbance by collisions. At high Mach numbers a relatively slight change in the trajectories of molecules passing through the skimmer can significantly affect the intensity of the beam. At lower Mach numbers a relatively greater trajectory change would be required for the same proportional reduction in beam intensity. From the perspective of fluid mechanics it is perhaps not at all surprising that Kn/M should be a powerful correlating parameter because it is essentially equivalent to an inverse Reynolds number. Reynolds number has long been used to account for viscous effects in continuum flow, and viscosity is, of course, a measure of collisional transport of momentum. In view of all these uncertainties and arbitrary features of the correlating parameter it is not particularly significant that there should appear in Figure 8 a general drift away from linearity at high values of Kn/M.

A much more serious departure from the correlation is indicated by the three distinct branches in Figure 8 which show a pronounced but orderly descent. Fenn and Deckers tried to "explain" these droops in terms of a boundary layer buildup in the skimmer. In our earlier discussion of the jet we have indicated that the recent results of Fenn and Anderson[8] have fairly well established that these abrupt departures from the correlation, which start at approximately the point where the maximum intensities occur in Figure 7, are due to scattering of jet molecules which otherwise would contribute to beam intensity by background gas in the nozzle exhaust chamber.

In summary, we can say that the overall character of the experimental results typified in Figure 7 can be accounted for by the fairly abrupt appearance at small nozzle–skimmer distances of a shock or shocklike structure in the stream at the skimmer entrance, the gradual attenuation of this shock with decreasing stream density as the nozzle–skimmer distance increases, and the scattering of jet molecules by background gas at still larger distances. We should add that it is possible to explain some other observations by this model. We mentioned earlier that Bier

and Hagena identified the abrupt increase in beam intensity which occurred when source pressures were increased as the onset of condensation in the jet. We suggest that such increases in intensity can be accounted for by the shock's being swallowed rather suddenly as the jet density increases with increasing source pressure. The phenomenon is analogous to what is clearly indicated in Figure 7 as the nozzle–skimmer distance is decreased at constant source pressure. Similarly, it is clear in Figure 7 that at some nozzle distance, e.g., at the location of the dotted lines, there is a marked increase in beam intensity as the source pressure goes from 10 to 50 to 100 torr. Another noteworthy item comes about because of the collisional cutoff discussed by Anderson and Fenn.[24] If the skimmer is downstream of the "surface" of transition from continuum to free molecule flow, the beam detector will "see" through the skimmer an area of this surface which is essentially a distributed effusive source of molecules that have superposed on their residual random thermal velocities the mean stream velocity. The contribution to detector signal from each point on this area will decrease inversely with the square of increasing detector–surface distance as the nozzle–skimmer separation is increased. At the same time the size of the area on the surface which is "seen" by the detector will increase with the square of the same distance. The net result is that in the absence of background scattering and skimmer effects the total detector signal will remain constant with increasing nozzle–skimmer separation as is shown in Eq. (7). If, on the other hand, one had presumed that continuum expansion obtained all the way to the skimmer so that the Mach number continued to increase with increasing nozzle–skimmer separation, then one would compute a "theoretical" intensity in terms of nozzle–skimmer separation which could be substantially lower than it should be.

For the sake of completeness and objectivity we must admit that there have been other explanations of the discrepancies between theory and experiment as far as intensity is concerned. Bier and Hagena,[7] in light of a schlieren study of jet–skimmer interaction by Bier and Schmidt,[35] proposed that low efficiencies and broad velocity distributions could be explained in terms of shock waves aft of the skimmer entrance or by shocks in the jet not caused by the skimmer, e.g., the Mach disk. It should be noted that these schlieren studies were carried out at much higher densities than those encountered in nozzle beam systems. In our view there is some doubt that such high-density results can be considered as true analogs of what happens at very low densities.

Oman presented an analysis of beam attenuation in terms of scattering effects due to molecules reflected forward from the external skimmer surfaces.[36] It is possible that this mechanism may be reasonable at very low densities, but it does not seem capable of explaining the extreme intensity losses which have been observed at relatively high jet densities. The Oman model can perhaps be considered as the residual vestige of what at higher densities seems to have at least some of the properties of a shock wave. Valleau and Deckers have made an attempt to account for the departures from theory in terms of self-scattering by collisions between the beam molecules themselves as a consequence of the high intensities and residual random velocity distribution.[37] This is an interesting approach but it is difficult to reconcile with the experiment with a cooled skimmer reported by Anderson et al.[9] A copper skimmer was immersed in a carbon dioxide jet. Observed intensities were higher by a factor of 3 when the skimmer was cooled with liquid nitrogen than when it was at room temperature. At liquid nitrogen temperatures a substantial fraction of the carbon dioxide molecules striking the skimmer surfaces were condensed and did not reflect. This experiment seems to comprise fairly conclusive evidence that it is the skimmer, or rather interaction between the skimmer and the jet, which causes loss of beam intensity.

Our discussion of the differences in nozzle beam performance between theory and experiment as affected by skimmer design and operation have thus far been largely in terms of observed beam intensities. Fully as important both for diagnosing system behavior and for ultimate use and application are the velocity distribution characteristics of nozzle beams. Only recently have velocity distribution results been obtained over any substantial range of operating conditions. We have already referred to some of these in our discussion of the jet characteristics. We will mention some others later when we consider the applications of nozzle beams. Now we would call attention to two results obtained by Anderson and Fenn[24] which seem pertinent to our present discussion of skimmer design. The first of these has to do with their observation that at large enough nozzle–skimmer separations there was no change in beam velocity distribution with increasing nozzle–skimmer distance. This constancy of velocity distribution even while intensities were decreasing because of background scattering of the jet implies at once that scattering cross sections are not strongly dependent upon velocity over the relatively narrow range of velocities which obtain at

high Mach number and that skimmer interactions are negligible at large enough nozzle–skimmer separations, i.e., low enough jet densities. Thus, it is possible to extract a beam from a high Mach number jet without perturbing the state of the molecules in the jet. This is a most important conclusion. The second result which is germane to our present discussion was their observation that as nozzle pressure was decreased at a fixed nozzle–skimmer separation, the velocity distribution fairly rapidly decreased in breadth. This decrease is entirely consistent with the model that proposes a shocklike structure at the skimmer inlet which is gradually attenuated as the stream density is lowered.

We conclude this rather lengthy discussion of skimmer behavior with some general remarks. It appears that skimmer interaction can be avoided if the parameter Kn/M has a value higher than unity. Thus the design optimum for maximum intensity would appear to be that in which the ratio of mean free path in the jet (calculated by assuming a constant viscosity cross section under source conditions) to the Mach number (calculated by the Owen-Thornhill relation or its equivalent) is equal to the skimmer inlet diameter. The possible intensity increases with skimmer diameter so the skimmer should be as large as available pumping speed aft of the skimmer will permit. Of course, an implicit limitation on skimmer size is the pumping speed in the nozzle exhaust chamber because it dictates the ratio of free-stream mean free path to Mach number which can be achieved. These general rules are subject to some modification due to jet scattering by background pressure and the consequence of transition from continuum to free molecule flow.

Insofar as the analogy between the skimmer and an oven aperture can be extended, it would seem that a two-dimensional slit geometry would be advantageous for the same reasons that it has proved useful in effusion systems. A slit-shaped skimmer should provide a higher ratio of beam intensity to area than a circular one because it could realize a value of Kn/M of unity at a higher jet density for the same area. These considerations lead to possible economies in pumping speed both fore and aft of the skimmer. Moreover, it is quite likely that in many experiments a ribbon-shaped beam would be better than a cylindrical one. We have carried out a few preliminary experiments with slit-shaped skimmers which seem to support these speculations.

Practically all of the experimental results which have been the basis for our discussion have been obtained with nozzle sources at room temperature. Therefore, the conclusions of this section may require

modification for situations in which the source temperature is substantially above room temperature. There are many good reasons for going to higher temperatures. Some results have been obtained, which we will discuss later, but the overall experience at higher source temperatures is not yet sufficient to provide a firm empirical basis for high-temperature operation. Consequently, there is still much to be done before the art of nozzle beam design can be considered fully developed.

IV. APPLICATIONS OF NOZZLE BEAMS

The possible applications of nozzle beams are in general the same as those of the more conventional beams. In a broad sense they fall into two main categories. In the first of these the beam is simply a diagnostic sampling device and the properties of the beams are a measure of the properties of the system being sampled. Thus, for example, the experimental verification of the Maxwell-Boltzmann distribution law of kinetic theory resulted from the velocity analysis of an oven beam. Because the jet from which a nozzle beam is extracted is a dynamic system, the properties of nozzle beams can be used as a measure of rate processes. Oven beam properties, on the other hand, would seem to be capable only of characterizing static equilibrium systems. In the second broad category of applications the beam itself plays a more active role. Its purpose is to provide a highly directed system of molecules which undergo no collisions among themselves so that their interactions with applied fields and various kinds of targets including unbound (gas phase) molecules can be studied more or less unambiguously. In all such experiments, the higher the beam intensity the bigger the signal. Consequently, nozzle beam techniques offer great prospective advantages over effusion beams. In this section we will review briefly what little has been done thus far with nozzle beams in each of these categories.

A. Sampling Experiments and Their Interpretation

We have already indicated that the velocity analysis of nozzle beams which has been carried out in order to elucidate overall performance and the nature of skimmer interaction effects has provided information about what might be called the relaxation rate of translational energy. So far, the reliable data are limited to helium and argon over a relatively narrow range of low static temperatures consequent to expansion of

source gas at room temperature. Extension of such studies to higher source temperatures and to other kinds of species remains to be exploited. We have also referred to the problem of nucleation-condensation kinetics and the opportunity for studying these processes which is promised by nozzle beam systems.

Another relaxation process occurring during expansion in the jet involves the internal degrees of freedom of the molecules. Clearly, if the expanded gas can reach a density so low that observable translational lags occur, i.e., the translational temperature lags behind the density decrease, then vibrational and rotational lags should also be observable. As an example, consider the combination comprising a molecule with a collision diameter of 4.5 Å, an initial density corresponding to a pressure of 100 torr at 300°K, and a converging nozzle with a 0.8 mm diameter throat. If 10^4 collisions are required for relaxation of internal energy, a typical value for vibration, the internal temperature will become "frozen" before a Mach number of about 1.5. If only 10 collisions are required for relaxation, as in some cases for rotation, the internal temperature will still lag about 20% behind the translational temperature at a Mach number of 4. These relaxation effects are important because they affect the mean velocity and translational temperature of the jet, which determine the intensity of the resulting beam. They also influence the internal states of the molecules in the beam.

In principle, it would seem possible to obtain information about vibrational and rotational relaxation times by the velocity analysis of the beams extracted from the rapidly expanding small jets. Hagena and Henkes have used this technique to study the vibrational lags in the expansion of carbon dioxide and uranium hexafluoride.[12] It should be remembered that on the basis of velocity distribution alone only the translational temperature can be measured. Therefore, rotation and vibration lags can be inferred only by an energy balance. Moreover, because the kinetic energy of the beam varies as the square of its mean velocity, any velocity deficiencies which are observed are likely to be a relatively insensitive measure of the residual internal energy. When both vibration and rotation are involved it would seem difficult to distinguish between the two. An independent means of measuring rotational or vibrational temperature in the beam molecules would be most valuable and hopefully will be ultimately achieved. The important realization in the present state of nozzle beam art is that the expansion process from small nozzles is sufficiently rapid that molecular internal energies can

apparently be frozen and the molecules with these internal energies can be "extracted" and examined without subjecting them to further collisional perturbation. In this connection it is clear that meaningful experiments can be made only if perturbation due to skimmer–jet interaction is entirely absent.

B. Direct Studies with Beam Molecules

So far there have been relatively few investigations in which a nozzle beam system has been used in the active sense. We will mention those that we know about as of this writing.

Koros, Deckers, and Boudart at Princeton developed a direct method of determining the sticking probability, or condensation coefficient, of water molecules on ice.[38] The nozzle system was used to produce a beam of water molecules having an intensity of 1.1×10^{15} molecules $cm^{-2}\,sec^{-1}$ over an area of about 6 cm^2 at the condensing surface. The surface was a copper sheet suspended from a quartz helix. The copper sheet was cooled by radiation to a liquid-nitrogen cooled shield (see Fig. 9). Two types of targets were used: one, a flat copper sheet for

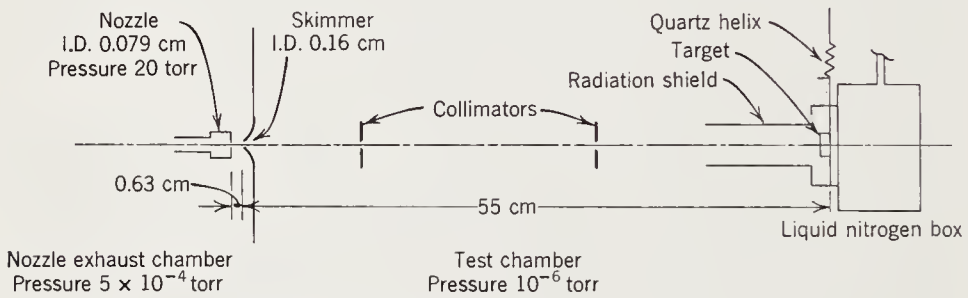

Fig. 9. Apparatus used by Koros et al. in measuring the sticking coefficient of water molecules on ice between −115 and −140°C.

single collisions; the other, a similar sheet with a cylindrical extension to allow multiple collisions, giving almost total condensation of the incoming molecules for measuring beam intensity. The increase in extension of the quartz helix provided a measurement of the weight gain of the target, giving a direct measurement of the condensation rate. The condensation coefficient was found to be 0.83 ± 0.15 for a target temperature range of −115 to −140°C. Nearly the same value has been reported by other investigators who studied evaporation of ice in the range from −40 to −80°C. The intensities available with oven beams

would have made this experiment much more difficult. However, there still exists some uncertainty in interpretation because of the possibility that some nucleation-condensation might have occurred in the jet so that some of the water molecules hitting the target could have been in the form of clusters or aggregates. Our best guess is that there was no condensation. We base this on the fact that intensities were not inordinately high as has been observed when condensation is known to occur. Moreover, Milne and Greene have indicated to us that they obtained very little evidence of condensation in water vapor even with a source pressure of 1 atm.[39] The source pressure in the Koros experiment was about 25 torr.

Nowak, Deckers, and Boudart at Princeton carried out a study of the interaction of a methane beam with a heated single crystal of silicon.[40] The sticking-reaction probability γ of cold methane molecules impinging on the surface was measured at surface temperatures of 750 to 875°C. Single crystal silicon wafers were suspended in the path of the beam by a quartz helix serving as a vacuum microbalance similar to that used by Koros. The targets were heated by radiation from a projection lamp placed in a polished ellipsoidal reflector. It was postulated that methane molecules decompose to carbon on the silicon surface and that the carbon thus formed diffuses into the silicon lattice. The measured value of the reaction probability varied from 0.05 to 0.67 over the temperature range studied. The data could be represented by the expression $\gamma = 2 \times 10^7 \exp[-E/RT]$, where E is about 40 kcal mole^{-1}. It is noteworthy that only one specimen of silicon of several tried resulted in any reaction at all. Results with this one specimen were reproducible.

Anderson and Boudart at Princeton studied the oxidation of single-crystal germanium wafers with oxygen beams.[41] The value of the reaction probability $\gamma = 0.04$ was obtained for all values of surface temperature from 470 to 900°C and nozzle gas temperatures from 30 to 450°C. Under the conditions of this experiment, the molecules of oxygen sticking to the surface reacted to form volatile germanium monoxide. The surface was kept clean by the continuous evaporation of the germanium monoxide formed. The technique of target heating and weight measurement was identical to that used by Nowak. The maximum oxygen beam intensity obtained was 1.4×10^{16} molecules cm^{-2} sec^{-1} over an area of several square centimeters.

An interpretation of the finding that the sticking probability was independent of both surface temperature and nozzle temperature over

wide ranges requires a knowledge of the state of the oxygen molecules striking the target. At present the lag in rotational relaxation during expansion in the jet can only be estimated. Thus, the rotational temperature of the oxygen molecules is uncertain. It is also uncertain whether increasing nozzle temperature from 30 to 450°C changes the rotational temperature to a significant extent.

Leonas of Moscow University used nozzle beam techniques to produce beams of carbon dioxide, argon, and nitrogen for an investigation of energy transfer with solid surfaces.[42] From measurements of the velocities of molecules reflected from aluminum, steel, and copper surfaces, he was able to estimate the energy transferred between beam molecules and the surfaces.

It is clear that a nozzle beam's advantages in high intensities and narrow velocity distributions make possible a large number of experiments of the sort we have mentioned. Offsetting these advantages up to now has been a lack of complete knowledge of the state of the molecules in the beam. When the beam formation process is more fully understood, the fruitful application of nozzle beams to a variety of problems will be expedited. The preliminary results which we have described serve at once to emphasize the brightness of future prospects and the importance of quantitative characterization of beam properties.

V. ENERGY LIMITATIONS AND THE USE OF MIXED GASES

A. The General Problem of Energy

The discussion thus far has been confined to cases in which pure gases are expanded through nozzles to form the supersonic flow field source. As we have tried to demonstrate, such sources lead in both theory and practice to much higher useful beam intensities than can be achieved by more conventional effusive source systems. There are still some disparities between theory and practice to be resolved but the soundness of the general principle seems well established.

In addition to intensity there is another limitation to classical oven beam technology which is particularly vexing to its use in the study of chemical kinetic problems which are a focal point for this volume. This limitation has to do with energy. Clearly, in the case of an oven beam, the translational kinetic energies which can be achieved are limited by the temperatures which can be maintained in the oven source. There is,

of course, a slight enhancement of mean beam energy due to the selectivity of the effusive slit for molecules of higher velocity. This amounts only to an additional $kT/2$ and is relatively inconsequential. In principle, also, there are available the high-energy molecules in the tail of the Maxwell-Boltzmann distribution and by appropriate velocity selection these could be used to form a "high-energy" beam. Unfortunately, such high-energy molecules are in a real minority. We have already observed that even total intensities in oven beams are frustratingly low. The possible partial intensities of high-energy molecules would seem to be hopelessly insignificant for experimental use. The net result of this limitation is that with about 3000°K as the practical upper limit for oven operating temperature, the maximum useful beam energies which can be obtained are of the order of half an electron volt or 10–12 kcal $mole^{-1}$. Such energies are at the low end of the scale applicable to chemical bonds. Dissociation energies for many simple molecules can be 20 times as high. There are many interesting chemical reactions which have activation energies several times this limit. Consequently, ordinary beam techniques suffer severe inhibitions in their applicability to many interesting chemical and physical problems.

The situation with nozzle beams of pure gases is only slightly different. The final beam energies which can be attained still depend essentially upon source temperature. Because the expansion process results in the conversion of total *enthalpy* into beam translational energy, final beam energies are higher than the mean thermal translational energy upstream of the nozzle by a factor which at Mach numbers above about 4 is approximately $2\gamma/3(\gamma - 1)$. Thus, with a nozzle operating at a temperature of about 3000°K, beam energies of the order of 1 eV could be achieved if completely relaxed expansion to high Mach number could be obtained.

In order to achieve beam energies higher than an electron volt by purely thermal means, therefore, it is necessary to have source temperatures substantially above 3000°K. One way to do this is to heat the gas upstream of the nozzle by means of a reflected shock wave. Such heating is transient so that the nozzle itself does not become too hot. Skinner at Cornell Aeronautical Laboratory has built such a shock tube driven nozzle beam and has reported preliminary success in obtaining a high-energy beam.[43] Recently, momentum transfer results for argon at about 1.2 eV were obtained by means of a ballistic pendulum.[44] Oman and his associates at Grumman Aircraft are also trying this

approach.[45] Although it is early to judge the merits of shock tube beams, there would seem to be two major difficulties inherent in the idea. Clearly the resulting beams will be of only short duration, a few milliseconds per shot, so that the rate of data accumulation will be small for many kinds of experiments even when multiparallel detection systems are used. The other problem relates to the state of the beam molecules. At source temperatures high enough to give energies much above 1 eV there will be dissociation and electronic excitation in the source gas. The extent of relaxation during the expansion process will have to be very carefully documented before the state of the final beam molecules can be characterized or controlled. We await with interest further progress in this direction.

Another approach is to use cooled nozzles and arc-heated source gases. Knuth at UCLA and McGinn at General Electric have built such arc jet beam systems and have made some preliminary runs with argon, achieving beam energies in excess of 1 eV.[10,13] As in the case of shock-heated gas, there would seem to be the need for detailed understanding of relaxation during arc jet expansion if the state of the final beam molecules is to be well known. There is the additional problem of possible electrode contamination of the expanding gas. Even though the contamination may be kept down to a few parts per million averaged over the entire jet, the relative concentration in the beam may be much higher because of the often observed preferential accumulation of heavy particles on the beam axis. We will have more to say about this heavy particle concentration effect.

Of course, there is an entirely different approach to the problem of high beam energy in which electrostatic acceleration of ions is followed by charge exchange to obtain a neutral beam. This technique is discussed in detail by Amdur and Jordan in Chapter 2 of this volume. In principle, it can lead to any desired energy in the final beam. Unfortunately, because of space charge effects the achievable beam intensity falls rapidly with decreasing beam energy. Consequently, most work with charge exchange beams has been at beam energies above 100 eV. The interesting range below 10 eV will probably be invaded only with difficulty by this technique but with sufficient ingenuity in focusing and detection methods it is quite possible that charge-exchange beams may become a powerful tool for studying collision processes in what is still the no-man's land between 1 and 10 eV. As a matter of fact, Amdur and his associates have studied some collision processes in this range

already by looking at collisions which result in low angle scattering. Recently, also, Utterback and Miller have reported measurable intensities at beam energies as low as 10 eV.[46] Still unachieved by this method and still most attractive for chemical kinetic work is a beam of relatively high intensity having an energy between 1 and 10 eV.

B. Nozzle Beams and Mixed Gases

Now there is implicit in the nozzle beam approach a means of obtaining beam energies in the desirable range above 1 eV. This possibility does not seem to have been appreciated by earlier workers in the field but it was in fact the main motivation behind the program in our laboratory. Consider what might be expected to happen when a binary gas mixture is expanded from the nozzle to form the supersonic jet source. If in the expansion process there are enough collisions to maintain energy and momentum equilibrium between the two species, then at the entrance to the skimmer both species will have the same velocity and the same static temperature. The actual values of velocity and temperature will correspond to those of a uniform gas having the same source temperature and values of molecular weight and specific heat ratio equivalent to the concentration-weighted averages of the two species for the particular mixture. Suppose the mixture comprises 1.0% of nitrogen in hydrogen. Then the mean jet velocity will be almost equal to that of pure hydrogen. The nitrogen molecules will have this same velocity. This means, of course, that the translational kinetic energy of the nitrogen molecules in the final beam will be higher than the corresponding energy obtained by expanding a pure gas by a factor approaching 14, the ratio of the molecular weight of nitrogen to that of hydrogen. Thus with such a 1% mixture of nitrogen in hydrogen, the energy of nitrogen molecules in the beam would be of the order of 1.3 eV if the nozzle temperature were 300°K and 13 eV if the nozzle temperature were 3000°K. Correspondingly higher energies would be obtained with heavier molecules in hydrogen.

This energy enhancement of heavy molecules in a light gas is a most exciting prospect but there are some caveats to be heeded. In the first place the energy values cited presume ideal expansion to infinite Mach number and apply strictly only to finite dilution of the heavy molecules. However, as long as Mach number is above about 4 and dilution is of the order of 1% the actual energy values will be only a few per cent below the ideal. Of more concern is the fact that only a small fraction

of the total beam intensity will consist of the desired high-energy heavy molecules. In absolute terms this circumstance is mitigated by two factors. Because of the very high total intensity of beams obtained with nozzles, the net intensity of heavy molecules will still be 10 to 100 times as high as total intensities from an oven source. In addition, the heavy species will have a much higher effective Mach number at the skimmer entrance and will, therefore, be preferentially focused on the centerline. The extent of preferential focusing is indicated by the $\frac{1}{2}\gamma M^2$ term in Eq. (7). Insofar as ideal collisionless flow is achieved from the skimmer inlet aft, the focusing ratio of heavy to light species approaches simply the molecular weight ratio at high Mach numbers. Thus, in the case of 1% nitrogen in hydrogen in the jet, under ideal conditions the beam would contain about 14% nitrogen. In short, the use of dilute gas mixtures does not seem to offer problems in absolute intensity. More serious than any relative absence of nitrogen molecules is the presence of hydrogen which will represent noise in many experiments. Fortunately, the marked differences in both molecular weight and energy of the species which will most likely be used in mixed gas beams would seem in principle to alleviate the difficulty of isolating their effects. To our knowledge, there have been no experiments yet undertaken or even designed in detail so that a real reading on this problem of the presence of light gas can be made. In fact, the whole idea of so-called "seeded" beams is still largely prospective.

As we have tried to indicate, there is much to be done in determining optimum operating conditions for nozzle beams generally, particularly with respect to the contradictory requirements of obtaining high Mach number and avoiding skimmer interaction effects, before mixed gas beams can be effectively exploited. The most pertinent work thus far has been reported by Klingelhofer and Lohse[47] consequent to the original observations by Becker and Henkes that the velocity of argon molecules in a beam generated of an argon–hydrogen mixture was of the order of the mean jet velocity. Klingelhofer and Lohse measured the velocity distribution and the composition of a beam obtained from expansion of room temperature hydrogen with 1% argon. They found that the velocity of the argon molecules was about 2100 m s^{-1} corresponding to an energy of about 1 eV. This value is disappointingly low because if the expansion had been completely relaxed the argon energy should have been of the order of 1.8 eV. Klingelhofer and Lohse explain the velocity deficiency by assuming that rotational relaxation of the hydro-

gen did not obtain. It is noteworthy that the measured composition of the beam indicated 40% argon whereas it should have been closer to 20% if indeed there had been ideal behavior in accordance with Eq. (7). We believe that both the low argon velocity and the high argon concentration may be due in part to skimmer–jet interaction in the form of a normal shock or shocklike structure at the skimmer inlet. We will set forth the background for this belief in the following section.

Before proceeding to that section we will mention some very recent results with mixed gas beams. Albright et al. produced beams with nitrogen–hydrogen and nitrogen–helium mixtures.[48] They passed these beams through a scattering chamber containing nitrogen and determined a total scattering cross section. They were able to obtain internal consistency with their results by assuming that the final beam was essentially pure nitrogen under most conditions, that the velocity of the nitrogen was that calculated by assuming isentropic expansion of the mixture to high Mach number, and that the scattering cross section was proportional to the $-\frac{2}{3}$ power of the beam velocity. This ingenious experiment seems to support the prospect of high energies by the use of gas mixtures. However, the assumptions underlying the conclusions need careful examination.

Belyaev and Leonas have obtained direct measurements of beam velocity for nitrogen–hydrogen mixtures. The results substantiate the predictions of increased velocity for the heavier component in a mixture.[49]

We would also mention the results obtained recently by French and O'Keefe.[50] They made composition and intensity distribution studies of the skimmer flux with an Omegatron partial pressure detector. The source gas was 1% argon in helium. At large nozzle–skimmer distances where skimmer interaction should be negligible, they found the centerline composition was about 10% argon. This is in agreement with what would be predicted by the ideal theory.

C. Related Experiments with Gas Mixtures

In their original paper on the formation of high-intensity hydrogen beams, Becker and Bier reported that they had observed remarkable increases in beam detector signal when the source hydrogen contained small quantities of higher molecular weight material. In one case they noted, for example, that 4% of argon produced an apparent beam intensity six times greater than that obtained with pure hydrogen. This

observation triggered a series of stimulating and valuable investigations of the separating nozzle or "trennduse" by Becker and his associates.[51-62] Separation effects of remarkable magnitude were found in various gas mixtures including isotopes such as uranium hexafluorides, where molecular weight differences are very small. In most of this work the skimmer was replaced by a simple sampling probe immersed in the supersonic jet resulting from expansion of the mixture to be studied through a small nozzle into an evacuated enclosure. Similar studies were carried out in this country at the Linde Company by Waterman and Stern and by Waterman, Stern, and Sinclair.[63,64] They generally verified the observations of Becker's group. At the University of California at Berkeley, Chow also found separation of nitrogen and oxygen in a supersonic jet of air at low pressure.[65] The accepted explanation of these separation effects was considered to be the preferential migration of the lighter species in a radial direction from the axis of the jet, thus leaving a higher concentration of heavy species on the jet axis. The mechanism underlying this preferential migration was in some dispute. Waterman and Stern proposed a free molecule model while the Becker group favored pressure diffusion, a continuum concept.

Clearly, this separation effect is of vital importance to the idea of using mixed gases to obtain high-energy beams. Therefore, we undertook a careful investigation of the expansion of nitrogen–hydrogen mixtures.[21] The net result of our studies seems to be that the separation cannot be due entirely to any radial migration model but is at least in part a consequence of the interaction of the probe with the jet. We found for the centerline that only when there is a detached shock wave in front of the probe is there any increase in the concentration of heavy species in the sampled gas over its original concentration in the gas admitted through the nozzle. Whenever we pumped the probe exit to such an extent that the shock wave was attached or swallowed, the sampled gas always had the same composition as the nozzle gas. The consequence of this observation, of course, is that whenever the composition of a beam obtained by expansion of a gas mixture is richer in heavy species than the preferential focusing factor of Eq. (7) permits, there is a strong possibility of a shocklike disturbance in the skimmer flow. Such a shock wave can also account for beam intensities below the theoretical prediction and the apparent low Mach numbers indicated by the early velocity distribution data. It is our view, therefore, that more often than not there have been skimmer–jet interactions in most

mixed gas nozzle beam experiments to date. The main task in the immediate future development of mixed gas nozzle beam systems is to characterize the nature of these interactions in more detail and, if possible, to identify the operating conditions necessary and sufficient to eliminate them. For this purpose, the careful study of beam velocity distributions seems to be the most promising approach.

References

1. A. Kantrowitz and J. Grey, *Rev. Sci. Instr.*, **22**, 328 (1951).
2. G. B. Kistiakowsky and W. P. Slichter, *Rev. Sci. Instr.*, **22**, 333 (1951).
3. E. W. Becker and K. Bier, *Z. Naturforsch.*, **9a**, 975 (1954).
4. H. M. Parker, A. R. Kuhlthau, R. N. Zapata, and J. E. Scott, Jr., in F. M. Devienne, ed., *Rarefied Gas Dynamics*, Pergamon Press, New York, 1960, pp. 69–79.
5. R. Campargue, *Rev. Sci. Instr.*, **35**, 111 (1964).
6. J. Deckers and J. B. Fenn, *Rev. Sci. Instr.*, **34**, 96 (1963).
7. K. Bier and O. Hagena, in J. A. Laurmann, ed., *Rarefied Gas Dynamics*, Vol. I, Academic Press, New York, 1963, pp. 478–496.
8. J. B. Fenn and J. B. Anderson, in *Rarefied Gas Dynamics*, J. H. de Leeuw, ed., Academic Press, New York, in press.
9. J. B. Anderson, R. P. Andres, J. B. Fenn, and G. Maise, in J. H. de Leeuw, ed., *Rarefied Gas Dynamics*, Academic Press, New York, in press.
10. E. L. Knuth, *Report. No. 63–30*, Department of Engineering, University of California at Los Angeles (1963).
11. E. L. Knuth and S. F. Iacobellis, in J. H. de Leeuw, ed., *Rarefied Gas Dynamics*, Academic Press, New York, in press.
12. O. Hagena and W. Henkes, *Z. Naturforsch.*, **15a**, 851 (1960).
13. J. H. McGinn, private communication (1964).
14. R. M. Fristrom, private communication (1964).
15. O. Hagena, *Z. Angew. Phys.*, **16**, 183 (1963).
16. K. Bier and O. Hagena, in J. H. de Leeuw, ed., *Rarefied Gas Dynamics*, Academic Press, New York, in press.
17. P. L. Owen and C. K. Thornhill, *Aeronautical Research Council (U.K.) R & M No. 2616* (1948).
18. F. S. Sherman, in J. A. Laurmann, ed., *Rarefied Gas Dynamics*, Vol. II, Academic Press, New York, 1963, pp. 228–260.
19. F. S. Sherman, *Lockheed MSC Tech. Rept., Fluid Mechanics* 6-90-63-61 (1963).
20. H. Ashkenas and F. S. Sherman, in J. H. de Leeuw, ed., *Rarefied Gas Dynamics*, Academic Press, New York, in press.
21. V. H. Reis and J. B. Fenn, *J. Chem. Phys.*, **39**, 3240 (1963).
22. E. W. Becker and W. Henkes, *Z. Physik*, **146**, 320 (1956).
23. J. A. Phipps, D. G. Griffith, and J. E. Scott, Jr., *Bull. Am. Phys. Soc. Ser. II*, **8**, 550 (1963).
24. J. B. Anderson and J. B. Fenn, *Phys. Fluids*, **8**, 780 (1965).
25. E. W. Becker, K. Bier, and W. Henkes, *Z. Physik*, **146**, 333 (1956).

26. E. W. Becker, R. Klingelhofer, and P. Lohse, *Z. Naturforsch.*, **17a**, 432 (1962).
27. P. G. Bentley, *Nature*, **190**, 432 (1961).
28. W. Henkes, *Z. Naturforsch.*, **16a**, 842 (1961).
29. W. Henkes, *Z. Naturforsch.*, **17a**, 786 (1962).
30. F. T. Greene and T. A. Milne, *J. Chem. Phys.*, **39**, 3150 (1963).
31. T. A. Milne, *Mass Spectrometry of Metal-containing Flames*, 7th Quarterly Tech. Summary Rept., Midwest Research Institute, Kansas City, 1963.
32. J. E. Scott, Jr. and D. E. Drewry, in J. A. Laurmann, ed., *Rarefied Gas Dynamics*, Vol. I, Academic Press, New York, 1963, pp. 516–538.
33. J. B. Fenn and J. Deckers, in J. A. Laurmann, ed., *Rarefied Gas Dynamics*, Vol. I, Academic Press, New York, 1963, pp. 497–515.
34. C. Muckenfuss, *Phys. Fluids*, **5**, 165 (1962).
35. K. Bier and B. Schmidt, *Z. Angew. Phys.*, **13**, 493 (1961).
36. R. A. Oman, *Phys. Fluids*, **6**, 1030 (1963).
37. J. P. Valleau and J. M. Deckers, *Can. J. Chem.*, **42**, 225 (1964).
38. R. M. Koros, Doctoral thesis, Princeton University, 1961.
39. T. A. Milne and F. T. Greene, private communication (1964).
40. E. J. Nowak, Doctoral thesis, Princeton University, 1962.
41. J. B. Anderson and M. Boudart, *J. Catalysis*, **3**, 216 (1964).
42. V. B. Leonas, *Teplo-i Massoperenos, Pervoe Vses. Soveshch., Minsk.*, **1961–3**, 540 (Pub. 1963).
43. G. T. Skinner, *Phys. Fluids*, **4**, 1172 (1961).
44. G. T. Skinner and B. H. Fetz, in J. H. de Leeuw, ed., *Rarefied Gas Dynamics*, Academic Press, New York, in press.
45. R. A. Oman, A. Bogan, C. H. Weiser, C. H. Li, and V. S. Calia, *Grumman Res. Dept. Rept.* **RE-166** (1963).
46. N. G. Utterback and G. H. Miller, *Phys. Rev.*, **124**, 1477 (1961); *Rev. Sci. Instr.*, **32**, 1101 (1961).
47. R. Klingelhofer and P. Lohse, *Phys. Fluids*, **7**, 379 (1964).
48. R. G. Albright, J. Peeters, M. Bourguignon, R. L. Le Roy, and J. M. Deckers, in J. H. de Leeuw, ed., *Rarefied Gas Dynamics*, Academic Press, New York, in press.
49. Yu. N. Belyaev and V. B. Leonas, *Vestn. Mosk. Univ. Ser. III, Fiz., Astron.*, **18**, 34 (1963).
50. J. B. French and D. R. O'Keefe, in J. H. de Leeuw, ed., *Rarefied Gas Dynamics*, Academic Press, New York, in press.
51. E. W. Becker, K. Bier, and H. Burghoff, *Z. Naturforsch.*, **10a**, 565 (1955).
52. E. W. Becker and R. Schutte, *Z. Naturforsch.*, **11a**, 679 (1956).
53. E. W. Becker, W. Beyrich, K. Bier, H. Burghoff, and F. Zigan, *Z. Naturforsch.*, **12a**, 609 (1957).
54. E. W. Becker, K. Bier, H. Burghoff, O. Hagena, P. Lohse, R. Schutte, P. Turowski, and F. Zigan, *Proc. 2nd U. S. Intern. Conf. Peaceful Uses At. Energy*, **4**, 455 (1958).
55. E. W. Becker and R. Schutte, *Z. Naturforsch.*, **15a**, 336 (1960).
56. E. W. Becker, R. Klingelhofer, and P. Lohse, *Z. Naturforsch.*, **15a**, 644 (1960).
57. K. Bier, *Z. Naturforsch.*, **15a**, 714 (1960).
58. E. W. Becker, K. Bier, and W. Bier, *Z. Naturforsch.*, **16a**, 1393 (1961).

59. F. Zigan, *Z. Naturforsch.*, **17a**, 772 (1962).
60. E. W. Becker, K. Bier, and W. Bier, *Z. Naturforsch.*, **17a**, 778 (1962).
61. E. W. Becker, K. Bier, W. Bier, and R. Schutte, *Z. Naturforsch.*, **18a**, 246 (1963).
62. K. Bier, *Fortschr. Physik.*, **11**, 325 (1963).
63. P. C. Waterman and S. A. Stern, *J. Chem. Phys.*, **31**, 405 (1959).
64. S. A. Stern, P. C. Waterman, and T. F. Sinclair, *J. Chem. Phys.*, **33**, 805 (1960).
65. R. R. Chow, *I.E.R. Tech. Rept.* **HE-150-175,** University of California at Berkeley (1959).

9. REACTIVE SCATTERING IN MOLECULAR BEAMS

D. R. HERSCHBACH

Department of Chemistry, Harvard University, Cambridge, Massachusetts

CONTENTS

I. Experimental Methods and Results 322
A. Apparatus and Experimental Conditions 322
B. Angular Distribution Measurements 328
C. Magnetic Deflection Analysis 341
D. Velocity Analysis of Products 344
E. Electric Deflection Analysis 347
F. Summary and Discussion 356
II. Chemical Forces in Charge-Transfer Reactions 367
A. The Harpooning Mechanism 368
B. Correlation with Electronic Structure 379
References 388

> *The atoms move in the void and catching each other up jostle together, and some recoil in any direction that may chance, and others become entangled with one another in various degrees according to the symmetry of their shapes and sizes and positions and order, and they remain together and thus the coming into being of composite things is effected.*
>
> SIMPLICIUS (*6th Century A.D.*)

It has long been recognized that molecular beam experiments offer the most direct means to study the dynamics of elementary chemical reactions. In effect the time resolution is reduced to the duration of a single collision, of the order of 10^{-13} sec. Thus, even quite primitive beam experiments can reveal the main features of the distribution of velocity vectors of the freshly formed product molecules and other properties inaccessible to traditional "bulb" methods of kinetics.

Until recently, chemical scattering experiments had yielded only meager results, and the small band of chemists who took up this work during the past decade was perhaps justly regarded as visionary. For a

method which depends so heavily on technology, an early period of evolutionary trauma had to be accepted. However, the newest developments, especially those of the past year, mark the end of this lean period, both in terms of experimental and theoretical methodology and in terms of results extensive enough to suggest chemical generalizations.

Reaction cross sections and angular distributions of both elastic and reactive scattering have now been measured for about twenty reactions of alkali metal atoms with halogen compounds which produce alkali halides,

$$M + XY \rightarrow MX + Y$$

The reactants XY include HX, RX, X_2, XX′, SX_2, PX_3, CH_2X_2, CHX_3, CX_4, SnX_4, SF_6, CF_3I, and also NO_2 and RNO_2 (which form MO and MNO_2). A complete summary is given in Table I (p. 357) and in the bibliography.[1–52] In a few cases, a direct velocity analysis of the MX product has been carried out. In others, the scattering has been subjected to analysis by inhomogeneous magnetic or electric deflecting fields. Mass spectrometric detection has also been employed, and it is expected that studies of reactions not involving alkali species will soon become feasible.

The theoretical apparatus required for detailed studies of reaction dynamics has also now reached working form. Until recently, the theory of scattering from a multidimensional potential-energy surface remained swaddled in formal theorems and the chemical implications of the reactive scattering experiments could only be discussed qualitatively. "Monte Carlo experiments" with computers have now opened up a new era for theoretical kinetics. As developed particularly by Bunker[26,27] and by Karplus,[32,33] these methods have made it feasible to examine vast numbers of exact trajectories for the general three-dimensional motion of a classical three-body system, without restrictive approximations. As yet, calculations have been reported for only one system ($K + ICH_3$, with CH_3 treated as a mass point), but the results indicate that the principal features of the potential surface can be established within fairly narrow limits from the dynamical properties determined in the beam experiments. Simple phenomenological models of the type popular in nuclear physics have also been explored, particularly the "optical potential" model, and it is found that some of the dynamical features of the Monte Carlo calculations are nicely simulated by such models.

The scattering experiments have already established a beautifully simple pattern for the dynamics of alkali atom–halogen reactions. There has emerged a strong correlation among the magnitude of the total reaction cross section, σ_r, the preferred direction of recoil of the products, and the shape of the angular distribution of elastic scattering of the reactants. A *rebound* mechanism is found for reactions with "small" cross sections, $\sigma_r \gtrsim 10$ Å^2 (e.g., reactions with CH_3I and other alkyl iodides); most of the alkali halide product recoils into the *backward* hemisphere with respect to the incoming alkali atom beam and the elastic scattering is very similar to that of nonreactive molecules. A *stripping* mechanism is found for reactions with large cross sections, $\sigma_r \gtrsim 100$ Å^2 (e.g., reactions with Br_2, PBr_3, CBr_4, and many others): most of the alkali halide recoils *forward* and the elastic scattering falls off very rapidly at wide angles. A spectrum of intermediate cases is found as σ_r varies from the rebound to the stripping limit (e.g., reactions of various alkali metals with CCl_4): the favored direction for recoil of the alkali halide gradually shifts from backwards to forwards and the falloff in the wide-angle elastic scattering becomes increasingly pronounced.

There are also several properties which hold regardless of the size of the reaction cross section. The total scattering (sum of elastically scattered M and reactively scattered MX) is very similar in both magnitude and angular distribution to that for nonreactive molecules of similar size and structure. Also, the anisotropy of the MX angular distributions indicates that both the rebound and stripping reactions proceed by a *direct* or *impulsive* mechanism; the duration of the reactive collisions must be very short, well below the average rotational period of a collision complex ($\gtrsim 5 \times 10^{-13}$ sec as a rough upper limit). For all the reactions, kinematic analysis of the reactive scattering indicates that the final relative translational kinetic energy of the products is comparable to the initial kinetic energy of the reactants, so that most of the chemical energy released appears as internal excitation of the products. As the electric deflection experiments have now demonstrated for several reactions that only a small part of this internal energy appears in rotation, most of it must be in vibrational excitation.

These general properties can all be accounted for by postulating that the reactions proceed via formation of an ion-pair, $M^+ + XY^-$. This "electron jump" model was proposed over thirty years ago to explain the large rate constants found in some of the Polanyi sodium flame

experiments, but not much could be done to test the model or to apply it elsewhere since knowledge of negative molecular ions has remained very scanty. Now, however, in addition to the evidence provided by the beam experiments, for many reactions it is possible to estimate the relevant potential curves for the XY^- ion by means of arguments developed for the analysis of charge-transfer spectra. Also, in some cases, use can be made of data and theory developed in recent electron-impact studies. In this way the chemical systematics associated with the transition from rebound to stripping behaviour and other details of the reaction dynamics can often be predicted by examining the electronic spectra and molecular orbital configuration of the reactant molecules XY. Simplicius would certainly have been very pleased with this.

Section I of this chapter illustrates the current status of experimental methods and summarizes the results which can be established directly from kinematic analysis of the data, without introducing theoretical models. The discussion is limited mainly to one prototype example, the $K + Br_2$ reaction, for which the most detailed results are available. Section II celebrates the chemical implications. The qualitative correlation of spectra and reactivity implied by the electron jump mechanism is emphasized and some speculative features are pointed out which should be accessible to experimental test.

I. EXPERIMENTAL METHODS AND RESULTS

As the early experiments and general aspects of the beam technique have been amply reviewed,[3,15,16,21,47] we shall illustrate here only the most important features of the recent reactive scattering studies carried out in our laboratory. Related work by other groups (at Birmingham, Oak Ridge, Brown, Wisconsin, and Bonn) receives only sporadic mention; however, Table I (in Section I–F) provides a complete listing of all the alkali reactions which have been studied in beams and a guide to the bibliography. In most essentials, the techniques employed in these experiments are derived from traditional practice of beam research in physics.[53–55] Many of the methods date back thirty or forty years, and our experience simply exemplifies the evolutionary principle, "Ontogeny Recapitulates Phylogeny."

A. Apparatus and Experimental Conditions

Most of the experiments have been carried out with an almost rudimentary apparatus.[15,24,38] As shown in Figure 1, the beams are

formed by thermal effusion from ovens mounted on a turntable which is rotated to sweep the angular distribution past the detector. The angle of intersection of the beams can be varied from about 60 to 135° but is usually 90°. In the plane of the incident beams the accessible range of the scattering angle is $\Theta = -60$ to 150° from the alkali beam. The out-of-plane scattering may be measured over a range of about $\Phi = -10$ to $+40°$ by vertical adjustment of the sliding detector flange or over $\Phi = -30$ to 90° by use of a special swivel mount for the detector.[24] In most of the experiments, the alkali metal beam was 0.5° wide and the gas beam 12° wide (full width at half intensity). The distance from the scattering center to the alkali oven is 11 cm, to the gas oven slit 1.7 cm, and to the detector usually about 10 cm. Use of a double-chamber oven for the alkali allows the temperature of the beam

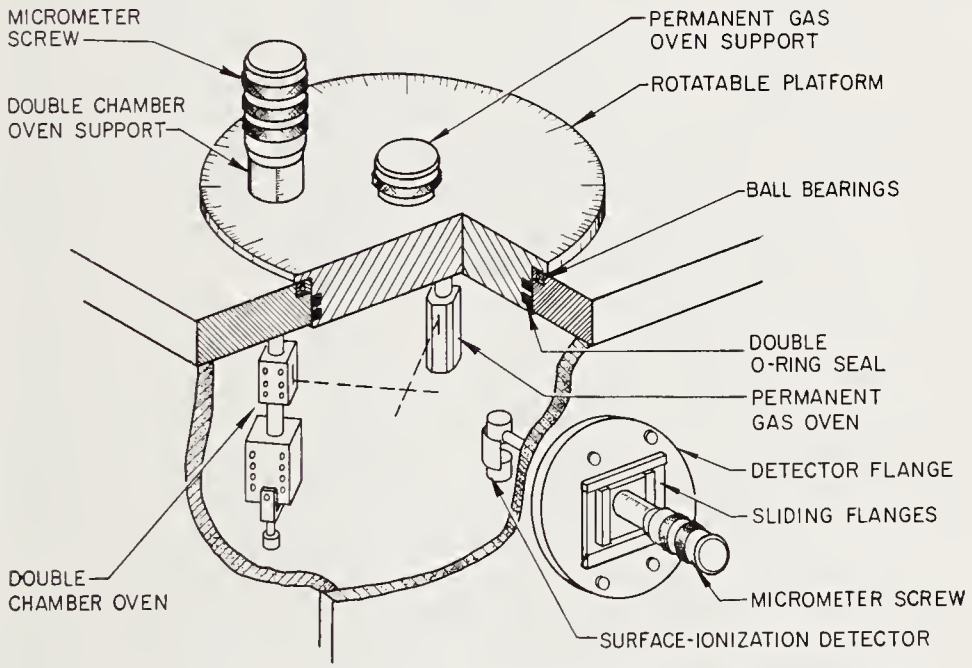

Fig. 1. Sketch of scattering chamber. Cold shields, collimating slits, shutters to interrupt the beams, and other details are omitted.

emerging from the upper chamber to be varied about 300° independently of the vapor pressure established in the lower chamber (about 0.1 mm Hg), which can then be maintained to provide the maximum intensity for effusive flow. The gas oven is connected to an external barostat

by a supply tube (not shown in Fig. 1) which passes through the support column in the rotating lid. Cold shields and collimating slits hide both ovens from the scattering center, and a cold shield also surrounds the detector. The entire scattering chamber is enclosed in a copper box attached to a large liquid nitrogen trap. For condensable reactants this provides a very high pumping speed (estimated as 2×10^5 liters/sec) and although this apparatus lacks the customary differential pumping of the beam sources, the background pressure remains at about 10^{-7} mm Hg during runs. As indicated in Figure 2, auxiliary equipment which surrounds the scattering chamber obscures somewhat the rudimentary character of the apparatus.

The detector must distinguish the reactively scattered MX molecules from the large background due to elastically scattered M atoms. A differential surface ionization technique was established by Taylor and Datz[2,56] in one of the early chemical scattering studies and this has been used in much of the subsequent work. Signals read on two surface ionization detectors are compared: one filament of tungsten or rhenium,[57] which is about equally sensitive to M and MX; the other a platinum–8% tungsten alloy, which under certain conditions is much more sensitive to M. For both M and MX, surface ionization produces M^+ ions. The mechanism which inhibits surface ionization of alkali halides on platinum is not understood, but evidently it requires that the surface be suitably contaminated.[57–59] If the platinum filament is operated in a sufficiently "clean" vacuum, it appears to be very similar to tungsten in surface ionization properties.[38,58] Many materials are found to *poison* the response of the platinum filament, and this frustrated early attempts to study the reactions of alkali metals with many halogen compounds, including the diatomic halogen molecules.[4,38] The difficulty has been eliminated by means of a *prepoisoning* procedure[38,39] due to Touw and Trischka.[59] They demonstrated that two distinct and reproducible surface conditions of the platinum–8% tungsten alloy filament could be produced: Mode D, obtained by heating the wire in oxygen, detects both M and MX with high efficiency; Mode N, obtained by heating the wire in methane, is essentially nondetecting for MX. Measurements of the electron emission from the filament show that the overall work function is higher for Mode D than for Mode N and provide a convenient means to monitor the state of the surface. These two modes are found to remain immune to halogens for long periods of time.

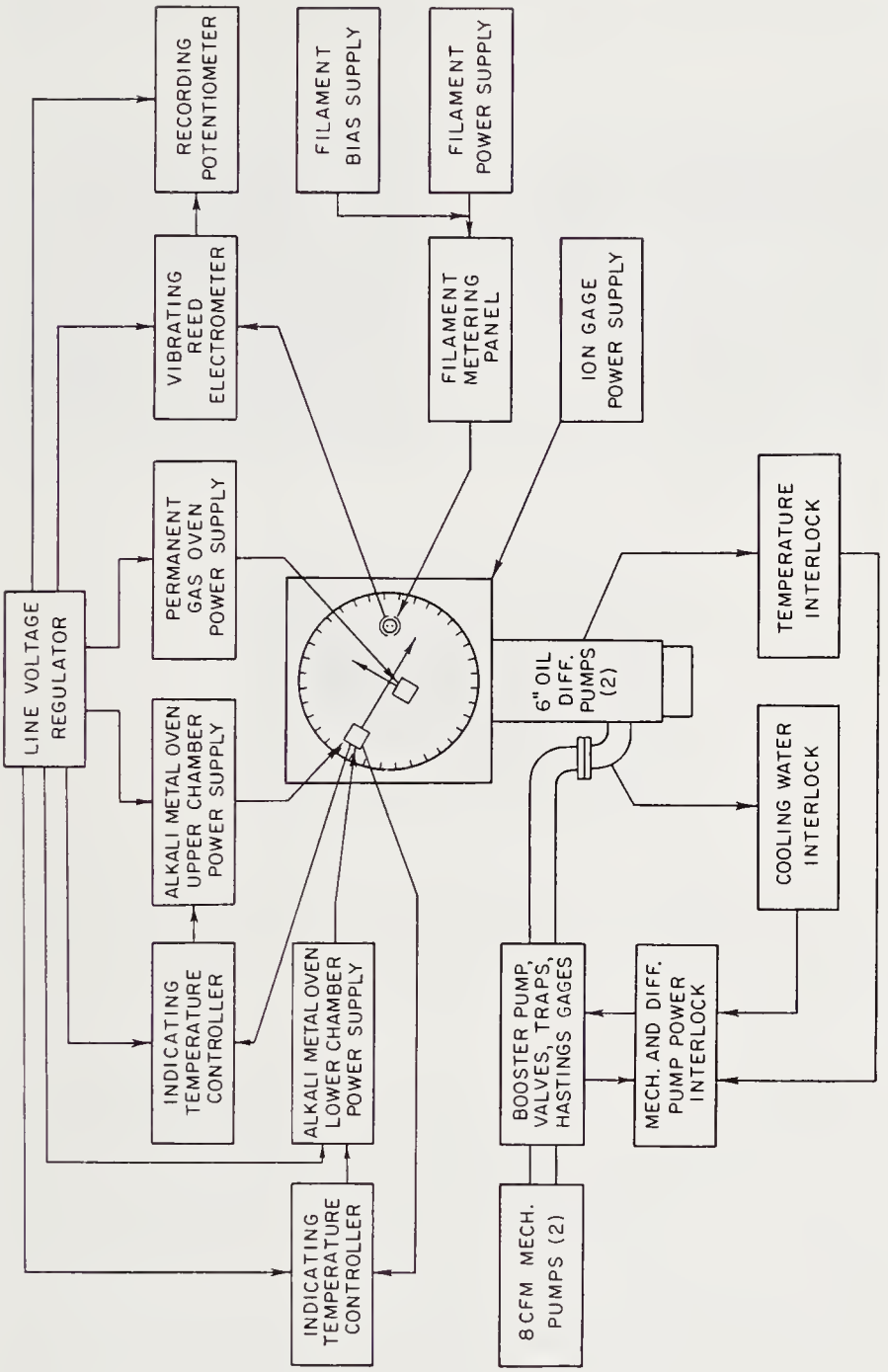
RECORDING POTENTIOMETER
FILAMENT BIAS SUPPLY
FILAMENT POWER SUPPLY
VIBRATING REED ELECTROMETER
FILAMENT METERING PANEL
ION GAGE POWER SUPPLY
LINE VOLTAGE REGULATOR
PERMANENT GAS OVEN POWER SUPPLY
ALKALI METAL OVEN UPPER CHAMBER POWER SUPPLY
6" OIL DIFF. PUMPS (2)
TEMPERATURE INTERLOCK
COOLING WATER INTERLOCK
INDICATING TEMPERATURE CONTROLLER
ALKALI METAL OVEN LOWER CHAMBER POWER SUPPLY
BOOSTER PUMP, VALVES, TRAPS, HASTINGS GAGES
MECH. AND DIFF. PUMP POWER INTERLOCK
INDICATING TEMPERATURE CONTROLLER
8 CFM MECH. PUMPS (2)

Fig. 2. Schematic diagram indicating auxiliary components of apparatus.

Recently, the detector flange shown in Figure 1 has been replaced with a side chamber in which the original detector is mounted behind one or the other of the analyzing elements pictured in Figure 3. In addition

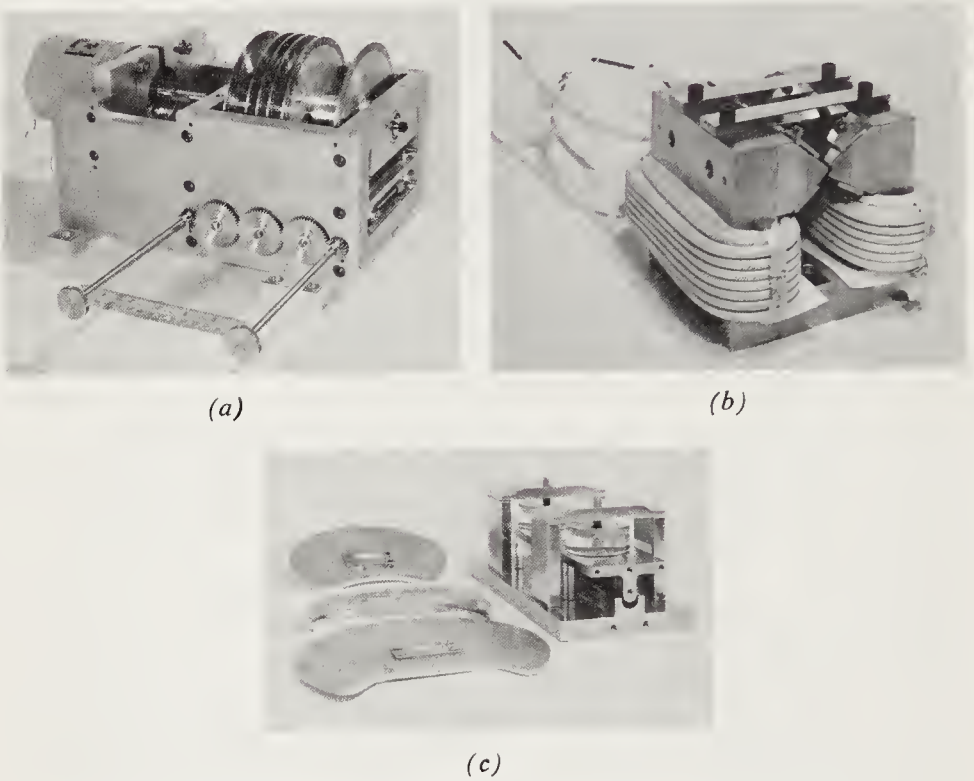

Fig. 3. Analyzing devices: (*a*) velocity selector; (*b*) inhomogeneous magnetic deflecting field; (*c*) inhomogeneous electric deflecting field. For (*a*), the distance between the first and last disk of the rotor is 10 cm; for (*b*) the field is 7 cm long and for (*c*) 15 cm.

to the spreading out of intensity imposed by the analysis, this reduces the solid angle subtended by the reaction volume at the detector by a factor of $\sim 10^2$–10^3, since the distance is considerably increased (up to $\sim$ 25–30 cm) and the analyzers require the use of narrow collimating slits ($\sim$ 0.005 cm for the velocity selector and 0.001 cm for the magnetic and electric fields). The loss in signal has been largely compensated by decreasing the detector noise level and by increasing the M atom beam flux. The noise from alkali metal impurities which previously had limited the detectable signal has been greatly reduced by the use of single-crystal tungsten filaments.[60] Signals as low as 3×10^{-16} A (2000

particles/sec) are now measurable. Another improvement of at least one order of magnitude could be obtained by use of beam modulation.[61] The flux increase has come from abandoning the traditional effusive flow conditions. The alkali oven is now equipped with thick slits shaped to conform to hydrodynamic criteria and the oven is operated at pressures up to 50-fold higher ($\sim$ 20 mm Hg) than allowed for effusive flow. The emergent beam is far from the mythical collision-free condition, but the scattering which occurs within the beam endows it with a "self-purifying" property. Measurements with the analyzers indicate that after traveling a few centimeters the beam approaches effusive flow. This simple method provides a tenfold or greater enhancement in intensity and a considerably narrower velocity distribution, and represents a modest step towards the supersonic jet or "Laval nozzle" technique which has been intensively developed during the past few years by chemical engineers.[62] It was first successfully applied to alkali beams by the Bonn group.[63]

The inhomogeneous magnetic deflecting field has been used to eliminate most of the background signal due to the paramagnetic M atoms and thus obtain a direct measurement of the distribution of the diamagnetic MX molecules.[31] With this the results derived from the modified differential surface ionization method have been verified for several reactions; also, measurements of the MX angular distributions have been much improved in the small-angle scattering region, which previously was almost inaccessible because the M atom background is very large there.

Since the velocity selector and electric deflecting field provide other means to sort atoms from molecules, as an incidental aspect of their function as analyzers, they also extend significantly the scope of the detection method. In the study of reactions of alkali atoms with NO_2, for example, the differential surface ionization method was unsuccessful.[38,45] Despite drastic efforts, the Pt–W filament could not be made to operate in the nondetecting mode; even the very low ambient concentration of NO_2 appears to be sufficient to stabilize the filament in the detecting mode. Use of the magnetic field also failed to separate the product, as practically the whole scattered signal was found to be paramagnetic. However, the electric field revealed that the reaction actually produces a large yield of polar molecules.[45] These deflection experiments show that the product is almost certainly the MO molecule (which until very recently had not been observed spectroscopically[64]).

A few preliminary experiments have been carried out with a Paul mass filter and ion multiplier behind the surface ionization detectors; this has made possible the study of reactions such as Rb + NaI → RbI + Na, which involve two different alkali metal atoms.[38]

In typical angular distribution experiments (made without the use of the analyzer devices or the Laval slits), the concentration of M atoms within the volume defined by the intersection of the beams is about 10^{10} atoms/cm^3, equivalent to a pressure of 10^{-6} mm Hg, and that of the gas molecules is about 100-fold greater. About 10^{14} M atoms/sec enter the reaction volume, of which roughly 0.1–1% react to form MX while about 10% undergo elastic scattering. The steady-state concentration of MX in the reaction volume is roughly 10^7–10^8 molecules/cm^3, the pressure 10^{-9}–10^{-8} mm Hg. At the peak of the MX angular distribution, about 10^{10}–10^{11} molecules/cm^2/sec arrive at the detector; for many of the reactions studied more than a month would be required to deposit a monolayer of MX molecules.

B. Angular Distribution Measurements

In reactive scattering experiments the object is to determine the direction and magnitude of the *recoil* velocity vectors **u** that carry the products away from the center-of-mass, which proceeds with constant velocity **C** regardless of the outcome of the collision. However, the observable spectrum of laboratory velocity vectors is a *vector sum*, $\mathbf{v} = \mathbf{u} + \mathbf{C}$. In the laboratory spectrum the (unknown) distributions in the recoil angle and energy therefore are usually strongly coupled and also may be drastically blurred by the (known) distribution in **C** vectors which arises from the spread in initial conditions. For systems with favorable kinematics it is nonetheless often possible to establish some of the main qualitative features of the recoil spectrum from laboratory angular distribution measurements, without resorting to velocity analysis of either reactants or products. This is so because in thermal energy crossed beam experiments the reactants usually have comparable velocities and the **C** velocity vector points sideways, at a wide angle intermediate between the directions of the incident beams. A rough measure of the recoil spectrum of a product thus may be obtained simply from the displacement of its laboratory angular distribution from the calculated distribution of **C** vectors.

This primitive method has now been used in many reactive scattering studies (see Table I). The kinematic analysis and results have been

discussed in detail in other reviews.[15,47] The method was first applied to $K + CH_3I$ and other alkyl iodide reactions.[7,15] It was found that the laboratory distribution (LAB, or $\mathbf{v}_{KI}$ distribution) of the KI product shows a broad peak at a wide angle (near $\Theta \sim 85°$, measured from the direction of the parent K beam, see Fig. 6), well beyond the peak in the distribution of **C** vectors (which is near $\Theta \sim 50°$). The kinematic analysis of the LAB distribution demonstrated that in the center-of-mass reference system (CM, or $\mathbf{u}_{KI}$ distribution) most of the KI must recoil into the *backward* hemisphere with respect to the incoming K atoms (see Fig. 9). This is characteristic of what is now called the *rebound* mechanism.[47,48,50] The kinematic analysis also provided a rough estimate of the magnitude of the most probable $\mathbf{u}_{KI}$ recoil vector. Since this is quite small ($\sim$ 100–200 m/sec), only a small part of the chemical energy released in the reaction (roughly 2–5 kcal/mole out of about 25 kcal/mole) can appear in the final relative translational motion of KI and CH_3; most of the energy must be present as vibrational or rotational excitation of the products.

Figures 4 and 5 illustrate the results obtained in a similar study[38,39] of the $K + Br_2$ reaction, which proved to be a prototype example of the *stripping* mechanism.[28,39,42,47] Here most of the KBr recoils into the *forward* hemisphere with respect to the incident K atoms, although again only a small fraction of the energy released appears in translational motion of the products.

The reaction yield is remarkably large. As illustrated by the primary data of Figure 4, the angular distribution of the *total scattering* (sum of K and KBr, as measured on the W filament or the Pt-W alloy in the "detecting" mode) shows a relatively gradual falloff at wide angles, whereas the *elastic scattering* (K intensity, as measured on the Pt-W filament in the "nondetecting" mode) falls off very rapidly. Note that the ordinate scale is logarithmic. Beyond $\Theta \gtrsim \pm 30°$ the KBr intensity is roughly an order-of-magnitude larger than the K signal, in contrast to the situation found for rebound reactions (see Fig. 11), where the reactive scattering is always accompanied by a comparable amount of elastic scattering. The nominal yield (integrated intensity of KBr divided by total K scattered from the parent beam) derived from Figure 4 is $\sim 10\%$, and this does not include the contribution from the out-of-plane scattering which misses the detector. The reaction cross section is thus $\gtrsim 10\%$ of the total beam-scattering cross section (compared with only $\sim 0.5\%$ for the $K + CH_3I$ case), or roughly $\gtrsim 100$ Å^2.

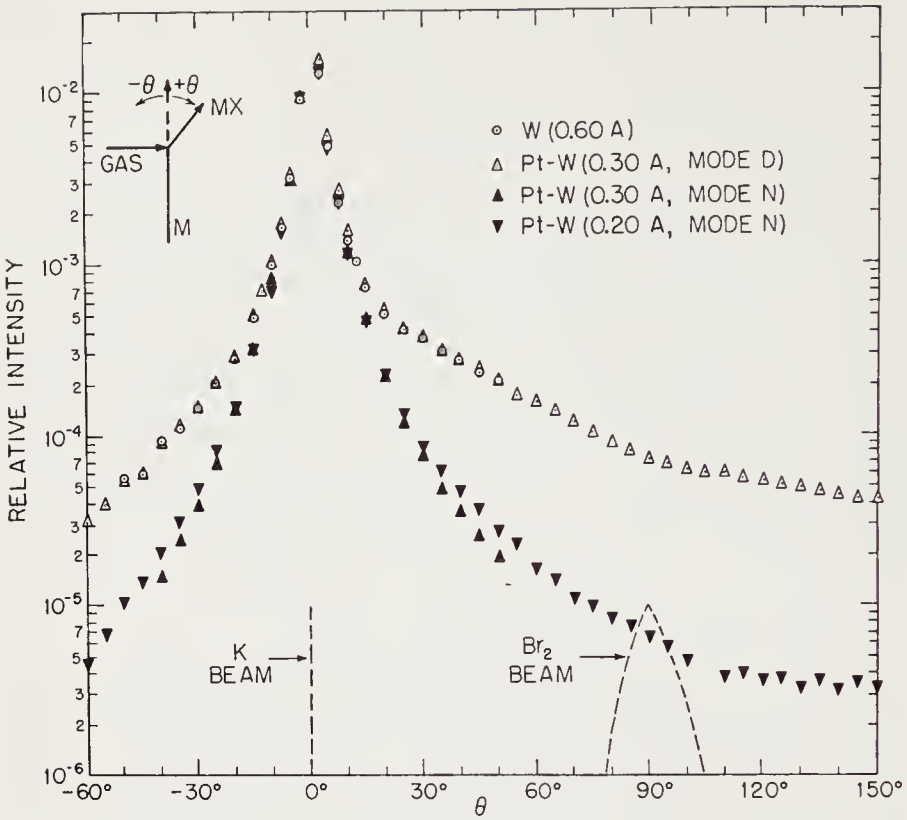

Fig. 4. Scattering of $K + Br_2$ measured on various surface ionization filaments. The ordinate scale gives the ratio of the actual signal to the attenuation of the parent K beam measured on the same filament. Readings on the W filament (○) or the Pt-W filament in the "detecting" mode (△) indicate the sum of scattered K and KBr; readings on Pt-W in the "nondetecting" mode (▲) indicate scattered K atoms.

Figure 5 shows the angular distribution of KBr and the main features of the kinematic analysis. The KBr relative intensity is derived by subtracting the mode N detector signal from the mode D result and dividing by the attenuation of the parent K beam. Outside the region $\Theta \gtrsim \pm 20°$ the subtraction is a small or negligible correction, but the uncertainty becomes large at small angles and points within $\Theta \gtrsim 5°$ had to be discarded. The experimental points shown are the average of three separate runs, and the error bars indicate the standard deviation. Although the precise location of the peak remains uncertain by a few degrees, the general form is well determined and has been verified closely in the magnetic deflection experiments (see Fig. 11).

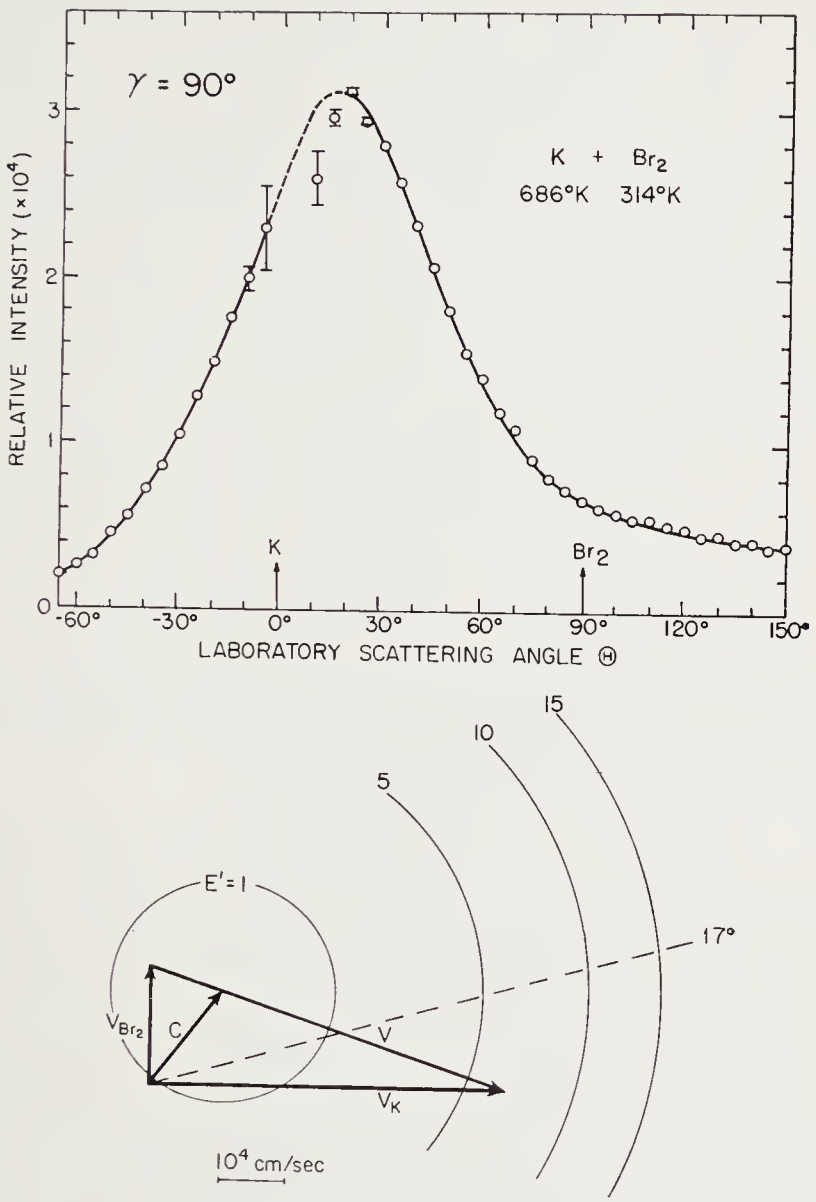

Fig. 5. Laboratory angular distribution of KBr from the K + Br_2 reaction (measured in the plane of the incident beams). The lower panel gives the kinematic diagram corresponding to the most probable velocities in the reactant beams; the circles indicate the length of recoil velocity vectors for KBr produced with various amounts of final relative translational kinetic energy E' (kcal/mole).

The kinematic analysis consists of comparing the observed product distribution with the spectrum of recoil vectors allowed by the conservation laws for energy and linear momentum.[10,15,50] Newtonian mechanics is rigorously applicable here. In quantum mechanics, the velocity vectors in the asymptotic initial and final states of a collision are subject to the same, essentially geometrical relationships; in these asymptotic translational states the beam particles are too far apart to interact, hence need not be precisely localized in space and can be assigned definite momenta despite Heisenberg's principle.

The qualitative features may be seen from the vector diagram given in the lower part of Figure 5, which we like to call a *Newton diagram.* The most probable velocity vectors in the reactant beams are shown; $\mathbf{V}$ denotes the *initial* relative velocity vector and $\mathbf{C}$ is the center-of-mass vector. As required by momentum balance, the tip of $\mathbf{C}$ partitions $\mathbf{V}$ into segments having lengths in the inverse ratio of the masses of the reactant molecules. The recoil velocity vectors of the products, $\mathbf{u} = \mathbf{v} - \mathbf{C}$, are likewise related to the *final* relative velocity vector $\mathbf{V}'$ by

$$\mathbf{u}_1 = (m_2/M)\mathbf{V}' \qquad \mathbf{u}_2 = -(m_1/M)\mathbf{V}' \tag{1}$$

where $1 \leftrightarrow$ Br, $2 \leftrightarrow$ KBr, and M is the total mass. The $\mathbf{V}'$ vector may take any direction, but energy conservation restricts its magnitude. The total energy available to the reaction products is

$$E' + W' = E + W + \Delta D_0 \tag{2}$$

where $E = \frac{1}{2}\mu V^2$ and $E' = \frac{1}{2}\mu' V'^2$ are the initial and final relative translational kinetic energy (μ and μ' are the reduced masses), W and W' denote the internal excitation of the reactants and products, respectively, and ΔD_0 is the difference in dissociation energies of the new and old bonds (measured from the zero-point vibrational levels). For the $K + Br_2$ reaction, the chemical energy released is $\Delta D_0 \simeq 45$ kcal/mole; the thermal distribution of initial relative kinetic energy is peaked at $E = 1.2$ kcal/mole; and the Br_2 is mostly (77%) in the ground vibrational state with a rotational distribution peaked near $W = 0.3$ kcal/mole (18% has an additional 0.9 kcal/mole in thermal excitation of the first vibrational state). Thus the possible spectrum of recoil vectors for KBr is represented by a set of spheres about the tip of $\mathbf{C}$, constructed from Eqs. (1) and (2), one for each value accessible to E' up to the maximum of about 48 kcal/mole.

From Figure 5 is it apparent that in order for the peak to appear near $\Theta \sim 17°$ in the LAB distribution, much of the KBr must recoil forward

(and the Br backward) in the CM distribution. A rough, *nominal* value of the recoil energy E' may be estimated by assuming that the KBr recoils directly forward along **V**; this gives $E' \sim 1$ kcal/mole and accordingly the internal excitation $W' \sim 45$ kcal/mole. This rather cavalier procedure has proven surprisingly useful. The nominal E' is also near 1 kcal/mole for many of the other reactions studied and often the shifts in the position of the LAB peak caused by changing either the angle of intersection or the temperature of the reactant beams are very close to predictions obtained from the nominal analysis. However, there is considerable leeway in the quantitative kinematic interpretation. Detailed calculations must be carried out to make allowance for distributions in both the recoil angle and energy and the blurring effect of the velocity distributions in the reactant beams.[42,50] Two features provide stringent requirements in deciding the *range* of recoil vectors compatible with the data. The scattering must have cylindrical symmetry about **V**, since the incident beams contain all possible molecular orientations and impact parameters. Also, an acceptable recoil distribution must conform to the Jacobian factor for the LAB $\leftrightarrow$ CM angle transformation, which often introduces severe distortions in the laboratory "image" of the recoil spectrum. Comparisons of the data with extensive trial calculations[42,65] (see Fig. 9, for example) indicate that for $K + Br_2$ at least 50% of the reactive scattering must come from recoil angles within $\pm 45°$ of the direction of **V** and recoil energy $E' \sim 0.3$ to 10 kcal/mole (or $W' \lesssim 35$ kcal/mole).

Much of the uncertainty is inherent in the kinematic analysis and arises from freedom in adjusting the distributions of both recoil angle and energy rather than from the velocity averaging. For the $Cs + Br_2$ reaction, a study using velocity selection of the Cs beam has been carried out at Oak Ridge.[28] As the Cs velocity varied from 300 to 450 cm/sec, the CsBr peak was found to shift to slightly smaller angles (from 22° to 18°) and to decrease appreciably in width (from 46° to 33° in the full width at half-intensity). These variations are closely simulated by a calculation which assumes the recoil is strictly forward along **V** with $E'/E = 0.3$ and averages a set of appropriate kinematic diagrams over the velocity distribution in the Br_2 beam. Although this calculation also accounts for about 60% of the observed width of the CsBr peaks, calculations which allow distributions in both angle and energy show that the range of recoil spectra compatible with the data is in this case nearly as broad as in the experiments without velocity selection.

Further aspects of the angular distribution studies are illustrated in Figures 6–9, which compare the results for prototype stripping and rebound reactions. The LAB distributions for the K + ICl and K + CH_3I systems are shown in Figures 6 and 7. Although the results for ICl and Br_2 are practically the same, ICl is chosen as the stripping example here since it offers a closer kinematic and chemical analogy to CH_3I. It is not possible to decide whether K + ICl yields mainly KI + Cl or KCl + I from analysis of the product distribution, however.[47,49] Figure 6 shows product distributions measured in successive runs with the same experimental conditions. As before, the ordinate scale gives the ratio of the product signal to the attenuation of the parent K beam; since the total scattering cross sections (determined essentially just by the van der Waals forces) are nearly the same for ICl and CH_3I, this normalization allows a direct comparison of the reaction yields. Note that not only is the total yield much greater for the stripping case, but even the scattering which corresponds to backward recoil in the CM system (which appears in the region 60–150° in the LAB distribution) is substantially larger than for the rebound case. Figure 7 brings out another striking property. Whereas the stripping and rebound cases show drastic differences in both reactive and nonreactive scattering, the *total* scattering is very similar in both magnitude and angular distribution.

In Figures 8 and 9 the comparisons are made in terms of CM angular distributions derived from an approximate kinematic analysis. Since in the CM system the results for various stripping reactions are very similar, Br_2 is again taken as the example. Figure 8 gives results for nonreactive scattering. The LAB intensity distributions measured on the Pt-W alloy filament in mode N were transformed to the CM system, multiplied by sin θ_{CM} in order to remove the form factor due to the solid-angle element in the differential cross section, and normalized in the small-angle region where the patterns should be perturbed negligibly by reactive scattering. The kinematic relations appropriate for the most probable velocities in the parent beams were used in carrying out the transformation to the CM system. It has been shown[22,65] that in the case of elastic scattering of a beam of fast light atoms from slow heavy molecules this procedure yields a close approximation to the average of the CM angular distribution over the distribution of relative kinetic energy. The heavy dashed curve shows the averaged distribution calculated[22] for elastic scattering produced by an Exp-6

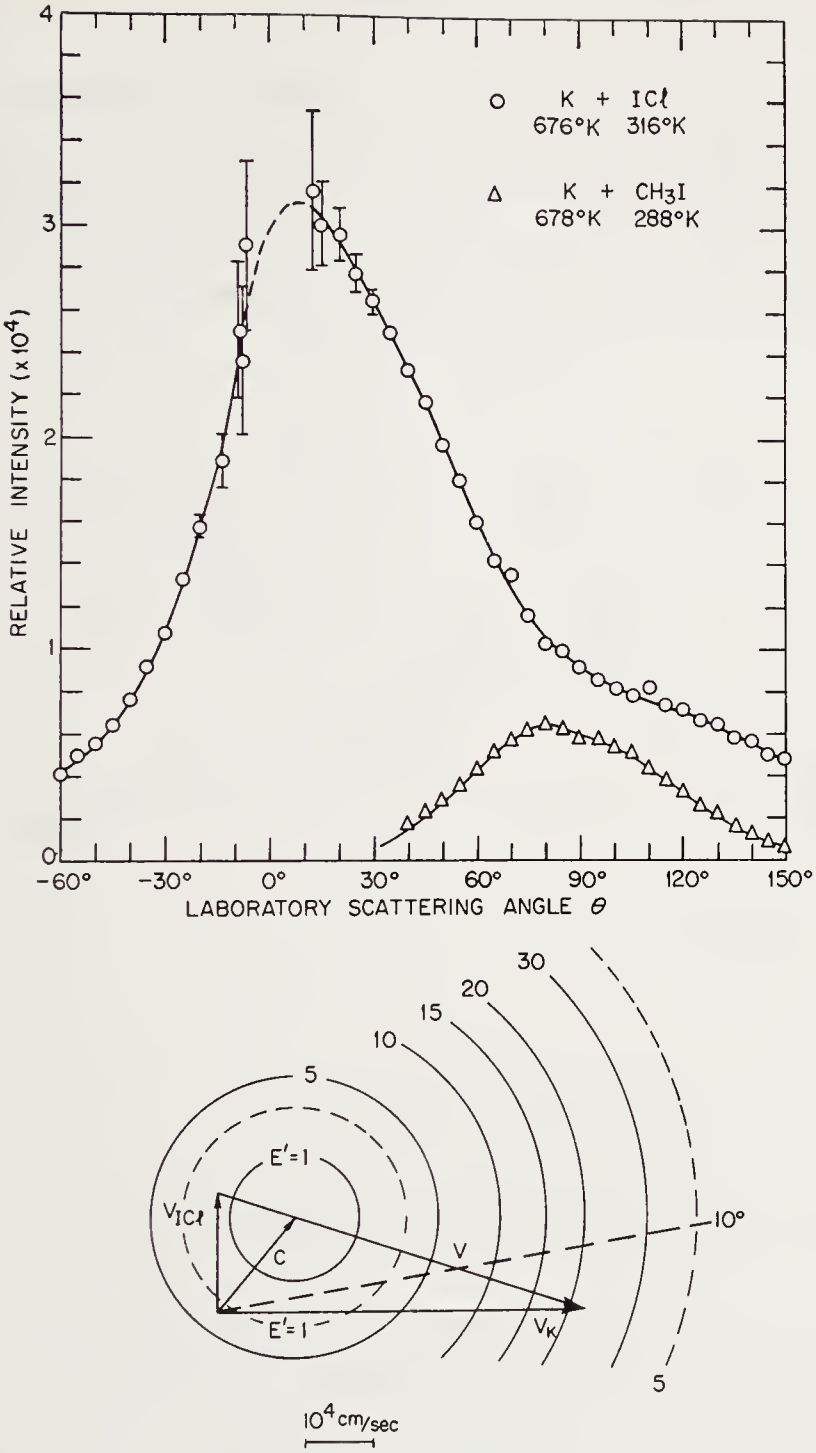

Fig. 6. Comparison of laboratory angular distributions of alkali halide product from the K + ICl and K + CH_3I reactions. The kinematic diagram applies to the K + ICl system; solid circles indicate the recoil energy E' when KI is the product, dashed circles when KCl is the product.

potential; a very similar distribution is obtained for a Lennard-Jones potential.

The angular distribution of K scattered from CH_3I closely resembles the pattern expected for an Exp-6 or Lennard-Jones potential, and in particular shows at wide angles the bowed shape characteristic for scattering from a repulsive wall. In contrast, the nonreactive scattering

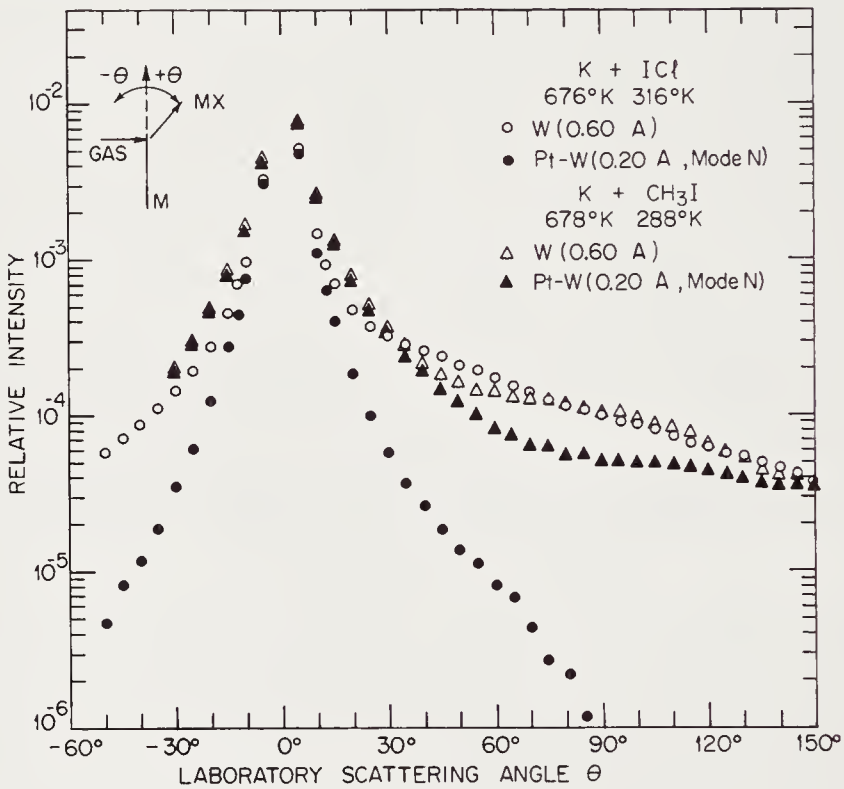

Fig. 7. Comparison of laboratory angular distributions of *total scattering* (sum of M and MX, indicated by ○ or △) and of *nonreactive scattering* (M only, indicated by ● or ▲) for the K + ICl and K + CH_3I systems.

from Br_2 shows an almost exponential falloff at wide angles. The usual contribution from repulsive core scattering is evidently almost entirely absent. Furthermore, as discussed later, the observed rate of decay of the intensity (by about $1/e$ in each 30° interval, as indicated by the light dashed curve in Fig. 8) is strong evidence that the only significant contributions to the wide-angle nonreactive scattering come from collisions at large impact parameters which involve "orbiting" outside a

centrifugal barrier. For stripping reactions, collisions at smaller impact parameters apparently lead almost exclusively to reaction, whereas for rebound reactions even close collisions give substantial contributions to the nonreactive scattering.

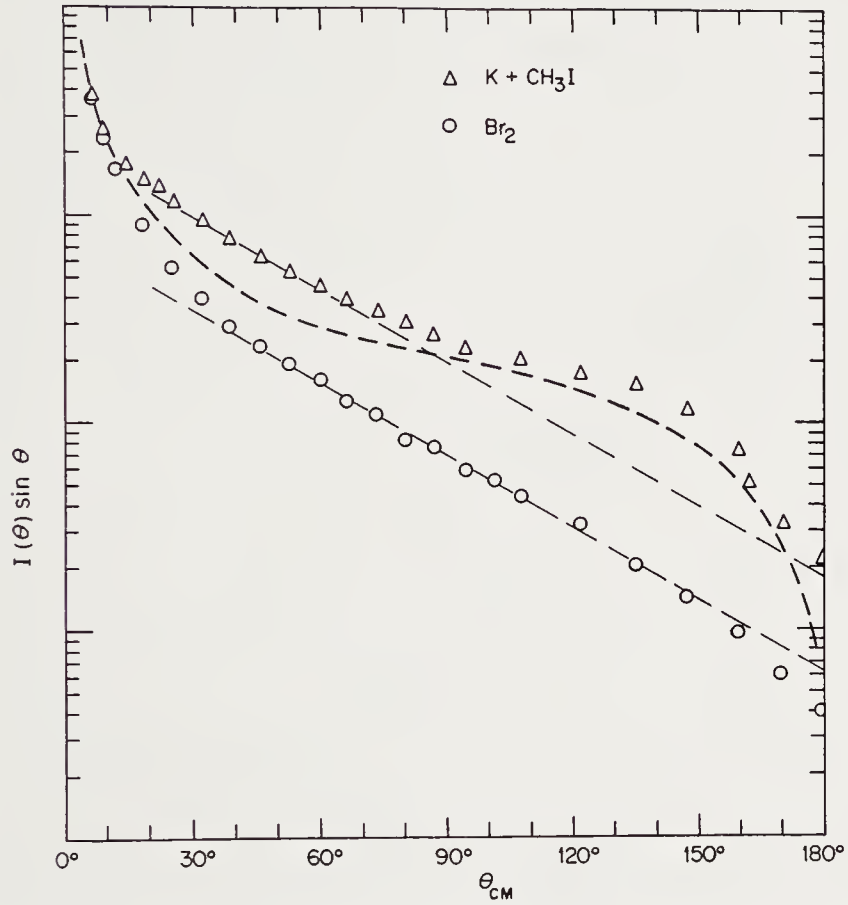

Fig. 8. Comparison of angular distributions (in the center-of-mass system) of K atoms scattered from CH_3I and from Br_2 without reaction. The heavy dashed curve shows the distribution expected for elastic scattering produced by an Exp-6 potential (with well depth $\varepsilon = 0.5$ kcal/mole and repulsive index $\alpha = 12$); the experimental curves are normalized to this in the small angle region. The light dashed curves are calculated from the orbiting collision model.

Figure 9 shows the CM angular distributions of reactive scattering obtained by using a "fixed-velocity" approximation to carry out the LAB → CM transformation.[65] This is analogous to the treatment applied in Figure 8 to elastic scattering. Only the most probable velocity vectors

in the reactant beams are considered and in addition it is assumed that the recoil energy E' has a fixed value. The requirement of cylindrical symmetry about the initial relative velocity vector means that for certain portions of the angular distribution different LAB angles should correspond to the same CM angle and intensity, and the value of E'

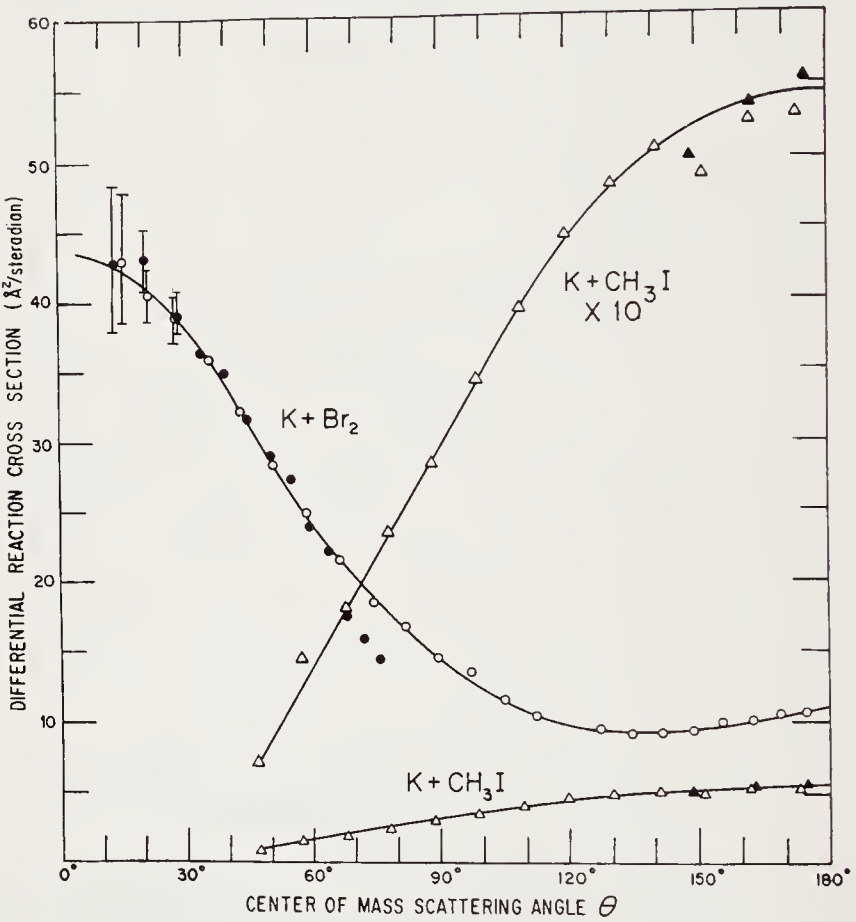

Fig. 9. Comparison of angular distributions (in the center-of-mass system) of alkali halide product from the $K + CH_3I$ and $K + Br_2$ reactions, as derived via the fixed velocity approximation.

is adjusted until the results satisfy this requirement as closely as possible. For stripping reactions, for example, the CM results derived from observations at negative LAB angles should match those from part of the range of positive LAB angles (see Figs. 4 and 5). For rebound reactions, the regions of redundant LAB angles are less well separated and accord-

ingly the results are less well defined. This procedure can give only a rough approximation to the actual CM angular distribution but (since it suppresses all the distributions in energy) it probably provides an upper limit estimate for the spread in CM recoil angles. The significance of the value of E' obtained is less definite; it appears to be higher than the most probable value, as indicated by comparison with other kinematic calculations and the velocity analysis experiment described in Section I-D (see Fig. 13). The analysis also provides an estimate of the total reaction cross section, σ_r. The ratio of σ_r to the total scattering cross section is evaluated by integration of the CM relative intensity distribution; this circumvents the difficulty encountered in the LAB system where often the out-of-plane scattering or other portions of the distributions are out of reach of the detector. In Figure 9, the points derived from the two branches of the LAB distributions are distinguished by open and solid figures. For the Br_2 reaction the best matching occurs for $E' = 3.6$ kcal/mole, and $\sigma_r = 210$ Å^2; for CH_3I, $E' = 6.3$ kcal/mole, and $\sigma_r = 30$ Å^2. The form of the CM product distributions indicated by this approximate analysis agree very nicely with results obtained from the Monte Carlo calculations.[27,32,66]

Outside the series of alkyl iodide reactions there are at present no other definitely established examples of rebound reactions. Many examples of stripping reactions involving polyatomic molecules have been found,[38,40,45,65,67] including M + SCl_2, PCl_3, PBr_3, CH_2I_2, $SnCl_4$, CBr_4, and SF_6. In all these the nominal recoil energy $E' \sim 1$ kcal/mole, and the reaction yield, forward peaking of the alkali halide distribution, and wide-angle falloff of the nonreactive scattering are remarkably similar to those found for the diatomic halogen reactions.

The nature of the transition between the rebound and stripping mechanisms has also been examined.[38] In the early Polanyi sodium flame experiments, several series of related polyhalide molecules were found to show drastic differences in reactivity, and beam studies have been carried out for such a series: M + $SiCl_4$, $CHCl_3$, CCl_4, $SnCl_4$. For M + $SiCl_4$ the reaction yield is too small to be reliably measured, but the scattering provides a reference for comparison with the other members of the series. As in Figure 7, the angular distribution of the *total scattering* for each of the reactive systems is found to be remarkably close to that for the $SiCl_4$ standard. Also, again the nominal recoil energy $E' \sim 1$ kcal/mole for the reactive systems. For M + $CHCl_3$ and M + CCl_4, the yield and other properties are intermediate between those

for the prototype rebound and stripping cases. The laboratory angular distributions of alkali halide appear to be bimodal and correspond to sideways, conical distributions of the recoil velocity vectors. In the wide-angle nonreactive scattering, a substantial contribution with the bowed shape characteristic of repulsive wall scattering appears to be superposed on the exponentially decaying contribution from orbiting collisions. This is illustrated for CCl_4 in Figure 10 (to be compared with Fig. 8), which includes the results for a drastic stripping case, $SnCl_4$, as well as the nonreactive standard, $SiCl_4$.

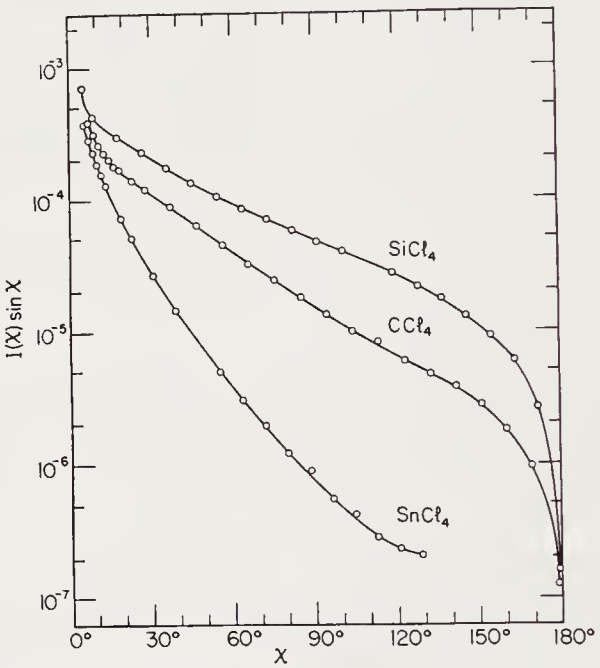

Fig. 10. Comparison of angular distributions (in the center-of-mass system) of Cs atoms scattered from tetrachloride molecules without reaction. (Here the CM scattering angle is denoted by χ rather than by θ as in Figure 8.)

The results for these polyhalide reactions indicate a strong correlation among the magnitude of the total reaction cross section, the preferred direction of recoil of the products, and the shape of the angular distribution of nonreactive scattering. As the reaction yield increases from the rebound range to the stripping limit, the favored direction for recoil of the alkali halide gradually shifts from backwards to forwards and the falloff in the wide-angle nonreactive scattering of the alkali atoms becomes increasingly pronounced.

C. Magnetic Deflection Analysis

The inhomogeneous magnet[45] shown in Figure 3*b* is of the traditional design,[53–55] with pole tips which conform to the cylindrical magnetic equipotential surfaces of the field produced by a pair of infinitely long parallel wires carrying equal and opposite currents. The copper tubing wound about the yoke (42 turns of 0.5-cm diameter tubing insulated with Fiberglas sheathing) carries both the energizing current and cooling water. A transistorized power supply is used which provides up to 100 A with less than 0.2% ripple. The magnet barrel is 7.0 cm long and the maximum width of the air gap is 0.32 cm. At an energizing current of 85 A, the induction in the air gap is $B \simeq 11$ kgauss and the transverse gradient is $\partial B/\partial z \simeq 34$ kgauss/cm.

For a given field, the deflection of an uncharged particle is proportional to μ_m/E_t, where μ_m is the magnetic moment and $E_t = \frac{1}{2}mv^2$ is the translational kinetic energy. Mass and velocity enter only via E_t, since the deflection is given by $\frac{1}{2}at^2$, with $a = (\mu_m/m)\partial B/\partial z$ the transverse acceleration and $t = L/v$ the time of passage through the field. With the field of Figure 3(*b*) operated at 85 A, an atom with $\mu_m = 1$ Bohr magneton and $E_t = 1$ kcal/mole is deflected by 0.05 cm in passing through the field ($L = 7.0$ cm). The deflection at the position of the detector is larger, about 0.11 cm, since the detector is an appreciable distance beyond the magnet ($D = 4.1$ cm, for the experiments of Fig. 11) and hence the deflection is magnified by a factor $1 + 2(D/L)$.

In the experiments of Figure 11 the magnet was used to eliminate most of the background signal due to the paramagnetic alkali atoms and thus permit a direct measurement of the distribution of diamagnetic alkali halide molecules produced by reactive scattering.[31,45] A test of the results which had been obtained from the two-filament subtraction method seemed very desirable because of the great difficulties experienced with "poisoning" in the initial studies of $K + Br_2$ and other stripping reactions. It appeared that the remarkably large yields and the remarkably similar form of the angular distributions for various reactions indicated by the two-filament results might be spurious.

In the deflection experiments, the magnet and detector assembly are mounted on a common flange and view the scattering chamber through two slits, each 0.01 cm wide; the first slit is 0.5 cm ahead of the magnet and 11.6 cm from the detector; the second slit 6.35 cm ahead of the first and 1.4 cm from the scattering chamber. It is essential that, with

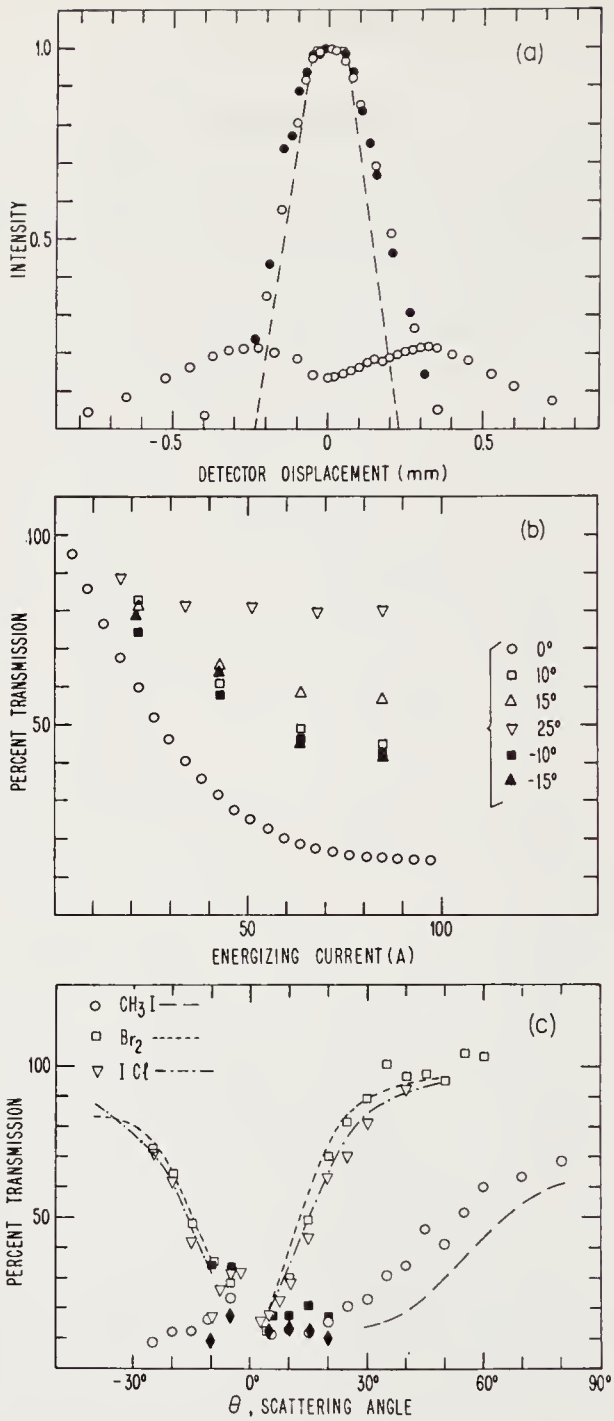

Fig 11. Magnetic deflection analysis: (*a*) Beam profile (for zero field) calculated from nominal slit geometry (*dashed trapezoid*) compared with profiles observed for parent K beam at 0° (○; unnormalized signal 5×10^{-10} A) and scattered signal at 25°(●; unnormalized signal 5×10^{-14} A). The Stern-Gerlach deflection pattern

the magnet off, the profile of the signal transmitted through the collimating slits and magnet barrel to the detector should remain independent of the observation angle Θ, since broadening of the profile by misalignment or background scattering can drastically reduce the effective deflecting power. Figure 11*a* shows a typical check of this requirement and an example of a deflection pattern. Since relatively wide slits had to be used, about 14% of the parent K beam (including high-velocity atoms and $\sim 1\%$ K_2 molecules) cannot be deflected.

Measurements of the magnetically filtered signal as a function of the magnet current are illustrated in Figure 11*b*; this demonstrates that for $K + Br_2$ a large fraction of the scattering at $\Theta = \pm 10°$ and beyond is due to a diamagnetic product.

In Figure 11*c* the results for reactions of K with CH_3I, Br_2, and ICl are compared. Results obtained for the nonreactive system K + cyclohexane are also shown; as expected, this exhibits the same transmission as the parent K beam. All of the data were obtained with a W filament except for a few points for $K + Br_2$ (solid squares), which were obtained with a Pt-W filament that had been heated in methane to make it insensitive to KBr. As the latter points are somewhat higher than those for cyclohexane, it appears that the Pt-W filament still detects some KBr, but with low efficiency ($\sim 5\%$). The results for the reactive systems are in very good agreement with calculated curves (shown dashed) derived from the previous two-filament measurements. There is clearly a striking difference between the CH_3I reaction, in which the diamagnetic product appears only at angles beyond $\Theta \simeq 30°$ and is accompanied by a comparable amount of elastic scattering, and the Br_2 and ICl reactions, in which the product is a substantial fraction of the signal within $\Theta < \pm 30°$ and practically 100% of the signal beyond $\Theta \simeq 30°$.

Magnetic deflection analysis has subsequently been applied to several other reactions,[45] including some involving nitrogen oxides for which the products could not be detected by the two-filament method.

---

for the parent beam (at a magnet current of 67.6 A) is also shown. (*b*) Signal reaching detector (at center of beam profile) as a function of the magnet current, for scattering of $K + Br_2$ at various angles. (*c*) Comparison of transmitted signal (at a magnet current of 84.4 A) versus laboratory scattering angle for beams of CH_3I (○, ———), ICl (△, —·—), and cyclohexane (◆) colliding with the parent K beam. Dashed curves are results predicted from data obtained with the two-filament technique.

D. Velocity Analysis of Products

The velocity selector[49] shown in Figure 3*a* is similar in design to that used by Hostettler and Bernstein[68] and others.[69,70] The rotor, which can be lowered out of the beam path by the gear arrangement, is driven by a hysteresis synchronous motor and a variable-frequency three-phase power supply. Each of the disks has 240 slots 0.080 cm wide, and the intermediate disks are positioned in such a way as to block the transmission of any "overtone" velocities.[68] A band of velocities with an approximately triangular intensity distribution is transmitted; the full width at half-intensity is 4.8% of the nominal transmitted velocity. The effective fractional open time to the incident beam is 0.32. At the highest attainable rotor speed (24,000 rpm) the transmitted velocity is 1200 m/sec.

As yet only a few studies[1,19,29,40,41,44] (a brief review is given in ref. 47) have employed velocity analysis of reaction products. Figure 12 shows results obtained for the $K + Br_2$ system.[40,41] In these experiments, the parent K beam (at 665°K) had most probable velocity $\alpha(K) = 530$ m/sec and the Br_2 beam (at 315°K) had $\alpha(Br_2) = 170$ m/sec. As before, the scattered K signal was detected with a "methanated" Pt-W surface ionization filament and the KBr signal was evaluated by taking the difference between readings on the W filament and the Pt-W filament. As in the experiments with the magnetic or electric analyzers, the apparatus alignment is very important. Only a small part of the zone of intersection of the parent beams is viewed by the detector, which is now 30 cm away and behind two additional collimating slits of width 0.005 cm placed before and after the velocity selector. Thus it is essential to establish that the two detector filaments continue to view the same portion of the scattering zone as the beam source assembly is rotated (see Fig. 1) about the scattering center. For the final alignment, the optimum "undisplaced" position of each filament was determined by scanning the parent K beam profile (at $\Theta = 0°$) with the detector running. Then an auxiliary experiment was carried out on the essentially nonreactive system $K + SiCl_4$, to verify that the velocity spectra (at various scattering angles Θ) measured on the two filaments were the same.

In Figure 12 the velocity distributions are given in terms of the "relative number density", $N(v) = S(v)/v^2$, obtained (aside from normalization) by dividing the detector signal by the square of the velocity. One of these factors of v corrects for the transmission of the velocity analyzer, which is proportional to velocity; the other factor of v

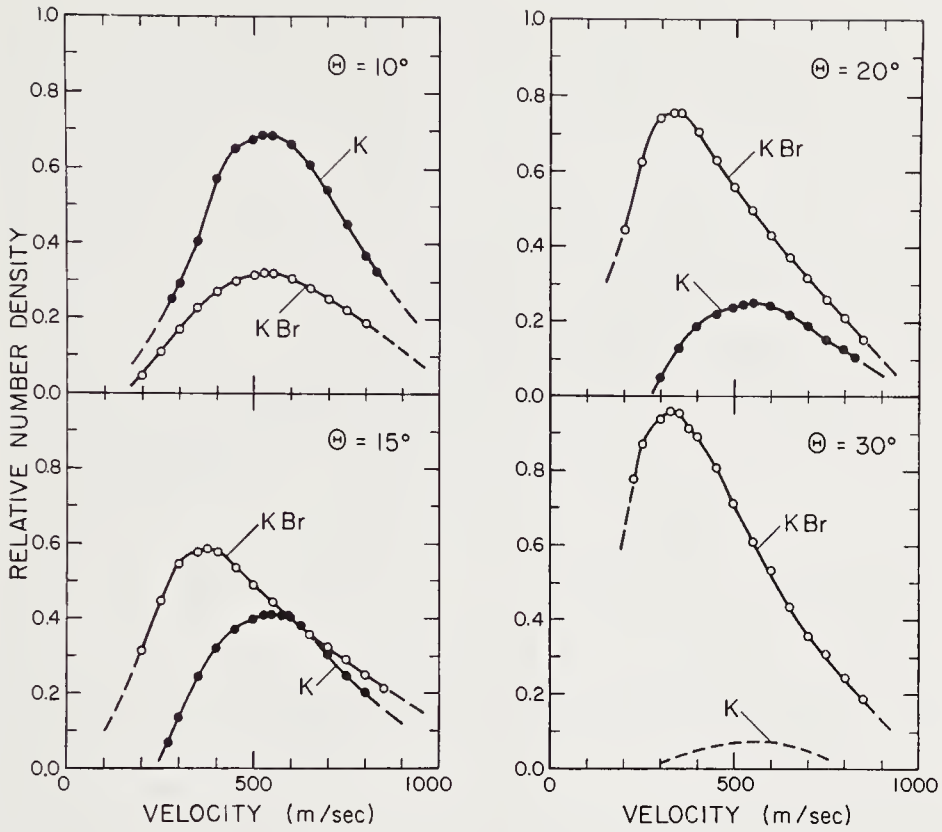

Fig. 12. Velocity analysis of $K + Br_2$ scattering at various laboratory angles. At each angle, the curves have been normalized so that the *sum* of the maximum ordinates for K and KBr is unity.

converts the flux density (particles/cm^2 sec) measured by the surface ionization detector into a number density (particles/cm^3). The distributions have been normalized at each angle so that the sum of the maximum ordinates for K and KBr is unity.

In agreement with the previous experiments (see Figs. 4 and 11), as Θ increases, the intensity of scattered K falls off much more rapidly than that of KBr, and at $\Theta \simeq 20°$ and beyond, the reactive scattering is dominant throughout the velocity spectrum. The distribution of scattered K peaks near 530 m/sec, the most probable velocity in the parent beam, and as Θ increases shows only a slight shift to higher velocities (as required by the kinematics of elastic scattering). The KBr distribution peaks at 510 m/sec for $\Theta = 10°$ but shifts rapidly to lower velocities as Θ increases; the peak appears at about 370, 350 and 310 m/sec for $\Theta = 15°$, 20°, and 30°, respectively. Although the velocity

analysis covers just the range 200–900 m/sec, it appears that only a small fraction of the total KBr yield occurs at higher velocities. Differences in conditions (especially the collimation of the parent beams and viewing zone of the detector) preclude a precise comparison with the previous experiments made without velocity analysis. However, the ratio of the integrated intensity in the KBr velocity distribution, including the extrapolated portions indicated in Figure 12, to the total KBr signal observed in the experiments without velocity analysis remains constant (within 10%) as Θ is changed.

These results nicely confirm the qualitative kinematic interpretation of the previous angular distribution measurements, and definitely establish that most of the chemical energy released in the $K + Br_2$ reaction, $\Delta D_0 \simeq 45$ kcal/mole, must appear in internal excitation rather than in translational motion of the products. In Figure 13 a contour map of the experimental LAB distribution of KBr is compared with the Newton diagram for the most probable velocities in the reactant beams. This indicates that the recoil energy in the CM system which corresponds to the peak in the LAB velocity distribution (shown by the open circles) varies from roughly $E' = 6$ kcal/mole at $\Theta = 10°$ to 3 kcal/mole at $\Theta = 15°$ and 1 kcal/mole at $\Theta = 30°$. The recoil energy distribution is quite broad, however, and along the contour with 50% of the peak intensity $E' \simeq 18$ kcal/mole at $\Theta = 10°$ and 8 kcal/mole at $\Theta = 30°$. A more useful description of the distribution may be given in terms of the cumulative intensity, or fraction of the total yield which appears below a specified recoil energy. For example, integration of the LAB distributions shown in Figure 12 gives

KBr velocity range	<500	<700	<900 m/sec
Approx. E' range	$\lesssim 5$	$\lesssim 10$	$\lesssim 20$ kcal/mole
Cumulative yield			
at $\Theta = 10°$	40%	79%	95%
at $\Theta = 20°$	61%	86%	94%

To pursue further the analysis of these results, it is necessary to examine the LAB $\rightarrow$ CM transformation in detail.[40,41] This will not be considered here except to note that the LAB intensity distributions used in constructing Figure 13 must be multiplied by a Jacobian factor to adjust to the CM velocity scale. This factor shifts the peak of the distributions outwards, and thereby moves the 100% contour further from the initial relative velocity vector $\mathbf{V}$ than it appears to be in Figure 13. There remains considerable uncertainty in the quantitative kinematic analysis because of the velocity distributions in the parent beams and

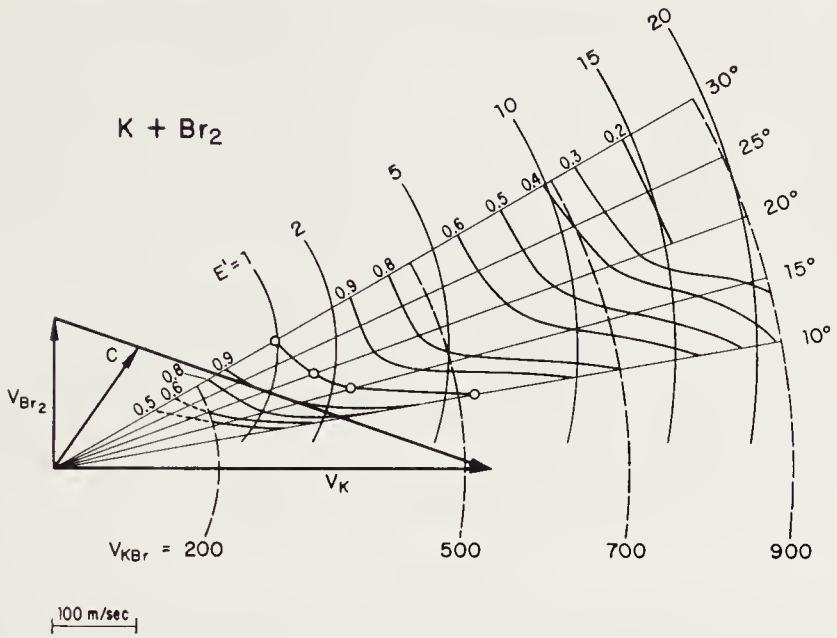

Fig. 13. Contour map indicating kinematic analysis of observed laboratory velocity distribution of KBr from K + Br_2 reaction. Solid circles show loci of $\mathbf{u}_{KBr}$ recoil vectors corresponding to various values of final relative energy E'; dashed circles show loci of $\mathbf{v}_{KBr}$ vectors corresponding to various laboratory velocities. Contours denote the percentage of maximum intensity at each laboratory angle; thus they do not indicate the angular variation of intensity but only the variation along the radius corresponding to the fixed value of Θ.

the inherent difficulty of evaluating separately the dependence on the recoil angle and energy.

The K + Br_2 reaction has been studied subsequently by the Wisconsin group,[44] with both velocity selection of the parent K beam and velocity analysis of the scattered K and KBr. Measurements were made at $\Theta = 20°$ with $v_K = 549$, 732, and 915 m/sec and at $\Theta = 15°$ and 10° with $v_K = 549$ m/sec. The KBr distributions obtained turn out to be remarkably similar in position and shape to those of Figure 12; selection and variation of the K velocity appears to have practically no effect on the KBr distribution! This striking property and the qualitative shape of the KBr distributions both find a ready explanation[40,41] in terms of the "electron jump" mechanism discussed in Section II.

E. Electric Deflection Analysis

Inhomogeneous electric deflecting fields have long been used in beam experiments designed to measure atomic polarizabilities or electric

dipole moments and also for selection of rotational states of polar molecules in electric resonance spectroscopy.[53–55] In scattering experiments, such fields offer a means to examine orientational effects,[71,72] inelastic rotational energy transfer,[73] and the distribution of angular momentum in reaction products.[45,46] The partitioning of angular momentum is of great interest for the theory of reaction dynamics.[10,13,15,27,32,47,52] It is intimately connected with the molecular mechanism of the reaction, since mass, velocity, and position all enter into the definition of angular momentum. Spectroscopic experiments have indicated the presence of high rotational excitation in some reactions but very little is known beyond this because rotational energy is relatively easily degraded by collisions.[74] Thus, beam experiments may make a particularly valuable contribution here.

Conservation of angular momentum provides that

$$\mathbf{L}' + \mathbf{J}' = \mathbf{L} + \mathbf{J} \tag{3}$$

where $\mathbf{L}$ and $\mathbf{L}'$ denote the initial and final orbital angular momenta associated with the relative motion of the collision partners and $\mathbf{J}$ and $\mathbf{J}'$ denote the rotational momenta of the reactants and products. Classically,

$$L = \mu V b \qquad \text{and} \qquad L' = \mu' V' b' \tag{4}$$

in terms of the reduced masses, relative velocities, and impact parameters of the reactants and products, respectively. For an A + BC → AB + C reaction,

$$W_{\text{rot}} = J^2/2I \qquad \text{and} \quad W'_{\text{rot}} = J'^2/2I', \tag{5}$$

in terms of the initial and final rotational excitation and the moments of inertia of BC and AB, respectively. As indicated in Figure 14*a*, the $\mathbf{L}$ vectors are perpendicular to the initial relative velocity $\mathbf{V}$, with all azimuthal orientations of $\mathbf{L}$ about $\mathbf{V}$ equally likely, whereas the initial $\mathbf{J}$ vectors are randomly oriented. The total angular momentum $\mathbf{L} + \mathbf{J}$ supplied by the reactants may be estimated roughly, as the thermal distributions of $\mathbf{V}$ and $\mathbf{J}$ are known and the range of impact parameters involved in the reaction probably does not extend much beyond $b^* \sim (\sigma_r/\pi)^{1/2}$, where σ_r is the total reaction cross section. For the alkali atom reactions this typically gives $\mathbf{L} \gg \mathbf{J}$, with L^* ranging from roughly 100 to 250 $\hbar$.

The partitioning of the angular momentum between $\mathbf{L}'$ and $\mathbf{J}'$ in the

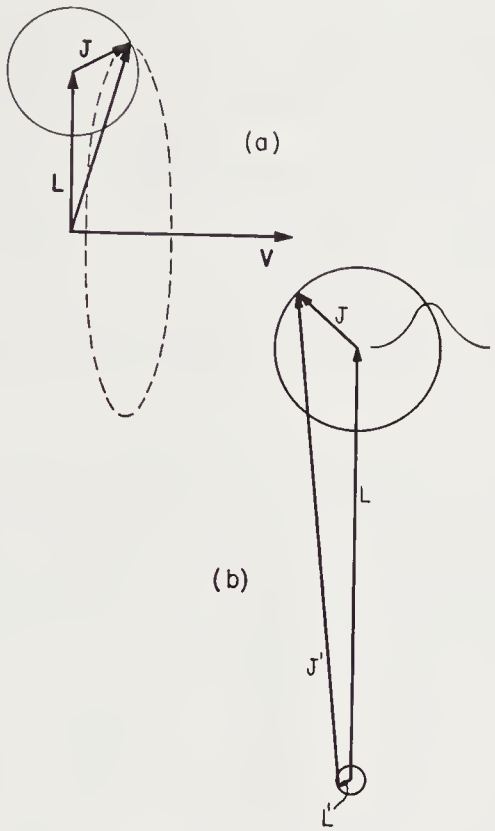

Fig. 14. Orientation of asymptotic angular momentum vectors: (*a*) In initial state of the collision the orbital angular momentum **L** is perpendicular to the relative velocity **V**, with all azimuthal orientations equally likely; the direction of the rotational angular momentum **J** of the reactants is uniformly distributed. (*b*) Example for which rotation of products must be polarized, with **J′** confined to directions nearly parallel to **L** and hence perpendicular to the initial relative velocity vector.

products is often only weakly constrained by the conservation laws. For example, if **L′** and **J′** are oppositely directed, Eq. (3) allows both to have much larger magnitude than $|\mathbf{L} + \mathbf{J}|$. Energy conservation limits the magnitude of **J′** according to Eqs. (2) and (5). However, for strongly exothermic reactions which produce molecules with large moments of inertia, this limit is rather weak; for example, if $J' \sim 300\ \hbar$, the rotational excitation is $W'_{\text{rot}} \sim 33$ kcal/mole for a KCl molecule, 21 kcal/mole for KBr, and only 9 kcal/mole for CsI. The accessible range of **L′** is linked by Eq. (4) to the final relative translational momentum and to the exit impact parameter. Also the centrifugal energy associated with the products, $L'^2/2\mu' R'^2$, must not exceed the available

energy (at a radius R' where $\mathbf{L}'$ and $\mathbf{J}'$ reach their asymptotic values). Again, for a strongly exothermic reaction, a wide range in $\mu' V'$ and centrifugal energy is usually compatible with energy conservation. The impact parameter b' is expected to be limited by the range of the forces and probably cannot become much larger than a typical bond length, but this usually allows a quite generous range for $\mathbf{L}'$. For example, in the $K + Br_2$ reaction, if $b' \sim 3$Å, then $L' \sim 100\ \hbar$ for $E' = 1$ kcal/mole and $\sim 300\ \hbar$ for $E' = 10$ kcal/mole.

A situation in which the partitioning of angular momentum is tightly constrained by the conservation laws occurs in the reactions

$$M + HX \rightarrow MX + H$$

Here it is expected[10,13,15] that most of the available angular momentum will appear in rotation of the MX molecule. On the reactant side, orbital angular momentum is dominant almost everywhere (except where b or V is very small), since the small moment of inertia of HX ensures that $\mathbf{J}$ is very small (only $\sim 3\ \hbar$ for HBr at the maximum of the thermal distribution for 300°K). On the product side, however, the orbital angular momentum is likely to be almost negligible; that is, $\mu' V' b'$ should have a much smaller range than $\mu V b$, since the reduced mass of the products (approximately just the mass of H) is far smaller than that of the reactants (26 times smaller for the K + HBr reaction, 50 for Cs + HBr). Because the reaction is only slightly exothermic, V' cannot become large enough to offset more than a fraction of the mass ratio; and the exit impact parameter b' would have to be unreasonably large to make the range of $\mathbf{L}'$ comparable to that of $\mathbf{L}$ (for example, $b' \sim 15$ Å at $E' \sim 2$ kcal/mole to make $L' \sim 100\ \hbar$). Therefore, since $\mathbf{L} \gg \mathbf{J}$ and $\mathbf{L} \gg \mathbf{L}'$, most of the initial orbital angular momentum must appear in product rotation, and $\mathbf{L} \approx \mathbf{J}'$.

The Monte Carlo studies of reaction dynamics[18,27,32] indicate that the condition $\mathbf{L} \approx \mathbf{J}'$ may also hold for a large class of reactions for which it is not required by the conservation laws. This occurs also for some of the reaction models discussed in Section II. The $\mathbf{L} \approx \mathbf{J}'$ situation has two interesting consequences for an electric deflection experiment.[10,15,45] First, as illustrated in Figure 14*b*, the rotation of MX should be strongly polarized, with $\mathbf{J}'$ aligned nearly perpendicular to the direction of the initial relative velocity vector. The predicted alignment for many reactions is much stronger than could be achieved with an external field and should have a pronounced effect on the electric

deflection patterns. Thus it will be possible to establish experimentally whether the condition $\mathbf{L} \approx \mathbf{J}'$ actually occurs. Second, when this does occur, a measurement of the distribution of the rotational momentum of MX will give information about the distribution of initial orbital angular momentum in those collisions which lead to reaction. From Eq. (4), this is equivalent to determining the reaction probability as a function of the initial impact parameter, $P(b)$, since the velocity dependence can be determined in separate experiments. The $P(b)$ function is basic for all theoretical calculations but the only other means of estimating $P(b)$ from scattering experiments is quite indirect and has to rely on the use of an optical potential model.[13,16,43]

The electric deflection experiment is essentially similar to magnetic deflection. However, the Stark effect of a polar molecule is much more complicated than the Zeeman effect of a paramagnetic atom, and the strength of the Stark effect varies drastically for the myriad rotational states that differ in magnitude and orientation of the angular momentum.[53–55] For heavy molecules such as alkali halides (unless the rotational excitation is extremely low) the effective dipole moment component in the field direction thus has a broad, practically continuous spectrum of values. Despite this, the main features of the rotational distribution can be readily characterized from the electric deflection patterns (if the distribution of transit times through the field is known from velocity analysis). The property most easily determined is the mean rotational energy. This may be evaluated by simply measuring the total fraction of the beam which is deflected and its variation with field strength, since rotation produces a "gyroscopic" quenching of the Stark effect. Information about the form of the rotational energy distribution and the spatial orientation of the angular momentum vectors can be obtained from the shape of the deflection pattern and its variation with the direction of the deflecting field.

The experiments carried out thus far[45,46] have used the apparatus of Figure 3*c*, which is well suited for measurements of the total deflection but not for measurements of the true shape of the deflection pattern. Since the onset of the field region is abrupt and the direction of the lines of force varies over a wide range, it is likely that any possible polarization would be blurred out by reorientation of the angular momentum within the field.[54] Also, since velocity selection was not used in these experiments, there is a broad spread in the direction of the axis of polarization (i.e., the initial relative velocity vector). Buffer

fields which will preserve the angular momentum quantization[54] must be installed before reliable measurements of the shape of the deflection pattern can be made. Thus, we shall consider here only the results derived from the total deflection measurements.

The experimental configuration is closely analogous to that used for magnetic deflection. The electric field and detector assembly are mounted on a common flange and view the scattering center through two slits, each 0.01 cm wide; the first slit is 1.6 cm ahead of the field and 29.8 cm from the detector; the second is 7.6 cm ahead of the first and 3.9 cm from the scattering center. The electrode configuration, as shown in Figure 3*c*, again has the "two-wire" form, which produces an electric field conjugate to that from two parallel line charges of opposite sign.[53,54] The electrodes are 15.2 cm long. The radius of the concave electrode is 0.396 cm and the radius of the convex electrode and the maximum width of the air gap are both 0.317 cm. The concave electrode is grounded and the convex electrode is charged by a transformer capable of supplying up to 50 kV at a current of 5 mA with less than 2% ripple. To minimize sparking, the electrodes are made of polished stainless steel and the insulators are quartz. In practice the sparking voltage is determined by surface contamination; in a good vacuum (no parent beams, background pressure $\lesssim 10^{-7}$ mm Hg) it is about 40 kV after the electrodes have been carefully cleaned and "purged" for several hours by repeatedly turning up the voltage to "spark away" specks of dirt, whereas with the parent beams present it drops to between 20 and 30 kV. The end plates shown in Figure 3*c* are attached to the grounded electrode when the apparatus is assembled; these carry some of the slits and provide part of the electrical shielding between the detector and field. The entire assembly (field, slits, detector, etc.) is enclosed in a 10-cm diameter brass tube attached to the main beam apparatus by a rotatable vacuum seal, and the fan shown in Figure 3*c* allows the electrical contact to be maintained as the orientation of the field is adjusted.

Auxiliary runs with thermal beams were carried out regularly to test the apparatus alignment and to provide a direct calibration of the deflecting power of the field. Calculations from Stark effect theory[45] were found to give excellent agreement with the deflection patterns observed in these runs if it was assumed that the beam passed 0.17 cm from the convex electrode (this is within the uncertainty in the position estimated from the nominal slit geometry). At this position the field

strength and transverse gradient calculated from the field geometry are $\mathscr{E} = 2.97\ V_0$ (kV/cm) and $\partial\mathscr{E}/\partial z = -8.63\ V_0$ (kV/cm^2), where V_0 (kV) is the applied potential. With this field operated at $V_0 = 30$ kV, a neutral particle with an effective dipole moment component of only 0.01 Debye and translational energy $E_t = 1$ kcal/mole will undergo a deflection of about 0.02 cm at the detector. An MX molecule has a permanent dipole moment of ~ 10 D and the magnitude of the effective moment (averaged over isotropic rotational orientations) remains larger than ~ 0.01 D until the rotational energy E_r exceeds ~ 20 kcal/mole (e.g., corresponding to $J' \lesssim 300\ \hbar$ for KBr).

Figure 15*a* shows typical beam profiles and deflection patterns observed for KBr from reactive scattering of K + Br_2 and for thermal Cs and CsCl calibration beams. The reproducibility of the apparatus alignment is illustrated by the close agreement (for runs made three months apart) with the zero-field profile calculated from the nominal slit geometry (dashed trapezoid). The deflection pattern for the Cs beam is shifted bodily towards the high-field region by the polarizability interaction (at 30 kV the induced dipole is about 0.015 D). The patterns for the reactively scattered KBr (at a laboratory angle $\Theta = 40°$ from the K beam) and the CsCl calibrating beam spread to both high and low field since the dipole moment has a range of orientations with respect to the field direction. The deflection pattern for the KBr product is seen to be very similar to that for a thermal beam. This is observed also for several other reactions which were studied, including the Cs + HBr reaction. Taken at face value, the shape of the pattern thus would correspond to an isotropic distribution of J' vectors. As already discussed, this may be a spurious result caused by experimental blurring of a polarized orientation, but the width of the deflection pattern remains a significant measure of the average rotational excitation.

Figure 15*b* shows measurements of the total deflection, in terms of the signal reaching the detector (at the center of the zero-field beam profile) as a function of the electrode voltage, for reactively scattered KBr from K + Br_2 and CsBr from Cs + HBr. Also shown are results for elastic scattering of K from cyclohexane (at $\Theta = 30°$, open diamonds) and for thermal beams of K, Cs, and CsCl. The reactive scattering curves have been corrected for the contributions from deflection of atoms elastically scattered at the same angle.

The results clearly demonstrate that in these reactions the mean rotational excitation of the newly formed products is comparable to the

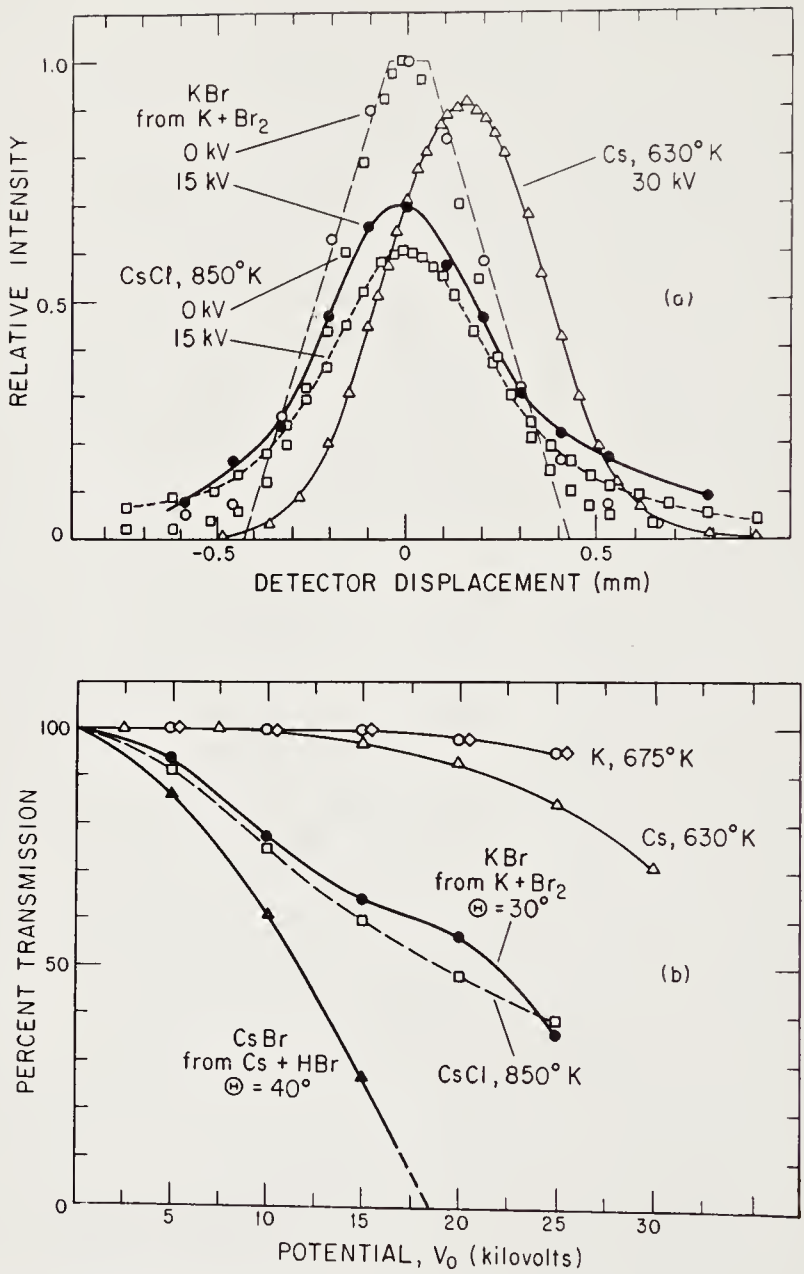

Fig. 15. Electric deflection analysis: (*a*) deflection patterns; (*b*) variation of transmission with electrode voltage.

thermal energy. As illustrated in Figure 16, the total deflection depends primarily on the ratio $\mu\mathscr{E}/\langle\bar{E}\rangle$, where $\mu\mathscr{E}$ is the Stark effect perturbation energy and $\bar{E} = (E_t E_r)^{1/2}$ is the geometric mean of the translational and rotational energy; in the accessible range the total deflection is insensitive both to the form of the distribution in E_r and to the orientation of the angular momentum vectors. A thermal translational distribution is assumed (temperature T_t). For K + Br_2 the direct measurements[41] show this is a good approximation (with $T_t \simeq 755°K$ at $\Theta = 30°$). For Cs + HBr, kinematics requires the CsBr to come off very near the center of mass; thus the velocity distribution is readily calculated and again it is approximately thermal (with $T_t \simeq 375°K$ at $\Theta = 40°$). For the

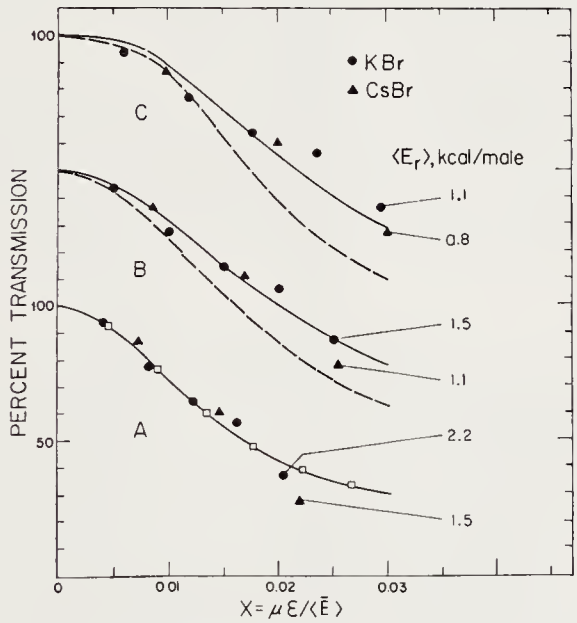

Fig. 16. Transmission functions calculated for various rotational energy distributions compared with experimental results.

rotational distribution, case A is a thermal distribution (temperature T_r), B is a constant up to a cutoff (denoted by E_B), C is a delta function (located at E_C); the first moments are related by

$$\langle E_r \rangle = kT_r = \tfrac{1}{2}E_B = E_C$$

The solid curves refer to isotropic orientation, dashed to polarization perpendicular to the field direction. The data have been fitted to the calculated curves by adjusting the value of $\langle E_r \rangle = \langle \bar{E} \rangle^2 / kT_t$; for each

case the isotropic orientation was used, since, as shown in Figure 15*a*, this corresponds closely to the measured deflection patterns.

As noted above, the total angular momentum available to the products may be roughly estimated from the magnitude of the observed reaction cross sections. For Cs + HBr ($\sigma_r \simeq 140$ Å^2), essentially all of it (175 $\hbar$, estimated from case *B*, polarized) appears to go into rotation of CsBr as predicted from analysis of the kinematic restrictions on this reaction.[10,13,15] For K + Br_2 ($\sigma_r \simeq 210$ Å^2, corresponding to at least 250 $\hbar$ available), kinematic restrictions are insignificant and the deflection experiments indicate the rotational momentum of KBr is appreciably smaller (case *B*, polarized gives the maximum as 135 $\hbar$) so that a substantial fraction must appear in the orbital angular momentum associated with the relative motion of KBr and Br.

Electric deflection measurements have been carried out also[45] for reactions of alkali metals with ICl, PBr_3, $SnCl_4$, and SF_6. The values found for $\langle \bar{E} \rangle$ range from 1 to 3.5 kcal/mole. Although the evaluation of $\langle E_r \rangle$ must await completion of velocity analysis experiments, these results show that in all of these reactions the exothermicity must appear mostly in vibrational excitation (or possibly electronic excitation) of the products.

F. Summary and Discussion

Table I and the bibliography[1–52] are intended to provide a complete list of molecular beam studies of reactive scattering and theoretical discussions of the results. References to the earliest proposals and inconclusive experiments are omitted since these can be found in other reviews.[3,47,53] Thus the bibliography goes back only ten years[1,2] and over two-thirds of the entries have appeared within the past two years. Also, studies of the elastic scattering of reactive molecules have been extensively reviewed elsewhere.[16,21,43] References to this work are not included in Table I (except when carried out concurrently with reactive scattering experiments) but are included in the bibliography. The same holds for a few preliminary studies of reactive scattering for which the present data are very incomplete or appear inconsistent with kinematic requirements.

The broad, qualitative features which have appeared again and again in the work of Table I may be summarized as:

1. Most of the chemical energy released appears as internal excitation of the products rather than as relative translational kinetic energy.

TABLE I
Reactions Studied in Molecular Beams[a]

Reaction	ΔD_0, kcal/mole	Refs.
$K + HBr \rightarrow KBr + H$	3.8	*2*,3,*5*,6,8,*13*,16,21,23,*29*,36, 43,*45*,*46*
$HI \rightarrow KI + H$	5.6	*25*,*35*,43
$M + RI \rightarrow MI + R$		*7*,10,14,15,16,21,*24*,
$M = Na, K, Rb, Cs$		26,27,*31*,32,*38*,47,*48*,
$R = CH_3, C_2H_5, \ldots, C_5H_{11}$	23–33	*49*,*50*
$R = CH_2{:}\ CHCH_2$	40	
$M + Br_2 \rightarrow MBr + Br$	44.8	*28*,*31*,*38*,*39*,*40*,*41*,*42*,*44*,*45*, *46*,47,66
$I_2 \rightarrow MI + I$	40.4	*38*,*39*,*42*,47
$ICl \rightarrow MI + Cl$	26.4	*31*,*39*,47,*49*
or $\rightarrow MCl + I$	51.0	
$IBr \rightarrow MI + Br$	34.1	*39*,47,*49*
or $\rightarrow MBr + I$	48.3	
$M + SCl_2 \rightarrow MCl + SCl$	~40	*40*
$M + PCl_3 \rightarrow MCl + PCl_2$	~22	*38*
$PBr_3 \rightarrow MBr + PBr_2$	~27	
$M + CH_2I_2 \rightarrow MI + CH_2I$	(30)	*65*
$M + CHCl_3 \rightarrow MCl + CHCl_2$	~32	*38*
$CHBr_3 \rightarrow MBr + CHBr_2$	~40	
$M + SnCl_4 \rightarrow MCl + SnCl_3$	~24	*38*,*45*
$CCl_4 \rightarrow MCl + CCl_3$	32	*1*,*38*,*45*,47
$CBr_4 \rightarrow MBr + CBr_3$	~40	*38*,*67*
$M + SF_6 \rightarrow MF + SF_5$	(50)	*45*
or $\rightarrow MSF_5 + F$	(?)	
$M + CF_3I \rightarrow MI + CF_3$	(23)	*75*
$M + NO_2 \rightarrow MO + NO$	(30)	*45*
$+ CH_3NO_2 \rightarrow MNO_2 + CH_3$	(20)	*45*

[a] The italicized references give experimental results, others give discussion or interpretation. The quantity ΔD_0 is the difference in dissociation energy of the M—X bond (from ref. 77) and the reactant R—X bond (from ref. 76), measured from the zero-point vibrational level. The values given refer to reactions with potassium; for a given halogen, the ΔD_0 values would be almost the same for reactions with rubidium, about 3–4 kcal/mole less for reactions with sodium, and about 5 kcal/mole larger for reactions with cesium. The listed values are all uncertain by about 1–2 kcal/mole due to uncertainty in the M—X bond strengths. For the cases indicated with an approximation mark there is a further uncertainty of perhaps 5 kcal/mole or more because only an average value of the R—X bond strength derived from the heat of atomization of the compound is available. Values given in parenthesis are much more uncertain, and in most cases are simply guesswork.

2. The angular distribution of products (in the CM system) is usually quite anisotropic. With respect to the incoming M atoms, most of the MX molecules recoil *backwards* in the rebound reactions (e.g., alkyl iodide reactions), *forwards* in the stripping reactions (e.g., diatomic halogens, SCl_2, PCl_3, $SnCl_4$), and *sideways* for intermediate reactions (e.g., CCl_4, $CHCl_3$, CF_3I).

3. The preferred direction of recoil of the products is strongly correlated with the magnitude of the total reaction cross section, σ_r, which varies from $\lesssim 10$ Å^2 for rebound reactions to $\gtrsim 100$ Å^2 for stripping reactions.

4. The shape of the angular distribution of elastic scattering (in the CM system) also is correlated with σ_r; for rebound reactions, it is similar to that of comparable nonreactive molecules, whereas for stripping reactions it falls off very rapidly at wide angles.

5. Regardless of the size of σ_r, the angular distribution of the total scattering (sum of elastically scattered M and reactively scattered MX) is similar to that for nonreactive molecules of similar size and structure.

More detailed properties, thus far studied for only a few reactions, include:

6. The shape of the angular distributions (CM system) of both the reactive and nonreactive scattering is almost identical for various alkali metals (M = K, Rb, Cs) but may differ appreciably for different reactant molecules (e.g., for Br_2 and I_2).

7. Variation of the K velocity has very little effect on the velocity of the KBr formed in the K + Br_2 reaction.

8. The mean rotational excitation of the products is comparable to their mean translational or thermal energy. In some cases, a large fraction of the initial angular momentum may be taken up in the orbital motion of the products (e.g., the K + Br_2 reaction); in others essentially all of it may go into rotational excitation (e.g., the Cs + HBr reaction).

We will consider in turn the interpretation to be attached to each of these properties. As a matter of doctrine, we wish to emphasize the three natural and distinct stages in analysis of chemical scattering studies: kinematic reduction of the data; stochastic comparison with theoretical models based on assumed force fields; and inference or speculation about the chemical basis of the forces. Passage between these stages should be made cautiously! Hence, in reviewing the experimental results we have restricted attention to the kinematic stage, and in order to indicate the proper distance between the experiments and

the final stage we have removed discussion of the chemical implications to Section II. In the stochastic comparison with theoretical models, the Monte Carlo calculations provide the surest guide. Several reviews are available,[26,27,32,74] although the experiments have since pulled ahead of the computers. Here we shall briefly discuss qualitative arguments which are in part supported or suggested by the Monte Carlo results. These interpretations are strictly heuristic.

Energy Disposal. The partitioning of the reaction exothermicity between the internal and external degrees of freedom available in the products (property *1*) had received a great deal of attention long before the molecular beam studies. The early Polanyi flame experiments[78–84] showed that many reactions of alkali metals with halogen compounds produced MX with internal excitation sufficient to excite resonance lines of the M atoms in subsequent collisions. However, the observed quantum yields of chemiluminescence were large for only two or three of the reactions; thus, only for these reactions is it possible to conclude that a large fraction of the MX produced must carry high internal excitation. The example universally quoted is the $X + Na_2$ reaction[78,79] (for which $\Delta D_0 = 80, 69, 55$ kcal/mole for X = Cl, Br, I as compared with 48 kcal/mole required to excite the Na D lines). This occurs as a secondary step following the $Na + X_2$ reaction, for which the flame studies give no information concerning the internal excitation since the exothermicity is not large enough to give NaX that could excite the Na D lines. Surprisingly, similar studies[80] of the $K + X_2$ systems seem to have been almost universally overlooked in texts and reviews. Here the exothermicity ($\Delta D_0 = 43, 45, 40$ kcal/mole for X = Cl, Br, I) exceeds the excitation energy of the K D lines (37 kcal/mole) and intense chemiluminescence due to the primary reaction was indeed observed. This was separated from a weaker contribution due to the secondary $X + K_2$ reaction by heating to temperatures sufficient to dissociate most of the K_2 molecules.

In recent years, vibrationally excited product molecules have been directly observed in many spectroscopic experiments. Extensive reviews of this work are available.[74,85–89] Again, however, it should be emphasized that as yet there are only a few studies from which it is possible to establish the order of magnitude of the relative yield of excited and unexcited products or to infer the initial distribution of vibrational excitation before degradation by collisions. For several hydrogen atom reactions, including reactions with Cl_2, ClNO, and NO_2, the spectroscopic

observations have shown that the products are formed predominantly in the ground vibrational state.[74,90,91]

The molecular beam and spectroscopic experiments are complementary, since the beam studies can directly determine only the initial translational and rotational energy distributions and the spectroscopic experiments only the steady-state vibrational and electronic excitation. We have recently given a more detailed review[47] of the beam results on energy partitioning. Here we shall only note that although the beam results for the $M + Br_2$ and $M + I_2$ reactions leave open the question whether the internal excitation is partly present as electronic excitation of the metastable $^2P_{1/2}$ states of the halogen atoms (10.5 and 21.7 kcal/mole above the ground states for Br and I, respectively), the diffusion flame experiments[80] offer evidence against this.

Early qualitative discussions[78,81] suggested a simple relation between the partitioning of the reaction exothermicity and the form of the potential energy surface. This applies to an $A + BC \rightarrow AB + C$ reaction without appreciable activation energy. If the surface is of the *attractive* or *early downhill* type, in which most of the exothermicity is released as the reactants approach rather than as the products separate, strong vibrational excitation of the newly formed AB bond is expected, whereas for a *repulsive* or *late downhill* surface most of the exothermicity is expected to appear in translational recoil of AB and C. The energy partitioning has been thoroughly examined in the Monte Carlo studies and found to obey this criterion although in extreme cases other features of the surface have some effect also.[27,33,74,89] Several instructive qualitative discussions of the operation of this criterion have also been given.[89,92–94]

Thus the reactions of alkali atoms and of hydrogen atoms with halogens appear to be prototype examples of the attractive and repulsive type, respectively. Chemical intuition, which always works best after the facts are established, hastens to suggest that these examples probably represent the limiting cases. The strongly attractive or early downhill character of the alkali reactions may be attributed to the transition from covalent (X_2) to ionic (M^+X^-) bonding (as discussed in Section II), the late downhill character of the hydrogen reactions to the small size and resistance to polarization of the atom, which delays the onset of chemical interaction.

Angular Distribution of Products. The marked forward–backward asymmetry observed in the angular distributions of alkali halides in both

the rebound and stripping reactions (property *2*, cf. Fig. 9) indicates that the products *remember* the direction of the initial relative velocity vector **V**. These reactions hence proceed mainly via a *direct* or *impulsive* mechanism, rather than via a collision complex whose decomposition could be treated as independent of its manner of formation.[10,15,47] The asymmetry implies that the collision complex usually decomposes before it can rotate through a half-turn. Since most of the collision complexes are formed with very large angular momentum, as required by the large reaction cross sections, and $\mathbf{L} + \mathbf{J} \simeq \mathbf{L}$ is essentially perpendicular to **V**, the average period for a forward-to-backward rotation is quite short. This leads to a rough upper limit of $\sim 5 \times 10^{-13}$ sec for the average lifetime of the collision complex.

Of the reactions studied thus far, only $M + CH_3NO_2$ appears to give an isotropic product distribution (in the CM system). Further work is required to identify definitely the product; however, magnetic deflection analysis[45] has shown that the product is diamagnetic and it is probably MNO_2. If so, it may be significant that this is the only case so far studied in which the product is formed by attack of the M atom on a central atom rather than a peripheral atom.[45] It should also be noted that for several of the reactions which are intermediate between rebound and stripping the product distributions may actually be essentially isotropic. Although the kinematic analysis indicates sideways peaking, for some of these reactions the uncertainty is too large to permit an isotropic distribution to be ruled out. Of course, whereas observation of forward–backward asymmetry points to a direct interaction mechanism, observation of an isotropic distribution cannot be taken as evidence for a statistical complex mechanism since (as illustrated in the discussion of Fig. 17) an isotropic distribution can also result from a direct interaction mechanism.

In the Monte Carlo computer studies the direct interaction mechanism appears to be quite general. Even for potential surfaces which do not give agreement with the beam experiments, it usually is found that most of the trajectories turn the corner smoothly and the products separate within 5×10^{-13} sec or less.[27,33] These results are of particular interest, since in theoretical chemical kinetics much more attention has been given to statistical collision complex models than to direct interaction models.

Transition between Rebound and Stripping. The correlation among the magnitude of the reaction cross section, the preferred direction of recoil

of the products, and the form of the wide-angle elastic scattering (properties *2–4*) has a simple heuristic interpretation which is illustrated in Figures 17–19. It is convenient to discuss this in terms of a rudimentary extension[47] of the semiclassical optical potential model for elastic scattering.[95] The qualitative features of interest here are definitely not unique to this model, but it nicely simulates some of the results of the Monte Carlo calculations.[32,66] The reactants A + BC are assumed to approach the region of chemical interaction along a two-body central force trajectory specified by an impact parameter b and kinetic energy E. A fraction $P(b,E)$ of these collisions lead to reaction, and the products AB + C depart along another two-body trajectory with impact parameter b' and kinetic energy E'. The differential scattering cross sections for elastic and reactive scattering then are given by

$$I_E(\theta) = [1 - P(b,E)]d(\pi b^2)/d\omega \tag{6a}$$

$$I_R(\theta') = P(b,E)d(\pi b^2)/d\omega' \tag{6b}$$

where $\theta(b,E)$ and $\theta'(b,E)$ are the elastic and reactive scattering angles (directions of recoil of A and AB, respectively) and $d\omega = 2\pi \sin\theta \, d\theta$ and $d\omega' = 2\pi \sin\theta' \, d\theta'$ are the corresponding solid angle elements in the CM system. In reactive collisions the scattering angle is the sum of contributions from the reactant and product portions of the trajectory,

$$\theta' = \theta_r(b,E) + \theta_p(b',E') \tag{7}$$

The lack of a third contribution representing the ABC complex makes apparent the "ultra-direct" character of this model. Further assumptions are required to relate b' and E' to b and E, as described below. With these relations both the elastic and reactive scattering may be evaluated from the usual semiclassical two-body collision mechanics, once the potentials and the reaction probability function $P(b,E)$ are specified.

For the rebound reactions, the main contributions evidently come from small impact parameters, since $(\sigma_r/\pi)^{1/2} \gtrsim 2$ Å. In this region the elastic scattering is dominated by the "repulsive wall" and in the hard-sphere approximation

$$\theta_r = \arccos(b/R) \tag{8}$$

with R the sphere radius. Since the switchover to products occurs for configurations with the A—B and B—C distances somewhere near the

equilibrium bond lengths, the exit impact parameter b' must also be small; thus the product interaction will likewise be mainly repulsive, and

$$\theta_p = \arccos(b'/R') \tag{9}$$

If the reaction is supposed to occur for a particular configuration of A—B—C, the relation between b and b' is fixed by simple geometry. For linear configurations the relation is one-to-one, as illustrated in Figure 17. For bent configurations, all azimuthal orientations about a

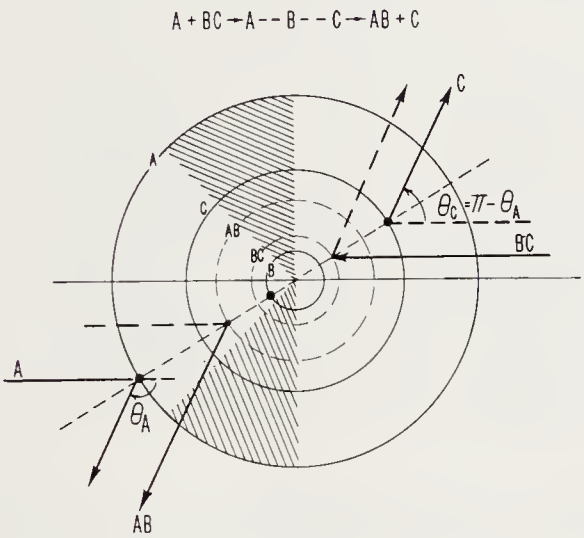

Fig. 17. Relation of elastic and reactive scattering in the primitive optical potential model for a *rebound* reaction. A collinear configuration of ABC is assumed, with both the incoming and outgoing portions of the trajectories governed by hard-sphere repulsion. For an impact parameter such that in elastic scattering the angle of A is θ_A, in the reactive scattering the product AB appears at the same angle, $\theta_{AB} = \theta_A$, and C at the "mirror image" angle, $\theta_C = \pi - \theta_A$. If A is incident on the unshaded area, both A and AB recoil into the backward hemisphere ($\theta_A \geq 90°$) whereas if A is incident on the shaded area they recoil forwards ($\theta_A \leq 90°$).

line from A through the center of mass of BC are equally likely, and this generates a broad spectrum of b' for each b; the averaged scattering evaluated by integrating over the azimuthal orientations closely resembles that for linear configurations, however, as indicated in Figure 18. For $R \simeq R'$, this model makes the averaged trajectories for reactively scattered AB approximate specular reflection, roughly parallel to the elastically scattered A. Thus the form factors $d(\pi b^2)/d\omega$ in Eqs. (6) are

both nearly constant; the angular distribution of reactive scattering is directly determined by $P(b,E)$, with $b = b(\theta')$, and the wide-angle elastic scattering is determined by $1 - P(b,E)$, with $b = b(\theta)$. Since for rebound reactions the elastic scattering is found to be very similar to that of nonreactive systems (see Fig. 8), the reaction probability $P(b,E)$ is evidently well below unity even for small impact parameters. If the reaction can occur only for $b < R/\sqrt{2}$ (unshaded region in Fig. 17, or average unshaded region in Fig. 18), the distribution of AB is entirely

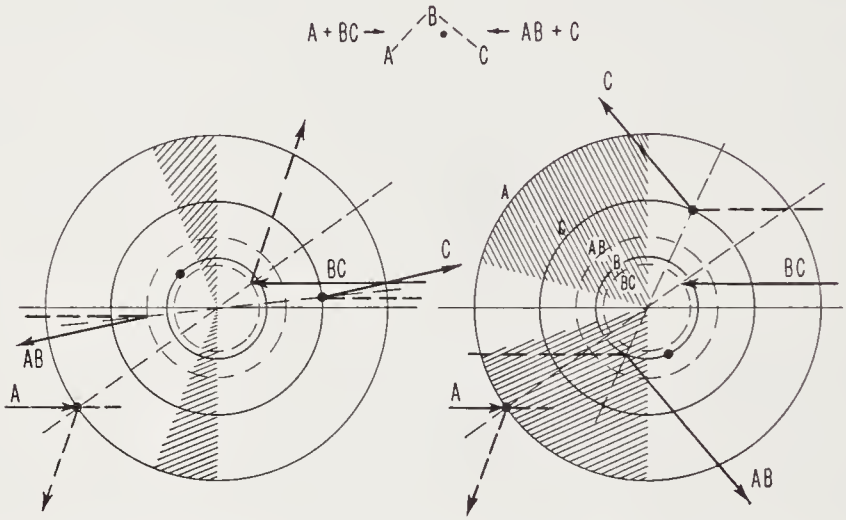

Fig. 18. Primitive rebound reaction model for a bent configuration of ABC. An everage must be taken over all azimuthal orientations of the BC axis about the line from A through the center of mass of BC. As illustrated by the two extreme cases pictured here, the relations shown for the collinear case in Fig. 17 are thereby broadened, but the average remains close to the collinear result.

confined to the backward hemisphere, whereas if reaction is equally probable for all impact parameters up to $b = R$, the angular distribution of AB becomes nearly isotropic. This same qualitative correlation between the range and form of the reaction probability and the form of the angular distributions has been found in the Monte Carlo calculations for a wide variety of potential surfaces, although the degree to which the wide-angle scattering of A and AB approach specular reflection varies considerably with the potential.[32,66]

For the stripping reactions, the remarkably big cross sections indicate that the reaction probability must be high for collisions with impact parameters as large as $(\sigma_r/\pi)^{1/2} = 6$ Å or more. Since there is no evidence

of a repulsive wall contribution in the elastic scattering, the residual wide-angle elastic scattering apparently comes solely from "orbiting" collisions in which the reactants are held apart by a centrifugal barrier (see Fig. 21). In this realm the deflection may be approximated by[96]

$$\theta = 2\theta_r = \theta_0 + a_0 \ln [(b - b_0)/b_0] \tag{10}$$

for $b > b_0$, where b_0 is the impact parameter for a trajectory which just reaches the top of the barrier. The corresponding angular distribution, evaluated from Eq. (6b), falls off as $\exp(-\theta/a_0)$ at wide angles. The decay parameter $a_0 \simeq 30°$ for any potential which goes as r^{-6} at long range and is almost independent of the collision energy (as long as E is within the orbiting realm). The observed wide-angle elastic scattering shows precisely this 30° exponential falloff (dashed line in Fig. 8).

The forward peaking of reactively scattered AB observed in stripping reactions is also readily obtained from the model. Since $P(b,E)$ is now taken as unity for b well beyond the hard sphere radius R, the terms considered for the rebound model, Eqs. (8) and (9), give an isotropic contribution. Superimposed on this are further contributions from the regions with $b > R$ or with $b' > R'$ in which attractive forces dominate. Here the deflections θ_r or θ_p are negative, whereas for $b < R$ or $b' < R'$ they were between 0 and 90°. Only the absolute value of the scattering angle,

$$|\theta'| = |\theta_r + \theta_p| \tag{11}$$

is observable and hence the regions in which θ_r and θ_p differ in sign (i.e., $b > R$, $b' < R'$ and $b < R$, $b' > R'$) favor forward scattering. The situation is illustrated in Figure 19, which corresponds to a collision with the reactant part of the trajectory attractive ($b > R$, $\theta_r < 0$) and the product part repulsive ($b' < R'$, $\theta_p > 0$). As is clear from the elastic scattering, contributions with $b > R$ must be very important, especially since they are heavily weighted by the target area distribution, $d(\pi b^2)$. Thus if the reaction cross section is large enough, the AB distribution should be strongly peaked forward. Although it is much weaker, there is also appreciable backward scattering of AB arising from the isotropic contribution. According to the model, the backward scattering should in fact be substantially larger than for rebound reactions, since in the rebound case $P(b,E)$ is well below unity. This again agrees with the experimental results (see Fig. 9).

The notion that all trajectories which surmount the centrifugal barrier

and reach the "hard collision" region will lead to reaction has been employed in many model calculations of total cross sections for various types of fast reaction processes.[52,97] The observed angular distributions now offer very strong evidence that this is actually the situation for stripping reactions.

For reactions intermediate between rebound and stripping, the prediction of the optical potential model is quite sensitive to the form of the reaction probability function. Thus, the product distribution will be essentially isotropic if $P(b,E)$ is roughly constant up to a cutoff in the vicinity of $b \simeq R$, whereas the distribution can be peaked sideways if $P(b,E)$ gives less weight to collisions with small impact parameters.

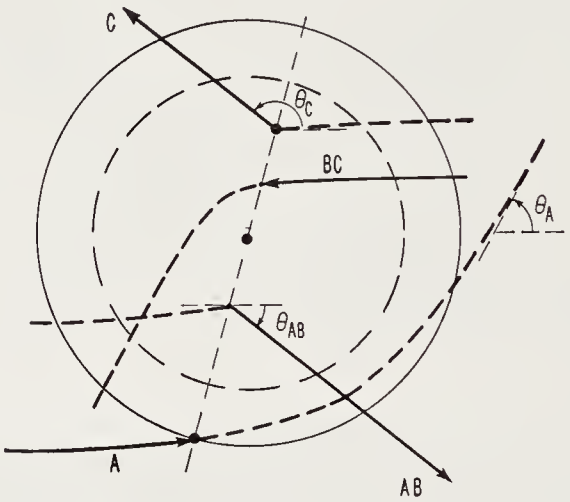

Fig. 19. Primitive optical potential model for a *stripping* reaction, illustrating the forward scattering of AB produced by reaction at impact parameters in the attractive zone (region outside the dashed sphere which represents the repulsive core considered in Figs. 17 and 18).

The proper interpretation of the approximate constancy observed in the sum of elastic and reactive scattering (property *5*) is not clear, especially since this property has not yet been examined in the Monte Carlo studies. The optical potential model does not necessarily lead to this result. However, if the scattering functions $\theta(b,E)$ and $\theta'(b,E)$ are not very different in form, or if the differences are blurred out by averaging over the velocity distributions, Eqs. (6) imply that the sum of elastic and reactive scattering should be approximately described by a common factor, $I(\theta) = d(\pi b^2)/d\omega$, which is independent of the $P(b,E)$ function.

In this case the total scattering in the LAB system would often resemble closely that for similar nonreactive molecules, as is observed, since often the velocity-averaged kinematic transformations (CM → LAB) are approximately the same for the elastic and reactive scattering.

Other Properties. Both the facts that the shape of the MX angular distribution (property *6*) is much more sensitive[38,42] to the identity of the reactant molecule XY than to the alkali atom M and that the velocity distribution (property *7*) is insensitive to changes in the initial collision energy[41,44,47] suggest that these properties are largely determined by the forces which govern the "pulling apart" of the XY molecule. (A specific mechanism for this correlation is discussed in Section II.) As yet, these properties have only been established for a few of the most exothermic stripping reactions (and they may not prove to hold elsewhere). For these reactions the M + XY interaction must be very strong and of long range (as indicated by properties *1–4*). Thus a *saturation effect* is to be expected: changes in the range and form of the $P(b,E)$ function due to changing the identity of M or the initial relative kinetic energy E will be "washed out" by the powerful acceleration between M and XY and consequently will have little effect on the distribution in angle and velocity of the products.

As discussed already in Section E, the partitioning of angular momentum between orbital and rotational motion in the products (property *8*) is also determined by the forces which govern the breakup of the collision complex.

II. CHEMICAL FORCES IN CHARGE-TRANSFER REACTIONS

The traditional physics professor is supposed to point to chemistry as a monumental demonstration of what can be done with electrons, a few nuclei, and Coulomb's law. He might even be surprised at how much fun can be had in exploring the simplest consequences of "the one-electron problem" in chemical dynamics. According to the electron jump model, the alkali reactions are, in effect, gas-phase acid–base or ion-recombination reactions, as

$$M + X{-}Y \rightarrow M^{+}{---}X^{-}{---}Y \rightarrow M^{+}X^{-} + Y \qquad (12)$$

Michael Polanyi suggested the picturesque term *harpooning* for this process: the attacking alkali atom tosses out its valence electron, hooks the halogen, and hauls it in with the Coulomb force. The basic features

of the mechanism have been developed in a nice theoretical study by Magee.[81,82] Since the contribution of this mechanism depends critically on the energy required to form the ion-pair, it is essential to know or guess the electron affinity of the acceptor molecule.

As the experimental information is very meager and unreliable,[98–100] we have adopted molecular orbital arguments developed by Mulliken and Person for the analysis of charge-transfer spectra.[101] This approach leads to a qualitative correlation between the reaction dynamics and the electronic spectra of the reactant molecule. It also brings out interesting implications of the model which depend intimately on the nature of the orbitals available to the harpooning electron.

A. The Harpooning Mechanism

The main points in Magee's discussion may be reviewed by reference to Figure 20, which gives the potential curves for the lowest few electronic states of an alkali halide molecule. In the ground state the molecule is essentially M^+X^- near its equilibrium bond distance and yet

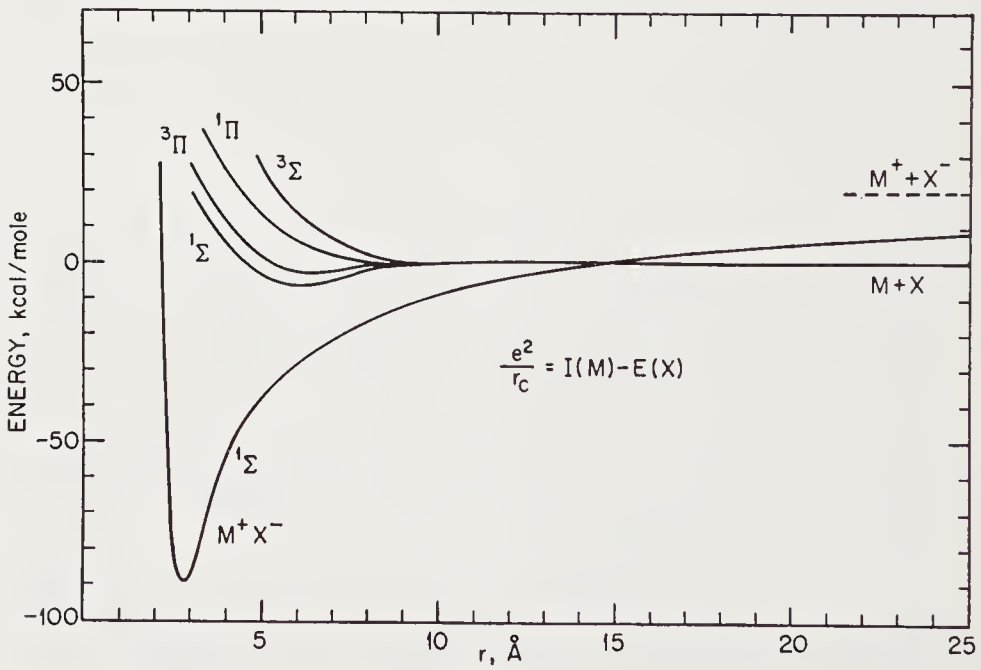

Fig. 20. Potential-energy curves for an alkali halide molecule (drawn for KBr) showing the "zeroth-order crossing" of the ionic and covalent states.

dissociates to form atoms. The zeroth-order potential curve for the "purely ionic" electron configuration therefore must cross that for the "purely covalent" configuration. As these configurations interact to some extent, they are mixed in a higher order of approximation. Hence the potential curves for the stationary states do not cross, but may approach very closely if the configuration mixing is weak.[102] The internuclear distance at the position of the zeroth-order crossing, r_c, is quite large ($\sim$ 15 Å for KBr) and since the Coulombic attraction is dominant there, r_c may be determined from the energy required to form the ion-pair,

$$e^2/r_c \simeq I(\mathrm{M}) - E(\mathrm{X}) \tag{13}$$

Here I(M) denotes the ionization potential of the alkali atom and E(X) the electron affinity of the halogen atom.

For the lowest stationary state, the electron distribution must undergo an abrupt change in the vicinity of r_c, from dominantly covalent outside to dominantly ionic inside. This corresponds to the jump of the electron from the alkali to the halogen atom. The Born-Oppenheimer approximation has been assumed, and accordingly the stationary states are eigenfunctions of the electronic Hamiltonian with the nuclei clamped in position. However, it should be noted (for later reference) that this approximation may fail if the crossing point occurs at a very large distance and the internuclear distance changes with appreciable velocity. The ionic–covalent configuration mixing will then be very weak and the electron will not have time to jump as the region of the crossing point is traversed. This is actually what occurs for the alkali halides.[103] The optical spectra corresponding to transitions from the ground to the lowest bundle of excited states are continuous rather than discrete as required by the Born-Oppenheimer approximation. The only exceptions are the molecules for which r_c is smallest (e.g., NaI, with $r_c \sim 7$ Å, and possibly LiI and LiBr); the spectra of these show some banded structure.

In an M + XY reaction the situation is essentially the same.[82] The potential surfaces for the M---X---Y and M^+---X^----Y electronic configurations must cross, and the electron jump can occur only in the close vicinity of the crossing. The nature of the crossing actually differs from that for the diatomic case, as here even the stationary-state potential surfaces can cross (except for the exactly collinear configuration, for which the "avoided intersection" situation still holds).[104] Also, the

MX distance at the crossing will vary with the position of the Y group, but again for configurations in which the Coulombic attraction is dominant,

$$e^2/r_c \simeq I(\mathrm{M}) - E^v(\mathrm{XY}) \tag{14}$$

where $E^v(\mathrm{XY})$ denotes the vertical electron affinity of the XY molecule (evaluated at the bond distance which obtains during the electron jump). In most cases, r_c for M + XY will be considerably smaller than for M + X, since very few XY molecules are expected to have electron affinity comparable to that of an X atom. Thus the Born-Oppenheimer approximation should usually hold, and most M + XY reactions are expected to take place on the lowest stationary-state potential energy surface. Of course, both Eqs. (13) and (14) become invalid if the calculated r_c is so small that Pauli repulsion forces or other interactions become comparable to the Coulomb attraction. In the case of M + XY reactions for which r_c does become large enough to inhibit the electron jump, Eq. (14) again must be amended; here the successful electron jumps will tend to become appreciably nonvertical and the vertical electron affinity should be replaced by one averaged over the appropriate portion of the potential curve for the XY^- ion.

Figure 21 gives an idea of the strength of the "harpoon potential" for interaction of $M + X_2$ as compared with an ordinary long-range van der Waals potential. We have chosen the convenient functional form

$$V_H(r) = V_I(r) \sin^2 \omega + V_C(r) \cos^2 \omega \tag{15}$$

where the mixing parameter ω describes the switchover from the covalent intersection (at $r > r_c$, $\omega \to 0°$) to the ionic interaction (at $r < r_c$, $\omega \to 90°$) and

$$V_C(r) = -C/r^6$$

$$V_I(r) = \Delta - e^2/r - \tfrac{1}{2}e^2(\alpha_1 + \alpha_2)/r^4 - 2e^2\alpha_1\alpha_2/r^7$$

$$\omega = (\pi/4)\,[1 - \tanh \gamma(r - r_c)]$$

At the large distances considered here, V_C is just the usual dispersion force term (with $C \simeq 5330$ kcal/mole Å^6 calculated from the Slater-Kirkwood approximation[105]). For V_I the Rittner potential[106] for a pair of polarizable ions is used. The parameter $\Delta = e^2/r_c$ is the energy required to form the ion-pair, as in Eq. (14), and the parameter γ

prescribes the abruptness of the switchover; for this example we have arbitrarily taken $\Delta = 50$ kcal/mole and $\gamma = 1$ Å^{-1}. The comparison potential (dashed curve) is an Exp-6 ($\alpha = 12$) function; the parameters are taken from scattering data for the K + HBr system.[12]

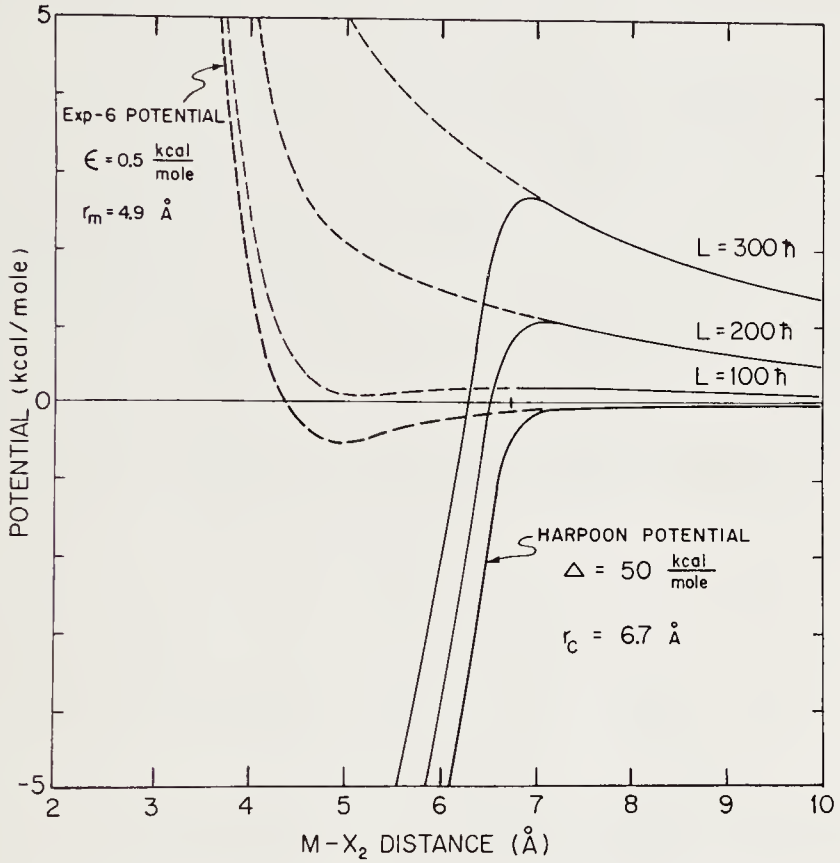

Fig. 21. Comparison of the effective potential energy curves (including the centrifugal repulsion term) for collision of K + Br_2 subject to ordinary van der Waals forces (dashed curves) or to the harpoon potential (solid curves).

Figure 21 also shows several of the effective potential curves which include the centrifugal repulsion term, $L^2/2\mu r^2$. These curves indicate the special role played by the centrifugal barrier for a screened Coulomb potential. For ordinary intermolecular potentials, qualitatively similar to the Exp-6 function, the position of the centrifugal barrier varies rapidly with the orbital angular momentum. Above a particular value ($L \simeq 125\ \hbar$ for this example) the centrifugal repulsion energy overcomes the attractive interaction and the effective potential curve becomes

monotonic. In contrast, when the attraction is Coulombic, the more slowly varying centrifugal term can never introduce a maximum. Thus for a screened Coulomb potential the centrifugal barrier is always confined to the switchover region. The location of the barrier is only weakly dependent on the angular momentum and its shape is largely determined by the width and form of the switchover function. Also, the effective potential curves for the harpoon potential cannot become monotonic until the centrifugal energy at r_c becomes of the order $\frac{1}{2}\Delta$ (or $L \sim 800\ \hbar$ for our example).

In reactions for which r_c is large enough to make Eq. (14) a fair approximation, just before the electron jump the X_2 molecule is nearly unaware of the presence of the M atom. Thus the arrival of the harpooning electron produces a Franck-Condon transition between the potential curves for the isolated X_2 and X_2^- molecules, as indicated in Figure 22. The X_2^- curve of course only defines the initial stage in the formation of the final products; as M^+ approaches, X_2^- is severely distorted by the strong electric field and dissociates. In the case pictured in Figure 22 the X_2^- ion is formed in a highly excited vibrational state, barely

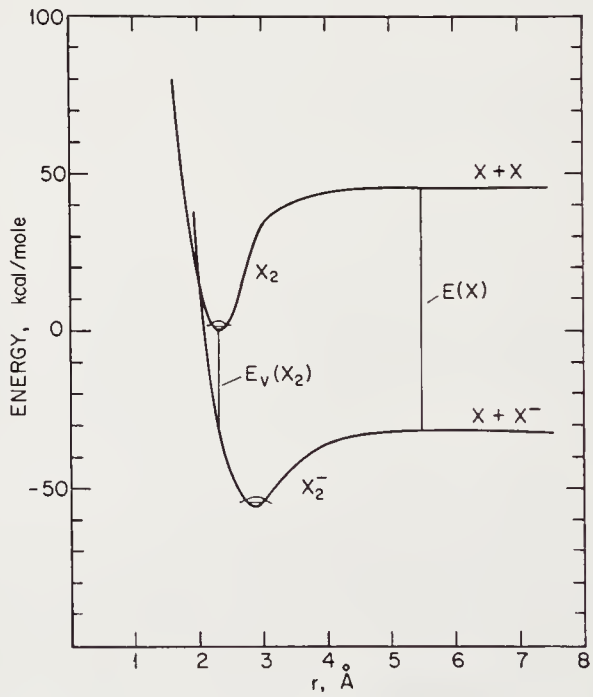

Fig. 22. Potential-energy curves for the ground electronic states of a diatomic halogen molecule and its negative ion (drawn for Br_2).

below the dissociation limit. Such an ion will readily break up in the electric field, which will exceed 3×10^9 V/cm when M^+ approaches within 7 Å. External fields of the order of 10^6 V/cm have been shown to produce efficient dissociation of free, vibrationally excited H_2^+ ions.[107,108]

The lag between the arrival of the harpooning electron and that of M^+ can be appreciable. For example, K^+ and Br_2^- ions starting 7 Å apart at rest and with no orbital angular momentum require $\sim 10^{-13}$ sec to reach 3 Å, the vicinity of the K^+Br^- equilibrium bond distance. The lag is only slightly shortened by the addition of initial thermal velocity, and with orbital angular momentum it becomes longer; for example, $\sim 2 \times 10^{-13}$ sec for $L \sim 200\ \hbar$. For the case of Figure 22, the time required for the breakup of X_2^- is less than the vibrational period, or $\gtrsim 10^{-13}$ sec. Thus, when the M^+ ion is delayed by centrifugal repulsion, it may find that only the X^- ion is at the scene as the X atom has already departed.

It should be emphasized that the harpooning mechanism has many variations. Although the main features are determined essentially just by the vertical electron affinity, many details of the reaction dynamics will differ with the shape and particularly the location of the asymptote of the potential curve for the negative molecule ion. (Some of the possibilities are classified in Figure 28.) In many reactions the negative ion will be formed in a purely repulsive state, or above the dissociation asymptote of an attractive state; in others it may appear in a low vibrational level of a state that would be stable if the electric field were not present. Thus the case of Figure 22 is quite special, although hopefully it is qualitatively correct for the diatomic halogen systems. The rough approximations[101] used to estimate the curve for X_2^- will be discussed later.

Also, it should be noted again that for large r_c the electronic transition is not vertical. This occurs with respect to the M—X_2 distance because the nuclei have some time to move while the electron makes its long-distance hop. It occurs also with respect to the X—X distance because the jump will incline to favor smaller electron affinity and thereby decrease r_c (see Fig. 24).

The harpooning model obviously offers ready qualitative explanations[39,42,47,89] for the main features of the reaction dynamics: the high level of product internal excitation arises because the potential surface is extremely attractive within the crossing radius; the impulsive interaction

mechanism is a Franck-Condon transition from a reactant to a product trajectory; the correlations associated with the transition between the rebound and stripping limits simply reflect the range over which the Coulombic attraction operates, as determined from Eq. (14). Here we shall only comment briefly on a few aspects of experimental tests of the harpooning mechanism.

Total Reaction Cross Section. There seems to be no other mechanism which can account for the very large cross sections found in the flame studies[78] of the $Na + X_2$ system ($\sigma_r \sim 50$–75 Å^2) and the beam studies[28,42] of the K, Rb, Cs + X_2 systems ($\sigma_r \sim 200$–250 Å^2). As seen in Figure 21, the centrifugal barrier remains very close to the crossing point, so that for harpooning σ_r is approximately given by πr_c^2 and should be nearly independent of energy. Figure 23 shows the dependence

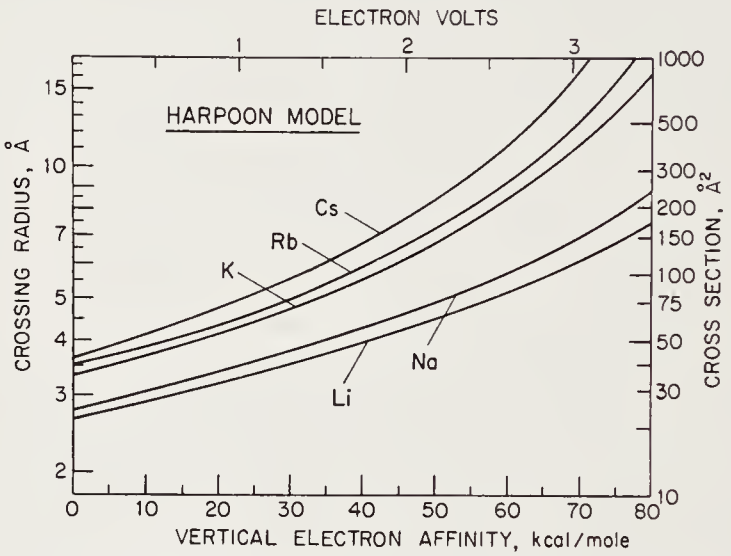

Fig. 23. Variation of the crossing radius, r_c, and the reaction cross section, $\sigma_r \simeq \pi r_c^2$, with the vertical electron affinity of the electron acceptor according to the harpoon model.

on the vertical electron affinity, according to Eq. (14). The model appears to be compatible with both the flame and the beam results, although the value indicated for the vertical electron affinity (~ 50 kcal/mole) is considerably higher than the estimates[101] to be discussed later. The systematic error in σ_r for both sets of experiments could easily be larger than the traditional factor of 2; it would be very desirable to have beam results on $Na + X_2$ for comparison. Also, the increase

in σ_r predicted on going from K to Cs (for fixed X_2) is not apparent in the present beam data. Possibly, this might arise from the saturation effect which is expected to appear in σ_r when r_c becomes large enough to inhibit the electron jump; the spectra of the alkali halides[103] suggests that this is likely to occur in the vicinity of $r_c \sim 7$ Å.

Energy Disposal. The Monte Carlo calculations show that high internal excitation in the products is evidence only for an early downhill potential and harpooning need not be invoked. Nonetheless, harpooning is very likely the chemical basis. An excellent detailed discussion has been given recently by J. C. Polanyi.[89] He was particularly concerned to show that the repulsion which appears between X^- and Y in Eq. (12) just after the electron jump need not show up in translational acceleration of the Y group with respect to M^+X^-. He pointed out that because of the Coulombic attraction between M^+ and X^- the momentum imparted to X^- in repulsion from Y will induce a momentum of opposite sign in M^+ and thus enhance the vibrational excitation rather than translational recoil. Computer studies have borne this out.[109] It may be noted that his discussion does not refer to the situation indicated in Figure 22 but to the case of a monotonic repulsive XY^- potential curve which is everywhere above the dissociation asymptote (labeled as case I^+C in Fig. 28). As we have seen for the Figure 22 case, the initial repulsion between X^- and Y will be relaxed very quickly and often their interaction will be attractive (or perhaps nil) by the time M^+ arrives.

Figure 24 gives an example of a potential energy surface derived from the harpoon model. The construction of this surface is described elsewhere[49]; it is similar to the procedure used in the first Monte Carlo calculations[14,32] except that terms involving the ions were brought in as in Eq. (15). The essential aspect of an early downhill surface which traps a large fraction of the exothermicity as vibrational excitation is that the attraction in the bond being formed is maintained until any appreciable repulsion between the products is dissipated.[89,109] As expected, the surface of Figure 24 nicely exemplifies this.

The surface also illustrates a rather peculiar feature of harpooning which may permit a specific experimental test of the mechanism. As shown by the dashed curve, the nominal jumping radius r_c varies quite rapidly with the Br—Br distance. As before, r_c was evaluated from Eq. (14), now using at each Br—Br distance (denoted by r') the value of the vertical electron affinity obtained from the difference of the Br_2 and Br_2^- potential curves in Figure 22. The affinity varies from near

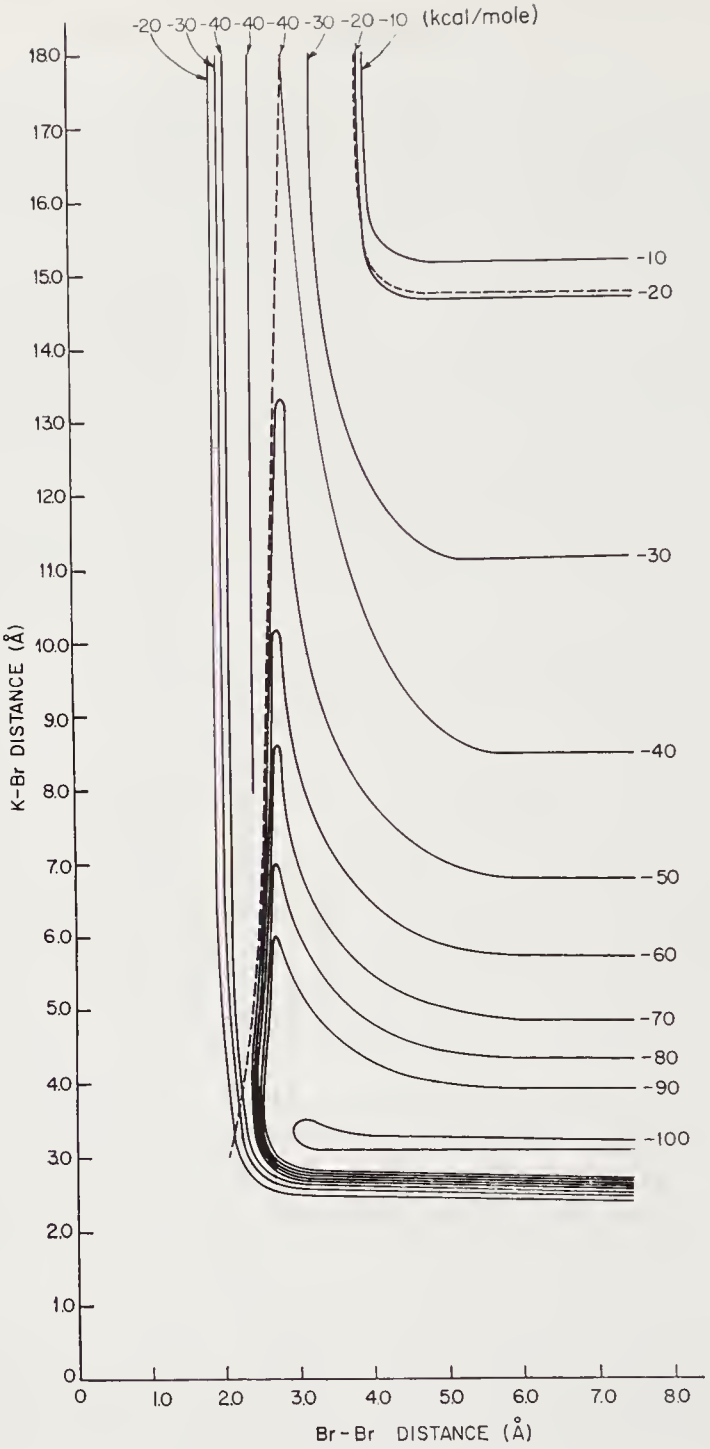

Fig. 24. Potential-energy surface for linear configurations of the K–Br–Br system, as derived from the harpoon model and the molecular potential curves of Figures 20 and 22. The solid curves are contours of constant energy; the energy zero corresponds to infinite separation of the three atoms. The dashed curve shows the variation of the crossing radius r_c with the Br—Br distance.

zero at $r' = 2$ Å to 25 kcal/mole at the equilibrium bond distance $r' = 2.28$ Å for Br_2 and reaches a maximum of 89 kcal/mole at $r' = 3.1$ Å. Thus if energy were supplied to prestretch the Br—Br bond, electron jumps would become possible at considerably larger values of r_c than that corresponding to the equilibrium Br_2 bond distance. Again, if r_c becomes too large, breakdown of the Born-Oppenheimer approximation would inhibit the jumps and make them nonvertical. If the cross sections for $M + X_2$ and other stripping reactions are indeed near the upper limit allowed by the Born-Oppenheimer breakdown, these may not be sensitive to initial vibrational excitation of the reactant molecule. However, if harpooning is also important for rebound and intermediate reactions these would be expected to be sensitive to initial vibrational excitation.

Angular Distributions. The evidence for orbiting[38,42,43] in the wide-angle elastic scattering of M from X_2 and other stripping reactions and the lack of rainbow structure[4,28,43] indicate that attenuation by reaction must be very strong up to distances of at least 6–7 Å. Even the very small angle elastic scattering[30] shows appreciable deviations from the pattern for comparable nonreactive molecules which indicate some deviation from the usual r^{-6} van der Waals force at distances up to ~ 15 Å. Again, it seems necessary to invoke ionic interactions to account for these observations. A particularly inviting prospect for further elastic scattering studies is apparent from Figure 21. Measurement of the velocity dependence of the scattering at collision energies well above those for which ordinary van der Waals orbiting is possible should show whether the centrifugal barrier persists in the vicinity of r_c and might give some information about the form of the switchover function. Some data of this kind is already available,[28,43] but it has not yet been analyzed in terms of the harpoon potential.

The observation[38,42] that for several stripping reactions the shape of the angular distribution of reactively scattered MX is much more sensitive to the identity of XY than to M fits in nicely with the harpooning picture. This would be expected to occur whenever r_c is large and the XY^- ion breaks up readily. The initial state of the XY^- ion and its resistance to decomposition may be quite different even for similar molecules, since they depend on the potential curves, whereas if r_c is large the shift in r_c due to changing the identity of M has little effect except to alter somewhat the electric field acting on XY^- as it breaks up.

Basis for Spectator Model. In nuclear stripping reactions [110,111] of the

type A + BC → AB + C, the characteristic feature is that the incident particle A interacts impulsively with only part B of the target. The products separate before there is time to transfer any momentum to the rest of the target, so that C just plays the role of a spectator. In this situation, once the interaction sets in, A + B and C behave as separate dynamical systems. Thus the final momentum carried by the product AB is given by the momentum of the center of mass of A + B just before the collision, or

$$m_{AB}\mathbf{C}_{AB} = m_A\mathbf{v}_A + m_B\mathbf{C}_{BC} + \mu_{BC}(\mathbf{v}_B - \mathbf{v}_C) \tag{16}$$

The second term is the momentum B acquires from motion of the center of mass of BC. The third is the internal momentum of B in vibrational and rotational motion relative to the center of mass of BC and $\mu_{BC} = m_B m_C/m_{BC}$ is the reduced mass of BC. The recoil momentum of AB relative to the center of mass of the whole system is thus given by

$$m_{AB}(\mathbf{C}_{AB} - \mathbf{C}) = (m_A m_C/M)\,\mathbf{V} + \mu_{BC}(\mathbf{v}_B - \mathbf{v}_C) \tag{17}$$

where M is the total mass and $\mathbf{V} = \mathbf{v}_A - \mathbf{C}_{BC}$ is the initial relative velocity of approach of A to BC. From Eq. (17) we see that this model always makes the distribution of AB recoil vectors peak forward along **V**, as the internal momentum distribution is isotropic. If the initial conditions are well enough defined to make the spread in **V** negligible, the observed breadth and shape of the angle and velocity distributions of AB are simply determined by the internal momentum distribution within BC just before reaction.

There is evidence that at high kinetic energies (> 5 eV) some proton transfer ion–molecule reactions conform to the spectator model.[112] At these energies this is plausible since the time scale for the external interaction of A + BC is much shorter than that for communication of momentum within BC. At lower energies the same reactions appear to proceed mainly by a collision complex mechanism.

The spectator model is also at least qualitatively useful for alkali atom stripping reactions. In the Oak Ridge study of the Cs + Br_2 reaction,[28] it was found that the location of the peak of the CsBr angular distribution and the slight forward shift and narrowing observed with increase of the Cs velocity agreed nicely with the spectator model. In this comparison the internal momentum term of (16) and (17) was not included. However, it has since been found that with this term the spectator model gives fairly good agreement for most of the alkali atom stripping reac-

tions thus far studied.[40,41] In particular, a detailed comparison has been made with the results obtained in the velocity analysis experiments on the K + Br_2 reaction.[41,44] A plausible assumed form for the internal momentum distribution can account for the observed approximately Maxwellian shape of the KBr velocity distributions, the variation with angle, and the insensitivity to the K velocity. Thus the present evidence for spectator dynamics in alkali reactions is substantial, although not conclusive because of the kinematic limitations in analysis of the data.

The spectator model would seem to be out of the question for ordinary thermal reactions, as the times required for external and internal momentum transfers are too nearly comparable. The appearance of apparent spectator dynamics here may be understood as another aspect of the harpooning mechanism. Merely switching on the Coulomb interaction of M^+ and X^- does not establish spectator conditions; even if M^+ is too far away to interact appreciably with Y, the interaction of X^- with Y ordinarily cannot be neglected. Thus in general a momentum transfer term must be added to Eqs. (16) and (17). However, if r_c is large the breakup of the XY^- ion often will be practically complete while M^+ is still far away. This isolates Y and thereby fixes the momentum transfer. Essentially, Eqs. (16) and (17) can be used again but with the external terms fixed before the electron jump and the internal term fixed after the breakup of XY^-. In the case considered in Figure 22, the net momentum transfer is expected to be relatively small, since the initial repulsion between X^- and Y is largely compensated by subsequent attraction. In this case $E^v(XY) \simeq E(X) - D(XY)$ and the energy required to form $M^+ + XY^-$ is essentially the same as to form $M^+ + X^- + Y$. In the more likely cases where this does not hold, the momentum transfer is apt to be larger.

B. Correlation with Electronic Structure

The analogy between the electron jump mechanism for alkali reactions and the theory of charge-transfer spectra is very close. The jumping condition of Eq. (14) corresponds to the workhorse approximation[113–115] for the frequency of the charge-transfer band,

$$h\nu_{CT} = I_D^v - E_A^v + \Delta G + \Delta X \tag{18}$$

where I_D^v is the vertical ionization potential of the free donor molecule, E_A^v is the vertical electron affinity of the accepter and ΔG and ΔX account for other interactions which influence the formation of the

charge-transfer complex. The transition between the ionic and covalent states of MX shown in Figure 20 is a primitive example of a charge-transfer transition.[115,116] Thus, many aspects of the extensive valence theory of charge-transfer complexes are of interest in exploring the chemical implications of the harpooning mechanism. Here we shall only consider what can be inferred about the X_2^- ions and a few others by applying simple molecular orbital arguments, coupled with spectroscopic and electron impact data where possible.

Diatomic Halogens. Complexes with I_2 are among the most thoroughly studied charge-transfer systems.[101,114] Several methods of analysis based on Eq. (18) have been used to deduce values of $E^v(I_2)$ from the spectra of various complexes. The results are in the range $E^v(I_2) \sim 15$–45 kcal/mole. These charge-transfer analyses have been discussed fully by Person.[101] He has also offered semiempirical estimates of some of the I_2^- potential curves and we shall briefly review this part of his paper.

In molecular orbital theory the electronic configuration of the ground state of I_2^- is given by

$$\ldots \sigma_g^2 \pi_u^4 \pi_g^4 \sigma_u \tag{19}$$

Only the orbitals made from the valence shell p orbitals of the atoms are shown. The σ_g (bonding) and σ_u (antibonding) orbitals are formed by constructive and destructive overlap of the atomic p_z orbitals; the π_u and π_g orbitals from overlap of the atomic p_x and p_y orbitals. The configuration (19) differs from I_2 only in the additional electron in the strongly antibonding σ_u orbital. In I_2 the π_u orbital is considered to be somewhat bonding, the π_g orbital somewhat antibonding.[117] Since both are filled, their net effect is probably nearly nonbonding, so that in I_2^- the bonding effect of the two σ_g electrons is partially cancelled by the one σ_u electron. Therefore we can expect that the ground state of I_2^- will be stable[82,117] and, as a first approximation, the dissociation energy will be about one-half that for I_2, or $D(I_2^-) \sim 18$ kcal/mole.

Various semiempirical rules and analogies[101,117] can be used to estimate the equilibrium bond length and vibrational frequency for I_2^-. For example, $r_e(I_2^-)$ must be between 4.3 Å (the sum of the van der Waals radii for two I atoms) and 2.67 Å (r_e for I_2). A literal interpretation of the "half-bond" expected for I_2^- would suggest a value halfway between these, or $r_e(I_2^-) \sim 3.5$ Å; other estimates indicate a somewhat smaller value.[117] For the symmetrical I_3^- ion the experimental result is 2.90 Å and this should be a lower limit for the bond length in I_2^-.

The most useful and convincing way[101] to estimate the properties of I_2^- is to appeal to the known properties of a suitable excited electronic state of I_2. The $^3\Pi_{0^+_u}$ excited state of I_2 has the configuration

$$\ldots \sigma_g{}^2 \pi_u{}^4 \pi_g{}^3 \sigma_u \tag{20}$$

which differs from that for the ground state of I_2^- only in that one of the weakly antibonding π_g electrons is missing. If the antibonding character of this orbital is weak enough, the properties of I_2^- would be expected to be very similar to those found for I_2 in the $^3\Pi_{0^+_u}$ state, namely: bond length, $r_e = 3.02$ Å; vibrational frequency, $\omega_e = 128$ cm^{-1}; bond strength, $D = 12$ kcal/mole.

From such considerations Person derived a rough estimate of the potential curve for the ground $^2\Sigma_u^+$ state of I_2^-. This is shown in Figure 25 along with curves for several excited states. The position of the asymptote for dissociation to $I + I^-$ relative to the asymptote for $I + I$ is accurately known from the electron affinity of the I atom, $E(I) = 70.6$ kcal/mole.[118] Person constructed the rest of the $^2\Sigma_u^+$ potential curve

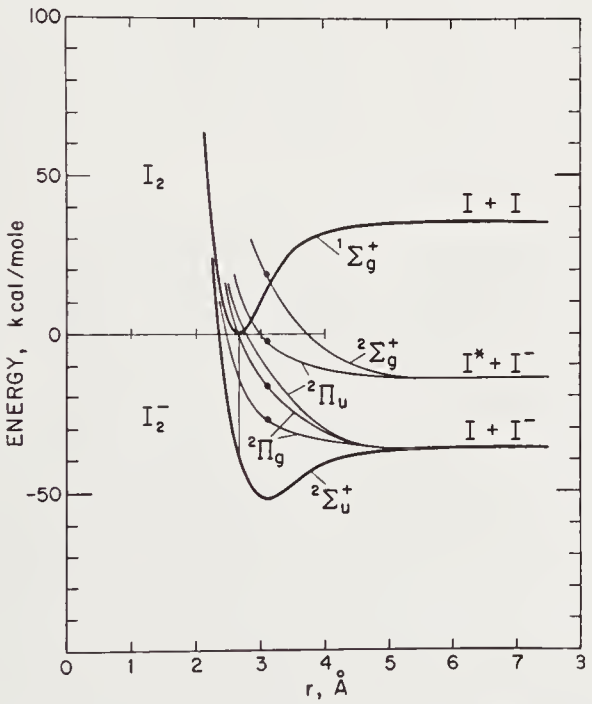

Fig. 25. Potential-energy curves for the ground electronic state of I_2 and several of the lowest group of electronic states of I_2^-.

by fitting a Morse function to this asymptote and his estimates of the parameters characterizing the minimum. The curve for Br_2^- shown in Figure 22 was estimated in the same way. Comparison of the X_2^- curve with that for X_2 gives the electron affinity as a function of the X—X distance. The value obtained for the vertical affinity is 37 kcal/mole for I_2 and 25 kcal/mole for Br_2. These estimates must be assigned an uncertainty of at least $\pm$ 10 kcal/mole because of the uncertainty in the X_2^- parameters and the use of the Morse function.

The curves for the excited states of I_2^- are repulsive since these states all involve electronic configurations with two electrons in the antibonding σ_u orbital. Figure 26 indicates the correlation of these states with

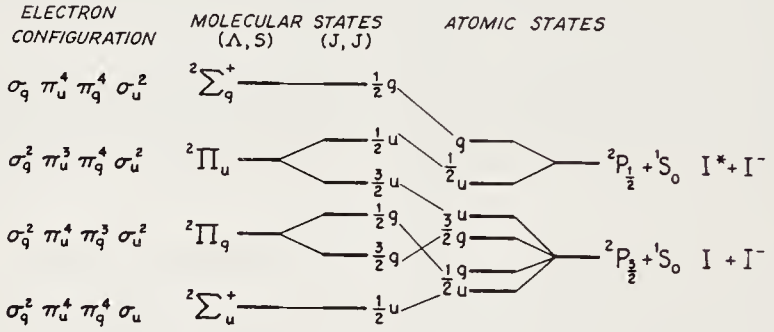

Fig. 26. Correlation of electronic states of the I_2^- ion and its dissociation products.

the two possible dissociation asymptotes ($I + I^-$ and $I^* + I^-$, the latter corresponding to excitation of the atom to the metastable $^2P_{1/2}$ state). The correlations are readily established by matching the *u,g* character and the value of the component of the total electronic angular momentum along the internuclear axis for the various possible atomic and molecular states.[119] The location of the excited-state potential curves above the minimum for the ground state has been derived from a study of certain color centers in doped alkali halide crystals.[120] The paramagnetic resonance spectra and the relative intensity and polarization behavior of the various absorptions observed in the optical spectra of these centers show exactly the properties expected for X_2^- ions. Thus this study gives the vertical energy differences between the curves for several of the excited electronic states and the potential minimum for the ground state. Flash photolysis of aqueous and ethanolic solutions of alkali halides

also gives rise to spectra that have been assigned to the X_2^- ions.[121] The results are summarized in Figure 27 and the positions of the states above the minimum are indicated by the dots placed on the curves of Figure 25.

The results of electron impact experiments on the halogens[122,123] have sometimes been regarded as indicating very small (or even somewhat negative) values for the vertical electron affinity. However, these experiments actually only show that the potential curve for some state of X_2^- must cross that of the ground state of the parent molecule near

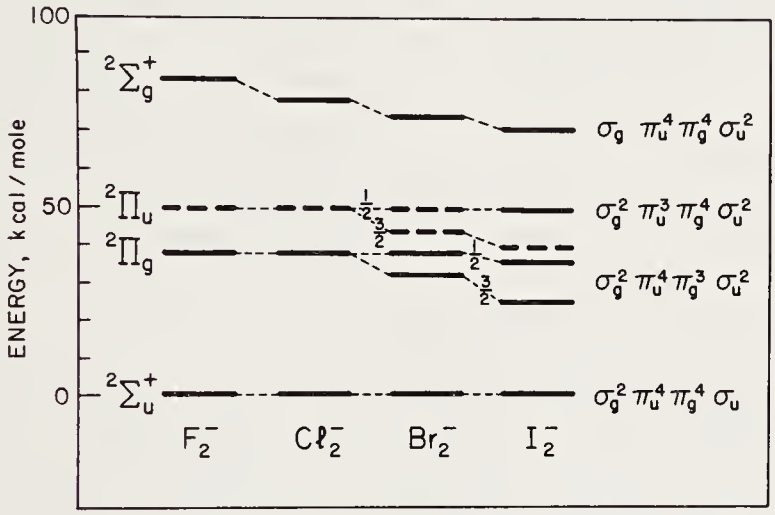

Fig. 27. Location of excited electronic states of the diatomic halogen molecule ions, as derived from spectra of color centers in alkali halide crystals. Transitions involving the levels shown by dashed lines have not been observed.

the minimum in the X_2 curve. There are several candidates for such a state among the excited electronic states of X_2^-, as seen in Figure 25 (although the uncertainty in the location of the curves is much too large to permit a definite assignment to be made). In the experiments, X_2^- ions are not found; the only low-energy process observed is dissociative electron capture to form $X + X^-$ (or possibly $X^* + X^-$). This is just what would be expected from Figure 25, since a stable X_2^- ion cannot be formed without some way of disposing of the considerable energy released in the electron capture (equal to the vertical electron affinity). The formation of stable negative molecule ions by direct electron capture is rare and appears to occur only for polyatomic

molecules large enough that the exothermicity can be taken up in vibrational excitation.[99,124] Observation of stable X_2^- ions formed in fragmentation of larger molecules has been reported.[125]

Despite the lack of a direct determination and the wide latitude in quantitative estimates, all the present evidence is compatible with the large values of $E^v(X_2)$ required by the harpooning mechanism for the $M + X_2$ reactions. It is also interesting to note what Figure 25 suggests concerning the possible role of the excited electronic states of X_2^- in these reactions. These states may not contribute at all. For all of them the jumping radius is well within that for the ground state, since $E^v(X_2)$ is much smaller. Thus if the reaction always occurs at the outermost radius r_c, the intermediate X_2^- ion will never be formed in an excited electronic state. In Figure 25 it is apparent that the states which could yield an excited I* atom are particularly unfavored and this may be why no sign of I* is found in these reactions. The best opportunity for participation of excited electronic states will occur when r_c for the ground state is so large as to inhibit the electron jump.[82] Accordingly, electronic excitation is more likely to be found for reactions of Cs atoms than for Na atoms (see Fig. 23).

It is conceivable that the probability of reaction by harpooning may depend on the orientation of the molecule in a way characteristic of the symmetry of the electronic state of the negative molecule ion. Recently, Dunn has given general arguments, based on group theory, which show that in many cases the probability of electron capture processes should exhibit a strong dependence on the relative orientation of the axis of the molecule and the incident electron beam.[126,127] His selection rules, if blithely carried over to harpooning reactions, predict that for parallel alignment of the parent X_2 molecule in its Σ_g^+ ground state the X_2^- ion can only be produced in the Σ_u^+ or Σ_g^+ states, and for perpendicular alignment only in the Π_u or Σ_g^+ states. For oblique alignments, all the states can be formed.

Other Molecules. The electronic structure of the negative XY^- ion formed in harpooning can be discussed in much the same way for many of the other reactant molecules in Table I. For most of these a detailed analysis of the molecular orbitals and the electronic spectrum of the parent molecule may be found in a very useful paper by Walsh.[128] As examples we will consider here only a few of the simplest cases, including methyl iodide, the hydrogen halides, and nitrogen dioxide. A convenient qualitative classification of the types of XY^- potential curves which may

occur is given in Figure 28. The category I or II is decided by the relative magnitude of the bond strength $D(XY)$ of the parent molecule and the affinity $E(X)$ of the atom which eventually acquires the electron. In both cases A and B, the free XY^- ion is stable, but for B as well as the unstable case C the vertical transition leads to immediate dissociation. As we have seen, the ground states of the X_2^- ions may belong to either case I^+A or I^+B.

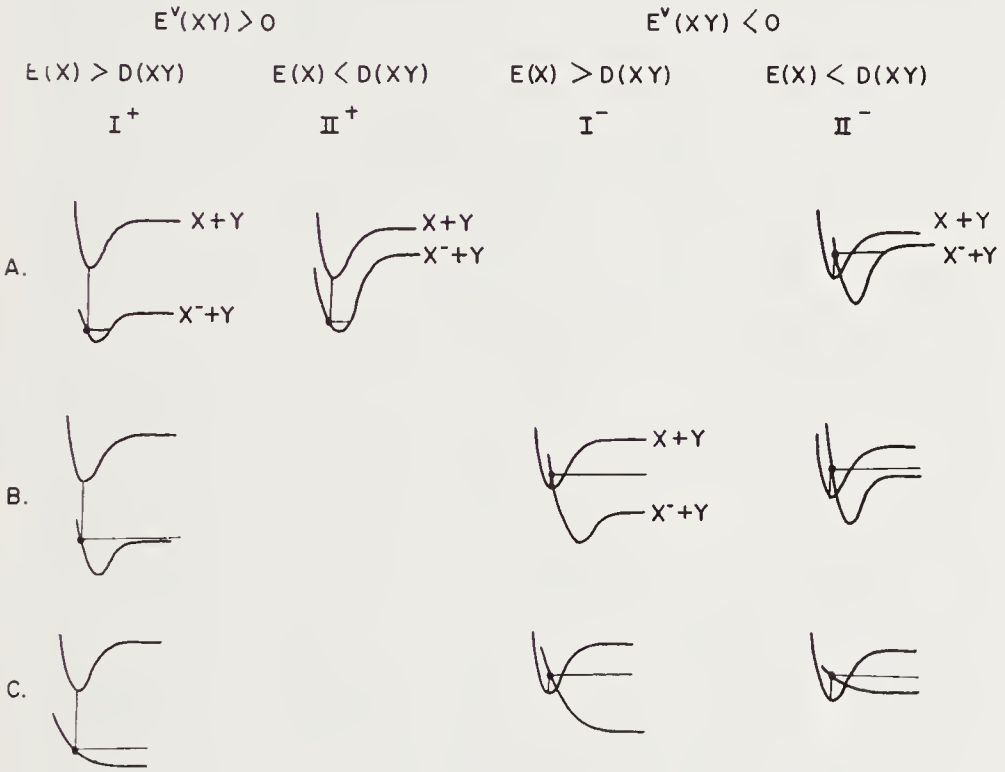

Fig. 28. Classification of electron impact processes producing negative molecule ions ($XY + e \rightarrow XY^-$).

For methyl iodide the complete molecular orbital description[128] is complicated but the features relevant here are closely analogous[129] to the diatomic halogen case. In the united atom approximation the CH_3 group shrinks into an F atom. Thus in diatomic notation the upper occupied orbitals in CH_3I^- may be denoted by $\ldots \pi^4\bar{\sigma}$, as in Eq. (19). Here the π orbital essentially consists of the $5p_x$ and $5p_y$ orbitals of the I atom and is approximately nonbonding,[129] whereas the $\bar{\sigma}$ orbital is

strongly antibonding. In the spectrum of CH_3I the transition to the excited electronic state corresponding to the configuration $\ldots \pi^3\bar{\sigma}^2$, analogous to Eq. (20), is well known.[128–130] In contrast to the X_2 case, this state is repulsive and leads to photodissociation of the molecule. The location and shape of this repulsive curve as derived from the absorption spectrum and the parameters $D(CH_3—I) = 55$ kcal/mole, $E(I) = 70.6$ kcal/mole require that the ground state of CH_3I^- be assigned to case I^-C of Figure 28. The value indicated[48] for the vertical electron affinity is $E^v(CH_3I) \simeq -20 \pm 20$ kcal/mole. Although this estimate is very rough, the qualitative result seems quite certain. It offers a very plausible explanation of why the $M + CH_3I$ reactions proceed by a rebound mechanism rather than by stripping.

For the hydrogen halides the topmost occupied orbitals and electronic spectra are somewhat similar to those for CH_3I. The rough arguments again give plausible results but here they are not needed, as the potential curves for the HX^- ions can be derived from a recent electron impact study.[131] In this case the observed electron capture must give the ground state of HX^- rather than an excited electronic state, as only the ground state correlates with $H + X^-$. All of these molecules belong to case II^-C of Figure 28. The HX^- curves are evidently rather flat near the minimum in the HX potential and $E^v(HX) \simeq E(X) - D(HX)$ with $E^v(HX) \sim -18$, -8, and 0 kcal/mole for HCl, HBr, and HI. Thus it is clear that in the $M + HX$ reactions a harpooning reaction could not occur except at distances well within the van der Waals radius, in agreement with the evidence from the elastic scattering studies.[43]

Nitrogen dioxide offers an intriguing example for study of the harpooning mechanism.[45] There is abundant spectral evidence to confirm the close analogy between the electronic structure of the NO_2^- ion and the O_3 molecule,[128,132] and the NO_2^- ion is well known in mass spectroscopy. Thus this ion is very stable and belongs to case II^+A of Figure 28. Although the electron affinity of the NO_2 molecule must be very high, no reliable measurements are yet available.[98–100] However, a rigorous lower limit is set by the observation that the charge exchange reaction

$$NO_2 + Cl^- \rightarrow NO_2^- + Cl$$

occurs at very low energies.[133] This requires that $E^v(NO_2) > E(Cl) = 83$ kcal/mole, and therefore in electron capture NO_2 acts as if it were a

"super-halogen atom." Consequently in the $M + NO_2$ reactions, the crossing radius will come at an extremely large distance ($r_c > 20$ Å for $K + NO_2$), larger even than that for an alkali halide molecule (see Fig. 20). The electron jump thus cannot take place to form the ground state of NO_2^-, except perhaps in the Na or Li reactions ($r_c > 8$ Å for Na). If the reactions observed[45] for K, Rb, and Cs proceed by harpooning, they must make use of an excited electronic state of NO_2^-. The lowest excited state is expected [128,132] to arise from raising one of the unshared electrons on the N atom to an antibonding $\bar{\pi}$ orbital of the ion ($n_N \rightarrow \bar{\pi}$). The results of the reactive scattering studies on NO_2 and related compounds are not yet complete, but can be reasonably interpreted on this basis.[45] The primary product is a polar, paramagnetic molecule, almost certainly the MO molecule. In the $Na + NO_2$ reaction, however, an additional diamagnetic contribution appears, which might be NaNO formed via the ground state of NO_2^-. For the analogous reactions of CH_3NO_2, the harpooning mechanism would be expected to use the ground state since the crossing radius would be pulled in (just as in the case of CH_3I compared to I_2), and indeed the experiments show only a diamagnetic product.

The harpooning mechanism is a charming model for reactions which can proceed via ion-pair intermediates and it appears to be qualitatively correct. Further studies of the detailed mechanics of chemical reactions will surely lead to broader correlations with electronic structure. The success enjoyed by the valence theory of charge-transfer complexes[113–115] for a broad spectrum of cases in which the electron transfer is only partial is an encouraging example. In fact, a striking correspondence has been found[134] in comparing electron absorption coefficients estimated from gas chromatography[135] with rate constants for the large class of "reactions with inertia" studied in the Polanyi sodium flame experiments. This extends over a factor of 10^4 in reactivity. Perhaps there is good prospect for replacing the harpoon with a needle.

Acknowledgments

The Berkeley and Harvard experiments listed in Table I extend over a very blissful period of five years. We have had no co-workers, but a working company: all of these experiments and much of the analysis presented here are due to G. H. Kwei, J. A. Norris, J. L. Kinsey, K. R. Wilson, R. R. Herm, J. H. Birely, E. A. Entemann, and M. C. Moulton. Support of the early work at Berkeley came primarily from the U. S. Atomic Energy Commission and that at Harvard from the National Science Foundation.

References

1. T. H. Bull and P. B. Moon, *Discussions Faraday Soc.*, **17**, 54 (1954). Cs + CCl_4; mechanically pulsed, accelerated beam, time-of-flight velocity analysis.
2. E. H. Taylor and S. Datz, *J. Chem. Phys*, **23**, 1711 (1955). K + HBr; differential surface ionization method.
3. S. Datz and E. H. Taylor, in *Recent Research in Molecular Beams*, I. Estermann, Ed., Academic Press, New York, 1959, p. 157. Review of chemical applications of beam techniques.
4. R. W. Roberts, "The Scattering of a Potassium Atomic Beam by a Crossed Beam of Bromine Molecules," Ph.D. thesis, Brown University, Providence, Rhode Island, 1959.
5. E. F. Greene, R. W. Roberts, and J. Ross, *J. Chem. Phys.*, **32**, 940 (1960). Energy dependence of yield in K + HBr reaction.
6. D. R. Herschbach, *J. Chem. Phys.*, **33**, 1870 (1960). Kinematic limitations on reactive scattering of K + HBr.
7. D. R. Herschbach, G. H. Kwei, and J. A. Norris, *J. Chem. Phys.*, **34**, 1842 (1961). K + CH_3I, K + C_2H_5I; anisotropy of recoil, internal excitation of products.
8. S. Datz, D. R. Herschbach, and E. H. Taylor, *J. Chem. Phys.*, **35**, 1549 (1961). Mechanics of crossed-beam reactions, analysis of K + HBr results.
9. H. Gienapp, *Z. Elektrochem.*, **65**, 417 (1961). K + Cl_2 and HI; influence of reactivity on total scattering cross section.
10. D. R. Herschbach, *Vortex*, **22**, 348 (1961). Review of reactive scattering experiments and analysis.
11. K. Kodera and T. Tamura, *Bull. Chem. Soc. Japan*, **34**, 566 (1961). Na + Cl_2; total scattering cross section unaffected by reaction.
12. D. Beck, *J. Chem. Phys.*, **37**, 2884 (1962). Velocity selected K + Ar and HBr; rainbow scattering.
13. D. Beck, E. F. Greene, and J. Ross, *J. Chem. Phys.*, **37**, 2895 (1962). Velocity selected K + HBr; reaction probability derived from optical potential analysis of elastic scattering.
14. N. C. Blais and D. L. Bunker, *J. Chem. Phys.*, **37**, 2713 (1962). Monte Carlo computer study of K + CH_3I reactive scattering.
15. D. R. Herschbach, *Discussions Faraday Soc.*, **33**, 149, 277, 278, 281 (1962). Restrictions imposed by conservation laws; review of reactive scattering of K, Rb, Cs with alkyl iodides.
16. J. Ross and E. F. Greene, *Proceedings of the Twelfth Solvay Conference* (1962); also, *Energy Transfer in Gases*, R. Stoops, Ed., Interscience, New York, 1964, p. 363. Review of studies of K + HBr, CH_3Br and CH_3I.
17. M. Ackerman, E. F. Greene, A. L. Moursund, and J. Ross, *Ninth International Symposium on Combustion*, Academic Press, Inc., New York, 1963. K + CH_3Br, optical potential analysis of elastic scattering.
18. N. C. Blais and D. L. Bunker, *J. Chem. Phys.*, **39**, 315 (1963). Monte Carlo computer study of A + BC reactions.
19. S. Datz and E. H. Taylor, *J. Chem. Phys.*, **39**, 1896 (1963). D + H_2; time-of-flight velocity analysis.

20. W. L. Fite and R. T. Brackmann, in *Atomic Collision Processes*, M. R. C. McDowell, Ed., North-Holland Pub. Co., Amsterdam, 1963, p. 955. $H + D_2$.
21. W. L. Fite and S. Datz, *Ann. Rev. Phys. Chem.*, **14**, 61 (1963). General review of chemical research with beams.
22. E. Gersing, E. Hundhausen, and H. Pauly, *Z. Physik*, **171**, 349 (1963). Evidence for reaction in $K + HgX_2$ and SnI_4 scattering.
23. D. R. Herschbach and G. H. Kwei, in *Atomic Collision Processes*, M. R. C. McDowell, Ed., North-Holland Pub. Co., Amsterdam, 1963, p. 972. Model calculation of elastic scattering of reactive molecules.
24. J. A. Norris, "Chemical Reactions in Crossed Molecular Beams," Ph.D. thesis, University of California, Berkeley, 1963. Also, *UCRL Report*, *10848*, Lawrence Radiation Laboratory, Berkeley, 1963.
25. M. Ackerman, E. F. Greene, A. L. Moursund, and J. Ross, *J. Chem. Phys.*, **41**, 1183 (1964). Velocity selected $K + HCl$ and HI; optical potential analysis of elastic scattering.
26. D. L. Bunker, *Sci. Am.*, **211**, 100 (1964). Review of Monte Carlo computer studies of reaction dynamics.
27. D. L. Bunker and N. C. Blais, *J. Chem. Phys.*, **41**, 2377 (1964). Monte Carlo calculations extended to three-dimensional collisions.
28. S. Datz and R. E. Minturn, *J. Chem. Phys.*, **41**, 1153 (1964). Velocity selected $Cs + Br_2$; stripping mechanism.
29. A. E. Grosser, A. R. Blythe, and R. B. Bernstein, *J. Chem. Phys.*, **42**, 1268 (1964). Velocity analysis of KBr from $K + HBr$.
30. R. Helbing and H. Pauly, *Z. Physik*, **179**, 16 (1964). Influence of reactivity on small-angle elastic scattering of $K + Br_2$ and several other halogen compounds.
31. R. R. Herm, R. Gordon, and D. R. Herschbach, *J. Chem. Phys.*, **41**, 2218 (1964). Magnetic deflection analysis of $K + CH_3I$, Br_2, and ICl scattering.
32. M. Karplus and L. Raff, *J. Chem. Phys.*, **41**, 1267 (1964). Monte Carlo method extended to three-dimensional collisions; study of $K + CH_3I$; correlation between size of reaction cross section and anisotropy of angular distribution.
33. M. Karplus, R. N. Porter, and R. D. Sharma, *J. Chem. Phys.*, **40**, 2033 (1964). Monte Carlo computer study of $D + H_2$ reactive scattering.
34. J. C. Light, *J. Chem. Phys.*, **40**, 3221 (1964). Statistical theory of reactions.
35. A. L. Moursund, "The Elastic and Reactive Scattering of K by HCl, CH_3Br, and HI in Crossed Molecular Beams," Ph.D. thesis, Brown University, Providence, Rhode Island, 1964.
36. R. J. Suplinskas, "Calculation of the Chemical Reaction Cross Section; $K + HBr$," Ph.D. thesis, Brown University, Providence, Rhode Island, 1964.
37. C. H. Williams, "The Dissociation of a Cesium Fluoride Molecule by Impact with a Fast Argon Atom," Ph.D. thesis, Brown University, Providence, Rhode Island, 1964.
38. K. R. Wilson, "Molecular Beam Studies of Chemical Dynamics," Ph.D. thesis, University of California, Berkeley, 1964. Also *UCRL Report*, *11605*, Lawrence Radiation Laboratory, Berkeley, 1964.
39. K. R. Wilson, G. H. Kwei, J. A. Norris, R. R. Herm, J. H. Birely, and D. R. Herschbach, *J. Chem. Phys.*, **41**, 1154 (1964). K, Rb, $Cs + Br_2$, I_2, ICl, and IBr; stripping mechanism.

40. J. H. Birely, "Product Excitation in Reactive Scattering," Ph.D. thesis, Harvard University, Cambridge, Mass., 1965.
41. J. H. Birely and D. R. Herschbach, *J. Chem. Phys.*, **43** (1965). Velocity analysis of KBr from K + Br_2.
42. J. H. Birely, R. R. Herm, K. R. Wilson, and D. R. Herschbach, *J. Chem. Phys.*, **43** (1965). K, Rb, Cs + Br_2 and I_2.
43. E. F. Greene, A. L. Moursund, and J. Ross, this volume, p. 135. Review of elastic scattering of reactive molecules and optical potential analysis.
44. A. E. Grosser and R. B. Bernstein, *J. Chem. Phys.*, **43**, 1140 (1965). Velocity analysis of KBr from K + Br_2.
45. R. R. Herm, "Electric and Magnetic Deflection Analysis of Reactive Scattering," Ph.D. thesis, Harvard University, Cambridge Mass., 1965. Also, *UCRL Reports 10526, 16039*, Lawrence Radiation Laboratory, Berkeley, 1962 and 1965.
46. R. R. Herm and D. R. Herschbach, *J. Chem. Phys.*, **43** (1965). Electric deflection analysis of K + Br_2 and Cs + HBr scattering; rotational excitation.
47. D. R. Herschbach, *Appl. Optics*, **Suppl. 2** (*Chemical Lasers*), 128 (1965). Review of alkali reactions, models for reaction dynamics.
48. J. L. Kinsey, G. H. Kwei, and D. R. Herschbach, *J. Chem. Phys.*, **43** (1965). Rb, Cs + alkyl iodides, optical potential model for rebound reactions.
49. G. H. Kwei, "Elastic and Reactive Scattering in Crossed Molecular Beams," Ph.D. thesis, University of California, Berkeley, 1965. Also, *UCRL Reports 11178, 11966*, Lawrence Radiation Laboratory, Berkeley, 1963 and 1965.
50. G. H. Kwei, J. A. Norris, and D. R. Herschbach, *J. Chem. Phys.*, **43** (1965). K + alkyl iodides; scattering kinematics.
51. P. Pechukas and J. C. Light, *J. Chem. Phys.*, **42**, 3281 (1965). Detailed balancing amendment to statistical theory.
52. P. Pechukas, J. C. Light, and C. Rankin, *J. Chem. Phys.*, **43** (1965). Statistical theory applied to atom exchange reactions.
53. R. G. J. Fraser, *Molecular Rays*, Cambridge University Press, Cambridge, 1931; *Molecular Beams*, Methuen, London, 1937.
54. N. F. Ramsey, *Molecular Beams*, Oxford University Press, Oxford, 1956.
55. P. Kusch and V. W. Hughes, in *Handbuch der Physik 37/1*, S. Flügge, Ed., Springer-Verlag, Heidelberg, 1959.
56. S. Datz and E. H. Taylor, *J. Chem. Phys.*, **25**, 389, 395 (1956).
57. K. R. Wilson and R. J. Ivanetich, *UCRL Repts. 10706, 11606*, Lawrence Radiation Laboratory, Berkeley, Cal., 1962 and 1965.
58. W. Schroen, *Z. Physik*, **176**, 237 (1963).
59. T. R. Touw and J. W. Trischka, *J. Appl. Phys.*, **34**, 3635 (1963).
60. Obtained from Linde Co., Crystal Products, 4120 Kennedy Ave., East Chicago, Indiana. A method of "growing" pure tungsten filaments has been described by E. F. Greene, *Rev. Sci. Instr.*, **32**, 860 (1961).
61. See, for example, R. B. Bernstein, *Science*, **144**, 141 (1964).
62. See, for example, J. P. Valleau and J. M. Deckers, *Can. J. Chem.*, **42**, 225 (1964).
63. E. Hundhausen and H. Pauly, Private communication (Bonn University, May, 1964).
64. R. A. Berg, L. Wharton, and W. Klemperer, *Bull. Am. Phys. Soc.*, **9**, 734 (1964);

A. Büchler, J. L. Stauffer, W. Klemperer, and L. Wharton, *J. Chem. Phys.*, **39** 2299 (1963).
65. E. A. Entemann, work in progress (Harvard University).
66. M. Karplus, private communication (Columbia University).
67. S. Datz and R. E. Minturn, private communication (Oak Ridge National Laboratory).
68. H. U. Hostettler and R. B. Bernstein, *Rev. Sci. Instr.*, **31**, 872 (1960).
69. H. G. Bennewitz, Dissertation, Physical Institute, Bonn, 1956.
70. S. M. Trujillo, P. K. Rol, and E. W. Rothe, *Rev. Sci. Instr.*, **33**, 841 (1962).
71. H. G. Bennewitz, K. H. Kramer, W. Paul, and J. P. Toennies, *Z. Physik*, **177**, 84 (1964).
72. K. H. Kramer and R. B. Bernstein, *J. Chem. Phys.*, **42**, 767 (1965).
73. J. P. Toennies, *Discussions Faraday Soc.*, **33**, 96 (1962); also in M. R. C. McDowell, Ed., *Atomic Collision Processes*, North-Holland Publishing Co., Amsterdam, 1963, p. 1113.
74. See, for example, J. C. Polanyi, *J. Quant. Spectr. Radiative Transfer*, **3**, 481 (1963); also, J. V. V. Kasper and G. C. Pimentel, *Phys. Rev. Letters*, **14**, 352 (1965).
75. M. C. Moulton, work in progress (Harvard University).
76. T. L. Cottrell, *The Strengths of Chemical Bonds*, Butterworths, London, 1958.
77. L. Brewer and E. Brackett, *Chem. Rev.*, **61**, 425 (1961).
78. M. Polanyi, *Atomic Reactions*, Williams and Norgate, London, 1932.
79. M. G. Evans and M. Polanyi, *Trans. Faraday Soc.*, **35**, 178 (1939).
80. M. Krocsak and G. Schay, *Z. Physik. Chem.* (*Leipzig*), **B19**, 344 (1932); E. Roth and G. Schay, *Ibid.*, **B28**, 323 (1935).
81. S. Glasstone, K. J. Laidler, and H. Eyring, *Theory of Rate Processes*, McGraw-Hill, New York, 1941.
82. J. L. Magee, *J. Chem. Phys.*, **8**, 687 (1940).
83. For reviews of subsequent alkali flame studies see C. E. H. Bawn, *Ann. Rept. Chem. Soc.*, **39**, 36 (1943) and E. Warhurst, *Quart. Rev. Chem. Soc.* (*London*), **5**, 44 (1951).
84. V. N. Kondratiev, *Chemical Kinetics of Gas Reactions*, Pergamon Press, London 1964, p. 87.
85. J. C. Polanyi, *J. Chem. Phys.*, **31**, 1338 (1959).
86. N. Basco and R. G. W. Norrish, *Can. J. Chem.*, **38**, 1769 (1960).
87. B. S. Rabinovitch and M. C. Flowers, *Quart. Rev. Chem. Soc.* (*London*), **18**, 122 (1964).
88. K. E. Shuler, T. Carrington, and J. C. Light, *Appl. Optics*, **Suppl. 2** (*Chemical Lasers*), 81 (1965).
89. J. C. Polanyi, *Appl. Optics*, **Suppl. 2** (*Chemical Lasers*), 109 (1965).
90. F. Kaufman, *Discussions Faraday Soc.* **33**, 138, 284, (1962).
91. J. R. Airey, R. R. Getty, J. C. Polanyi, and D. R. Snelling, *J. Chem. Phys.*, **41**, 3255 (1964).
92. F. T. Smith, *J. Chem. Phys.*, **31**, 1352 (1959).
93. J. Simons, *Nature*, **186**, 551 (1960).
94. D. L. Bunker, *Nature*, **194**, 1277 (1962).
95. See, for example, R. M. Eisberg and C. E. Porter, *Rev. Mod. Phys.*, **33**, 190 (1961).

96. K. W. Ford and J. A. Wheeler, *Ann. Phys.* (*N.Y.*) **7**, 259 (1959).
97. See, for example, B. H. Mahan, *J. Chem. Phys.*, **32**, 362 (1960); K. Yang and T. Ree, *J. Chem. Phys.*, **35**, 588 (1961); H. S. Johnston and P. Goldfinger, *J. Chem. Phys.*, **37**, 700 (1962); and references cited therein.
98. H. O. Pritchard, *Chem. Rev.*, **52**, 529 (1953).
99. F. H. Field and J. L. Franklin, *Electron Impact Phenomena*, Academic Press, New York, 1957, p. 148.
100. L. M. Branscomb, *Advan. Electron Phys.*, **9**, 43 (1957); *Atomic and Molecular Processes*, D. R. Bates, Ed., Academic Press, New York, 1962, p. 100.
101. W. B. Person, *J. Chem. Phys.*, **38**, 109 (1963).
102. See, for example, W. Kauzmann, *Quantum Chemistry*, Academic Press, New York, 1957, p. 536.
103. R. S. Berry, *J. Chem. Phys.*, **27**, 1288 (1957).
104. E. Teller, *J. Phys. Chem.*, **41**, 109 (1937); G. Herzberg and H. C. Longuet-Higgins, *Discussions Faraday Soc.*, **35**, 77 (1963).
105. J. C. Slater and J. G. Kirkwood, *Phys. Rev.*, **37**, 682 (1931).
106. E. S. Rittner, *J. Chem. Phys.*, **19**, 1030 (1951).
107. A. C. Riviere and D. R. Sweetman, *Phys. Rev. Letters*, **5**, 560 (1960); H. Wind, *Proc. Phys. Soc.* (*London*), **84**, 617 (1964).
108. J. R. Hiskes, *Phys. Rev.*, **122**, 1207 (1961); *Nucl. Fission*, **2**, 38 (1962).
109. J. C. Polanyi, private communication (University of Toronto).
110. S. T. Butler, *Nuclear Stripping Reactions*, Wiley, New York, 1957.
111. See, for example, C. A. Levinson and M. K. Banerjee, in F. Ajzenberg-Selove, Ed., *Nuclear Spectroscopy*, Academic Press, New York, 1960, Chap. VB.
112. A. Henglein and G. A. Muccini, *Z. Naturforsch.*, **17a**, 452 (1962); **18a**, 753 (1963); A. Henglein, K. Lacmann, and G. Jacobs, *Ber. Bunsenges. Physik. Chem.*, **69**, 279, 286, 292 (1965).
113. R. S. Mulliken, *J. Am. Chem. Soc.*, **74**, 811 (1950).
114. G. Briegleb, *Elektron-Donator-Acceptor Komplexe*, Springer-Verlag, Berlin, 1961.
115. R. S. Mulliken, *J. Chim. Phys.*, **61**, 20 (1963).
116. R. N. Zare and D. R. Herschbach, *J. Mol. Spectry.* **15**, 462 (1965).
117. R. S. Mulliken, *J. Am. Chem. Soc.*, **72**, 600 (1950); **77**, 884 (1955).
118. R. S. Berry and C. W. Reimann, *J. Chem. Phys.*, **38**, 1540 (1963).
119. A. G. Gaydon, *Dissociation Energies*, Chapman and Hall, London, 2nd Ed., 1953, p. 45.
120. C. J. Delbecq, W. Hayes, and P. H. Yuster, *Phys. Rev.*, **121**, 1043 (1961); *Proc. Roy. Soc.* (*London*), **A271**, 243 (1963).
121. G. Dobson and L. I. Grossweiner, *Radiation Res.*, **23**, 290 (1964) and earlier papers cited therein.
122. M. A. Biondi and R. E. Fox, *Phys. Rev.*, **109**, 2012 (1958).
123. D. C. Frost and C. A. McDowell, *J. Chem. Phys.*, **29**, 964 (1958); *Can. J. Chem.*, **38**, 407 (1960).
124. See, for example, R. I. Reed, *Ion Production by Electron Impact*, Academic Press, New York, 1962, pp. 87 and 116; C. A. McDowell, *Mass Spectrometry*, McGraw-Hill, New York, 1963, p. 526.

125. V. M. Dukelskii and V. M. Sokolov, *J. Exptl. Theoret. Phys.* (*USSR*), **32**, 394 (1957); S. Buchel'nikova, *ibid.*, **34**, 519 (1959).
126. G. H. Dunn, *Phys. Rev. Letters*, **8**, 62 (1962).
127. R. N. Zare and D. R. Herschbach, *Proc. I.E.E.E.*, **51**, 173 (1963); *Appl. Optics Suppl.*, **2**, 193 (1965).
128. A. D. Walsh, *J. Chem. Soc.*, **1953**, 2260.
129. R. S. Mulliken, *Phys. Rev.*, **47**, 413 (1935).
130. G. Herzberg, *Discussions Faraday Soc.*, **35**, 7 (1963).
131. D. C. Frost and C. A. McDowell, *J. Chem. Phys.*, **29**, 503 (1958).
132. W. G. Trawick and W. H. Eberhardt, *J. Chem. Phys.*, **22**, 1462 (1954).
133. R. K. Curran, *Phys. Rev.*, **125**, 910 (1962).
134. K. R. Wilson and D. R. Herschbach, *Nature*, **207** (1965).
135. J. E. Lovelock and N. L. Gregory in N. Brenner, J. E. Callear, and M. D. Weiss, Eds., *Gas Chromatography*, Academic Press, New York, 1962, p. 227; J. E. Lovelock, *Anal. Chem.*, **35**, 474 (1963).

APPENDIX

SELECTED REFERENCES ON MOLECULAR BEAM RESEARCH

General

R. G. J. Fraser, *Molecular Rays*, Cambridge University Press, London, 1931.

H. S. W. Massey and E. H. S. Burhop, *Electronic and Ionic Impact Phenomena*, Oxford University Press, Oxford, 1952.

K. F. Smith, *Molecular Beams*, Methuen and Company, Ltd., London, 1955.

N. F. Ramsay, *Molecular Beams*, Oxford University Press, London, 1956.

I. Estermann, Ed., *Recent Research in Molecular Beams*, Academic Press, New York, 1959.

D. R. Bates, Ed., *Atomic and Molecular Processes*, Academic Press, New York, 1962.

E. W. McDaniel, *Collision Phenomena in Ionized Gases*, Wiley, New York, 1964.

W. Fite and S. Datz, *Ann. Rev. Phys. Chem.*, **14**, 61 (1963).

V. B. Leonas, *Uspekhi*, **7**, 121 (1964).

J. C. Zorn, Resource Letter MB-1 on Experiments with Molecular Beams, *Am. J. Phys.*, **32**, 721 (1964).

Scattering Theory

N. F. Mott and H. S. W. Massey, *Theory of Atomic Collisions*, 2nd ed., Clarendon Press, Oxford, 1949.

T. Wu and T. Ohmura, *Quantum Theory of Scattering*, Prentice Hall, New Jersey, 1962.

M. L. Goldberger and K. M. Watson, *Collision Theory*, Wiley, New York, 1964.

Intermolecular Forces

J. O. Hirschfelder, C. F. Curtiss, and R. B. Bird, *Molecular Theory of Gases and Liquids*, Wiley, New York, 1954.

AUTHOR INDEX*

A

Aberth, W., 269 (ref. 100), 270 (ref. 100), *273*
Abrahamson, A. A., 30 (ref. 5), 67 (ref. 5), *71*
Ackerman, M., 105 (ref. 22), *133*, 138 (refs. 10, 13), 141 (ref. 13), 142 (ref. 13), 157 (ref. 10), 166 (ref. 13), *168*, *169*, 320 (refs. 17, 25), 356 (refs. 17, 25), 357 (ref. 25), *388*, *389*
Afrosimov, V. V., 202, 215, 216, 218, *243*, *244*
Airey, J. R., 360 (ref. 91), *391*
Albright, R. G., 313, *316*
Allison, S. K., 60 (ref. 47), *72*, 196, 206, 236, 237, *243*
Amdur, I., 29, 30 (ref. 1), 32 (refs. 11, 12), 33 (refs. 1, 16, 17), 35 (ref. 19), 46 (refs. 19, 26), 47 (refs. 19, 27, 28), 49 (refs. 29, 30), 50 (refs. 27, 28), 52 (ref. 38), 56 (refs. 17, 26, 29), 57 (ref. 26), 59 (ref. 46), 61 (refs. 38, 46, 48), 62 (refs. 26, 50), 64 (refs. 19, 26), 65 (refs. 17, 28), 67 (refs. 27, 29), 68 (refs. 1, 60), 70 (ref. 69), *71–73*, 83, *131*, 174, *191*, 310
Amme, R. C., 227, *245*
Anderson, J. B., 275, 283, 287–290, 300–302, 307, *315*, *316*
Andres, R. P., 275, 283 (ref. 9), 287 (ref. 9), 290 (ref. 9), 302 (ref. 9), *315*
Arthurs, A. M., 126, *134*, 267, *273*
Ashkenas, H., 285, *315*

B

Babeliowsky, T. P. J. H., 259, *272*
Bailey, T. L., 69, *73*, 202, *243*
Baker, C. E., 269 (ref. 97), *273*
Banerjee, M. K., 377 (ref. 111), *392*
Barnes Engineering Co., 62 (ref. 51), *72*
Barnett, C. F., 205, 208 (ref. 28), 210–212, 236, 237, *244*, *245*
Basco, N., 359 (ref. 86), *391*
Bassel, R. H., 236, *245*
Bates, D. R., 14, *27*, 55 (ref. 41), *72*, 235, 236, 240, 242 (ref. 98), *243*, *245*, *246*, 254–256, 267 (ref. 86), 268, *272*, *273*, 368 (ref. 100), 386 (ref. 100), *392*, *395*
Bawn, C. E. H., 359 (ref. 83), *391*
Beck, D., 105 (ref. 22), 131 (ref. 49), *133*, *134*, 138 (refs. 5, 6), 141 (refs. 5, 6), 142 (refs. 5, 6), 166 (refs. 5, 6), *168*, 190, *193*, 320 (refs. 12, 13), 348 (ref. 13), 350 (ref. 13), 351 (ref. 13), 356 (refs. 12, 13), 357 (ref. 13), 371 (ref. 12), *388*
Beckel, C. L., 124 (ref. 35), *133*
Becker, E. W., 276, 285, 287, 288, 290, 294, 299, 312–314, *315–317*
Bederson, B., 1, 2 (refs. 3, 4), 14, 15, 21 (ref. 4), *26*
Belyaev, Yu. N., 313, *316*
Bennewitz, H. G., 344 (ref. 69), 348 (ref. 71), *391*
Bentley, P. G., 290, *316*
Benton, E. E., 188, 189 (ref. 58), *192*
Berg, R. A., 327 (ref. 64), *390*
Bernstein, R. B., 32 (ref. 14), *71*, 75, 85 (ref. 6c), 86 (refs. 6c, 10–12), 87 (refs. 6c, 10, 11), 90 (ref. 15), 92 (refs. 6c, 17a), 94 (ref. 6c), 103 (ref. 21), 105 (refs. 6c, 21b, 22, 25, 25a), 117 (ref. 10a), 118 (ref. 10a), 119 (refs. 6c, 31, 32), 120 (ref. 31), 121 (refs. 6c, 25, 31, 34), 122 (refs. 31, 34), 123 (refs. 31b, 34a), 124 (refs. 31, 34, 35), 125 (refs. 31b, 34, 38, 40), 127 (ref. 45), 128 (ref. 6), *132–134*, 136, 182 (ref. 47),

* Italic numbers refer to pages carrying full bibliographic listings.

183 (ref. 47), *192*, 320 (refs. 29, 44), 327 (ref. 61), 344, 347 (ref. 44), 348 (ref. 72), 356 (refs. 29, 44), 357 (refs. 29, 44), 367 (ref. 44), 379 (ref. 44), *389–391*
Berry, R. S., 369 (ref. 103), 375 (ref. 103), 381 (ref. 118), *392*
Bertrand, R. R., 33 (ref. 17), 56 (ref. 17), 65 (ref. 17), *72*, 83 (ref. 4), *131*
Beyrich, W., 314 (ref. 53), *316*
Bier, K., 276, 283–285, 288, 290, 294, 295, 299–301, 313, 314 (refs. 51, 53, 54, 57, 58, 60–62), *315–317*
Bier, W., 314 (refs. 58, 60, 61), *316*, *317*
Biondi, M. A., 383 (ref. 122), *392*
Bird, R. B., 7 (ref. 10), *26*, 77 (ref. 1), 80 (ref. 1), 83 (ref. 1), 92 (ref. 15d), 105 (ref. 1a), 114 (ref. 1), *131*, *132*, *395*
Birely, J. H., 138 (ref. 12), *169*, 320 (refs. 39–42), 324 (ref. 39), 329 (refs. 39, 42), 333 (ref. 42), 339 (ref. 40), 344 (refs. 40, 41), 346 (refs. 40, 41), 347 (refs. 40, 41), 355 (ref. 41), 356 (refs. 39–42), 357 (refs. 39–42), 367 (refs. 41, 42), 373 (refs. 39, 42), 374 (ref. 42), 377 (ref. 42), 379 (refs. 40, 41), *389*, *390*
Blais, N. C., 64 (ref. 55), 65 (ref. 55), 67 (ref. 55), *73*, 320 (refs. 14, 18, 27), 339 (ref. 27), 348 (ref. 27), 350 (refs. 18, 27), 356 (refs. 14, 18, 27), 357 (refs. 14, 27), 359–361 (ref. 27), 375 (ref. 14), *388*, *389*
Blythe, A. R., 320 (ref. 29), 344 (ref. 29), 356 (ref. 29), 357 (ref. 29), *389*
Boelrijk, N. A. I. M., 259, 261, 265 (ref. 68), *272*
Bogan, A., 310 (ref. 45), *316*
Bohm, D., 34 (ref. 18), 53 (ref. 18), *72*
Boudart, M., 306, 307, *316*
Bourguignon, M., 313 (ref. 48), *316*
Boyd, T. J. M., 240, *246*
Brackett, E., 357 (ref. 77), *391*
Brackett, J. W., 86 (ref. 9), 87 (ref. 9), *132*
Brackmann, R. T., 172 (refs. 3, 11), 173 (ref. 20), 175 (ref. 3), 178 (ref. 3), *191*, 219, 230 (ref. 65), 239 (ref. 89), *244–246*, 320 (ref. 20), 356 (ref. 20), *389*
Branscomb, L. M., 220 (ref. 46), 239 (ref. 46), 240 (ref. 46), *244*, 368 (ref. 100), 386 (ref. 100), *392*
Bransden, B. H., 236, *245*
Breit, G., 175 (ref. 27), 178 (refs. 27, 35), *191*, *192*
Brewer, L., 357 (ref. 77), *391*
Briegleb, G., 379 (ref. 114), 380 (ref. 114), 387 (ref. 114), *392*
Brinkman, H. C., 235, *245*
Browne, J. C., 269 (ref. 94), *273*
Buchel'nikova, S., 384 (ref. 125), *393*
Buchma, I., 224, *244*
Buck, P., 172 (ref. 13), *191*
Buckingham, R. A., 7, 8, *26*, 86 (ref. 7), 126 (ref. 40a), *132*, *134*, 183, *192*
Büchler, A., 327 (ref. 64), *391*
Bukhteev, A. M., 208 (ref. 29), 224, *244*, *245*
Bull, T. H., 320 (ref. 1), 344 (ref. 1), 356 (ref. 1), 357 (ref. 1), *388*
Bunker, D. L., 162 (ref. 16), *169*, 320, 339 (ref. 27), 348 (ref. 27), 350 (refs. 18, 27), 356 (refs. 14, 18, 26, 27), 357 (refs. 14, 26, 27), 359 (refs. 26, 27), 360 (refs. 27, 94), 361 (ref. 27), 375 (ref. 14), *388*, *389*, *391*
Burghoff, H., 314 (refs. 51, 53, 54), *316*
Burhop, E. H. S., 55 (ref. 40), *72*, 84 (ref. 6a), 91 (ref. 6a), 92 (ref. 6a), 94 (ref. 6a), 128 (ref. 6), *132*, 180 (ref. 38), *192*, 196, 197 (ref. 1), *243*, 253 (ref. 39), 256 (ref. 39), *272*, *395*
Butler, S. T., 377 (ref. 110), *392*
Bydin, Yu. F., 208 (ref. 29), 224, *244*, *245*

C

Calia, V. S., 310 (ref. 45), *316*
Camparque, R., 283, *315*
Caplinger, E., 222, 224, *244*
Carbone, R. J., 32 (ref. 15), *72*, 213–215 (ref. 34), 218 (ref. 34), *244*
Carleton, N. P., 178 (ref. 30), 179 (ref. 30), *192*, 229, *245*
Carrington, T., 359 (ref. 88), *391*

Cermák, V., 188, 189, 190 (ref. 61), *192*, *193*, 249, 251, 258, *271*, *272*
Chamberlain, G. E., 2, 12–15, 20, *26*, *27*, 182 (ref. 46), *192*
Chkuaseli, D. V., 222, 224, 225, *244*
Choi, S., 92 (ref. 15c), *132*
Chow, R. R., 314, *317*
Chupka, W. A., 250 (ref. 13), 252 (ref. 13), *271*
Clapp, T., 172 (ref. 4), 174 (ref. 4), *191*
Clarke, E. M., 266, 267, 270 (ref. 83), *273*
Clausing, P., 52 (ref. 33), *72*
Clements, T. C., 248 (ref. 4), *271*
Cloney, R. D., 269, *273*
Cohen, E. G. D., 86 (ref. 8), *132*
Colegrove, F. D., 180 (ref. 42), *192*
Colgate, S. O., 46 (ref. 26), 56 (ref. 26), 57 (ref. 26), 62 (ref. 26), 64 (ref. 26), 65 (ref. 52), *72*
Comes, F. J., 248 (ref. 3), 269, *271*, *273*
Condon, E. U., 3 (ref. 6), *26*
Cook, C. J., 268, *273*
Cook, G. R., 189 (ref. 62), *193*
Cottrell, T. L., 357 (ref. 76), *391*
Crable, G. F., 251, *271*
Cramer, W. H., 202, *243*
Cristofori, F., 232, *245*
Cuevas, J., 60 (ref. 47), *72*
Curran, R. K., 256, *272*, 386 (ref. 133), *393*
Curtiss, C. F., 7 (ref. 10), *26*, 77 (ref. 1), 80 (ref. 1), 83 (ref. 1), 92 (ref. 15c), 105 (refs. 1a, 25a), 114 (ref. 1), *131–133*, *395*

D

Dahler, J. S., 251 (ref. 28), *271*
Dalgarno, A., 5, 7, 8, 14, 21 (ref. 21), 24 (ref. 21), *26*, *27*, 126, 127 (ref. 45), *134*, 182 (ref. 45), 183, *192*, 235, 236, 239, 240, 242 (ref. 99), *245*, *246*, 267, *273*
Damgaard, A., 14, *27*
Das, T. P., 240, *246*
Datz, S., 138 (refs. 4, 11), 139 (ref. 14), 165, *168*, 320 (refs. 2, 3, 8, 19, 21, 28), 322 (refs. 3, 21), 324, 329 (ref. 28), 333 (ref. 28), 339 (ref. 67), 344 (ref. 19), 356 (refs. 2, 3, 8, 19, 21, 28), 357 (refs. 2, 3, 8, 21, 28, 67), 374 (ref. 28), 377 (ref. 28), 378 (ref. 28), *388*, *389*, *391*, *395*
Davidson, N., 162 (ref. 16), *169*
Davies, A. R., 86 (ref. 7), *132*
Davis, D. H., 52 (ref. 34), *72*
Davison, W. D., 126, *134*
Dawson, P. H., 268, *273*
DeBoer, J., 86 (ref. 8), *132*
Deckers, J. M., 283, 295–300, 302, 306, 307, 313 (ref. 48), *315*, *316*, 327 (ref. 62), *390*
Dehmelt, H. G., 268, *273*
Dekabrun, L. L., 250 (ref. 15), *271*
Delbecq, C. J., 382 (ref. 120), *392*
Demkov, Yu. N., 222, 240, *244*
Dobson, G., 383 (ref. 121), *392*
Donahue, T. M., 202, *243*
Donnally, B. L., 172 (ref. 4), 174, *191*
Dorrestein, R., 174 (ref. 23), 180, *191*, *192*
Drake, C. W., 172 (ref. 14), *191*
Drewry, D. E., 295, 298, 299, *316*
Düren, R., 121, 122 (ref. 33), *133*, 183 (ref. 48), *192*
Dukelskii, V. M., 384 (ref. 125), *393*
Dunn, G. H., 229, 230 (ref. 64), 232, *245*, 384 (ref. 126), *393*
Dunoyer, L., 176, *192*

E

Eberhardt, W. H., 386 (ref. 132), 387 (ref. 132), *393*
Eck, J. van, 232, *245*
Eckart, C., 95 (ref. 19), *132*
Ehrhardt, H., 204, 205, 221 (ref. 49), 222, 242 (ref. 49), *243*, *244*
Eisberg, R. M., 362 (ref. 95), *391*
Eisinger, J., 2 (ref. 3), 15 (ref. 3), *26*
Eliason, M. A., 128, *134*
Entemann, E. A., 333 (ref. 65), 334 (ref. 65), 337 (ref. 65), 339 (ref. 65), 357 (ref. 65), *391*
Epofeev, V. I., 250 (ref. 15), *271*
Erdelyi, A., 95 (ref. 19), *132*
Estermann, I., *395*

Evans, M. G., 359 (ref. 79), *391*
Everhart, E., 32 (ref. 15), *72*, 213–215, 218, *244*
Evett, A. A., 269 (ref. 93), *273*
Eyring, H., 265, 266, *273*, 359 (ref. 81), 360 (ref. 81), 368 (ref. 81), *391*

F

Faddeyev, 88 (ref. 12a), *132*
Fallon, R. J., 49 (ref. 32), 68 (ref. 32), *72*
Fedorenko, N. V., 202, 215, 216 (ref. 41), 217, *243*, *244*
Feldman, P., 172 (ref. 9), 178 (ref. 9), *191*
Fenn, J. B., 275, 283, 286, 287–289, 290 (ref. 9), 295–302, 314 (ref. 21), *315*, *316*
Ferguson, A. F., 239, 240, *245*, *246*
Ferguson, E. E., 188 (ref. 58), 189, *192*
Fetz, B. H., 309, *316*
Field, F. H., 188 (ref. 54), *192*, 247 (ref. 2), 251 (refs. 25, 28, 29), 258 (ref. 2), 260 (ref. 2), 261 (refs. 2, 65), 263 (ref. 72), 264, *271–273*, 368 (ref. 99), 384 (ref. 99), 386 (ref. 99), *392*
Filippenko, L. G., 215, *244*
Fineman, M. A., 251 (ref. 32), 270 (ref. 32), *271*
Firsov, O. B., 39 (ref. 22), *72*, 208, 218, 222, 224, 240, *244*, 267, *273*
Fite, W. L., 172 (refs. 3, 11), 173 (ref. 20), 175, 178 (ref. 3), *191*, 219, 220 (refs. 46, 47), 221, 230 (ref. 65), 238, 239, 240 (ref. 46), 242, *244–246*, 249 (ref. 41), 251, 252 (ref. 33), 254 (ref. 41), 255, 256, 270 (refs. 32, 41), *271*, *272*, 320 (refs. 20, 21), 322 (ref. 21), 356 (refs. 20, 21), 357 (ref. 21), *389*, *395*
Flaks, I. P., 208, 215, *244*
Flowers, M. C., 359 (ref. 87), *391*
Foner, S. N., 172 (refs. 10, 19), 175, *191*
Fontana, P. R., 119 (ref. 32), *133*
Ford, K. W., 77 (ref. 2), 78 (ref. 2), 83 (ref. 2), 85, 86 (ref. 2), 94, 103, 105 (ref. 2), 114, *131*, 137 (ref. 2), 138 (ref. 2), 167, *168*, 365 (ref. 96), *392*
Fox, J. W., 86 (ref. 7), 126 (ref. 40a), *132*, *134*
Fox, R. E., 172 (ref. 7), *191*, 383 (ref. 122), *392*
Francis, W. E., 196, 224, 240, 241, 243, *243*, 255, 256, *272*
Frankevich, E. L., 250 (ref. 15), *271*
Franklin, J. L., 188 (ref. 54), *192*, 247 (ref. 2), 251 (refs. 25, 28, 29), 258 (ref. 2), 260 (ref. 2), 261 (refs. 2, 65), *271*, *272*, 368 (ref. 99), 384 (ref. 99), 386 (ref. 99), *392*
Fraser, R. G. J., 105 (ref. 27), 107 (ref. 27), *133*, 322 (ref. 53), 341 (ref. 53), 348 (ref. 53), 351 (ref. 53), 352 (ref. 53), 356 (ref. 53), *390*, *395*
French, J. B., 313, *316*
Friedman, L., 259 (ref. 59), 260, 262 (refs. 59, 70), 263–265, 266 (ref. 64), *272*
Frigerio, G. E., 232 (ref. 69), *245*
Fristrom, R. M., 284, *315*
Froman, N., 89 (ref. 14), 91 (ref. 14), 124 (ref. 14), 128 (ref. 14), *132*
Froman, P., 89 (ref. 14), 91 (ref. 14), 124 (ref. 14), 128 (ref. 14), *132*
Frost, D. C., 383 (ref. 123), 386 (ref. 131), *392*, *393*
Fueno, T., 265 (ref. 80), *273*
Fuls, E. N., 213–215 (ref. 34), 218 (ref. 34), *244*
Futrell, J. H., 251 (ref. 23), *271*

G

Gal, E., 126 (ref. 40a), *134*
Galli, A., 251 (refs. 21, 22), *271*
Garcia-Munoz, M., 60 (ref. 47), *72*, 196, 206, *243*
Garstang, R. H., 179, *192*
Gaydon, A. G., 382 (ref. 119), *392*
Gebelle, R., 229, 230 (ref. 64), 231, 232, *245*
Gerjuoy, E., 236, 237, *245*
Gersing, E., 105 (ref. 22), *133*, 138 (ref. 8), *168*, 320 (ref. 22), 334 (ref. 22), 356 (ref. 22), *389*
Getty, R. R., 360 (ref. 91), *391*
Giardini-Guidoni, A., 251 (refs. 21, 22), *271*

Gienapp, H., 320 (ref. 9), 356 (ref. 9), *388*
Giese, C. F., 206, *243*, 247, 250, 252 (ref. 37), 253, 257 (ref. 37), 259 (ref. 60), 261 (ref. 17), 262 (ref. 60), 263, 264, 265 (ref. 37), 266 (ref. 74), 267 (refs. 17, 74, 87), *271–273*
Gilbody, H. B., 56 (ref. 44), *72*, 200, 201, 221 (ref. 48), 223, 225 (ref. 11), *243*, *244*, 249 (ref. 104), 257 (ref. 52), 270 (ref. 104), *272*, *273*
Gilles, D. C., 86 (ref. 7), *132*
Gioumousis, G., 162 (ref. 15), *169*, 259, 260 (ref. 61), 265, 266, *272*
Glassgold, A. E., 128, *134*
Glasstone, S., 359 (ref. 81), 360 (ref. 81), 368 (ref. 81), *391*
Glick, C. F., 52 (ref. 38), 61 (ref. 38), *72*
Goldberger, M. L., *395*
Goldfinger, P., 366 (ref. 97), *392*
Goldman, F., 200, *243*
Goodman, L., 176, *192*
Gordeev, Yu. S., 215 (ref. 41), 216 (ref. 41), *244*
Gordon, R., 320 (ref. 31), 327 (ref. 31), 341 (ref. 31), 356 (ref. 31), 357 (ref. 31), *389*
Greene, E. F., 105 (ref. 22), 131 (ref. 49), *133*, *134*, 135, 138 (refs. 6, 10, 13), 141 (refs. 6, 13), 142 (refs. 6, 13), 157 (ref. 10), 166 (refs. 6, 13), *168*, *169*, 320 (refs. 5, 13, 16, 17, 25, 43), 322 (ref. 16), 326 (ref. 60), 348 (ref. 13), 350 (ref. 13), 351 (refs. 13, 16, 43), 356 (refs. 5, 13, 16, 17, 25, 43), 357 (refs. 5, 13, 16, 25, 43), 377 (ref. 43), 386 (ref. 43), *388–390*
Greene, F. T., 290, 307, *316*
Gregory, N. L., 387 (ref. 135), *393*
Greider, K. R., 128, *134*
Grey, J., 276, 279, 280, 284, *315*
Griffith, D. G., 287, *315*
Grishin, V. D., 250 (ref. 15), *271*
Groblicki, P. J., 103 (ref. 21), 125 (ref. 38), *133*
Gröbner, W., 96 (refs. 20a, 20b), *132*
Grosof, G. M., 172 (ref. 13), *191*
Grosser, A. E., 320 (refs. 29, 44), 344 (refs. 29, 44), 356 (refs. 29, 44), 357 (refs. 29, 44), 367 (ref. 44), 379 (ref. 44), *389*, *390*
Grossweiner, L. I., 383 (ref. 121), *392*
Guldamashvili, A., 222, 224, *244*
Gurnee, E. F., 240, 242 (ref. 94), *246*
Gustafsson, E., 203 (ref. 20), 205, 225 (ref. 20), *243*, 250 (ref. 8), 252 (ref. 8), *271*

H

deHaas, E., 57 (ref. 45), *72*
Hagen, K. E., 230 (ref. 65), *245*
Hagena, O., 283, 287, 288, 290, 294, 295, 301, 305, 314 (ref. 54), *315*, *316*
Hagstrum, H. D., 174, *191*
Hamill, W. H., 261, 262, 264, 265, 268, *272*, *273*
Hamilton, J., 86 (ref. 7), *132*
Harkness, A. L., 35 (ref. 19), 46 (ref. 19), 47 (ref. 19), 49 (ref. 29), 56 (ref. 29), 64 (ref. 19), 67 (ref. 29), *72*, 174 (ref. 22), *191*
Harris, L., 61 (ref. 49), *72*
Harrison, A. G., 258 (ref. 55), *272*
Harrison, H., 124 (ref. 35), *133*
Hartree, D. R., 21 (ref. 18), *27*
Hartree, W., 21 (ref. 18), *27*
Hasted, J. B., 56 (ref. 44), *72*, 172 (ref. 12), 174 (ref. 12), 180, *191*, 196, 200 (ref. 12), 201, 206, 225, *243*, *244*, 257 (ref. 52), *272*
Hatfield, L. L., 229, *245*
Hayes, W., 382 (ref. 120), *392*
Head, H. N., 251 (ref. 25), *271*
Heer, F. J. de, 232, *245*
Helbing, R., 105 (ref. 26), 110 (refs. 26b, 26c), 114, *133*, 138 (ref. 9), *168*, 320 (ref. 30), 356 (ref. 30), *389*
Hendrickson, J. B., 70 (ref. 68), *73*
Henglein, A., 251 (ref. 24), 256, 258, 263 264, *271–273*, 378 (ref. 112), *392*
Henkes, W., 284, 287, 288, 290, 305, 312, *315*, *316*
Herm, R. R., 138 (ref. 12), *169*, 320 (refs. 31, 39, 42, 45, 46), 324 (ref. 39), 327 (refs. 31, 45), 329 (refs. 39, 42),

333 (ref. 42), 339 (ref. 45), 341 (refs. 31, 45), 343 (ref. 45), 348 (refs. 45, 46), 350 (ref. 45), 351 (refs. 45, 46), 352 (ref. 45), 356 (refs. 31, 39, 42, 45, 46), 357 (refs. 31, 39, 42, 45, 46), 361 (ref. 45), 367 (ref. 42), 373 (refs. 39, 42), 374 (ref. 42), 377 (ref. 42), 386 (ref. 45), 387 (ref. 45), *389*, *390*

Herman, F., 21 (ref. 19), *27*

Herman, Z., 188, 189 (ref. 61), 190 (ref. 61), *192*, *193*, 251, 258, *271*, *272*

Herschbach, D. R., 131 (ref. 49), *134*, 136, 138 (refs. 4, 7, 12), 165, *168*, *169*, 319, 320 (refs. 6–8, 10, 15, 23, 31, 39, 41, 42, 46–48, 50), 322 (refs. 15, 47), 324 (ref. 39), 327 (ref. 31), 329 (refs. 7, 15, 39, 42, 47, 48, 50), 332 (refs. 10, 15, 50), 333 (refs. 42, 50), 334 (ref. 47), 341 (ref. 31), 344 (ref. 41), 346 (ref. 41), 347 (ref. 41), 348 (refs. 10, 15, 46, 47), 350 (refs. 10, 15), 351 (ref. 46), 355 (ref. 41), 356 (refs. 6–8, 10, 15, 23, 31, 39, 41, 42, 46–48, 50), 357 (refs. 6–8, 10, 15, 23, 31, 39, 41, 42, 46–48, 50), 360 (ref. 47), 361 (refs. 10, 15, 47), 362 (ref. 47), 367 (refs. 41, 42, 47), 373 (refs. 39, 42, 47), 374 (ref. 42), 377 (ref. 42), 379 (ref. 41), 380 (ref. 116), 384 (ref. 127), 386 (ref. 48), 387 (ref. 134), *388–390*, *392*, *393*

Herzberg, G., 369 (ref. 104), 386 (ref. 130), *392*, *393*

Herzfeld, K. F., 70 (ref. 64), *73*

Hirschfelder, J. O., 7 (ref. 10), *26*, 77 (ref. 1), 80 (ref. 1), 83 (ref. 1), 90 (ref. 15), 92 (ref. 15d), 105 (refs. 1a, 24), 114 (ref. 1), 128, *131–134*, 266 (ref. 81), *273*, *395*

Hiskes, J. R., 373 (ref. 108), *392*

Hofreiter, N., 96 (refs. 20a, 20b), *132*

Hornbeck, J., 188, *192*

Hostettler, H. U., 103 (ref. 21), 105 (refs. 21b, 22), *133*, 344, *391*

Howard, W. M., 52 (ref. 36), *72*

Hoyland, J. R., 269, *273*

Hoyt, F. C., 39 (ref. 21), *72*

Hudson, R. L., 172 (refs. 10, 19), 175, *191*

Hughes, R. H., 229, 232, *245*

Hughes, V. W., 11, 13 (ref. 16), *26*, *27*, 172 (refs. 6, 14), *191*, 322 (ref. 55), 341 (ref. 55), 348 (ref. 55), 351 (ref. 55), *390*

Hummer, D. G., 172 (ref. 3), 173 (ref. 20), 175 (ref. 3), 178 (ref. 3), *191*, 220 (refs. 46, 47), 239, 240, *244*, *246*

Hundhausen, E., 105 (ref. 22), *133*, 137 (ref. 3), 138 (ref. 8), *168*, 320 (ref. 22), 327 (ref. 63), 334 (ref. 22), 356 (ref. 22), *389*, *390*

Hushfar, F., 202, *243*

Hussain, M., 206, *244*

Hutchison, D., 258 (ref. 54), *272*

Hylleraas, E. A., 88, *132*

I

Iacobellis, S. F., 284, *315*

Iczkowski, R. P., 52 (ref. 35), *72*

Imam-Rahajoe, S., 105 (ref. 25a), *133*

Inghram, M. G., 252 (ref. 37), 257 (ref. 37), 265 (ref. 37), *271*

Ionescu-Pallas, N., 240, *246*

Iovitsu, I. P., 240, *246*

Ireland, J. V., 200 (ref. 12), 201 (ref. 12), *243*

Ivanetich, R. J., 324 (ref. 57), *390*

J

Jackson, J. D., 235, *245*

Jacobs, G., 378 (ref. 112), *392*

Jeffreys, B. S., 89, 92 (ref. 13), 95 (ref. 19), *132*

Jeffreys, H., 95 (ref. 19), *132*

Jesse, N., 251 (ref. 27), *271*

Johnston, H. S., 366 (ref. 97), *392*

Jones, P. R., 213–215 (ref. 34), 218 (ref. 34), *244*

Jordan, J. E., 29, 33 (ref. 17), 46 (ref. 26), 47 (ref. 27), 50 (ref. 27), 56 (refs. 17, 26), 57 (ref. 26), 59 (ref. 46), 61 (ref. 46), 62 (ref. 26), 64 (ref. 26), 65 (refs. 17, 53), 67 (ref. 27), *72*, *73*, 83 (ref. 4), *131*, 310

K

Kaminker, D. M., 202, 217, *243*, *244*
Kantrowitz, A., 276, 279, 280, 284, *315*
Karmohapatro, S. B., 240, *246*
Karplus, M., 320, 339 (refs. 32, 66), 348 (ref. 32), 350 (ref. 32), 356 (refs. 32, 33), 357 (refs. 32, 66), 359 (ref. 32), 360 (ref. 33), 361 (ref. 33), 362 (refs. 32, 66), 364 (refs. 32, 66), 375 (ref. 32), *389*, *391*
Kasper, J. V. V., 348 (ref. 74), 359 (ref. 74), 360 (ref. 74), *391*
Kaufman, F., 360 (ref. 90), *391*
Kaul, W., 188 (ref. 55), *192*, 259 (ref. 58), *272*
Kauzmann, W., 369 (ref. 102), *392*
Kay, I., 39 (ref. 23), *72*
Kearns, G. L., 251, *271*
Keller, J. B., 39 (ref. 23), *72*
Kells, M. C., 39 (ref. 25), *72*
Kennard, E. H., 39 (ref. 24), 40 (ref. 24), *72*, 77 (ref. 1), 80, 83 (ref. 1), 114 (ref. 1), *131*
Kerwin, L., 208, 209, 226–228, *244*, *245*
Kim, S. K., 162 (ref. 17), *169*
King, N. M., 236, *245*
Kingston, A. E., 5, 14, 21 (ref. 21), 24 (ref. 21), *26*, *27*, 182 (ref. 45), *192*
Kinsey, J. L., 320 (ref. 48), 329 (ref. 48), 356 (ref. 48), 357 (ref. 48), 386 (ref. 48), *390*
Kirkwood, J. G., 7, 8, *26*, 370, *392*
Kistemaker, J., 57 (ref. 45), *72*, 232, *245*
Kistiakowsky, G. B., 276, *315*
Klemperer, W., 327 (ref. 64), *391*
Klingelhofer, R., 290 (ref. 26), 312, 314 (ref. 56), *316*
Knewstubb, P. F., 252, *271*
Knox, R. S., 21, *27*
Knuth, E. L., 284, 310, *315*
Kock, H. v., 225 (ref. 58), *245*, 250 (ref. 9), 252 (ref. 9), 253 (ref. 9), 259 (ref. 59), 262 (ref. 59), *271*, *272*
Kodera, K., 320 (ref. 11), 356 (ref. 11), *388*
Kolos, W., 30 (ref. 4), *71*
Kondratiev, V. N., 359 (ref. 84), *391*
Koros, R. M., 306, 307, *316*
Kramer, K. H., 86 (ref. 10), 87 (ref. 10), 117 (ref. 10a), 118 (ref. 10a), *132*, 348 (refs. 71, 72), *391*
Kramers, H. A., 235, *245*
Kraus, K., 256 (ref. 51), *272*
Kreevoy, M. M., 70, *73*
Krocsak, M., 359 (ref. 80), 360 (ref. 80), *391*
Kruithoff, A. A., 187 (ref. 52), *192*
Kuhlthau, A. R., 279 (ref. 4), 294, *315*
Kusch, P., 11, *26*, 35 (ref. 20), 46 (ref. 20), *72*, 179 (ref. 37), *192*, 322 (ref. 55), 341 (ref. 55), 348 (ref. 55), 351 (ref. 55), *390*
Kushnir, R., 224, *244*, *245*
Kwei, G. H., 131 (ref. 49), *134*, 138 (refs. 7, 12), *168*, *169*, 320 (refs. 7, 23, 39, 48–50), 324 (ref. 39), 329 (refs. 7, 39, 48, 50), 332 (ref. 50), 334 (ref. 49), 344 (ref. 49), 356 (refs. 7, 23, 39, 48–50), 357 (refs. 7, 23, 39, 48–50), 373 (ref. 39), 375 (ref. 49), 386 (ref. 48), *388–390*

L

Lacmann, K., 378 (ref. 112), *392*
Laidler, K. J., 359 (ref. 81), 360 (ref. 81), 368 (ref. 81), *391*
Lamb, W. E., Jr., 172 (ref. 2), *191*
Lampe, F. W., 247 (ref. 2), 258 (ref. 2), 260 (ref. 2), 261 (refs. 2, 65), 263 (ref. 72), 269, *271–273*
Landau, L. D., 54, *72*, 89, 91 (ref. 14), 111, 118, 124 (ref. 14), 128 (ref. 14), *132*, *133*
Larin, I. K., 266 (ref. 82), *273*
Lauroskaya, G. K., 250 (ref. 15), *271*
Lauterbach, U., 259 (ref. 58), *272*
Lawrence, T. R., 229, *245*
LeBlanc, F. J., 205, *243*
Ledsham, K., 267 (ref. 86), *273*
Lee, A. R., 200 (ref. 12), 201 (ref. 12), 206, *243*, *244*
Lehrle, R. S., 250, *271*
Leonas, V. B., 308, 313, *316*, *395*

Le Roy, R. L., 313 (ref. 48), *316*
Lessmann, W., 248 (ref. 3), *271*
Levenson, L. L., 52 (ref. 34), *72*
Levine, 15
Levinson, C. A., 377 (ref. 111), *392*
Levinson, N., 124, *133*
Li, C. H., 310 (ref. 45), *316*
Lichten, W., 172 (refs. 13, 15–18), 174 (ref. 16), 175, 176, 177 (ref. 15), 178 (ref. 15), *191*
Lifshitz, E. M., 54, *72*, 89, 91 (ref. 14), 111, 118, 124 (ref. 14), 128 (ref. 14), *132*, *133*
Light, J. C., 264, 266, 267 (ref. 75), 273, 320 (refs. 34, 51, 52), 348 (ref. 52), 356 (refs. 34, 51, 52), 359 (ref. 88), 366 (ref. 52), *389–391*
Lin, S., 229, *245*
Lind, S. C., 251 (ref. 31), 264 (ref. 31), *271*
Linde Co., 326 (ref. 60), *390*
Lindholm, E., 203, 205, 225, *243*, *245*, 250, 252, 253, *271*
Lint, V. A. J. van, 252 (ref. 33), *271*
Lippincott, E. R., 30 (refs. 6, 9), *71*
Litovitz, T. A., 70 (ref. 64), *73*
Lockwood, G. J., 212 (ref. 37), 213 (refs. 34, 37), 214, 215, 218, *244*
Löwdin, P. O., 85
Lohse, P., 290 (ref. 26), 312, 314 (refs. 54, 56), *316*
Longmire, M. S., 47 (ref. 28), 50 (ref. 28), 65 (refs. 28, 54), *72*, *73*
Longuet-Higgins, H. C., 369 (ref. 104), *392*
Lorents, D. C., 269 (ref. 100), 270 (ref. 100), *273*
Lorquet, A. J., 261 (ref. 66), *272*
Lovell, S. E., 105 (ref. 24), *133*
Lovelock, J. E., 387 (ref. 135), *393*
Lurio, A., 172 (ref. 14), 178 (ref. 32), *191*, *192*
Lynn, N., 242 (ref. 98), *246*, 254–256, *272*
Lyubimova, A. K., 250 (ref. 15), *271*

M

McCarroll, R., 196, 236, 238–240, *243*, *245*
McDaniel, E. W., 196, *243*, *395*
McDermott, M. N., 172 (ref. 17), 175, *191*
McDowell, C. A., 348 (ref. 73), 383 (ref. 123), 384 (ref. 124), 386 (ref. 131), *391–393*
McDowell, M. R. C., 239, 240, *246*
McElroy, M. B., 238, *245*
McGinn, J. H., 284, 310, *315*
McGowan, J. W., 208, 209, 226–228, *244*, *245*
McGuire, J. M., 269 (ref. 97), *273*
McIntyre, H. A. J., 7 (ref. 9), 8 (ref. 9), *26*
McNamee, J. M., 7 (ref. 9), 8 (ref. 9), *26*
Magee, J. L., 240, 242 (ref. 94), *246*, 359 (ref. 82), 368, 369 (ref. 82), 380 (ref. 82), 384 (ref. 82), *391*
Mahadevan, P., 172 (ref. 12), 174 (ref. 12), 180, *191*
Mahan, B. H., 366 (ref. 97), *392*
Maier, W. B., II, 206, *243*, 250, 251 (ref. 18), 253, 257 (ref. 53), 261 (ref. 17), 267 (ref. 17), *271*, *272*
Maisch, W. G., 30 (refs. 7–9), *71*
Maise, G., 283 (ref. 9), 287 (ref. 9), 290 (ref. 9), 302 (ref. 9), *315*
Major, F. G., 268, *273*
Mandelberg, H. I., 232, *245*
Mann, J. B., 64 (ref. 55), 65 (ref. 55), 67 (ref. 55), *73*
Mapleton, R. A., 235–237, *245*
Marchi, R. P., 86 (ref. 9), 87 (ref. 9), 105 (ref. 9b), *132*, 187
Marcus, A. B., 202 (ref. 14), *243*
Margrave, J. L., 52 (ref. 35), *72*
Marino, L. L., 173 (ref. 21), *191*, 222, 224, 225, *244*
Markin, M. I., 266 (ref. 82), *273*
Marmet, P., 228, *245*, 268 (ref. 91), *273*
Mason, E. A., 30 (refs. 3, 6–9), 31, 32 (refs. 10, 13), 47 (refs. 27, 28), 49 (refs. 29, 30, 32), 50 (refs. 27, 28), 56 (ref. 29), 63 (ref. 10), 64 (ref. 70), 65

(ref. 28), 67 (refs. 27, 29), 68, 69 (refs. 61, 62), 70, *71–73*, 77 (ref. 3), 78, 82, 83 (refs. 3, 5), 105, 110, 112, 113 (ref. 26d), 114 (ref. 26d), *131–133*, 136 (ref. 1), 137 (ref. 3), 163, 164 (refs. 1a, 1b), *168*, *192*, 269 (refs. 98, 99, 102), *273*

Massey, H. S. W., 55 (ref. 40), *72*, 83, 84 (ref. 6a), 86 (ref. 7), 91 (ref. 6a), 92 (refs. 6a, 16), 93, 94, 102 (ref. 16b), 105, 107, 117, 127 (ref. 45), 128 (ref. 6), *132–134*, 180 (ref. 38), *192*, 196, 197, 239 (ref. 87), *243*, *245*, 253, 256, *272*, *395*

Matsen, F. A., 183 (ref. 50), 187 (ref. 50), 188 (ref. 58), 189 (ref. 58), *192*, 269 (ref. 94), *273*

Melton, C. E., 251 (refs. 26, 30, 31), 264 (ref. 31), *271*

Messiah, A., 84 (ref. 6a), 91 (ref. 6a), 92 (ref. 6a), 94 (ref. 6a), 128 (ref. 6), *132*

Michels, A., 86 (ref. 8), *132*

Miller, G. H., 202, *243*, 311, *316*

Milleron, N., 52 (ref. 34), *72*

Milne, T. A., 290, 307, *316*

Minturn, R. E., 138 (ref. 11), *168*, 320 (ref. 28), 329 (ref. 28), 333 (ref. 28), 339 (ref. 67), 356 (ref. 28), 357 (refs. 28, 67), 374 (ref. 28), 377 (ref. 28), 378 (ref. 28), *389*, *391*

Mittleman, M. H., 55 (ref. 42), *72*

Mizushima, M., 14, *27*

Moe, D. E., 202, *243*

Mohr, C. B. O., 92 (ref. 16), 93, 102 (ref. 16b), 105, 107, 117, *132*, *133*

Moiseiwitsch, B. L., 240, *246*

Molho, N., 232 (ref. 69), *245*

Molnar, J. P., 178 (ref. 33), 188, *192*

Monchick, L., 105 (refs. 22e, 25a), *133*, 137 (ref. 3), *168*

Montague, J. H., 208 (ref. 27), *244*

Moon, P. B., 320 (ref. 1), 344 (ref. 1), 356 (ref. 1), 357 (ref. 1), *388*

Moore, G. E., 268 (ref. 92), *273*

Moran, T. F., 262, 267, *272*

Morgan, G. H., 212–214 (ref. 37), 215, *244*

Morrison, J. D., 268 (ref. 91), *273*

Morse, F. A., 86 (ref. 11), 87 (ref. 11), 105 (ref. 22), *132*, *133*

Moses, H. A., 213–215 (ref. 34), 218 (ref. 34), *244*

Mott, N. F., 83, 84 (ref. 6a), 91 (ref. 6a), 92 (ref. 6a), 94, 128 (ref. 6), *132*, 239 (ref. 87), *245*, *395*

Moulton, M. C., 357 (ref. 75), *391*

Moursund, A. L., 105 (ref. 22), *133*, 135, 138 (refs. 10, 13), 141 (ref. 13), 142 (ref. 13), 157 (ref. 10), 166 (ref. 13), *168*, *169*, 320 (refs. 17, 25, 35, 43), 351 (ref. 43), 356 (refs. 17, 25, 35, 43), 357 (refs. 25, 35, 43), 377 (ref. 43), 386 (ref. 43), *388–390*

Muccini, G. A., 251 (ref. 24), 256, 258, 263, *271*, *272*, 378 (ref. 112), *392*

Muckenfuss, C., 298, *316*

Mueller, C. R., 86 (ref. 9), 87 (ref. 9), 105 (ref. 9b), *132*

Müller, E. W., 248 (ref. 4), *271*

Müller-Duysing, W., 257 (ref. 51), *272*

Mulliken, R. S., 178 (ref. 31), *192*, 379 (refs. 113, 115), 380 (refs. 115, 117), 385 (ref. 129), 386 (ref. 129), 387 (refs. 113, 115), *392*, *393*

Munn, R. J., 105 (ref. 25a), *133*

Munson, M. S. B., 188 (ref. 54), *192*, 251 (refs. 28, 29), *271*

Muschlitz, E. E., Jr., 69, *73*, 171, 172 (ref. 8), 175 (ref. 26), 176, 184 (ref. 26), 185 (ref. 26), 188, 189, 190 (ref. 60), *191*, *192*, 269 (ref. 97), *273*

N

Nakhleh, J., 124 (ref. 35), *133*

Neuert, H., 257 (ref. 51), *272*

Neynaber, R. H., 123 (ref. 34b), 125 (refs. 37, 39), *133*, 147, 173, 181 (refs. 43, 44), *191*, *192*

Niehaus, A., 190 (ref. 64), *193*

Nikoleishvili, U., 222, 224, *244*

Norris, J. A., 138 (refs. 7, 12), *168*, *169*, 320 (refs. 7, 24, 39, 50), 322 (ref. 24),

323 (ref. 24), 324 (ref. 39), 329 (refs. 7, 39, 50), 332 (ref. 50), 356 (refs. 7, 24, 39, 50), 357 (refs. 7, 24, 39, 50), 373 (ref. 39), *388–390*
Norrish, R. G. W., 359 (ref. 86), *391*
Novick, R., 172 (ref. 9), 178 (refs. 9, 32), *191*, *192*
Nowak, E. J., 307, *316*

O

O'Brien, T. J. P., 123, 124 (ref. 34a), *133*
Ogawa, M., 189 (ref. 62), *193*
Ogurtsov, G. N., 215, *244*
Ohmura, T., 83 (ref. 5), 91 (ref. 6b), 94 (ref. 6b), 128 (ref. 6), *131*, *132*, *395*
O'Keefe, D. R., 313, *316*
Oldenburg, O., 178 (ref. 30), 179 (ref. 30), *192*
Oman, R. A., 302, 309, *316*
Oppenheimer, J. R., 235, *245*
Osberghaus, O., 190, *193*
Owen, P. L., 285, *315*

P

Padov, M. N., 215 (ref. 41), 216 (ref. 41), *244*
Palyukh, B., 224, *245*
Parker, H. M., 279, 294, *315*
Parkinson, D., 14, *27*
Paul, W., 348 (ref. 71), *391*
Pauly, H., 83 (ref. 5), 87 (ref. 5c), 105 (refs. 22, 26), 109, 110, 114, 121, 122 (ref. 33), *131*, *133*, 137 (ref. 3), 138 (refs. 8, 9), *168*, 180 (ref. 39), 183 (ref. 48), *192*, 320 (refs. 22, 30), 327 (ref. 63), 324 (ref. 22), 356 (refs. 22, 30), *389*, *390*
Pearlman, H., 32 (ref. 11), 52 (ref. 38), 61 (refs. 38, 48), *71*, *72*, 83 (ref. 4), *131*
Pechukas, P., 320 (refs. 51, 52), 348 (ref. 52), 356 (refs. 51, 52), 366 (ref. 52), *390*
Peeters, J., 313 (ref. 48), *316*
Penning, F. M., 187, *192*
Percival, I. C., 127 (ref. 45), *134*
Person, W. B., 368, 374 (ref. 101), 380, 381, *392*
Pettersson, E., 203 (ref. 20), 225 (ref. 20), *243*, 250 (ref. 12), 252 (ref. 12), *271*
Phelps, A. V., 178 (ref. 33), 180 (ref. 41), *192*
Phillipson, P. E., 30 (ref. 2), 66, *71*
Philpot, J. L., 232, *245*
Phipps, J. A., 287, *315*
Pietenpol, J., 178 (ref. 36), *192*
Pimentel, G. C., 348 (ref. 74), 359 (ref. 74), 360 (ref. 74), *391*
Pobo, L., 258 (ref. 54), *272*
Polanyi, J. C., 348 (ref. 74), 359 (refs. 74, 85, 89), 360 (refs. 74, 89, 91), 373 (ref. 89), 375, *391*
Polanyi, M., 359, 360 (ref. 78), 367, 374 (ref. 78), *391*
Pollack, E., 2 (ref. 4), 14, 15 (ref. 4), 21, *26*
Porter, C. E., 362 (ref. 95), *391*
Porter, R. N., 320 (ref. 33), 356 (ref. 33), 360 (ref. 33), 361 (ref. 33), *389*
Poshusta, R. D., 183 (ref. 50), 187 (ref. 50), *192*
Pottie, R. F., 261 (ref. 66), 264, *272*, *273*
Powers, R. S., 92 (ref. 15c), *132*
Pretzer, D., 229, 230 (ref. 64), 231, *245*
Pritchard, H. O., 368 (ref. 98), 386 (ref. 98), *392*

R

Rabi, I. I., 52 (ref. 37), *72*, 172 (ref. 13), *191*
Rabinovitch, B. S., 359 (ref. 87), *391*
Raff, L., 320 (ref. 32), 339 (ref. 32), 348 (ref. 32), 350 (ref. 32), 356 (ref. 32), 357 (ref. 32), 359 (ref. 32), 362 (ref. 32), 364 (ref. 32), 375 (ref. 32), *389*
Ramsey, N. F., 13 (ref. 15), *26*, 172, *191*, 322 (ref. 54), 341 (ref. 54), 348 (ref. 54), 351 (ref. 54), 352 (ref. 54), *390*, *395*
Rankin, C., 320 (ref. 52), 348 (ref. 52), 356 (ref. 52), 366 (ref. 52), *390*
Rapp, D., 196, 224, 240, 241, 243, *243*, 254 (ref. 40), 255, 256, *272*
Raw, C. J. G., 105 (ref. 26), 110 (ref. 26d), 112–114 (ref. 26d), *133*
Reagan, P. N., 269 (ref. 94), *273*

Ree, T., 265 (ref. 80), *273*, 366 (ref. 97), *392*
Ree, T. S., 265 (ref. 80), *273*
Reed, R. I., 384 (ref. 124), *392*
Reimann, C. W., 381 (ref. 118), *392*
Reis, V. H., 286, 287, 297, 314 (ref. 21), *315*
Retherford, R. C., 172 (ref. 2), *191*
Reuben, B. G., 260, 263–265, 266 (ref. 64), *272*
Reynolds, H. K., 236, 237, *245*
Rhoderick, E., 172 (ref. 6), *191*
Ribe, F., 208 (ref. 26), *244*
Rice, W. E., 64 (ref. 70), *73*
Richards, H. L., 175 (ref. 26), 184, 185 (ref. 26), *191*
Rittner, E. S., 370, *392*
Riviere, A. C., 232, 234, *245*, 373 (ref. 107), *392*
Robb, J. C., 250, *271*
Roberts, C. S., 126, *134*
Roberts, R. W., 320 (refs. 4, 5), 324 (ref. 4), 356 (refs. 4, 5), 357 (ref. 5), 377 (ref. 4), *388*
Robertson, W. W., 188 (ref. 58), 189 (ref. 58), *192*
Robinson, E. J., 1, 2 (ref. 4), 15, 21 (ref. 4), *26*
Robinson, S. M., 52 (ref. 35), *72*
Rol, P. K., 121 (ref. 34), 122 (ref. 34), 124 (ref. 34), 125 (refs. 34, 37), *133*, 147, 181 (ref. 44), 182 (ref. 47), 183 (ref. 47), *192*, 344 (ref. 70), *391*
Roothan, C. C. J., 30 (ref. 4), *71*
Rosenstock, H., 263 (ref. 73), 265, 267 (ref. 73), *272*
Rosin, S., 52 (ref. 37), *72*
Ross, J., 30 (refs. 1, 3), 33 (ref. 1), 68 (ref. 1), *71*, 92 (ref. 15c), 105 (ref. 22), 131 (ref. 49), *132–134*, 135, 138 (refs. 6, 10, 13), 141 (refs. 6, 13), 142 (refs. 6, 13), 157 (ref. 10), 162 (ref. 17), 166 (refs. 6, 13), *168*, *169*, 320 (refs. 5, 13, 16, 17, 25, 43), 322 (ref. 16), 348 (ref. 13), 350 (ref. 13), 351 (refs. 13, 16, 43), 356 (refs. 5, 13, 16, 17, 25, 43), 357 (refs. 5, 13, 16, 25, 43), 377 (ref. 43), 386 (ref. 43), *388–390*
Roth, E., 359 (ref. 80), 360 (ref. 80), *391*
Roth, W., 269 (ref. 103), *273*
Rothe, E. W., 121 (ref. 34), 122 (ref. 34), 123 (ref. 34b), 124 (ref. 34), 125 (refs. 34, 37, 39), *133*, 147, 173 (ref. 21), 181, 182 (ref. 47), 183 (ref. 47), *191*, *192*, 344 (ref. 70), *391*
Rubin, K., 2 (ref. 3), 15 (ref. 3), *26*
Rudolph, P. S., 251 (ref. 31), 264 (ref. 31), *271*
Russek, A., 214, 215, 218, *244*
Rutherford, J. A., 252 (ref. 33), *271*

S

Salop, A., 2 (refs. 3, 4), 14, 15, 17, 18, 20, 21 (ref. 4), *26*
Samson, J. A. R., 189 (ref. 62), *193*
Sanders, W. A., 86 (ref. 9), 87 (ref. 9), *132*
Saporoschenko, M., 264 (ref. 79), *273*
Sawyer, W., 172 (ref. 4), 174 (ref. 4), *191*
Schatz, P. N., 30 (ref. 3), *71*
Schay, G., 359 (ref. 80), 360 (ref. 80), *391*
Schearer, L. D., 180 (ref. 42), *192*
Scheffers, H., 2, 9, *26*
Schiff, H., 235, *245*
Schiff, L. I., 118, *133*
Schissler, D. O., 259, *272*
Schlier, C., 105 (ref. 23), *133*
Schmidt, B., 301, *316*
Schmoys, J., 39 (ref. 23), *72*
Schroen, W., 324 (ref. 58), *390*
Schultz, M., 172 (ref. 4), 174 (ref. 4), *191*
Schulz, G. J., 172 (ref. 7), *191*
Schutte, R., 314 (refs. 52, 54, 55, 61), *316*, *317*
Schwartz, C., 21 (ref. 20), 24 (ref. 20), *27*
Scott, B. W., 125 (ref. 37), *133*, 147
Scott, J. E., Jr., 279 (ref. 4), 287, 294, 295, 298, 299, *315*, *316*
Secrest, D. H., 90 (ref. 15), *132*
Sena, L., 224, *245*
Shapiro, J., 178 (ref. 35), *192*
Sharma, R. D., 320 (ref. 33), 356 (ref. 33), 360 (ref. 33), 361 (ref. 33), *389*

Sherman, F. S., 285, *315*
Sholette, W. P., 188, 189 (ref. 57), *192*
Shortley, G. H., 3 (ref. 6), *26*
Shuler, K. E., 359 (ref. 88), *391*
Simons, J. H., 69, *73*, 202 (ref. 13), *243*, 360 (ref. 93), *391*
Sinanôgou, O., 49, *72*
Sinclair, T. F., 314, *317*
Skillman, S., 21 (ref. 19), *27*
Skinner, G. T., 309, *316*
Skurat, V. E., 250 (ref. 15), *271*
Slater, J. C., 370, *392*
Slichter, W. P., 276, *315*
Sluyter, T. J. M., 57 (ref. 45), *72*
Smit, J. H., 180, *192*
Smith, A. C. H., 204, 205, 219, 221–224, 238, 242, *243*, *244*, 249 (refs. 41, 104), 254 (ref. 41), 255 (ref. 41), 256, 270 (refs. 41, 104), *272*, *273*
Smith, F. J., 105 (ref. 25a), *132*, *133*, 268, *273*
Smith, F. T., 105 (ref. 25a), 128, *133*, *134*, 187, 360 (ref. 92), *391*
Smith, G. M., 172 (ref. 8), *191*
Smith, N. F., *395*
Smith, R. A., 93, *132*
Snelling, D. R., 360 (ref. 91), *391*
Snow, W. R., 219, *244*, 252 (ref. 33), *271*
Sokolov, V. M., 384 (ref. 125), *393*
Solov'ev, E. S., 208, *244*
Sona, P. G., 232 (ref. 69), *245*
Speiser, R., 224, *244*
Spotz, 92 (ref. 15d), *132*
Stark, J., 2, 9, *26*
Stauffer, J. L., 327 (ref. 64), *391*
Stebbings, R. F., 172 (refs. 3, 5), 173, 175 (ref. 3), 178 (ref. 3), 180, *191*, 195, 204, 205, 219, 220 (refs. 46, 47), 221–223, 238, 239 (refs. 46, 89), 240 (ref. 46), 242, *243*, *244*, *246*, 249 (refs. 41, 104), 251 (ref. 32), 254, 255 (ref. 41), 256, 270 (refs. 32, 41, 104), *271–273*
Steiner, B., 252 (ref. 37), 257 (ref. 37), 265 (ref. 37), *271*
Stern, S. A., 314, *317*
Sternheimer, R. M., 2 (ref. 1), 7, 8, 14, *26*
Stevenson, D. P., 162 (ref. 17), *169*, 259, 260 (ref. 61), 263 (ref. 71), 265, 266, *272*
Stewart, A. L., 267 (ref. 86), *273*
Stier, P. M., 205, 208 (ref. 28), 210–212, 236, 237, *244*
Stogryn, D. A., 92 (ref. 15d), *132*
Stone, G., 32 (ref. 15), *72*, 213–215 (ref. 34), 218 (ref. 34), *244*
Sundbom, M., 14, *27*
Suplinskas, R. J., 320 (ref. 36), 356 (ref. 36), 357 (ref. 36), *389*
Swan, P., 124 (ref. 36), *133*
Sweetman, D. R., 232, 234, *245*, 373 (ref. 107), *392*
Szegö, G., 109, 115 (ref. 28), *133*

T

Tait, J. M. S., 258 (ref. 55), *272*
Takayanagi, K., 126, *134*, 255, *272*
Tal'roze, V. L., 247 (ref. 1), 250, 251, 253, 258 (ref. 1), 259, 266 (ref. 82), *271–273*
Tamura, T., 320 (ref. 11), 356 (ref. 11), *388*
Tantsyrev, G. D., 250 (ref. 15), *271*
Taubert, R., 188 (ref. 55), *192*, 259 (ref. 58), *272*
Taylor, E. H., 138 (ref. 4), 139 (ref. 14), *168*, *169*, 320 (refs. 2, 3, 8, 19), 322 (ref. 3), 324, 344 (ref. 19), 356 (refs. 2, 3, 8, 19), 357 (refs. 2, 3, 8), *388*
Taylor, H. S., 266 (ref. 81), *273*
Teller, E., 175 (ref. 27), 178 (ref. 27), *191*
Theard, L. P., 261 (ref. 67), *272*
Thomas, D. W., 250, *271*
Thomas, E. W., 200 (ref. 12), 201 (ref 12), *243*
Thomas, M. T., 218, *244*
Thornhill, C. K., 285, *315*
Thorson, W. R., 66, *73*
Tickner, A. W., 252, 268, *271*, *273*
Tiernan, T. O., 251 (ref. 23), *271*
Toennies, J. P., 348 (ref. 73), *391*
Touw, T. R., 324, *390*
Trawick, W. G., 386 (ref. 132), 387 (ref. 132), *393*
Trischka, J. W., 324, *390*

Trujillo, S. M., 125 (refs. 37, 39), *133*, 147, 173 (ref. 21), 181 (refs. 43, 44), *191*, *192*, 344 (ref. 70), *391*
Tuan, T. F., 237, *245*
Tucker, G., 172 (ref. 6), *191*
Turner, B. R., 251 (ref. 32), 256, 270 (ref. 32), *271*, *272*
Turowski, P., 314 (ref. 54), *316*

U

Utterback, N. G., 56 (ref. 43), *72*, 202, 227, *243*, *245*, 311, *316*

V

Valleau, J. P., 302, *316*, 327 (ref. 62), *390*
Vanderslice, J. T., 30 (refs. 6–9), 31, 32 (refs. 10, 13), 49 (ref. 32), 63 (ref. 10), 68, 70 (ref. 65), *71–73*, 83 (ref. 5), 105 (ref. 26), 110 (ref. 26d), 112–114 (ref. 26d), *131*, *133*, *192*, 269, *273*
Varnerin, L. J., Jr., 174, *191*
Vernon, R., 224, *244*
Vetrov, O. D., 250 (ref. 15), *271*
Volpi, G. G., 251 (refs. 21, 22), *271*

W

Wadsworth, P. A., 263 (ref. 71), *272*
Wagner, C. D., 263 (ref. 71), *272*
Wainfan, N., 189 (ref. 62), *193*
Walker, R. E., 67 (refs. 57–59), *73*
Walker, W. C., 189 (ref. 62), *193*
Walsh, A. D., 384, 385–387 (ref. 128), *393*
Walters, G. K., 180 (ref. 42), *192*
Warhurst, E., 359 (ref. 83), *391*
Waterman, P. C., 314, *317*
Watson, K. M., *395*
Weber, G. G., 125 (ref. 40), *133*
Weingartschofer, A., 266, 267, 270 (ref. 83), *273*
Weinreich, G., 172 (refs. 6, 14), *191*
Weiser, C. H., 310 (ref. 45), *316*
Weiss, M. J., 189, 190 (ref. 60), *192*
Weissler, G. L., 189 (ref. 62), *193*
Weissman, S., 49 (ref. 32) 68 (ref. 32), 69 (ref. 62), 70 (ref. 65), *72*, *73*
Westenberg, A. A., 67 (refs. 57–59), *73*
Wexler, S., 251 (ref. 27), *271*
Wharton, L., 327 (ref. 64), *390*, *392*
Wheeler, J. A., 77 (ref. 2), 78 (ref. 2), 83 (ref. 2), 85, 86 (ref. 2), 94, 103, 105 (ref. 2), 114, *131*, 137 (ref. 2), 138 (ref. 2), 167, *168*, 365 (ref. 96), *392*
White, J. A., 172 (ref. 14), *191*
Whiteman, A. S., 200 (ref. 12), 201 (ref. 12), *243*
Wilkinson, P. G., 178 (ref. 31), *192*
Williams, C. H., 320 (ref. 37), 356 (ref. 37), *389*
Wilmenius, P., 225 (ref. 58), *245*, 250 (refs. 10, 11), 252 (refs. 10, 11), *271*
Wilson, K. R., 138 (ref. 12), *169*, 320 (refs. 38, 39, 42), 322 (ref. 38), 324 (refs. 38, 39, 57), 327 (ref. 38), 328 (ref. 38), 329 (refs. 38, 39, 42), 339 (ref. 38), 356 (refs. 38, 39, 42), 357 (refs. 38, 39, 42), 367 (refs. 38, 42), 373 (refs. 39, 42), 374 (ref. 42), 377 (refs. 38, 42), 387 (ref. 134), *389*, *390*, *393*
Wolf, F., 205, *243*
Wu, T. Y., 83 (ref. 5), 91 (ref. 6b), 94 (ref. 6b), 128 (ref. 6), *131*, *132*, *395*

Y

Yadav, H. N., 240, *246*
Yang, K., 366 (ref. 97), *392*
Yukhvidin, A. Ya., 250 (ref. 15), *271*
Yun, K. S., 69 (refs. 61, 62), *73*
Yuster, P. H., 382 (ref. 120), *392*

Z

Zapata, R. N., 279 (ref. 4), 294, *315*
Zare, R. N., 380 (ref. 116), 384 (ref.127), *392*, *393*
Ziemba, F. P., 212–215, 218 (ref. 34), *244*
Zigan, F., 314 (refs. 53, 54, 59), *316*, *317*
Zorn, J. C., 2, 12–15, 20, *26*, *27*, 182 (ref. 46), *192*, *395*
Zyl, B. van, 231, *245*

SUBJECT INDEX

A

AA (asymptotic approximation). See *JWKB approximation.*
Absolute reaction rate theory, 265–266
Accidental resonance. See *Charge transfer, accidental resonance.*
Activated complex. See *Reaction complex.*
Adiabatic hypothesis, 201, 212
Adiabatic potentials, 66–67
Adiabatic transitions, 198, 254, 257, 267, 269
Airy function, 89–90, 104, 167
Alkali metals, polarizabilities of, 9–20
Amplitude function, 83
Angular distribution. See also *Cross section, differential* and *Interference pattern.*
  in harpooning, 377
  in reactive scattering, 328–340, 360–361
  in violent charge transfer, 212–215
Appearance potential, 175, 191, 227–228, 252
Arc jet nozzle beams, 310
Argon, polarizability of metastable, 20–25
Aston bands, 209
Asymmetric charge transfer. See *Charge transfer, asymmetric.*
Asymmetric resonance. See *Charge transfer, accidental resonance.*
Asymptotic approximation (AA). See *JWKB approximation.*
Atomic polarizability, 1–27
  of alkali atoms, 8–20
  average, 4
  beam measurements of, 9–26
  calculation of, 6–9
  of metastable $^3P_2$ argon, 20–25
  theory of, 2–6
Atomic polarizability anisotropy, 5–6, 21
Atomic polarizability tensor, 3–4, 20–21, 25
Attenuation in transverse fields, fast-particle detection by, 209–212
Auger effect, 21, 174–175
Autoionization, 178

B

Background scattering, 41–42, 50–53, 62
Backscattering, 44, 46, 106
Barycentric coordinates. See *Coordinate systems.*
Beam detectors, 58, 61–62, 139–141, 249–252, 270, 324–328
  for charge transfer, 200–218 *passim*, 228–234
  for excited species, 174–177, 228–234
  geometry of, 38–39, 46–47
  for unstable gases, 219–222, 225
Beam sources, 57–60, 69, 139, 248–249, 323–324
  See also *Nozzle beams.*
  for excited species, 172–174, 225–227
  for unstable gases, 219, 221–222
"Black-sphere" model, 128
Born (B) approximation, 92–93, 129
Born-Oppenheimer approximation, 31–32, 34, 66, 369–370, 377
Bound states, maxima in impact spectra and, 124–126

C

Center-of-mass coordinates. See *Coordinate systems.*
Central forces, elastic scattering by, 35–47

Centrifugal barrier, 92, 162, 261, 263, 265, 371–372
Charge exchange. See *Charge transfer.*
Charge transfer, 195–246
  accidental (asymmetric) resonance, 197–198, 254–256
    theory of, 242–243
  asymmetric, 197
    theory of, 240–241
  chemical forces in, 367–387
  cross section measurements of, 200–218
  dissociative, 202–206, 228, 250
    energetics of, 252–253
  excited products of, 174, 228–234
  low-energy, 248, 250, 252–257
  with metastable primary beams, 196, 225–228
  neutral beam production by, 57, 60–61, 174, 310–311
  symmetric resonance, 197–198, 254
    theory of, 239–240
  theoretical considerations in, 234–243
  threshold behavior of endothermic, 256–257
  with unstable gases, 218–225
Chemical forces, in charge-transfer reactions, 367–387
Chemically unstable gases, scattering in, 218–225
Classical deflection function, 77–81, 95, 100, 114, 136–137
  in semiclassical approximation, 95–98
Classical mechanics, criterion for applicability of, 53
Classical turning point, 77, 85, 89, 92
CM (center-of-mass) system, 329
  See also *Coordinate systems.*
Coincidence detection, 215–218, 249, 270
Collisional breakup, 199
Collision chamber techniques, for unstable gases, 222–225
Collision complex. See *Reaction complex.*
Collision cross section. See *Cross section.*
Collision energy, 34, 77
  reduced, 77, 136–137
Collisions. See also *Scattering.*
  impulsive, 268
  intimate, 266–267
  violent. See *Violent collisions.*
Condensation coefficient. See *Sticking probability.*
Condenser method, for slow-ion detection, 200–202
Congruency of electric and magnetic fields, 15–18
Coordinate systems, 37, 40, 48–49, 140–141, 253, 261, 329–339 *passim*
Crossed beam measurements, 139–141, 251, 270, 322–325
  with unstable gases, 218–222
Cross section, 35
  averaging of, for noncentral forces, 49–50
  background scattering correction to, 50–53
  charge transfer, 197–199, 225, 236–243
    apparent total, 201
    low-energy. See *Charge transfer, low-energy.*
    measurement of, 200–218, 220–222, 227–228
  differential, 37–39, 83
    See also *Elastic cross section, differential.*
  elastic. See *Elastic cross section.*
  inelastic. See *Inelastic cross section.*
  ionization, 55–57, 188–190
  phenomenological, 259–260
  polar, 139
  quantum correction to, 53–54
    See also *Quantum scattering.*
  reaction. See *Reaction cross section.*
  total, 37–39, 83
    See also *Elastic cross section, total.*
    "conservation" of, 127–131
    "incomplete," 83

D

Deflection function. See *Classical deflection function.*
Differential cross section. See *Cross section, differential.*

Diffraction scattering. See *Shadow scattering.*
"Diffraction theory" treatment of reactive scattering, 128–130
Dipole radiation, 172, 178–179
Divergent beams, analysis of, 44–46
Double photon emission, 178

E

Early downhill energy surface, 360, 375
E–H gradient balance method, 9, 14–26
Elastic atom–atom impact spectra, 123–126
Elastic cross section. See also *Cross section* and *Elastic scattering.*
differential, 76–79, 137
for collisions of excited species, 179, 183–187
effective, 141, 166–168
low-angle, 81, 105–109, 112–114
quantum, 53–54, 83, 86–88, 99–100, 104–105
in reactive systems, 131, 141–168 *passim*, 269, 362
reduced, 79–82
inelastic correction to, 39, 54–57, 127–131
See also *Inelastic scattering.*
for ion–neutral reactions, 269
total, 39–45, 76
approximations for, 117–120
for collisions of excited species, 179–183, 186
extrema in, 120–124
for helium–helium scattering, 62–67
measurement of, 57–62
volume averaging of, 40–42
Elastic scattering, 33–35, 136–137
See also *Elastic cross section.*
by central forces, classical analysis of, 35–47, 76–83
of excited species, 179–187
of high-energy beams, 29–73
inelastic effects on. See *Inelastic scattering.*
in ion–neutral reactions, 248, 269
by noncentral forces, 47–50
quantum effects in, 53–54, 75–134
in reactive systems, 135–169, 321, 329, 336–337, 362–367
energetics of, 151–153
experimental techniques for, 139–141
Electric deflection analysis, 9–10, 15–16, 175, 249, 326–327
of reactive scattering, 347–356
Electric field ionization, 234, 248, 268
Electric fields, congruent, 15–18
inhomogeneous. See *Electric deflection analysis.*
quenching in, 175, 351
Electron capture. See *Charge transfer.*
Electron energy in ion–neutral reactions, selection of, 270
variation of, 258–259
Electronic structure, harpooning and, 379–387
Electron impact, 257, 383
production of excited species by, 173–174, 184, 226–227
production of primary ions by, 248–249
"Electron jump" model, 321–322, 367, 379
See also *Reactive scattering.*
Electron transfer. See *Charge transfer.*
Energy defect, 197, 256
Energy disposal, in harpooning, 375–377
in reactive scattering, 359–360
Energy exchange, in fast molecular ion collisions, 232
rotation-translation, 141, 151–154
vibration-translation, 141, 151–155
Energy parameter, 136–137, 144, 165
Equilibrium beam method, 207–208
Excitation transfer, 180
Excited atoms and molecules, 32, 171–193
and charge transfer, 196, 225–234
detection of beams of, 174–175
elastic collisions of, 179–187
inelastic collisions of, 187–190
lifetimes of, 175–179

polarizability of, 20–25
production of beams of, 69, 172–174
Exp-six potential, 77, 105, 136–138, 162, 334–337
differential cross section for, 163–164
parameters for, from scattering in reactive systems, 144–147, 165–168
Extrema effect, 120–126

F

Fast particles, detection of, 206–212
Fixed-velocity approximation, 337–339
Forbidden transitions, 179
Forward scattering. See *Low-angle scattering.*
Forward scattering ratio, 107–108, 115
Franck-Condon principle, 257, 373

G

Gaseous discharge. See also *Glow discharge.*
production of excited species by, 172–173, 178
Glory, 114
Glory interference effect, 114–117
and total cross section, 122
"Glory phase." See *Maximum phase.*
Glow discharge, 248, 252, 268

H

Halogens, charge-transfer reactions of, 380–384
Harpooning, 367–368
and electronic structure, 379–387
mechanism of, 368–379
Harpoon potential, 370
Hartree approximation, 6
Hartree-Fock approximation, 7, 26
Helium, metastable, polarizability of, 21, 24
scattering of, 180–189
Helium–helium cross sections, 62–67
excited, 183–184
High-velocity approximation for charge transfer, 234–238
High-velocity neutral beams, elastic scattering of, 29–73
Hornbeck-Molnar process, 188

I

Impact parameter, 38, 77
critical, 265
glory, 114, 120
reduced, 77, 86, 136
threshold, 154, 165
Impact parameter method, 215, 234, 240, 255
Impact spectra, 123–124
and bound states, 124–126
Impulsive mechanism, 321
Induced dipole–quadrupole effect, 119
Inelastic cross section, 127–131
See also *Inelastic scattering.*
Inelastic energy loss,in violent collisions, 212–218
Inelastic scattering. See also *Reactive scattering.*
contribution of, to total scattering, 32, 39, 54–57, 65–66, 126–131, 179
of excited species, 179, 187–190
in ion–neutral collisions, classification of, 199–200, 248
Interference pattern, 76
See also *Glory interference effect.*
approximations for, 98–103
near rainbow angle, 104–105
Intermolecular potential, 31–33, 76–77
See also individual potential functions.
in charge transfer, 235–236
for ion–neutral reactions, 265
between nonspherical molecules, 47–49
from phase shifts, 88
quantum calculations of, compared with experiment, 66–68
reduced, 77
at small distances, 30, 32–33, 82
applications of, 68–70
from high-energy scattering, 43, 63–68

Inverse-power potential, 32, 76, 83
low-angle scattering by, 109–116
Ion counting, 270
Ionization, 55–56, 187–190, 199, 202
See also *Charge transfer* and *Ion–neutral reactions.*
Ionization potential, 197, 240, 257, 379
Ion–molecule reactions. See *Ion–neutral reactions.*
Ion–neutral reactions. See also *Charge transfer.*
high-energy, 69
low-energy, 247–273
electron energy variation in, 258–259
future work with, 269–270
isotopic effects in, 262–266
measurements of, 248–252
repeller effects in, 260–262
temperature effects in, 259–260
theory of, 265–268
types of, 248
Ionosphere, 254, 256
Ion sources. See *Beam sources.*

J

JB approximation. See *Jeffreys-Born approximation.*
Jeffreys (J) approximation, 93
Jeffreys-Born (JB) approximation, 93–94, 111, 117–118
Jeffreys–WKBL approximation. See *JWKB approximation.*
Jets, supersonic. See *Supersonic jets.*
JWKB approximation, 89–92
See also *Semiclassical approximation.*

K

Kennard approximation, 80
Kihara potential, 77, 105
extrema analysis with, 122–123
Knudsen number, 289
correlation of, with Mach number, 297–300, 303
nozzle, 291
skimmer, 293

L

LAB (laboratory) system, 329
See also *Coordinate systems.*
Laboratory coordinates. See *Coordinate systems.*
Landau-Lifshitz (LL) approximation, 111, 118
Late downhill energy surface, 360
Lennard-Jones (12,6) potential, 77, 78–105 *passim*
extrema analysis with, 120–123
for scattering of excited species, 182–184
"Level-counting" technique, 124–125
Levinson's theorem, 124
L.-J. potential. See *Lennard-Jones potential.*
LL approximation. See *Landau-Lifshitz approximation.*
London dispersion, 119
Low-angle scattering, 78, 80–82, 96, 105–117
energy dependence of, 116–117
glory interference effect in, 114–117
Low-velocity approximation for charge transfer, 239–240

M

Mach disk, 285, 291, 301
Mach number, 281–285, 293–295
See also *Nozzle beams.*
correlation of, with Knudsen number, 297–300, 303
effective, 282, 312
freezing of, 288–291
terminal or maximum, 289
velocity distribution and, 277–279, 287–289
Magnetic deflection analysis, 15, 175, 327
for reactive scattering, 341–343
Magnetic fields, congruent, 15–18
inhomogeneous. See *Magnetic deflection analysis.*
Mass analysis, of fast particles, 208–209
of ion–neutral reactions, 250–252
of slow ions, 202–206

Massey criterion, 253, 256–257, 268
Massey-Mohr (MM) approximation, 93, 109, 117–118, 120–121
Maximum phase ("glory phase"), 115, 120, 122–124
Metastable species. See *Excited atoms and molecules.*
MM approximation. See *Massey-Mohr approximation.*
Monomolecular reactions, 176, 190
Monte Carlo calculations, 320, 350, 359–362, 364, 366, 375
Morse potential, 77, 105, 382
Mutual collision cross section. See *Cross section, total.*

N

Near-adiabatic hypothesis, 197–198
Near-resonance. See *Charge transfer, accidental resonance.*
Newton diagram, 173, 331–332
Noncentral forces, elastic scattering by, 47–50
Nonspherical molecules, 47–50
Nozzle beams, 275–317, 327
  applications of, 304–308
  basic principles of, 277–282
  design considerations for, 282–304
  energy limitations on, 308–311
  of mixed gases, 311–315
  and oven beams, 277–278, 282, 308–309
  pumping speed requirements for, 283–284
  separation effect in, 313–315
  theoretical performance of, 279–282
Nozzle–jet system, 284–292
Nuclear moments, 26

O

One-electron approximation, 6
Opacity, 129–130
Optical potential model, 128, 351, 362, 366–367
Optical theorem, 107, 121, 129–130
Orbiting, 92, 105, 137, 162, 336–337, 365, 377
Orbiting-tunneling phenomenon, 105, 125
Oscillator strengths, 4–5, 14
Oven beams, compared with nozzle beams, 277–278, 282, 308–309

P

Partial waves, method of, 84
Penning ionization, 187–189
Persistent complexes, 264–265
Perturbation theory, 2–3, 6–7, 14, 85, 175
Phase. See *Phase shifts.*
Phase shifts, 84–86
  See also *Quantum scattering.*
  approximations for, 91–93, 95, 100
  in low-angle scattering, 106, 110
    See also *Random-phase approximation.*
  maximum or "glory." See *Maximum phase.*
  potential deduction from, 88
  near rainbow angle, 103
  "reduced," 78, 85
Photoemission, 177
Photoionization, 189–190, 248, 252, 257, 260, 262, 270
Poisoning of ionization detectors, 324, 341
Polarizability, atomic. See *Atomic polarizability.*
  molecular, 26
Polarization force, 255, 263, 268
Potassium beams, elastic scattering of, in reactive systems, 139–168 *passim*
Potential functions. See *Intermolecular potential.*
Potential surfaces, for harpooning, 375–377
  for reactive systems, 147–148, 360
Prepoisoning, 324
Pressure measurement, 61
Primary ions. See also *Charge transfer* and *Ion–neutral reactions.*
  detection of, 248–249
  metastable, 225–228

Probability of reaction, 149–162 *passim*, 261, 362–366
See also *Reaction cross section.*

Q

Quadrupole moment, 5–6
Quadrupole radiation, 178–179
Quadrupole shielding factor, 2
Quantum parameter, 98, 100–102
Quantum scattering, 75–134
approximation methods for, 88–126
correction for, 53–54
theory of, 83–88
Quasiclassical approximation. See *Semiclassical approximation.*
Quenching, beam detection by, 175
"gyroscopic," 351

R

Radial wave function, 84–85, 88
approximations for, 89–91
"reference," 84
Radiative capture, 264
Rainbow angle, 78–79, 137–138
See also *Rainbow scattering.*
Rainbow effect. See *Rainbow scattering.*
Rainbows, supernumerary, 105, 137
Rainbow scattering, 78–80, 86, 137–139, 144, 147, 157, 161–162, 377
approximations for, 103–105
Random-phase approximation (rph), 105–109, 117, 120, 127
RE. See *Recombination energy.*
Reaction complex, 190, 261, 263, 266–267
persistent, 264–265
Reaction cross section, 128–131
See also *Cross section, charge transfer* and *Reactive scattering.*
differential, 362–366
"multichannel," 128
for ion–molecule reactions, 259–262, 267, 269
total, 129, 157–165
for harpooning, 374–375
reduced, 157
Reaction kinetics, 128
Reaction probability. See *Probability of reaction.*
Reactive cross section. See *Reaction cross section.*
Reactive scattering, 128–131, 319–393
See also *Charge transfer* and *Ion–neutral reactions.*
angular distribution in, 328–340, 360–361
apparatus for, 322–328
electric deflection analysis of, 347–356
energy disposal in, 359–360
magnetic deflection analysis of, 341–343
mechanisms of, 321–322, 361–367
optical model for. See *Optical potential model.*
summary of measurements on, 356–358
velocity analysis of products of, 343–347
Reactive systems. See also *Reactive scattering.*
elastic scattering in. See *Elastic scattering.*
Rebound mechanism, 321, 329, 358
See also *Reactive scattering.*
and stripping, transition between, 361–367
Recombination energy (RE), 252–253
Repeller effects, in ion–molecule reactions, 260–262
Repulsive forces. See *High-velocity neutral beams* and *Intermolecular potential at small distances.*
Retardation effect, 119
Reynolds number, 285, 300
Rigid-sphere potential, 102
low-angle scattering by, 106–109, 113
Rittner potential, 370–371
Rotational excitation, 126
rph. See *Random-phase approximation.*

S

Sampling experiments with nozzle beams, 304–306

Scattering, background. See *Background scattering.*
elastic. See *Elastic scattering.*
inelastic. See *Inelastic scattering.*
low-angle. See *Low-angle scattering.*
quantum. See *Quantum scattering.*
rainbow. See *Rainbow scattering.*
reactive. See *Reactive scattering.*
shadow. See *Shadow scattering.*
Scattering amplitude, 83–84
approximations for, 94–99
glory, 114–115
low-angle, 107–111
near rainbow angle, 103
Scattering cross section. See *Cross section.*
Scattering geometries, 35–37, 44–47, 64, 253
Scattering volume, 36, 45–46
Scheffers and Stark experiment, 2, 13
Schiff-Landau-Lifshitz (SLL) approximation, 118–119, 121–123
Screening, 6, 9
Secondary electron emission, 174, 201
"Seeded" beams, 312
Semiclassical approximation, 54, 76, 86, 88–131 *passim*, 137, 167–168, 362
Semiclassical equivalence relationship, 95, 97
Separating nozzle, 314
Separation effect, in nozzle beams, 313–315
Shadow scattering, 106–107, 128–130
See also *Low-angle scattering.*
Shock tubes, nozzle beams driven by, 309–310
research with, 269
Short-range forces. See *Intermolecular potential at small distances.*
Single collisions, method of, 208–209
Size parameter, 136–137, 144
estimation of, in reactive systems, 154–157, 162, 168
Skimmer, 277–278, 292–304
See also *Nozzle beams.*
SLL approximation. See *Schiff-Landau-Lifshitz approximation.*
Slow ions, detection of, 200–206
Small-angle scattering. See *Low-angle scattering.*
S-matrix formalism, 126–128
Spectator model, 377–379
Spin orientation, study of, with ion–neutral reactions, 268
Stark effect, 351
See also *Electric deflection analysis.*
Stationary phase, method of, 94–97, 103–104, 114–115
Sternheimer procedure, 6–7, 14
Sticking probability, nozzle beam measurements of, 306–308
Stripping, 199, 202, 321, 329, 358
See also *Reactive scattering.*
and rebound mechanism, transition between, 361–367
"Strong field" deflection, 9–13
Supersonic jets, 276
See also *Nozzle beams.*
condensation in, 290
flow field of, 285
viscous effects in, 284–287, 297–300
Supersonic nozzle beams. See *Nozzle beams.*
"Swallowed shock," 297
Symmetric resonance. See *Charge transfer, symmetric resonance.*

T

Tensor polarizability. See *Atomic polarizability tensor.*
Thermal energies, 37
scattering at, 119–120, 123, 125, 187
Threshold behavior, of endothermic charge transfer, 256–257
in reactive systems, 150, 153–154, 157, 162–164
Total cross section. See *Cross section, total.*
Transfer ionization, 199, 202
Transition probabilities, 55–56, 126–127
"Trennduse," 314
Tunneling-orbiting phenomenon, 105, 125

Turning point. See *Classical turning point.*

U

Unstable gases. See *Chemically unstable gases.*

V

Velocity distribution, 10, 141, 166
  in beams of excited species, 177–178
  in nozzle beams, 277–279, 287–289, 311–315
  of products of reactive scattering, 344–347
Velocity selection, 15, 25, 139–141, 166, 177, 181, 326–327, 333, 344
Vibrational states of two-body system, 124–126
Violent collisions, 197–207
  angular and energy distribution in, 212–218

W

"Weak field" deflection, 9, 13–15
Workhorse approximation, 379

Date Due

MAY 1 2 '[illegible]			
OCT 1 4 1971			
JAN - 5 1972			
[illegible]	[illegible]		
NOV	1 1984		
DEC 1 5 1984			
MAR	1 1 1993		
MAR	1 2 1993		
JAN	1 2 2012		

NOV 1 9 1979

CAT. NO. 23 233 PRINTED IN U.S.A.

TRENT UNIVERSITY
0 1164 0085770 6

QD453 .A27 v.10 1966

Advances in chemical physics.

DATE | ISSUED TO 61264

61264